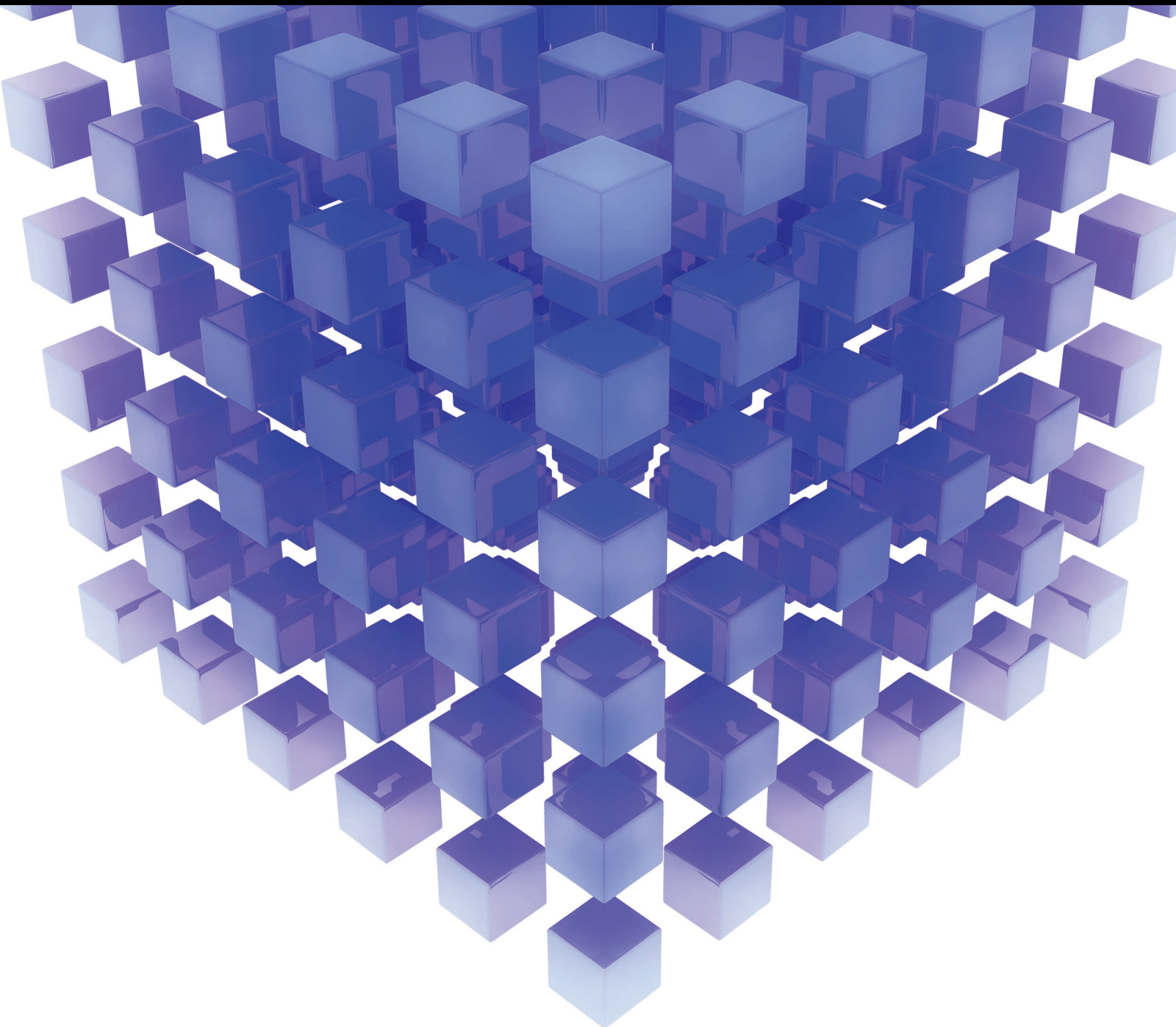


Mathematical Problems in Engineering

Recent Advancements in Signal Processing and Machine Learning

Guest Editors: Gelan Yang, Su-Qun Cao, and Yue Wu





Recent Advancements in Signal Processing and Machine Learning

Mathematical Problems in Engineering

Recent Advancements in Signal Processing and Machine Learning

Guest Editors: Gelan Yang, Su-Qun Cao, and Yue Wu



Copyright © 2014 Hindawi Publishing Corporation. All rights reserved.

This is a special issue published in “Mathematical Problems in Engineering.” All articles are open access articles distributed under the Creative Commons Attribution License, which permits unrestricted use, distribution, and reproduction in any medium, provided the original work is properly cited.

Editorial Board

- Mohamed Abd El Aziz, Egypt
Eihab M. Abdel-Rahman, Canada
Rashid K. Abu Al-Rub, USA
Sarp Adali, South Africa
Salvatore Alfonzetti, Italy
Igor Andrianov, Germany
Sebastian Anita, Romania
W. Assawinchaichote, Thailand
Er-wei Bai, USA
Ezzat G. Bakhoum, USA
José Manoel Balthazar, Brazil
Rasajit Kumar Bera, India
Jonathan N. Blakely, USA
Stefano Boccaletti, Spain
Stephane P. A. Bordas, USA
Daniela Boso, Italy
M. Boutayeb, France
Michael J. Brennan, UK
Salvatore Caddemi, Italy
Piermarco Cannarsa, Italy
Jose E. Capilla, Spain
Carlo Cattani, Italy
Marcelo Cavalcanti, Brazil
Diego J. Celentano, Chile
Mohammed Chadli, France
Arindam Chakraborty, USA
Yong-Kui Chang, China
Michael J. Chappell, UK
Kui Fu Chen, China
Kue-Hong Chen, Taiwan
Xinkai Chen, Japan
Jyh-Horng Chou, Taiwan
Slim Choura, Tunisia
Cesar Cruz-Hernandez, Mexico
Erik Cuevas, Mexico
Swagatam Das, India
Filippo de Monte, Italy
Yannis Dimakopoulos, Greece
Baocang Ding, China
Joao B. R. Do Val, Brazil
Daoyi Dong, Australia
B. Dubey, India
Horst Ecker, Austria
M. Onder Efe, Turkey
Elmetwally Elabbasy, Egypt
Alex Elías-Zúñiga, Mexico
Anders Eriksson, Sweden
Vedat S. Erturk, Turkey
Moez Feki, Tunisia
Ricardo Femat, Mexico
Robertt Fontes Valente, Portugal
Claudio Fuerte-Esquivel, Mexico
Zoran Gajic, USA
Ugo Galvanetto, Italy
Xin-Lin Gao, USA
Furong Gao, Hong Kong
Behrouz Gatmiri, Iran
Oleg V. Gendelman, Israel
Paulo Batista Gonçalves, Brazil
Oded Gottlieb, Israel
Fabrizio Greco, Italy
Quang Phuc Ha, Australia
Tony Sheu Wen Hann, Taiwan
Thomas Hanne, Switzerland
Katica R. Hedrih, Serbia
M. I. Herreros, Spain
Wei-Chiang Hong, Taiwan
Jaromir Horacek, Czech Republic
Gordon Huang, Canada
Huabing Huang, China
Chuangxia Huang, China
Yi Feng Hung, Taiwan
Hai-Feng Huo, China
Asier Ibeas, Spain
Anuar Ishak, Malaysia
Reza Jazar, Australia
Zhijian Ji, China
Jun Jiang, China
J. J. Judice, Portugal
Tadeusz Kaczorek, Poland
Tamas Kalmar-Nagy, USA
Tomasz Kapitaniak, Poland
Hamid R. Karimi, Norway
Metin O. Kaya, Turkey
Farzad Khani, Iran
Ren-Jieh Kuo, Taiwan
Jurgen Kurths, Germany
Claude Lamarque, France
Usik Lee, Korea
Marek Lefik, Poland
Stefano Lenci, Italy
Roman Lewandowski, Poland
Shihua Li, China
Ming Li, China
S. Li, Canada
Jian Li, China
Teh-Lu Liao, Taiwan
Panos Liatsis, UK
Kim Meow Liew, Hong Kong
Yi-Kuei Lin, Taiwan
Shueei M. Lin, Taiwan
Jui-Sheng Lin, Taiwan
Wanquan Liu, Australia
Bin Liu, Australia
Yuji Liu, China
Paolo Lonetti, Italy
Vassilios C. Loukopoulos, Greece
Chien-Yu Lu, Taiwan
Junguo Lu, China
Alexei Mailybaev, Brazil
Manoranjan K. Maiti, India
Oluwole Daniel Makinde, South Africa
Rafael Martínez-Guerra, Mexico
Driss Mehdi, France
Roderick Melnik, Canada
Xinzhu Meng, China
Jose Merodio, Spain
Yuri Vladimirovich Mikhlin, Ukraine
Gradimir Milovanović, Serbia
Ebrahim Momoniat, South Africa
Trung Nguyen Thoi, Vietnam
Hung Nguyen-Xuan, Vietnam
Ben T. Nohara, Japan
Sotiris K. Ntouyas, Greece
Claudio Padra, Argentina
Bijaya Ketan Panigrahi, India
Francesco Pellicano, Italy
Matjaž Perc, Slovenia
Vu Ngoc Phat, Vietnam
Maria do Rosário Pinho, Portugal
Seppo Pohjolainen, Finland
Stanislav Potapenko, Canada
Sergio Preidikman, USA
Carsten Proppe, Germany
Hector Puebla, Mexico

Justo Puerto, Spain
Dane Quinn, USA
Kumbakonam Rajagopal, USA
Gianluca Ranzi, Australia
Sivaguru Ravindran, USA
G. Rega, Italy
Pedro Ribeiro, Portugal
J. Rodellar, Spain
Rosana Rodriguez-Lopez, Spain
Alejandro J. Rodriguez-Luis, Spain
Carla Roque, Portugal
Rubén Ruiz García, Spain
Manouchehr Salehi, Iran
Miguel A. F. Sanjuán, Spain
Ilmar Ferreira Santos, Denmark
Nickolas S. Sapidis, Greece
Evangelos J. Sapountzakis, Greece
Bozidar Sarler, Slovenia
Andrey V. Savkin, Australia
Massimo Scalia, Italy
Mohamed A. Seddeek, Egypt
Leonid Shaikhet, Ukraine
Cheng Shao, China
Bo Shen, Germany
Jian-Jun Shu, Singapore
Zhan Shu, UK
Dan Simon, USA
Luciano Simoni, Italy

Grigori M. Sisoiev, UK
Christos H. Skiadas, Greece
Davide Spinello, Canada
Sri Sridharan, USA
Hari M. Srivastava, Canada
Rolf Stenberg, Finland
Changyin Sun, China
Xi-Ming Sun, China
Jitao Sun, China
Andrzej Swierniak, Poland
Yang Tang, Germany
Allen Tannenbaum, USA
Cristian Toma, Romania
Gerard Olivar Tost, Colombia
Irina N. Trendafilova, UK
Alberto Trevisani, Italy
Jung-Fa Tsai, Taiwan
Kuppapalle Vajravelu, USA
Victoria Vampa, Argentina
Josep Vehi, Spain
Stefano Vidoli, Italy
Yijing Wang, China
Cheng C. Wang, Taiwan
Dan Wang, China
Xiaojun Wang, China
Qing-Wen Wang, China
Yongqi Wang, Germany
Moran Wang, China

Youqing Wang, China
Gerhard-Wilhelm Weber, Turkey
Jeroen Witteveen, The Netherlands
Kwok-Wo Wong, Hong Kong
Ligang Wu, China
Zhengguang Wu, China
Gongnan Xie, China
Wang Xing-yuan, China
Xi Frank Xu, China
Xuping Xu, USA
Jun-Juh Yan, Taiwan
Xing-Gang Yan, UK
Suh-Yuh Yang, Taiwan
Mahmoud T. Yassen, Egypt
Mohammad I. Younis, USA
Bo Yu, China
Huang Yuan, Germany
S.P. Yung, Hong Kong
Ion Zaballa, Spain
Ashraf M. Zenkour, Saudi Arabia
Jianming Zhan, China
Yingwei Zhang, China
Xu Zhang, China
Lu Zhen, China
Liancun Zheng, China
Jian Guo Zhou, UK
Zexuan Zhu, China
Mustapha Zidi, France

Contents

Recent Advancements in Signal Processing and Machine Learning, Gelan Yang, Su-Qun Cao, and Yue Wu
Volume 2014, Article ID 549024, 4 pages

Strategies for Exploiting Independent Cloud Implementations of Biometric Experts in Multibiometric Scenarios, P. Peer, Ž. Emeršič, J. Bule, J. Žganec-Gros, and V. Štruc
Volume 2014, Article ID 585139, 15 pages

A Joint Learning Approach to Face Detection in Wavelet Compressed Domain, Szu-Hao Huang and Shang-Hong Lai
Volume 2014, Article ID 548791, 13 pages

Lower Power Design for UHF RF CMOS Circuits Based on the Power Consumption Acuity, Niu Xiang-jie and Li Hua
Volume 2014, Article ID 512398, 8 pages

Image Encryption Using the Chaotic Josephus Matrix, Gelan Yang, Huixia Jin, and Na Bai
Volume 2014, Article ID 632060, 13 pages

Language Recognition Using Latent Dynamic Conditional Random Field Model with Phonological Features, Sirinoot Boonsuk, Atiwong Suchato, Proadpran Punyabukkana, Chai Wutiwiwatchai, and Nattanun Thatphithakkul
Volume 2014, Article ID 250160, 16 pages

Efficient LED-SAC Sparse Estimator Using Fast Sequential Adaptive Coordinate-Wise Optimization (LED-2SAC), T. Yousefi Rezaii, S. Beheshti, and M. A. Tinati
Volume 2014, Article ID 317979, 8 pages

Human Skeleton Model Based Dynamic Features for Walking Speed Invariant Gait Recognition, Jure Kovač and Peter Peer
Volume 2014, Article ID 484320, 15 pages

Penalized Maximum Likelihood Algorithm for Positron Emission Tomography by Using Anisotropic Median-Diffusion, Qian He and Lihong Huang
Volume 2014, Article ID 491239, 7 pages

Linear Chromatic Adaptation Transform Based on Delaunay Triangulation, Rok Kreslin, Pilar M. Calvo, Luis G. Corzo, and Peter Peer
Volume 2014, Article ID 760123, 9 pages

Minimum Error Thresholding Segmentation Algorithm Based on 3D Grayscale Histogram, Jin Liu, Jianhong Zheng, Quanhua Tang, and Weidong Jin
Volume 2014, Article ID 932695, 13 pages

A Simple and High Performing Rate Control Initialization Method for H.264 AVC Coding Based on Motion Vector Map and Spatial Complexity at Low Bitrate, Yalin Wu and Sun-Woo Ko
Volume 2014, Article ID 595383, 11 pages

The New Mathematical Model of Motion Compensation for Stepped-Frequency Radar Signal, Yun Lin, Xiaochun Xu, Jinfeng Pang, Bin Li, and Ruolin Zhou
Volume 2014, Article ID 142482, 9 pages

A Model for Recognizing Key Factors and Applications Thereof to Engineering, Baofeng Shi and Guotai Chi
Volume 2014, Article ID 862132, 9 pages

A Novel Machine Learning Strategy Based on Two-Dimensional Numerical Models in Financial Engineering, Qingzhen Xu
Volume 2013, Article ID 659809, 6 pages

Efficient Interaction Recognition through Positive Action Representation, Tao Hu, Xinyan Zhu, Wei Guo, and Kehua Su
Volume 2013, Article ID 795360, 11 pages

Human Walking Pattern Recognition Based on KPCA and SVM with Ground Reflex Pressure Signal, Zhaoqin Peng, Chun Cao, Qiusheng Liu, and Wentao Pan
Volume 2013, Article ID 143435, 12 pages

Subband Adaptive Filtering with l_1 -Norm Constraint for Sparse System Identification, Young-Seok Choi
Volume 2013, Article ID 601623, 7 pages

Improvement and Simulation of an Autonomous Time Synchronization Algorithm for a Layered Satellite Constellation, Feijiang Huang, Xiaochun Lu, Guangcan Liu, Liping Sun, Wang Sheng, and Yingde Wang
Volume 2013, Article ID 136301, 7 pages

A Heuristic Feature Selection Approach for Text Categorization by Using Chaos Optimization and Genetic Algorithm, Hao Chen, Wen Jiang, Canbing Li, and Rui Li
Volume 2013, Article ID 524017, 6 pages

Unsupervised Optimal Discriminant Vector Based Feature Selection Method, Su-Qun Cao and Jonathan H. Manton
Volume 2013, Article ID 396780, 7 pages

Video Shot Boundary Recognition Based on Adaptive Locality Preserving Projections, Yongliang Xiao, Limin Xia, Shaoping Zhu, Dazu Huang, and Jianquan Xie
Volume 2013, Article ID 353261, 9 pages

Active Semisupervised Clustering Algorithm with Label Propagation for Imbalanced and Multidensity Datasets, Mingwei Leng, Jianjun Cheng, Jinjin Wang, Zhengquan Zhang, Hanhai Zhou, and Xiaoyun Chen
Volume 2013, Article ID 641927, 10 pages

Application of Fuzzy Set Theory to Quantitative Analysis of Correctness of the Mathematical Model Based on the ADI Method during Solidification, Xiaofeng Niu, Guanqian Wang, Wei Liang, Hua Hou, Hongxia Wang, and Jinshan Zhang
Volume 2013, Article ID 894384, 7 pages

Tensorial Kernel Principal Component Analysis for Action Recognition, Cong Liu, Xu Wei-sheng, and Wu Qi-di
Volume 2013, Article ID 816836, 16 pages

An Initial Value Calibration Method for the Wheel Force Transducer Based on Memetic Optimization Framework, Guoyu Lin, Weigong Zhang, Fan Yang, Han Pang, and Dong Wang
Volume 2013, Article ID 275060, 10 pages

Application of Global Optimization Methods for Feature Selection and Machine Learning, Shaohua Wu, Yong Hu, Wei Wang, Xinyong Feng, and Wanneng Shu
Volume 2013, Article ID 241517, 8 pages

An Efficient Web Usage Mining Approach Using Chaos Optimization and Particle Swarm Optimization Algorithm Based on Optimal Feedback Model, Lu Dai, Wei Wang, and Wanneng Shu
Volume 2013, Article ID 340480, 8 pages

Low-Complexity Compression Algorithm for Hyperspectral Images Based on Distributed Source Coding, Yongjian Nian, Mi He, and Jianwei Wan
Volume 2013, Article ID 825673, 7 pages

A Novel Fusion Method by Static and Moving Facial Capture, Shuai Liu, Weina Fu, Wenshuo Zhao, Jiantao Zhou, and Qianzhong Li
Volume 2013, Article ID 503924, 6 pages

A Virtual Channels Scheduling Algorithm with Broad Applicability Based on Movable Boundary, Ye Tian, Qingfan Li, Yongxin Feng, and Xiaoling Gao
Volume 2013, Article ID 391493, 13 pages

Comprehensive Models for Evaluating Rockmass Stability Based on Statistical Comparisons of Multiple Classifiers, Longjun Dong and Xibing Li
Volume 2013, Article ID 395096, 9 pages

A Routing Algorithm for WiFi-Based Wireless Sensor Network and the Application in Automatic Meter Reading, Li Li, Xiaoguang Hu, and Baochang Zhang
Volume 2013, Article ID 320894, 9 pages

Accurate Counting Bloom Filters for Large-Scale Data Processing, Wei Li, Kun Huang, Dafang Zhang, and Zheng Qin
Volume 2013, Article ID 516298, 11 pages

Analysis and Denoising of Hyperspectral Remote Sensing Image in the Curvelet Domain, Dong Xu, Lei Sun, Jianshu Luo, and Zhihui Liu
Volume 2013, Article ID 751716, 11 pages

Editorial

Recent Advancements in Signal Processing and Machine Learning

Gelan Yang,¹ Su-Qun Cao,² and Yue Wu³

¹ College of Information Science and Engineering, Hunan City University, Yiyang 413000, China

² Faculty of Mechanical Engineering, Huaiyin Institute of Technology, Huai'an 223003, China

³ Department of Electrical and Computer Engineering, Tufts University, Medford, MA 02155, USA

Correspondence should be addressed to Gelan Yang; glyang@mail.ustc.edu.cn

Received 26 March 2014; Accepted 26 March 2014; Published 14 April 2014

Copyright © 2014 Gelan Yang et al. This is an open access article distributed under the Creative Commons Attribution License, which permits unrestricted use, distribution, and reproduction in any medium, provided the original work is properly cited.

Recent advances of consumer electronics, like iPhone 5s, Google glasses, Xbox Kinect, and so forth, bring people revolutionary experiences of human-machine interactions. Behind these innovations are the successes of various recent cutting-edge technologies, including voice recognition, object recognition, and motion recognition. Though many of these technologies are still far from perfect, these examples demonstrate the usefulness and importance of signal processing and machine learning (SPML) research.

SPML, however, clearly goes far beyond these well-known recognition technologies and roots deeply in many aspects of academic research and industrial development. Indeed, wherever digital sensors require signal processing, and wherever decision-making problems can be formed in a machine learning manner. Moreover, SPML is also deeply involved: on one hand, ML could take digital signals as raw features to learn rules; on the other hand, many statistical SP techniques are essentially ML solutions. For example, wavelet transform proposed for SP now has been widely used as a preprocessing for many machine learning applications, while probabilistic graphical models often used in an expert system now show their potentials in image segmentation and recognition.

For these reasons, the aim of this special issue is to consider the recent advancements in SPML together. In total, this special issue contains thirty-four papers studying various SPML problems including image registration, pattern recognition, texture analysis, surveillance, biometrics, human-machine interface, image/video compression/encryption, image enhancement, and face recognition. A summarized description of these papers is given below.

“Strategies for exploiting independent cloud implementations of biometric experts in multibiometric scenarios” by P. Peer et al. presents an analysis of different strategies for combining independent cloud implementations of biometric experts into a multibiometric recognition system. Analysis results suggest that fixed fusion rules combining single expert systems at the matching score level are the most suitable for the studied task as they provide a good balance among expected performance gains and other important factors.

“Linear chromatic adaptation transform based on Delaunay triangulation” by R. Kreslin et al. suggests a method using Delaunay triangulation and linear transformations in order to transform the input image. It relies on the color values of the patches of the Macbeth color checker captured under the same illuminant as the input image must be known. Objective evaluation showed that the proposed method outperforms existing CAT methods by more than 21%, which performs statistically significantly better than that of other existing methods.

“Language recognition using latent dynamic conditional random field model with phonological features” by S. Boonsuk et al. proposes an acoustic SLR system based on the latent-dynamic conditional random field (LDCRF) model using phonological features (PFs). Evaluated on the NIST LRE 2007 corpus, the proposed method showed an improvement over the baseline systems. Additionally, it showed comparable result with the acoustic system based on *i*-vector. This research demonstrates that utilizing the PF attributes as a mean to integrate linguistic information with the acoustic approach can enhance the performance.

“*Human skeleton model based dynamic features for walking speed invariant gait recognition*” by J. Kovač et al. proposes a skeleton model based gait recognition system focusing on modelling gait dynamics and eliminating the influence of subject appearance on recognition. Furthermore, this paper tackles the problem of walking speed variation and proposes space transformation and feature fusion that mitigates its influence on recognition performance.

“*Efficient LED-SAC sparse estimator using fast sequential adaptive coordinate-wise optimization (LED-2SAC)*” by T. Yousefi Rezaii et al. presents a novel method benefits from the sparsity of the signal both in the optimization criterion (LED) and its solution path, denoted by Sparse SAC (2SAC). The new reconstruction method is consequently more efficient and considerably faster compared to the LED-SAC algorithm, in terms of adaptability and convergence rate with a much lower computational complexity.

“*A joint learning approach to face detection in wavelet compressed domain*” by S.-H. Huang et al. carries out a novel face detection system working directly in the wavelet compressed domain. This methodology involves a feature space warping process, a paired feature learning scheme, an ID3-like joint feature plane quantization method, and a weak Bayesian classifier. Experimental results on the benchmarking face datasets showed that the proposed face detection system working in the compressed domain achieves similar accuracy to that of Viola and Jones’ face detector.

“*Improvement and simulation of an autonomous time synchronization algorithm for a layered satellite constellation*” by F. Huang et al. investigates the autonomous time synchronization algorithm that corresponds to the layered constellation structure, analyzes the main error of the time synchronization algorithm, and proposes methods to improve the characteristics of satellite movement in the constellation. Its simulation results show that in a condition with simulation errors, the time synchronization precision of this improved algorithm can be controlled within 5 ns and used in high-precision autonomous time synchronization between layered satellite constellations.

“*The new mathematical model of motion compensation for stepped-frequency radar signal*” by Y. Lin et al. presents a novel mathematical method to estimate target speed for the stepped-frequency radar. Its numeric simulation results confirm that this new method is effective and predominant in terms of much higher estimation accuracy in a low SNR and much larger estimation range of target speed.

“*Human walking pattern recognition based on KPCA and SVM with ground reflex pressure signal*” by Z. Peng et al. investigates an algorithm based on the ground reflex pressure (GRF) signal obtained from a pair of sensing shoes for human walking pattern recognition. Experimental results showed that algorithm fusing SVM and KPCA had better recognition performance.

“*Application of global optimization methods for feature selection and machine learning*” by S. Wu et al. proposes a novel immune clonal genetic algorithm for the feature selection problem. The proposed algorithm largely simplifies the feature selection process without trading off its effectiveness.

It shows higher classification accuracy than compared feature selection algorithms.

“*An initial value calibration method for the wheel force transducer based on memetic optimization framework*” by G. Lin et al. proposes an automatic solution without additional calibration equipment or manual operation. In this method, a vehicle with the wheel force transducer (WFT) is driven on a flat road with a constant speed. A real WFT data is used to verify the proposed method and result shows that it is superior to traditional solutions and can improve the measurement accuracy effectively.

“*A routing algorithm for WiFi-based wireless sensor network and the application in automatic meter reading*” by L. Li et al. introduces a new architecture of WiFi-based wireless sensor network, which is suitable for the next generation AMR system. It also proposes a new improved routing algorithm called energy saving-based hybrid wireless mesh protocol (E-HWMP).

“*An efficient web usage mining approach using chaos optimization and particle swarm optimization algorithm based on optimal feedback model*” by L. Dai et al. proposes an efficient particle swarm chaos optimization mining algorithm. It uses a user feedback model to provide a listing of best-matching webpages for user. Its test results show that this approach significantly outperforms other algorithms in the aspects of response time, execution time, precision, and recall.

“*Video shot boundary recognition based on adaptive locality preserving projections*” by Y. Xiao et al. introduces a novel video shot boundary recognition method. It firstly defines the discriminating similarity with mode prior probabilities and an adaptive neighborhood selection strategy and then uses an optimized multiple kernel support vector machine to classify video frames into boundary and nonboundary frames.

“*A virtual channels scheduling algorithm with broad applicability based on movable boundary*” by Y. Tian et al. presents a novel algorithm for virtual channel scheduling based on movable boundary. It divides slots into synchronous ones and asynchronous ones, reduces the scheduling delay, and improves the channel utilization ratio. The proposed method outperforms the DSA algorithm, when the time delay and applicability scope are concerned. In addition, the algorithm is suitable for the scheduling of diverse data sources.

“*Comprehensive models for evaluating rock mass stability based on statistical comparisons of multiple classifiers*” by L. Dong and X. Li demonstrates the applicability and feasibility of RF, SVM, Bayes (NBC), Fisher, LR, and NN classification models to evaluate the rockmass stability of slope. Results show that the established RF, SVM, Bayes, Fisher, LR, and NN classification models can evaluate the slope status with a high accuracy.

“*Unsupervised optimal discriminant vector based feature selection method*” by S.-Q. Cao and J. H. Manton proposes an efficient unsupervised feature selection method based on unsupervised optimal discriminant vector. It aims to find important features without using class labels. Two experiments on Wine dataset and fault diagnosis demonstrate that the proposed method is able to find important features and is a reliable and efficient feature selection methodology compared to SUD and Relief-F methods.

“Penalized maximum likelihood algorithm for positron emission tomography by using anisotropic median-diffusion” by Q. He and L. Huang presents an approach to improving the quality of positron emission tomography images. By fusing an anisotropic median-diffusion filter to maximum-likelihood expectation-maximization algorithm, testing results demonstrate high-quality image reconstruction and denoising with better edge preserving capacities.

“A novel fusion method by static and moving facial capture” by S. Liu et al. introduces a fusion facial detection method in moving environment in the field of face recognition. Experimental results show that this method has better robustness and accuracy.

“Lower power design for UHF RF CMOS circuits based on the power consumption acuity” by N. Xiang-jie and L. Hua conveys a lower power design for UHF RF CMOS circuit based on the power consumption acuity due to the excessive energy consumption of UHF tag. The simulation results show that the leakage power of rectifier in this method is obviously less than the conventional rectifier. The proposed design method is suitable for various industrial productions, public management, and daily life use.

“Accurate counting bloom filters for large-scale data processing” by W. Li et al. proposes a multilevel optimization approach to build an accurate counting bloom filter (ACBF) for reducing the false positive probability. Experiments on realistic datasets show that ACBF can greatly reduce the false positive probability as well as the map outputs. Meanwhile, compared to the classic solution, this method also improves the join execution times by 20%.

“A heuristic feature selection approach for text categorization by using chaos optimization and genetic algorithm” by H. Chen et al. proposes a novel text categorization algorithm called chaos genetic feature selection optimization. Experimental results show that the proposed algorithm effectively simplifies the feature selection process which can also obtain higher classification accuracy with a smaller feature set.

“A simple and high performing rate control initialization method for H.264 AVC coding based on motion vector map and spatial complexity at low bitrate” by Y. Wu and S.-W. Ko describes a simple and high performance initial QP determining method based on motion vector map. Simulation results indicate that this algorithm outperforms conventional methods under many objective and subjective criteria.

“Subband adaptive filtering with l_1 -norm constraint for sparse system identification” by Y.-S. Choi introduces a normalized subband adaptive filter NSAF integrating a new weighted l_1 -norm constraint. Numerical results prove that the l_1 -norm regularized NSAFs outperform the classical NSAF solutions, especially for identifying a sparse system.

“Image encryption using the chaotic Josephus matrix” by G. Yang et al. introduces a new image encryption solution using the chaotic Josephus matrix. It extends the conventional Josephus traversing to a matrix form and proposes a treatment to improve the randomness of this matrix by mixing chaotic maps. The proposed CJPM is parametric and is uniquely dependent on the set of parameters, which is sufficiently large to provide a secure size of key space. Simulation results demonstrate that an encrypted image of using this method

is very random-like from the perspective of human visual inspection.

“Active semisupervised clustering algorithm with label propagation for imbalanced and multidensity datasets” by M. Leng et al. provides an active semisupervised clustering algorithm based on active data selection and semisupervised clustering algorithm on multidensity and imbalanced datasets. Testing results show that the proposed semisupervised clustering has higher accuracy and stable performance compared to other clustering and semisupervised clustering algorithms, especially in case of the datasets are multidensity and imbalanced.

“A novel machine learning strategy based on two-dimensional numerical models in financial engineering” by Q. Xu puts forward a two-dimensional numerical model for machine learning to simulate major US stock market index, which uses a nonlinear implicit finite-difference method to find numerical solutions of the two-dimensional simulation model. For the purpose of better prediction of the future trend of the index, experimental results show that the proposed algorithm reduces the prediction error and improve forecasting precision.

“Analysis and denoising of hyperspectral remote sensing image in the curvelet domain” by D. Xu et al. provides a new denoising algorithm based on the characteristics of hyperspectral remote sensing image (HRSI) in the curvelet domain. The detailed subband images in the same scale and same direction from different wavelengths of HRSI are stacked to obtain new 3D datacubes of the curvelet domain. The multiple linear regression method is also introduced. The simulated data experimental results show that the proposed algorithm is superior to the compared algorithms in the reference in terms of SNR.

“Efficient interaction recognition through positive action representation” by T. Hu et al. proposes a novel approach to decompose two-person interaction into a positive action and a negative action for more efficient behavior recognition. In this way, interaction recognition can be simplified to positive action-based recognition. Also, they created a new dataset with six types of complex human interaction. Experimental results showed that the proposed recognition technique is more accurate than the traditional method, shortens the sample training time, and hence achieves comprehensive superiority.

“Tensorial kernel principal component analysis for action recognition” by C. Liu et al. proposes a novel tensorial kernel principal component analysis (TKPCA) for feature extraction from action objects, which extends the conventional principal component analysis (PCA) in two perspectives: working directly with multidimensional data (tensors) in their native state and generalizing an existing linear technique to its nonlinear version by applying the kernel trick. Experiments with real action datasets show that the proposed method is insensitive to both noise and occlusion and performs well compared with state-of-the-art algorithms.

“Low-Complexity compression algorithm for hyperspectral images based on distributed source coding” by Y. Nian et al. proposes distributed compression algorithm for realizing

both lossless and lossy compression. It is implemented by performing scalar quantization strategy on the original hyperspectral images followed by distributed lossless compression. Multilinear regression model is introduced for improving the quality of side information. Experimental results show that the compression performance of the proposed algorithm is competitive with that of state-of-the-art compression algorithms for hyperspectral images.

“Model for recognizing key factors and applications thereof to engineering” by B. Shi and G. Chi presents a model for recognizing key factors while using collinearity diagnostics for deleting factors of repeated information and logistic regression for selecting factors. Experimental results from 2044 observations in financial engineering show that the 13 indicators are recognized as key factors to distinguish the good customers from the bad customers and thus demonstrate the effectiveness of the proposed method.

“Application of fuzzy set theory to quantitative analysis of correctness of the mathematical model based on the ADI method during solidification” by X. Niu et al. proposes a model based on the equivalent specific heat method and the ADI method aiming at improving the computational efficiency. Experimental results show that for a thick-walled position, the time step influences the simulation results of the temperature field and the number of casting meshes has little influence on the simulation results of temperature field, while for a thin-walled position a larger influence exists.

“Minimum error thresholding segmentation algorithm based on 3D grayscale histogram” by J. Liu et al. proposes a novel algorithm called three-dimensional minimum error thresholding (3D-MET) according to the relative entropy theory. The 3D histogram is obtained by combining raw information of pixel intensity distribution and relevant information of neighboring pixels within an image. Experimental results indicate that the proposed approach provides superior segmentation performance compared to other methods for gray image segmentation.

Acknowledgments

Thanks are due to the authors of the special issue for their contributions and thanks to the reviewers for their valuable comments on the submissions. Gelan Yang acknowledges the support by Scientific Research Fund of Hunan Provincial Education Department (Grant no. 12B023). Su-Qun Cao acknowledges the support by the National Spark Plan of China (Grant no. 2013GA690404).

Gelan Yang
Su-Qun Cao
Yue Wu

Research Article

Strategies for Exploiting Independent Cloud Implementations of Biometric Experts in Multibiometric Scenarios

P. Peer,¹ Ž. Emeršič,¹ J. Bule,¹ J. Žganec-Gros,² and V. Štruc³

¹ Faculty of Computer and Information Science, University of Ljubljana, Tržaška cesta 25, 1000 Ljubljana, Slovenia

² Alpineon d.o.o., Ulica Iga Grudna 15, 1000 Ljubljana, Slovenia

³ Faculty of Electrical Engineering, University of Ljubljana, Tržaška cesta 25, 1000 Ljubljana, Slovenia

Correspondence should be addressed to V. Štruc; vitomir.struc@fe.uni-lj.si

Received 18 October 2013; Revised 8 January 2014; Accepted 22 January 2014; Published 13 March 2014

Academic Editor: Yue Wu

Copyright © 2014 P. Peer et al. This is an open access article distributed under the Creative Commons Attribution License, which permits unrestricted use, distribution, and reproduction in any medium, provided the original work is properly cited.

Cloud computing represents one of the fastest growing areas of technology and offers a new computing model for various applications and services. This model is particularly interesting for the area of biometric recognition, where scalability, processing power, and storage requirements are becoming a bigger and bigger issue with each new generation of recognition technology. Next to the availability of computing resources, another important aspect of cloud computing with respect to biometrics is accessibility. Since biometric cloud services are easily accessible, it is possible to combine different existing implementations and design new multibiometric services that next to almost unlimited resources also offer superior recognition performance and, consequently, ensure improved security to its client applications. Unfortunately, the literature on the best strategies of how to combine existing implementations of cloud-based biometric experts into a multibiometric service is virtually nonexistent. In this paper, we try to close this gap and evaluate different strategies for combining existing biometric experts into a multibiometric cloud service. We analyze the (fusion) strategies from different perspectives such as performance gains, training complexity, or resource consumption and present results and findings important to software developers and other researchers working in the areas of biometrics and cloud computing. The analysis is conducted based on two biometric cloud services, which are also presented in the paper.

1. Introduction

Biometric technology is slowly gaining ground and is making its way into our daily lives. This development is exemplified best by the last generation of smart-phones, which is starting to adopt fingerprint technology as means of improving security and is bringing biometrics closer to our minds than ever. While biometric technology for personal devices, such as notebooks and mobile phones, is slowly gaining traction, its broader use on the Internet is still quite modest. The main reason for this setting pertains mainly to open issues with respect to the accessibility and scalability of the existing biometric technology [1]. Scalability issues are also of relevance to other deployment domains of biometrics, such as forensics or law-enforcement, where biometric databases are expected to grow significantly over the next few years to accommodate several hundred millions (or even billions) of identities [2]. To meet these demands, it is necessary to

develop scalable biometric technology, capable of operating on large amounts of data, and to ensure sufficient storage capacity and processing power [1].

A possible solution for the outlined issues is the development of biometric technology for the cloud, where the cloud platform ensures appropriate scalability, sufficient amount of storage, and parallel processing capabilities. With the widespread availability of mobile devices, the cloud also provides an accessible entry point for various applications and services relying on mobile clients [1]. The enormous potential of cloud-based biometric solutions was also identified by various companies which are currently developing or have only recently released their biometric cloud services to the market.

While a cloud platform can ensure the necessary infrastructure and resources for the next generation of biometric technology, the technology itself must ensure the best possible recognition (e.g., verification) performance. In this

respect, it is necessary to stress that biometric techniques relying on a single biometric trait (i.e., unimodal biometric experts) can only be improved to a certain extent in terms of performance. From a certain point forward, it may be either too costly or not yet feasible to further improve their performance. However, if performance is of paramount importance, the use of multibiometrics may represent a feasible solution.

The term multibiometrics refers to biometric technology that exploits several biometric experts and, hence, relies on several biometric traits of the same individual for identity inference. Multibiometric systems can offer substantial improvements in terms of accuracy and improvements in terms of flexibility and resistance to spoofing attacks. They also introduce higher tolerance to noise and data corruption and also reduce the failure-to-enroll rate [3].

In this paper, we address the problem of building (cloud-based) multibiometric systems based on existing implementations of unimodal biometric experts. Building (cloud-based) multibiometrics systems from existing implementations of biometric experts, instead of developing the system from scratch, has several advantages. The most obvious advantage is the reduction in effort needed to implement a multibiometric system. Furthermore, it is possible to choose the single expert systems from different vendors according to the desired specifications and performance capabilities. On the other hand, it is necessary to understand the process of combining the single expert systems from the perspectives of potential performance gains, additional resources needed, implementation complexity, and the like. Ideally, we would like to combine different (existing) biometric cloud services into a multibiometric service with significant performance gains and hence large improvements in security, but without the need for large modifications of existing client applications. Such multibiometric services would be of great interest to existing end-users of biometric cloud services and would exhibit significant market value.

To better understand the problem outlined above, we present in this paper an analysis of different (fusion) strategies for combining existing cloud-based biometric experts. To be as thorough as possible, we conduct the analysis under the assumption that only limited information, such as classification decisions or similarity scores, can be obtained from the existing cloud services (i.e., from the unimodal biometric experts). The fusion strategies are analyzed from different perspectives such as performance gains, training complexity, or resource consumption. The analysis is carried out based on two biometric cloud services developed in the scope of the KC CLASS project [1], the first being a face recognition cloud service and the second being a fingerprint recognition cloud service. The results of the analysis are important to engineers, software developers, and other researchers working in the areas of biometrics, cloud computing, and other related areas.

The rest of the paper is structured as follows. In Section 2, prior work in the area of multibiometrics is surveyed. In Section 3, the baseline (cloud-based) unimodal biometric experts are introduced. In Section 4, different strategies for combining the biometric experts are presented and their characteristics are discussed. In Section 5, a detailed analysis

of all fusion strategies is presented and nonperformance related characteristics of the fusion strategies are also presented and elaborated on. The paper is concluded with some final comments and directions for future work in Section 6.

2. Related Work

The problem of combining unimodal biometric experts into multibiometric systems has been studied extensively in the literature (see, e.g., [3–9]). In general, the process of combining unimodal systems (usually referred to as fusion) can be conducted at the following [3].

- (i) *The Signal or Sensor Level.* Sensor level fusion can benefit multisample systems which capture multiple snapshots of the same biometric. The process commonly referred to as mosaicing, for example, captures two or more impressions of the same biometric trait and creates an enhanced composite biometric sample that is better suited for recognition [3, 10].
- (ii) *The Feature Level.* Fusion at the feature level involves integrating evidence of several biometric feature vectors of the same individual [3] obtained from multiple information sources. It is generally believed that fusion at this level ensures better recognition results than fusion at the later levels (i.e., the decision or matching score levels) as the features sets typically contain richer information about the raw biometric samples [3, 11].
- (iii) *The Matching Score Level.* The matching scores still contain relatively rich information about the input biometric samples and it is also rather easy to combine matching scores of different experts. Consequently, information fusion at the matching score level is the most commonly used approach in multibiometric systems [3]. The matching score data from different biometric experts may not be homogeneous, may not be on the same numerical scale, or do not follow the same probability distribution [3]. These reasons make score level fusion a demanding problem.
- (iv) *The Decision Level.* This type of fusion is sensible when the unimodal biometric experts provide access only to the final stage in the process of biometric recognition, namely, the final classification result [3]. Different techniques can be considered at this level, for example, the AND- and OR-rules, majority voting, weighted majority voting, and others [3, 9, 12].

Among the different types of fusion techniques studied in the literature, fusion techniques applied at the matching score level are by far the most popular. This is also evidenced by Table 1, where a short overview of recent studies on biometric fusion is presented. Note that matching score level fusion techniques clearly dominate the research in this area.

When exploiting existing implementations of biometric experts, such as in our case, not all of the listed fusion levels are possible. Fusion at the first two levels requires data to be extracted right after the sample acquisition or the feature

TABLE 1: A few multibiometric systems discussed in the recent literature.

Author and year	Biometric modalities	Fusion level	Approach used
Nandakumar et al., 2008 [4]	Face, fingerprint, speech, iris	Matching score level	Likelihood ratio-based fusion
Maurer and Baker, 2008 [38]	Fingerprint, speech	Matching score level, quality-based fusion	Quality estimates via a Bayesian belief network (modified sum-rule)
Poh et al., 2009 [39]	Face, fingerprint, iris	Matching score level	Benchmarking 22 different biometric fusion algorithms
Lin and Yang, 2012 [40]	Face	Matching score level	Enhanced score-level fusion based on boosting
Tao and Veldhuis, 2009 [21]	Face (two face recognition algorithms)	Matching score level, decision level	Optimal fusion scheme at decision level by AND- or OR-rule (score levels: sum-rule, likelihood ratio, SVM)
Vatsa et al., 2010 [41]	Face (two face recognition algorithms)	Matching score level	Sequential fusion algorithm (likelihood ratio test + SVM)
Poh et al., 2010 [42]	Face, fingerprint	Matching score level	Quality-based score normalization
Poh et al., 2010 [43]	Face, fingerprint, iris	Matching score level	Addressing missing values in multimodal system with neutral point method
Nanni et al., 2011 [44]	Fingerprint, palm print, face	Matching score level	Likelihood ratio, SVM, AdaBoost of neural networks
Poh and Kittler, 2012 [45]	Face, fingerprint	Matching score level, quality-based fusion	A general Bayesian framework
Nagar et al., 2012 [46]	Face, fingerprint, iris	Feature level	Feature level fusion framework using biometric cryptosystems
Tao and Veldhuis, 2013 [47]	Face, speech	Matching score level	Native likelihood ratio via ROC

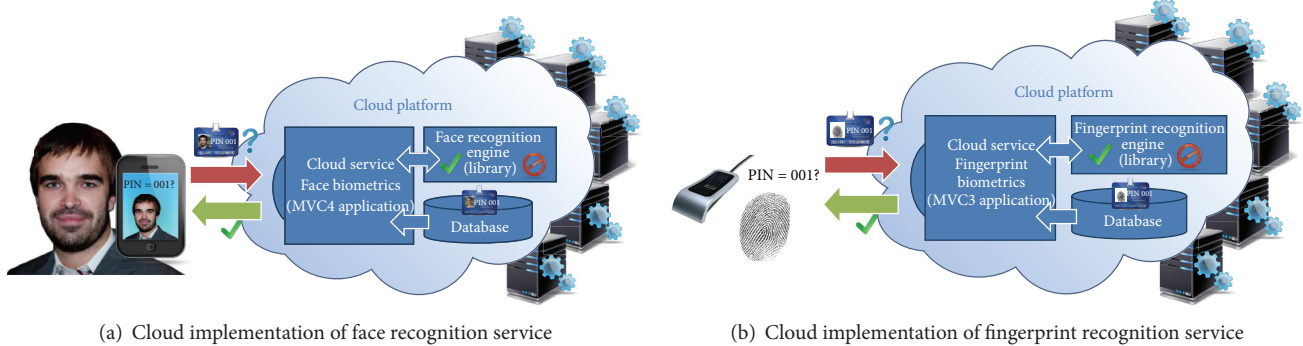


FIGURE 1: Illustration of basic architecture of the biometric cloud services.

extraction process, which is usually not possible, as existing (e.g., commercial) services commonly do not expose APIs for accessing the required data (i.e., signals or features). Existing cloud services typically only allow access to the decision and/or the matching score level. Hence, these two levels also form the basis for our assessment presented in the experimental section.

3. Baseline Systems

To be able to evaluate different strategies for combining independent implementations of biometric experts into a multibiometric cloud service, we first require access to unimodal biometric cloud services. In this section, we briefly introduce the basics of the unimodal face and fingerprint

services that were used for the evaluation presented in the experimental section.

3.1. *The Cloud Implementations.* As we can see from Figure 1, both (i.e., face and fingerprint) services share a similar architecture, which is more or less a characteristic for biometric cloud services. Both services feature a background worker (i.e., typically implemented in the form of a programming library), which represents the recognition engine of the cloud service. The biometric database is implemented in the form of an SQL database, while the communication with potential clients of the services is conducted through a RESTful Interface. Note that both services are implemented and optimized for the task of biometric verification (and not biometric identification) and as such are capable of

returning either the verification result (i.e., the class label) or a matching score indicating the similarity between the input biometric sample and the template of the claimed identity. These characteristics are common to most biometric cloud-based verification systems and define the boundaries for possible strategies that may be explored for combining existing implementations of biometric cloud services.

3.2. The Face Recognition Engine. The core component of the face recognition service is the face recognition engine, which relies on Gabor-LBP features (LBP-Local Binary Patterns). Below, we briefly summarize the basics.

- (i) *Face Detection, Localization, and Preprocessing.* Facial images are first preprocessed to remove illumination artifacts and then subjected to the Viola-Jones face detector to extract the facial region [13]. Next, facial landmark localization with PSEF correlation filters is performed to find anchor points in the faces that serve as the basis for geometrical normalization of the images [14]. The normalized images are rescaled to a fixed size of 128×128 pixels and finally subjected to the photometric normalization technique presented by Tan and Triggs in [15].
- (ii) *Feature Extraction and Supporting Representation.* The main feature representation used by the face recognition service relies on Gabor magnitude responses and Local Binary Patterns (LBPs). Here, the normalized facial images are first filtered with a bank of 40 Gabor filters. The Gabor magnitude responses are then encoded with the LBP operator and local LBP histograms are computed from patches of all computed responses. The local histograms are ultimately concatenated into a global feature vector that forms the template for the given identity. To improve recognition performance, a vector of the first few DCT coefficients of the normalized facial image is also added to the template.
- (iii) *Verification.* In the verification stage, the claim of identity is validated by comparing the template computed from the test/live/input image to the template of the claimed identity. Here, the Bhattacharyya distance is used to measure the similarity between the histograms of the LBP encoded Gabor magnitude responses and a simple whitened cosine similarity measure is used to match the DCT coefficients. Both similarity scores are then stacked together with image-quality measures (see [16] for details—Q-stack) and the newly combined feature vector is subjected to an AdaBoost classifier to obtain the final matching score based on which identity inference is conducted.

3.3. The Fingerprint Recognition Engine. The core component of the fingerprint recognition service is the minutiae-based fingerprint recognition engine first presented in [17]. Below, we briefly summarize the basics.

- (i) *Segmentation and Image Enhancement.* Fingerprint scans are first subjected to a segmentation procedure, where the fingerprint pattern is separated from the background. Through the segmentation procedure, the processing time is shortened and the matching accuracy is increased. Since fingerprints are often degraded due to various external factors, the fingerprint patterns are enhanced by binarizing the captured fingerprint samples and ridge profiling [18].
- (ii) *Minutiae Extraction.* The minutiae pattern is obtained from the binarized profiled image by thinning of the ridge structures, removal of structure imperfections from the thinned image, and the final process of minutiae extraction. For each detected minutia, its type (bifurcation or ending), spatial coordinates (x, y) , and the orientation of the ridge containing the minutia are stored as the templates for each given identity [18].
- (iii) *Matching and Verification.* Given a claimed identity and an input fingerprint sample, the claim of identity is validated by comparing the template computed from the test/live/input sample and the template corresponding to the claimed identity using a minutiae-based matching algorithm. Here, two fingerprints match when a sufficient number of minutiae match by type, location, and orientation.

4. Fusion Strategies

The task of combining different experts into a multiexpert system is common to many problems in the areas of pattern recognition and machine learning and is not restricted solely to the area of biometric recognition. Nevertheless, each problem has its specifics and it is important to understand the fusion task in the context of the specific problem one is trying to solve. The cloud implementations of the two biometric experts presented in the previous section were designed for the problem of biometric verification. We, therefore, commence this section by formalizing the problem of biometric verification and introducing the fusion task with respect to the presented formalization. In the second part of the section, we introduce different fusion strategies and elaborate on their characteristics.

4.1. Prerequisites. Let us assume that there are N identities registered in the given biometric system and that these identities are labeled with $\omega_1, \omega_2, \dots, \omega_i, \dots, \omega_N$ and that there are a total of J biometric experts at our disposal. Furthermore, let us assume that we are given a feature vector $\mathbf{x}^{(j)}$ of the j th expert, where $j \in \{1, 2, \dots, J\}$ and a claimed identity ω_i from the pool of the N enrolled identities (in general, there could be a different number of identities enrolled in each of the J biometric experts, but for the sake of simplicity, we assume that this number (i.e., N) is the same for all experts). The aim of biometric verification is to assign the pair $(\omega_i, \mathbf{x}^{(j)})$ to class C_1 (a genuine/client claim) if the claim of identity is found to be genuine and to class C_2 (an illegitimate/impostor claim) otherwise. Commonly, the validity of the identity

claim is determined based on the so-called matching score $d^{(j)}$, which is generated by comparing the feature vector $\mathbf{x}^{(j)}$ to the template corresponding to the claimed identity ω_i [19, 20]; that is,

$$(\omega_i, \mathbf{x}^{(j)}) = \begin{cases} C_1, & \text{if } d^{(j)} \leq \theta \text{ for } j \in \{1, 2, \dots, J\} \\ C_2, & \text{otherwise,} \end{cases} \quad (1)$$

where θ stands for the decision threshold. Here, we assume that small matching scores correspond to large similarities and large matching scores correspond to small similarities.

In multibiometric systems, several (i.e., J) biometric experts are available for classifying the given pair $(\omega_i, \mathbf{x}^{(j)})$, where $i \in \{1, 2, \dots, N\}$ and $j \in \{1, 2, \dots, J\}$, with respect to (1). Thus, after the verification process, the following families of results are typically available:

$$\begin{aligned} \mathcal{C} &= \{C_k^{(j)} \mid j = 1, 2, \dots, J; k \in \{1, 2\}\}, \\ \mathcal{D} &= \{d^{(j)} \mid j = 1, 2, \dots, J\}, \end{aligned} \quad (2)$$

where $C_k^{(j)}$ denotes the classification result and $d^{(j)}$ is the matching score produced by the j th expert; $k \in \{1, 2\}$.

Applying different functions on the results of the verification procedure from (2) gives rise to different fusion procedures. Some of these procedures that also represent valid fusion strategies with respect to the two cloud implementations presented in one of the previous sections are presented in the remainder of the paper. Note also that we will assume that $J = 2$ from this point on, since we only have two cloud services at our disposal. All presented strategies are, however, easily extended for the case, where $J > 2$.

4.2. Decision-Level Fusion Rules. The first strategy for combining the verification results of two independent cloud implementations of biometric experts one may consider is to combine the results at the decision level. The decision level represents the most basic way of combining expert opinions of several biometric systems. The experts are simply queried for the classification result $C_k^{(j)}$ (for $j = 1, 2, \dots, J$ and $k \in \{1, 2\}$) and the results are then combined into the final decision:

$$\psi : \{C_k^{(1)}, C_k^{(2)}, \dots, C_k^{(J)}\} \longrightarrow C_k^{\text{fused}}, \quad \text{where } k \in \{1, 2\}, \quad (3)$$

where C_k^{fused} is the combined classification result and $k \in \{1, 2\}$.

Several options are in general available for choosing the fusion function ψ , but two of the most common are the AND- and OR-rules [21]. In the context of the two cloud-based biometric experts at our disposal, the two rules, which assume that the class labels C_1 and C_2 are binary encoded, that is, $C_1 = 1$ and $C_2 = 0$, are defined as

$$\begin{aligned} \psi_{\text{AND}}(C_k^{(1)}, C_k^{(2)}) &= C_k^{\text{fused}} = C_k^{(1)} \& C_k^{(2)}, \\ \psi_{\text{OR}}(C_k^{(1)}, C_k^{(2)}) &= C_k^{\text{fused}} = C_k^{(1)} \mid C_k^{(2)}, \end{aligned} \quad (4)$$

where $\&$ and \mid denote the logical AND and OR operators and the superscript indices $^{(1)}$ and $^{(2)}$ stand for the face and fingerprint experts, respectively, and $k \in \{1, 2\}$.

While the decision level fusion strategies are easy to implement and offer a straightforward way of consolidating experts opinions, potential client applications relying on these strategies do not possess the flexibility of freely choosing the operating point of the combined biometric system. Instead, the operating point is determined by the operating points of the single expert systems.

4.3. Matching-Score-Level Fusion Rules. The second strategy that can be exploited to combine the verification results of several biometric experts is fusion at the matching score level using fixed fusion rules [5]. Most cloud-based biometric services (including our two) can be queried for a similarity score rather than the final classification decision. The client application then implements the classification procedure (see (1)) using a desired value for the decision threshold θ . Such an operating mode is implemented in most biometric services as it gives the client applications the possibility of choosing their own operating points and, hence, selecting a trade-off between security and user-convenience.

The general form for consolidating several expert opinions at the matching score level is

$$\phi : \{d^{(1)}, d^{(2)}, \dots, d^{(J)}\} \longrightarrow d^{\text{fused}}, \quad (5)$$

where ϕ is the fusion function and $d^{\text{fused}} \in \mathbb{R}$ represents the combined matching score that can be exploited for the final identity inference using (1). Note that the decision threshold for the fused scores needs to be recalculated for all desired operating points and cannot be found in the specifications of the cloud services anymore.

For our assessment presented in the experimental section, we implemented two fixed matching-level fusion rules, namely, the weighted sum-rule and the weighted product-rule. The two rules are defined as follows:

$$\phi_{\text{SUM}}(d^{(1)}, d^{(2)}) = d^{\text{fused}} = w d^{(1)} + (1 - w) d^{(2)}, \quad (6)$$

$$\phi_{\text{PRO}}(d^{(1)}, d^{(2)}) = d^{\text{fused}} = (d^{(1)})^w \cdot (d^{(2)})^{(1-w)}, \quad (7)$$

where the superscript indices $^{(1)}$ and $^{(2)}$ again denote the face and fingerprint experts, respectively, d^{fused} represents the combined matching score, and the real-valued $w \in [0, 1]$ stands for the weighting factor balancing the relative importance of the face and fingerprint scores. Note here that the weighted product-rule in (7) could also be represented as a weighted log-sum fusion rule making it very similar to the weighted sum-rule in (6). However, as shown in [9], the two fusion rules are based on different assumptions. The interested reader is referred to [9] for more information on this topic.

It should be emphasized here that the matching scores of independent biometric systems are typically of a heterogeneous nature—they are not on the same numerical

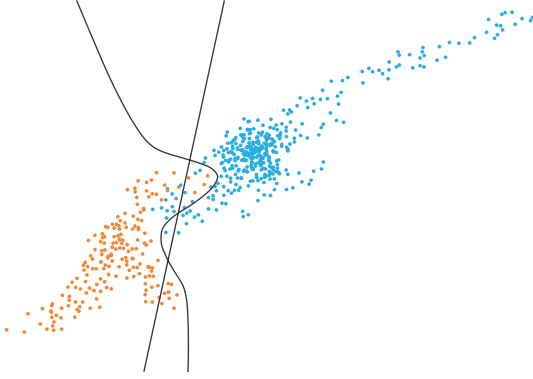


FIGURE 2: The linear and nonlinear decision boundaries are displayed, dividing genuine (in blue) and impostor (in red) classes.

range. Score normalization is, therefore, used to transform the scores to a common range prior to combining them [22, 23]. In this work, min-max normalization is used as it is quite simple and typically gives satisfactory results. Min-max normalization transforms all the scores to a common range of $[0, 1]$.

4.4. Fusion with Classifiers. The third strategy one may consider when combining biometric experts (again at the matching score level) is to use pattern classifiers. Similar to the fixed fusion rules presented in the previous section, it is first necessary to obtain similarity scores from the cloud services rather than classification labels. Rather than combining the scores to a single scalar value using fixed rules, the matching scores are concatenated into “new” feature vectors which are then classified into one of two classes: “genuine” or “impostor” (i.e., classes C_1 and C_2 in (1)) [3]. In this setting, the classifier is actually used to indirectly learn the relationship between the vector of matching scores provided by the biometric experts and the a posteriori probabilities of the genuine and the impostor classes [3]. Once trained, the discriminant function associated with the given classifier can be used to produce combined matching scores.

The described procedure can be formalized as follows:

$$\xi : \{d^{(1)}, d^{(2)}, \dots, d^{(J)}\} \longrightarrow d^{\text{fused}} = \delta(\mathbf{x}'), \quad (8)$$

where $\mathbf{x}' = [d^{(1)}, d^{(2)}, \dots, d^{(J)}]^T$ denotes the new feature vector and $\delta(\cdot)$ stands for the discriminant function of the given classifier.

The classifier learns a decision boundary between the two classes, which can be either linear or nonlinear, depending on the choice of classifier. In Figure 2, where a toy example is presented, the impostor class is represented with red color and the genuine class with blue. The straight line represents a linear decision boundary between the two classes, whereas the curved line represents a nonlinear boundary. Note that during verification, any new matching score vector is classified into the genuine/impostor class depending on which side of the decision boundary it falls. Thus, most existing implementations of the most common classifiers return

the class label instead of the output of their discriminant functions. However, with a little bit of tweaking, most existing implementations can be altered to return the output of the discriminant function as well.

Different from the fixed fusion rules, classifiers are capable of learning the decision boundary irrespective of how the feature vectors are generated. Hence, the output scores of the different experts can be nonhomogeneous (distance or similarity metric, different numerical ranges, etc.) and no processing is required (in theory) prior to training the classifier [3].

In the experimental section, we assess the relative usefulness of the classifier-based fusion strategy based on two classifiers: a Support Vector Machine (SVM) (with a linear kernel) [24, 25] and a Multilayer Perceptron (MLP) [26] classifier. The former falls into the group of linear classifiers (in our case), while the latter represents an example of a nonlinear classifier.

5. Experiments

5.1. Database, Protocol, and Performance Measures. To evaluate the different fusion strategies, a bimodal chimeric database is constructed from the XM2VTS and FVC2002 databases [27, 28]. A chimeric database represents a database in which biometric modalities from different databases are combined and assigned common identities. Since the biometric samples in the initial databases are not taken from the same identities, this procedure creates artificial (chimeric) subjects. Note that such a procedure is reasonable due to the fact that biometric modalities are generally considered to be independent one from another (e.g., a facial image says nothing about the fingerprint of the subject and vice versa) [29]. The constructed chimeric database consists of facial imagery and fingerprint data of 200 subjects with each subject having a total of 8 biometric samples for each modality. A few sample images from the chimeric database are presented in Figure 3.

For the experiments, the data is divided into two disjoint parts of 100 subjects (with 8 biometric samples per each modality). The first part is used for learning open hyperparameters of the fusion procedures (e.g., fusion weights, decision thresholds, etc.), while the second is used for evaluating the fusion techniques on unseen testing data with fixed hyperparameters. Each of the experimental runs consists of enrolling each of the 800 biometric samples (i.e., face and fingerprint samples) from the given part into the corresponding (biometric) cloud service and matching the same 800 samples against all enrolled samples. This experimental setup results in 640,000 matching scores (800×800) for the training and testing parts, out of which 6400 correspond to genuine verification attempts and 633600 correspond to illegitimate verification attempts. Note that prior to the experiments the matching scores are normalized using min-max score normalization [23].

For evaluation purposes, standard performance measures typically used in conjunction with two-class recognition problems are adopted, namely, the false acceptance error rate

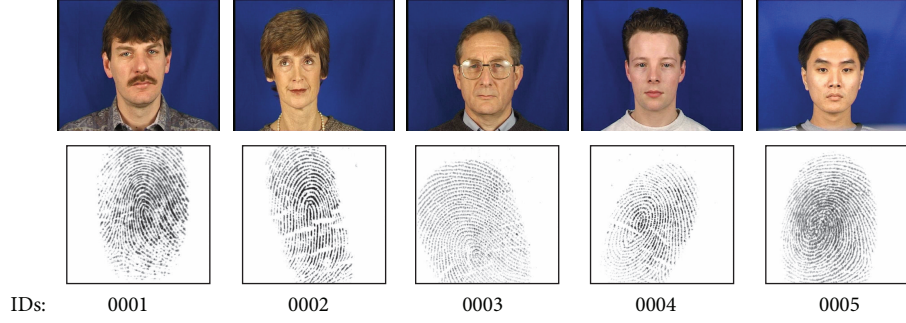


FIGURE 3: Sample images from the constructed chimeric database.

(FAR) and the false rejection error rate (FRR). The two error rates are defined as [30–33]

$$\text{FAR}(\theta) = \frac{|\{d_{\text{imp}} \mid d_{\text{imp}} \leq \theta\}|}{|\{d_{\text{imp}}\}|}, \quad (9)$$

$$\text{FRR}(\theta) = \frac{|\{d_{\text{cli}} \mid d_{\text{cli}} > \theta\}|}{|\{d_{\text{cli}}\}|},$$

where $\{d_{\text{cli}}\}$ and $\{d_{\text{imp}}\}$ represent sets of client and impostor scores generated during the experiments, $|\cdot|$ denotes a cardinality measure, and θ represents the decision threshold, and the inequalities assume that dissimilarity measures were used to produce the matching scores (it is assumed that large similarities between biometric samples result in small values of the matching scores and vice versa).

Note that both error rates, FAR and FRR, represent functions of the decision threshold θ . Selecting different values of the decision threshold, therefore, results in different error rates that form the basis for various performance metrics. In this paper, three such metrics are used, namely, the equal error rate (EER), which is defined with the decision threshold that ensures equal values of the FAR and FRR on the training set, that is,

$$\text{EER} = \frac{1}{2} (\text{FAR}(\theta_{\text{eer}}) + \text{FRR}(\theta_{\text{eer}})), \quad (10)$$

where

$$\theta_{\text{eer}} = \underset{\theta}{\operatorname{argmin}} |\text{FAR}(\theta) - \text{FRR}(\theta)|, \quad (11)$$

the verification rate at the false acceptance error rate of 0.1% (VER@0.1FAR), which is defined as

$$\text{VER@0.1FAR} = 1 - \text{FRR}(\theta_{\text{ver01}}), \quad (12)$$

where

$$\theta_{\text{ver01}} = \underset{\theta}{\operatorname{argmin}} |\text{FAR}(\theta) - 0.001|, \quad (13)$$

and the verification rate at the false acceptance error rate of 0.01% (VER@0.01FAR):

$$\text{VER@0.01FAR} = 1 - \text{FRR}(\theta_{\text{ver001}}), \quad (14)$$

where

$$\theta_{\text{ver001}} = \underset{\theta}{\operatorname{argmin}} |\text{FAR}(\theta) - 0.0001|. \quad (15)$$

The presented performance metrics are typically computed based on client and impostor score populations generated on the training data. To obtain an estimate of the generalization capabilities of a given fusion technique on unseen data, the thresholds θ_{eer} , θ_{ver01} , and θ_{ver001} are applied to client and impostor score populations generated on the evaluation data. Thus, during test time, the FAR and FRR defined in (9) are computed based on the fixed thresholds and then combined into the half-total error rate (HTER) as follows:

$$\text{HTER}(\theta_k) = \frac{1}{2} (\text{FAR}_e(\theta_k) + \text{FRR}_e(\theta_k)), \quad (16)$$

where $k \in \{\text{eer}, \text{ver01}, \text{ver001}\}$ and the subscript index e indicates that the error rates FAR and FRR were computed on the evaluation set. Alternatively, it is also possible to evaluate the verification rate and the false acceptance error rate at a specific decision threshold set during training; that is,

$$\text{VER}_e(\theta_k) = 1 - \text{FRR}_e(\theta_k), \quad \text{with } \text{FAR}_e(\theta_k), \quad (17)$$

where, in our case, k again stands for $k \in \{\text{eer}, \text{ver01}, \text{ver001}\}$.

In addition to the quantitative performance metrics, performance curves are also used to present the results of the experiments. Specifically, Receiver Operating Characteristic (ROC) Curves and Expected Performance Curves (EPC) are generated during the experiments to better highlight the differences among the assessed techniques [34]. ROC curves plot the dependency of the verification rate (VER) and the false acceptance rate (FAR) with respect to varying values of the decision threshold θ . ROC curves are usually plotted using a linear scale on the x - and y -axes; however, to better highlight the difference among the assessed procedures at the lower values of the false acceptance rate, a log scale for the x -axis is used in this paper.

To generate EPC, two separate image sets are needed. The first image set, that is, the training set, is used to find a decision threshold that minimizes the following weighted error (WER) for different values of α :

$$\text{WER}(\theta, \alpha) = \alpha \text{FAR}(\theta) + (1 - \alpha) \text{FRR}(\theta), \quad (18)$$

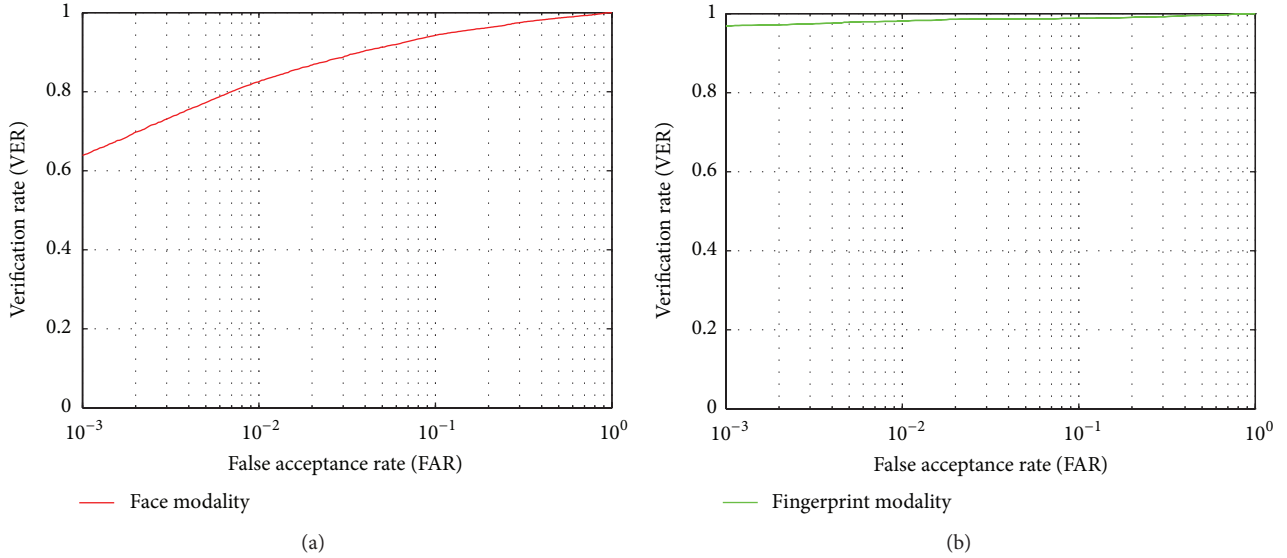


FIGURE 4: ROC curves of the experiments: face recognition (a) and fingerprint recognition (b).

TABLE 2: Quantitative comparison of the biometric modalities.

Procedure	EER	VER@0.1FAR	VER@0.01FAR
Face	0.0720	0.6394	0.3748
Fingerprint	0.0163	0.9691	0.9556

where α denotes a weighting factor that controls the relative importance of the FAR and FRR in the above expression. Next, the second image set, that is, the testing/evaluation image set, is employed to estimate the value of the HTER at the given α and with the estimated value of the decision threshold θ . When plotting the HTER (obtained on the testing/evaluation image sets) against different values of the weighting factor α , an example of an EPC is generated [35].

5.2. Single Expert Assessment. Before evaluating the feasibility and efficiency of different strategies for combining the cloud implementations of the biometric experts, it is necessary to establish the baseline performance of the unimodal biometric systems, that is, the face and fingerprint systems. To this end, the training data (note that the data used during this series of experiments represents the training data for the fusion techniques; for the unimodal systems, data is still valid testing/evaluation data) from our chimeric database is used to generate all of the relevant performance metrics and performance curves introduced in the previous section. The results of the experiments are presented in the form of ROC curves in Figure 4 and with quantitative performance metrics in Table 2.

As expected, the fingerprint recognition system performs much better than the face recognition system, especially at the lower values of the false acceptance error rates. At the equal error rate, for which the cloud-based biometric experts were also optimized, the face modality results in an error of around

7%, while the fingerprint modality ensures an error rate of a little more than 1.5%.

It is interesting to look at the distribution of the client and impostor similarity scores of the single experts in the *fingerprint—versus face-score—space*; see Figure 5. Since the optimal decision boundary appears to be different from a horizontal or vertical line (this would correspond to conducting identity inference based on one of the biometric experts), performance gains (at least on the matching score level) can be expected by combining the two experts. Different strategies for doing so are evaluated in the remainder.

5.3. Assessing Decision-Level Strategies. One possible strategy for combining the outputs of the cloud implementations of the face and fingerprint recognition experts is to consolidate the opinions of the two experts at the decision level. In this setting, the cloud services are asked to make a decision regarding the validity of the identity claim made with the given biometric sample. Since no similarity scores are sent to the client application, the operating point (i.e., the ratio of the FAR and FRR) of the cloud recognition service cannot be changed and is determined by the settings on the service side. In our case, the operating point of the cloud services is set to the equal error rate (EER).

Two decision-level fusion schemes are implemented for the experiments, namely, the AND- and OR-rules, as described in Section 4. The results of the experiments (on the training data) are shown in Table 3 in the form of various performance metrics. Note that it is not possible to generate ROC curves for this series of experiments, since no similarity scores are available.

Several observations can be made based on the presented results. Both fusion strategies result in similar performance in terms of the HTER with the difference that the AND-rule favors small FARs, while the OR-rule favors small FRRs. When compared to the performance of the single

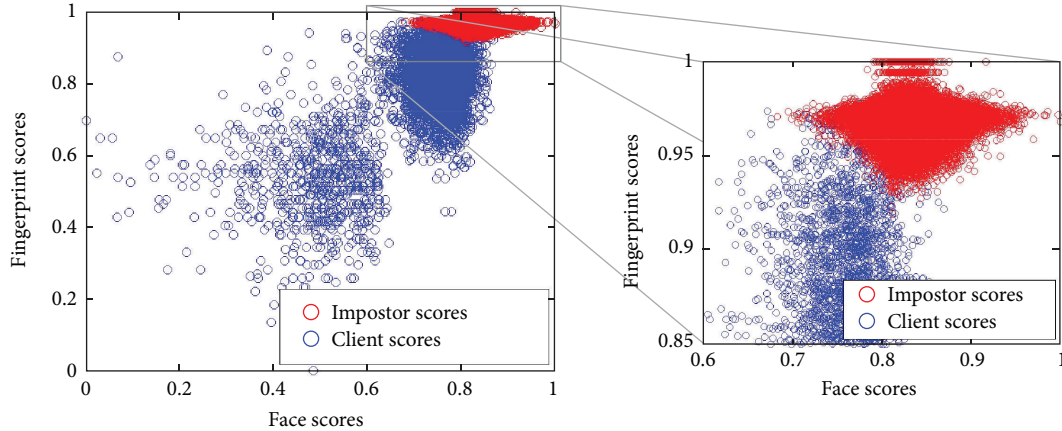


FIGURE 5: Plot of scores in the face-fingerprint-score plane.

TABLE 3: Quantitative comparison of the decision-level fusion rules (training data).

Procedure	HTER	FAR	FRR
AND-rule	0.0440	0.0011	0.0869
OR-rule	0.0440	0.0862	0.0014

expert systems presented in Table 2, the decision-level fusion schemes performed better than the face expert but a little worse than the fingerprint expert. All in all, the decision-level fusion rules did not prove to be too useful for improving the recognition performance of the single expert systems but should rather be considered as a way of changing the operating point of the combined system toward lower FARs or FRRs in cases where only decision-level outputs can be obtained from cloud implementations of biometric experts.

5.4. Assessing Matching-Score-Level Strategies. When assessing matching-score-level strategies for combining the two biometric experts, we first focus on the fixed fusion rules and present experiments related to classifier fusion strategies in the second part of this section.

The performance of the sum and product fusion rules is first examined on the training part of the constructed chimeric database. Before reporting the final performance, it is necessary to find (or learn) appropriate values for the open hyperparameter w of the sum and product fusion rules ((6) and (7)). To this end, the value of w is gradually increased from 0 to 1 with a step size of 0.1 and the values of EER, VER@0.1FAR, and VER@0.01FAR are computed for each value of w . The results of this series of experiments are shown in Figure 6. Note that both the sum and product fusion rules peak in their performance at a value of $w = 0.3$. This value is, therefore, selected for both fusion rules for all the following experiments.

To compare the performance of the sum and product fusion rules with fixed hyperparameters to that of the single expert systems, we generate ROC curves from the scores obtained on the training part of the chimeric database. The performance curves are shown in Figure 7 and the

corresponding performance measures in Table 4. Note that the sum and product fusion rules perform very similarly; both are significantly better than the unimodal (single expert) systems. The EER, for example, falls by more than 50% with both fusion rules when compared to the better performing single expert system. While these results are encouraging, it needs to be taken into account that the ROC curves for the fusion techniques shown in Figure 7 were generated by optimizing the open hyperparameter w on the same data that was used for constructing the curves in the first place. This means that the performance of the fusion techniques may be somewhat biased. To analyze this issue, we present comparative experiments on the evaluation/testing data of the constructed chimeric database in Section 5.5.

Next to fixed fusion rules, the second possibility for combining the similarity scores of the single expert systems is to stack the similarity scores into a two-dimensional feature vector and use the constructed vector with a classifier. To evaluate this possibility, the training part of the chimeric database is used to train SVM (Support Vector Machine [24, 25]) and MLP (Multilayer Perceptron [26]) classifiers. For the SVM classifier, a linear kernel is selected, and for the MLP classifier, an architecture with two hidden layers (each with 5 neurons) is chosen. This setting results in a classifier capable of finding linear decision boundary between the client and impostor classes (i.e., the SVM) and a classifier capable of setting the decision boundary in a nonlinear manner (i.e., the MLP). Once trained, both classifiers are applied to the training data to compute performance metrics and construct performance curves. The results of this series of experiments are shown in Figure 8 and Table 5. Note that with most existing software solutions for training SVM and MLP classifiers (see, e.g., [36, 37]) a little of tweaking is needed to obtain the similarity scores required for constructing ROC curves, as the classifiers usually output only class labels. When looking at the performance of the SVM and MLP classifiers, it is obvious that they did not ensure any additional performance improvements when compared to the fixed fusion rules. While this could be expected for the linear SVM classifier, it is somehow unexpected that the MLP classifier did not improve the performance over

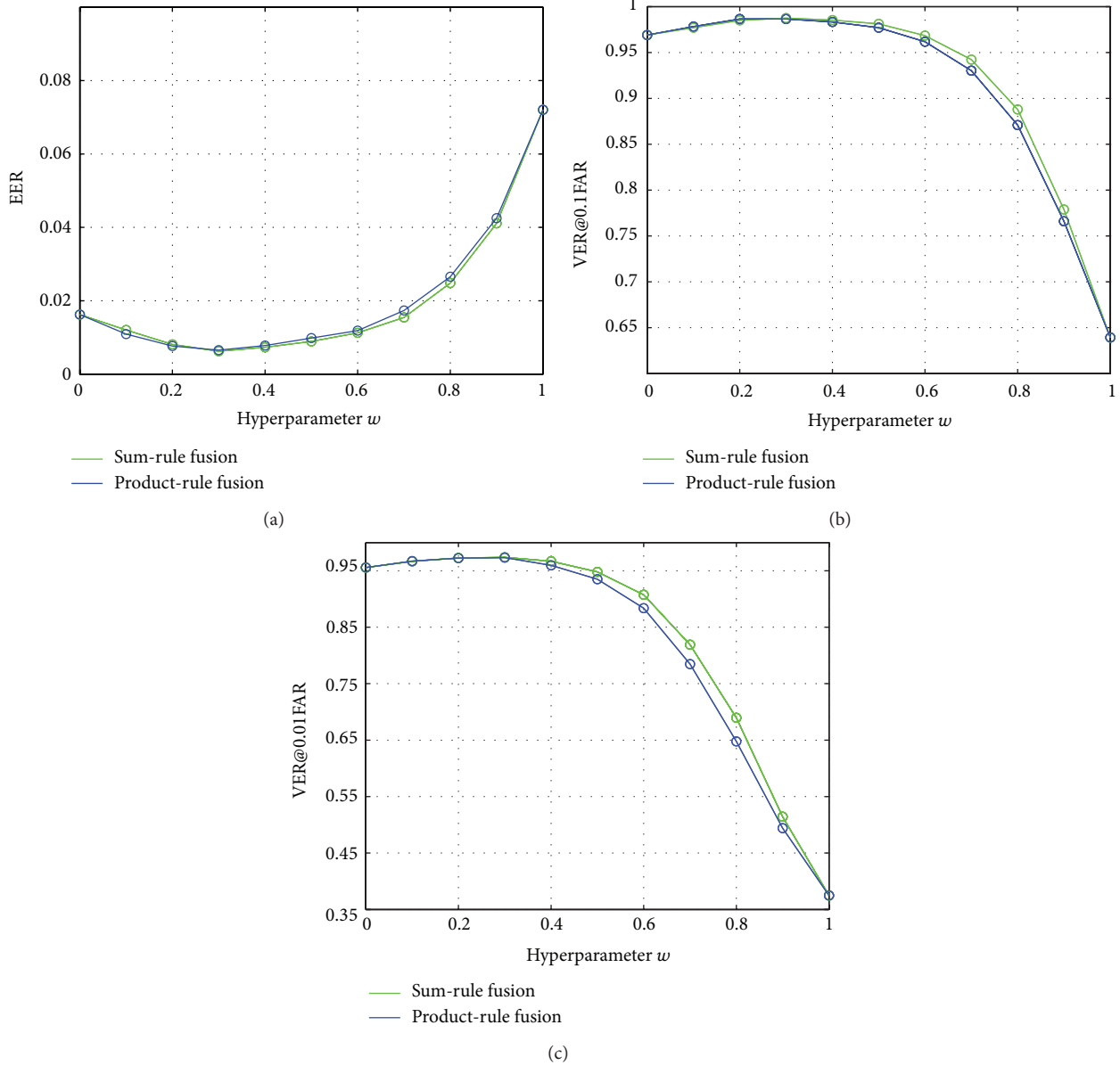


FIGURE 6: EERs, VER@0.1FARs, and VER@0.01FARs for the sum and product fusion rules for different values of the hyperparameter w .

the fixed sum and product fusion rules. It seems that, without any additional information such as quality or confidence measures, it is extremely difficult to significantly improve upon the performance fixed fusion rules on our chimeric database.

5.5. Generalization Capabilities of Different Strategies. The last series of verification experiments aimed at examining the generalization capabilities of the fusion strategies on the evaluation/testing part of the chimeric database. Here, all decision thresholds and hyperparameters of all assessed fusion strategies are fixed on the training part of the data. The testing/evaluation data is then used to generate performance metrics and curves, which are shown in Figure 9 and Table 6 for this series of experiments.

The first thing to notice from the presented results is the fact that, similar to the training data, all fusion strategies (except for the decision-level fusion techniques) result in performance improvements when compared to either of the two single expert systems. Next, the performance achieved on the training data is also achieved on the evaluation/testing data, which suggests that no overfitting took place during training. Especially important here is also the fact that all results are very well calibrated indicating that a desired operating point (i.e., the ratio between the FAR and FRR) can easily be selected and maintained even after the fusion process.

Last but not least, it is also important to stress that, among the matching-score-level fusion strategies, no particular strategy has a clear advantage in terms of performance on

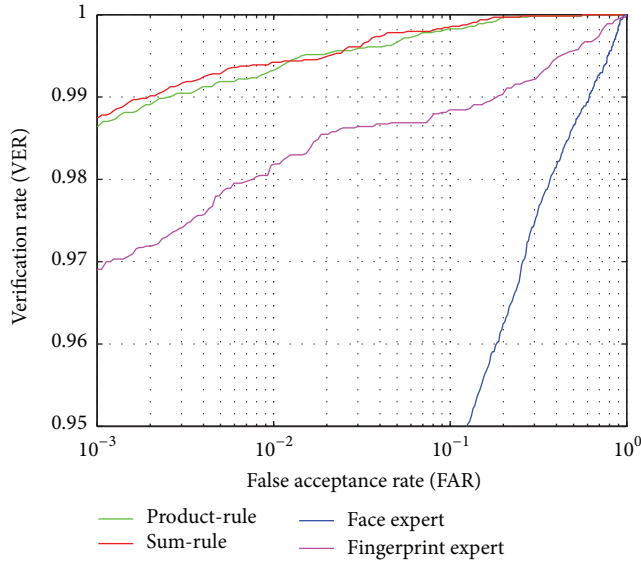


FIGURE 7: ROC curves for the fusion rules (training data).

TABLE 4: Quantitative comparison of the fusion rules with learned parameter w ($w = 0.3$ for both techniques)—training data.

Procedure	EER	VER@0.1FAR	VER@0.01FAR
Product-rule	0.0066	0.9866	0.9733
Sum-rule	0.0063	0.9875	0.9736

our chimeric database. This suggests that other criteria next to performance should be taken into account when selecting the best strategy for combining different cloud-based biometric experts.

5.6. Subjective Analysis. In the previous sections, different fusion strategies for combining cloud implementations of biometric experts were assessed only from the perspective of performance. However, when combining different biometric experts into a multibiometric system, other criteria are important as well. One may, for example, be interested in how existing client applications need to be modified to enable multiexpert biometric recognition, how difficult it is to reach a specific operating point in the multibiometric system, whether additional libraries need to be included in the client applications, and so forth. To evaluate the fusion strategies based on other (nonperformance related) criteria as well, a grade (low—L, medium—M, or high—H) was assigned to each strategy in seven different categories (note that these grades are of a subjective nature and reflect the perception of the authors). These categories include the following.

- (i) Training complexity: the complexity of the training procedure for the given fusion strategy (e.g., training the classifier, setting hyperparameters, etc.).
- (ii) Run-time complexity: the run-time complexity required to apply the given fusion strategy to the data (e.g., applying the trained classifier to the data, etc.).

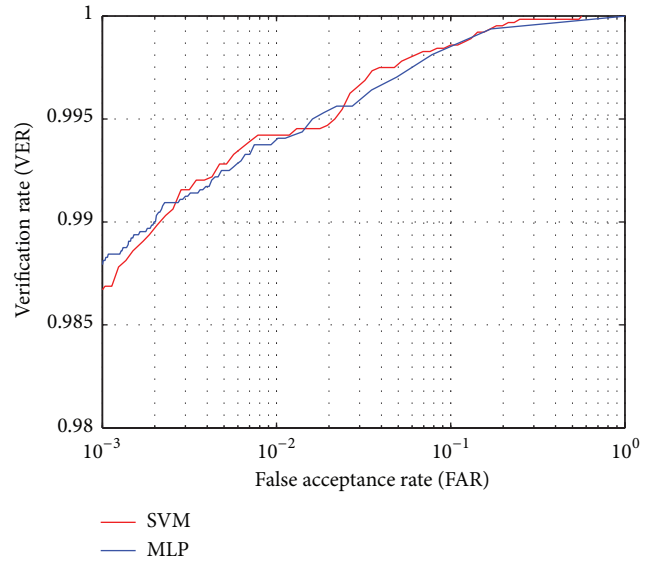


FIGURE 8: ROC curves for fusion techniques with classifiers (training data).

TABLE 5: Quantitative comparison of fusion techniques with classifiers (training data).

Procedure	EER	VER@0.1FAR	VER@0.01FAR
SVM	0.0064	0.9869	0.9733
MLP	0.0063	0.9881	0.9731

- (iii) Storage requirements: memory requirements for storing metadata needed by the given fusion strategy (e.g., for storing support vectors, hyperparameters, etc.).
- (iv) Performance gains: performance related criterion that reflects the results of the experiments conducted in the previous sections.
- (v) Client disturbance: relating to the amount of work needed to rewrite existing client applications and the need for including additional external resources (e.g., programming libraries, etc.).
- (vi) Calibration: referring to the generalization capabilities of the given fusion strategy and the capability of ensuring the same operating point across different data sets.
- (vii) OP complexity: relating to the complexity of setting a specific operating point for the multibiometric system (e.g., the EER operating point, etc.).

Our ratings are presented in Table 7 in the form of grades and in Figure 10 in the form of Kiviati graphs. With the generated graphs, a larger area represents a more suitable fusion strategy according to the selected criteria (note that the same weight has been given here to all criteria. If a certain criterion is considered more important than others, this could be reflected in the final Kiviati graphs).

Note that the fixed fusion rules (i.e., the sum- and product-rules) turned out to be suited best for combining

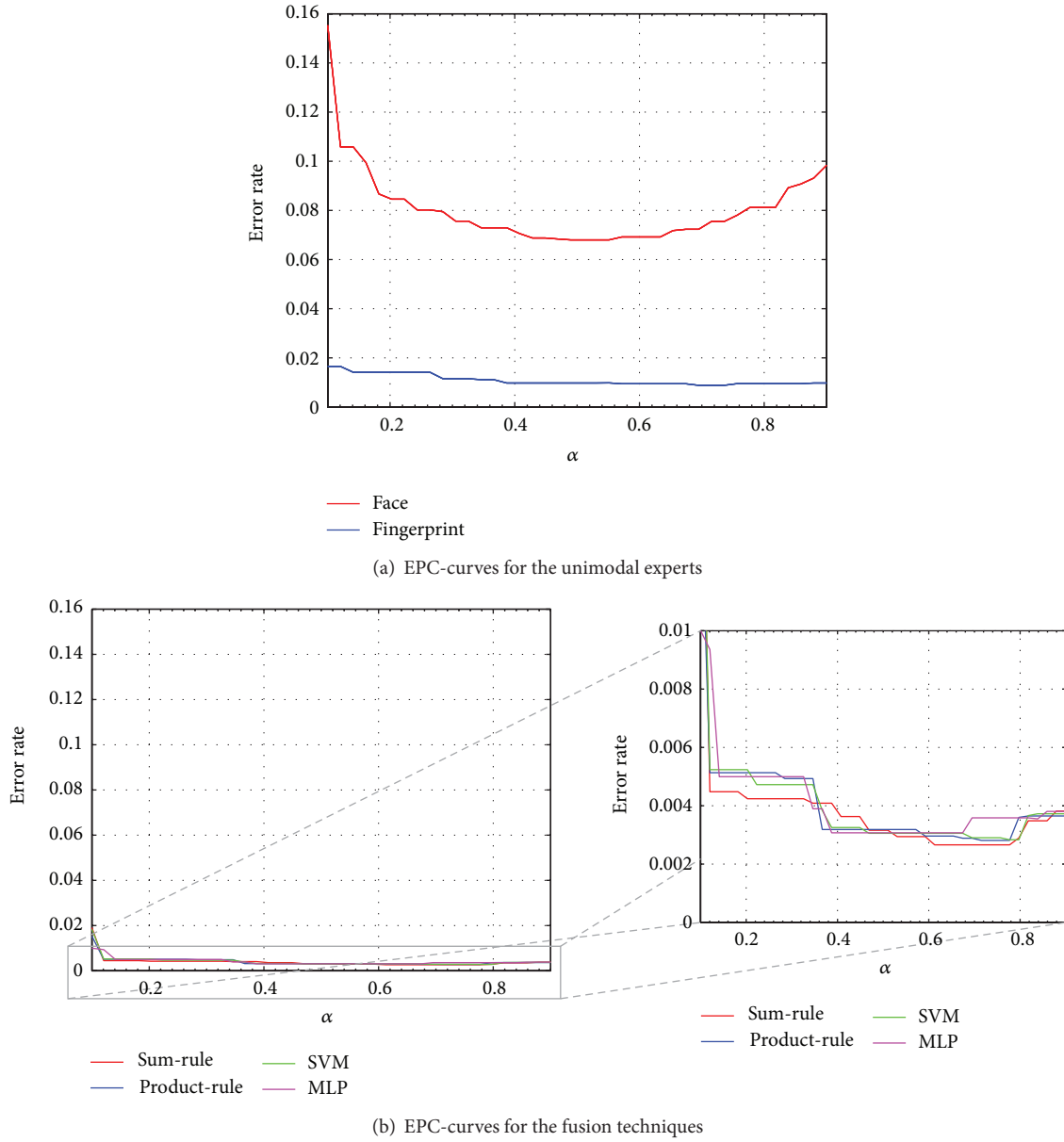


FIGURE 9: EPC-curves of the experiments on the evaluation data.

TABLE 6: Quantitative comparison of the fusion rules on the evaluation/testing data. Here, the symbol n/a stands for the fact that this value is not computable.

	$HTER_e$	$@\theta_{eer}$ VER_e	FAR_e	$HTER_e$	$@\theta_{ver01}$ VER_e	FAR_e	$HTER_e$	$@\theta_{ver001}$ VER_e	FAR_e
Face	0.0716	0.9280	0.0712	0.1808	0.6394	0.0010	0.3126	0.3748	$9.95E-5$
Fingerprint	0.0133	0.9897	0.0162	0.0096	0.9819	0.0012	0.0129	0.9744	$1.78E-4$
Sum-rule	0.0045	0.9973	0.0064	0.0034	0.9944	0.0011	0.0061	0.9880	$1.14E-4$
Product-rule	0.0046	0.9972	0.0065	0.0033	0.9945	0.0011	0.0063	0.9875	$1.25E-4$
AND-rule	0.0411	0.0811	0.0012	n/a	n/a	n/a	n/a	n/a	n/a
OR-rule	0.0411	0.0013	0.0863	n/a	n/a	n/a	n/a	n/a	n/a
SVM	0.0046	0.9972	0.0063	0.0032	0.9947	0.0011	0.0060	0.9881	$1.36E-4$
MLP	0.0046	0.9973	0.0066	0.0036	0.9939	0.0012	0.0062	0.9877	$1.10E-4$

TABLE 7: Comparison of the fusion strategies based on the perception of the authors and conducted experimentation. High, medium, and low are denoted by H, M, and L, respectively.

Fusion technique	Training complexity	Run-time complexity	Storage requirements	Performance gains	Client disturbance	Calibration	OP complexity
Sum-rule	L	L	L	M	L	H	L
Product-rule	L	L	L	M	L	H	L
AND-rule	L	L	L	L	L	L	H
OR-rule	L	L	L	L	L	L	H
SVM	H	M	M	M	M	H	M
Neural network	M	L	L	M	M	H	L

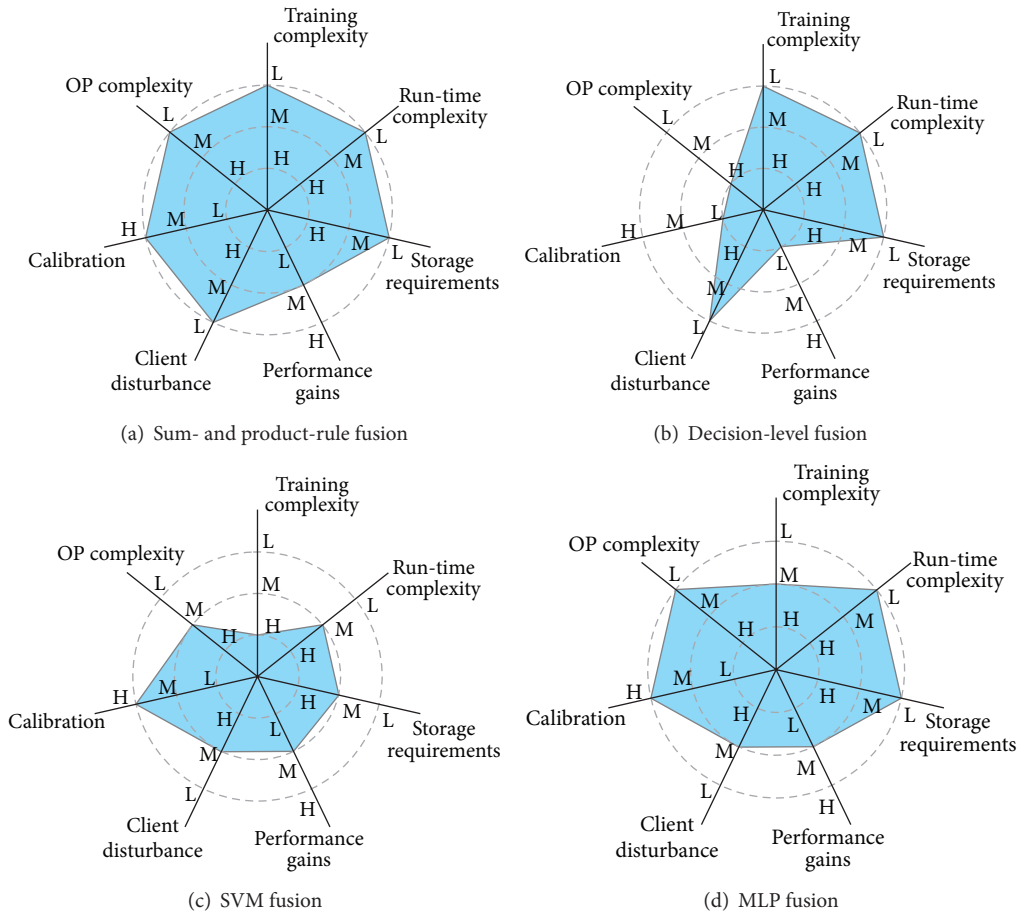


FIGURE 10: Kiviati graphs of the fusion techniques generated based on the selected evaluation criteria.

different cloud implementations of biometric experts into a multibiometric system as they provide a good trade-off between the complexity of the training and run-time procedures, expected performance gains, flexibility in setting the operating point, calibration, and the need for modifying existing client applications.

6. Conclusion

We have presented an analysis of different strategies for combining independent cloud implementations of biometric

experts into a multibiometric recognition system. For the analysis, we used our own implementations of cloud-based face and fingerprint verification services and a specially constructed chimeric database. The results of our analysis suggest that fixed fusion rules that combine the single expert systems at the matching score level are the most suitable for the studied task as they provide a good trade-off between expected performance gains and other important factors such as training complexity, run-time complexity, calibration, and client disturbance. As part of our future work, we plan to examine possibilities of including confidence measures in

the fusion strategies, as these have the potential to further improve the recognition performance of the combined multi-biometric system. We also plan to develop biometric cloud services combining more than two single expert systems.

Conflict of Interests

The authors declare that there is no conflict of interests regarding the publication of this paper.

Acknowledgments

The work presented in this paper was supported in part by The National Research Program P2-0250(C) Metrology and Biometric Systems, by the National Research Program P2-0214 Computer Vision, and by the EU, European Regional Fund, in scope of the framework of the Operational Programme for Strengthening Regional Development Potentials for the Period 2007–2013, Contract no. 3211-10-000467 (KC Class), the European Union's Seventh Framework Programme (FP7-SEC-2011.20.6) under Grant agreement no. 285582 (RESPECT), and the European Union's Seventh Framework Programme (FP7-SEC-2010-1) under Grant agreement no. 261727 (SMART). The authors additionally appreciate the support of COST Actions, IC1106 and IC1206.

References

- [1] P. Peer, J. Bule, J. Zganec Gros, and V. Štruc, "Building cloud-based biometric services," *Informatica*, vol. 37, no. 1, pp. 115–122, 2013.
- [2] E. Kohlwey, A. Sussman, J. Trost, and A. Maurer, "Leveraging the cloud for big data biometrics: meeting the performance requirements of the next generation biometric systems," in *Proceedings of the IEEE World Congress on Services (SERVICES '11)*, vol. 1, pp. 597–601, July 2011.
- [3] A. Ross, K. Nandakumar, and A. Jain, *Handbook of Multibiometrics*, Springer Science+Business Media, LLC, New York, NY, USA, 2006.
- [4] K. Nandakumar, Y. Chen, S. C. Dass, and A. K. Jain, "Likelihood ratio-based biometric score fusion," *IEEE Transactions on Pattern Analysis and Machine Intelligence*, vol. 30, no. 2, pp. 342–347, 2008.
- [5] L. Kuncheva, *Combining Pattern Classifiers: Methods and Algorithms*, Wiley-Interscience, Hoboken, NJ, USA, 2004.
- [6] A. B. Khalifa and N. B. Amara, "Bimodal biometric verification with different fusion levels," in *Proceedings of the 6th International Multi-Conference on Systems, Signals and Devices (SSD '09)*, vol. 1, pp. 1–6, March 2009.
- [7] L. I. Kuncheva, "A theoretical study on six classifier fusion strategies," *IEEE Transactions on Pattern Analysis and Machine Intelligence*, vol. 24, no. 2, pp. 281–286, 2002.
- [8] F. Alkoot and J. Kittler, "Experimental evaluation of expert fusion strategies," *Pattern Recognition Letters*, vol. 20, no. 11–13, pp. 1361–1369, 1999.
- [9] J. Kittler, M. Hatef, R. P. W. Duin, and J. Matas, "On combining classifiers," *IEEE Transactions on Pattern Analysis and Machine Intelligence*, vol. 20, no. 3, pp. 226–239, 1998.
- [10] X. Xia and L. O'Gorman, "Innovations in fingerprint capture devices," *Pattern Recognition*, vol. 36, no. 2, pp. 361–369, 2003.
- [11] A. Ross and R. Govindarajan, "Feature level fusion using hand and face biometrics," in *Proceedings of the SPIE Conference on Biometric Technology for Human Identification*, vol. 5779, pp. 196–204, March 2005.
- [12] L. Lam and C. Y. Suen, "Application of majority voting to pattern recognition: an analysis of its behavior and performance," *IEEE Transactions on Systems, Man, and Cybernetics A*, vol. 27, no. 5, pp. 553–568, 1997.
- [13] P. Viola and M. J. Jones, "Robust real-time face detection," *International Journal of Computer Vision*, vol. 57, no. 2, pp. 137–154, 2004.
- [14] V. Štruc, J. Zganec Gros, and N. Pavešić, "Principal directions of synthetic exact filters for robust real-time eye localization," in *Lecture Notes in Computer Science*, vol. 6583, pp. 180–192, 2011/2011.
- [15] X. Tan and B. Triggs, "Enhanced local texture feature sets for face recognition under difficult lighting conditions," *IEEE Transactions on Image Processing*, vol. 19, no. 6, pp. 1635–1650, 2010.
- [16] K. Kryszczuk and A. Drygajlo, "Improving biometric verification with class-independent quality information," *IET Signal Processing*, vol. 3, no. 4, pp. 310–321, 2009.
- [17] U. Klopčič and P. Peer, "Fingerprint-based verification system: a research prototype," in *Proceedings of the 17th International Conference on Systems, Signals and Image Processing (IWSSIP '10)*, A. Conci and F. Leta, Eds., vol. 1, pp. 150–153, 2010.
- [18] J. Fierrez-Aguilar, J. Ortega-Garcia, J. Gonzalez-Rodriguez, and J. Bigun, "Kernel-based multimodal biometric verification using quality signals," in *Proceedings of the Biometric Technology for Human Identification Conference*, pp. 544–554, April 2004.
- [19] A. K. Jain, A. Ross, and S. Prabhakar, "An introduction to biometric recognition," *IEEE Transactions on Circuits and Systems for Video Technology*, vol. 14, no. 1, pp. 4–20, 2004.
- [20] V. Štruc and N. Pavešić, "The corrected normalized correlation coefficient: a novel way of matching score calculation for LDA-based face verification," in *Proceedings of the 5th International Conference on Fuzzy Systems and Knowledge Discovery (FSKD '08)*, pp. 110–115, Shandong, China, October 2008.
- [21] Q. Tao and R. Veldhuis, "Threshold-optimized decision-level fusion and its application to biometrics," *Pattern Recognition*, vol. 42, no. 5, pp. 823–836, 2009.
- [22] S. Chaudhary and R. Nath, "A multimodal biometric recognition system based on fusion of palmprint, fingerprint and face," in *Proceedings of the International Conference on Advances in Recent Technologies in Communication and Computing (ART-Com '09)*, pp. 596–600, October 2009.
- [23] A. Jain, K. Nandakumar, and A. Ross, "Score normalization in multimodal biometric systems," *Pattern Recognition*, vol. 38, no. 12, pp. 2270–2285, 2005.
- [24] C. Cortes and V. Vapnik, "Support-vector networks," *Machine Learning*, vol. 20, no. 3, pp. 273–297, 1995.
- [25] V. Vapnik, *Statistical Learning Theory*, Wiley-Interscience, New York, NY, USA, 1998.
- [26] C. Bishop, *Neural Networks for Pattern Recognition*, Oxford University Press, Oxford, UK, 1995.
- [27] K. Messer, J. Matas, J. Kittler, J. Luetten, and G. Maitre, "Xm2vtsdb: the extended m2vts database," in *Proceedings of the 2nd International Conference on Audio and Video-based Biometric Person Authentication (AVBPA '99)*, vol. 1, pp. 72–77, 1999.

- [28] D. Maio, D. Maltoni, R. Cappelli, J. Wayman, and A. Jain, "Fvc 2002: second fingerprint verification competition," in *Proceedings of the 16th International Conference on Pattern Recognition*, vol. 1, pp. 811–814, 2002.
- [29] N. Poh and S. Bengio, "Using chimeric users to construct fusion classifiers in biometric authentication tasks: an investigation," in *Proceedings of the International Conference on Acoustics, Speech and Signal Processing (ICASSP '06)*, vol. 1, pp. V1077–V1080, May 2006.
- [30] R. Gajšek, F. Mihelič, and S. Dobrišek, "Speaker state recognition using an hmm-based feature extraction method," *Computer Speech & Language*, vol. 27, no. 1, pp. 135–150, 2013.
- [31] R. Gajšek, S. Dobrišek, and F. Mihelič, *Analysis and Assessment of State Relevance in Hmm-Based Feature Extraction Method*, Lecture Notes in Computer Science, Springer, New York, NY, USA, 2012.
- [32] B. Vesnicer and F. Mihelič, "The likelihood ratio decision criterion for nuisance attribute projection in gmm speaker verification," *EURASIP Journal of Advances in Signal Processing*, vol. 2008, Article ID 786431, 11 pages, 2008.
- [33] M. Günther, A. Costa-Pazo, C. Ding et al., "The 2013 face recognition evaluation in mobile environment," in *Proceedings of the 6th IAPR International Conference on Biometrics*, June 2013.
- [34] S. Bengio and J. Marithoz, "The expected performance curve: a new assessment measure for person authentication," in *Proceedings of the Speaker and Language Recognition Workshop (Odyssey)*, pp. 279–284, Toledo, Spain, 2004.
- [35] V. Štruc and N. Pavešić, "The complete gabor-fisher classifier for face recognition under variable lighting," *EURASIP Journal of Advances in Signal Processing*, vol. 2010, no. 31, pp. 1–26, 2010.
- [36] C.-C. Chang and C.-J. Lin, "LIBSVM: a library for support vector machines," *ACM Transactions on Intelligent Systems and Technology*, vol. 2, no. 3, pp. 1–27, 2011.
- [37] S. Nissen, "Implementation of a fast artificial neural network library (fann)," Tech. Rep., Department of Computer Science, University of Copenhagen, Kbenhavn, Denmark, 2003.
- [38] D. E. Maurer and J. P. Baker, "Fusing multimodal biometrics with quality estimates via a Bayesian belief network," *Pattern Recognition*, vol. 41, no. 3, pp. 821–832, 2008.
- [39] N. Poh, T. Bourlai, J. Kittler et al., "Benchmarking quality-dependent and cost-sensitive score-level multimodal biometric fusion algorithms," *IEEE Transactions on Information Forensics and Security*, vol. 4, no. 4, pp. 849–866, 2009.
- [40] W.-Y. Lin and C.-J. Yang, "An enhanced biometric score fusion scheme based on the adaboost algorithm," in *Proceedings of the International Conference on Information Security and Intelligence Control (ISIC '12)*, pp. 262–265, 2012.
- [41] M. Vatsa, R. Singh, A. Noore, and A. Ross, "On the dynamic selection of biometric fusion algorithms," *IEEE Transactions on Information Forensics and Security*, vol. 5, no. 3, pp. 470–479, 2010.
- [42] N. Poh, J. Kittler, and T. Bourlai, "Quality-based score normalization with device qualitative information for multimodal biometric fusion," *IEEE Transactions on Systems, Man, and Cybernetics A*, vol. 40, no. 3, pp. 539–554, 2010.
- [43] N. Poh, D. Windridge, V. Mottl, A. Tatarchuk, and A. Eliseyev, "Addressing missing values in kernel-based multimodal biometric fusion using neutral point substitution," *IEEE Transactions on Information Forensics and Security*, vol. 5, no. 3, pp. 461–469, 2010.
- [44] L. Nanni, A. Lumini, and S. Brahmam, "Likelihood ratio based features for a trained biometric score fusion," *Expert Systems with Applications*, vol. 38, no. 1, pp. 58–63, 2011.
- [45] N. Poh and J. Kittler, "A Unified framework for biometric expert fusion incorporating quality measures," *IEEE Transactions on Pattern Analysis and Machine Intelligence*, vol. 34, no. 1, pp. 3–18, 2012.
- [46] A. Nagar, K. Nandakumar, and A. K. Jain, "Multibiometric cryptosystems based on feature-level fusion," *IEEE Transactions on Information Forensics and Security*, vol. 7, no. 1, pp. 255–268, 2012.
- [47] Q. Tao and R. Veldhuis, "Robust biometric score fusion by naive likelihood ratio via receiver operating characteristics," *IEEE Transactions on Information Forensics and Security*, vol. 8, no. 2, pp. 305–313, 2013.

Research Article

A Joint Learning Approach to Face Detection in Wavelet Compressed Domain

Szu-Hao Huang¹ and Shang-Hong Lai²

¹ Department of Industrial Engineering and Engineering Management, National Tsing Hua University, Hsinchu 300, Taiwan

² Department of Computer Science, National Tsing Hua University, Hsinchu 300, Taiwan

Correspondence should be addressed to Szu-Hao Huang; shhuang@ie.nthu.edu.tw

Received 27 September 2013; Revised 16 January 2014; Accepted 30 January 2014; Published 11 March 2014

Academic Editor: Yue Wu

Copyright © 2014 S.-H. Huang and S.-H. Lai. This is an open access article distributed under the Creative Commons Attribution License, which permits unrestricted use, distribution, and reproduction in any medium, provided the original work is properly cited.

Face detection has been an important and active research topic in computer vision and image processing. In recent years, learning-based face detection algorithms have prevailed with successful applications. In this paper, we propose a new face detection algorithm that works directly in wavelet compressed domain. In order to simplify the processes of image decompression and feature extraction, we modify the AdaBoost learning algorithm to select a set of complimentary joint-coefficient classifiers and integrate them to achieve optimal face detection. Since the face detection on the wavelet compression domain is restricted by the limited discrimination power of the designated feature space, the proposed learning mechanism is developed to achieve the best discrimination from the restricted feature space. The major contributions in the proposed AdaBoost face detection learning algorithm contain the feature space warping, joint feature representation, ID3-like plane quantization, and weak probabilistic classifier, which dramatically increase the discrimination power of the face classifier. Experimental results on the CBCL benchmark and the MIT + CMU real image dataset show that the proposed algorithm can detect faces in the wavelet compressed domain accurately and efficiently.

1. Introduction

Automatically detecting specific objects from images has been a popular research topic for intelligent image analysis and understating with many applications, including face recognition, face tracking, expression cloning, face pose estimation, and 3D head model reconstruction from images. These applications usually assume the face regions are detected correctly as the first step. A lot of researchers from computer vision and image processing have proposed many different approaches for this problem.

Most previous face detection methods focused on detecting faces from a single gray-scale image. The survey paper [1] by Yang et al. classified the face detection methods into four categories, namely, knowledge-based methods, feature-based methods, template matching methods, and appearance-based methods. The appearance-based approach has evolved to a major stream in the face detection research. Since it is very hard to describe a general face in an image by some explicit characterization or feature description, the appearance-based

approach learns a face classifier from a large number of face and nonface examples. The training stage in this approach is to decide a two-class classifier from training examples. After collecting a large number of training face images, most researchers focus on finding a suitable feature representation and a powerful classifier for face detection.

In recent years, with the popularity of digital camera and camcorder, the demand for real-time face detection is increasing. Detecting faces directly in a compressed domain, instead of the original image, is an interesting approach that can save time in the decompression process and reduce the complexity of hardware and software design, especially that most digital images in the world are stored in a compressed form. However, not much previous research work was focused on detecting faces in a compressed domain [2, 3]. Detecting faces directly from a compressed domain can skip parts of the decompression and feature extraction process. In this paper, we propose a novel joint feature representation based on the wavelet coefficients and improve the AdaBoost-based learning for fast and accurate face detection.

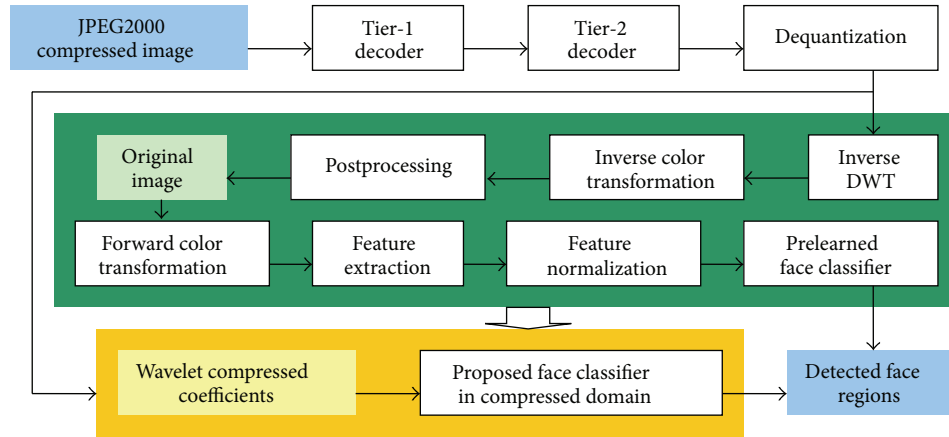


FIGURE 1: The block diagram of face detection in the original image space and the wavelet compressed domain for JPEG2000 [15, 16] compressed images. Note that the decompression and feature extraction blocks in the middle green area can be skipped in the proposed face detector.

In the detection process, the proposed system accesses the corresponding wavelet coefficients and executes the cascade classifier efficiently with a sliding-window search fashion.

Some previous face detection works proved that the wavelet representation [4–7] or Haar-like features [8–14] can well describe faces. However, if we apply the famous AdaBoost face detector [8, 11] with the features replaced by the wavelet coefficients, the resulting accuracy turns out to be unsatisfactory for the following two reasons. Firstly, the feature discrimination is limited by the restricted wavelet compresses feature space. Secondly, it is difficult to implement image contrast normalization directly in the wavelet compressed domain. Thus, this work is motivated by achieving a discriminative face detector in the restricted wavelet feature space. We proposed a paired feature representation and an improved learning framework to achieve a robust classifier with high accuracy in the wavelet compressed domain.

Figure 1 shows the flow diagram of detecting faces directly in the compressed image, such as JPEG2000 [15, 16]. Note that some decompression and feature extraction processes, that is, the blocks in green zone in Figure 1, will be skipped in the proposed method.

Increasing the discrimination in the limited wavelet compressed feature space is the main goal of our learning mechanism. We propose a space warping technique to increase the representation capability of each feature via reweighted learning of the sample distributions. In addition, the joint feature representation projects learning samples onto a paired-feature plane to improve the discrimination power. We propose an improved AdaBoost system based on learning with this joint feature representation.

In order to avoid the information loss in the feature learning procedure, some modified components are developed to preserve more information. For example, the ID3-like quantization is applied after the join feature space representation. Compared with traditional quantization methods, the proposed ID3-like quantization considers the positive and negative sample distribution in 2D pair feature space to

achieve the best discrimination by separating samples into different bins with their labels. Moreover, instead of a binary classifier, Bayesian weak learners are adopted to compute the ratio between positive and negative samples for each bin as the output for the classifier. With simple prelearned look-up tables, the weak classifier can provide more detailed classification result than a hard decision.

Finally, the trained face classifier can be applied directly in the wavelet compressed domain with very efficient calculation. The learning framework preserves the essential information in quantization tree and some look-up tables. The execution process of the face detector is simplified to some low-complexity computation, such as accessing corresponding coefficients and querying look-up tables. Although the input features of the proposed algorithm are restricted to the wavelet compressed coefficients without normalization, our experimental results show the accuracy of the proposed face detector is comparable to some state-of-the-art methods which detect faces in the uncompressed image domain.

The rest of this paper is organized as follows. Section 2 reviews the previous related works and the AdaBoost learning algorithm [8, 11], since our learning framework is based on this algorithm. Section 3 gives the details of the proposed learning framework for our face detector, including feature space warping, joint feature representation, ID3-like quantization, and weak probabilistic classifier. Subsequently, we describe the execution flow of the proposed face detector applied in the wavelet compressed domain in Section 4. In Section 5, we show several experimental results on two popular benchmarking databases. Finally, we conclude this paper in Section 6.

2. Related Works

Automatic object detection is an important issue in computer vision and image. In addition to face detection, researchers have proposed algorithms for car detection [5], pedestrian detection [6, 17–20], and even generic object detection [21]. In this section, we will first briefly review some previous face

detection techniques. Then, we will describe the AdaBoost learning algorithm [22, 23].

2.1. Previous Face Detection Techniques. Our focus in this paper is on frontal face detection from still gray-scale images. The survey paper [1] by Yang et al. reviewed some face detection methods in the early period, such as manually established facial rules and predefined symmetric attributes. These methods are intuitive but lack robustness, because the natural sense includes too much variety and the simple heuristic rules or models can not cover all possible variations well. The appearance-based methods became the mainstream of face detection research. It normally consists of collecting a lot of training samples, projecting these samples onto an appropriate feature space, and applying machine learning techniques to form a classifier from the distribution of samples in the feature space. Most initial appearance-based methods used the pixel brightness values from the sliding windows in an image as the features. Then, some well-developed learning algorithms, such as support vector machine [24], neural network [25], eigen space analysis [26], and Sparse Network of Winnows [27], were applied to develop the face detectors.

In order to tolerate more scale and pose variations, Fleuret and Geman [28] proposed a coarse-to-fine face detector based on an edge feature descriptor. Schneiderman and Kanade [5] employed the histogram of wavelet features for face and car detection with out-of-plane rotation. In the meantime, Papageorgiou and Poggio [6] developed their multipurpose object detection system by using the wavelet features with the support vector machine classifier. In addition, Heisele et al. [29] partitioned a face region into several local patches and applied support vector machines to develop a component-based face detector. In 2001, Viola and Jones [8] presented the first real-time face detection system based on AdaBoost learning in conjunction with block sum difference features easily computed with an integral image. The efficient computation and acceptable accuracy of this system bring the face detection into real applications. More details in the AdaBoost learning will be discussed in the next subsection. Later, Liu [30] applied Bayesian Discriminating Features (BDF) technique to develop an accurate face detection system with a very low false detection rate.

Although detecting faces in gray-scale images is the most general approach, some researchers also employed the color information to simplify the face detection problem. By using the color information, the face detection system can extract more discriminative information and increase the speed and accuracy dramatically. Traditional works [4, 31] collected a large number of pixels of skin regions to determine a skin color distribution and filter. Hsu et al. [32] proposed a face detector that contains a lighting compensation step and eye/mouth color maps. Huang and Lai [7] developed a color face classifier by learning face appearance in the color feature space. Tsalakanidou et al. [33] used extra 3D range data acquired by a 3D sensor to improve the performance of color face detection under illumination and expression variations.

Detecting faces in video [7, 34, 35] has been another interesting face detection approach in recent years. Combining video tracking techniques and the face appearance

models can extend the face detection from still images to video sequences. These methods proved that they can recover missed face detections and eliminate false positives by temporally integrating the face detection results.

Furthermore, multipose face detection techniques have been researched to extend the previous frontal face detection methods in recent years. Schneiderman and Kanade [5] first applied the statistical histogram representation for detecting faces in profile as well as frontal views. Then, a convolutional neural network architecture [36] and an AdaBoost method with pose estimator [10] are proposed to extend the upright and frontal face classifier to detect faces with large pose variations, with rotation up to ± 30 degrees in image plane (RIP) and up to ± 60 degrees for out-of-plane rotation (ROP). More recently, Huang et al. [14] proposed the width-first-search structure and vector boosting algorithm to accomplish the face detection with arbitrary RIP angles and the ROP angles up to ± 90 degrees.

In addition, some more related works were developed for different problem settings and different applications. For example, detecting small faces from degraded images [13] focused on detecting low-resolucional faces. There were previous methods proposed to detect faces in the DCT compressed domain [2, 3], which is somewhat related to the problem setting of this paper. The major difference between the previous works and the proposed method is that our method can be applied directly in the wavelet compressed domain without wavelet decomposition or intensity normalization, and it can still achieve high accuracy comparable to the state-of-the-art face detection methods.

In addition to the face detection, face identification and recognition is another challenging problem which had been widely discussed in computer vision research field. After the face region is detected precisely from the input image, the face recognition system would analyze the frontal facial image patch and determine or verify the identity of the person. Zhao et al. [37] had extensively reviewed early machine recognition systems and surveyed several psychological studies which focused on human faces. These works can be roughly categorized into two types: face recognition from single still image and face recognition from video sequences. Wright et al. [38] proposed a new classification framework based on sparse representation techniques and provided new insights into two crucial issues: feature extraction and robustness to occlusion. To solve the face identification under uncontrolled environments or with a lack of training samples, Schwartz et al. [39] employed a large and rich set of feature descriptors and used partial least squares regression model to increase the discriminant ability of recognizer across varying conditions.

2.2. AdaBoost Learning. AdaBoost, short for adaptive boosting, is a meta-algorithm that can cooperate with other machine learning techniques to improve their performance. The AdaBoost algorithm was originally proposed by Freund and Schapire [22], and this original algorithm is listed in Algorithm 1.

As shown in Algorithm 1, after a series of labeled data put into the learning machine, we need to initialize the weights of each learning sample. In most two-class classification

Input: sequence of N labeled examples $\langle (x_1, y_1), \dots, (x_n, y_n) \rangle$
 Distribution D over N examples
 Weak learning algorithm **WeakLearn**
 integer T specifying number of iterations

Initialize the weight vector $w_i^1 = D(i)$ for $i = 1, \dots, N$

Do for $t = 1, 2, \dots, T$

- (1) Set $p^t = w^t / \sum_{i=1}^N w_i^t$
- (2) Call **WeakLearn**, providing it with the distribution p^t ; get back a hypothesis $h_t: X \rightarrow [0, 1]$
- (3) Calculate the error of h_t : $\epsilon_t = \sum_{i=1}^N p_i^t |h_t(x_i) - y_i|$
- (4) Set $\beta_t = \epsilon_t / (1 - \epsilon_t)$
- (5) Set the new weight vector to be $w_i^{t+1} = w_i^t \beta_t^{1 - |h_t(x_i) - y_i|}$

Output the hypothesis

$$h_f(x) = \begin{cases} 1 & \text{when } \sum_{t=1}^T \left(\log \frac{1}{\beta_t} \right) h_t(x) \geq \frac{1}{2} \sum_{t=1}^T \log \frac{1}{\beta_t} \\ 0 & \text{otherwise} \end{cases}$$

ALGORITHM 1: The AdaBoost algorithm [22].

problems without prior knowledge of the training examples, the weight summations of all positive and negative data will be set equally and each learning sample belonging to the same category has the same weight. Another issue is about an adequate quantity of training samples, which is very difficult to determine for a practical machine learning problem. Bootstrap learning architecture provides a solution to resolve this problem.

In the AdaBoost algorithm depicted in Algorithm 1, WeakLearn is a function or an algorithm that performs the hypothesis to classify the input samples into different categories by considering the current sample weights. The word “weak” means the hypothesis is not expected to be very powerful since it only uses very simple features and calculation in the weak classifier. In most applications, the WeakLearn function is normally designed in a simple way, such as a binary function of a feature value. The basic idea is that the WeakLearn classification functions are very easy to calculate and at least slightly better than random guess. Thus, the AdaBoost learning algorithm is applied to select a set of discriminating and complementary weak classifiers to form a final strong classifier.

The input integer T specifies the number of iterations in the learning system. One obvious advantage of AdaBoost is that it did not need any tuning parameters except T . The selection of T depends on different applications. Selecting a larger T value will decrease the error measure in the training data, but it may lead to the overfitting problem. The value h_t is decided in each iteration and the sample weights are updated from the error measure. The basic idea in the AdaBoost is to assign more weighting to the samples misclassified in the previous iterations to achieve a global optimization process.

AdaBoost has been very popular in computer vision and image processing research fields since the first real-time face detection method proposed by Viola and Jones [8]. For face detection, there were some improved versions, such as Kullback-Leibler Boosting [40], FloatBoost [9], and asymmetric AdaBoost [41] algorithm, to increase the accuracy and efficiency of learning performance. Some modifications of

the learning framework extended Viola and Jones’ method to different applications, such as detecting faces in video [7], detecting faces in degraded images [13], and detecting pedestrians via motion and appearance patterns [17]. A similar technique of AdaBoost was also applied in different feature space to solve other two-class learning problems. The image retrieval with relevance feedback [42, 43] was also an important application of AdaBoost.

At the end of this section, we list some improved versions of the AdaBoost algorithm in Table 1. Although most applications applied the AdaBoost algorithm to solve the two-class classification problems, there were some extensions of the AdaBoost algorithm to the regression [22] and multiclass classification problem [23].

3. Proposed Learning Method

The proposed learning system is an improved version of Viola and Jones’ face detector [8, 11] to adapt to our requirement, that is, detecting faces directly from wavelet compressed domain. The fundamental structure is similar to most appearance-based learning methods. An initial training data set, including 4916 face image blocks and 7872 nonface (negative) image blocks, is prepared for the learning of the face classifier. When the trained AdaBoost classifier can separate samples in the training dataset well, the current classifier is applied to a large image database to accumulate false positive blocks as the negative samples in the next training dataset. In the bootstrap learning system, the growing negative learning samples are extracted from 100 different categories of Corel PhotoStock database, totally 10000 natural images.

For the proposed face detector, a 3-leveled wavelet transformation is applied for each training image to obtain the 576-dimensional features. The LL band of highest level from 24×24 images is skipped because this part cannot be recovered when we execute the face detection directly from compressed domain without any decompressed process.

TABLE 1: Variants of the AdaBoost algorithm.

Algorithm	Authors and references	Description
AdaBoost	Freund and Schapire [22]	Original algorithm
RealBoost	Schapire and Singer [23]	A real version of weak hypothesis
AdaBoost.M1/M2	Freund and Schapire [22]	Multiple class extension of original AdaBoost algorithm
AdaBoost.R	Freund and Schapire [22]	Solving regression problems
AdaBoost.MO/MH/MR	Schapire and Singer [23]	Multiclass, multilabel extensions
Kullback-Leibler Boosting	Liu and Shum [40]	Incorporate Kullback-Leibler divergence into AdaBoost
FloatBoost	Li and Zhang [9]	Replace exponential error function by backtrack mechanism

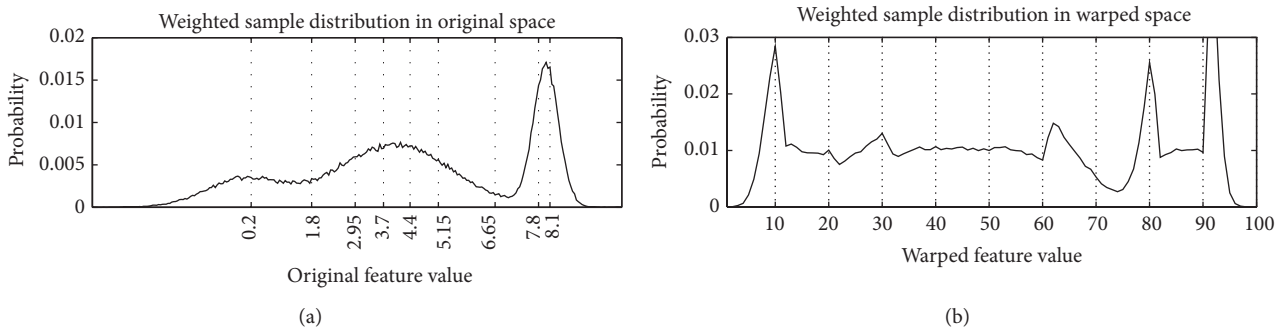


FIGURE 2: The feature space warping representation: (a) the landmarks in the original distribution and (b) the weighted distribution in the warped feature space.

3.1. Learning System Overview. The goal of the improved AdaBoost learning algorithm is to learn an efficient face detector from a restricted wavelet feature space. Without wavelet decomposition and intensity-based normalization processes, the feature discrimination power for face detection is weak. The improved AdaBoost learning system contains four major improvements based on two principles: higher discrimination and more information preservation. Algorithm 2 gives an overview of the proposed system. More details of each step will be described in the following parts of this section.

3.2. Feature Space Warping. The function of feature space warping is similar to the histogram equalization for image enhancement. The basic idea is that we should use more levels in the area with dense data distribution and less levels in the area with sparse data for the feature quantization. In actual implementation, the distribution of the training data samples should be reweighted by the current weights. We need a nonlinear transformation for each feature to increase the feature representation capability.

A discrete cumulative density function is estimated to find some landmark points, such as the feature value located in 50% weighted distribution. After we have these landmarks, a simple space warping, which linearly interpolates samples between these points, is applied. Figure 2(a) shows the landmarks of original weighted data distribution, and Figure 2(b) shows the weighted distribution after space warping. After the space warping process, the distance measure of a single feature between two different samples is driven by the current sample weights and distributions.

3.3. Joint Feature Representation. Schneiderman and Kanade [5] have first adopted the idea of joint distribution of a pair of features to represent objects. Mita et al. [12] simply extended the AdaBoost detector proposed by Viola and Jones and combined three binary weak classifiers to the three-digit code learning. In the proposed method, we map all learning samples onto paired wavelet feature spaces and estimate the corresponding 2D distributions before selecting the weak classifiers. Because of the feature space warping step, the data distribution appears approximately uniform when only considering a single feature. After the joint feature representation, mapping data to higher dimension is a strategy to increase the feature variety instantly. With the processes of permutation and combination, it provides higher possibility to explore more discrimination.

The original feature dimension for a three-level wavelet transform of a 24-by-24 block image is 576. After the cross-level and cross-band combinations of a pair of wavelet coefficients, the feature dimension is increased to 160,461 dramatically without extracting any additional information. Instead of the paired feature representation, a cubic or even higher dimensional mapping is another aggressive possibility. However, the efficiency of the AdaBoost learning system should be considered, especially when the computational cost for the AdaBoost learning from the paired feature spaces is already very high.

The major design principle for the feature space warping and the joint feature representation is to explore high discrimination from the limited set of wavelet coefficients. After the joint feature representation is created, the following steps are designed for preserving more information in the

(i) Given example images $(x_1, y_1), \dots, (x_n, y_n)$, where y_i takes the value 0 for negative examples or 1 for positive examples, respectively.

(ii) Initialize weights $w_{1,i} = 1/(2m)$ for $y_i = 0$ or $w_{1,i} = 1/(2l)$ for $y_i = 1$, where m and l denote the total numbers of negative and positive images, respectively.

(iii) For $t = 1, \dots, T$

- (1) Estimate feature space warping function $W_j(x_i)$ via the sample distribution $[x_{1,j}, x_{2,j}, \dots, x_{n,j}]$ and weights w_t
- (2) For each possible feature pair (j, k) , map all training sample onto paired plane via warped feature value $W_j(x_i)$ and $W_k(x_i)$
- (3) Apply ID3-like tree method to each axis of paired feature plane in rotation, and find the quantization function $f_{j,k}(x_i)$ which will try to separate positive and negative samples into different bins.
- (4) Compute the conditional probability as the Bayesian classification result for each weak classifier $C_{j,k}(x_i)$.
- (5) Estimate the error $\varepsilon_{j,k}$ for each feature pair (j, k) as follows:

$$\varepsilon_{j,k} = \sum_{i=1}^n w_{t,i} \times |y_i - C_{j,k}(x_i)|$$
- (6) Select the paired feature $h(t)$ with minimum error $\varepsilon_{j,k}$

$$h(t) = \arg \min_{(j,k)} \varepsilon_{j,k}$$
- (7) Update the weights for all training samples as follows:

$$w_{t+1,i} = w_{t,i} \times \beta_t^{1-|y_i - C_{h(t)}(x_i)|},$$
 where $\beta_t = \varepsilon_{h(t)} / (1 - \varepsilon_{h(t)})$.
- (8) Normalize the weights by

$$w_{t+1,i} = \frac{w_{t+1,i}}{\sum_{i=1}^n w_{t+1,i}}$$

(iv) The final classifier is given by

$$SC(x) = \begin{cases} \text{face} & \text{when } \sum_{t=1}^T \alpha_t C_{h(t)}(x) \geq \frac{1}{2} \sum_{t=1}^T \alpha_t, \\ \text{non-face} & \text{otherwise} \end{cases},$$

where $\alpha_t = \log(1/\beta_t)$.

ALGORITHM 2: The proposed AdaBoost-based learning algorithm for face detection.

feature quantization before going into the AdaBoost learning procedure.

3.4. ID3-Like Plane Quantization. After the joint feature representation, we can estimate the positive and negative data distributions for each feature pair from the training data. To develop weak classifiers for all possible pair features for AdaBoost learning, we quantize the paired feature plane for computing the conditional probabilities of the joint features for positive and negative cases. Our strategy is to segment the paired feature plane into several representative regions and use the ratio of the conditional probabilities in each quantized region for classification. In other words, we want to quantize the continuous paired feature plane such that each quantized segment has its own dominant sample label. With this strategy, the system can separate the positive and negative into different segments as good as possible to achieve high discrimination capability.

To achieve the above goal, we employ the ID3-like plane quantization on the paired feature space. This quantization for each feature is determined based on the distribution of the training data with the current weight function. Compared to other traditional quantization methods, our ID3-like approach can retain more information with a little bit more

computational effort. The main algorithm of ID-3 decision tree [44] is to select the best boundary in each node such that it can divide the data passing through this node into two classes with the highest information gain. It means that the boundary is selected such that each branch contains as much data of the same class as possible. In other words, we want to find appropriate boundaries to divide the data into intervals of maximal uniformity.

In the ID3-decision tree, we first define the entropy and information gain as follows:

$$\begin{aligned} \text{Entropy}(S) &= -p(y_i = 1 | x_i \in S, W_t) \\ &\quad \times \log p(y_i = 1 | x_i \in S, W_t) \\ &\quad - p(y_i = 0 | x_i \in S, W_t) \\ &\quad \times \log p(y_i = 0 | x_i \in S, W_t), \\ \text{Gain}(S, A) &\equiv \text{Entropy}(S) - \sum_{v \in \text{leaf_nodes}} \frac{|S_v|}{|S|} \text{Entropy}(S_v), \end{aligned} \quad (1)$$

where W_t is the weighting function for each training sample at the t th iteration and the symbol A denotes a function that can classify samples from a parent node S to a different leaf node S_v . Because our ID3-like balance tree quantization is

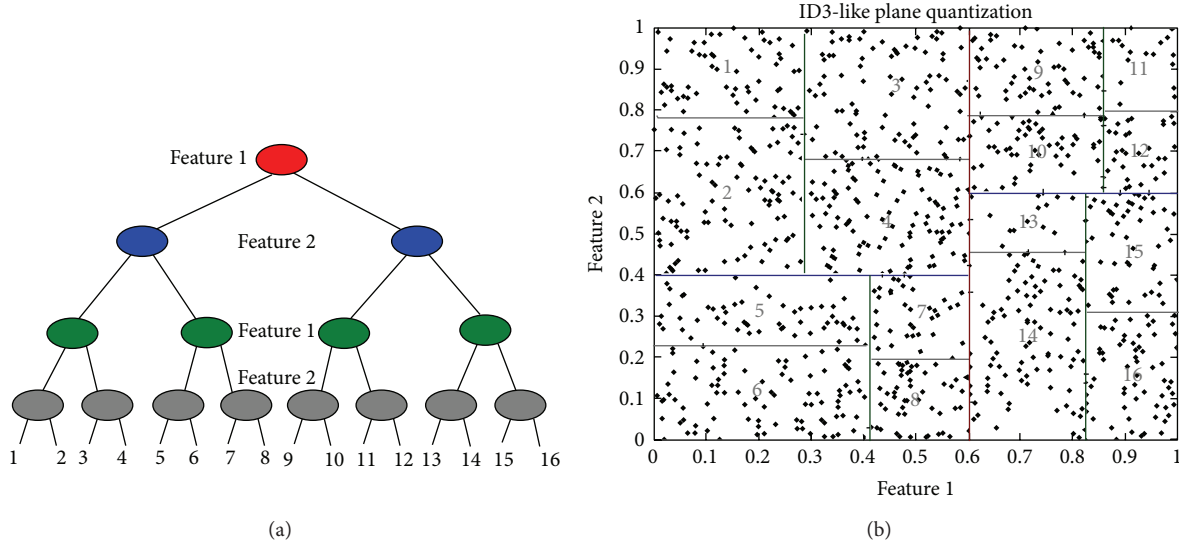


FIGURE 3: ID3-like plane quantization representation: (a) a 4-layer ID3 tree structure and (b) the corresponding quantization regions and boundaries in the feature plane.

a binary tree, the function A can be represented by a list of thresholds that divide a feature value into left or right leaf nodes recursively. Then, we can select the best seed value that maximizes the information gain as follows:

$$\text{selected}_{\text{boundary}} = \arg \text{Max}_A (\text{Gain}(S, A)). \quad (2)$$

First, entering all learning samples into root node can find the best boundary in one of the axes to separate the space into two parts. In these two regions, we turned the seed selection process in another axis independently. The ID3-like plane quantization involves repeating the above process recursively and alternatively along the two axes to determine a quantization function $f_{j,k}(x)$. If the processing time is a critical issue, histogram equalization can provide the initial seeds to speed up the computation with similar performance. In practical setting, a four-layer decision tree is constructed just like Figure 3(b) to quantize the pair feature plane into 16 different regions, as shown in Figure 3(a).

3.5. Weak Probabilistic Classifier. For each pair of features, we can train a weak classifier based on the corresponding joint conditional probability determined from the training data. The AdaBoost training algorithm is then used to select some powerful and complementary weak classifiers and combine them to form a final classifier for face detection. For each weak classifier, we apply the Bayes rule based on the conditional probability density function in each interval to decide the class. By thresholding the ratio of face to nonface conditional probabilities for a given paired feature vector in a quantized interval, we obtain a number of weak classifiers that can be used in the AdaBoost training algorithm.

Making a binary decision in the weak classifier does not fully exploit the information computed in the conditional probabilities. Therefore, we replace the binary decision in the

weak classifier by the conditional probability in the AdaBoost learning algorithm.

By applying the Bayes rule, we can compute the conditional probability as follows:

$$\begin{aligned} C_{j,k}(x_i) &= \frac{p(y_i = 1 | f_{j,k}(x_i), W_t)}{p(y_i = 0 | f_{j,k}(x_i), W_t) + p(y_i = 1 | f_{j,k}(x_i), W_t)} \\ &= (p(f_{j,k}(x_i) | y_i = 1, W_t)) \\ &\quad \times \left(p(f_{j,k}(x_i) | y_i = 1, W_t) + p(f_{j,k}(x_i) | y_i = 0, W_t) \right. \\ &\quad \left. \times \frac{p(y_i = 0)}{p(y_i = 1)} \right)^{-1}, \end{aligned} \quad (3)$$

$$\begin{aligned} p(f_{j,k}(x_i) | y_i = 1, W_t) &= \frac{\sum_{\text{all } m, \text{ let } f_{j,k}(x_m) = f_{j,k}(x_i)} y_m W_{t,m}}{\sum_{m=1}^n y_m W_{t,m}}, \end{aligned} \quad (4)$$

where $C_{j,k}(x)$ means the probability of the (j, k) th pair feature for image x to be class 1, that is, face class and $f_{j,k}(x)$, which denotes the leaf node index of ID3 tree determined from the plane quantization. Equation (4) measures the conditional distribution of $f_{j,k}(x)$ under the situation that label $y_i = 1$ and the sample weights w_t are updated after t iterations of the AdaBoost learning algorithm. Equation (3) returns a probability value between 0 and 1, which indicates the face conditional probability. We use $C_{j,k}(x)$ to be the Bayesian weak classifier in the AdaBoost system.

In our implementation, we segment the paired feature plane into 16 regions and a look-up table containing 16

- (i) Given a test image represented in N -layered wavelet compressed domain
- (ii) Each layered-coefficient plane L_i is composed of three sub-bands, L_i^{LH} , L_i^{HL} and L_i^{HH}
- (iii) Preprocessing
 - (1) Apply the bi-linear interpolation to down-sample each sub-band to 1/1.25, 1/1.5, and 1/1.75 scales, respectively, and form three additional wavelet layer sets.
- (iv) For each of these four sets of the wavelet-layer representation, run the sliding window face detection with the scale i initialized to 1
 - (1) Apply the AdaBoost face classifier to each sliding window which is constructed from the coefficients in the planes from L_i to L_{i+2} .
 - (2) If the classifier determines the region is a face, calculate and save the position and size of the corresponding window in the original image space based on the shift, downsample, and layer information.
 - (3) Repeat the previous two steps with the scale i incremented by one until the scale $i > N - 2$.
- (v) Postprocessing
 - (1) Eliminate the overlapped face regions based on the scores provided by the AdaBoost classifier.
 - (2) Output the detected faces.

ALGORITHM 3: The proposed face detection algorithm in the wavelet compressed domain.

Bayesian probabilities is used for the AdaBoost learning and testing processes.

4. Detecting Faces on Wavelet Compressed Domain

In this section, we describe how the trained AdaBoost face classifier is applied for face detection from the wavelet representation of the whole image. The previous AdaBoost face detector is featured for its simple computation. Although we add several complicated components into our learning system to increase the overall discrimination for face detection from a restricted feature space, the resulting AdaBoost classifier only needs a very small amount of computation with some look-up tables and quantization tree structures. Algorithm 3 depicts the complete algorithm of the proposed face detection on the wavelet compressed domain. Sections 4.1 and 4.2 give more details of our implementation.

4.1. Face Detection in a Single Sliding Window. First, we describe how the trained AdaBoost classifier is applied in a sliding window search strategy for face detection from a wavelet compressed image. When focusing on a single block of a whole image to determine whether it is a face region, we can access the corresponding wavelet coefficients from HL, HH, and LH bands of three contiguous levels. Since the LL bands for all levels are not available without a complete decompression process, we do not include them into our feature space learning.

In each iteration t , the selected hypothesis $h_t(x)$ from our system refers to a weak classifier associated with a feature pair (j, k) . The first step is to retrieve the coefficient values of features j and k . These two feature values are quantized through the corresponding ID3-like plane quantization, as described above, with only four comparison operators. Then, a simple look-up table is used to access the corresponding weak classifier output value for the quantized feature region, which can be done very efficiently. Finally, the accumulated

sum of the products of α_t , provided from the AdaBoost training, and the weak Bayesian classifier probability output is used to determine if this window is a face region or not.

4.2. Face Detection in a Whole Image. When detecting faces in a whole image, the position and scale of sliding windows should cover all the possible image blocks where faces could appear. The minimal detection window is as large as the training samples with 24×24 pixels. The shift of the sliding window in the wavelet compressed domain can be easily implemented by adding relative shift terms when seeking the corresponding feature values. The shift at one higher level is twice the shift at the previous level. Figure 4 is a simple chart that describes the corresponding spatial relationship of the window shifting. The gray solid rectangle shifts one coefficient in level 3 from the red rectangle. The relative shifts in level 2 and level 1 are 2 and 4, respectively. Recovering to the original image domain, the gray detected window shifts 8 pixels in horizontal direction from red one. This kind of scanned windows with full correspondence is not dense enough for face detection. Therefore, shifting windows of the corresponding coefficients in lower level and rounding the shifts in higher level could achieve higher accuracy.

In addition to the shift, the various scales of the sliding windows in the compressed domain are not easy to implement without wavelet decomposition. The multilevel structure of wavelet decomposition provides a basis to find the corresponding features from different scales, but it is restricted to the detected windows with power-of-2 scales of the template face window. For example, if we can detect faces of size 48-by-48 from wavelet levels $N - 2$, $N - 1$, and N , then the coefficients related to 96-by-96 faces are positioned in levels $N - 3$ to $N - 1$. In order to detect faces of sizes between these two scales, we apply the bilinear interpolation to the wavelet coefficient plane. Downsampling these coefficient planes to 1/1.25, 1/1.5, and 1/1.75 of the original width and height will create three different starting scale bases. Thus, between sizes 24 and 48, we can have sizes 30, 36, and

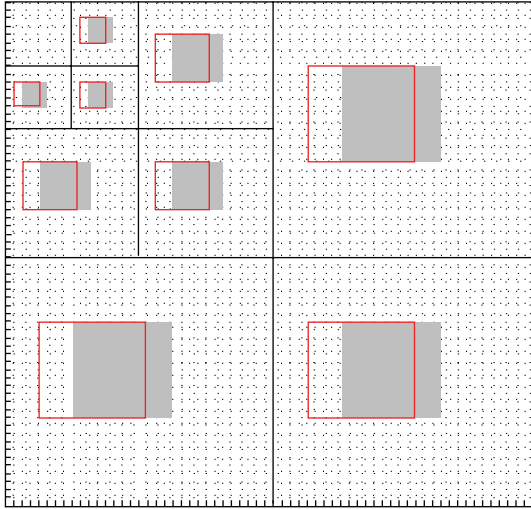


FIGURE 4: The corresponding coefficients in compressed domain of different detected window.

42 for different window widths with the same framework. The downsampled plane with 1/1.25 ratio can provide the coefficients of 30-by-30 detection windows and its higher wavelet levels should cover the sizes 60,120,..., and so forth, in the original image scale. An additional postprocessing is required to decrease the detected face regions which are overlapped with each other. The positive windows with higher scores in strong classifier will be reserved as the final decision.

5. Experimental Results

In this section, we show four sets of experiments to verify the improvement of the proposed AdaBoost learning system to demonstrate the performance and efficiency of the proposed face detector directly on the wavelet compressed domain. We first adopted CBCL face database which contains separate training and testing image datasets for evaluating the AdaBoost learning results. Totally 24,045 testing clipped images are examined after one-time learning from 6,977 training image blocks. Then, the MIT + CMU face database is used for the testing of face detection from whole images with bootstrap learning. Our experimental results show that the proposed learning system significantly improves the accuracy of face detection on the restricted wavelet compresses domain.

5.1. Learning System Improvement Benchmarks. To justify the improved AdaBoost-based learning system, we need a benchmark to evaluate the performance of the proposed method. MIT CBCL face dataset provides a fair benchmarking database to compare the performance of face classifiers. The training dataset contains 6,977 image blocks (2,429 face blocks and 4,548 nonface blocks) and the testing data set is composed of 24,045 image blocks (472 face blocks and 23,573 nonface blocks).

All the experiments in this part have three different learning system settings: AdaBoost learning with Viola and

Jones' feature space [11], AdaBoost learning in conjunction with the 567-dimensional wavelet feature space, and the proposed learning system on the paired wavelet feature space.

The first benchmarking experiment is performed for each of the three learning systems with 10 weak classifiers only. The results are depicted in Figure 5(a). It is obvious that changing the feature space from the original feature space in Viola and Jones' method to the restricted wavelet feature space degrades the face detection accuracy dramatically. However, with our improved AdaBoost learning, the detection rates of the proposed face detector are better than all the other two systems under the same false positive rates. One may argue that the comparison is unfair because the proposed paired feature learning strategy adopts two features for each iteration, that is, weak classifier. Therefore, we performed another experiment, shown in Figure 5(b), which restricted each of the three final classifiers can only include 20 wavelet coefficients. The result is more reasonable from our expectation. When the false alarm is equal to 0.2, the detection rate of Viola and Jones' method is 0.79. The same learning method with wavelet features only has 0.65 detection rate, while the proposed system with paired wavelet features can improve the face detection rate to 0.76. In addition, the proposed method can obtain better results in this benchmark comparison when the false alarm rate increases to 0.35.

In order to examine the limit of the learning systems, we increase the accessing feature number to 200. In other words, the standard AdaBoost classifiers contain 200 iterations and the proposed paired feature learning system consists of 100 weak classifiers. As shown in Figure 5(c), it has similar result to that of Figure 5(b), and the proposed system outperforms Viola and Jones' method when the false alarm rate is larger than 0.185.

5.2. ROC Curve of MIT + CMU Dataset. The second experiment is mainly used to examine the performance of the proposed learning system after bootstrap learning. Our system is designed for face detection in wavelet compressed domain, so the input to our face detection system is the wavelet representation of the whole testing image.

MIT + CMU face dataset is widely used in the face detection research. There are 130 gray-scale images containing 507 faces in this dataset. Figure 6 depicts three ROC curves and detection rates with respect to different numbers of false positives, obtained by applying the three different face detection algorithms to the entire dataset. The experimental results show that the proposed method can improve the detection rate from 0.68 to 0.89 under 100 false positives, which is near the 0.92 detection rate in raw image.

The curve of Viola and Jones' method was published in their paper [11] and adopted here for comparison. Another ROC curve is obtained by applying the same AdaBoost learning algorithm with the wavelet features. It is obvious from Figure 6 that the proposed learning system with the paired wavelet features improves the ROC curve with the restricted wavelet features significantly and it is close to the ROC curve of Viola and Jones' face detector, which is based on a large number of features.

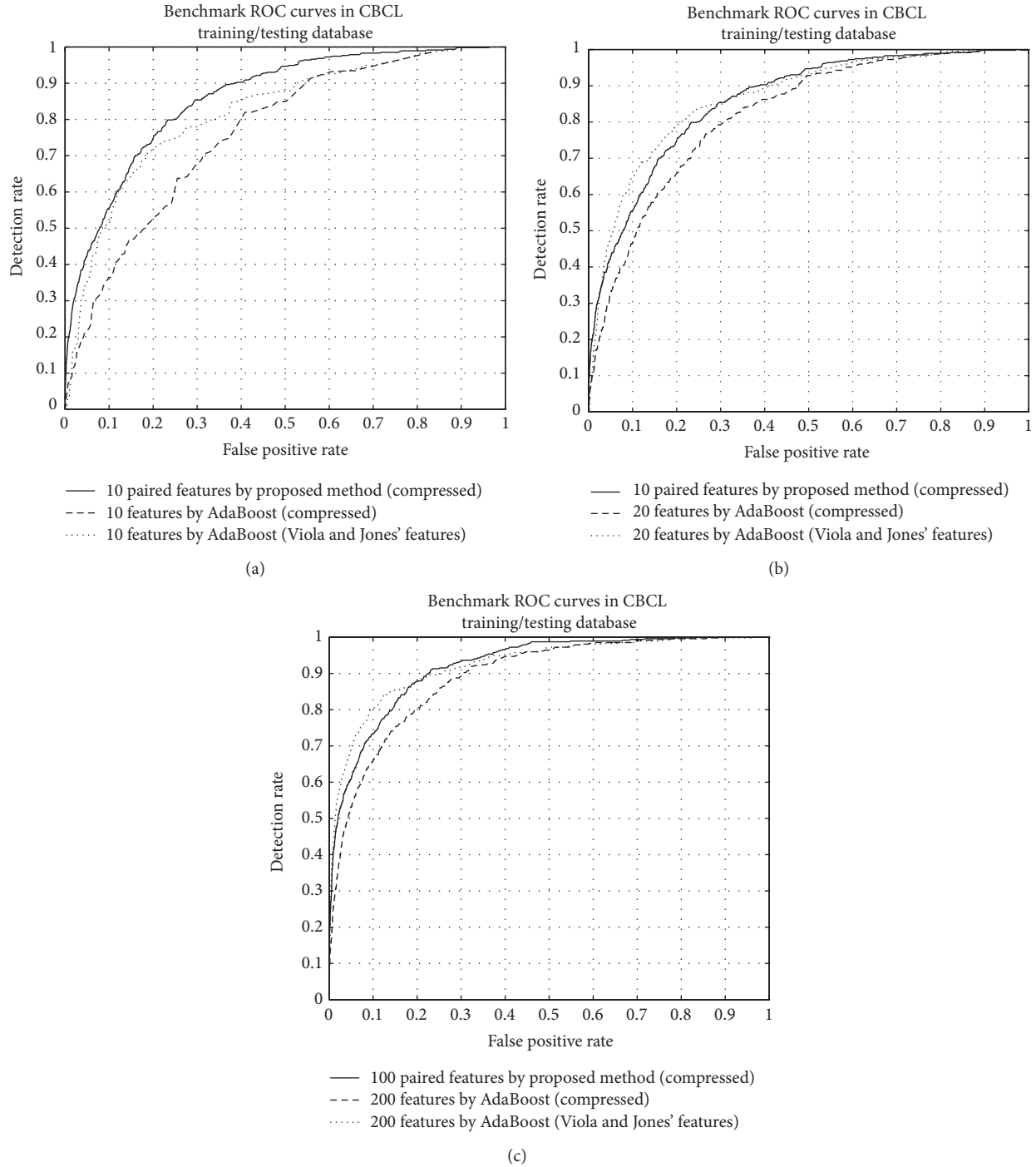


FIGURE 5: The benchmark comparison on the CBCL database: (a) three different learning systems with 10 weak classifiers adopted, (b) three different learning systems with 20 features adopted, and (c) three different learning systems with 200 features adopted.

5.3. More Comparisons on MIT + CMU Dataset. In this experiment, we provide more results and comparisons between the proposed face detection system and other systems. The experimental setting is similar to that in the previous two experiments. The detection rates under different numbers of false detection of the proposed face detector and some previous methods on the MIT + CMU face dataset are depicted in Table 2.

In this comparison, we can see that the accuracy of the proposed method is about 1%~5% lower than that of Viola-Jones' method under different rates of false positives. We think it is a reasonable accuracy decrease since the proposed face detection algorithm is restricted to the limited wavelet feature space and it can save the decompression cost. Figure 7 depicts the face detection results of the proposed algorithm in the test images of MIT + CMU dataset.

TABLE 2: The detection rates under different false detections of several different face detection systems.

Detection method	False detections							
	10	31	50	65	78	95	167	422
AdaBoost (compressed)	56.1%	62.5%	63.9%	65.9%	66.5%	67.9%	70.9%	75.9%
Proposed method (compressed)	79.8%	85.2%	87.3%	88.1%	88.5%	89.2%	90.9%	93.3%
Viola and Jones [8]	76.1%	88.4%	91.4%	92.0%	92.1%	92.9%	93.9%	94.1%
Viola and Jones (voting) [11]	81.1%	89.7%	92.1%	93.1%	93.1%	93.2%	93.7%	—
Rowley et al. [25]	83.2%	86.0%	—	—	—	89.2%	90.1%	89.9%

TABLE 3: The execution time (ms) of the proposed face detector and the original AdaBoost face detector for detecting faces from wavelet compressed images.

Image size (pixels)	Sliding windows	Tier 1 + Tier 2	Method	IDWT	Integral images	Feature extraction	Classifiers	Processing time	Total time
3320 × 240	8,411	27.6	Original	18.4	1.8	19.5	9.7	49.4	77.0
			Proposed	—	5.4	—	14.1	19.5	47.1
640 × 480	41,243	95.7	Original	75.2	7.2	96.6	47.5	226.5	322.2
			Proposed	—	21.4	—	69.3	90.7	186.4
1024 × 768	113,789	207.4	Original	183.7	18.3	263.8	131.1	596.9	804.3
			Proposed	—	55.3	—	190.7	246.0	453.4
1600 × 1200	291,580	488.1	Original	432.9	43.7	677.1	334.2	1,487.9	1,976.0
			Proposed	—	135.7	—	492.8	628.5	1,116.6

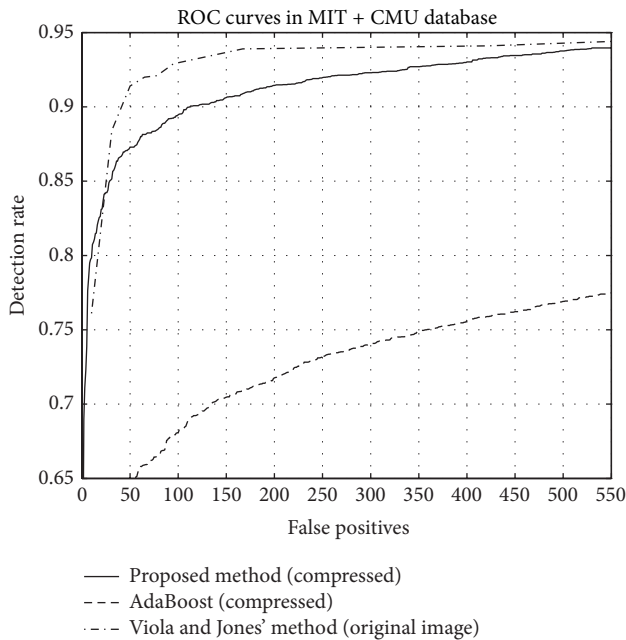


FIGURE 6: The ROC curve of the final classifier in MIT + CMU database.



FIGURE 7: Face detection results of proposed methods in MIT + CMU dataset.



FIGURE 8: False positives and missing of proposed face detection methods in MIT + CMU dataset.

The experimental results show that our system can detect face regions correctly not only in the natural photos but also in the paintings and sketches. Moreover, Figure 8 displays some false positives and missing detection of proposed method in the same database. We observe that the proposed system misses several faces with partial occlusions or higher rotation angles as shown in Figure 8. In addition, balancing the number of missing and false positive rate is critical for a binary decision system design. The false positives shown in Figure 8 can be eliminated with a tighter detector and the detection rate will also be decreased to 87.3%.

5.4. Execution Time Analysis. Table 3 depicts the execution time of the components in the proposed face detection system that operates directly in the wavelet domain and the original AdaBoost face detector [8, 11] that detects faces after wavelet decomposition. This experiment is performed on a

regular PC with Intel E6320 CPU (Dual 1.87 GHz Cores) and 2 G RAM. The face detector was applied from 36×36 blocks to full image size with 1.25 times scale increase. In the spatial domain, the sliding window is scanned on the image for face detection with step 1/8 window width in both horizontal and vertical directions for speed consideration.

The proposed wavelet-domain face detector skips the IDWT procedure and the feature extraction process to achieve more efficient detection. Our experiments show that the processing time, which skips the tier 1 and tier 2 decoding time, on a 320×240 image is only 19.5 ms. When discussing the total execution time of detecting faces from a compressed image, our face detector only requires 57% computation time of the original AdaBoost face detector [8, 11].

6. Conclusion

In this paper, we proposed a face detection system working directly in the wavelet compressed domain. The main contributions of the proposed face detection algorithm are an improved AdaBoost-based learning framework and a series of joint feature representation strategies, which can produce a strong face classifier on the restricted wavelet feature space.

The proposed face detection system involves a feature space warping process, a paired feature learning scheme, an ID3-like joint feature plane quantization method, and a weak Bayesian classifier. Although some complicated components which increase the power of classifiers are included in the face detection system, the execution of the final face classifier is quite simple. With tree structure quantization and look-up tables, the proposed face detector can work very efficiently and directly on the wavelet compressed domain. Our experimental results on the benchmarking face datasets showed that the proposed face detection system working in the compressed domain can achieve similar accuracy to that of Viola and Jones' face detector [8, 11].

Conflict of Interests

The authors declare that there is no conflict of interests regarding the publication of this paper.

Acknowledgments

The authors would like to thank the National Science Council of the Republic of China, Taiwan, for partially financially supporting this research under Contract nos. NSC 102-2221-E-007-082 and NSC 102-2622-E-007-019-CC3. This work was also supported by the Advanced Manufacturing and Service Management Research Center (AMSMRC), National Tsing Hua University.

References

- [1] M.-H. Yang, D. J. Kriegman, and N. Ahuja, "Detecting faces in images: a survey," *IEEE Transactions on Pattern Analysis and Machine Intelligence*, vol. 24, no. 1, pp. 34–58, 2002.
- [2] S. Lee and M. H. Hayes, "A simple and fast color-based human face detection scheme for content-based indexing and retrieval," in *Proceedings of the International Conference on Image Processing (ICIP '04)*, vol. 1, pp. 701–704, October 2004.
- [3] P. Fonseca and J. Nesvadba, "Face detection in the compressed domain," in *Proceedings of the International Conference on Image Processing (ICIP '04)*, vol. 3, pp. 2015–2018, October 2004.
- [4] C. Garcia and G. Tziritas, "Face detection using quantized skin color regions merging and wavelet packet analysis," *IEEE Transactions on Multimedia*, vol. 1, no. 3, pp. 264–277, 1999.
- [5] H. Schneiderman and T. Kanade, "A statistical method for 3D object detection applied to faces and cars," in *Proceedings of the IEEE Conference on Computer Vision and Pattern Recognition (CVPR '00)*, pp. 746–751, June 2000.
- [6] C. Papageorgiou and T. Poggio, "A trainable system for object detection," *International Journal of Computer Vision*, vol. 38, no. 1, pp. 15–33, 2000.
- [7] S.-H. Huang and S.-H. Lai, "Real-time face detection in color video," in *Proceedings of the 10th International Multimedia Modelling Conference (MMM '04)*, pp. 338–345, January 2004.
- [8] P. Viola and M. Jones, "Rapid object detection using a boosted cascade of simple features," in *Proceedings of the IEEE Computer Society Conference on Computer Vision and Pattern Recognition*, vol. 1, pp. 1511–1518, December 2001.
- [9] S. Z. Li and Z. Zhang, "FloatBoost learning and statistical face detection," *IEEE Transactions on Pattern Analysis and Machine Intelligence*, vol. 26, no. 9, pp. 1112–1123, 2004.
- [10] R. Xiao, M.-J. Li, and H.-J. Zhang, "Robust multipose face detection in images," *IEEE Transactions on Circuits and Systems for Video Technology*, vol. 14, no. 1, pp. 31–41, 2004.
- [11] P. Viola and M. J. Jones, "Robust real-time face detection," *International Journal of Computer Vision*, vol. 57, no. 2, pp. 137–154, 2004.
- [12] T. Mita, T. Kaneko, and O. Hori, "Joint Haar-like features for face detection," in *Proceedings of the 10th IEEE International Conference on Computer Vision (ICCV '05)*, vol. 2, pp. 1619–1626, October 2005.
- [13] S. Hayashi and O. Hasegawa, "A detection technique for degraded face images," in *Proceedings of the IEEE Computer Society Conference on Computer Vision and Pattern Recognition (CVPR '06)*, pp. 1506–1512, June 2006.
- [14] C. Huang, H. Ai, Y. Li, and S. Lao, "High-performance rotation invariant multiview face detection," *IEEE Transactions on Pattern Analysis and Machine Intelligence*, vol. 29, no. 4, pp. 671–686, 2007.
- [15] ISO/IEC 15444-1, "JPEG2000 Image Coding System," 2000.
- [16] D. S. Taubman and M. W. Marcellin, *JPEG2000: Image Compression Fundamentals, Practice and Standards*, Kluwer Academic Publishers, Boston, Mass, USA, 2002.
- [17] P. Viola, M. J. Jones, and D. Snow, "Detecting pedestrians using patterns of motion and appearance," in *Proceedings of the 9th IEEE International Conference on Computer Vision*, vol. 2, pp. 734–741, October 2003.
- [18] N. Dalal and B. Triggs, "Histograms of oriented gradients for human detection," in *Proceedings of the IEEE Computer Society Conference on Computer Vision and Pattern Recognition (CVPR '05)*, vol. 1, pp. 886–893, June 2005.
- [19] Q. Zhu, M.-C. Yeh, K.-T. Cheng, and S. Avidan, "Fast human-detection using a cascade of histograms of oriented gradients," in *Proceedings of the IEEE Computer Society Conference on Computer Vision and Pattern Recognition*, vol. 2, pp. 1491–1498, 2006.

- [20] Q. Zhu, S. Avidan, M.-C. Yeh, and K.-T. Cheng, "Fast human detection using a cascade of histograms of oriented gradients," in *Proceedings of the IEEE Computer Society Conference on Computer Vision and Pattern Recognition (CVPR '06)*, vol. 1, pp. 1491–1498, June 2006.
- [21] A. Opelt, A. Pinz, M. Fussenegger, and P. Auer, "Generic object recognition with boosting," *IEEE Transactions on Pattern Analysis and Machine Intelligence*, vol. 28, no. 3, pp. 416–431, 2006.
- [22] Y. Freund and R. E. Schapire, "A decision-theoretic generalization of on-line learning and an application to boosting," *Journal of Computer and System Sciences*, vol. 55, no. 1, pp. 119–139, 1997.
- [23] R. E. Schapire and Y. Singer, "Improved boosting algorithms using confidence-rated predictions," *Machine Learning*, vol. 37, no. 3, pp. 297–336, 1999.
- [24] E. Osuna, R. Freund, and F. Girosi, "Training support vector machines: an application to face detection," in *Proceedings of the IEEE Computer Society Conference on Computer Vision and Pattern Recognition*, pp. 130–136, June 1997.
- [25] H. A. Rowley, S. Baluja, and T. Kanade, "Neural network-based face detection," *IEEE Transactions on Pattern Analysis and Machine Intelligence*, vol. 20, no. 1, pp. 23–38, 1998.
- [26] K.-K. Sung and T. Poggio, "Example-based learning for view-based human face detection," *IEEE Transactions on Pattern Analysis and Machine Intelligence*, vol. 20, no. 1, pp. 39–51, 1998.
- [27] D. Roth, M. H. Yang, and N. Ahuja, "A SNoW-based face detector," in *Proceedings of the Conference on Advances in Neural Information Processing Systems*, vol. 12, pp. 855–861, 2000.
- [28] F. Fleuret and D. Geman, "Coarse-to-fine face detection," *International Journal of Computer Vision*, vol. 41, no. 1-2, pp. 85–107, 2001.
- [29] B. Heisele, T. Serre, and T. Poggio, "A component-based framework for face detection and identification," *International Journal of Computer Vision*, vol. 74, no. 2, pp. 167–181, 2007.
- [30] C. Liu, "A Bayesian discriminating features method for face detection," *IEEE Transactions on Pattern Analysis and Machine Intelligence*, vol. 25, no. 6, pp. 725–740, 2003.
- [31] H. Wu, Q. Chen, and M. Yachida, "Face detection from color images using a fuzzy pattern matching method," *IEEE Transactions on Pattern Analysis and Machine Intelligence*, vol. 21, no. 6, pp. 557–563, 1999.
- [32] R.-L. Hsu, M. Abdel-Mottaleb, and A. K. Jain, "Face detection in color images," *IEEE Transactions on Pattern Analysis and Machine Intelligence*, vol. 24, no. 5, pp. 696–706, 2002.
- [33] F. Tsalakanidou, S. Malassiotis, and M. G. Strintzis, "Face localization and authentication using color and depth images," *IEEE Transactions on Image Processing*, vol. 14, no. 2, pp. 152–168, 2005.
- [34] R. Choudhury Verma, C. Schmid, and K. Mikolajczyk, "Face detection and tracking in a video by propagating detection probabilities," *IEEE Transactions on Pattern Analysis and Machine Intelligence*, vol. 25, no. 10, pp. 1215–1228, 2003.
- [35] E. Loutas, I. Pitas, and C. Nikou, "Probabilistic multiple face detection and tracking using entropy measures," *IEEE Transactions on Circuits and Systems for Video Technology*, vol. 14, no. 1, pp. 128–135, 2004.
- [36] C. Garcia and M. Delakis, "Convolutional face finder: a neural architecture for fast and robust face detection," *IEEE Transactions on Pattern Analysis and Machine Intelligence*, vol. 26, no. 11, pp. 1408–1423, 2004.
- [37] W. Zhao, R. Chellappa, P. J. Phillips, and A. Rosenfeld, "Face recognition: a literature survey," *ACM Computing Surveys*, vol. 35, no. 4, pp. 399–458, 2003.
- [38] J. Wright, A. Y. Yang, A. Ganesh, S. S. Sastry, and Y. Ma, "Robust face recognition via sparse representation," *IEEE Transactions on Pattern Analysis and Machine Intelligence*, vol. 31, no. 2, pp. 210–227, 2009.
- [39] W. R. Schwartz, H. Guo, J. Choi, and L. S. Davis, "Face identification using large feature sets," *IEEE Transactions on Image Processing*, vol. 21, no. 4, pp. 2245–2255, 2012.
- [40] C. Liu and H.-Y. Shum, "Kullback-Leibler boosting," in *Proceedings of the IEEE Computer Society Conference on Computer Vision and Pattern Recognition*, vol. 1, pp. 1/587–1/594, June 2003.
- [41] J. Wu, S. C. Brubaker, M. D. Mullin, and J. M. Rehg, "Fast asymmetric learning for cascade face detection," *IEEE Transactions on Pattern Analysis and Machine Intelligence*, vol. 30, no. 3, pp. 369–382, 2008.
- [42] K. Tieu and P. Viola, "Boosting image retrieval," in *Proceedings of the IEEE Conference on Computer Vision and Pattern Recognition (CVPR '00)*, pp. 228–235, June 2000.
- [43] S.-H. Huang, Q.-J. Wu, and S.-H. Lai, "Improved AdaBoost-based image retrieval with relevance feedback via paired feature learning," *Multimedia Systems*, vol. 12, no. 1, pp. 14–26, 2006.
- [44] T. M. Mitchell, *Machine Learning*, MIT Press, McGraw-Hill, 1997.

Research Article

Lower Power Design for UHF RF CMOS Circuits Based on the Power Consumption Acuity

Niu Xiang-jie and Li Hua

School of Computer and Information Engineering, School of Economics & Management, Beijing University of Agriculture, Beijing 102206, China

Correspondence should be addressed to Li Hua; huahua.lili@yeah.net

Received 25 September 2013; Revised 29 November 2013; Accepted 30 December 2013; Published 10 March 2014

Academic Editor: Gelan Yang

Copyright © 2014 N. Xiang-jie and L. Hua. This is an open access article distributed under the Creative Commons Attribution License, which permits unrestricted use, distribution, and reproduction in any medium, provided the original work is properly cited.

Excessive energy consumption of UHF tag is the bottleneck of energy saving in its wide range of applications. To address this issue, a lower power design for UHF RF CMOS circuits based on power consumption acuity is proposed in this paper. Through in-depth analysis of the static and dynamic power generation principle of UHF RF circuits in the work, the power consumption acuity can be calculated by using the correlation of circuit power and input vector. Subsequently, under the guide of this acuity, the UHF RF CMOS circuits with better energy saving can be designed. Furthermore, according to the performance indicators of EPC CIG2 UHF RFID in UHF identification, the corresponding circuit is designed and implemented. The test results show that the design of UHF RF circuit based on the acuity of power consumption can reduce 35%–40% power consumption.

1. Introduction

Compared to other automatic identification technologies, the most prominent feature of RFID is that it is the fast noncontact technology in identification of moving objects and has high accuracy, security, and resistances to harsh environment, which can also identify multiple recognition objects and so on [1, 2]. RFID technology is widely used in industrial production and all aspects of daily life, such as dangerous goods management, supply chain management, ticketing, security, mall management, and access control [3, 4]. RFID system is different which is depending on its application. However, in general, the tag, interrogator, and processor are the basic three composed parts [5]. With the application of large-scale RF technology, the power consumption of RF chip becomes the focus in this research field [6].

The researches of UHF and microwave bands tag chip got a late start, and most of them have focused in 2003–2006. Among them, the paper about tag chip research published in the literature [7, 8] is the most representative. In Karthaus and Fischer's [9] research, the minimum input RF (radio

frequency) power in UHF passive RFID tag chip is only $16.7 \mu\text{W}$. It used the read-write EEPROM memory to support the design and the IC was implemented in a $0.5 \mu\text{m}$ digital two-poly two-metal digital CMOS technology with EEPROM and Schottky diodes. In this paper, it mainly focused on how to improve energy conversion efficiency in the RF energy acquisition, but how to achieve low-power technology in specific circuit was not addressed, and the requirements of Schottky diode did not exist in the standard COMS process. The literature [10] proposed a design of ultralow-cost UHF RFID tag chip for SCM (Supply chain management). The design process was the $0.25 \mu\text{m}$ standard CMOS, and the nonvolatile memory could be implemented by using of self-adaptive silicon approach in CMOS technology, which could greatly reduce the costs of the chip production. The power matching in the front end of RF analog, the acquisition circuit of RF energy, the energy conversion efficiency, and another key technology were studied in this paper. However, it only established a supply voltage model by using physical method to dynamically adjust the voltage. The threshold could not be changed and the effort was poor. Digital control

logic and memory were accounted for the main part cost and power consumption of RFID tag chip. In the literature [11], the implementation method for embedded memory and digital controller which is suitable for RFID tag chip was investigated. In this paper, the asynchronous circuit was applied to achieve the core of RFID tag chip. However, there is a big restriction that this method is applied in RFID tags chip, since it is not compatible with standard CMOS process and high cost. The literature [12] introduced a new nonvolatile memory to reduce the tag chip's power consumption. It was also the trend of development in future. For example, in July 2005, the memory in the RFID tags chips MB89R119 produced by Fujitsu was 256 Byte FRAM (Ferroelectric Random Access Memory). The power consumption of FRAM was lower than an EEPROM, but its production cost was higher than EEPROM, which is the main reason that FRAM is not widely used in the RFID tag chip currently. The literature designed a UHF passive tag chip, in which the antenna gain was -0.5 dB, reader transmit power was 4 W EIRP, the minimum input power of the tag was 16.7 μ w, and the reading distance was about 9.25 m, but in this tag, by using the EEPROM and Schottky diodes technology, the cost of 8 chips was high and power consumption was excessive. In the literature [13], it did not contain EEPROM and digital control circuits, but the data communication rate could reach 10 Mb/s, the simulation consumption was 62.9 μ w, and the calculation distance was 6.58 m, while the tape-out was not realized. The literature [14] proposed that the passive RFID system did not have a very reliable security mechanism, which could not guarantee a high reliability of data security, and the data stored within the system was vulnerable to attack mainly because the RFID chip itself and chips in the process of reading and writing data will easily be hacked. In the literature [15], the recognition rate was another problem of RFID system. For the energy intensive of liquid and metal objects, the highest accurate recognition rate of RFID tag only could be reached to around 80%. Obviously, there is a large distance before the recognition rate that can be applied in practice.

The remainder of the paper is organized as follows. Section 2 analyzes the generation principle of static and dynamic power consumption in the work of the high-frequency RF; Section 3 proposes the concept of using power acuity and the view on UHF RF circuit design on the basis of power acuity; Section 4 gives the experiment; and Section 5 is the conclusions.

2. Power Consumption of UHF RF IC Integrated Circuits

Power consumption of CMOS circuit can be divided into static and dynamic power consumption. The static power consumption is caused by the charging and discharging of large parasitic capacitance, which is considered the main source of power consumption in the circuit. The dynamic power consumption is mainly caused by the PH junction leakage current, gate leakage, and subthreshold current of

the transistor; it is the important part of the overall power consumption.

2.1. The Dynamic Power Consumption of UHF RF Circuit.

Dynamic power consumption is considered to be the main source of power consumption of UHF RF CMOS circuits, which is produced from the handover of tag identification circuit between two stable operating states. It consists of two parts: one is the power consumption of capacitor caused by the charging and discharging of capacitor in RF circuit reverser; the other is the power consumption of moment conduction generated by the instant conduction of tubes T_1 and T_2 . Dynamic power consumption, power consumption of capacitor, and power consumption of moment conduction are represented by P_a , P_C , and P_T , respectively; therefore, the equation is as follows: $P_a = P_C + P_T$.

(1) *The Power Consumption Generation Principle of Capacitor in UHF RF Circuit.* As shown on Figure 1(a), UHF RF CMOS inverter tube normally consists of tubes T_1 , T_2 and the load capacitance C_L , where tube T_1 is made by PMOS technology and tube T_2 is made by NMOS technology and C_L is connected to the inverter output end.

According to the working principle of UHF RF inverter, when the jump-behavior of the CMOS inverter input end v_i occurs, the charge and discharge currents will be caused. As it can be seen from Figure 1, the current generation process of charging and discharging is like this: if v_i is 1, tube T_1 turns off, and T_2 turns on, then v_0 is 0, whereas when v_i changes from 1 to 0, tube T_1 is turned from off to on and T_2 is just the opposite; consequently CMOS inverter v_0 will be changed from 0 to 1 and C_L will be charged from V_{DD} through the tube T_1 . Conversely, if v_i is 0, tube T_1 turns on, and T_2 turns off, then v_0 is 1; but when v_i changes from 0 to 1, tube T_1 is turned from on to off, and tube T_2 is turned from off to on, then CMOS inverter v_0 will be changed from 1 to 0 and C_L will be charged from V_{DD} through the tube T_2 .

In the process of UHF RF circuit operation, the average power consumption P_C generated by charge current i_N and discharge current i_P are shown as follows:

$$P_C = \frac{1}{T} \left[\int_0^{T/2} i_N v_0 dt + \int_{T/2}^T i_P (V_{DD} - v_0) dt \right]. \quad (1)$$

In the above formula, P_C is the average power when the UHF RF circuit is working, T represents a cycle of operation of the circuit, i_N represents the current when the inverter of UHF frequency circuit is charging, i_P represents the current when the inverter of UHF frequency circuit is discharging, V_{DD} denotes the pin elements inside the inverter, and v_0 is the tag in which the value is only 0 or 1; it is used to mark the beginning of the charging or discharging state.

It can be obtained from the principle of charging and discharging of the CMOS inverter: $i_N = -C_L(dv_0/dt)$, $i_P = C_L(dv_0/dt) = -C_L(d(V_{DD} - v_0)/dt)$.

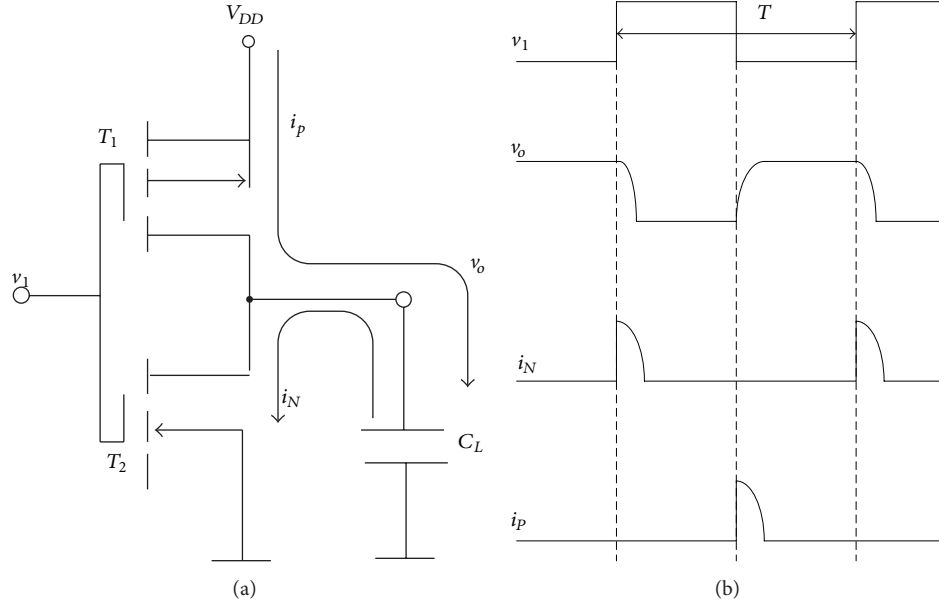


FIGURE 1: The charging and discharging of the load capacitance from UHF RF inverter.

Therefore, it can be obtained as (2) after i_N and i_P are substituted into (1):

$$P_C = \frac{1}{T} \left[C_L \int_{v_{dd}}^0 -v_0 dv_0 + C_L \int_{v_{dd}}^0 -(V_{DD} - v_0) d(V_{DD} - v_0) \right] \quad (2)$$

$$= f C_L \left[\frac{1}{2} V_{DD}^2 + \frac{1}{2} V_{DD}^2 \right] = C_L f V_{DD}^2.$$

In the above formula, $f = 1/T$ is the repetition frequency of v_i . From formula (2), it can be seen that the power consumption generated by the charging current or discharge current is $0.5C_L V_{DD}^2$. The power consumption of capacitor C_L is proportional to f and V_{DD} .

(2) *The Generated Power Consumption of Instantaneous Conduction.* If it takes $V_{DD} > |V_{TP}| + V_{TN}$ and $V_{IH} \approx V_{DD}$, then v_i has the state of $v_i > V_{TN}$, and $V_{DD} - v_i > |V_{TP}|$ in the process of change between high and low electrical levels. The instantaneous current i_T will be produced when tubes T_1 and T_2 are simultaneously turned on. The average value is shown in (3):

$$I_{TAV} = \frac{1}{T} \left[\int_{t_1}^{t_2} i_T dt + t \int_{t_3}^{t_4} i_T dt \right]. \quad (3)$$

Thus, the power consumption of instantaneous conduction is

$$P_T = V_{DD} I_{TAV}. \quad (4)$$

I_{TAV} is related to the frequency of v_i ; the higher the f is, the larger the I_{TAV} is. The power consumption of instantaneous conduction P_T is related to the input signal

frequency f and the voltage V_{DD} , the higher the frequency f and voltage V_{DD} are, the larger of P_T is. In addition, P_T will also be affected by the rise and fall time of v_i , the power voltage of CMOS tube, and others.

2.2. *The Generated Static Power of UHF RF Circuit.* When UHF RF circuit is in a steady state, the leakage current of inverter exists, which is the reason of static power generation. If P represents power consumption of inverter, P_D is the static power of inverter, then $P = P_a + P_D = P_C + P_T + P_D$.

It is the solution equation of subthreshold leakage current, while subthreshold leakage current is measured value which cannot be ignored in test circuit simulation of BSIM. BSIM is the industrial standard of test circuit simulation, which is developed by University of California in Berkley and used to test circuit simulation and development of CMOS technology. It is software simulation system based on physics and occupies the characters like preciseness, upgradability, robustness, and language, which can also provide the data of Dc analysis, transient analysis, and Ac analysis of standard circuit. It is the current between source and drain electrode when the circuit is at rest. BSIM model can accurately test the subthreshold leakage current [16], as formula (5) that is shown below:

$$I_{sub} = \mu_0 \frac{W_{eff}}{L_{eff}} v_T^2 \sqrt{\frac{q\epsilon_s N_{cheff}}{2\phi_s}} (1 - e^{-(V_{ds}/v_T)}) \times \exp \left[\frac{V_{gs} - V_t - \gamma V_{sb} + \eta V_{ds}}{nv_T} \right]. \quad (5)$$

In this equation, in the solution process of subthreshold leakage current I_{sub} , V_{gs} , V_{ds} , and V_{sb} are the voltage between grid-source, drain-source, and source-body area of transistor,

respectively. ϵ_s is the dielectric constant of material of transistor, η is linearized effect factor of the leakage inductance of the barrier drop effect, V_{ds} is drain-source voltage, μ_0 is the carrier mobility, W_{eff} and L_{eff} are the effective width and length of transistor, respectively, γ is the linearized influence factor of body area effect, and ϕ_s is surface potential. V_t is the voltage threshold at zero bias. In the calculation process, the thermal availability voltage v_T is unknown; in order to solve the thermal availability voltage effectively, we assumed that Plank's constant is κ , the temperature of carrier is T , and the electron charge is of per unit; then the calculation formula of V_T can be shown as follows: $V_T = \kappa T/q$.

With the deepening of the process, the increasing of gate leakage current is much faster than subthreshold leakage current, which can be indicated in formula (6), where A_g and B_g are associated with the process of physical parameters and ϕ_{ox} is the barrier height of the tunneling electron (or holes).

Consider the following:

$$I_{\text{gate}} = WL_{\text{SDE}}A_g \left(\frac{V_{dd}}{T_{\text{ox}}} \right)^2 \times \exp \left\{ \frac{-B_g \left[1 - (1 - V_{dd}/\phi_{\text{ox}})^{3/2} \right]}{V_{dd}} T_{\text{ox}} \right\}. \quad (6)$$

When the strong electric field is formed between reverse-biased P-N junctions, it will form BTBT (Reverse Biased Band to Band Tunneling) leakage current; it can be represented by using formula (7) as follows:

$$I_{\text{BTBT}} = \sum_{k=\text{side, bottom}} WL_k A \frac{\xi_k}{E_g^{1/2}} V_{dd} \exp(-BE_g^{3/2}/\xi_k). \quad (7)$$

L_{side} and L_{bottom} refer to the sides and bottom length of the P-N junction, ξ_{side} and ξ_{bottom} mean the electric field of the side and bottom of P-N junction, and A and B are the physical parameters associated with the process [17].

3. The Saving Design of UHF RF Circuits Based on the Acuity of Power Consumption

By the preceding theory, the dynamic power of UHF RF circuit is essentially the valid statistics for jump variables of input signal. In this section, the power acuity analysis is researched in-depth. Acuity of power consumption is the correlation degree of power consumption and input vector. It is a very important character of power consumption. It also can be used in low power design. If the acuity of power consumption is considered enough in the design of UHF RF circuit, it can perform an UHF RF circuit with relatively small power consumption.

3.1. The Analysis Method of Power Acuity. The power consumption of UHF RF circuit is generally divided into static and dynamic power consumption. Dynamic power consumption is considered to be the main source of power consumption of UHF RF circuits. It is produced from the switching process of UHF RF circuit between two stable

operating states, which consists of two parts: one is the power consumption of capacitor caused by the charging and discharging of capacitor in RF circuit reverser, the other one is the power consumption of moment conduction generated by the instant conduction of T_1 and T_2 tubes. In the ideal case static power should be zero, but this does not mean that the static power is really zero, and actually the static power of UHF RF circuit is due to the leakage current of circuit. The leakage current includes subthreshold current, gate leakage current, and source-drain reverse bias leakage current. The acuity of power consumption is a very important character of power consumption. It means the change degree of power consumption is compared to the input vector. For better understanding, some related definitions and theorems of power acuity are introduced.

The probability of which signal is set to 1 and signal activity are the important indicator to measure power consumption acuity. It can reflect validly the active character of circuit and reflect the power consumption acuity directly. Assume that the action of UHF RF circuit is the 0-1 process of each state, which is represented by the function $g(t)$. Therefore, in this case, the signal probability of which signal is set to 1 and the jumping of rate signal activity can be used to indicate the activities feature of digital circuit. In the time interval $(-T, T)$, T represents the activity period of UHF RF circuit; the unit is μs . The probability of which signal is set to 1 can be defined as follows.

Signal probability can be represented by formula (8) [18]:

$$P(g) = \lim_{T \rightarrow \infty} \frac{1}{2T} \int_{-T}^{+T} g(t) dt. \quad (8)$$

T represents the activity period of UHF RF circuit; $n_g(T)$ is the activity frequency in time interval $(-T, T)$. Signal activity is defined as follows:

$$A(g) = \lim_{T \rightarrow \infty} \frac{n_g(T)}{2T}. \quad (9)$$

By means of analysis, when the random probability of which signal is set to 1 is 1/2, signal activity is 1/2, and the effect of power consumption acuity is the best.

As the same definition, the signal activity of v_i from high level to low level is A_{10} , and the signal activity of v_i from low level to high level is represented by A_{01} . When the random probability of signal probability is 1/2, signal activity is 1/2, and A_{10} and A_{01} values are 1/4.

After defining the signal probability and signal activity, the transmission characters of signal probability and signal activity are further to define.

The transmission characters of the probability which signal is set to 1 are that the signal probability of basic logic gate output signal is represented by a function of the input signal probability. Assume that a two-input gate AND input signal probability is $P_1 \cdot P_2$, then the output signal probability is $P_1 \cdot P_2$. As to the gate OR, assuming its input signal probabilities are P_1 and P_2 , respectively, then the output signal probability is $1 - (1 - P_1) \cdot (1 - P_2)$. Propagation of signal activity is to use the transition rate of basic logic gate input signal to indicate the output signal transition rate. After a number of

logic gates, the random signal changes generally have certain regularity.

For n input gate AND, only when the other input $n-1$ is 1, the jump of the n pin can be passed out at the output side; on the contrary, if one of the logic gate values is 0 and keeps the same value, which means that this kind of jumping is blocked. So that other input jumping cannot be passed out smoothly, and 0 is the control value of gate AND, as it can be seen from Figure 2.

After the research on the character of signal probability and signal activity, the transmission characteristics of the basic logic gate transition rate are available. On the basis of this, power consumption acuity can be analyzed. In the circuit design process, the method of low-power design is based on the transmission character of jump rate: if the circuit logic gate with a larger probability is near to the control value, then the design of UHF RF circuits will be with the relatively small power consumption.

The power consumption acuity is the correlation degree of power consumption and input vector. It is a very important character of power consumption.

Power consumption acuity is the changing rate of circuit power consumption probability which is set to 1. The definition is as follows:

$$S_{P(x_i)} = \lim_{\Delta P(x_i) \rightarrow 0} \frac{\Delta \text{Power}_{\text{avg}}}{\Delta P(x_i)} = \frac{\partial \text{Power}_{\text{avg}}}{\partial P(x_i)}. \quad (10)$$

In this equation, $S_{P(x_i)}$ is the signal activity of power consumption when the signal is set to 1, $\Delta \text{Power}_{\text{avg}}$ represents the average power consumption per unit, $\Delta P(x_i)$ is the probability of which x_i is set to 1, $\Delta \text{Power}_{\text{avg}}$ represents the partial derivatives of the average dynamic power consumption for x_i , and $\partial P(x_i)$ represents the partial derivative of the transition rate for x_i .

Consider the following:

$$S_{A(x_i)} = \lim_{\Delta A(x_i) \rightarrow 0} \frac{\Delta \text{Power}_{\text{avg}}}{\Delta A(x_i)} = \frac{\partial \text{Power}_{\text{avg}}}{\partial A(x_i)}. \quad (11)$$

In this equation, $S_{A(x_i)}$ is the power consumption rate of change on the signal activity, $\Delta \text{Power}_{\text{avg}}$ represents the average dynamic power consumption per unit, and $\partial A(x_i)$ represents the probability of signal activity of x_i .

Through the previous studies on signal probability and signal activity and their transmission characteristics, a simple calculation method for power consumption acuity based on the transmission characteristics of transition rate can be obtained. Firstly, the signal probability and signal activity of given input vector can be adopted to make statistical analysis, and through the transmission character of signal probability, the signal probability of each circuits gate can be calculated. The signal activity of circuit input signal is set to the signal activity of input vectors, and then by the transmission characteristics of signal activity, the input and output signal activity value of the entire logic gate at the input terminal can be obtained. The sum of signal activity values of

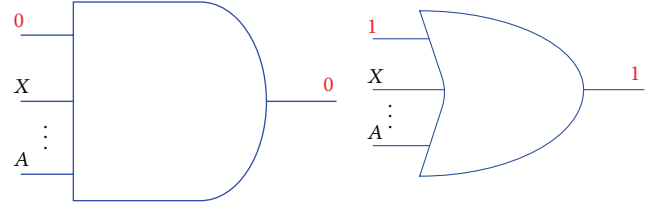


FIGURE 2: The hopping transfer characteristics of basic logic gates figure.

the input and output is a measure of the power consumption acuity at this terminal:

$$S_{a(x_i)} = \frac{\sum_{\text{fanout gate } g \text{ of } x_i} [\Delta A_{10}(g) + \Delta A_{01}(g)]}{\Delta a(x_i)}. \quad (12)$$

Conclusion 1. The average of dynamic power consumption of UHF RF circuit is correlated with an approximate linear relationship to its signal activity of each gate. By the following derivation, it can be demonstrated that

$$\begin{aligned} P_{\text{avg}} &= \lim_{T \rightarrow +\infty} \frac{\sum_{t=1}^T \sum_{g=1}^{\zeta} \{ (f_g[(t-1)] \oplus f_g[t]) \cdot F(g) \}}{2T} \\ &= \lim_{T \rightarrow +\infty} \frac{\sum_{g=1}^{\zeta} \{ \sum_{t=1}^T \{ (f_g[(t-1)] \oplus f_g[t]) \cdot F(g) \} \}}{2T} \\ &= \sum_{g=1}^{\zeta} \left\{ \lim_{T \rightarrow +\infty} \frac{\sum_{t=1}^T [(f_g[(t-1)] \oplus f_g[t])] \cdot F(g)}{2T} \right\} \\ &= \sum_{g=1}^{\zeta} \left[\frac{n_g(T)}{2T} \cdot F(g) \right] = \sum_{g=1}^{\zeta} [A_g \cdot F(g)], \end{aligned} \quad (13)$$

wherein, $n_g(T)$ is the total jumping time in the range of gate g and gate $(T, -T)$, $f_g[t]$ is status value that logic gate g is on t . So, by calculating the signal activity of each gate in the circuit, the average dynamic power consumption of circuit can be directly obtained.

Conclusion 2. The linear signal probability of the logic gate can be used to describe the average leakage power of UHF RF circuits, and the derivative process can be shown as follows:

$$\begin{aligned} \text{Leak}_{\text{avg}} &= \lim_{L \rightarrow +\infty} \frac{\sum_{i=1}^L \text{Leak}(V_i)}{L} \\ &= \lim_{L \rightarrow +\infty} \frac{\sum_{i=1}^L \sum_{j=1}^N I(T_j, V_{j,i}, M_j)}{L} \\ &= \sum_{i=1}^N \lim_{L \rightarrow +\infty} \frac{\sum_{j=1}^L I(T_i, V_{i,j}, M_i)}{L} \\ &= \sum_{i=1}^N \lim_{L \rightarrow +\infty} \frac{\sum_{j=1}^{2^{M_i}} n_{i,j} I(T_i, S_j, M_i)}{L} \end{aligned}$$

$$\begin{aligned}
&= \sum_{i=1}^N \sum_{j=1}^{2^{M_{ij}}} \left\{ \lim_{L \rightarrow +\infty} \frac{n_{i,j}}{L} I(T_i, S_j, M_i) \right\} \\
&= \sum_{i=1}^N \sum_{j=1}^{2^{M_{ij}}} \left\{ \text{prob}_{i,j} I(T_i, S_j, M_i) \right\}.
\end{aligned} \tag{14}$$

Conclusion 3. Supposing each v_i of UHF RF circuit is independently of one another, and then the circuit power consumption under specific input signal vector can be expressed by the acuity parameter equation linear of its input terminal power consumption, it is as follows:

$$P = P_{\text{avg}} + \sum_{i=1}^{I_{\text{num}}} \Delta a(x_i) S_{a(x_i)}. \tag{15}$$

In this formula, i is the variable, and x_i represents the i th logical gate. P_{avg} represents the average power consumption circuit, $S_{a(x_i)}$ is calculated by the previous measure formula, and $\Delta a(x_i)$ is the difference between $a(x_i)$ and signal activity when the a circuit obtains the average power.

3.2. The Design Process of UHF RF Circuit Based on Power Acuity. By using the acuity analysis of the power consumption, the average dynamic and static power consumption of UHF RF circuit can be calculated.

In the process of UHF RF circuit design, in order to reduce power consumption, it can be considered to reduce the power consumption acuity in low power design. If the logic gate of UHF RF circuit exists with a greater probability at the value in the control, the designed UHF RF circuit will have relatively small power consumption compared to the other. According to this conclusion, minimizing the power consumption acuity can make the circuit relatively stable in the UHF RF circuit design. Definitely, the appropriate transformations of the circuit can also lead to lower power requirement in UHF RF circuit design. The acuity in the respective input terminal of the circuit is difference, and one of the greater acuities can be selected as the control parameter, and the phase deviation of the UHF RF can be suppressed effectively. The power consumption is reduced greatly.

4. Experimental Analysis

Experiment circumstance: the experiments about acuity analysis of energy consumption are presented; the analysis is achieved by C++; the platform is VC++6.0, at the same time, running on the Precision T7610 ((Inter xeon processor E5-2620 v2 (6 cores HT, 2.1GHz Turbo, 15 MB) Windows 7 professional 64 bit, 16 GB (4 × 4 GB) 1866 MHz DDR3 ECC RDIMM, 1TB, 3.5 inch Serial ATA (7,200 Rpm) HDD, 2 GB NVIDIA Quadro K2000 (2DP & 1DVI-I) (2DP-DVI & 1DVI-VGA adapter))) workstation.

To validate the effectiveness and energy efficiency of the proposed design of UHF RF circuit based on the power consumption acuity, according to the performance indicators of EPC CIG2 UHF RFID and the power acuity theory, a UHF

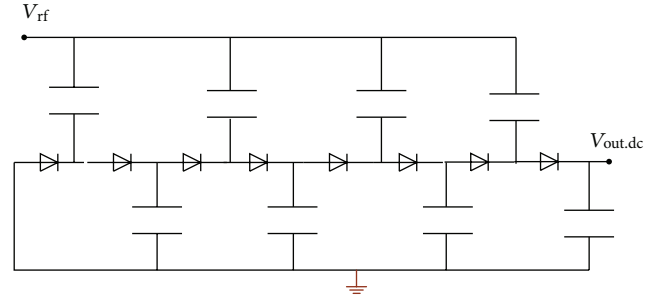


FIGURE 3: The in front-end rectifier of UHF RF circuit.

RF front-end circuit with the reset terminal which is suitable for the power-sensitive work is presented here. The general structure is shown in Figure 3; some NOT gates are not shown in the figure, wherein the gate NOT, NAND, and NOR use transmission gate logic to reduce the fosp/snfP asymmetry.

Compared with the conventional rectifier, the delay of rectifying portion in the front end of UHF RF is small, and the leakage is low under the same operating voltage. In order to reduce the static and dynamic power consumption of circuit, the increase of circuit drive capability makes the size of the rectifier relatively large; this is not obvious for the small-scale digital circuit. When the circuit is operating in strong inversion region, it can reflect its superiority. Figure 4 shows simulation results of the structural power consumption of the standard rectifier. The simulation is performed in the typical condition, the temperature is 20°C, and the power supply voltage is 300 mv. Figure 4(a) is the result of conventional rectifier; Figure 4(b) is the result of our designed rectifier. It can be seen from Figure 4 that the maximum transient dynamic current (7 sA) of the conventional rectifier is less than the maximum transient dynamic current (20 nA) in this paper. However, the leakage power of the former is obviously larger than the latter.

As it is shown in Table 1, the overall power consumption and the clock frequency of the different process corners and different temperatures in the two rectifier working processes are 10 kHz, respectively.

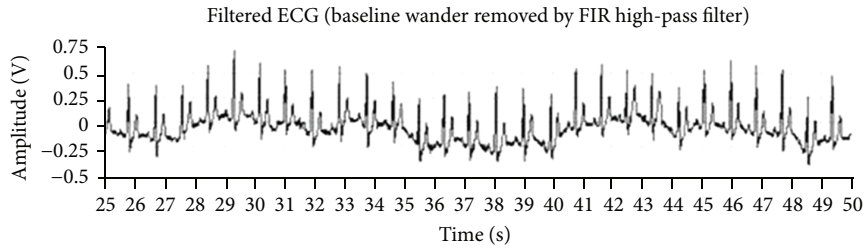
According to the theory of acuity analysis, in this paper we use the transmission gate structure and increase the width to length ratio of transistor appropriately. The delay of the rectifiers designed in this paper is smaller than the traditional structure for 9.6 us under the same supply voltage and load (the NOT gate in this paper), and the consumption decreases by around 36%.

For a long time statistical analysis, the total loss curve $U_1 - \sum P$ of the UHF RF rectifier circuit and the corresponding total loss error curve $U_1 - \delta(\sum P)$ are shown in Figure 5. As we can see from Figure 5, when the regulating voltage is below 20 V, the total loss error of circuit is increasing; when the regulating voltage is more than 20 V, the loss error of circuit is almost 0. For the reason that operating voltage of the UHF RF circuit is generally higher than 22 V, it can be calculated according to approximate solution, and the total loss is lower.

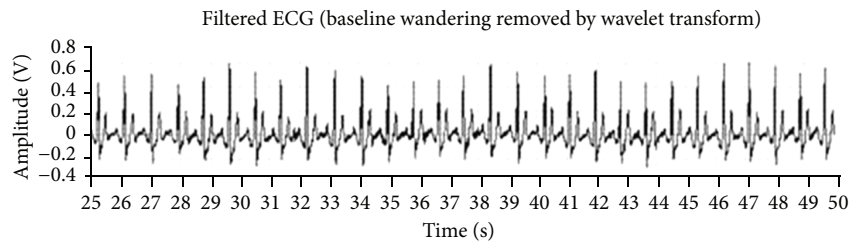
In accordance with the approximate solution and the exact solution, the optimal voltage curve $T_L - U_1^*$ varies with

TABLE 1: Energy consumption of different triggers.

Temp	80°C			66°C			-30°C		
Comer	<i>tt</i>	<i>fnsP</i>	<i>snfp</i>	<i>tt</i>	<i>fnsP</i>	<i>snfp</i>	<i>tt</i>	<i>fnsP</i>	<i>snfp</i>
V_{dd}	0.245V	0.346V	0.325V	0.345V	0.446V	0.425V	0.345V	0.456V	0.416V
P_T (DFFI) _{conventional}	1.77n	2.8n	3.55n	211.5P	321.44P	265.65P	234.5P	314.44P	265.65P
P_T (DFFI) _{thiswork}	1.43n	1.96n	2.77n	111.4P	223.44P	162.46P	175.4P	267.44P	162.46P



(a)



(b)

FIGURE 4: Comparison results of power consumption.

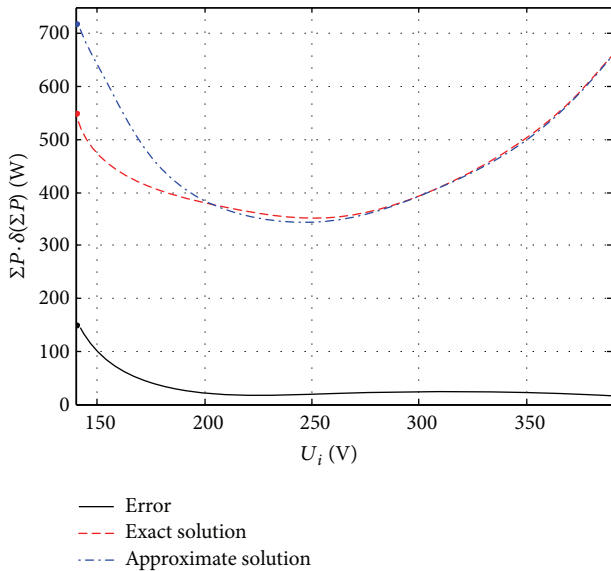


FIGURE 5: Comparison of minimum loss.

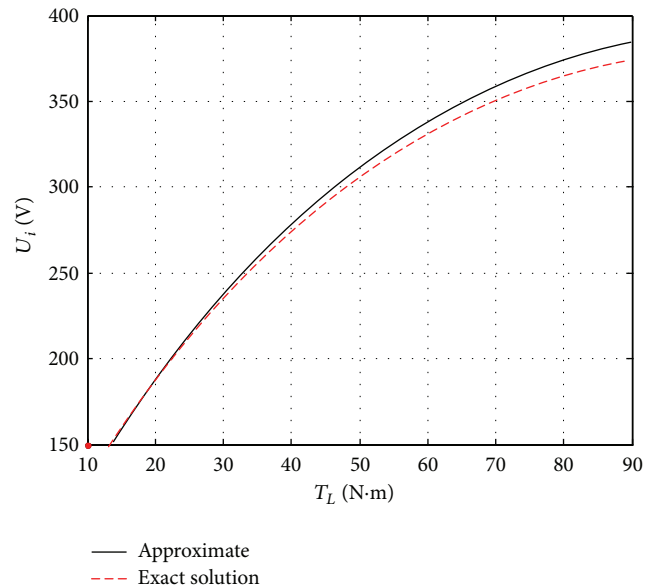


FIGURE 6: Comparison of optimal voltage.

load can be available. As it can be seen from Figure 6, the optimal voltage error will increase with the changes of load, but in the operating voltage range of UHF RF circuit, the optimal voltage error is calculated to be less than 7 V. Thus,

the front-end of UHF RF circuit load is small and the power consumption is relatively low.

5. Conclusions

In this paper, we reviewed the design approach or procedures of UHF tags. In response to the problem of high energy consumption, we present a lower power design for UHF RF CMOS circuit based on the power consumption acuity. The simulation results show that (1) the leakage power of rectifier in this method is obviously less than the conventional rectifier; (2) the delay of the rectifiers designed in this paper is smaller than the traditional structure; (3) the total loss is lower; (4) the design of UHF RF circuit based on the power consumption acuity can reduce 35%–40% power consumption. The proposed design method can be used for various industrial productions, public management and daily life, and so forth, and it will improve the development and efficiency of its application field.

Conflict of Interests

The authors declare that they have no conflict of interests.

Acknowledgment

This work was supported by Beijing modern agricultural technology system, Poultry innovation Team, 2013 Beijing New Rural Base Constructional Project.

References

- [1] R. Want, "An introduction to RFID technology," *IEEE Pervasive Computing*, vol. 5, no. 1, pp. 25–33, 2006.
- [2] J. Landt, "The history of RFID," *IEEE Potentials*, vol. 24, no. 4, pp. 8–11, 2005.
- [3] R. Angeles, "RFID technologies: supply-chain applications and implementation issues," *Information Systems Management*, vol. 22, no. 1, pp. 51–65, 2005.
- [4] R. Weinstein, "RFID: a technical overview and its application to the enterprise," *IT Professional*, vol. 7, no. 3, pp. 27–33, 2005.
- [5] C. M. Roberts, "Radio frequency identification (RFID)," *Computers and Security*, vol. 25, no. 1, pp. 18–26, 2006.
- [6] F. Zhou, C. Chen, D. Jin, C. Huang, and H. Min, "Evaluating and optimizing power consumption of anti-collision protocols for applications in RFID systems," in *Proceedings of the International Symposium on Lower Power Electronics and Design (ISLPED '04)*, pp. 357–362, ACM, August 2004.
- [7] K. V. S. Rao, P. V. Nikitin, and S. F. Lam, "Antenna design for UHF RFID tags: a review and a practical application," *IEEE Transactions on Antennas and Propagation*, vol. 53, no. 12, pp. 3870–3876, 2005.
- [8] P. V. Nikitin, K. V. S. Rao, S. F. Lam, V. Pillai, R. Martinez, and H. Heinrich, "Power reflection coefficient analysis for complex impedances in RFID tag design," *IEEE Transactions on Microwave Theory and Techniques*, vol. 53, no. 9, pp. 2721–2725, 2005.
- [9] U. Karthaus and M. Fischer, "Fully integrated passive UHF RFID transponder IC with 16.7- μ W minimum RF input power," *IEEE Journal of Solid-State Circuits*, vol. 38, no. 10, pp. 1602–1608, 2003.
- [10] R. Glidden, C. Bockorick, S. Cooper et al., "Design of ultra-low-cost UHF RFID tags for supply chain applications," *IEEE Communications Magazine*, vol. 42, no. 8, pp. 140–151, 2004.
- [11] S. Roundy, B. P. Otis, Y. h. Chee, J. M. Rabaey, and P. Wright, "A 1.9 GHz RF transmit beacon using environmentally scavenged energy," *Optimization*, vol. 4, no. 2, p. 4, 2003.
- [12] R. Banakar, S. Steinke, B.-S. Lee, M. Balakrishnan, and P. Marwedel, "Scratchpad memory: a design alternative for cache on-chip memory in embedded systems," in *Proceedings of the 10th International Symposium on Hardware/Software Codesign (CODES '02)*, pp. 73–78, ACM, May 2002.
- [13] K. M. Ramakrishnan and D. D. Deavours, "Performance benchmarks for passive UHF RFID tags," in *Proceedings of the 13th GI/ITG Conference in Measuring, Modelling and Evaluation of Computer and Communication Systems (MMB '06)*, VDE, 2006.
- [14] S. L. Garfinkel, A. Juels, and R. Pappu, "RFID privacy: an overview of problems and proposed solutions," *IEEE Security and Privacy*, vol. 3, no. 3, pp. 34–43, 2005.
- [15] H. Vogt, "Multiple object identification with passive RFID tags," in *Proceedings of the IEEE International Conference on Systems, Man and Cybernetics*, pp. 651–656, October 2002.
- [16] R. Rao, A. Srivastava, D. Blaauw, and D. Sylvester, "Statistical analysis of subthreshold leakage current for VLSI circuits," *IEEE Transactions on Very Large Scale Integration (VLSI) Systems*, vol. 12, no. 2, pp. 131–139, 2004.
- [17] A. Keshavarzi, S. Narendra, S. Borkar, C. Hawkins, K. Roy, and V. De, "Technology scaling behavior of optimum reverse body bias for standby leakage power reduction in CMOS IC's," in *Proceedings of the 1999 International Conference on Low Power Electronics and Design (ISLPED '99)*, pp. 252–254, August 1999.
- [18] G. M. Vitetta, U. Mengali, and D. P. Taylor, "Error probability formula for noncoherent orthogonal binary FSK with dual diversity on correlated Rician channels," *IEEE Communications Letters*, vol. 3, no. 2, pp. 43–45, 1999.

Research Article

Image Encryption Using the Chaotic Josephus Matrix

Gelan Yang,¹ Huixia Jin,¹ and Na Bai²

¹ Department of Computer Science, Hunan City University, Yiyang, Hunan 413000, China

² School of Electronics and Information Engineering, Anhui University, Hefei, Anhui 230039, China

Correspondence should be addressed to Na Bai; realbain@gmail.com

Received 3 October 2013; Accepted 14 January 2014; Published 6 March 2014

Academic Editor: Yue Wu

Copyright © 2014 Gelan Yang et al. This is an open access article distributed under the Creative Commons Attribution License, which permits unrestricted use, distribution, and reproduction in any medium, provided the original work is properly cited.

This paper presents a new image encryption solution using the chaotic Josephus matrix. It extends the conventional Josephus traversing to a matrix form and proposes a treatment to improve the randomness of this matrix by mixing chaotic maps. It also derives the corresponding encryption primitives controlled by the chaotic Josephus matrix. In this way, it builds up an image encryption system with very high sensitivities in both encryption key and input image. Our simulation results demonstrate that an encrypted image of using this method is very random-like, that is, a uniform-like pixel histogram and very low correlations in adjacent pixels. The design idea of this method is also applicable to data encryption of other types, like audio and video.

1. Introduction

Encryption is the process of transforming information (referred to as plaintext) using an algorithm (referred to as a cipher) to make the encrypted information (referred to as ciphertext) unreadable to anyone except those authorized users with special knowledge (referred to as a key) [1]. Encryption has been long used by militaries and governments to facilitate secret communications. Since the digital revolution in the 1980s, the demands of digital encryption in various applications have quickly increased because digital storage and communication are widely used. Encryption is now commonly used in protecting information within many types of civilian systems, like personal emails and patient documents.

Digital image is a major data type of two dimensions. Although a digital image can be extracted in order and becomes a one-dimensional data, its distinctive characteristics make conventional ciphers developed for one dimensional data unsuitable [2], for example, those based on Data Encryption Standard (DES) [3] and Advanced Encryption Standard (AES) [4]. As a result, digital image encryption has become an attractive research area in the past decade [5–11].

The chaotic map is considered a wise choice for data encryption because of its ergodicity, mixing property, high

sensitivity to the initial conditions, high deterministic properties, high unpredictable random behaviors, and so forth [2, 5, 9, 12–15]. However, the chaotic encryption method is criticized for its vulnerability to attacks via certain basin structures [16], its low efficiency for encrypting the whole image [2], its deteriorated randomness property from its use of the finite precision with fixed-point arithmetic [17], and nonuniform distribution of the chaos sequence [18].

In computer science [19] and mathematics [20], the Josephus problem is a theoretical problem related to a certain counting-out game. If the counting-out order is recorded as a sequence, a Josephus traversing is obtained because all elements in the game are traversed without repetition. The Josephus traversing has already been used in data encryption field for years. The Josephus traversing is simple to realize and fast to compute, but previous attempts focused more or less on the scrambling purposes [21, 22]. However, scrambling based encryption is vulnerable to statistical attack, ciphertext-only attack, and known plaintext attack [23] because it never changes pixel values.

In order to achieve higher security level, many recent efforts adopt the hybrid idea to use one encryption system to suppress disadvantages of another system while keeping advantages unchanged. For example, [24] incorporates the chaotic map to DES; [25, 26] combine the chaotic map into

```

Input:   $t$ , the initial total number of persons in a circle
           $s$ , the starting position in the circle
           $n$ , the counting period
Output:  $q_\pi$ , the Josephus permutation sequence according to parameter set  $(t, s, n)$ 
count = 0; done = 0; pos = s; label = zeros(1, t);  $q_\pi = []$ ; % initial settings
while (~done) % main loop
    todo = label(pos);
    if (todo == 0) % if this person has not been taken out
        count = count + 1;
        if (count ==  $n$ ) % if this is the  $n$ th person
             $q_\pi(\text{end} + 1) = \text{pos}$ ; count = 0; label(pos) = 1;
            if (length( $q_\pi$ ) ==  $t$ )
                done = 1;
            end
        end
    end
    pos = pos + 1;
    if (pos >  $t$ )
        pos = 1;
    end
end
end

```

ALGORITHM 1: The generation of a Josephus permutation sequence.

conventional transform domain encryption; [27, 28] add chaotic map to Sudoku puzzles for encryption. In this paper, we develop a new image encryption method by combining the ideas of the chaotic map, the Josephus traversing sequence, and conventional substitution and transposition ciphers. The remainder of the paper is organized as follows: in Section 2, the Josephus permutation and the Logistic chaotic map are briefly reviewed; in Section 3, the CJPM and its generator are given; in Section 4, the proposed image encryption method based on CJPM is fully discussed including its flowchart and functions for each part; in Section 5, simulation results are shown and various security analyses are applied; in Section 6, the paper is concluded.

2. Preliminary

2.1. Josephus Permutation. The Josephus permutation or Josephus problem is well known in computer science and mathematics. It is named after Flavius Josephus, a Jewish historian lived in the 1st century. It is a theoretical problem related to a certain counting-out game that works by having t people standing in a circle, with consecutive tags from 1 to t . Starting at predetermined person, you count around the circle. Once you reach the n th person, take them out of the circle and have the members to close the circle. Then repeat the process, until only one person is left. That person wins the game. If we record the tags of people who have been taken out at each round as a sequence, then this sequence is a permutation of a natural number sequence and is called Josephus permutation sequence.

It is clear that three parameters are involved in the Josephus problem, namely, the initial total number of persons in a circle t , the starting position in the circle s , and the counting period n . Therefore, a Josephus permutation sequence q_π

can be denoted as follows, where J denotes the Josephus permutation according to the set of parameters t , s , and n . A Josephus permutation sequence can be easily implemented by linked lists and dynamic arrays. Algorithm 1 describes a

$$q_\pi = J(t, s, n). \quad (1)$$

For example,

$$\begin{aligned} q_\pi &= J(18, 1, 4) \\ &= [4, 8, 12, 16, 2, 7, 13, 18, 6, 14, 3, 11, 5, 17, 15, 1, 10, 9], \end{aligned} \quad (2)$$

$$\begin{aligned} q_\pi &= J(18, 1, 7) \\ &= [7, 14, 3, 11, 1, 10, 2, 13, 6, 18, 16, 15, 17, 5, 12, 4, 8, 9], \end{aligned} \quad (3)$$

$$\begin{aligned} q_\pi &= J(18, 4, 7) \\ &= [10, 17, 6, 14, 4, 13, 5, 16, 9, 3, 1, 18, 2, 8, 15, 7, 11, 12]. \end{aligned} \quad (4)$$

It is clear that (1) compared with the length t natural number sequence, a Josephus permutation sequence q_π changes a lot, especially considering that none of the two neighbor numbers is consecutive; (2) for a fixed length t , different pairs of (s, n) give distinct Josephus permutation sequences. However, it is weak in that (1) q_π 's very first several elements divulge the parameter of counting period n ; (2) the difference between two q_π s may disclose the difference between their starting positions; for example, the difference between the two first elements of q_π s in (3) and (4) is 3, which is the difference of their parameters of starting positions. Therefore, it is not completely random for a Josephus permutation sequence.

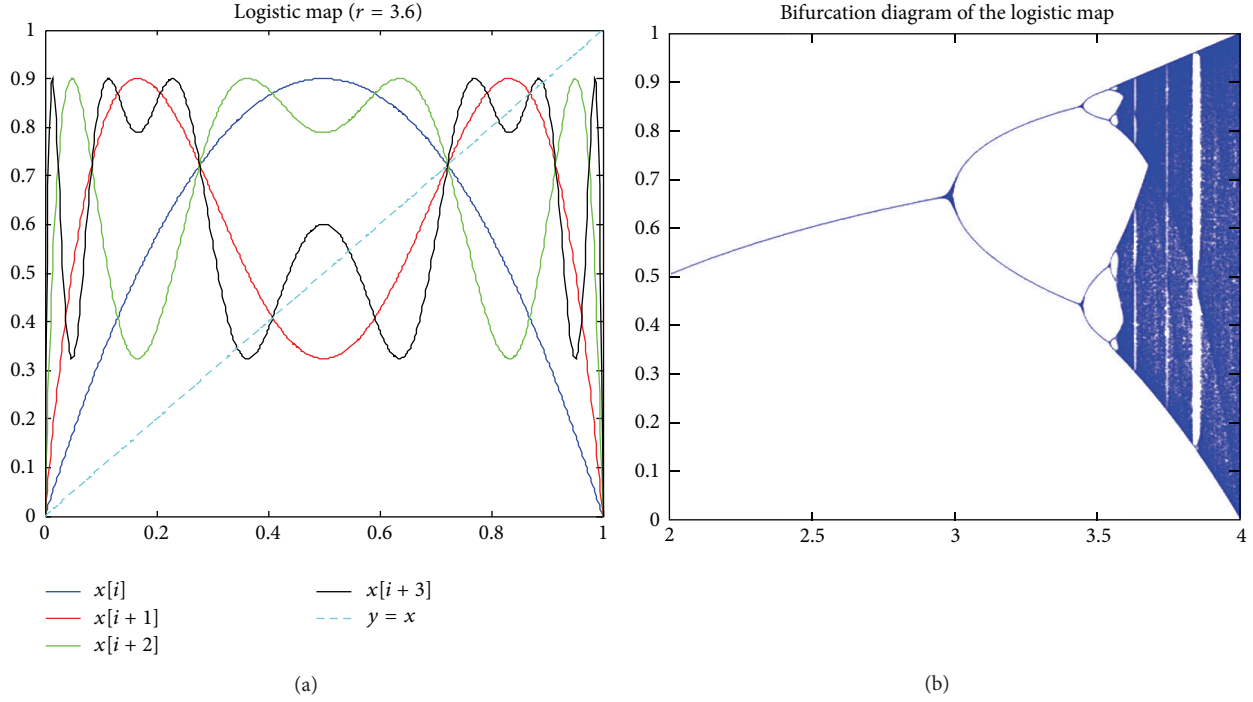


FIGURE 1: The Logistic map.

2.2. *Chaotic Logistic Map.* The Logistic map is a polynomial mapping of degree two. It was introduced by the biologist Robert May in 1976 [31]. The Logistic map is written as (5), where symbol \mathcal{L} is used to denote the Logistic map; $X_i \in [0, 1]$ and represents the population at year i and hence X_0 represents the initial population at year 0; r is a positive number and represents the combined rate for reproduction and starvation [32]. This map is often cited as an example of how complex chaotic behaviors can arise from a very simple nonlinear dynamic equation. Consider

$$X_{i+1} = \mathcal{L}(X_i) = rX_i(1 - X_i). \quad (5)$$

The Logistic map has been well studied. The plots of the first few iterations of the Logistic map and its bifurcation diagram are shown in Figure 1. It is well known that when $r \in [3.57, 4]$ (approximately), the Logistic map has chaotic behaviors for most values, but there are still certain isolated ranges of r that show nonchaotic behavior; for example, $r \approx 3.83$, which corresponds to a big gap in its bifurcation diagram.

In reality, the Logistic sequence is controlled by a set of parameters of (X_0, r, N, m) , where (X_0, r) are parameters in the Logistic map, N is the length of sequence, and m denotes the number of thrown-away samples. Therefore, a Logistic sequence X can be denoted as (6). Based on this logistic sequence X of length N , sorted sequence X' can be obtained by sorting X in the ascending order. It is certain that X' is a permutation of the original X . Therefore, X and X' satisfy (7),

where p_π is a permutation mapping sequence and i denotes sequence element index. Consider

$$X = \mathcal{L}(X_0, r, N, m), \quad (6)$$

$$X'_i = X_{p_\pi(i)} \quad (7)$$

$$X = [0.4000, 0.9120, 0.3050, 0.8055, 0.5954, 0.9154, 0.2943, 0.7892, 0.6322, 0.8836, 0.3908, 0.9047, 0.3277, 0.8372, 0.5179, 0.9488, 0.1846, 0.5721], \quad (8)$$

$$X' = [0.1846, 0.2943, 0.3050, 0.3277, 0.3908, 0.4000, 0.5179, 0.5721, 0.5954, 0.6322, 0.7892, 0.8055, 0.8372, 0.8836, 0.9047, 0.9120, 0.9154, 0.9488], \quad (9)$$

$$p_\pi = L(0.4, 3.8, 18, 0) = [17, 7, 3, 13, 11, 1, 15, 18, 5, 9, 8, 4, 14, 10, 12, 2, 6, 16]. \quad (10)$$

For example, if $(X_0, r, N, m) = (0.4, 3.8, 18, 0)$, then X and X' are shown in (8) and (9), respectively. Correspondingly, the permutation sequence p_π is determined as (10).

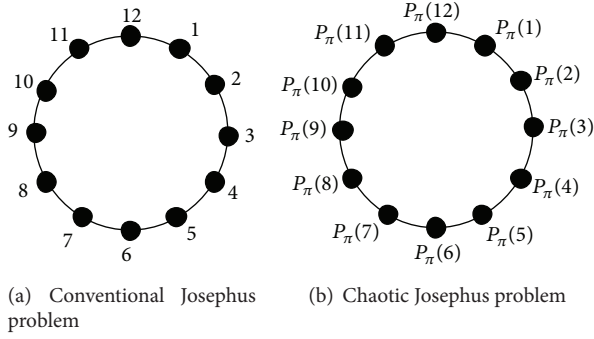


FIGURE 2: The chaotic Josephus problem.

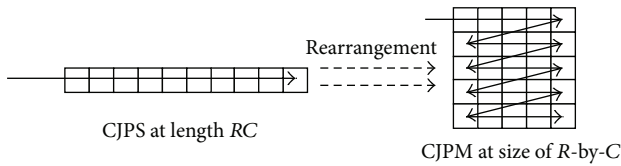


FIGURE 3: Rearranging a CJPS to a CJPM.

3. Chaotic Josephus Permutation Matrix (CJPM)

3.1. Chaotic Josephus Permutation Sequence (CJPS). From previous sections, it is clear that the Josephus permutation sequence q_π and the chaotic permutation sequence p_π are obtained from different mechanisms. The Josephus permutation sequence q_π is easy to obtain but not completely random-like, while the chaotic permutation sequence p_π is random-like but requires a large amount of computations for maintaining accuracy. It is desirable that a permutation sequence be random-like and only costs moderate computations.

In order to achieve the above objective, the new Josephus permutation sequence based on a chaotic permutation sequence p_π is defined, whose initial positions on the circle are not consecutive numbers like those in the conventional Josephus problem. This new problem can be restated as follows: (1) t people with numbered tags stand in a circle (these numbers together form a permutation sequence according to sorting a chaotic sequence); (2) starting at predetermined person, you count around the circle until you reach the n th person; take him out of the circle and have the members to close the circle and record his tag number; (3) repeat the process, until only one person is left. If we record the tags of people who have been taken out of the circle as a sequence, then a chaotic Josephus permutation sequence is obtained.

It is noticeable that the chaotic Josephus problem has parameters for both the chaotic Logistic map and for the conventional Josephus problem. In other words, a chaotic Josephus permutation sequence cq_π is determined by (11), where parameters t, s, n have the same meanings as in (1), X_0 and r are parameters in the Logistic map, and m determines

the number of thrown-away samples in the chaotic Logistic sequence. Consider

$$cq_\pi = cJ(t, s, n, X_0, r, m). \quad (11)$$

In the conventional Josephus problem (controlled by parameters (t, s, n) ; see (1)), a natural number sequence 1 to t is used to denote the tags for people standing in the circle, while a permuted sequence p_π (controlled by parameters (X_0, r, N, m) ; see (6)) is used in the chaotic Josephus problem as the tags. In order to match the sequence lengths of p_π and q_π , $t = N$ is the condition that has to be satisfied. The conventional Josephus problem and the chaotic Josephus problem for $t = N = 12$ are illustrated in Figure 2.

Therefore, the new Josephus permutation sequence cq_π can be denoted as a composed function of a conventional Josephus permutation sequence q_π and a chaotic permutation sequence p_π :

$$cq_\pi = p_\pi \circ q_\pi = p_\pi(q_\pi). \quad (12)$$

For example, if $q_\pi = J(18, 1, 4)$ in (2) and $p_\pi = L(0.4, 3.8, 18, 0)$ in (10) are preknown, $cq_\pi = cJ(18, 1, 4, 0.4, 3.8, 0)$ is obtained as (13) shows by using (12). Similarly, (14)–(16) can be also obtained. Consider

$$\begin{aligned} cq_\pi &= cJ(18, 1, 4, 0.4, 3.8, 0) \\ &= [13, 18, 4, 2, 7, 15, 14, 16, 1, 10, 3, 8, 11, 6, 12, 17, 9, 5] \end{aligned} \quad (13)$$

$$\begin{aligned} cq_\pi &= cJ(18, 1, 7, 0.4, 3.8, 0) \\ &= [15, 10, 3, 8, 17, 9, 7, 14, 1, 16, 2, 12, 6, 11, 4, 13, 18, 5] \end{aligned} \quad (14)$$

$$\begin{aligned} cq_\pi &= cJ(18, 4, 7, 0.4, 3.8, 0) \\ &= [9, 6, 1, 10, 13, 14, 11, 2, 5, 3, 17, 16, 7, 18, 12, 15, 8, 4] \end{aligned} \quad (15)$$

$$\begin{aligned} cq_\pi &= cJ(18, 4, 7, 0.40001, 3.8, 0) \\ &= [8, 6, 1, 10, 11, 12, 13, 2, 9, 15, 7, 18, 3, 5, 14, 17, 4, 16]. \end{aligned} \quad (16)$$

Compared to the previous conventional Josephus permutation sequence (see (2)–(4)), the chaotic Josephus permutation sequences (see (12)–(15)) are more random-like because (1) the difference between its very first elements is not related to its counting period anymore; (2) the difference between two cq_π s, which are only different in their starting positions, is no longer equal to the difference of their starting positions; (3) slight perturbations in chaotic map parameters lead to big changes in resulting cq_π s; (4) two neighbor elements in cq_π may or may not be consecutive. Therefore, the chaotic Josephus permutation sequence is more random-like than the conventional Josephus permutation sequence.

3.2. Chaotic Josephus Permutation Matrix (CJPM). Based on chaotic Josephus permutation sequence(s), a chaotic Josephus permutation matrix can be generated via various ways.

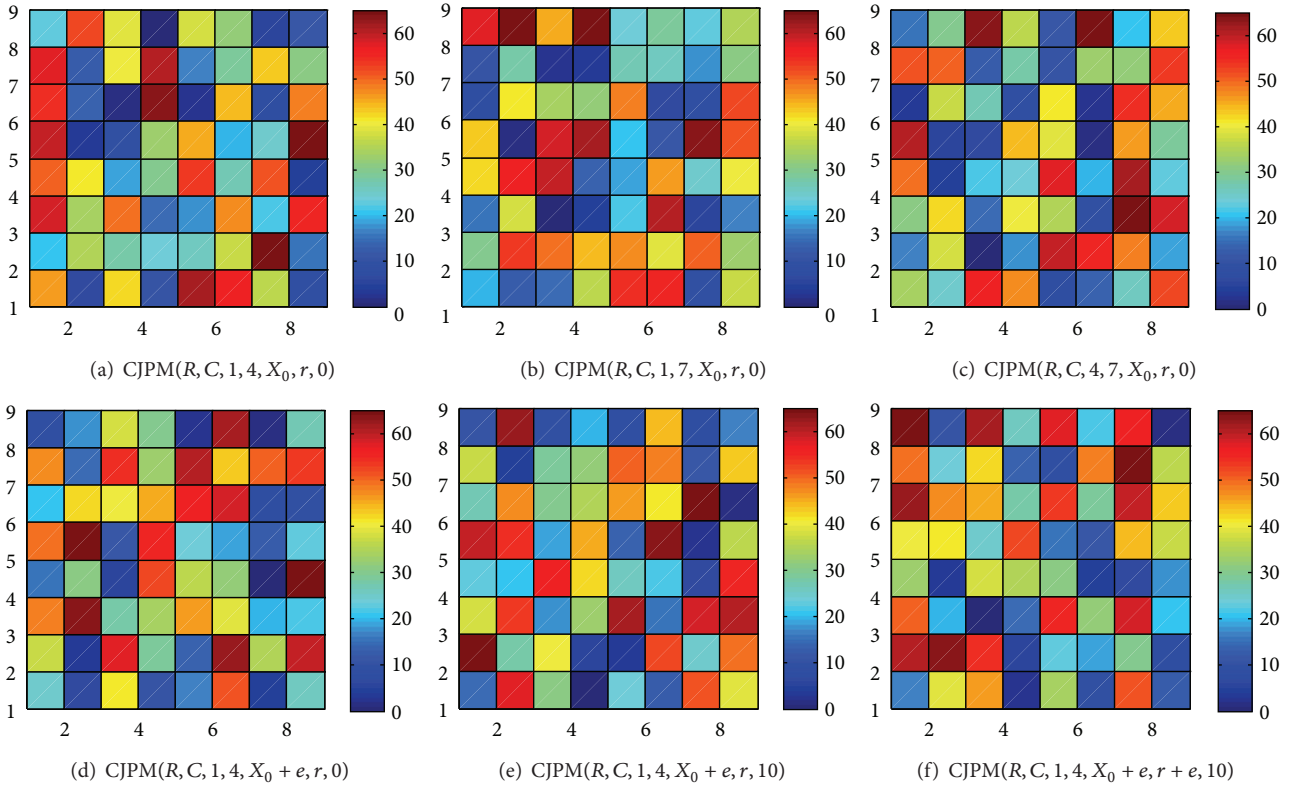


FIGURE 4: Parametric CJPMs (Note: $R = 8, C = 8, X_0 = 0.4, r = 3.8,$ and $e = 0.0001.$)

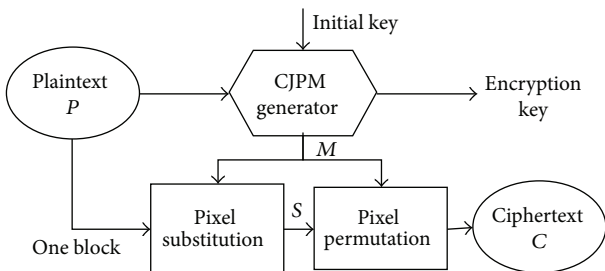


FIGURE 5: Image encryption method based on CJPM.

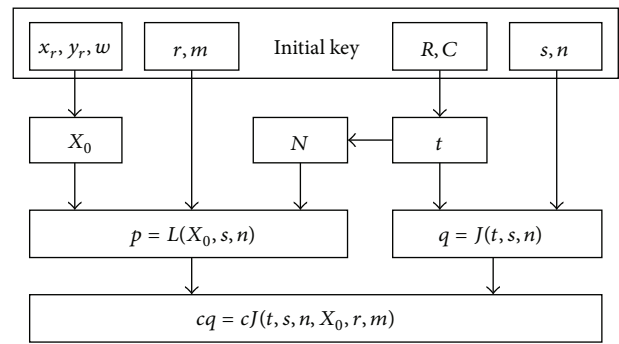


FIGURE 6: Key functions in CJPM.

Among these methods, Algorithm 2 illustrates a straightforward method to obtain a CJPM via a CJPS by rearranging CJPS elements to a matrix.

It is noticeable that Algorithm 2 is equivalent to rearranging a sequence of elements into a matrix following the order illustrated in Figure 3.

Therefore, a CJPM is determined by the same set of parameters controlling a CJPS. In order to emphasize the matrix property, the parameter t in CJPS is replaced by two parameters of height R and width C , where $t = RC$. Similarly, a CJPM is uniquely determined by a set of parameters (R, C, s, n, X_0, r, m) as for a CJPS. Mathematically, this claim can be denoted as

$$M = \text{CJPM}(R, C, s, n, X_0, r, m). \quad (17)$$

Figure 4 illustrates various CJPMs via Algorithm 2 according to different parameter sets. It is clear that CJPM is very sensitive to its parameters and small changes in the parameter set lead to distinct CJPMs.

4. Image Encryption Algorithm Based on CJPM

In 1949, Claude Shannon, the father of “Information Theory,” proposed that confusion and diffusion are two properties of the operation of a secure cipher, where the term confusion refers to making the relationship between the encryption key and the ciphertext a very complex and developed one

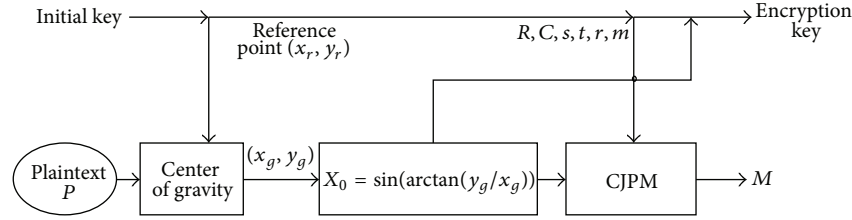


FIGURE 7: The internal structure of CJPM generator.

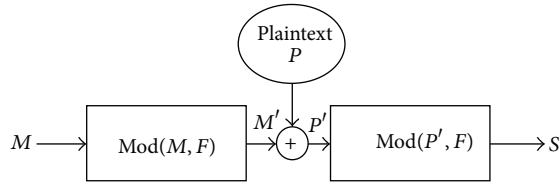


FIGURE 8: The internal structure of CJPM generator.

[33], and the term diffusion refers to the property that the redundancy in the statistics of the plaintext is “dissipated” in the statistics of the ciphertext [33]. In other words, for a secure cipher, it has to have good confusion and diffusion properties: (1) different ciphertexts are desired to have similar statistics; (2) any slight change in a plaintext is desired to lead to big difference in its ciphertext. The image encryption algorithm based on CJPM is proposed in this section to meet these two criteria.

4.1. Flowchart of Image Encryption Algorithm Based on CJPM. Since the CJPM is parametric and random-like, it can be used for image encryption directly. However, considering the requirements from confusion and diffusion properties, the encryption procedure can be described as Figure 5 shows. The plaintext image is first sent to the CJPM generator, which is a preparation stage for generating a CJPM M for future use. Later, this CJPM M is used as a reference matrix to permute and substitute image pixels for each image block in the stages of pixel permutation and pixel substitution, respectively. The decryption procedure is simply to reverse the encryption procedure.

4.2. Key Schedule. It is clear that the CJPM is the core of the cipher and thus key is related to the used CJPM reference matrix M . Initial key is composed of parameters $(x_r, y_r, w, r, m, R, C, s, n)$, where (x_r, y_r, w) is used in CJPM generator for obtaining plaintext-dependent parameter X_0 used in the Logistic map; (R, C) are used as the parameter t in (1) and the parameter N in (6). The functions of each part of the initial key are shown in Figure 6.

The output encryption key is composed of (R, C, s, n, X_0, r, m) , all of which are directly required for determining a CJPM according to (17). Among these parameters, R, C, s, n , and m are restricted to integers; x_r, y_r, r , and X_0 are decimals. More specifically, R and C should be positive

integers smaller than the plaintext image size; s and n should be positive integers below the product of RC ; r should be a number in between $[3.6, 4]$; (x_r, y_r) is an arbitrary point on xy plain with weight w and m is a nonnegative integer.

4.3. CJPM Generator. In order to enhance the resistance to differential attacks, the CJPM generator used in Figure 5 is designed to be plaintext dependent. Recall that a CJPM is determined by a set of parameters (R, C, s, n, X_0, r, m) shown in (17). In the CJPM generator for image encryption, only the parameter X_0 is not directly given by the initial key but by the plaintext and a reference point (x_r, y_r) controlling the weight in calculating the center of gravity. Once X_0 is generated, it is stored in the encryption key. The whole procedure of translating the initial key to a plaintext-dependent CJPM matrix M and encryption key is shown in Figure 7.

A plaintext is considered as an object of pixels where its upper-left corner pixel is the reference point located at $(1, 1)$. Correspondingly, pixels next to it along x and y directions are $(2, 1)$ and $(1, 2)$, respectively. The center of gravity of this plaintext is calculated via (18), where P_i denotes the i th pixel intensity value and x_i and y_i denote the location of the i th pixel in the image with respect to the upper-left corner. Once the center of gravity (x_g, y_g) is obtained, the initial value of Logistic map X_0 is also determined via (19), where $\arctan(\cdot)$ is the arc tangent function and $\sin(\cdot)$ is the sine function. It is easy to verify that the range of (19) is $[0, 1]$, which satisfies restrictions for the initial value X_0 in the Logistic map. Finally, all required parameters for a CJPM, that is, (R, C, s, n, X_0, r, m) , are obtained and thus a CJPM M is generated. Meanwhile, the used parameters are stored as the encryption key, which can be used in the decryption process. Consider

$$x_g = \frac{x_r \cdot w + \sum x_i P_i}{w + \sum P_i}, \quad (18)$$

$$y_g = \frac{y_r \cdot w + \sum y_i P_i}{w + \sum P_i},$$

$$X_0 = 0.5 \left[\sin \left(\arctan \left(\frac{y_g}{x_g} \right) \right) + 1 \right]. \quad (19)$$

It is worth noting that the plaintext-dependent CJPM generator guarantees that the proposed cipher has good diffusion property: any slight changes in plaintext lead to big difference in ciphertext. This is because the resulting

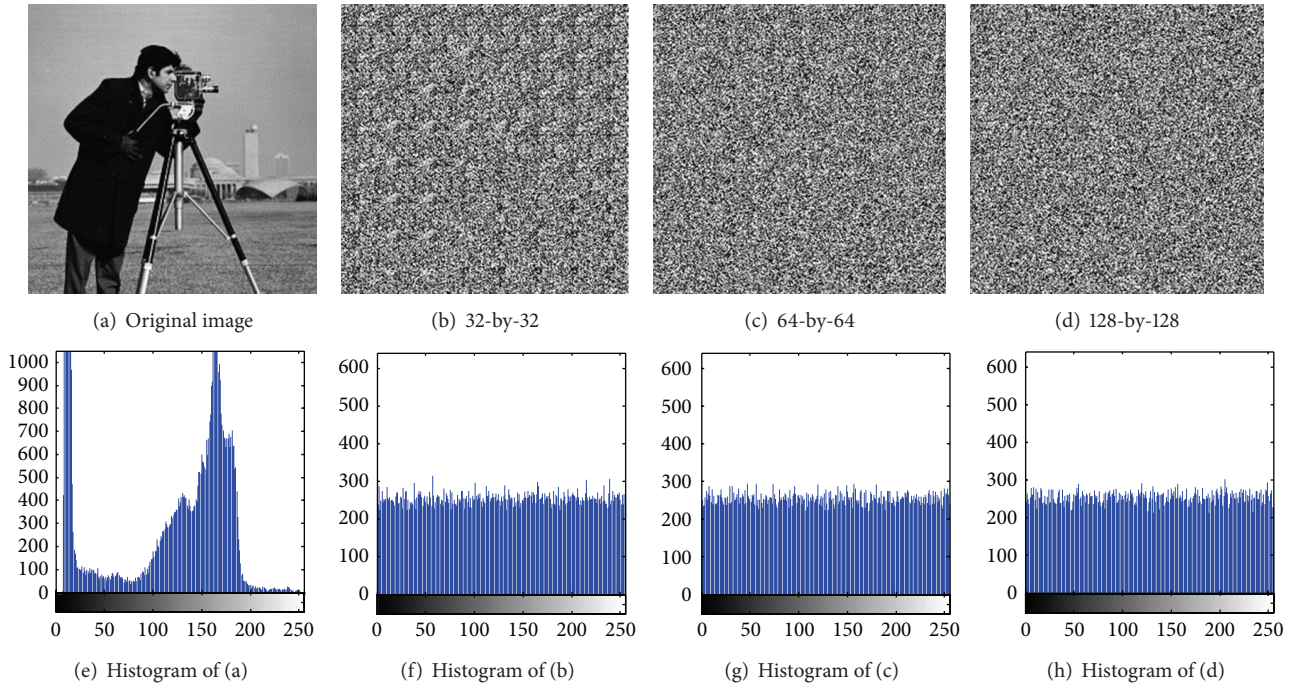


FIGURE 9: Pixel substitution results for CJPM at various sizes.

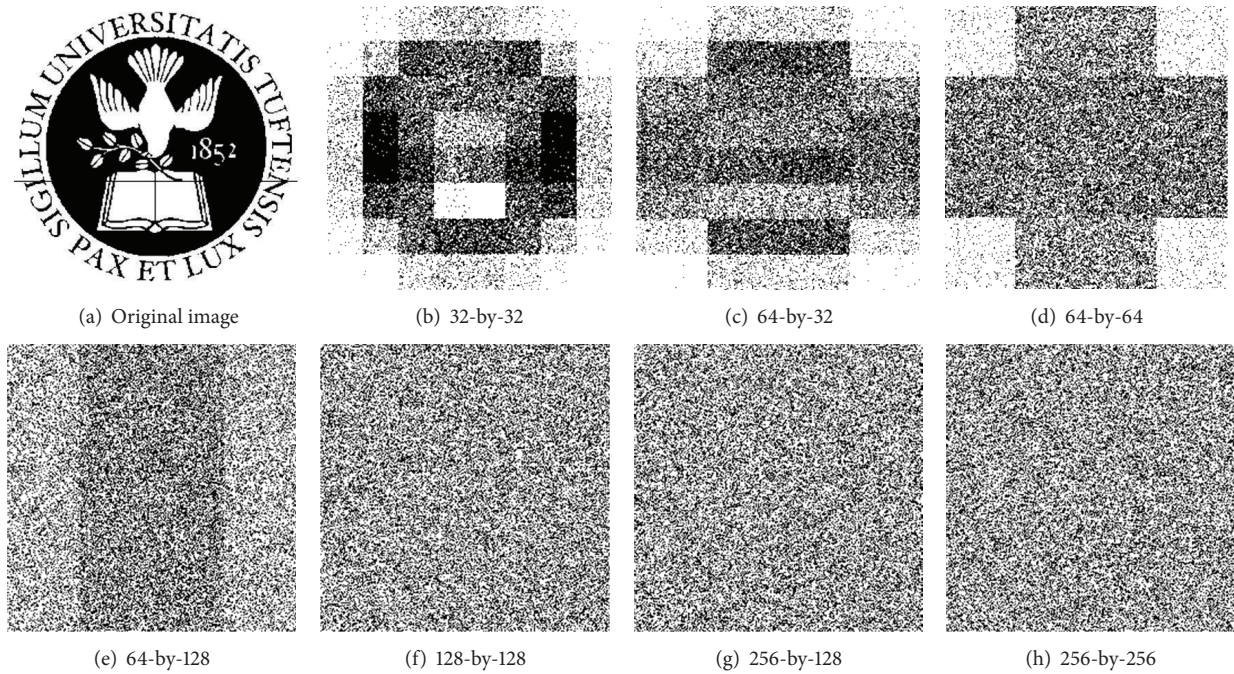


FIGURE 10: Pixel permutation results for CJPM at various sizes.

CJPM matrix M is dependent on the parameter X_0 and the parameter X_0 is dependent on the center of gravity for the plaintext, while the center of the plaintext gravity alters for any slight change in plaintext. Furthermore, this X_0 is the parameter in the chaotic map, and thus any slight change

in initial value leads to a completely different trajectory as the bifurcation diagram in Figure 1 shows. Consequently, a completely different CJPM is obtained as the reference matrix. Eventually, this new reference matrix leads to a distinct ciphertext. It can be demonstrated that without

```

Input:  $cq_\pi$ , a CJPS at length  $t = R \times C$ 
Output:  $M$ , a CJPM of size  $R$ -by- $C$ 
for  $i = 1: R$ 
    for  $j = 1: C$ 
         $M(i, j) = cq_\pi((i - 1)R + j)$ ;
    end
end

```

ALGORITHM 2: Reshape a CJPS into a CJPM.

preknowing the reference point's coordinate (x_r, y_r) and its weight w , there is no way to slightly change plaintext image pixels so that its gravity center is unchanged.

4.4. Pixel Substitution. Pixel substitution refers to the process of changing pixel values. From the point of view of statistics, this process is to change the statistics of a plaintext image, so that the statistics of resulting ciphertext image is completely different. Moreover, it is desired that different ciphertext images have similar statistics, which implies that ciphertext images tell little information about keys and plaintext images. As a result, the confusion property is achieved.

The proposed pixel substitution block is shown in Figure 8, where symbol $F = 2^b$ and b denotes the number of bits supported by the format of the plaintext image. For example, if plaintext P is an 8-bit gray image, then $F = 2^8 = 256$; if plaintext P is a binary image, then $F = 2^1 = 2$. It can be noticed that the reference CJPM M is first to convert to M' , whose format is compatible with the format of the plaintext image; later M' and P are added over the space of F ; finally the encrypted image S is obtained.

Because elements in a CJPM matrix M are uniformly distributed on integer set $[1, t]$, after "Mod" operation, M' still has a uniform-like distribution for its elements on $[0, F]$. As a result, when this M' is used to randomly shift the pixel value in plaintext, the resulting pixel value in ciphertext has an equal opportunity to be any value on $[0, F]$. As a result, a uniform-like histogram is achieved in the ciphertext.

Pixel substitution results based on CJPMs are shown in Figure 9. It is clear that histograms before and after pixel substitution are very different and ciphertext histograms are very flat compared to plaintext ones. It is also noticeable that as the size of the reference CJPM increases the ciphertext has a better encryption quality from the point view of human visual inspection.

4.5. Pixel Permutation. Pixel permutation refers to the process scrambling the positions of pixels in plaintext to disguise information contained in an image. Denote an image before and after pixel permutation as B and A , respectively. Assume the way of indexing image pixels is the same as the order to rearrange elements in a CJPM as Figure 3 shows. Then the pixel permutation process can be mathematically defined as a permutation f_π between domain B and range A : $\forall i, j \in$

$\{1, 2, \dots, t\}, \exists A_i = B_j = B_{f_\pi(i)}$, where t is the total number of pixels in the image. As we mentioned in previous sections, a CJPM is generated from a CJPS, which is a permutation sequence. Therefore, a CJPM can be directly used for pixel permutation that is given a CJPM M , and its pixel permutation can be defined as $f_\pi(i) = M(i)$.

For example, Figure 10 illustrates pixel permutation results of the "Tufts" logo image for different CJPMs. It is clear that pixels are well shuffled within the image block. As long as the size of CJPM/processing image block increases, the resulting shuffled image looks better and better. When the block size reaches to or over 128-by-128, pixels in the plaintext are almost evenly shuffled.

It is clear that images after pixel permutation look very different from the plaintext image. It is also worth noting that a CJPM also depends on a set of parameters besides the size and that any change in other parameters will lead to a completely different permuted image.

5. Simulation Results and Security Analysis

An excellent encryption method should be both robust and effective. Robustness means that the cipher should be applicable to any plaintext image written in a supported format. Effectiveness implies that the cipher is able to generate eligible ciphertext images, which hide information from possible intruders.

In this section, we focus on discussing the performance of the CJPM based image cipher described in Section 4. It is worth noting that all following computer simulations are run under MATLAB 2010a and Windows XP environment with Core 2 Quad 2.6 GHz processors.

5.1. Histogram Analysis. Histogram analysis is one of the most straightforward evaluations for ciphertext quality for it directly analyzes the pixel distribution of a ciphertext image.

Figure 11 illustrates image encryption results for various plaintext images: image "113" is a binary handwriting scanned image selected from ICDAR 2009 database; image "Lena" is a commonly used image of gray type; image "5.1.13" and "testpat.1k" are used to mimic the possible complex patterns in plaintext and they are both selected from USC-SIPI database. It is worth noting that the used CJPM is at size of 256-by-256.

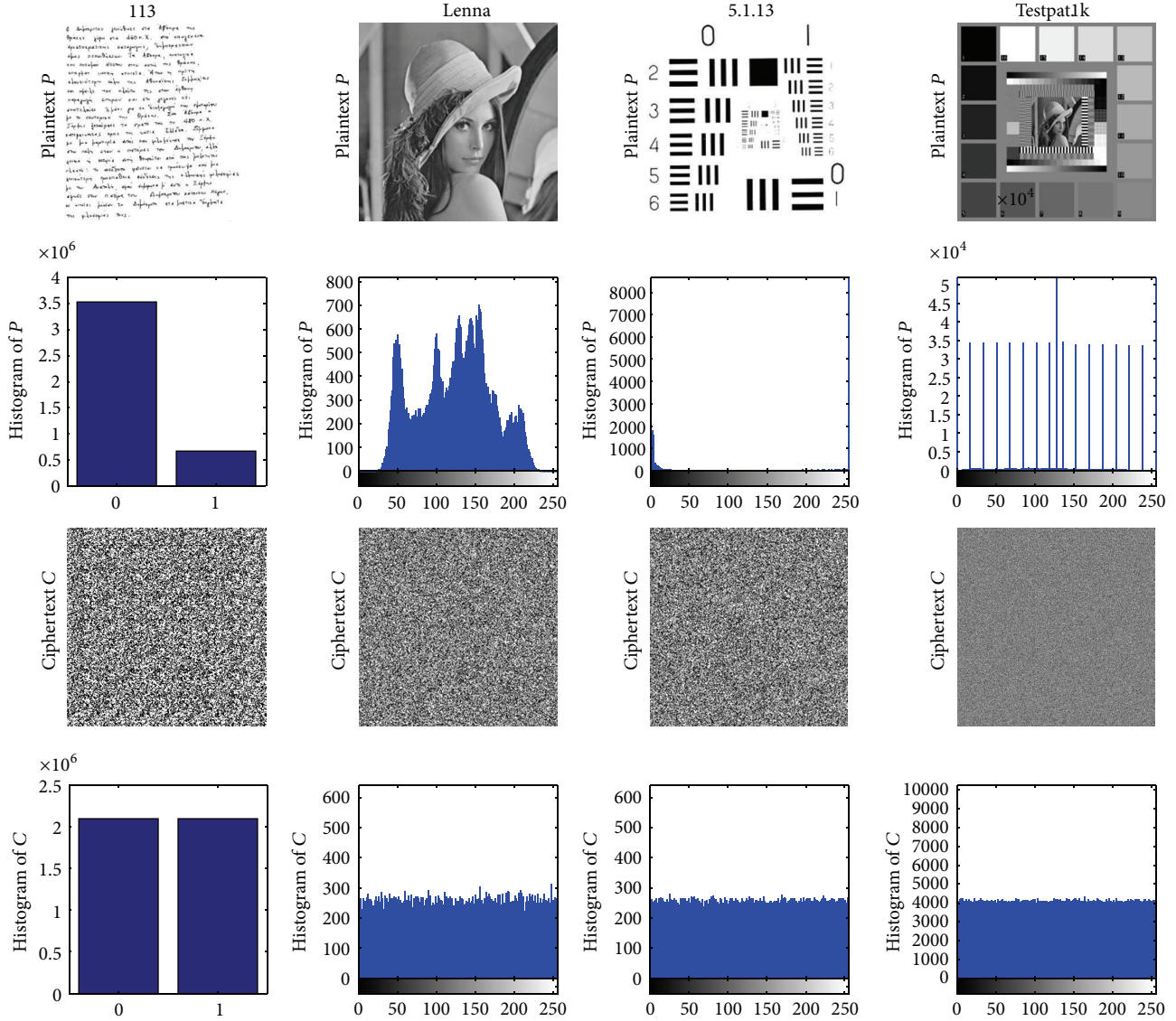


FIGURE 11: Histogram analysis for image encryption based on CJPM.

It is clear that no matter what histogram a plaintext image has, the histogram of its ciphertext image is flat, which implies that the pixel distribution is almost uniform. Complex patterns and large homogenous regions in plaintext images are completely unintelligible and become random-like in ciphertext images. These results imply that the proposed image encryption method based on CJPM is robust and effective for various image formats and contents.

5.2. Adjacent Pixel Autocorrelation (APAC) Analysis. High correlations of adjacent pixels can be utilized to carry out cryptanalysis. Therefore, a secure encryption algorithm should break the high correlation relationship between adjacent pixels.

In statistics, the autocorrelation R_a of a random process X describes the correlation between values of the process at different points in time, as a function of the two times or of the time difference. The autocorrelation coefficient R_a is defined in (20), where d is the time difference, μ is the mean value defined by (21), and σ is the standard deviation defined by (22); the definition of mathematical expectation is given in (23):

$$R_a(m) = \frac{E[(X_t - \mu)(X_{t+d} - \mu)]}{\sigma^2}, \tag{20}$$

$$\mu = E[X], \tag{21}$$

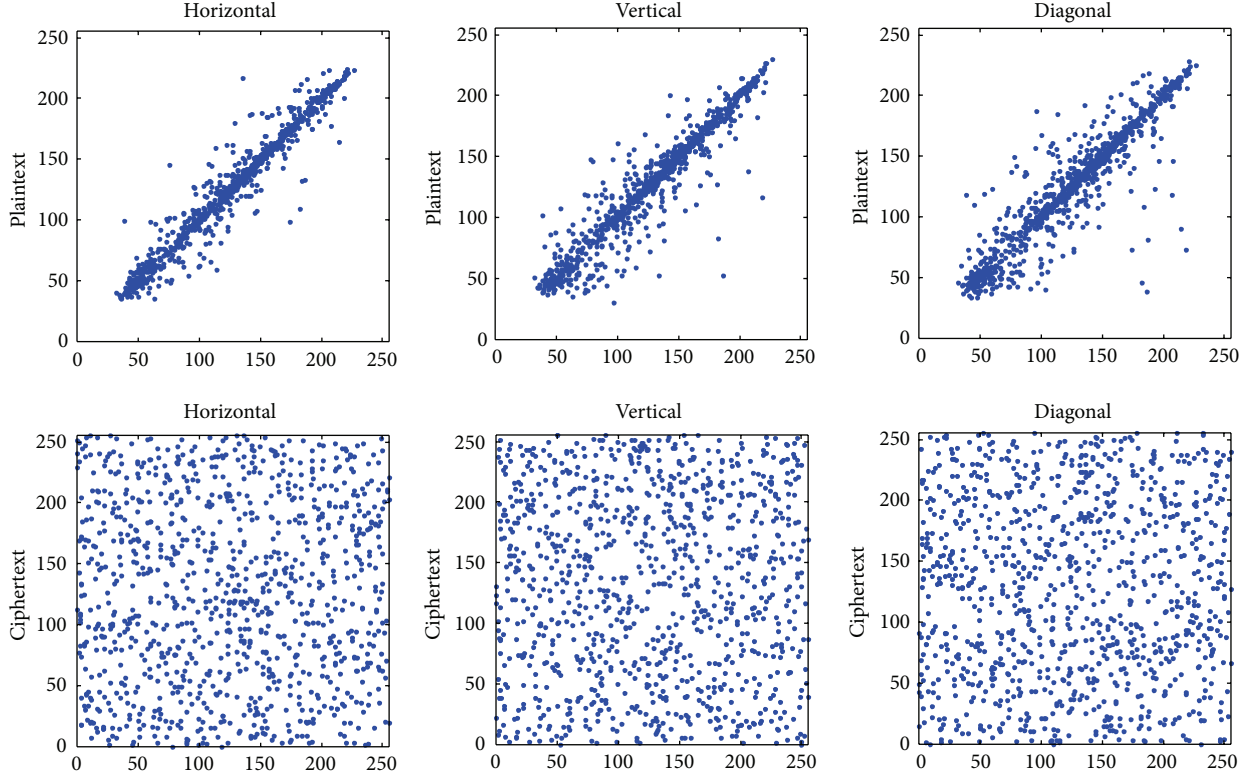


FIGURE 12: APAC analysis for image encryption based on CJPM.

TABLE 1: Adjacent pixel autocorrelation analysis.

Correlation coefficients (10^{-3})		Horizontal	Vertical	Diagonal
Plaintext	Lena	939.9652	970.9000	970.9894
	CJPM	-2.2281	-0.3709	3.265
	[6]	2.0970	16.1870	17.805
	[8]	-2.5000	-1.0000	-9.3000
Ciphertext	[5]	5.7765	28.434	20.662
	[29]	-12.7212	-60.2579	62.4427
	[9]	-13.4000	1.2000	39.8000
	[30]	-15.8900	-65.3800	-32.3100
	[16]	81.5860	-40.0530	-4.7150
	[10]	125.7000	58.1000	50.4000

$$\sigma = \sqrt{E[(X - \mu)^2]}, \quad (22)$$

$$E[x] = \sum_{i=1}^N \frac{x_i}{N}. \quad (23)$$

The closer to zero this coefficient is, the weaker the relationship two different time functions have. Specifically, in adjacent pixel correlation test, we let X be the image pixel sequence and let d be 1; that is, compare to the adjacent pixel sequence.

Based on the reference direction, there are three ways of extracting a two-dimensional image to a one-dimensional sequence and they are the horizontal adjacent correlation

coefficient, the vertical adjacent correlation coefficient, and the diagonal adjacent correlation coefficient.

“Lena” image in the 2nd column of Figure 11 is used as the test plaintext image because its APAC is widely reported by other encryption methods. Peer comparison results of the proposed CJPM cipher and cited encryption methods on APAC are shown in Table 1 (best results are bolded).

In addition, Figure 12 shows the result of randomly selected 1024 pairs of two adjacent pixels from the plaintext and the ciphertext along horizontal, vertical, and diagonal directions, where x - and y -axes denote the intensity values of a randomly selected pixel and its adjacent pixel, respectively. It is clear that after applying the CJPM based image cipher, the high correlations between adjacent pixels in plaintext are broken.

5.3. Plaintext Sensitivity Analysis. In order to test the resistance of the cipher to differential attacks, plaintext sensitivity analysis is required for a secure cipher. In differential attacks, an adversary attempts to extract meaningful relationship between a plaintext image and its ciphertext image by making a slight change, usually only one pixel, in the plaintext image while encrypting the plaintext image with the same encryption key. By comparing the change in ciphertext images, the encryption key might be cracked and furthermore the information contained in ciphertext might be leaked.

Although there are other measures [34, 35] to evaluate the resistance of plaintext attacks, two classic measures are the Number of Pixel Change Rate (NPCR) and Unified Average

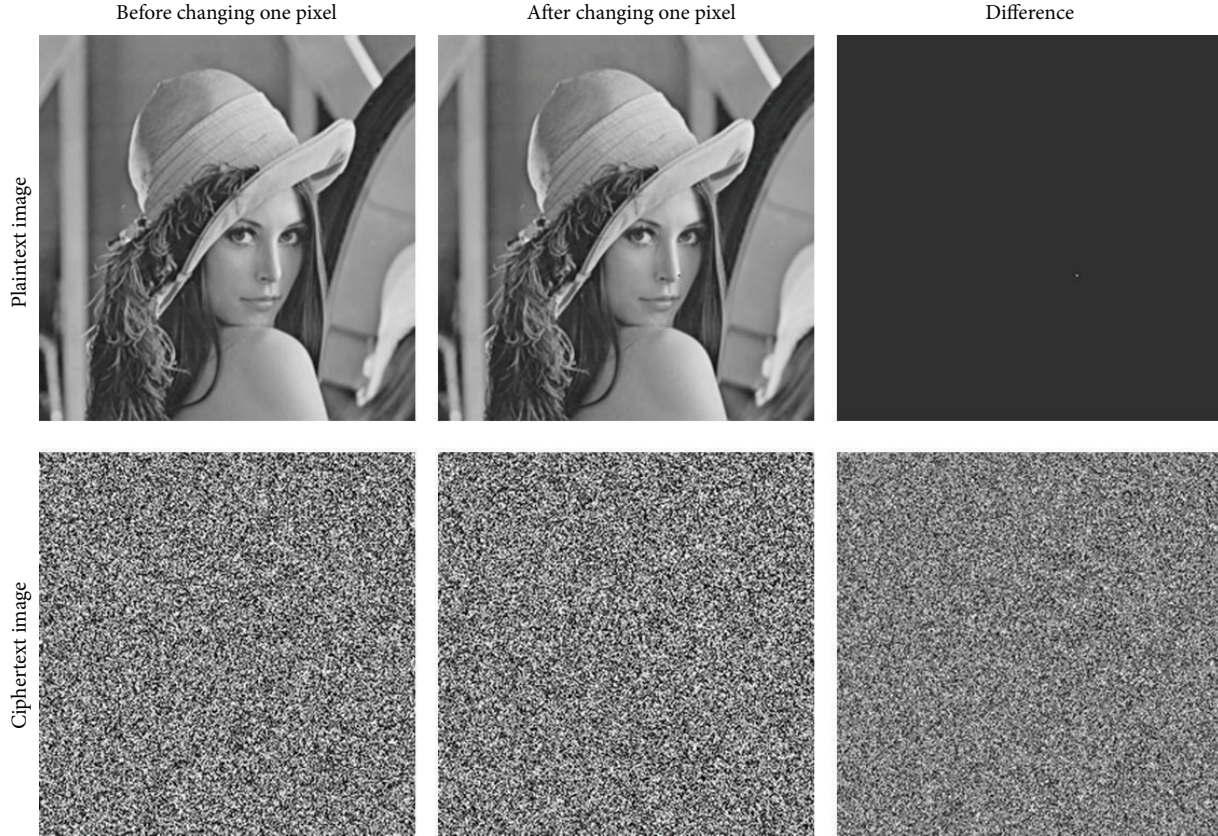


FIGURE 13: Plaintext sensitivity analysis (differential attacks) for image encryption based on CJPM.

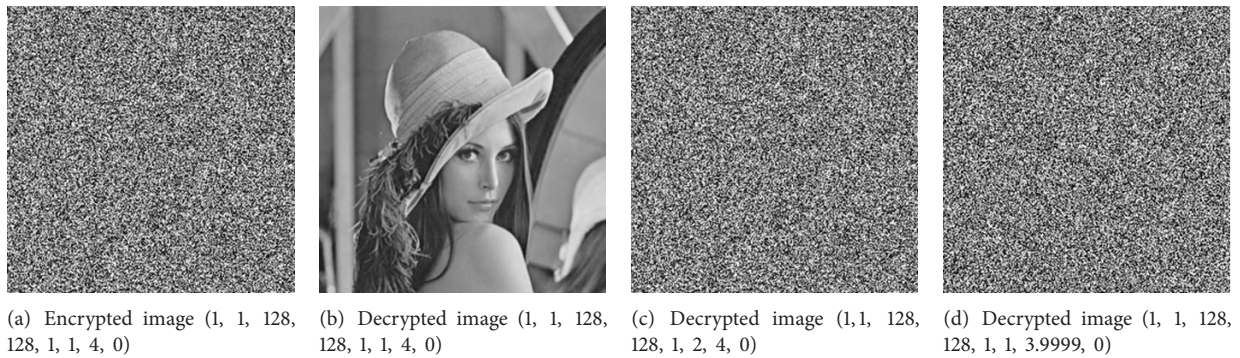


FIGURE 14: Key sensitivity analysis.

Changing Intensity (UACI) [5]. The NPCR is used to measure the percentage of the number of pixels changed in ciphertext after making a slight change in plaintext. Therefore, the theoretical greatest upper-bound of the NPCR is 100%. The UACI is used to measure the averaged intensity change for pixels in ciphertext images after making a slight change in a plaintext image. It is demonstrable that the UACI of an ideal cipher for 8-bit gray images is about 0.3346 [36].

Suppose ciphertext images before and after one pixel change in a plaintext image are C^1 and C^2 , respectively; the pixel values at grid (i, j) in C^1 and C^2 are denoted as $C^1(i, j)$ and $C^2(i, j)$; a bipolar array D is defined as (24), then the

NPCR and UACI can be mathematically defined as (25) and (26), respectively, where symbol N denotes the total number of pixels in the ciphertext, symbol F denotes the largest supported pixel value compatible with the ciphertext image format, and $|\cdot|$ is the absolute value function. Consider

$$D(i, j) = \begin{cases} 1, & \text{if } C^1(i, j) = C^2(i, j) \\ 0, & \text{if } C^1(i, j) \neq C^2(i, j) \end{cases} \quad (24)$$

TABLE 2: NPCR and UACI analyses on “Lena” image.

CPJM size	16-by-16	32-by-32	64-by-64	128-by-128	256-by-256
NPCR %	99.6170	99.6246	99.5895	99.5850	99.6338
UACI %	33.8205	33.8379	33.4048	33.4076	33.4040

$$\text{NPCR} = \sum_{i,j} \frac{D(i,j)}{N} \times 100\% \quad (25)$$

$$\text{UACI} = \sum_{i,j} \frac{|C^1(i,j) - C^2(i,j)|}{(F \cdot N)} \times 100\%. \quad (26)$$

Table 2 shows the NPCR and UACI results for one pixel change in the “Lena” image. It is clear that, for CJPMs at various sizes, the proposed cipher has good performances in both the NPCR and UACI analyses. Simulation results fit the expectations of the ideal cipher very well.

Figure 13 shows a differential attack on “Lena” image while keeping the encryption key unchanged. It is noticeable that the difference between two plaintext images is the pixel on Lena’s nose. However, the ciphertext images are so different that the image of their difference is still random-like. As a result, the one pixel change in the plaintext image is “dissipated” in ciphertext. From this point view, this plaintext sensitivity is closely related to the diffusion property of a cipher. In other words, it is reasonable to claim that a cipher has good NPCR and UACI results if it has good diffusion properties.

5.4. Key Space Analysis. The encryption key in the proposed image encryption method using CPJM is composed of a set of parameters $(x_r, y_r, w, R, C, s, n, r, m)$, where (x_r, y_r) is an arbitrary point on xy plain; w is a nonnegative decimal; R and C should be positive integers smaller than the plaintext image size; s and n should be positive integers below the product of RC ; r should be a number in between $[3.6, 4]$; and m is a nonnegative integer. Therefore, theoretically, the key space of the proposed cipher is infinitely large.

Because the chaotic Logistic map is used as the trigger for pseudorandom sequences, the proposed cipher has high key sensitivities as well. The results of key sensitivity analysis are shown in Figure 14, where the set of parameters written in parenthesis is the used key. It is clear that unless the correct decryption key is applied, a ciphertext image cannot be restored.

6. Conclusion

In this paper, we discussed the generation of a chaotic Josephus permutation matrix by using the conventional Josephus permutation sequences and the logistic chaotic map. The proposed CJPM is parametric and is uniquely dependent on the set of parameters, which is sufficiently large to provide a secure size of key space. As another heritage from the chaotic Logistic map, the CJPM is highly sensitive to its initial values (parameters). Any slight change in parameters

leads to significant differences in resulting CJPM. Simulation results show that (1) the ciphertext image is random-like from the perspective of human visual inspection; (2) the encryption quality is almost independent of the plaintext image; (3) the proposed encryption method is able to encrypt plaintext images with large homogeneous regions to secure ciphertext images; (4) histogram analysis also shows that different ciphertext images tend to have the uniform distribution on $[0, F]$; (5) adjacent pixel correlation analysis shows that neighbor pixels in ciphertext have lower correlations than many existing encryption methods; (6) the proposed cipher is highly sensitive to encryption key and plaintext; (7) experimental UACI results of the proposed cipher are very close to those of the ideal one.

The proposed cipher can be used for various image types, for example, binary images, 8-bit gray images, 16-bit gray images, RGB images, and so forth. The same encryption idea may also be applied to audio, video, or other types of digital formats.

Conflict of Interests

The authors declare that there is no conflict of interests regarding the publication of this paper.

Acknowledgments

This work was supported by the Scientific Research Fund of Hunan Provincial Education Department under Grant (no. 12B023). It is also supported by the National Natural Science Foundation of China (nos. 61204039 and 61106029) and Scientific Research Foundation for Returned Scholars, Ministry of Human Resources, and Social Security of the People’s Republic of China.

References

- [1] D. Stinson, *Cryptography: Theory and Practice*, CRC Press, 2006.
- [2] M. Yang, N. Bourbakis, and S. Li, “Data-image-video encryption,” *IEEE Potentials*, vol. 23, no. 3, pp. 28–34, 2004.
- [3] FIPS PUB 46: Data Encryption Standard, National Bureau of Standards, 1977.
- [4] FIPS PUB 197: Advanced Encryption Standard, Announcing the Advanced Encryption Standard (AES), 2001.
- [5] Y. Mao and G. Chen, *Chaos-Based Image Encryption*, Springer, Berlin, Germany, 2005.
- [6] H. Yang, K.-W. Wong, X. Liao, W. Zhang, and P. Wei, “A fast image encryption and authentication scheme based on chaotic maps,” *Communications in Nonlinear Science and Numerical Simulation*, vol. 15, no. 11, pp. 3507–3517, 2010.
- [7] J. Hu and F. Han, “A pixel-based scrambling scheme for digital medical images protection,” *Journal of Network and Computer Applications*, vol. 32, no. 4, pp. 788–794, 2009.
- [8] Z. Shuo, C. Ruhua, J. Yingchun, and G. Shiping, “An image encryption algorithm based on multiple chaos and wavelet transform,” in *Proceedings of the 2nd International Congress Image and Signal Processing (CISP ’09)*, pp. 1–5, 2009.

- [9] G. Ye, "Image scrambling encryption algorithm of pixel bit based on chaos map," *Pattern Recognition Letters*, vol. 31, no. 5, pp. 347–354, 2010.
- [10] C. K. Huang and H. H. Nien, "Multi chaotic systems based pixel shuffle for image encryption," *Optics Communications*, vol. 282, no. 11, pp. 2123–2127, 2009.
- [11] X. Liao, S. Lai, and Q. Zhou, "A novel image encryption algorithm based on self-adaptive wave transmission," *Signal Processing*, vol. 90, no. 9, pp. 2714–2722, 2010.
- [12] S. Fu-Yan, L. Shu-Tang, and L. Zong-Wang, "Image encryption using high-dimension chaotic system," *Chinese Physics*, vol. 16, no. 12, pp. 3616–3623, 2007.
- [13] V. Patidar, N. K. Pareek, and K. K. Sud, "A new substitution-diffusion based image cipher using chaotic standard and logistic maps," *Communications in Nonlinear Science and Numerical Simulation*, vol. 14, no. 7, pp. 3056–3075, 2009.
- [14] Y. Wu, J. P. Noonan, G. Yang, and H. Jin, "Image encryption using the two-dimensional logistic chaotic map," *Journal of Electronic Imaging*, vol. 21, no. 1, Article ID 013014, 2012.
- [15] Y. Wu, J. P. Noonan, and S. Agaian, "A wheel-switch chaotic system for image encryption," in *Proceedings of the International Conference on System Science and Engineering (ICSSE '11)*, pp. 23–27, June 2011.
- [16] L. Zhang, X. Liao, and X. Wang, "An image encryption approach based on chaotic maps," *Chaos, Solitons and Fractals*, vol. 24, no. 3, pp. 759–765, 2005.
- [17] H. S. Kwok and W. K. S. Tang, "A fast image encryption system based on chaotic maps with finite precision representation," *Chaos, Solitons and Fractals*, vol. 32, no. 4, pp. 1518–1529, 2007.
- [18] J. Jian, Y. Shi, C. Hu, Q. Ma, and J. Li, "Encryption of digital image based on chaos system," in *Computer and Computing Technologies in Agriculture II*, vol. 2, pp. 1145–1151, 2009.
- [19] P. Van-Roy and S. Haridi, *Concepts, Techniques, and Models of Computer Programming*, MIT Press, 2004.
- [20] P. Schumer, *Mathematical Journeys*, Wiley-Interscience, 2004.
- [21] G. Ye, X. Huang, and C. Zhu, "Image encryption algorithm of double scrambling based on ASCII code of matrix element," in *Proceedings of the International Conference on Computational Intelligence and Security (CIS '07)*, pp. 843–847, December 2007.
- [22] X. Desheng and X. Yueshan, "Digital image scrambling based on josephus traversing," *Computer Engineering and Applications*, no. 10, pp. 44–46, 2005.
- [23] B. Furht and D. Kirovski, *Multimedia Security Handbook*, CRC Press, 2005.
- [24] Y.-P. Zhang, Z.-J. Zhai, W. Liu, X. Nie, S.-P. Cao, and W.-D. Dai, "Digital image encryption algorithm based on chaos and improved DES," in *Proceedings of the IEEE International Conference on Systems, Man and Cybernetics (SMC '09)*, pp. 474–479, October 2009.
- [25] J. Lang, R. Tao, and Y. Wang, "Image encryption based on the multiple-parameter discrete fractional Fourier transform and chaos function," *Optics Communications*, vol. 283, no. 10, pp. 2092–2096, 2010.
- [26] S. Yang and S. Sun, "Video encryption method based on chaotic maps in DCT domain," *Progress in Natural Science*, vol. 18, no. 10, pp. 1299–1304, 2008.
- [27] V. Wu, J. P. Noonan, and S. Agaian, "Binary data encryption using the Sudoku block cipher," in *Proceedings of the IEEE International Conference on Systems, Man and Cybernetics (SMC '10)*, pp. 3915–3921, October 2010.
- [28] Y. Wu, Y. Zhou, J. P. Noonan, K. Panetta, and S. Agaian, "Image encryption using the Sudoku matrix," in *Proceedings of the Mobile Multimedia/Image Processing, Security, and Applications*, April 2010.
- [29] G. Chen, Y. Mao, and C. K. Chui, "A symmetric image encryption scheme based on 3D chaotic cat maps," *Chaos, Solitons and Fractals*, vol. 21, no. 3, pp. 749–761, 2004.
- [30] H. Gao, Y. Zhang, S. Liang, and D. Li, "A new chaotic algorithm for image encryption," *Chaos, Solitons and Fractals*, vol. 29, no. 2, pp. 393–399, 2006.
- [31] R. M. May, "Simple mathematical models with very complicated dynamics," *Nature*, vol. 261, no. 5560, pp. 459–467, 1976.
- [32] J. Thompson and H. Stewart, *Nonlinear Dynamics and Chaos*, John Wiley & Sons, 2002.
- [33] C. E. Shannon, "Communication Theory of Secrecy Systems," *Bell Systems Technical Journal*, vol. 28, pp. 656–715, 1949.
- [34] Y. Wu, Y. Zhou, G. Saveriades, S. Agaian, J. P. Noonan, and P. Natarajan, "Local Shannon entropy measure with statistical tests for image randomness," *Information Sciences*, vol. 222, no. 323, 342 pages, 2013.
- [35] Y. Wu, S. Agaian, and J. P. Noonan, "A novel method of testing image randomness with applications to image shuffling and encryption," in *Defense, Security, and Sensing*, Proceedings of the SPIE, pp. 875507–875507, 2013.
- [36] Y. Wu, J. P. Noonan, and S. Agaian, "NPCR and UACI randomness tests for image encryption," *Cyber Journals*, pp. 31–38, 2011.

Research Article

Language Recognition Using Latent Dynamic Conditional Random Field Model with Phonological Features

Sirinoot Boonsuk,¹ Atiwong Suchato,¹ Proadpran Punyabukkana,¹
Chai Wutiw WATCHAI,² and Nattanun Thatphithakkul²

¹ Department of Computer Engineering, Chulalongkorn University, Bangkok 10330, Thailand

² HLT, National Electronics and Computer Technology Center (NECTEC), Bangkok 10400, Thailand

Correspondence should be addressed to Atiwong Suchato; atiwong.s@chula.ac.th

Received 27 September 2013; Revised 23 December 2013; Accepted 23 December 2013; Published 20 February 2014

Academic Editor: Yue Wu

Copyright © 2014 Sirinoot Boonsuk et al. This is an open access article distributed under the Creative Commons Attribution License, which permits unrestricted use, distribution, and reproduction in any medium, provided the original work is properly cited.

Spoken language recognition (SLR) has been of increasing interest in multilingual speech recognition for identifying the languages of speech utterances. Most existing SLR approaches apply statistical modeling techniques with acoustic and phonotactic features. Among the popular approaches, the acoustic approach has become of greater interest than others because it does not require any prior language-specific knowledge. Previous research on the acoustic approach has shown less interest in applying linguistic knowledge; it was only used as supplementary features, while the current state-of-the-art system assumes independency among features. This paper proposes an SLR system based on the latent-dynamic conditional random field (LDCRF) model using phonological features (PFs). We use PFs to represent acoustic characteristics and linguistic knowledge. The LDCRF model was employed to capture the dynamics of the PFs sequences for language classification. Baseline systems were conducted to evaluate the features and methods including Gaussian mixture model (GMM) based systems using PFs, GMM using cepstral features, and the CRF model using PFs. Evaluated on the NIST LRE 2007 corpus, the proposed method showed an improvement over the baseline systems. Additionally, it showed comparable result with the acoustic system based on *i*-vector. This research demonstrates that utilizing PFs can enhance the performance.

1. Introduction

Spoken language recognition (SLR) is the task of determining the language of a spoken utterance. SLR has become an important component in many speech processing applications such as being the preprocessor of multilingual speech recognition systems and of automatic selection of the appropriate language for information service applications. Recent research works on SLR can be divided into two approaches: (1) the *acoustic approach* [1, 2] which directly models the distributions of acoustic features from speech signals; and (2) the *phonotactic approach* [3, 4] which utilizes phone-sequences tokenized from speech utterances to construct language modeling of *n*-grams of these phones. An obvious shortcoming of the phonotactic approach is that manual phonetic transcription of speech data is required for constructing

language modeling. The acoustic approach has become a popular alternative to overcome this issue due to the fact that it does not require prior knowledge of a specific language and transcription of phonetic data. Furthermore, the acoustic approach captures the differences in spectral features between languages and directly models the distribution of the spectral features given in the speech utterance in each language. The acoustic system based on *i*-vector approach [5] that provided superior performance has become state-of-the-art in the language recognition field.

The performance of the overall language recognition system depends on preprocessing techniques, feature extraction, and classification techniques. Some research studies focused on feature extraction to improve the performance of SLR system. A typical acoustic-based SLR system uses the Gaussian mixture model (GMM) [6, 7] to model conventional

speech features by applying Mel-frequency cepstral coefficients (MFCC) or perceptual linear prediction (PLP). In [1], a shifted-delta cepstral coefficient (SDC) which is employed to capture longer temporal information across multiple frames has improved the performance of the acoustic-based and it is the most commonly used feature in SLR. Recent work by [8] enhanced acoustic-based SLR by using MLP for feature extraction and achieved a better result than using conventional features. However, those features modeled the behavior of the human auditory system. By relying only on the conventional speech features, the SLR system may be limited in its ability to incorporate linguistic knowledge to improve the performance. Linguistic knowledge components such as articulatory features have been proposed to improve accuracy in speech applications [9] and to increase the tolerance in noisy environment [10]. Articulatory features have played an important role in language since the properties of sound segments in each language can be described by the articulatory configuration; however, there have been few research studies using these features in SLR.

Another factor that impacts the SLR performance is the modeling technique. Traditional acoustic-based SLR systems model the spectral features by using a generative model such as GMM [6]. In the past few decades, many approaches to SLR have been developed by exploiting discriminative models in acoustic system. Whereas recent approaches have used discriminative models, such as the support vector machine (SVM) with a polynomial kernel [11], SVM with a generalized linear discriminant sequence kernel (GLDS) [12, 13], GMM-MMI (which is GMM trained with the discriminative maximum mutual information) [11, 14], and a hybrid SVM/GMM (which used a GMM supervector as a feature vector of SVM) [15–18]. The results showed significant improvement over the previously reported results. Over the last few years, the Joint Factor Analysis (JFA) [19] and *i*-vector [20] that have achieved a success in speaker verification have shown excellent performance when applied to language recognition task. Recent modeling techniques used to improve the acoustic systems based on the *i*-vector [5, 21] have provided superior improvement in language recognition. Nevertheless, discriminative modeling in previous acoustic-based SLR studies assumed independency among speech features. It needed feature space transformation for extracting a new feature vector before applying to the discriminative model. Moreover, the recent research failed to consider the sequence of feature vectors; that is, the model was estimated based on the assumption of independence between the input features.

This study utilizes phonological features (PFs) to capture the acoustic characteristics of speech signals and to integrate linguistic information into SLR to represent the language characteristics. PF attributes can represent relation between articulatory configurations and phone units in spoken languages. They can meaningfully describe the cooccurrence of articulatory gesture patterns and can describe articulatory transition better than using conventional cepstral features. We used PFs as an alternative frame-based speech features to represent language information. Typically, a speech utterance is mapped to a bundle of PF attributes. Each PF correlates with a particular articulatory attribute and it corresponds

with other articulatory attributes. As each PF attribute correlates with others, we require a modeling technique that considers a sequence of these feature bundles and captures the relationship between the bundles of PF attributes. As a language classifier, this paper focuses on utilizing the latent-dynamic conditional random field (LDCRF) model which is a successful discriminative model applied to sequential data.

The purpose of this study was to employ the LDCRF model in an SLR system to capture the behaviors of PF attributes that reflect language characteristics. Baseline systems were conducted to evaluate the proposed method. The evaluation of the effectiveness of using PF attributes as speech representation was undertaken by comparing the SLR system using PF attributes with a system using spectral features such as MFCC, PLP coefficients, and SDC features. To measure the performance of classifier, we compared the SLR using the LDCRF model with that using the GMM model. Moreover, the performance of the proposed system is compared with state-of-the-art acoustic SLR system based on *i*-vector space [5].

This paper is organized as follows. Section 2 presents the literature review while Section 3 describes the background of PF. Section 4 presents the LDCRF model. Section 5 outlines the proposed SLR system. In Section 6 the experimental setup including the speech corpus, configuration of the feature extraction, and classification is described and the experimental results and discussion are presented in Section 7. Finally, the conclusion and suggestions for further work are presented in Section 8.

2. Related Works

PF research has focused on two areas: (1) PF extraction which estimates the underlying phonology in speech signals and (2) integrating PFs to improve their performance in SLR.

In general, extracting PFs can be achieved by manually mapping the phone transcriptions to PF attributes. The disadvantage is that it lacks the flexibility to integrate a new language. To avoid manual mapping, many different techniques have been developed, such as using multilayer perceptron artificial neural networks (MLP ANNs) [22], time-delay recurrent neural networks (RNN) [23], the hidden Markov model (HMM) [24], and the GMM [25] and SVM [26–28] techniques. Due to the popularity and success of MLP used in speech recognition, we make use of an MLP model to detect PF attributes in this paper.

The literature on the integration of PFs into an SLR system shows that few studies have employed PFs in an acoustic-based SLR system. In [26], the combination of SDC features and distinctive features (which are similar to PF attributes) is used as an input for acoustic GMM system and it showed better results than only using SDC features.

Another line of research in modeling techniques suggested utilizing a statistical model that considered the dependence of the assumptions between the input features. Conditional random field (CRF), a discriminative model, is proposed to solve sequential labeling (i.e., a kind of sequential data problem). The label sequence is calculated over the entire

sequences from a log-linear combination of input features. It showed a significant improvement in speech recognition [29] such as phone classification [30] and phone recognition [31]. In [32], the integration of PFs into the phone recognition task by using CRF achieved superior performance compared with conventional features. Furthermore, the deep structure CRF [33] also yielded a better result than other discriminative models in SLR. Although CRF can capture the extrinsic dynamics between the behaviors of features, it cannot capture the intrinsic dynamics of feature sequences.

LDCRF, a variant of CRF, has been successfully applied to continuous gesture recognition tasks [34–36] and it outperformed CRF. It was designed to learn the substructure sequential label. The advantage of using LDCRF is that it captures the intrinsic dynamics of the sequence of the features and it also explicitly learns the substructure of the features as well as the extrinsic dynamics between the class labels. In this paper, LDCRF is used to capture the dynamic characteristic of articulatory configurations within each phone and across phone sequences to represent a model of language.

This paper proposes an acoustic-based SLR system using LDCRF with PF attributes. The contribution of this paper is to incorporate linguistic information and acoustic information to improve the performance of the SLR system. In addition, employing LDCRF to learn the dynamic sequences of PF attributes for modeling the language can resolve the problem of the independence of observations. Furthermore, this work provides analysis on the language discriminative ability of PFs compared with conventional cepstral features.

3. Phonological Features

In linguistics, phonological features (PFs) represent speech sounds as bundles of positive-valued (+) or negative-valued (–) features where positive value shows a presence of the feature while otherwise, the value is negative. The phonological component, mapping speech production characteristics to phones, is considered to be a linear sequence of these feature bundles. Many studies proposed different PF concepts [23] such as the Sound Pattern of English (SPE), the Government Phonology (GP), the multi-valued (MV) features, and the hybrid features (HF). These concepts are defined from different articulatory, acoustical or phonological aspects and the different concepts of relationships between those aspects. In this paper, we use the Sound Pattern of English (SPE) definition, a widely used definition for describing phone inventory, since it has no redundant mapping rules. SPE, defined by Chomsky and Halle [37], illustrates speech production as binary values. According to the SPE definition, each phone can be broken down into 14 PF attributes: vocalic, consonantal, high, low, back, round, tense, continuant, anterior, coronal, voice, nasal, strident, and silence as shown in Table 1. They are classified as (1) the major class features which describe the obstruction in the way of airstream: vocalic, consonantal, and nasal; (2) the manner of articulation features which describe the primary constriction of air flow: continuant; (3) the place of articulation features which describe the body of tongue: coronal, anterior, and

TABLE 1: Example of phonological features in the Thai word “khun.”

IPA	[k ^h]	[u]	[n]
Vocalic	–	+	–
Consonantal	+	–	+
High	+	+	–
Back	+	+	–
Low	–	–	–
Anterior	–	–	+
Coronal	–	–	–
Round	–	+	–
Tense	–	+	–
Voice	–	+	+
Continuant	–	+	–
Nasal	–	–	+
Strident	–	–	–
Silence	–	–	–

round; (4) the source features: voice, strident, and tense; (5) vowel features which describe the position of tongue: back, high, and low; and (6) other features: silence.

Table 1 shows an example of the word “khun” in Thai (defined as [k^hun] by IPA) which means “you.” Each column represented a sequence of phone segments, and each segment is characterized by a set of PF attributes.

Moreover, the patterns of PF sequences occur differently for each language. For instance, some diphthongs occur in some languages, but they are not allowed in others. The diphthong /aw/, representing an articulatory configuration running from the vowel [a] to the glide [w], occurs in Thai but not in Russian. In Japanese, the onset of a velar nasal /ŋ/ is allowed but this does not occur in English. This causes the absence of a movement pattern of articulatory configuration from the velar nasal to vowel in English. With the benefit of different patterns of PF sequences in different languages, we can utilize the sequential PF attributes to discriminate between languages.

4. LDCRF for Language Classification

The latent-dynamic conditional random field (LDCRF) model is discriminative and relaxes the conditional independence assumptions between input features. It was designed to identify the substructure sequence label; thus, it captures the intrinsic characteristics within a class and interclass of patterns by associating a set of hidden states with each class label. To apply this in the SLR task, we used these hidden states to model the internal substructures of different language patterns and provide the overall likelihood for classification. Each hidden state can be treated similarly to a CRF. The overall likelihood is the sum of individual likelihoods from the hidden states. In a language recognition problem, we assume a training set of N speech utterances given as $X = \{x^1, x^2, \dots, x^N\}$ which contains speech utterances from the class label of languages. The corresponding label can be denoted as $Y = \{y^1, y^2, \dots, y^N\}$ where each y^n is a member

of a set of possible speech labels. Given the above definitions, a latent conditional model is defined as

$$P(Y | X, \theta) = \sum_h p(Y | h, X, \theta) p(h | X, \theta), \quad (1)$$

where x is the concatenation of all feature vectors x_i for the entire sequence of the utterance and $\theta\{x_i\}$ are the parameters of the training model.

4.1. Problem Formulation. SLR problems can be represented in mathematical formulation as $L = \{l_1, l_2, \dots, l_k\}$, where L denotes a set of n different languages. Given that X denotes the input speech signal, the most likely recognized language, L^* , can be represented as

$$L^* = \arg \max_L P(L | X). \quad (2)$$

Since the problem of SLR is a multiclass classification problem, this study broke the problem down into multiple binary classifications by using a one-versus-one schema. In language classification, we focus on the presence or absence of languages; thus, the class label from each LDCRF model is limited to the binary value $y^n \in \{0, 1\}$. For example, the class label $y^n \in \{\text{Chinese}, \text{Arabic}\}$ represents the pair language classification between *Chinese* and *Arabic*.

The task of the LDCRF model is to learn the mapping between the sequence of observation inputs $X = \{x_1, x_2, \dots, x_T\}$ and the sequence of class labels $Y = \{y_1, y_2, \dots, y_T\}$. Each y_i is a class label for the i th frame of speech sequence and is a member of a set L of possible class labels. We assign $y_1 = y_2 = y_T$ because one training speech utterance has one language. Each frame of observation is represented by a feature vector x_i . The LDCRF model incorporates a vector of hidden state variables $h = \{h_1, h_2, \dots, h_n\}$ to model the substructure of the speech sequence. Each h_i is a member of the set of all possible hidden states H and the hidden variables are not observable in the training examples.

The model is limited to having disjointed sets of hidden states corresponding to each class label. Given each $h_i \in H_{y_i}$ where H_{y_i} is the possible hidden states for the class label y_i and H is the set of all possible hidden states which is the union of all sets H_{y_i} , then a sequence has $P(Y | h, X, \theta) = 0$ for any $h_i \notin H_{y_i}$, or otherwise 1. The model is shown as

$$P(Y | X, \theta) = \sum_{h: \forall h_i \in H_{y_i}} p(h | X, \theta), \quad (3)$$

where $p(h | X, \theta)$ is the conditional random field. It is defined as

$$P(h | X, \theta) = \frac{1}{Z(X, \theta)} \exp\left(\sum_k \theta_k \cdot F_k(h, X)\right), \quad (4)$$

where the partition function Z is a normalization value with respect to all candidate paths for the input sequence. It can be written as

$$Z(X, \theta) = \sum_h \exp\left(\sum_k \theta_k \cdot F_k(h, X)\right), \quad (5)$$

and the feature vector F_k is defined as

$$F_k(h, X) = \sum_{i=1}^T f_k(h_{i-1}, h_i, X, i). \quad (6)$$

The $F_k(h, X)$ vector is the sum over all feature functions. In (6), each feature function $f_k(h_{i-1}, h_i, X, i)$ can be represented by two kinds of feature functions: a state function $s_k(h_i, X, i)$ or a transition function $t_k(h_{i-1}, h_i, X, i)$. The state function s_k depends on a single hidden variable in the model while the transition function t_k can depend on pairs of hidden variables.

4.2. Training LDCRF. Given a training set consisting of n labeled sequences (X_i, Y_i) for $i = 1, \dots, n$, the objective function for training is defined similarly to the reported work on CRF [38, 39] as

$$L(\theta) = \sum_{i=1}^n \log p(Y_i | X_i, \theta) - \frac{1}{2\sigma^2} \|\theta\|^2, \quad (7)$$

where the log-likelihood of the first term is given by the conditional log-likelihood of each training sequence and the second term is the Gaussian prior likelihood with the variance σ^2 (i.e., $P(\theta) \sim \exp(1/2\sigma^2 \|\theta\|^2)$). The gradient ascent technique was used to optimize the parameter values $\theta^* = \arg \max_{\theta} L(\theta)$.

4.3. Feature Functions. The state functions are considered by a subset of observations preceding the current variable because the dependency of the entire observation sequence is ignored. It can be said that $s_k(h_i, X, i) = s_k(h_i, \bar{X}_i, i)$ where $\bar{X}_i = [X_{i-m}, \dots, X_i]$ is a window of size $m + 1$ preceding the variable at the i th frame. The state function $s_k(h_i, X, i)$ represents the value of hidden states with a neighborhood relationship with the entry in \bar{X}_i . The details of state function are described in Section 5.2.

4.4. Inference on LDCRF. To classify a test sequence X , we find the most likely label sequence Y^* that maximizes the conditional model. In the inference phase, we use the optimal model parameter θ^* obtained from training data to estimate the model output as

$$Y^* = \arg \max_Y p(Y | X, \theta^*). \quad (8)$$

Because the LDCRF model is incorporating hidden states, it cannot be produced directly by a searching path like CRF. Thus, the most probable sequence can be estimated from summing the probabilities of the hidden paths, where each class label is associated with the sets of hidden states. It can be written as

$$Y^* = \arg \max_Y \sum_{h: \forall h_i \in H_{y_i}} p(h | X, \theta^*). \quad (9)$$

Applying the LDCRF model in SLR, the likelihood for estimating a specific language l is equal to the marginal

probability $P(Y_i = l \mid X, \theta^*)$. The belief propagation algorithm is employed to estimate the marginal probabilities. This probability is equal to the summation of the marginal probabilities of the hidden states of the subset H_i :

$$p(Y_i = l \mid X, \theta^*) = \sum_{h: \forall h_i \in H_i} p(h \mid X, \theta^*), \quad (10)$$

where X is the concatenation of the feature vector x_i for the entire sequence of speech. The observation X can be represented by speech features (see Section 5.1 for details). The model parameter θ^* is learned during the training phase.

5. Proposed SLR System

The block diagram of the proposed SLR system is shown in Figure 1. It consists of two main components: feature extraction and language classification. In feature extraction, the input speech is first converted into PF attributes by MLP attribute detectors. Then, the feature vectors are used as the input to language classifiers. Additionally, the feature vectors can be PF attributes or PF attributes applied with the shift delta operation. The language classifiers, which are trained for each target language, are used to determine the most likely language.

5.1. Feature Extraction. The main goal of the feature extraction is to extract discriminative speech representations that highlight the relevant information of language. A continuous speech is converted to a sequence of feature vectors containing information of language characteristics. Then, the feature vectors are used as the input to the language classification component.

5.1.1. Phonological Features (PFs). The PFs are the linguistic knowledge that conveys language information. They contain articulatory characteristics and different patterns of articulatory configuration movements. For PF attributes extraction, we employed MLP to detect the PF attributes from speech utterance. The MLP attribute detectors were applied to input speech and classify the values of the attribute for each frame.

The MLP attribute detectors were trained on the TIMIT speech corpus. The TIMIT database is a corpus recorded readings of a large set of English sentences. It contains 6,300 sentences, 10 sentences spoken by each of 630 speakers, recorded from male and female speakers of eight dialects of American English. The TIMIT corpus has been divided into a training set (4,620 utterances from 462 speakers) and a test set (1,680 utterances from 168 speakers). The training set was used for training each MLP attribute detector and each MLP attribute detector was evaluated on the test set.

For training MLP attribute detectors, we generated labeling of PF attribute from TIMIT phonetic transcription. We used the set of 13 PF attributes (excluding silence) that followed the SPE definition shown in Section 3. The mapping between phone transcription and PF values is based on [23]. The MLPs used PF transcription to separately train the attribute detector. Speech parameters were 39-coefficient

TABLE 2: The tuning result of MLP attribute detectors with the number of hidden units.

Number of hidden units	Accuracy
100	82.2
150	85.6
200	87.6
250	87.9
300	87.9

MFCC vector (12 Mel-frequency cepstral coefficients and energy plus their delta and acceleration coefficients) with 25 ms window length and 10 ms frame shift. Thirteen MLP attribute detectors (one for each PF attribute) were trained by using the NICO toolkit [40]. Each MLP consisted of three layers and the input layers had 39 nodes. The optimal number of hidden units was determined through MLP that provided the best performance in tuning experiments. Thus, each MLP was trained with the various numbers of hidden units. From the tuning results shown in Table 2, the MLP with 250 hidden units provided the best performance. The output layer of MLP was an estimation of the posterior probability of the PF attributes. Each MLP has two output nodes representing binary values of PF attribute. The results of thirteen MLP attribute detectors were composed to a 26-dimensional feature vector. Then, the feature vectors were used as the input of language classifiers.

Table 3 shows the performance of the MLP attribute detectors evaluated on the test set. The 39-MFCCs feature vectors were used to test classification performance of MLP attribute detectors. The results show that the MLP attribute detector using the nasal attribute outperformed other attributes (silence was not considered). The average accuracy of overall MLP attribute detectors was 87.95% and the range of classification accuracy at the frame level for each attribute detector had value between 81% and 98%.

Figure 2 represents the spectrogram and PF attributes of Thai utterance “ฟังโทรมาครึ่งสอง” which can be transcribed as /pvng[^] toz[^] maz[^] kraang[^] thiiiz[^] s@ng[^]/, along with the canonical values of PFs. The top subplot shows the spectrogram of the speech utterance. The values of PF attributes, as derived from MLP attribute detectors, are presented on the 2nd to 8th subplots. The outputs are the continuous values between 0 and 1, where 1 represents the most likely classifying PF attribute. Although each PF attribute was derived from separately-trained attribute detectors, the result shows that the values of each PF correlate with others. That is, the PFs did not perform frame synchronous as the manual mapping did while they change in similar pattern. For example, the vowel features that describe the position of tongue: *Back* and *High* attributes (on the 7th and 8th subplot) and the *Round* attribute, the feature describing the body of tongue and involving vowel (on the 6th subplot), simultaneously change in the same manner. For another example, the relationship between three features *Vocalic*, *Consonantal*, and *Continuant* attributes (on the 2nd, 3rd, and 5th subplot, resp.) is correlated. The rising of *Vocalic* and

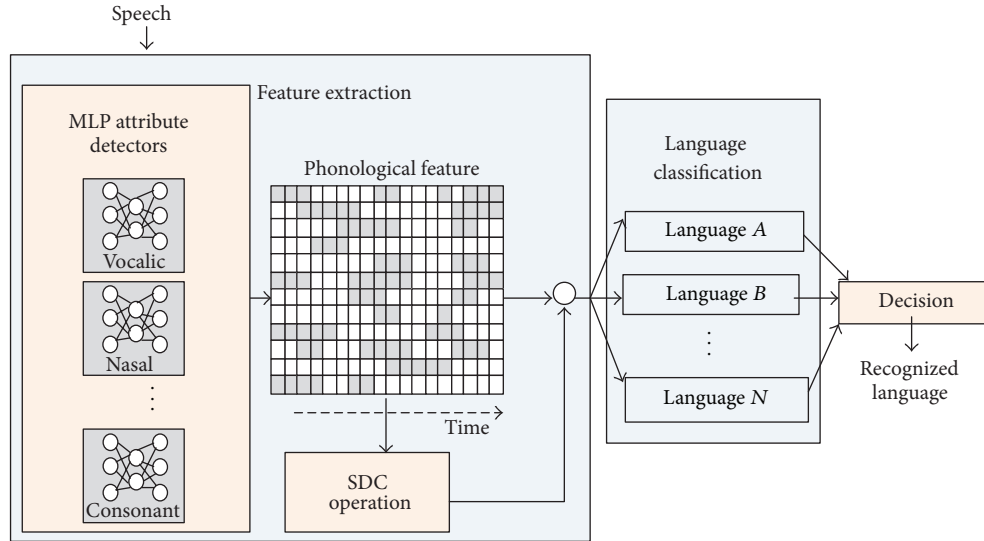


FIGURE 1: Proposed SLR system.

TABLE 3: Percentage accuracy of MLP attribute detectors tested on TIMIT corpus.

Attribute	Accuracy
High	81.9
Back	82.6
Coronal	82.8
Vocalic	82.8
Anterior	83.3
Tense	84.3
Consonantal	84.8
Continuant	88.7
Low	88.8
Voice	90.3
Round	91.7
Strident	95.0
Nasal	95.8
Silence	98.5
Average	87.95

The high accuracy result is displayed in bold.

Continuant feature simultaneously occurred with the falling of *Consonantal* feature.

In addition, the feature values do not switch instantaneously and all features do not always change simultaneously at the phone boundaries. It means that each feature makes the smooth transition between the side of target-like and non-target-like values. With the manner of using detector, it helps relaxing the limitation of value changing at phone boundaries. It has low possibility for the insertion error to occur. We can make use of the loosening and the properly asynchronous manner of the features to use these outputs as features rather than the output derived from the manually mapping procedure.

5.1.2. Shifted Delta Coefficient Operation. In this paper, the shifted delta operation was applied to compute delta PF attributes across successive frames, denoted as SDPF, since shifted delta coefficients (SDCs) have been successfully used in SLR [41, 42] to capture the cepstral dynamics of a long temporal window. We used the shifted delta operation to estimate the changes of PF attributes in multiple frames and to capture the language characteristic resulting from the pattern of the changes. The SDC features are obtained by stacking delta cepstral coefficients across multiple speech frames. The computation of the shifted delta operation is shown in Figure 3. There are four parameters, N - d - P - k , which are used in computing a shifted delta operation. The parameter N is the total dimension of the coefficients in each time frame. The parameter d is the time advance and delay for the delta computation. The parameter k is the number of blocks whose delta coefficients are concatenated to form the final feature vector. The parameter P is the time shift between consecutive blocks. In this study, the four parameters in a shifted delta operation were set to 7-1-3-7 following the configuration which has been successfully used in SLR [21]. The SDC feature vector at frame time t is given by the concatenation of all the blocks of delta vectors, $\Delta c(t + iP)$, where

$$\Delta c(t + iP) = c(t + iP + d) - c(t + iP - d). \quad (11)$$

5.2. Language Classification. In the language classification, the classifiers employed the feature vectors as input and provided a decision score of the hypothesis language as output. We used a binary classifier scheme to construct language classifiers. Each language classifier is performed using speech features extracted from Section 5.1. For recognition, the language of speech utterance is determined from the result of sequence classification of language classifiers. This result is obtained from the summation of sequence of classification

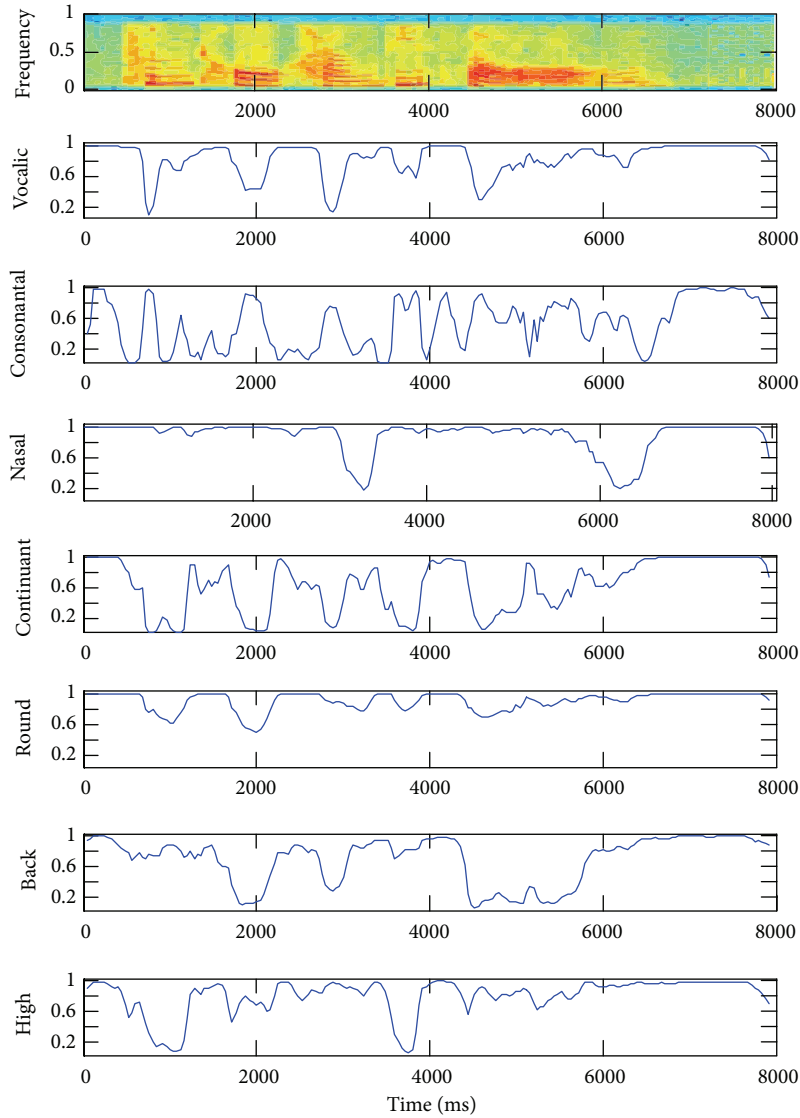


FIGURE 2: Spectrogram and PF attributes of the sentence “ฟัง โทรมมาครึ่งสอง”, resulting from MLP attribute detectors.

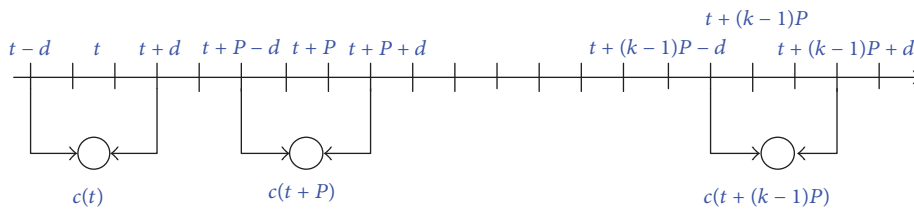


FIGURE 3: Computation of SDC feature vector at frame t for the parameters $N-d-P-K$.

scores. The performance of the classifiers is evaluated by considering the correctness of the sequence classification.

In this paper, we investigated the use of the outputs of the MLP attribute detector to construct feature functions for the LDCRF model. We used the posterior probability values obtained by the MLP attribute detectors to determine their frame-level result as state feature functions of the LDCRF model.

The feature functions for PF attributes are defined using the language label/PF attribute pairs. Let state feature function $s_{\phi, \text{Att}}(h_i, X, i)$ depend on a single hidden variable to link the output label of language ϕ . The feature function that ties together the output label of language ϕ is based on the output of the MLP attribute detector for feature Att. This allows for the association between a language ϕ and the Att attribute even if the Att attribute is not traditionally associated with

language ϕ . Thus, the state feature function is defined as follows:

$$s_{\phi, \text{Att}}(h_i, X, i) = \begin{cases} \text{MLP}_{\text{Att}}(x_i), & \text{if } h_i = \phi \\ 0; & \text{otherwise,} \end{cases} \quad (12)$$

where the output of the MLP detector for feature Att at time i is $\text{MLP}_{\text{Att}}(x_i)$. For example, the state feature function is defined for the output label language ϕ where the MLP output of feature *vocalic* can be defined as

$$s_{\phi, \text{vocalic}}(h_i, X, i) = \begin{cases} \text{MLP}_{\text{vocalic}}(x_i), & \text{if } h_i = \phi \\ 0; & \text{otherwise,} \end{cases} \quad (13)$$

where $\text{MLP}_{\text{vocalic}}(x_i)$ is the output of the MLP detector for the vocalic attributes at frame i of speech sequence X . As for the language classifier model above, state feature functions are defined for all possible language label/phonological attribute pairings, not just for the canonical attributes for the label. The $|H| \times |H|$ transitions functions t_k are defined as one for each hidden state pair (h', h'') . Each transition function is expressed as

$$t_k(h_{i-1}, h_i, X, i) = \begin{cases} 1, & \text{if } h_{i-1} = h', h_i = h'' \\ 0; & \text{otherwise.} \end{cases} \quad (14)$$

Weights associated with a transition function for hidden states that are in the subset H_y will model the substructure patterns.

Furthermore, we also used the PF attributes applied with shifted delta operation and other speech attributes from the feature extraction as features in the LDCRF model. The definition of feature functions or the state function of the LDCRF model is similar to the above described function; the only difference is we used the dimension of the feature vector of the speech attribute instead of the output from the MLP attribute detector to define the feature function.

For LDCRF model training, the speech utterance was labeled on the frame level either as a target language or as a nontarget language. The configuration parameters of the LDCRF model in the training and validation phase were set as follows: the hidden states were set to 3 and the window size was set to 3, while the regularization term used in BFGS was set to 300. It was observed that 3 hidden states per label gave better results. The LDCRF model was trained using the objective function described in Section 4. For performance evaluation, the LDCRF model was compared with two classification models: the CRF and the GMM models.

6. Experimental Method and Data

6.1. Speech Corpus. In the language classification and recognition tasks, the speech corpus from a portion of the NIST 2007 language recognition evaluation (LRE) [43] development data set was used as a speech corpus for training and testing. The corpus contains 7,530 utterances in eight languages: Arabic (Arb), Bengali (Ben), Thai (Tha), Urdu (Urd), Russian (Rus), Chinese-Cantonese or Yue Chinese (CH.can),

Chinese-Min (CH.min), and Chinese-Wu (CH.wuu). The language recognition task experiment focused on closed-set recognition where target languages must be included in the test set.

6.2. Language Classifiers. The speech features were extracted from speech utterances into a sequence of feature vectors and they were used to train the language classifiers. In this experiment, the classification problem of eight target languages was broken down into a pairwise language classification. Thus, the total number of classifiers was an elementary combination $C(n, k) = C(8, 2) = 28$.

6.3. Performance Evaluation. Performance evaluation of the proposed system by k -fold cross validation ($k = 5$) was used to reduce the bias of the trained model and to generalize classification ability of the model. Under fivefold cross-validation, the speech dataset was randomly partitioned to form five disjoint subsets. Four sets were used for training and the remaining set was test set. The average accuracy and average error rate were calculated by repeating training and testing five times on different combinations of data sets.

Receiver operating characteristic (ROC) curve is used as another evaluation method of the performance of a language pair classifier. It used the maximal marginal probabilities of (10), which was computed from the 5-fold models. ROC shows the relation of the true positive rate, which is computed as the ratio of the number of recognized frames and the total number of ground truth frames, and the false positive rate, which is computed as the ratio of the number of falsely recognized frames and the total number frames of the nontarget class.

Additionally, the performance of language classifiers can be statistically measured by applying a paired t -test at the significance level 0.01 to consider whether or not the classifiers using different speech features are significantly different.

6.4. Preliminary Studies

6.4.1. Preliminary Studies on the Discriminative Ability of Speech Features Using MANOVA. Based on the hypothesis that the distributions of PF attributes of each language are different and they have the capability to discriminate between languages, this experiment was conducted to study the variance of the distribution of speech features occurring in different languages.

MANOVA (multivariate analysis of variance) was used to analyze the difference of the means of features among all the languages. It is an extension of the F -test which analyzes the distribution of features with more than one dependent variable. We used MANOVA for observing the means of the values of the speech attributes and for analyzing the distribution of the speech features across different languages.

The discriminating powers of features were evaluated using two different criteria, the F -ratio and the P value. The feature is more significant if the F -value is very large and the P -value is small. A level of significance of 0.01 was used as the criterion for checking the statistical significance

TABLE 4: MANOVA of language classification using MFCC, PLP, and PF attributes.

Attribute	P value	F -ratio
PF	0	1425.43
MFCC	0	22.63
PLP	1	0.11

of the P value. In this study, we compared three speech features: PF, MFCC, and PLP, which were obtained from eight languages.

In Table 4, the P value and the F -ratio of three speech features are listed in descending order of F -value. The P value of PF attributes which is less than 0.01 indicates that the distribution of PF attributes for at least one of the eight languages was different. The PF attributes showed the largest F -ratio; thus, they contributed the most to discriminating between languages. The MFCC with a smaller F -ratio had less discriminative ability than the PFs. Based on the discrimination factors of PLP where the P value was 1, the mean values of PLP were not significantly different among eight languages.

6.4.2. Preliminary Studies on the Variance of the Distribution of PF Attributes Using ANOVA. The purpose of this experiment was to study the variance of the distribution of each PF attribute occurring in different languages. To analyze the distributions of each PF occurring in each language, the PF attributes were extracted by using MLP attribute detectors corresponding to the phonetic features.

The variance of the means of the PF attribute distributions were compared among the eight languages. ANOVA (analysis of variance) was used to analyze the difference of the means of the PF attributes among all the languages and in pairwise analysis. F -ratios and P values were used to evaluate the differences. A level of significance of 0.01 was used as the criterion for statistical significance of the F -ratios for the individual ANOVA. The number of language pairwise combinations from the eight languages was 28 language pairs. Thus, there were 364 cases used to analyze the distribution of 13 PFs.

Table 5 shows the results of the overall ANOVA analysis of PF attributes in terms of the F -ratio and P value. The P values of all PF attributes were less than 0.01 indicating that the distribution of the PF attributes for at least one of the eight languages is different. It showed that there were significant differences among the eight languages. The results of the F -ratio analysis show that (i) the low attribute, a member of the vowel features, has the best discriminative ability; (ii) the features involving obstruction in the vocal tract (*Vocalic* and *Continuant* attributes) show better discriminative ability than the *Consonantal* attribute; (iii) among the vowel features of the *High*, *Back*, and *Low* attributes, the *Low* attribute is more discriminative than the others; and (iv) three attributes (including *Consonantal*, *Nasal*, and *Round*) showed poorer discriminative ability.

For the language pairwise analysis, there were 296 cases out of 364 (about 81%) where the pairwise P values were less than 0.01. The results show that the mean values of the PF

TABLE 5: F -ratio and P value statistics for each PF attribute from pairwise analysis.

PF classes	F -ratio	P
Vocalic	3706.52	0
Consonantal	830.29	0
Nasal	970.02	0
Continuant	4984.65	0
Coronal	3414.93	0
Anterior	4919.50	0
Round	748.32	0
Voice	2683.94	0
Strident	2695.36	0
Tense	5237.42	0
Back	3041.22	0
High	3214.64	0
Low	6597.28	0

attributes were statistically different between two languages. From the results of the pairwise analysis, the discriminating capability of each PF attribute was different. Thus, incorporating all PF attributes can provide supplementary information that reflects the language characteristics and can compensate for the discriminating ability of a weak PF attribute.

From analyzing *Consonantal* attribute, there were 6 out of 28 pairs where the pairwise P values were greater than 0.01 which means that there are no differences between the two languages. They were CH.min versus Arb, CH.min versus Ben, CH.min versus Tha, CH.min versus CH.can, Rus versus Arb, and Rus versus CH.wuu. It can be noticed that the *Consonantal* attribute of CH.min had less ability to discriminate between languages. From observing the *Nasal* attribute on language pairwise analysis, about 15% of all pairwise cases were having P values that were greater than 0.01 (such as Arb versus Rus, Arb versus Tha, Arb versus Urd, and Ben versus CH.can). The reason that the mean values of the PF attributes were not statistically different could be due to the occurrence of nasal vowel and nasal consonant. The nasal vowel, which is vowel that is adjacent to nasal consonants, is allowed in some languages such as Bengali, Urdu, CH.min, and CH.wuu. Thus, nasal vowel can be used to discriminate between languages. Some nasal consonants such as velar nasal [ŋ] (which represents the sound /ng/) is allowed in some languages (e.g., CH.min, CH.can, CH.wuu, Urdu, Thai, and Russian) but it is not allowed in others. From observing *Round* attribute, there were three cases, including CH.min versus CH.can, CH.min versus CH.wuu, and CH.min versus Thai, where pairwise P values were larger than 0.01. The mean values of *Round* attribute among Chinese languages are not significantly different. It is interesting to describe why the *Round* attribute is not good to distinguish among these languages. Since *Round* attribute is one of vowel characteristics, we used the vowel chart to illustrate the manner of occurrence of this attribute. Vowels occurred in each language are summarized in the vowel chart and used to analyze the possibility of vowel feature in each language. From vowel chart analyzing as shown in Figure 4, we found

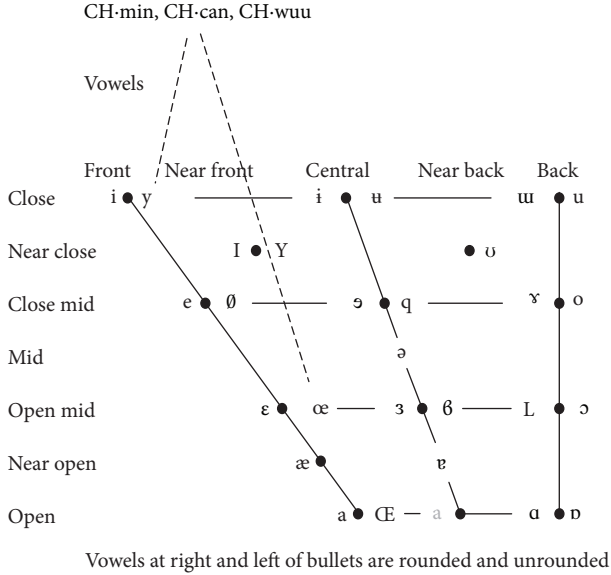


FIGURE 4: IPA vowel chart.

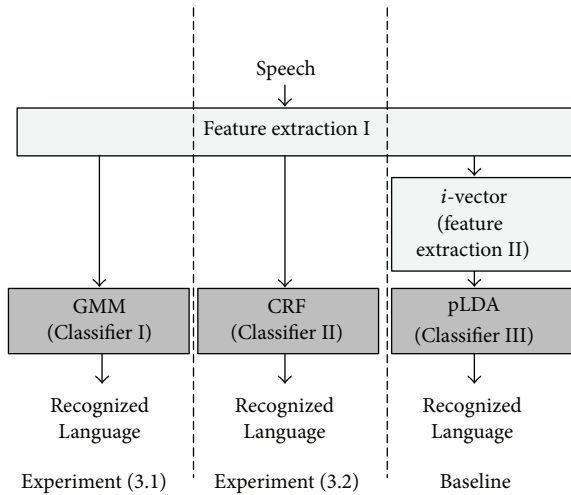


FIGURE 5: The baseline systems.

that that some rounded vowels are commonly present in Chinese languages such as the close front rounded vowel (represented as [y]) and the open-mid front rounded vowel (represented as [œ]). These examples of rounded vowels occur in Chinese languages (CH.min, CH.wuu, and CH.can) and are not present in others. The benefit of *Round* attribute can be used to distinguish Chinese languages from others but it cannot separate among Chinese dialects. Additionally, the mean value of *Round* attribute was not statistically different between CH.min and Thai because the rounded vowels can be often found in Thai and CH.min.

6.5. Baseline Systems and Experimental Evaluation. The architecture of baseline system and experimental evaluation is shown in Figure 5. It consists of two feature extraction methods and three classifiers. There are one baseline system

TABLE 6: Summary of speech features used in the experiment.

Feature	Description	Dimension
PF	Phonological features	26
SDPF	SDC over PF	182
PLP	C0 + 7 PLPs	8
MFCC	(12 MFCCs + E) + Δ + $\Delta\Delta$	39
SDCPLP	C0 + 7 PLPs + shifted delta cepstral	49
SDC + PLP	Concatenation of SDCPLP and 7 PLPs	56

and two experiments (as described in Section 6.6) which utilize different feature extractions and classifiers. The speech utterance is decoded by different feature extractions; then the feature vectors are fed into classifiers to determine the language of speech utterance. We evaluated the discriminative LDCRF model against the GMM to compare ability with generative model and we also evaluated it against the CRF model to examine the ability of discriminative model. Additionally, the performance of proposed system was also compared to the acoustic system based on *i*-vector space.

For comparing performance of proposed feature, the LDCRF language classifiers using different speech features were compared with conventional speech features in the acoustic-based SLR system. Summary of speech features used and compared in the experiment is provided in Table 6. There are six types of speech features: PF, SDPF, PLP, MFCC, SDC, and SDC + PLP. The details of the speech features are described in the following section.

6.5.1. Cepstral Feature. Typically, speech utterance is represented by cepstral feature vectors (including MFCC and PLP) which have been demonstrated to perform well in speech applications. This paper used these features to compare the discriminative ability for language classification. For MFCC and PLP feature extraction, the frames of speech utterance were analyzed using a 25 ms window with a 10 ms overlap. The MFCC feature vectors with 13 dimensions, including 12 MFCCs and energy, along with their first and second temporal derivatives, were calculated for each frame. For the PLP feature vector, we used the 7th order of PLP cepstral coefficients.

6.5.2. Shifted Delta Coefficients of Cepstral Features. The typical SDC that has been successfully and widely used in acoustic-based SLR systems is computed from the changes of the cepstral features across multiple frames. In this study, we used it to compare the discriminating ability with the proposed features.

In this experiment, we focused on two features which were computed from the SDC operation: SDCPLP (which is a result from applying the SDC operation to PLP features) and SDC + PLP (which is the concatenation of the PLP features and their SDC coefficients), as shown in Table 6.

6.5.3. Baseline Systems (*i*-Vector). Among the most popular modeling techniques used in acoustic systems, the *i*-vector

which is usually applied to model spectral features is the state-of-the-art in language recognition. To evaluate the effectiveness of the proposed system, we compared the performance between the proposed SLR system and the acoustic system based on i -vector.

The i -vector approach was motivated by the success of JFA, which models language and channel variability separately. In contrast with JFA, the i -vector concept utilizes the total variability subspace to model all variability in the same low dimensional subspace. That is, the total variability space contains the language and channel variability. The idea of total variability subspace is that the adapting of the Universal Background Model (UBM) to eigenvoice where the UBM is trained from all languages used in this experiment. The language-dependent and channel-dependent supervector M is a concatenation of all mean vectors of adapted GMM component. The GMM supervector M is obtained as (15) which is defined by the matrix T :

$$M = m + Tw, \quad (15)$$

where m is the UBM supervector (i.e., a language- and channel-independent component), T is a low rank rectangular matrix called the total variability, and w is the i -vector, which is random vector with a normal distribution $N(0, 1)$. The i -vector w is obtained for a given speech utterance.

To recognize language, the i -vector space, a log-likelihood ratio, is used to obtain a similarity score between a testing i -vector and the i -vectors of training class. There are many scoring methods for computing the similarity between two i -vectors w_1 and w_2 . The most successful model for modeling i -vector in speaker recognition is the generative Probabilistic Linear Discriminant Analysis (pLDA) [44]; thus, the pLDA log-likelihood ratio is used to compute the distance score between two i -vectors in this paper. It is computed as follows:

$$\begin{aligned} \text{score}(w_1, w_2) = & \log N \left(\begin{bmatrix} w_1 \\ w_2 \end{bmatrix}; \begin{bmatrix} w_1 \\ w_2 \end{bmatrix}, \begin{bmatrix} \Sigma_{\text{tot}} & B \\ B & \Sigma_{\text{tot}} \end{bmatrix} \right) \\ & - \log N \left(\begin{bmatrix} w_1 \\ w_2 \end{bmatrix}; \begin{bmatrix} w_1 \\ w_2 \end{bmatrix}, \begin{bmatrix} \Sigma_{\text{tot}} & 0 \\ 0 & \Sigma_{\text{tot}} \end{bmatrix} \right), \end{aligned} \quad (16)$$

where w_1 and w_2 are the two i -vectors, $N(\cdot)$ is the normal Gaussian probability density function, and Σ_{tot} is the total covariance matrix of training i -vectors and B denotes the between-class covariance matrix of training i -vectors. The i -vectors within each class (i.e., language) are averaged and represented as one i -vector.

The feature extraction used in this experiment was similar to that employed in [5]. The 7 MFCCs extracted and the SDC with 7-1-3-7 configuration were obtained. The final 56-dimensional feature vectors, a concatenation of MFCCs and its SDC, were converted to an i -vector based on GMM with 2048-components by using ALIZE [45]. The components involving i -vector of training class such as the UBM, the T matrix, and total and between-class matrices were trained using the training set (as 5-fold in Section 6.3).

6.6. *Experimental Setup.* There were four experiments described as follows.

Experiment (1). This experiment was a comparison of the discriminative ability of PF attributes with other features. The purpose of this experiment was to compare the performance of language classifiers using proposed PF features and using conventional features. The 28 language classifiers were trained from different speech features and the capabilities of discrimination were evaluated for each feature.

Experiment (2). This experiment was a study of the performance of language classifiers when reducing the effect of confused target classes. The purpose of this experiment was to evaluate the classifier performance when the ambiguous languages, that is, Chinese-Min and Chinese-Wu, were removed. That is, we simplified the classification problem in language recognition by ignoring the varieties of Chinese language. We compared the performance of the language classifiers of the five target languages with the results from Experiment (1). Thus, the number of classifiers was represented as an elementary combination by $C(6, 2) = 15$.

Experiment (3). The purpose of this experiment was to demonstrate the superiority of the discriminative model by using the LDCRF model for the language recognition task. The PF attributes were used as the speech features for training and testing language classifiers in this experiment. In addition, the PLP features were used to construct classifiers based on the GMM model. In total, language classifiers trained on the LDCRF, CRF, and GMM models using PFs and language classifiers trained on PLP were applied.

Experiment (3.1). This was a comparison of the discriminative model with the generative model. The language classifiers using the LDCRF model were compared with the one using the GMM model. Firstly, the acoustic GMM system that employed the PLP feature was compared to LDCRF system with PLP features. Secondly, the LDCRF language classifiers using PF attributes were compared with the GMM system using PFs, in order to compare the performance between employing PFs with the discriminative model and employing PF with generative model. The GMM model was trained on speech utterances from each language using the expectation maximization (EM) algorithm. The best configuration contained 256 Gaussians and was initialized using 10 iterations with the maximum likelihood (ML) criterion.

Experiment (3.2). This was a comparison of the discriminative LDCRF model with the CRF model. The language classifiers based on LDCRF were compared with the classifiers based on CRF, which is another discriminative model technique in a sequential problem. We conducted the language classifiers trained from the CRF model using similar configuration parameters to the parameters used for training the LDCRF model.

Experiment (4). This was a study of the effect of dimension reduction on the PF features and a study of how the language

TABLE 7: Error of language classifiers using different speech feature sets (averaged across 28 pairs).

Feature	Error (%)
PF	17.46
SDPF	21.07
MFCC	25.48
PLP	19.51
SDCPLP	23.36
SDC + PLP	21.15

The least error result is displayed in bold.

classifiers were affected when missing PF attributes. The feature vector of PF attributes used in Experiments (1–3) consisted of 13 PF attributes. In this experiment, we iteratively removed one of the PF attributes from the feature vector. Thus, in each round, these 12 PF attributes were concatenated to 24-dimensional feature vector. The same configuration parameters as Experiment (1) were used to train the LDCRF model of language classifiers. The language classifiers were trained from the feature vector by removing one of the PF attributes. The results of this experiment were compared with the results of Experiment (1) which used a total of 13 PF attributes.

Experiment (5). The purpose of this experiment was to evaluate the performance of the proposed system with the state-of-the-art acoustic system, based on *i*-vector approach [5]. In this experiment, we used the *i*-vector space with pLDA scoring method. The concepts of *i*-vector approach and *i*-vector feature extraction are described in Section 6.5.3.

7. Results and Discussion

The performance of the experiments (as described in Section 6.6) was measured across the 28 language classifiers. The average values of accuracy and errors were computed from 5-fold cross-validation. The results from each experiment are described as follows.

For Experiment (1), Table 7 compares the performance of the language classifiers using PF, SDPF, MFCC, PLP, SDCPLP, and SDC + PLP as input features. It shows that the classifiers using the PF features were superior to the other speech features. The average error of the 28 language pairs using the PF attributes was 17.46% which was the smallest. From Table 7, the error of classifiers using different features can be represented in descending order as PF < PLP < SDPF < SDC + PLP < SDCPLP < MFCC, which indicates that it is less beneficial applying SDC to compute the SDPF and SDCPLP features, with a relative error increase of 17.13% and 16.48%, respectively.

Comparing the experiments using varying features of PLP, namely, PLP, SDCPLP, and SDC + PLP (a combination of PLP attributes and the SDC computed from PLP), the performance of PLP was better than SDC + PLP and SDCPLP. The SDCPLP option was better than SDC + PLP. However, there was no significant difference among these features

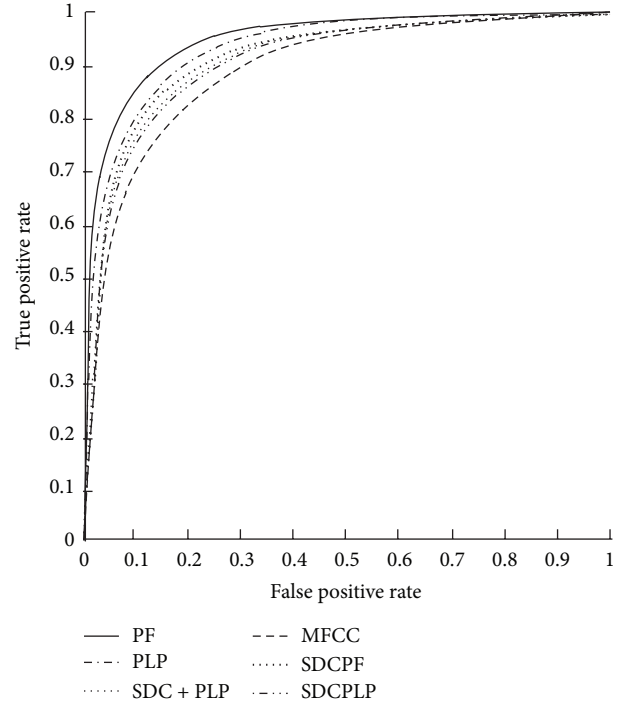


FIGURE 6: ROC curve classification results from 28 language pair classifiers using PF attributes versus others.

because they are highly correlated and they are derived from the same front-end feature, PLP.

Interestingly, the features performed relatively poorly when the SDC was applied to the original features, in contrast to the other research studies where applying the SDC to features achieved a better performance. This may have been caused as a result of these features being highly correlated with the original features and the LDCRF model that does not have strong dependence assumption and has the ability to incorporate the correlated observation.

Figure 6 compares the ROC curves of the classifiers using different speech features. The ROC curve of the classifier using PFs was higher than the classifier using conventional features and its SDC, which indicates that the classifier using PF features outperformed all the other classifiers.

Figure 7 compares the percentage of errors of the LDCRF language classifiers on different speech features. It demonstrates that the language classifiers using PF attributes outperformed those using the conventional features, but their performance was poorer when combining PF with the SDCs. From Figure 7, it can be noticed that different features in language classifiers also have the same trend and most of the classifiers using PFs achieved the best performance.

The performance of classifiers was also measured statistically using the paired *t*-test. There were 22 language classifiers using PFs that had better performance than the ones using PLP, three of which were significantly different: Rus.Can, Tha.Wu, and Urd.Wu. On the other hand, there were six language classifiers using PF attributes that were worse performers than using PLP: Min.Wu, Min.Urd, Arb.Urd,

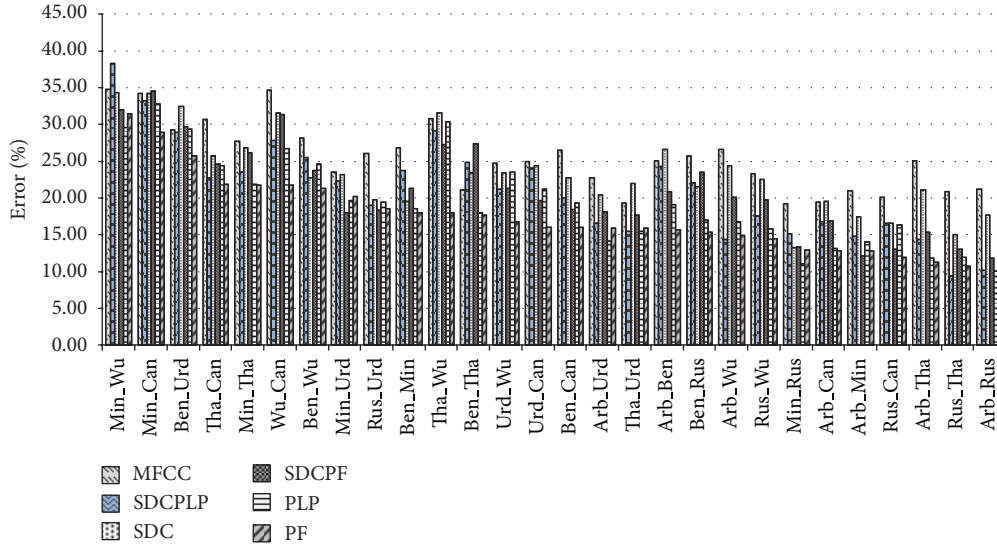


FIGURE 7: Errors for each of 28 language classifiers trained with LDCRF using PF attributes versus others.

Tha_Urd, Min_Rus, and Arb_Rus. Furthermore, there was no significant difference in language classifiers between using PF and PLP. There were 16 language classifiers using PFs that were significantly better than using SDCs. Additionally, there were 25 language classifiers using PFs that were better performers than SDC + PLP of which ten were significantly different: Arb_Ben, Ben_Min, Ben_Rus, Ben_Tha, ben_wuu, Min_Wu, Rus_Can, Tha_Wu, Urd_Wu, Urd_Can, and Wu_Can. Three PF language classifiers achieved better performance than using SDC such as Rus_Can, Tha_Wu, and Urd_Wu. Twenty-seven of the classifiers using PFs were better performers than SDCPF, and eight of them were significantly different. There is one pair of language classifier using PFs, Min_Urd, was poorer than SDCPF. The performances of all classifiers using PFs was better than using MFCC and 24 pairs had significant differences.

For Experiment (2), Table 8 shows the results of the language classifiers after removing the ambiguous Chinese languages. The results support that the discriminative ability of PF is superior to the other speech features. From comparing Tables 7 and 8, removing the confusing languages (Min Chinese and Wu Chinese) yielded better classification performance. The performance of language classifiers using PF, SDCPF, MFCC, PLP, SDC, and SDC + PLP attributes achieved relative error reductions of 10.08%, 8.58%, 6.33%, 10.87%, 6.09%, and 9.99%, respectively. In future work, we plan to extend the analysis on feature reduction when removing confusing languages and to observe if there is any feature which helps improving the performance of some language classifier.

Table 9 compares the language classifier error from training with the LDCRF, CRF, and GMM models using PFs (as described in Experiment (3)). It shows that the LDCRF model achieved 17.46% error which was lower than for the CRF and GMM models. However, it was not significantly different between the LDCRF and CRF models.

TABLE 8: Language classifier error using different speech feature sets (averaged across 15 pairs).

Feature	Error (%)
PF	15.70
SDPF	19.26
MFCC	23.87
PLP	17.39
SDC	21.94
SDC + PLP	19.04

The least error result is displayed in bold.

TABLE 9: Error of language classifiers trained on LDCRF, CRF, and GMM models using PFs and classifiers trained on GMM using PLP (averaged across 28 pairs).

Model	Error (%)
LDCRF (PF)	17.46
CRF (PF)	19.11
GMM (PF)	30.63
GMM (PLP)	52.28

The least error result is displayed in bold.

Moreover, the classifiers modeled by GMM were compared with using PFs and using the PLP as input features. The results of the experiment using PFs achieved better performance than from using the PLP, which could be due to the PFs having more discriminative ability than the PLP.

Figure 8 compares the confidence score results of CRF and LDCRF classifiers from Experiment (3) using different modeling techniques. The ROC curves of the LDCRF classifiers were slightly higher than for the CRF classifiers.

For Experiment (4), Table 10 shows the error of language classifiers trained from the feature vector that removed one of the PF attributes. The results showed that the classifiers

TABLE 10: Error of language classifiers trained from the feature vector after removal of one PF attribute (averaged across 28 pairs).

Removed attribute	Error (%)
None (Full PF)	17.46
High	17.79
Tense	17.80
Voiced	17.87
Strident	18.00
Anterior	18.02
Low	18.05
Vocalic	18.10
Continuant	18.12
Coronal	18.15
Nasal	18.17
Round	18.31
Consonantal	18.44
Back	18.60

The least error result is displayed in bold.

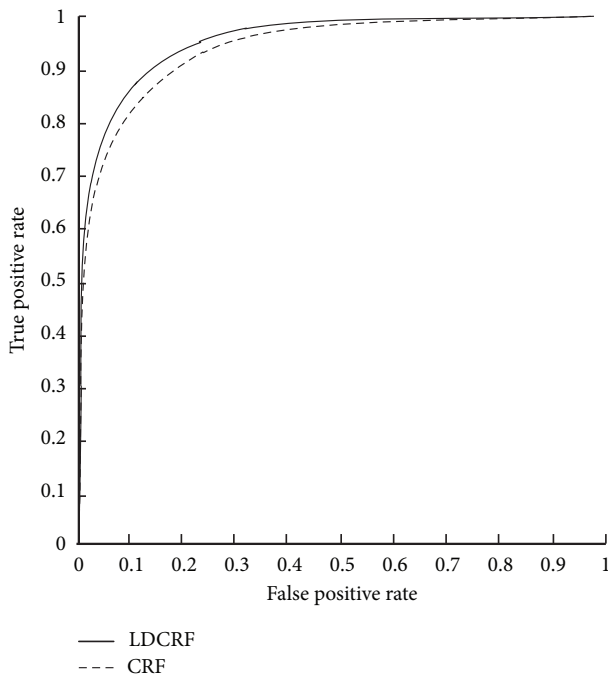


FIGURE 8: ROC curve classification results of LDCRF and CRF models (from 28 language classifiers).

achieved comparable performance with the one trained from the full set of PFs. Thus, removing one of the PF attributes did not significantly improve the performances of the classifiers.

The results of removing one PF attribute do not seem to be consistent. However, the overall classification results performed relatively poorly when one of PF attributes was removed from the feature vectors. This indicates that while

TABLE 11: Error of language classifiers trained on LDCRF using PFs and acoustic based on *i*-vector approach.

Model	Error (%)
LDCRF (PF)	17.46
<i>i</i> -vector	19.94

The least error result is displayed in bold.

the removal of a “*High*” attribute yielded a poorer performance in the experiment, performance was not as bad when a “*Back*” attribute was removed from the feature vector. In 11 out of 28 cases, the classifiers, with removing one PF attribute, were significantly different from the classifiers using the full set of PFs. Furthermore, there was a significant improvement when the “*Nasal*” attribute was removed from the feature vector (i.e., language classifier Arb_Urd).

From the results, we noticed that the removal of one attribute from the feature vector had a small effect on the overall accuracy. This was caused by the fact that the classifiers can use information from the other PF attributes which are in the same group of features. For example, “*High*” attribute can use information from “*Low*,” “*Back*,” and “*Round*” attributes (which are in the same group of vowel features). Another example is the removal of “*voiced*” attribute, which is correlated with “*Vocalic*” and “*Consonantal*” attributes, so the language can be classified by using other features instead. However, the removal of one attribute decreased the overall performance. Although each PF attribute was derived from separately-trained attribute detectors, the removal of PF attributes did not have a great impact on the performance. It can be concluded that the PF attributes in the feature vector are not truly independent.

For Experiment (5), Table 11 shows the averaged error of language classifiers trained on LDCRF using PFs and the acoustic approach based on *i*-vector space (baseline system). The error of proposed system based on LDCRF using PFs was 17.46% and 19.94% for the baseline system. The result shows that the performance of the proposed system based on LDCRF with PFs was comparable to the performance of the acoustic system based on *i*-vector space. Even though ALIZE has been widely used to extract the *i*-vector, the tuning is needed to acquire the satisfying performance. However, it is not the main focus of this study. There were 21 language classifiers using LDCRF with PFs that had better performance than the baseline while two of them, Rus_Can and Rus_Wu, were significantly different. On the other hand, there were seven language classifiers using PF attributes that were worse performers than baseline system: Ben_Rus, Min_Rus, Rus_Tha, Tha_Wu, Urd_Wu, and Tha_Urd. However, they were not significantly different from the LDCRF models and baseline systems. The performance of the baseline system using *i*-vector was not good because it has not been fine tuned. In addition, it could be concluded from the several following reasons. Firstly, the *i*-vector approach is advantageous when sufficiently/large speech data across language is available for training the UBM supervector and adapting the language- and channel-dependent vectors; however, the speech corpus used in this paper is small; thus, it may be not suitable for the

i -vector approach. Secondly, the measurement, used to obtain a likelihood score of a testing i -vector is a generative pLDA model scoring. Another technique can be applied to improve the classifying of i -vector space. Further experiment has to employ discriminative classifiers such as SVM and Logistic Regression to classify language in i -vector space. Moreover, we will adapt the i -vector paradigm to model the proposed PF feature for SLR task in future work.

8. Conclusion

We have presented an acoustic approach SLR system applying the LDCRF model with PF attributes. From the experimental results, applying the SLR system with the discriminative LDCRF model showed significant improvement compared to the generative GMM model. In addition, employing LDCRF to learn the dynamic sequences of PF attributes for modeling the language can enhance the SLR performance. It can be an alternative discriminative method that pays attention to solving the problem of the independency among features. In terms of the discriminative ability of the speech attributes, the performance of the SLR system using PFs outperformed that using conventional speech features. The most notable conclusion that could be drawn from the experiment was that the PF attributes achieved better performance in language classification than the conventional speech features.

Conflict of Interests

The authors declare that there is no conflict of interests regarding the publication of this paper.

Acknowledgments

This work was partially funded by Thailand Graduate Institute of Science and Technology (TGIST), NSTDA, and by CU Graduate School Thesis Grant.

References

- [1] P. A. Torres-Carrasquillo, E. Singer, M. A. Kohler, R. J. Greene, D. A. Reynolds, and J. Deller Jr., "Approaches to language identification using Gaussian mixture models and shifted delta cepstral features," in *Proceedings of the International Conference on Spoken Language Processing (ICSLP '02)*, pp. 33–36, 2002.
- [2] E. Wong, J. Pelecanos, S. Myers, and S. Sridharan, "Language identification using efficient Gaussian mixture model analysis," in *Proceedings of the Australian International Conference on Speech Science and Technology*, p. 7.6, 2000.
- [3] M. A. Zissman, "Comparison of four approaches to automatic language identification of telephone speech," *IEEE Transactions on Speech and Audio Processing*, vol. 4, no. 1, pp. 31–44, 1996.
- [4] H. Li, B. Ma, and C.-H. Lee, "A Vector space modeling approach to spoken language identification," *IEEE Transactions on Audio, Speech and Language Processing*, vol. 15, no. 1, pp. 271–284, 2007.
- [5] O. P. B. L. Martínez, G. David, F. Luciana, and S. Nicolas, "Language recognition in iVector space," in *Proceedings of the 9th Annual Conference of the International Speech Communication Association (INTERSPEECH '11)*, Florence, Italy, 2011.
- [6] P. A. Torres-Carrasquillo, D. A. Reynolds, and J. R. Deller Jr., "Language identification using Gaussian mixture model tokenization," in *Proceedings of the IEEE International Conference on Acoustics, Speech, and Signal Processing (ICASSP '02)*, pp. I-757–I-760, May 2002.
- [7] K. E. Wong, *Automatic spoken language identification utilizing acoustic and phonetic speech information [Ph.D. thesis]*, Queensland University of Technology, 2004.
- [8] C. C. L. Haipeng Wang, T. Lee, B. Ma, and H. Li, "Shifted-delta MLP features for spoken language recognition," *IEEE Signal Processing Letters*, vol. 20, pp. 15–18, 2013.
- [9] O. S. B. Launay, O. Siohan, A. C. Surendran, and C.-H. Lee, "Towards knowledge-based features for HMM based large vocabulary automatic speech recognition," in *Proceedings of the IEEE International Conference on Acoustics, Speech, and Signal Processing (ICASSP '02)*, pp. I-817–I-820, Orlando, Fla, USA, May 2002.
- [10] K. Kirchhoff, *Robust speech recognition using articulatory information [Ph.D. thesis]*, Universität Bielefeld, 1999.
- [11] L. Burget, P. Matějka, and J. Černocký, "Discriminative training techniques for acoustic language identification," in *Proceedings of the IEEE International Conference on Acoustics, Speech and Signal Processing (ICASSP '06)*, pp. I209–I212, May 2006.
- [12] W. M. Campbell, E. Singer, P. A. Torres-Carrasquillo, and D. A. Reynolds, "Language recognition with support vector machines," in *Proceedings of the Speaker and Language Recognition Workshop (ODYSSEY '04)*, 2004.
- [13] W. M. Campbell, J. P. Campbell, D. A. Reynolds, E. Singer, and P. A. Torres-Carrasquillo, "Support vector machines for speaker and language recognition," *Computer Speech and Language*, vol. 20, no. 2-3, pp. 210–229, 2006.
- [14] P. A. Torres-Carrasquillo, D. Sturim, D. A. Reynolds, and A. McCree, "Eigen-channel compensation and discriminatively trained Gaussian mixture models for dialect and accent recognition," in *Proceedings of the 9th Annual Conference of the International Speech Communication Association (INTERSPEECH '08)*, pp. 723–726, September 2008.
- [15] W. M. Campbell, D. E. Sturim, and D. A. Reynolds, "Support vector machines using GMM supervectors for speaker verification," *IEEE Signal Processing Letters*, vol. 13, no. 5, pp. 308–311, 2006.
- [16] F. Castaldo, D. Colibro, E. Dalmaso, P. Laface, and C. Vair, "Acoustic language identification using fast discriminative training," in *Proceedings of the 8th Annual Conference of the International Speech Communication Association (INTERSPEECH '07)*, pp. 389–392, August 2007.
- [17] W. M. Campbell, "A covariance Kernel for SVM language recognition," in *Proceedings of the IEEE International Conference on Acoustics, Speech and Signal Processing (ICASSP '08)*, pp. 4141–4144, April 2008.
- [18] C. H. You, H. Li, and K. A. Lee, "A GMM-supervector approach to language recognition with adaptive relevance factor," in *Proceedings of the 18th European Signal Processing Conference*, pp. 1993–1997, 2010.
- [19] P. Kenny, G. Boulianne, P. Ouellet, and P. Dumouchel, "Joint factor analysis versus eigenchannels in speaker recognition," *IEEE Transactions on Audio, Speech and Language Processing*, vol. 15, no. 4, pp. 1435–1447, 2007.
- [20] N. Dehak, P. J. Kenny, R. Dehak, P. Dumouchel, and P. Ouellet, "Front-end factor analysis for speaker verification," *IEEE Transactions on Audio, Speech and Language Processing*, vol. 19, no. 4, pp. 788–798, 2011.

- [21] B. L. Martínez González David, F. Luciana, and S. Nicolas, "Ivector-based prosodic system for language identification," in *Proceedings of the International Conference on Acoustics Speech and Language (ICASSP '12)*, pp. 4861–4864, Kyoto, Japan, 2012.
- [22] K. Kirchhoff, *Robust speech recognition using articulatory information [Ph.D. thesis]*, Universität Bielefeld, 1999.
- [23] S. King and P. Taylor, "Detection of phonological features in continuous speech using neural networks," *Computer Speech and Language*, vol. 14, no. 4, pp. 333–353, 2000.
- [24] J. Li and C.-H. Lee, "On designing and evaluating speech event detectors," in *Proceedings of the 9th European Conference on Speech Communication and Technology*, pp. 3365–3368, September 2005.
- [25] S. Stüker, T. Schultz, F. Metze, and A. Waibel, "Multilingual articulatory features," in *Proceedings of the IEEE International Conference on Acoustics, Speech, and Signal Processing*, vol. 1, pp. I-144–I-147, April 2003.
- [26] D. Harwath and M. Hasegawa-Johnson, "Phonetic landmark detection for automatic language identification," *Urbana*, vol. 51, 2010.
- [27] U. V. Chaudhari and M. Picheny, "Articulatory feature detection with support vector machines for integration into ASR and phone recognition," in *Proceedings of the IEEE Workshop on Automatic Speech Recognition and Understanding (ASRU '09)*, pp. 93–98, December 2009.
- [28] S. Kanokphara, J. Macek, and J. Carson-Berndsen, "Comparative study: HMM and SVM for automatic articulatory feature extraction," in *Proceedings of the 19th International Conference on Advances in Applied Artificial Intelligence: Industrial, Engineering and other Applications of Applied Intelligent Systems (IEA/AIE '06)*, pp. 674–681, 2006.
- [29] Y. H. Abdel-Haleem, *Conditional random fields for continuous speech recognition [Ph.D. thesis]*, University of Sheffield, 2006.
- [30] A. Gunawardana, M. Mahajan, A. Acero, and J. C. Platt, "Hidden conditional random fields for phone classification," in *Proceedings of the 9th European Conference on Speech Communication and Technology*, pp. 1117–1120, September 2005.
- [31] D. Yu and L. Deng, "Deep-structured hidden conditional random fields for phonetic recognition," in *Proceedings of the 11th Annual Conference of the International Speech Communication Association (INTERSPEECH '10)*, pp. 2986–2989, September 2010.
- [32] J. Morris and E. Fosler-Lussier, "Conditional random fields for integrating local discriminative classifiers," *IEEE Transactions on Audio, Speech and Language Processing*, vol. 16, no. 3, pp. 617–628, 2008.
- [33] D. Yu, S. Wang, Z. Karam, and L. Deng, "Language recognition using deep-structured conditional random fields," in *Proceedings of the IEEE International Conference on Acoustics, Speech, and Signal Processing (ICASSP '10)*, pp. 5030–5033, March 2010.
- [34] L.-P. Morency, A. Quattoni, and T. Darrell, "Latent-dynamic discriminative models for continuous gesture recognition," in *Proceedings of the IEEE Computer Society Conference on Computer Vision and Pattern Recognition (CVPR '07)*, pp. 1–8, June 2007.
- [35] A. J. Quattoni, *Object recognition with latent conditional random fields [M.S. thesis]*, Massachusetts Institute of Technology, 2005.
- [36] V. Deufemia, M. Risi, and G. Tortora, "Sketched symbol recognition with a latent-dynamic conditional model," in *Proceedings of the 20th International Conference on Pattern Recognition (ICPR '10)*, pp. 1100–1103, August 2010.
- [37] N. Chomsky and M. Halle, *The Sound Pattern of English*, 1968.
- [38] J. Lafferty, A. McCallum, and F. C. N. Pereira, "Conditional random fields: probabilistic models for segmenting and labeling sequence data," in *Proceedings of the 8th International Conference on Machine Learning*, pp. 282–289, 2001.
- [39] S. Kumar and M. Hebert, "Discriminative random fields: a discriminative framework for contextual interaction in classification," in *Proceedings of the 9th IEEE International Conference on Computer Vision*, pp. 1150–1157, October 2003.
- [40] N. Strom, "The NICO toolkit for artificial neural networks," <http://www.speech.kth.se/NICO>.
- [41] F. Allen, E. Ambikairajah, and J. Epps, "Language identification using warping and the shifted delta cepstrum," in *Proceedings of the IEEE 7th Workshop on Multimedia Signal Processing (MMSP '05)*, Shanghai, China, November 2005.
- [42] P. Matějka, L. Burget, O. Glembek et al., "BUT language recognition system for NIST 2007 evaluations," in *Proceedings of the 9th Annual Conference of the International Speech Communication Association (INTERSPEECH '08)*, pp. 739–742, September 2008.
- [43] "NIST LRE-2007 Evaluation Plan," 2007, <http://www.itl.nist.gov/iad/mig/tests/lre/2007/LRE07EvalPlan-v8b.pdf>.
- [44] L. Burget, O. Plchot, S. Cumani, O. Glembek, P. Matějka, and N. Brümmer, "Discriminatively trained Probabilistic Linear Discriminant Analysis for speaker verification," in *Proceedings of the 36th IEEE International Conference on Acoustics, Speech, and Signal Processing (ICASSP '11)*, pp. 4832–4835, May 2011.
- [45] A. Larcher, J. F. Bonastre, B. Fauve et al., "ALIZE 3.0—open source toolkit for state-of-the-art speaker recognition," in *Proceedings of the 9th Annual Conference of the International Speech Communication Association (INTERSPEECH '13)*, 2013.

Research Article

Efficient LED-SAC Sparse Estimator Using Fast Sequential Adaptive Coordinate-Wise Optimization (LED-2SAC)

T. Yousefi Rezaii,¹ S. Beheshti,² and M. A. Tinati¹

¹ Faculty of Electrical and Computer Engineering, University of Tabriz, 29 Bahman Avenue, Tabriz 51666-15813, Iran

² Department of Electrical and Computer Engineering, Ryerson University, Toronto, ON, Canada M5B 2K3

Correspondence should be addressed to T. Yousefi Rezaii; tohidusefi@gmail.com

Received 7 October 2013; Accepted 29 December 2013; Published 6 February 2014

Academic Editor: Yue Wu

Copyright © 2014 T. Yousefi Rezaii et al. This is an open access article distributed under the Creative Commons Attribution License, which permits unrestricted use, distribution, and reproduction in any medium, provided the original work is properly cited.

Solving the underdetermined system of linear equations is of great interest in signal processing application, particularly when the underlying signal to be estimated is sparse. Recently, a new sparsity encouraging penalty function is introduced as Linearized Exponentially Decaying penalty, LED, which results in the sparsest solution for an underdetermined system of equations subject to the minimization of the least squares loss function. A sequential solution is available for LED-based objective function, which is denoted by LED-SAC algorithm. This solution, which aims to sequentially solve the LED-based objective function, ignores the sparsity of the solution. In this paper, we present a new sparse solution. The new method benefits from the sparsity of the signal both in the optimization criterion (LED) and its solution path, denoted by Sparse SAC (2SAC). The new reconstruction method denoted by LED-2SAC (LED-Sparse SAC) is consequently more efficient and considerably fast compared to the LED-SAC algorithm, in terms of adaptability and convergence rate. In addition, the computational complexity of both LED-SAC and LED-2SAC is shown to be of order $\mathcal{O}(d^2)$, which is better than the other batch solutions like LARS. LARS algorithm has complexity of order $\mathcal{O}(d^3 + nd^2)$, where d is the dimension of the sparse signal and n is the number of observations.

1. Introduction

Compressed sensing (CS) signal processing has gained a lot of popularity due to the lower sampling rate needed for reconstruction of the original signal compared to that of Nyquist lower bound of sampling rate. Consequently, the signal is sampled in a compressed manner via the sampler and there is no need for an additional compression procedure (as it is common in conventional signal processing).

The main challenge in CS signal processing is how to recover the original signal using the few samples from the sampler. Suppose the sparse signal, $\theta^* \in \mathbb{R}^d$, $\|\theta^*\|_0 = K \ll d$, is to be estimated via the following linear regression model:

$$y_i = \mathbf{x}_i^T \theta^* + v_i \quad i = 1, 2, \dots, n, \quad (1)$$

where y_i , $\mathbf{x}_i \in \mathbb{R}^d$, and v_i are the observation, regressor and observation noise at time index i , respectively. v_i is assumed to be additive white Gaussian noise with mean 0 and variance

σ^2 . In the matrix form, the linear regression model (1) will have the following form:

$$\mathbf{y} = \mathbf{X}\theta^* + \mathbf{v}, \quad (2)$$

where $\mathbf{y} = [y_1, \dots, y_n]^T$, $\mathbf{X} = [\mathbf{x}_1^T, \dots, \mathbf{x}_n^T]^T$, and $\mathbf{v} = [v_1, \dots, v_n]^T$ are the observation vector, regression matrix (also called measurement matrix in CS), and noise vector, respectively.

Variable selection and high prediction accuracy are two major issues in sparse signal estimation. Variable selection is necessary for sparsity aware signal estimation. The common approach is to introduce a penalty to the overall objective function which will guarantee sparsity in the estimated signal. In order to ensure high prediction accuracy, a suitable loss function must be introduced. The most common loss function is the L_2 loss function due to its convexity which results in the well-known least squares solution. A general form of the objective functions to be minimized in order to

recover the sparse solution, which is also accepted through this paper, is as follows:

$$\mathcal{J}(\boldsymbol{\theta}^*) = \frac{1}{2n} \|\mathbf{y} - \mathbf{X}\boldsymbol{\theta}^*\|_2^2 + \tau \mathcal{P}(|\boldsymbol{\theta}^*|), \quad (3)$$

where $\mathcal{P}(\cdot)$ is the penalty function and τ is a tuning parameter that balances the prediction accuracy and sparsity.

Depending on the choice of the loss and sparsity encouraging functions and the techniques used for solving the optimization problem, extensive works have been presented in the literature. Some sophisticated and relatively high precision approaches are basis pursuit [1] and greedy [2, 3] reconstruction algorithms which perform batch-based estimation. The other class of batch-based sparse estimation algorithms is based on the L_p norm ($p < 1$) as the sparsity encouraging factor [4–8]. As it is reported, using the L_p norm in the objective function will effectively reduce the number of required measurements compared to that of the L_1 norm reconstruction. However, there is no analytic guarantee.

Adaptive signal reconstruction is of interest in applications where the sparse signal of interest undergoes variations in its support as well as the magnitude of its nonzero entries. Furthermore, in most signal acquisition devices, the observations are obtained sequentially. Thus, the variations in the support of the unknown signal can be sensed by sequentially processing the observations rather than batch processing.

In [9], observations are received in sequence and without any prior assumptions on the signal sparsity; the reconstruction error is computed between observations in order to decide whether enough samples have been obtained. Variational adaptive filters are extensively used to sparse signal reconstruction as in [10–18]. The resulting estimators are sequential but too slow. Furthermore, due to the lack of a direct variable selection stage, like a thresholding rule, exact reconstruction of the zero parameters is impossible.

Recently, the family of Least-Absolute Shrinkage and Selection Operator (Lasso) objective functions has gained a lot of popularity in sparse signal reconstruction context [19]. Lasso in its standard form includes the L_1 penalized least squares error criterion, which continuously shrinks the parameters toward zero. The Least Angle Regression (LARS) is the most famous batch-based algorithm to solve the Lasso problem [20] (a similar solution is also already proposed by Osborne et al. [21]).

It is shown that the standard Lasso objective function leads to biased estimator, which is due to the pure soft thresholding stage used in the estimation procedure [22–25]. SCAD (Smoothly Clipped Absolute Deviation) and adaptive Lasso are two alternatives which are presented in [22, 24], respectively, in order to make the standard Lasso an unbiased estimator. We have presented the LED objective function in [26] as another alternative for Lasso objective function and it is demonstrated that the resulting estimator outperforms the SCAD and adaptive Lasso estimators.

Based on the SCAD and adaptive Lasso objective functions, the TNWL and AdaLasso algorithms are presented in [27, 28, 32], respectively, which are the adaptive and sequential implementation of these objective functions. We have also

developed an adaptive and sequential solution for the LED objective function in [29], namely, LED-SAC, by solving the objective function in a coordinate-wise manner. It is shown that the proposed algorithm satisfies the oracle properties of asymptotic normality and consistency in variable selection and reaches better tracking performance compared to TNWL and AdaLasso.

Although the LED-SAC is a sparse reconstruction algorithm, it doesn't take the advantage of the sparsity of the signal to be estimated in its solution path. In this paper, we first study the complexity of LED-SAC algorithm. Then, a solution path is presented for LED-SAC algorithm, which benefits the sparsity of the signal to be estimated. More specifically, the most effective coordinates of the sparse signal are detected and the update procedure is done merely for those coordinates. Consequently, the resulting estimator, that is LED-2SAC, is more efficient and faster in terms of convergence rate compared to original one and it is shown that it has the same order of complexity as LED-SAC.

2. Summary of LED-SAC Reconstruction Algorithm

The exponentially decaying sparsity encouraging penalty function presented in [26] is as follows:

$$\mathcal{P}_{\tau_n, \gamma}(|\boldsymbol{\theta}^*|) = \begin{cases} \tau_n |\boldsymbol{\theta}^*|, & |\boldsymbol{\theta}^*| \leq \tau_n, \\ \tau_n^2 + \tau_n \gamma (1 - e^{-(|\boldsymbol{\theta}^*| - \tau_n)/\gamma}), & \text{otherwise,} \end{cases} \quad (4)$$

where τ_n and γ are the parameters of the penalty function which define its shape. Considering the penalty function in (4), the penalization rate reduces from a constant value to 0 (unlike standard Lasso), and the transition is smooth and controlled by the parameter γ , contrary to SCAD penalty, which has rough and linear decaying rate.

The overall objective function, which is obtained by augmenting the least squares loss function to the penalty function in (4), is nonconvex and cannot be solved via well-established convex optimization tools. Moreover, solving this nonconvex optimization problem may lead to a local minimum which is not the sparsest solution. In [26], we have obtained a convex approximation for this objective function by locally linearizing it using Taylor series expansion around some consistent estimate of $\boldsymbol{\theta}^*$. The resulting objective function is called LED objective function which is given as

$$\hat{\boldsymbol{\theta}} = \arg \min_{\boldsymbol{\theta}} \frac{1}{2n} \|\mathbf{y} - \mathbf{X}\boldsymbol{\theta}\|_2^2 + \sum_{j=1}^d \mathcal{P}'_{\tau_n, \gamma}(|\boldsymbol{\theta}^{j,o}|) |\boldsymbol{\theta}^j|, \quad (5)$$

where $\boldsymbol{\theta}^o$ is a consistent estimator of $\boldsymbol{\theta}^*$, such as the ordinary least squares solution (In [29] we have demonstrated the effects of decreasing the number of observations, n , while $\boldsymbol{\theta}^o$ is the ordinary least squares solution. The results show that, decreasing the number of observations degrades the performance of the sparse reconstruction algorithm. In this case, the solution of other suitable estimators like ridge regression estimator can be used, which is experimentally shown to

perform better). The properties of asymptotic normality and consistency hold for the LED objective function as long as the two constraints of $\lim_{n \rightarrow \infty} \tau_n \rightarrow 0$ and $\lim_{n \rightarrow \infty} \sqrt{n} \tau_n \rightarrow \infty$ are met, as n goes to infinity and the observation noise has finite variance [26].

In order to solve the approximated objective function in (5), one needs to solve a multivariate optimization problem, which is computationally too expensive to solve especially for sparse signals of higher dimension. In [29], a sequential and adaptive solution path is developed in order to solve the LED objective function in (5), called LED-SAC. The basic idea lies behind the fact that the objective function is convex and separable for each variables of the sparse signal θ . Therefore, the optimization problem is well suited to solve via the coordinate-wise optimization method. The proposed LED-SAC algorithm is capable of tracking the time variations in the support of the underlying sparse signal. The uniqueness of the LED-SAC algorithm is that it uses a novel sparsity-encouraging penalty and solves the overall objective function sequentially. As it is reported in [29], the LED-SAC estimator outperforms the TNWL and AdaLasso estimators in terms of mean squared error as well as tracking capability.

In what follows, we will explore the possibility of improving the convergence rate of the solution path for the LED-SAC algorithm. If so, a solution path is given to solve the objective function in (5), which itself is sparse in the sense that it has the sparsity of the signal to be estimated in mind, while pursuing the solution path. Therefore, the optimization method is itself sparse, which also leads to the sparsest solution. Consequently, the tracking capability of the algorithm will be increased, that is vital for online implementation, particularly in time varying sparse signal scenario.

3. The Proposed LED-Sparse SAC (LED-2SAC) Reconstruction Algorithm

Although the LED-SAC estimator restricts the solution of the under determined system of equations in (5) to the sparsest solution, it ignores the sparsity of the signal to be estimated in the solution path. This is due to the fact that at each iteration, it updates all of the coordinates of the sparse signal in cyclic manner, no matter which one of them belongs to the support of the true signal. This will significantly increase the number of observation needed to reach the desired precision in the reconstructed signal. As the signal of interest is sparse, most of its coordinates are zero and need not to be updated. Furthermore, in time varying sparse signal scenario, detecting and updating the coordinate, which has the most variation in its value, will significantly increase the tracking ability of the estimator.

Therefore, despite all advantages, updating whole coordinate set in a cyclic manner while most of them have zero values will still remain as the main shortcoming of LED-SAC estimator. This kind of blindly processing the coordinates of the signal to be estimated makes the reconstruction algorithm inefficient and rather slow to converge to a solution.

In order to consider the sparsity of the signal in the solution path and implement the LED-SAC more efficiently, one needs to introduce a procedure to detect the most effective coordinate/coordinates at each iteration and perform the update procedure for those coordinates. The objective function in (5) can be decomposed into two parts as follows:

$$\begin{aligned} \mathcal{F}(\theta) &= \overline{\mathcal{F}}(\theta^j) + \text{constant} \\ &= \frac{1}{2} [\mathbf{C}_\alpha(n)]_{jj} \theta^{j^2} \\ &\quad - \frac{1}{n} \beta(n, j) \theta^j + \mathcal{P}'_{\tau_n, \gamma}(|\theta^{j,o}|) |\theta^j| + \text{constant}, \end{aligned} \quad (6)$$

where $\overline{\mathcal{F}}(\theta^j)$ is the portion of $\mathcal{F}(\theta)$ which merely depends on θ^j and the term ‘‘constant’’ is a function of all of the entries of the parameter vector θ except θ^j , so it can be considered as constant with respect to θ^j .

Let us define $\Delta \overline{\mathcal{F}}(\theta^j)$ as the difference between $\overline{\mathcal{F}}(\theta_{(n)}^j)$ and $\overline{\mathcal{F}}(\theta_{(n-1)}^j)$, such that

$$\begin{aligned} \Delta \overline{\mathcal{F}}^j &= \overline{\mathcal{F}}(\theta_{(n)}^j) - \overline{\mathcal{F}}(\theta_{(n-1)}^j) \\ &= \frac{1}{2} [\mathbf{C}_\alpha(n)]_{jj} (\theta_{(n)}^{j^2} - \theta_{(n-1)}^{j^2}) \\ &\quad - \frac{1}{n} \beta(n, j) (\theta_{(n)}^j - \theta_{(n-1)}^j) \\ &\quad + \mathcal{P}'_{\tau_n, \gamma}(|\theta_{(n)}^{j,o}|) (|\theta_{(n)}^j| - |\theta_{(n-1)}^j|), \end{aligned} \quad (7)$$

where $\theta_{(n)}^j$ is the j th entry of the parameter vector θ at time n . One can select the most effective coordinate as the coordinate which makes the most changes to $\Delta \overline{\mathcal{F}}^j$, as [30]:

$$j^* = \arg \max_j \Delta \overline{\mathcal{F}}^j. \quad (8)$$

Selecting the most effective coordinate as in (8) leads to the best tracking performance for the adaptive estimator; however, it is to some extent computationally expensive. This is due to the fact that before obtaining j^* using (8), one has to obtain the estimated values for all of the elements of the sparse vector θ at the current time step, that is $\theta_{(n)}$, which is not a suitable strategy for online implementation of the reconstruction algorithm.

Another alternative which is much more straight forward, and has lower computational burden, is to use the directional derivatives of the objective function $\overline{\mathcal{F}}(\theta_{(n-1)}^j)$ in order to detect the most effective coordinate at each iteration. This approach is initially introduced in [31] for Lasso penalized regressions. In order to proceed in this way, we need to define the forward and backward derivatives of $\overline{\mathcal{F}}(\theta_{(n-1)}^j)$ with respect to $\theta_{(n-1)}^j$ as follows:

$$\begin{aligned} d_{+e^j} \overline{\mathcal{F}}(\theta_{(n-1)}^j) &= \lim_{\varepsilon \rightarrow 0} \frac{\overline{\mathcal{F}}(\theta_{(n-1)}^j + \varepsilon e^j) - \overline{\mathcal{F}}(\theta_{(n-1)}^j)}{\varepsilon} \\ d_{-e^j} \overline{\mathcal{F}}(\theta_{(n-1)}^j) &= \lim_{\varepsilon \rightarrow 0} \frac{\overline{\mathcal{F}}(\theta_{(n-1)}^j - \varepsilon e^j) - \overline{\mathcal{F}}(\theta_{(n-1)}^j)}{\varepsilon}, \end{aligned} \quad (9)$$

where e^j is the coordinate direction, along which $\theta_{(n-1)}^j$ varies. Taking the derivatives, we have

$$\begin{aligned} d_{+e^j} \overline{\mathcal{F}}(\theta_{(n-1)}^j) &= [\mathbf{C}_\alpha(n)]_{jj} \theta_{(n-1)}^j - \frac{1}{n} \beta(n, j) \\ &\quad + \mathcal{P}'_{\tau_n, \gamma}(|\theta^{j,0}|) \operatorname{sgn}(\theta_{(n-1)}^j), \\ d_{-e^j} \overline{\mathcal{F}}(\theta_{(n-1)}^j) &= -[\mathbf{C}_\alpha(n)]_{jj} \theta_{(n-1)}^j + \frac{1}{n} \beta(n, j) \\ &\quad - \mathcal{P}'_{\tau_n, \gamma}(|\theta^{j,0}|) \operatorname{sgn}(\theta_{(n-1)}^j). \end{aligned} \quad (10)$$

Considering the directional derivatives of $\overline{\mathcal{F}}(\theta_{(n-1)}^j)$ with respect to $\theta_{(n-1)}^j$ in (10), the most effective coordinate is the one which has the most negative value either for forward or backward derivatives as

$$j^* = \arg \min_j \{d_{+e^j} \overline{\mathcal{F}}(\theta_{(n-1)}^j), d_{-e^j} \overline{\mathcal{F}}(\theta_{(n-1)}^j)\}. \quad (11)$$

It is noteworthy that one can obtain the m most effective coordinates by finding the m coordinates which have the most negative values among d coordinates. This is of interest in the situations in which the signal sparsity, K , is known or there exists an approximate value for that. Furthermore, in the case of unknown sparsity, increasing the value of m will increase the convergence rate of the estimator. However, this will come at the cost of increasing the computational burden.

In the next section, we will give the complexity analysis for both LED-SAC and LED-2SAC algorithms and show that they both have the same order of complexity.

4. Complexity Analysis of LED-SAC and LED-2SAC Algorithms

The solution flow of the LED-SAC algorithm for one of the elements of the sparse signal, that is $\hat{\theta}_{(n)}^j$, at time index n , is shown in Figure 1 where the shrinkage and update procedures are given in (12), (13), and (14), respectively, as follows:

$$\begin{aligned} \hat{\theta}_{(n)}^j &= \arg \min_{\theta^j} \overline{\mathcal{F}}(\theta^j) \\ &= \frac{1}{[\mathbf{C}_\alpha(n)]_{jj}} \operatorname{shrink} \left[\frac{1}{n} \beta(n, j), \mathcal{P}'_{\tau_n, \gamma}(|\theta^{j,0}|) \right], \end{aligned} \quad (12)$$

$$\mathbf{C}_\alpha(n) = a \mathbf{C}_\alpha(n-1) + \frac{1}{n} \mathbf{x}_n \mathbf{x}_n^T, \quad (13)$$

$$\beta(n, j) = a \beta(n-1, j) + x_n^j [y_n - \hat{y}_n] + (x_n^j)^2 \hat{\theta}_{(n-1)}^j, \quad (14)$$

where the shrink (\cdot) operator in (12) is defined such, that $\operatorname{shrink}(a, b) = (|a| - b)_+ \operatorname{sgn}(a)$, where $(z)_+ = z$ if $z > 0$ and it is 0 otherwise. According to Figure 1, the input parameters are the observation and the corresponding regressor at time index n . In order to obtain $\hat{\theta}_{(n)}^j$, which is the estimate of the j th coordinate at time index n , using the shrinkage procedure in (12) one needs to have the j th simple least

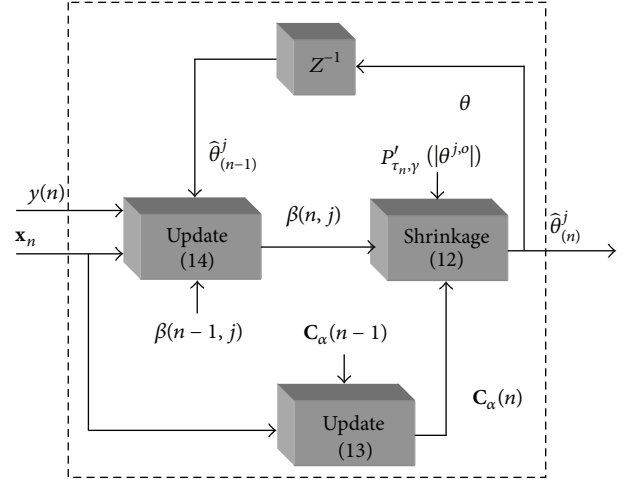


FIGURE 1: Block diagram of the estimation of one of the elements of the underlying sparse signal at the current time index, $\hat{\theta}_{(n)}^j$, for LED-SAC algorithm.

squares coefficient, that is $\beta(n, j)$, as well as $\mathbf{C}_\alpha(n)$, at the current time index. At each iteration, updating $\mathbf{C}_\alpha(n)$, having $\mathbf{C}_\alpha(n-1)$, needs $\mathcal{O}(d^2)$ algebraic operations. Having $\mathbf{C}_\alpha(n)$, obtaining $\beta(n, j)$ via (7), needs $\mathcal{O}(d)$ algebraic operations. Due to the fact that the recursive least squares estimate is used as the consistent estimate of the sparse signal θ_j^0 in (14), and considering the complexity of the recursive least squares algorithm, which is of order $\mathcal{O}(d^2)$, the overall complexity of the LED-SAC algorithm at each time step is $\mathcal{O}(d^2)$ whereas the computational complexity of the well-known batch-based algorithm such as LARS, which performs multivariate optimization, is of order $\mathcal{O}(d^3 + nd^2)$. Thus, the LED-SAC algorithm is cheaper in terms of computational burden, especially for signals of higher dimensionality, while it is capable of tracking the variations in the sparse signal contrary to the LARS algorithm.

4.1. Computational Complexity of the LED-2SAC Algorithm. Taking into account the sparse solution path given in Section 3 and the recursive relations for the parameters $\mathbf{C}_\alpha(n)$ and $\beta(n, j)$ in (13) and (14), respectively, the pseudo code for efficient and fast implementation of the LED-SAC algorithm using the directional derivatives is given as LED-2SAC algorithm in Algorithm 1. The implementation is done for m most effective coordinates of the underlying sparse signal.

According to Algorithm 1, the computational complexity of LED-2SAC algorithm is the same as LED-SAC, except for the stage in which the indices of the most effective coordinates are to be estimated. For the case of $m = 1$, one needs to compute the forward and backward derivatives of $\overline{\mathcal{F}}(\theta_{(n-1)}^j)$ via (10), having the estimate of the sparse signal from the previous time step, that is $\theta_{(n-1)}$, and the simple least squares coefficients $\beta(n, j)$ for $j = 1, \dots, d$. Computing $d_{+e^j} \overline{\mathcal{F}}(\theta_{(n-1)}^j)$ and $d_{-e^j} \overline{\mathcal{F}}(\theta_{(n-1)}^j)$ for $j = 1, \dots, d$ requires $\mathcal{O}(d)$ operations,

```

Fast LED-SAC Algorithm
for  $n = 1, 2, \dots, n_{\max}$ 
    Obtain  $y_n$  and the corresponding  $\mathbf{x}_i$ 
    Update  $\mathbf{C}_\alpha(n)$  via (13)
    Update  $\beta(n, j)$  for  $j = 1, \dots, d$  via (14)
    Obtain the index of the  $m$  most effective set of coordinates via (11), as  $\Omega$ 
    Update  $\hat{\theta}_{(n)}^j = \hat{\theta}_{(n-1)}^j, \forall j \notin \Omega$ 
    Update  $\hat{\theta}_{(n)}^j, \forall j \in \Omega$  via (12)
end
    
```

ALGORITHM 1: The pseudo code of the LED-2SAC algorithm.

which do not affect the complexity order of the original algorithm, LED-SAC, which is of order $\mathcal{O}(d^2)$. Therefore, the presented algorithm, LED-2SAC, reaches higher convergence rate and tracking capability compared to LED-SAC algorithm with just a little increase in the computational burden.

5. Simulation Results

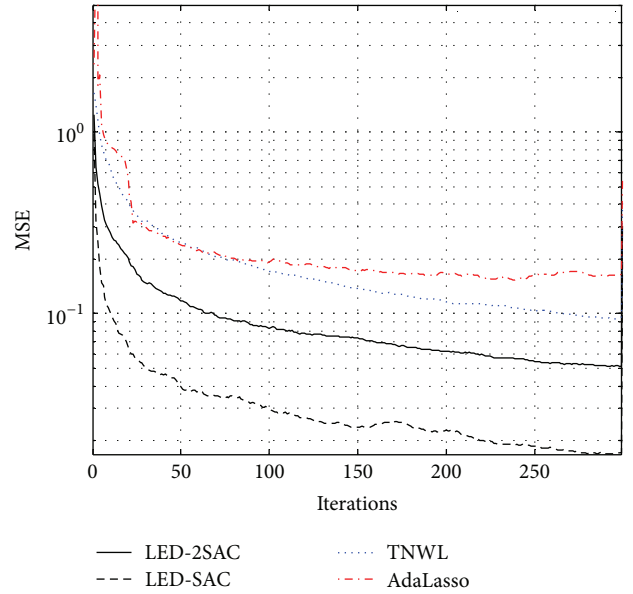
In what follows, the simulation results for the presented LED-2SAC reconstruction algorithm are given and compared to the former version, that is LED-SAC in [29], as well as TNWL reconstruction algorithm in [32] and AdaLasso algorithm presented in [24, 28].

Likewise [26, 29], the data set T is generated according to the model in (1) with $d = 30$ and $v_i \sim \mathcal{N}(0, 1)$. The regressors \mathbf{x}_i are also assumed to be samples from a Gaussian density of the form $\mathbf{x}_i \sim \mathcal{N}(\mathbf{0}_d, \mathbf{I}_d)$. The parameter vector $\boldsymbol{\theta}$ comprises K randomly allocated ± 1 entries, while all the other remaining entries are set to 0. Therefore, the tuning parameters for the parameter $\tau_n = n^{-\delta} \sqrt{\lambda \sigma^2 \log(d)}$ are set to the same values as in [26], which are extracted from cross validation, that is $(\lambda, \delta, \gamma) = (2.5, 2.7, 0.25)$.

In Figure 2, the learning curves of the algorithms are given in terms of the MSE plots. The MSE plots are obtained over 50 repetition of the experiment. The sparsity of the underlying signal to be estimated is set to 3 and the observation noise variance is set to 0.5. Comparing the convergence rate and the steady state error for the presented algorithm and the others reveals the superiority of the LED-2SAC algorithm. As it can be seen, the LED-2SAC algorithm has significantly improved the MSE performance, even compared with its former version, that is LED-SAC. This is due to the efficient implementation of the presented algorithm, such that at each iteration the most effective coordinate is detected and updated first.

In the next experiment, the sparsity of the signal is set to 10, and the results are shown in Figure 3. As it is seen, decreasing the sparsity of the signal has less affected the LED-2SAC algorithm, which is an interesting property for a sparsity aware reconstruction algorithm, since most of the existing methods fail to maintain their performance for lower sparsity levels.

In order to compare the performance of the algorithms in terms of variable selection capability, the percentage of


 FIGURE 2: MSE curves over 100 iterations with $d = 30$, $K = 3$, and $\sigma^2 = 0.5$.

exact model selection is given in Figure 4 for two different observation noise powers versus the number of iterations (or number of observations in online implementation). As it is seen, the LED-2SAC algorithm reaches the best model selection rates in different situations. The TNWL and AdaLasso algorithms have almost the same performance in terms of variable selection, as reported in [29], which are overcome by LED-2SAC and LED-SAC algorithms.

The plots of percentage of exact model selection for the algorithms are also given in Figure 5 for two different sparsity levels. Again, in this case, the presented LED-2SAC has retained the superior performance. As it was expected, the performance of the algorithms gets better by increasing the sparsity of the signal and vice versa.

The presented LED-2SAC algorithm is a sequential and adaptive reconstruction algorithm as LED-SAC, TNWL, and AdaLasso. So, we have to demonstrate its ability to track the variations in the support of the sparse signal. In the following, the adaptation capabilities of the algorithms are compared. For this purpose, in an arbitrary iteration (after all of the

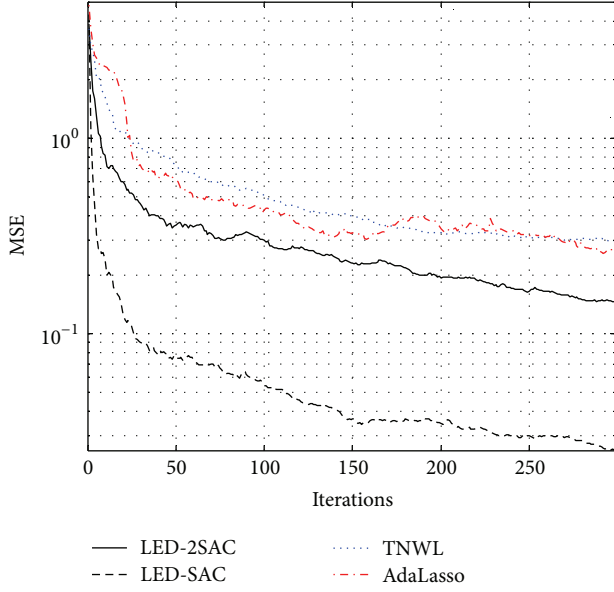


FIGURE 3: MSE curves over 100 iterations with $d = 30$, $K = 10$, and $\sigma^2 = 0.5$.

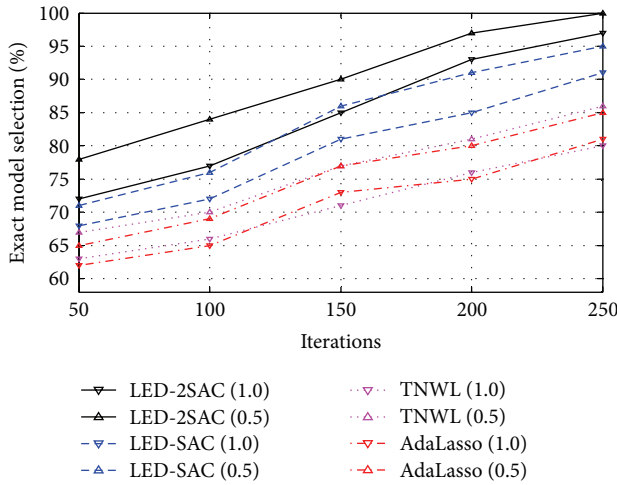


FIGURE 4: Percentage of exact model selection (different noise variances are denoted in the brackets).

algorithms are settled in their steady state performance), the support of the sparse signal is changed in the following fashion: one of the active coordinates is set to zero (inactive) and one of the inactive coordinates is set to 1 (active). The MSE curves are given in Figure 6 for $K = 3$.

As it is shown in Figure 6, the presented LED-2SAC algorithm has significantly improved the tracking capability of the former version, LED-SAC. However, both of the algorithms have outperformed the TNWL and AdaLasso algorithms. Figure 7 shows the same results for the case of $K = 10$. As it was expected from the results of Figures 2 and 3, the LED-2SAC algorithm has maintained its performance as the sparsity of the underlying signal is decreased.

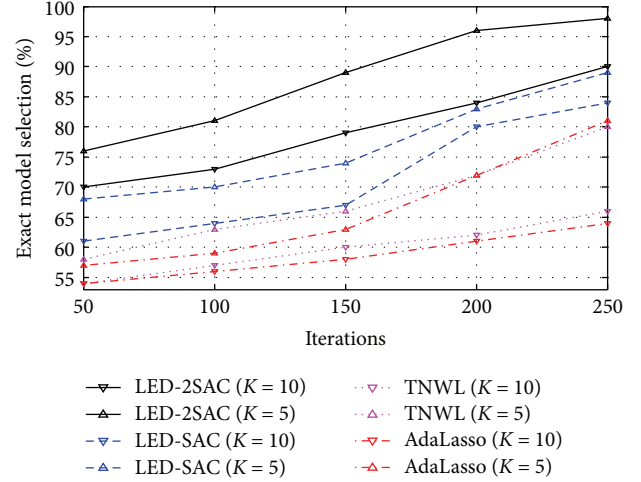


FIGURE 5: Percentage of exact model selection (different sparsity levels are denoted in the brackets).

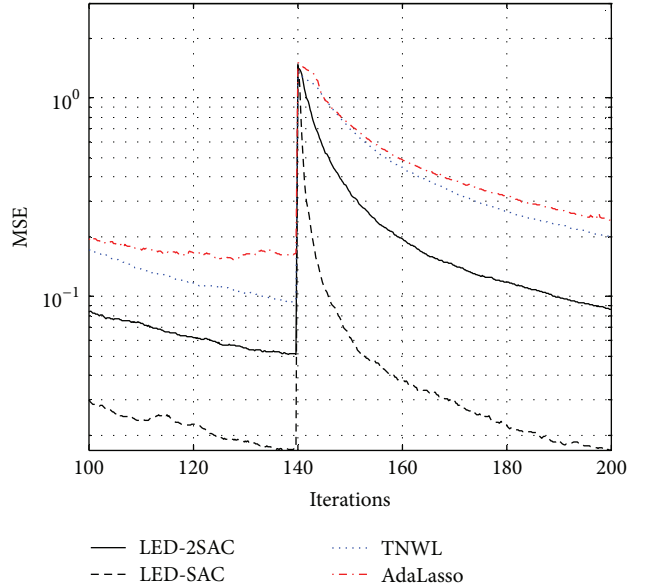


FIGURE 6: MSE when one of the active elements is set to zero and one of the inactive elements is set to one, $d = 30$, $K = 3$, and $\sigma^2 = 0.5$.

Finally, the estimation trajectories for an active coordinate becoming inactive and an inactive coordinate becoming active are shown in Figures 8 and 9, respectively. The LED-2SAC algorithm has outperformed all of the competitors as it was expected from the results of Figures 6 and 7. The interesting thing about Figure 8 is the fact that the LED-2SAC algorithm has almost abruptly detected and updated the inactive element. Although this is not the case for the entire coordinates, it happens more often.

6. Conclusion

In this paper, an efficient solution is proposed to sequentially solve the LED-based objective function that unlike the

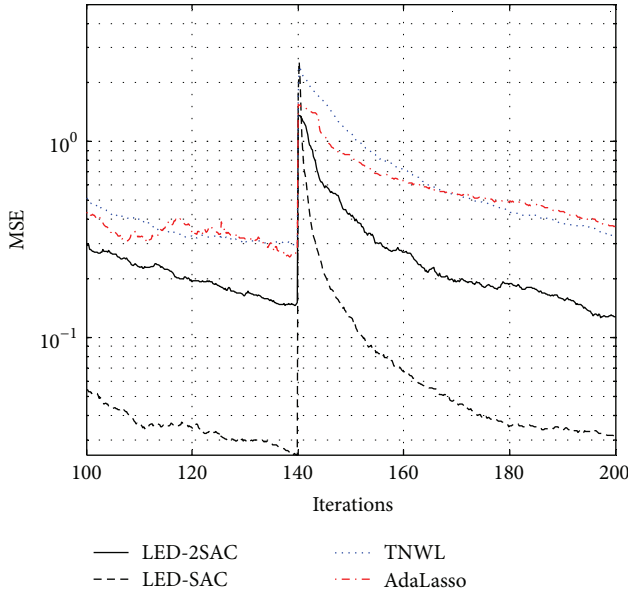


FIGURE 7: MSE when one of the active elements is set to zero and one of the inactive elements is set to one, $d = 30$, $K = 10$, and $\sigma^2 = 0.5$.

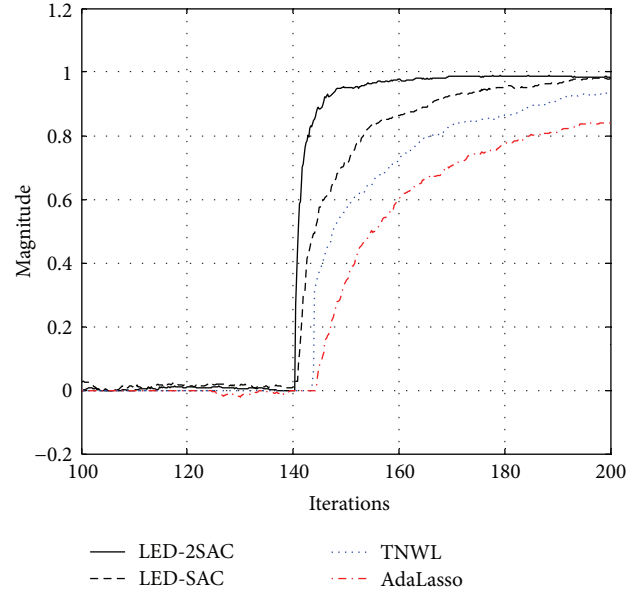


FIGURE 9: Estimation trajectory of the estimate of an inactive parameter becoming active.

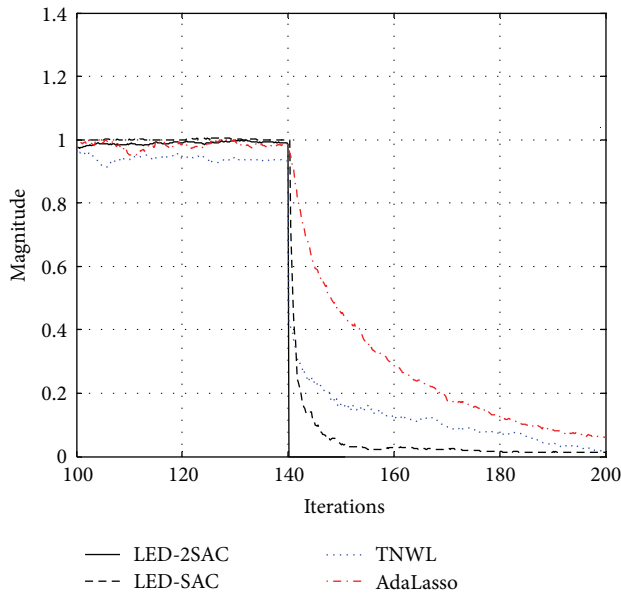


FIGURE 8: Estimation trajectory of the estimate of an active parameter becoming inactive.

existing SAC solution considers the sparsity of the signal to be estimated. Consequently, the proposed algorithm, denoted by LED-2SAC, leads to a significant improvement in the convergence rate and tracking capability of the original LED-SAC algorithm. Moreover, the complexity analysis of LED-SAC and LED-2SAC algorithms shows that both methods have the same order of complexity with additional improved convergence and adaptability behavior in LED-2SAC. Finally, the simulation results are given for the proposed algorithm. Comparing the performance of the presented algorithm with

the original one, as well as two other existing methods, confirms the superiority of the LED-2SAC in terms of convergence rate and adaptation capability.

Conflict of Interests

The authors declare that there is no conflict of interests regarding the publication of this paper.

References

- [1] S. S. Chen, D. L. Donoho, and M. A. Saunders, "Atomic decomposition by basis pursuit," *SIAM Journal on Scientific Computing*, vol. 20, no. 1, pp. 33–61, 1998.
- [2] J. A. Tropp, "Greed is good: algorithmic results for sparse approximation," *IEEE Transactions on Information Theory*, vol. 50, no. 10, pp. 2231–2242, 2004.
- [3] Y. Li and S. Osher, "Coordinate descent optimization for L_1 minimization with application to compressed sensing: a greedy algorithm," *Inverse Problems and Imaging*, vol. 3, no. 3, pp. 487–503, 2009.
- [4] M. Çetin, D. M. Malioutov, and A. S. Willsky, "A variational technique for source localization based on a sparse signal reconstruction perspective," in *Proceedings of the IEEE International Conference on Acoustic, Speech, and Signal Processing (ICASSP '02)*, pp. 2965–2968, May 2002.
- [5] E. J. Candès, M. B. Wakin, and S. P. Boyd, "Enhancing sparsity by reweighted L_1 minimization," *The Journal of Fourier Analysis and Applications*, vol. 14, no. 5-6, pp. 877–905, 2008.
- [6] R. Chartrand, "Exact reconstruction of sparse signals via non-convex minimization," *IEEE Signal Processing Letters*, vol. 14, no. 10, pp. 707–710, 2007.
- [7] R. Chartrand and W. Yin, "Iteratively reweighted algorithms for compressive sensing," in *Proceedings of the IEEE International*

- Conference on Acoustics, Speech and Signal Processing (ICASSP '08)*, pp. 3869–3872, Las Vegas, Nev, USA, April 2008.
- [8] C. J. Miosso, R. von Borries, M. Argàez, L. Velazquez, C. Quintero, and C. M. Potes, “Compressive sensing reconstruction with prior information by iteratively reweighted least-squares,” *IEEE Transactions on Signal Processing*, vol. 57, no. 6, pp. 2424–2431, 2009.
 - [9] D. M. Malioutov, S. R. Sanghavi, and A. S. Willsky, “Sequential compressed sensing,” *IEEE Journal on Selected Topics in Signal Processing*, vol. 4, no. 2, pp. 435–444, 2010.
 - [10] J. Benesty and S. L. Gay, “An improved PNLMS algorithm,” in *Proceedings of the IEEE International Conference on Acoustic, Speech and Signal Processing (ICASSP '10)*, pp. 1881–1884, May 2002.
 - [11] D. L. Duttweiler, “Proportionate normalized least-mean-squares adaptation in echo cancelers,” *IEEE Transactions on Speech and Audio Processing*, vol. 8, no. 5, pp. 508–517, 2000.
 - [12] T. Gänslér, S. L. Gay, M. M. Sondhi, and J. Benesty, “Double-talk robust fast converging algorithms for network echo cancellation,” *IEEE Transactions on Speech and Audio Processing*, vol. 8, no. 6, pp. 656–663, 2000.
 - [13] O. Hoshuyama, R. A. Goubran, and A. Sugiyama, “A generalized proportionate variable step-size algorithm for fast changing acoustic environments,” in *Proceedings of the IEEE International Conference on Acoustics, Speech, and Signal Processing (ICASSP '04)*, pp. 161–164, May 2004.
 - [14] J. Benesty, C. Paleologu, and S. Ciochina, “Proportionate adaptive filters from a basis pursuit perspective,” *IEEE Signal Processing Letters*, vol. 17, no. 12, pp. 985–988, 2010.
 - [15] Y. Chen, Y. Gu, and A. O. Hero III, “Sparse LMS for system identification,” in *Proceedings of the IEEE International Conference on Acoustics, Speech, and Signal Processing (ICASSP '09)*, pp. 3125–3128, April 2009.
 - [16] Y. Gu, J. Jin, and S. Mei, “ L_0 norm constraint LMS algorithm for sparse system identification,” *IEEE Signal Processing Letters*, vol. 16, no. 9, pp. 774–777, 2009.
 - [17] J. Jin, Y. Gu, and S. Mei, “A stochastic gradient approach on compressive sensing signal reconstruction based on adaptive filtering framework,” *IEEE Journal on Selected Topics in Signal Processing*, vol. 4, no. 2, pp. 409–420, 2010.
 - [18] E. M. Ekşioğlu, “RLS adaptive filtering with sparsity regularization,” in *Proceedings of the 10th International Conference on Information Sciences, Signal Processing and Their Applications (ISSPA '10)*, pp. 550–553, May 2010.
 - [19] R. Tibshirani, “Regression shrinkage and selection via the lasso,” *Journal of the Royal Statistical Society B*, vol. 58, no. 1, pp. 267–288, 1996.
 - [20] B. Efron, T. Hastie, I. Johnstone, and R. Tibshirani, “Least angle regression,” *The Annals of Statistics*, vol. 32, no. 2, pp. 407–499, 2004.
 - [21] M. R. Osborne, B. Presnell, and B. A. Turlach, “A new approach to variable selection in least squares problems,” *IMA Journal of Numerical Analysis*, vol. 20, no. 3, pp. 389–403, 2000.
 - [22] J. Fan and R. Li, “Variable selection via nonconcave penalized likelihood and its oracle properties,” *Journal of the American Statistical Association*, vol. 96, no. 456, pp. 1348–1360, 2001.
 - [23] M. Yuan and Y. Lin, “On the nonnegative Garotte estimator,” Tech. Rep., Georgia Institute of Technology, School of Industrial and Systems Engineering, 2005.
 - [24] H. Zou, “The adaptive lasso and its oracle properties,” *Journal of the American Statistical Association*, vol. 101, no. 476, pp. 1418–1429, 2006.
 - [25] P. Zhao and B. Yu, “On model selection consistency of Lasso,” *Journal of Machine Learning Research*, vol. 7, pp. 2541–2563, 2006.
 - [26] T. Yousefi Rezaii, M. A. Tinati, and S. Beheshti, “Sparsity aware consistent and high precision variable selection,” *Journal of Signal, Image and Video Processing*, 2012.
 - [27] D. Angelosante and G. B. Giannakis, “RLS-weighted Lasso for adaptive estimation of sparse signals,” in *Proceedings of the IEEE International Conference on Acoustics, Speech, and Signal Processing (ICASSP '09)*, pp. 3245–3248, April 2009.
 - [28] M. A. Tinati and T. Y. Rezaii, “Adaptive sparsity-aware parameter vector reconstruction with application to compressed sensing,” in *Proceedings of the International Conference on High Performance Computing and Simulation (HPCS '11)*, pp. 350–356, July 2011.
 - [29] T. Y. Rezaii, M. A. Tinati, and S. Beheshti, “Adaptive efficient sparse estimator achieving oracle properties,” *IET Signal Processing*, vol. 7, no. 4, pp. 259–268, 2013.
 - [30] Y. Li and S. Osher, “Coordinate descent optimization for L_1 minimization with application to compressed sensing: a greedy algorithm,” *Inverse Problems and Imaging*, vol. 3, no. 3, pp. 487–503, 2009.
 - [31] T. T. Wu and K. Lange, “Coordinate descent algorithms for lasso penalized regression,” *The Annals of Applied Statistics*, vol. 2, no. 1, pp. 224–244, 2008.
 - [32] D. Angelosante, J. A. Bazerque, and G. B. Giannakis, “Online adaptive estimation of sparse signals: where RLS meets the L_1 -norm,” *IEEE Transactions on Signal Processing*, vol. 58, no. 7, pp. 3436–3447, 2010.

Research Article

Human Skeleton Model Based Dynamic Features for Walking Speed Invariant Gait Recognition

Jure Kovač and Peter Peer

Faculty of Computer and Information Science, University of Ljubljana, Tržaška 25, 1000 Ljubljana, Slovenia

Correspondence should be addressed to Jure Kovač; jure.kovac@fri.uni-lj.si

Received 1 October 2013; Revised 19 December 2013; Accepted 23 December 2013; Published 21 January 2014

Academic Editor: Yue Wu

Copyright © 2014 J. Kovač and P. Peer. This is an open access article distributed under the Creative Commons Attribution License, which permits unrestricted use, distribution, and reproduction in any medium, provided the original work is properly cited.

Humans are able to recognize small number of people they know well by the way they walk. This ability represents basic motivation for using human gait as the means for biometric identification. Such biometrics can be captured at public places from a distance without subject's collaboration, awareness, and even consent. Although current approaches give encouraging results, we are still far from effective use in real-life applications. In general, methods set various constraints to circumvent the influence of covariate factors like changes of walking speed, view, clothing, footwear, and object carrying, that have negative impact on recognition performance. In this paper we propose a skeleton model based gait recognition system focusing on modelling gait dynamics and eliminating the influence of subjects appearance on recognition. Furthermore, we tackle the problem of walking speed variation and propose space transformation and feature fusion that mitigates its influence on recognition performance. With the evaluation on OU-ISIR gait dataset, we demonstrate state of the art performance of proposed methods.

1. Introduction

Psychological studies showed that humans have small but significant ability to recognize people they know well by their gait. This ability has encouraged the research for using gait as the means of biometric identification. Early studies on Point Light Displays (PLD) [1], which enable isolated study of motion by removing all other contexts from observed subjects, confirmed this ability.

Commonly used biometrics based on fingerprints, face, iris, and so forth have two obvious deficiencies. They perform badly at low image resolutions and need active user participation. Gait on the other hand does not suffer from these deficiencies. It can be captured with ordinary equipment without individual's awareness or even consent. The main deficiencies of such biometrics are the unknown level of uniqueness and covariate factors that change gait characteristics. These can be external (changes of view, direction, or speed of movement, illumination conditions, weather, clothing, footwear, terrain, etc.) or internal (changes due to illness, injuries, ageing, pregnancy, etc.). Problems are also caused by uncertain measurements, occlusions, and the

use of noninvasive acquiring techniques (without sensors or markers). All these negatively influence the recognition performance in real-life environment, which is still too weak for efficient use in biometry.

Methods can be categorized into two main groups. Model based approaches [2–5] build the model of human body or its movement in 3D and acquire gait parameters from this model (e.g., step dimensions, cadence, human skeleton, body dimensions, locations and orientations of body parts, joint kinematics, etc.). The methods of this group mostly focus on gait dynamics and less on appearance of individuals, which makes them more resistant to problems like changes of view and scale but in general do not achieve as good results as methods that also consider appearance. Furthermore, such methods are computationally demanding and especially susceptible to problems like occlusions.

Model-free approaches [6–9] acquire gait parameters by performing measurements directly on 2D images, without adopting specific model of human body or motion. Feature correspondence in consecutive images is obtained by prediction of speed, shape, texture, and color. They mostly use geometric representations like silhouettes, optical flow,

joint trajectories, history of movement, and so forth. The methods do not rely only on gait dynamics, but also measure the individual during movement—with it they also take appearance of individual into consideration. Methods are therefore less sensitive to covariate factors that result in variations of gait dynamics (e.g., ageing, illness, and walking speed change) but more susceptible to factors that result in changes of appearance (e.g., clothing, obesity, hairstyle, etc.), changes of view, and direction of movement.

Although several gait recognition methods demonstrate impressive performance under controlled (in-lab) environment setups [2, 3, 5–7, 9, 10], the use of gait recognition in real-life application is still limited, mostly because of covariate factors that influence individual's gait and therefore make recognition task more difficult (e.g., view changes, walking speed changes, occlusions, etc.). Nevertheless, examples of real-life applications using gait analysis exist. Authors in [11, 12] demonstrate how monitoring gait motion parameters of residents in the senior housing facility can detect anomalies in resident's movements [11] and also discriminate and recognize facility residents and visitors [12]. Such monitoring can be used for fall risk assessment, detection of health problems, and monitoring of patients during rehabilitation. Although authors do not specifically handle covariate factors, they propose an efficient way for eliminating walking samples that do not conform to constraints posed by gait analysis methods.

However, often in other real-life scenarios only limited number of individual's walking samples are available (e.g., security cameras), which can also be short, contain only a few steps, and are influenced by several previously mentioned covariate factors. Under such circumstances these covariate factors must be dealt with in order to make walking samples useful for gait analysis. Our work focuses on variations of walking speed, since it represents one of the major covariate factors that affect gait recognition performance, is almost always present in real-life environment, and therefore requires special attention. Several approaches handling changing walking speed exist in the literature. The most outstanding are summarized below, but, as opposed to our work, none of them are model based and none of them uses solely gait dynamics for recognition task.

Authors in [8] researched the influence of walking speed changes to recognition performance based on cadence and step length and suggested the improvement by silhouette normalization. Authors proposed a stride normalization of double-support gait silhouettes based on a statistical relation between the walking speed and the stride. They used baseline algorithm [7] on only five silhouettes of gait cycle (two single-support images and three double-support images) for recognition and discarded the other still informative images.

Furthermore authors in [13] used geometrical transformations to apply walking speed normalization to averaged silhouette [6] and Probabilistic Spatiotemporal Model (PSTM) [10] and demonstrated how negative effects of walking speed changes can be mitigated to improve recognition performance.

Authors in [14] proposed a HMM-based time-normalized gait feature extraction with standard gait poses and tested it

on the slow and fast walking data. The method does, however, not consider spatial changes (e.g., stride changes).

Authors in [15] introduced a spatiotemporal Shape Variation-Based Frieze Pattern (SVB frieze pattern) representation for gait, which captures motion information over time and represents normalized frame difference over gait cycles. A temporal symmetry map of gait patterns is constructed and combined with vertical/horizontal SVB frieze patterns for measuring the dissimilarity between gait sequences.

Authors in [16] proposed an approach based on Dynamic Time Warping (DTW), which uses a set of DTW functions to represent the distribution of gait patterns using uniform and wrapped-Gaussian distributions.

Authors in [17] proposed a three-way (x -, y -, and time-axis) method of autocorrelation that effectively extracted spatio-temporal local geometric features to characterize motions called Cubic Higher-order Local Autocorrelation (CHLAC). It is relatively robust against variations in walking speed, since it only uses the sums of local features over a gait sequence and, thus, does not explicitly use the phase information of the gait. Researchers have assumed that walking speed does not change much within or across gait sequences.

Authors in [18] separated static and dynamic features from gait silhouettes by fitting a human model and then created a factorization based speed transformation model for the dynamic features using a training set for multiple persons on multiple speeds. The model can transform the dynamic features from a reference speed to another arbitrary speed.

Authors in [19] propose a new descriptor named Higher-order derivative Shape Configuration (HSC), which can generate robust feature when body shape changes due to varying walking speed. Procrustes shape analysis was used for gait signature and HSC is able to retain discriminative information in the gait signatures, while it is still able to tolerate the varying walking speed. They upgraded the method by introducing a Differential Composition Model (DCM) [20], which differentiates different effects caused by walking speed changes on various human body parts.

Human body skeleton model is proved to be an effective tool for representing human motion and was therefore adapted by several model based gait recognition approaches [3, 4]. Similar as authors in [3], we acquire gait signature by segmenting 2D human skeleton from silhouette images and then use this model to further extract motion parameters. On the other hand, authors in [4] first acquire individual's gait's characteristics by the principle of deformable template matching and then use view decomposing principle of general viewing angle and prior constraints from general knowledge of human body to impose gait characteristics to generic 3D skeleton model.

Authors in [3, 4] both assume that subjects are walking with constant (i.e., normal) speed. Moreover, authors in [3] do not handle any covariate factors at all, while authors in [4] achieve some degree of view invariance by reconstructing a 3D body model. Both works mainly use static gait parameters like subject's height, gait frequency, stride length, and even walking speed itself, which are all highly discriminative under unchanged, normal-walking conditions, but on the

other hand very susceptible to, for example, perspective deformations caused by view change and gait dynamics transformations caused by walking speed change. Although dynamic gait parameters are also used, they are not fully utilized for the recognition task. Authors in [3] use only means and standard deviations of main joint angles, while authors in [4] only use motion trajectories of main joints. Both are similarly susceptible to covariate factors as static features.

As opposed to both of these works our focus is on dynamic motion parameters only. We observe time series of changing joint angles, angle phase differences, mass ratios of different body parts, distances of body parts from body center, and so forth, through the entire gait sequence. These are less sensitive to covariate factors that greatly affect the appearance of individual's gait.

We argue that although dynamic features are claimed to be less discriminative than static features, they still contain enough discriminator power to achieve comparable recognition performance to appearance based methods, and are at the same time more resistant and easily adoptable to handle covariate factors that exist in real-life scenarios. Our main contributions are as follows:

- (i) feature space transformation based on statistical model of different walking speeds to compensate for walking speed changes in dynamic gait features;
- (ii) feature fusion scheme that enables the use of per feature classifiers as a weak classifiers that are fused into the final distance based classifier;
- (iii) image moments based cycle detection stage that enables almost perfect gait phase alignment among different video sequences, which is crucial for distance based classification on time series signal based features.

The remainder of this paper is organized as follows. In Section 2 we will introduce the procedure for extracting human skeletons from silhouette images. Section 3 will discuss the details of acquiring gait signals and motion parameters from skeleton models and introduce the proposed feature space transformation, which helps mitigate the effects of changed walking speed on recognition performance. In Section 4 we will describe classification procedure based on proposed feature fusion scheme and in Section 5 we will present the results and analysis of performed experiments together with comparison to related walking speed invariant state-of-the-art methods. Finally, we will provide some directions for future work in the conclusion.

2. Skeleton Segmentation

Input video must first be processed to acquire silhouettes of walking subjects. We use Gaussian mixture based background subtraction to acquire motion foreground, which corresponds to subjects's silhouettes that are further processed by morphology operations to improve their quality. Since

most of the gait datasets already provide extracted silhouettes, we use standard procedures for silhouette extraction when required and do not pay special attention to motion segmentation procedure as this is another active research area (see [21] for recent advancements). Therefore, we assume that silhouettes of decent quality are either provided or acquired as the input to our method. It means that extracted silhouettes must conform to the constraints posed by relatively complex skeleton segmentation procedure. For example, walking subjects, which are far away from the camera, might appear too small in the video to effectively distinguish human body parts (limbs, head, etc.). Despite the silhouette quality constraint posed in this work, we still provide methods for handling low quality and noisy silhouettes in Section 4.5.

We adopt the skeleton extraction procedure from [3], since their method uses simple segmentation steps for deriving skeletons based on single view 2D motion sequences, which turned out to supply sufficient gait information for gait based identification. Our segmentation procedure contains the following steps.

First, we extract silhouette contour from every image of the sequence. Then calculate body height and segment lengths based on average anatomical properties of human body [22]. For a body height H , the initial estimate of the vertical position of the neck, shoulder, waist, pelvis, knee, and ankle was set to be $0.870H$, $0.818H$, $0.530H$, $0.480H$, $0.285H$, and $0.039H$, respectively.

Next, we divide silhouette into individual body parts (head, neck, torso, waist, upper legs, bottom left, right leg, and left and right feet) based on calculated segment lengths (Figure 1(a)). For each body segment we then find left most and right most contour points and calculate their middle (Figure 1(b)). After that, we fit lines through this points using Hough transformation and chose the line with largest value in accumulation field. Such fitting is more robust to errors as opposed to linear regression used in [3] (Figure 1(c)).

While upper body part segmentation is straightforward, the lower body part (thighs and shins) is much harder to extract and must therefore be specially handled. First we detect shin bones. Especially during single support phase, only one segment is detected in lower body part. Therefore, both legs are represented by single body segment. In this case, left and right most contour points are used as left and right bone angles. In the case of double support, each shin is represented by its own body segment and middle points of both segments are used, similar to those in upper body part. The thigh bone angles are then derived from torso lower midpoint and starting points of both left and right shins. Finally, we compute bone endpoints from bone starting points, derived angles and segment length estimations (Figure 1(d)).

Extracted bones form a simplified (no arms, shoulders, etc.) skeleton of human body for single silhouette frame. Raw gait signature is then acquired by detecting skeletons on all frames of the input video. Such signature enables direct extraction of bone and joint angles, which form time-series signals that can be used for recognition.

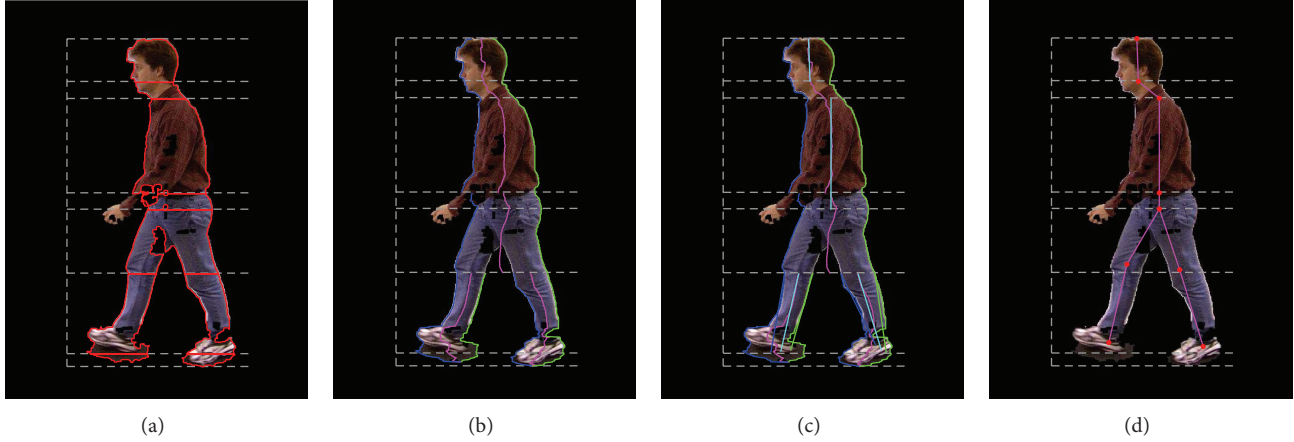


FIGURE 1: Skeleton segmentation algorithm in steps.

3. Gait Signal Extraction

Several gait signals are extracted from acquired skeleton signatures:

- (i) body part angles: head, neck, torso, left and right thighs, and left and right shins;
- (ii) joint locations: left and right knees and ankles;
- (iii) masses and centres of mass (COM) for the whole silhouette and individual body parts;
- (iv) silhouette width and height.

All these so-called raw signals represent the basis for the derived signals, which are actually used in recognition system later. By definition, joint angles are measured as one joint relative to the other, so relative joint angles are derived from extracted raw angle values. At normal walking, torso is almost vertical, so relative hip angle (thigh bone angle) is the same as extracted value, while relative knee angle is calculated as

$$\theta_{\text{knee}} = \theta_{\text{thigh}} - \theta_{\text{shin}}. \quad (1)$$

Phase difference of thighs and shins describe the correlation among left and right thighs or left and right shins and can be very specific for walking subjects:

$$\theta_{\text{tphs}} = \theta_{\text{thigh}_1} - \theta_{\text{thigh}_2}. \quad (2)$$

Body part mass ratio represents the ratio between masses of specific body parts and the mass of entire body:

$$Q_{m_i} = \frac{m_i}{m}. \quad (3)$$

Body part center of mass distance represents the distances of center of mass of specific body parts to the center of mass for the entire body:

$$D_{c_i} = \sqrt{(c_{i,x} - c_x)^2 + (c_{i,y} - c_y)^2}. \quad (4)$$

The total of 64 feature signals are extracted and later used in classification.

3.1. Image Moments Based Motion Parameters. Image moments for binary images and its derivatives, especially COM, turned out very useful for gait motion parameters estimation. Their use for estimating gait frequency, gait cycle starts, and gait phases (double, single support) is described below.

Image moments are defined as

$$M_{ij} = \sum_x \sum_y x^i y^j I(x, y), \quad (5)$$

where ij is the order of the moment and $I(x, y)$ is the image value at point (x, y) . Since binary silhouette images contain values either 0 or 1, its COM can be computed as

$$\mathbf{C} = \left[\frac{M_{10}}{M_{00}}, \frac{M_{01}}{M_{00}} \right], \quad (6)$$

where M_{10} and M_{01} are the sums of all x and y coordinates of all nonzero image elements, respectively, and M_{00} is the number of all non-zero image elements also referred to as mass. Both COM \mathbf{C} and mass M_{00} are also useful as gait features.

3.1.1. Gait Cycle Detection. Walking sequences are not synchronized among subjects and can start at any phase of the gait cycle. To be able to compare the cycles later, we must define at which phase gait cycle should start. Double support is the easiest to detect, therefore, we set all cycles to start at double support.

First, we determine gait frequency based on frequency analysis of extracted signals. The most appropriate signals for gait frequency detection are vertical movement of COM, body mass and silhouette width. The main property of these signals is that the signal has its peaks at double support (max) and single support (min) phases of gait cycle. When subject is observed from side view, COM is at its lowest point (highest y value), and subject's mass is at its highest point, since hands and legs are spread and occupy more space than at single support, and the same goes for subject's width. Among these subject's width is the most sensitive to noisy silhouettes and

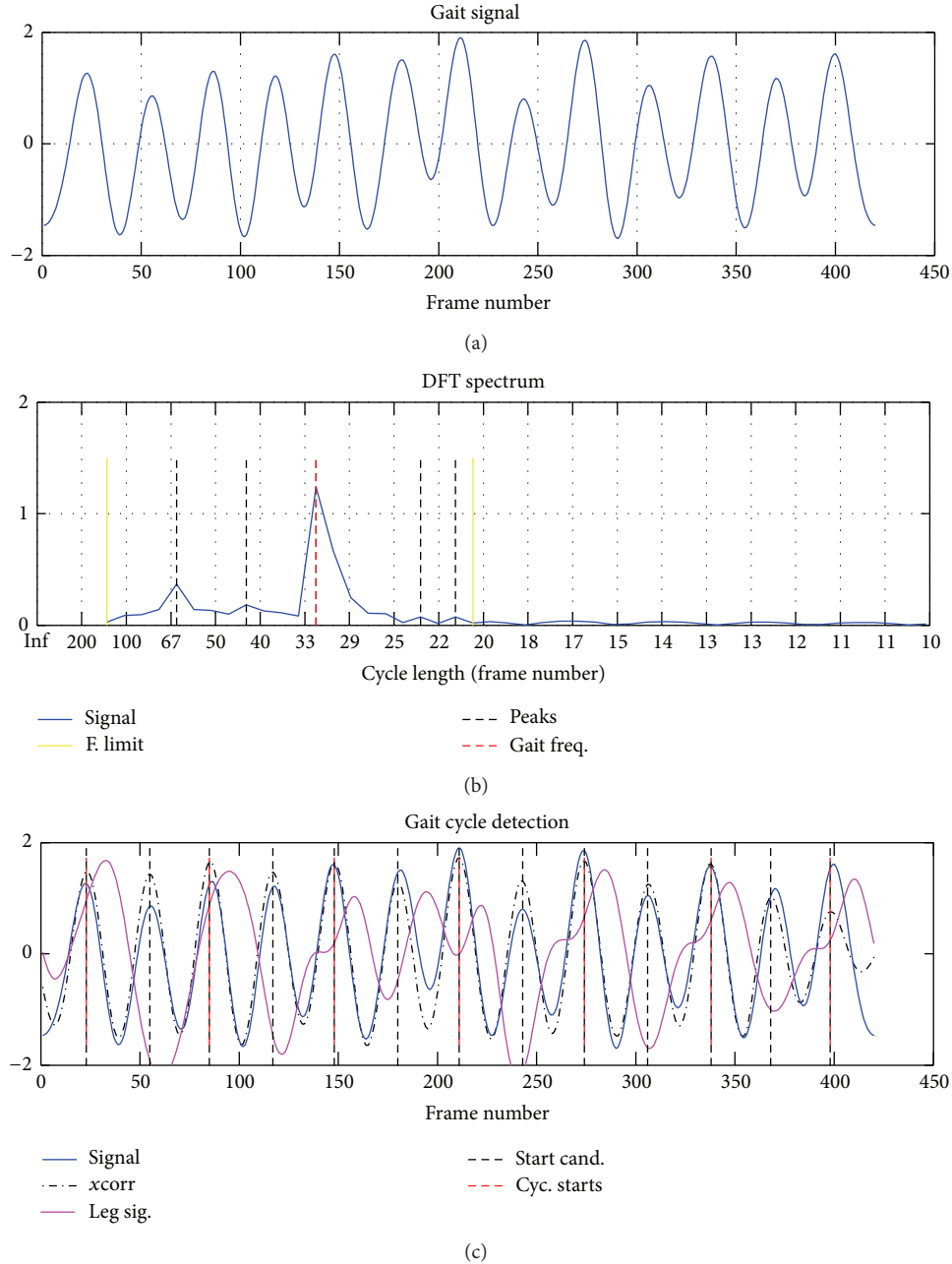


FIGURE 2: Gait frequency analysis: (a) shows COMy signal with peaks at double support phases (half gait cycle); (b) shows DFT spectrum with one outstanding frequency indicating half gait cycle length; (c) shows gait cycle starts detection, where left leg double support is detected by leg signal value at main signal autocorrelation peaks.

also the least reliable, since it is severely affected by hand movements and is therefore the least appropriate. COM is the most resistant to noisy silhouettes, but a bit less stable in finding double support peaks than subject’s mass. Therefore, the best way is to use mass when dealing with high quality silhouettes and COM when silhouettes are noisy.

We analysed the signal with Discrete Fourier Transform (DFT) to determine frequency spectra. Two frequencies with highest amplitudes stand out (Figure 2). F_s represents one half of the gait cycle, which usually has the highest

amplitude since it corresponds to subject’s steps, which are most common in the signal. F_g has slightly lower amplitude and represents the gait frequency (two steps): $F_g \approx 2F_s$.

3.1.2. *Left Leg Double Support Detection.* To be able to compare these signals later, it is essential to detect the same double support for every subject (e.g., the one with left leg in front), so that cycles of all the subjects start with the same leg in front (e.g., left) and are therefore roughly aligned. Merely

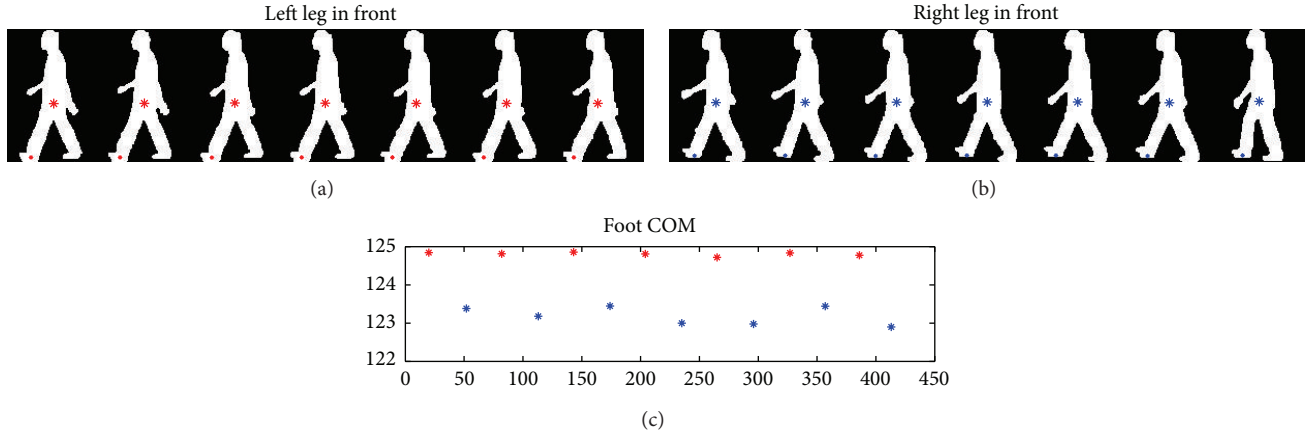


FIGURE 3: Double support detection: (a) shows double support when left leg is in front, (b) shows double support when right leg is in front. Red and blue markers indicate a location of body and leg COMs. (c) demonstrates a clear gap in COM y value between left and right leg double support. x axis denotes time in frames, and y axis denotes y coordinate of COM.

switching the legs at the later stage does not help here, because all other features are also affected.

We solve this by exploiting constraint posed by perspective projection. It can be observed that because of perspective projection when looking at walking subject from side view, the leg closer to the camera appears a bit lower in the image (Figure 3). That is when left leg is in front, it appears lower than when the right leg is in front. We use this property when analysing another signal. The y coordinate of front leg foot COM is observed at double support phases. When the leg closer to the camera (e.g., left) is in front, the value of COM y of the foot is higher than foot COM y value of the leg that is farther away from the camera.

Finally, we derive cycle starts based on estimated gait frequency and detected left leg double support phases, which are used as initial estimates for cycle length and start of the first cycle. So obtained signal part is then cross-correlated against entire signal and its peaks represent starts of gait cycles (Figure 2(c)).

3.1.3. Leg Crossover Detection. One of the problems with the extracted signature represents the crossing of the legs. When observing subject from side view, which is most commonly the case, the legs are crossed during single support phase. Previously described algorithm for skeleton extraction cannot detect the crossing, instead it always tracks the front leg as leg number 1 and rear leg as leg number 2. When legs get crossed, the leg that was previously in the front (e.g., left leg) now goes to the back and vice versa.

Authors in [3] use physical constraints (e.g., foot does not move forward when in contact with the floor) to detect the crossover. Such constraint gets broken, for example, when walking on a treadmill. Therefore, we use vertical movement of COM, which turns out to be more appropriate for the given task.

It can be observed that single support phase location corresponds to local minima in COM y or mass signal. This is similar as double support detection by local maxima in

the same signal described earlier. Gait signature is then adopted by softly switching left and right thigh angle signals at detected leg switches locations. Softly we denote interpolation through small time frame window during single support. Shin angles and joint locations are adopted according to changed thigh angle values afterwards (see Figure 4).

3.2. Signal Postprocessing. Signals in gait signature are prone to erratic detections, which manifest as spikes in gait signals. The spikes are detected by applying moving median filter through entire signal. Moving median enables local detection of spikes.

First, we compute the difference $d(t)$ between signal $s(t)$ and moving median $s_m(t)$. Then spikes are detected according to

$$d(t) = \|s(t) - s_m(t)\|, \quad (7)$$

$$s(t) = \begin{cases} \text{NaN} & d(t) > \alpha * 1.4826 * s_{m\sigma}(t), \\ s(t), & \text{else,} \end{cases}$$

where $s(t)$ is the value of the signal at time t , α is a parameter determining the size of the spike, $s_{m\sigma}$ is median deviation, which is similar to standard deviation, and except deviation is calculated based on median mean instead of average mean. Scaling median mean by factor 1.4826 gives median-absolute mean, which is on average equal to standard deviation for Gaussian distributions. When spike is detected, signal values are set to undefined NaN.

For example, in the case of bone angle signals, we detect spikes for both thighs and both shins and then interpolate the missing values with spline interpolation. After that, bone structures (joints and angles) must be adopted accordingly (e.g., changing angle of left thigh also affects left shin position). Moreover, all the signals are additionally filtered by trigonometric polynomials used when building gait descriptor (see Section 4.2).

As human gait is cyclic in nature, all gait signals are then sliced to smaller pieces based on found cycle starts. This

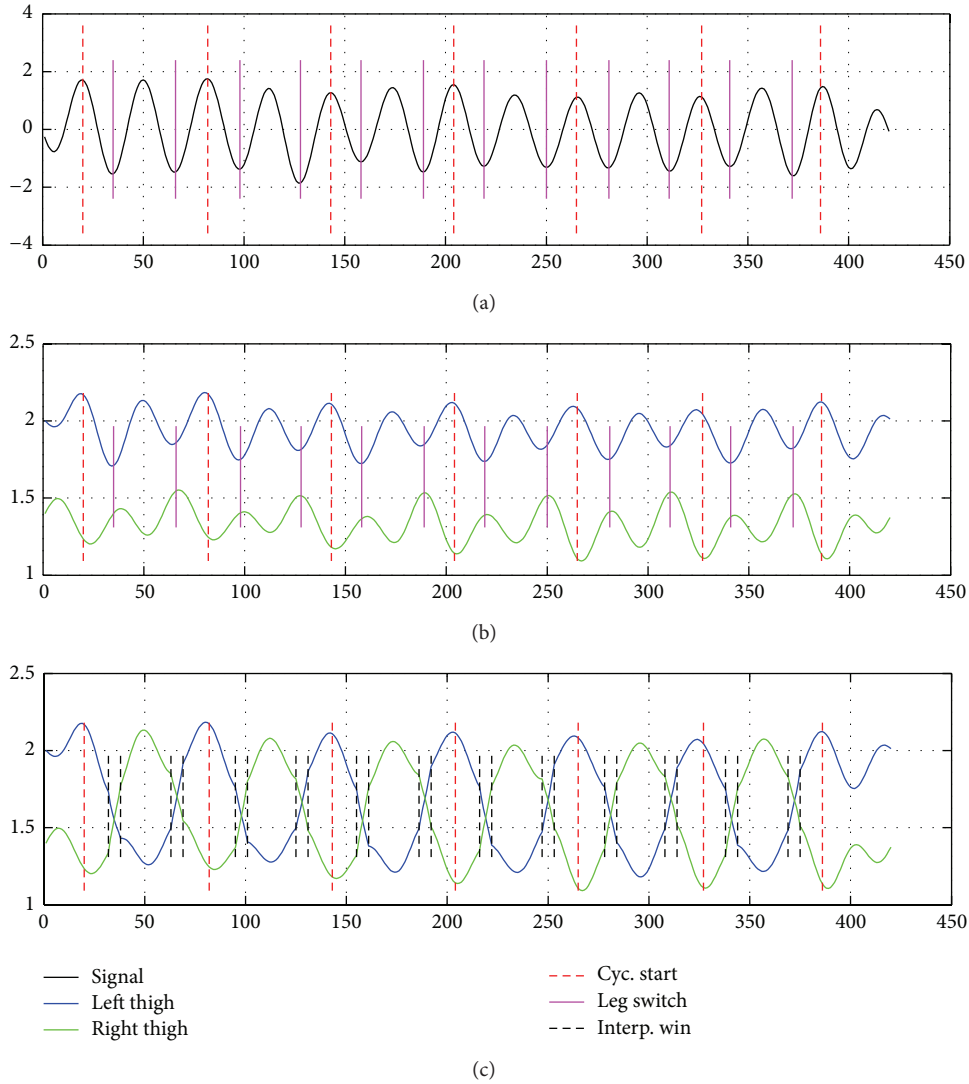


FIGURE 4: Leg crossover detection: (a) shows COM y signal (full-black line), detected cycle starts (dashed-red vertical lines), and leg crossover locations (full-magenta vertical lines). (b) shows front (blue) and rear (green) thigh angle signals as extracted from skeleton. (c) shows thigh angle signals interpolated into left (blue) and right (green) thigh angles. x axis denotes time in frames and y axis represents normalized signal values.

also implies that gait cycles of the same subject are similar under unchanged conditions. For acquired signals this also means that the next cycle should start with approximately the same values as previous cycle and also that cyclic signal should end with approximately the same values as it has started [10]. Because of noisy segmentation this is not always the case. Therefore, signals are adopted to correspond to this assumption. We make the signals cyclic by finding the difference between cycle start and cycle end and interpolating the entire signal to negate this difference:

$$S_i = S_i - \frac{2i - (L - 1)}{2(L - 1)} * D, \quad (8)$$

where S is the part of the signal corresponding to some specific gait cycle, S_i is the value at point i of that gait cycle, L

is the gait cycle length, and D is the difference between cycle start and cycle end.

Also, different people walk with different speeds, which affect gait frequency and with that the duration of the gait cycle. If gait is sampled by the same sampling frequency (e.g., camera frame rate), cycle lengths differ in the number of acquired samples in one gait cycle. To be able to compare gait cycles of different subjects (and also gait cycles of the same subject acquired with different sampling frequencies), gait cycle signals must be resampled to the same length by interpolation and decimation.

Each gait cycle now contains only parts of the original signals corresponding to this gait cycle. These signal parts are called features (see examples in Figure 5). Each feature corresponds to one gait cycle of some extracted signal. Figure also demonstrates the difference in inter- and intraclass

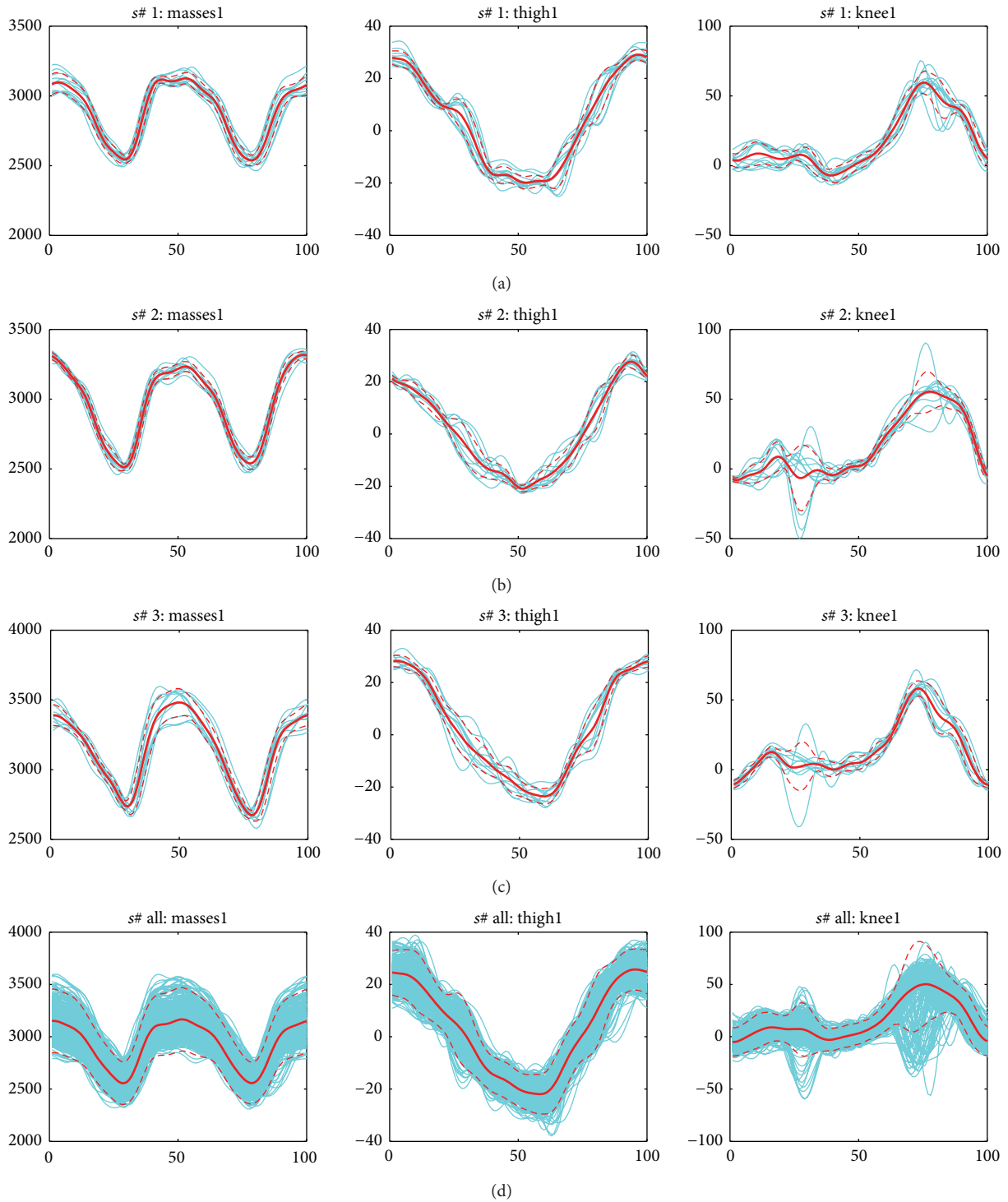


FIGURE 5: Example of extracted features: image shows extracted mass, thigh1, and knee1 signals (in columns) of several gait cycles for three subjects (rows (a), (b), and (c)) denoted by s# 1, s# 2 and s# 3. Blue lines indicate signals, red-thick lines indicate signals mean, and red-dashed lines indicate intraclass variance. Row (d) shows mean and variance (interclass) of all the signals for all subjects (s# all).

variance. It is evident that the latter is smaller, which is good for recognition purposes.

3.3. Feature Space Transformation. Changes in walking speed present one of the major covariate factors with negative impact on recognition results. When a person changes

walking speed, dynamic features (e.g., stride length and joint angles) are changed, while static features (e.g., thigh and shin lengths) remain unchanged. From top row of Figure 6, it can be seen, how single subjects's features differ for different walking speeds (red—fast walk, blue—slow walk). As we only deal with dynamic features, we have to compensate for such changes.

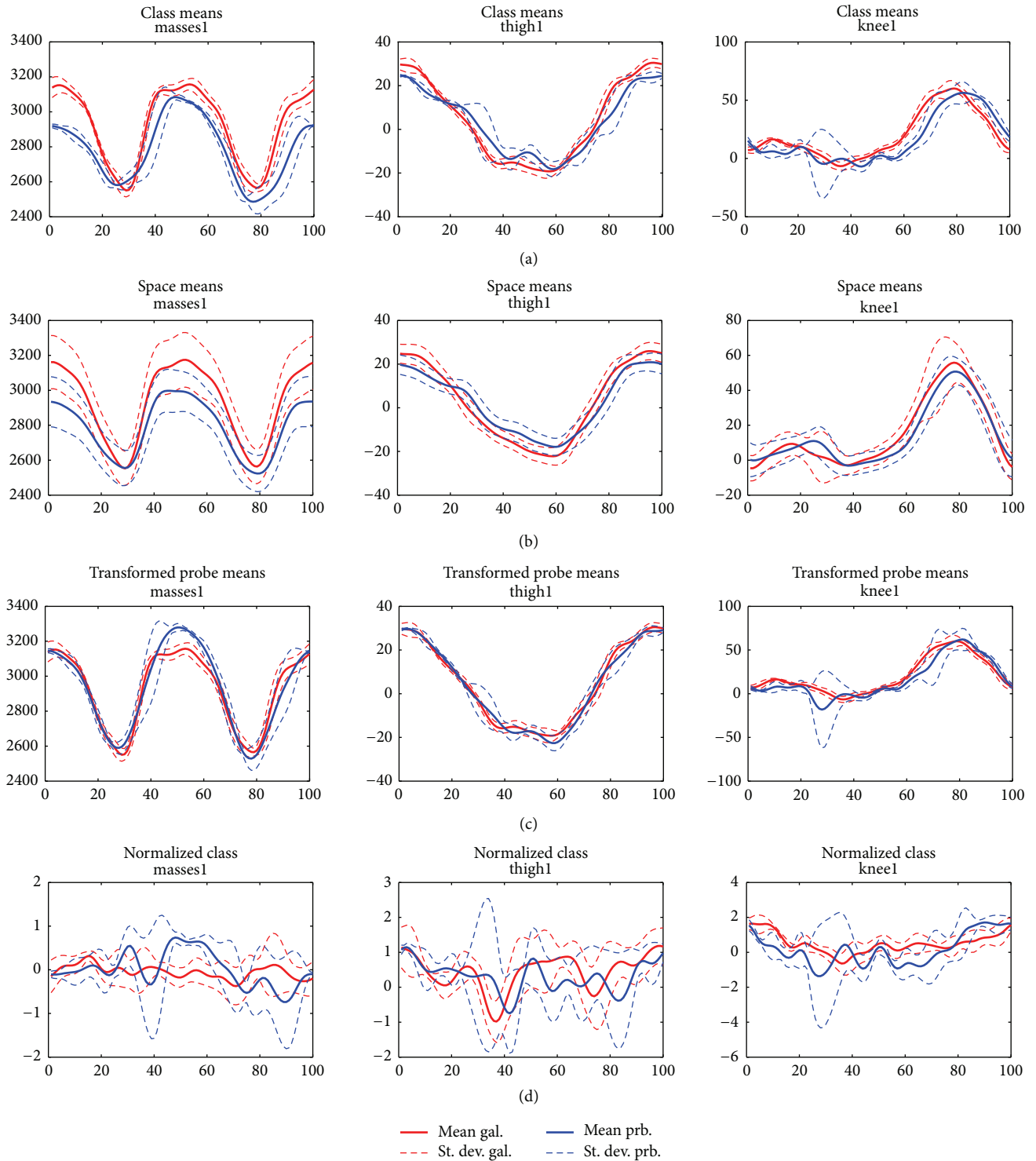


FIGURE 6: Feature space transformation: (a) single subject's features for fast walk (red) and slow walk (blue). (b) Slow and fast walk group mean and st. dev. (c) Slow walk features transformed to fast walk space. (d) Remaining differences after transformation. Note that y axis in rows (a), (b), and (c) shows absolute (measured) values, while row (d) shows differences after normalization, which therefore appear relatively small compared to measured values. x axis denotes the percent of gait cycle.

We perform a feature space transformation based on statistical model of feature space for gallery and probe groups, which contain subjects walking with different speeds. First, we calculate the main statistical measures for each group belonging to certain walking speed, based only on a few randomly chosen subjects from that group. Then we derive group mean and standard deviation (Figure 6 2nd row) and transform the feature signals of all the samples (all subjects, all gait cycles) in that group by

$$\vec{s} = \frac{\vec{s} - \vec{\mu}_g}{\vec{\sigma}_g}, \quad (9)$$

where \vec{s} is the signal vector of single feature of single gait cycle sample, $\vec{\mu}_g$ is the mean vector of the same feature for target group, and $\vec{\sigma}_g$ is the vector of standard deviations for the same group. All operations are element wise.

Such transformation removes major group space deviations caused by varying walking speed and retains only interclass differences based on which subjects can be discriminated (Figure 6, 4th row). The transformation is performed on both gallery and probe groups and subjects within these groups are now comparable. For a demonstration, probe features of slow walk are transformed by inverse transformation to fast walking feature space of the gallery (Figure 6, 3rd row). It is evident that the signals are closer together after transformation.

4. Classification

4.1. Phase Alignment. Classification is done by comparing the probe subjects with the subject stored in the gallery. The comparison is based on Euclidean distance. To make this comparison feasible, gait and probe features must be perfectly aligned. This is roughly achieved in cycle detection phase; however, cycle starts can still differ by a few frames, therefore, more precise alignment is required before classification.

We perform phase alignment by finding the offset of two subject's gait cycles based on a few selected features (COMy, mass, and width). We shift one subject's gait cycles in the range of few frames and calculate the distances of selected features for these shifts. The one with minimal distance is chosen and probe cycles are then shifted accordingly:

$$o = \arg \min_{i=-10}^{i=10} d(\vec{F}_1, \vec{F}_2),$$

$$\vec{F}_1 = [\vec{f}_{c_y,1}, \vec{f}_{m,1}, \vec{f}_{w,1}], \quad (10)$$

$$\vec{F}_2 = [\vec{f}_{c_y,2}, \vec{f}_{m,2}, \vec{f}_{w,2}],$$

where o is the offset, d is distance, and \vec{F}_j is the feature vector of subject j composed of feature vectors $\vec{f}_{i,j}$ of specific features. c_y, m , and w denote COMy, mass, and width. It is important to limit the shifting to small ranges (e.g., $[-10 \cdots 10]$), since larger ranges can result in shifting the gait cycle to the next double support (with the wrong leg in front).

Prior to classification all subjects in the gallery are aligned to one chosen subject (e.g., first) and also all probes are aligned to the same subject.

4.2. Gait Descriptor. Only after such alignment we can compose gait descriptors for all cycles of all subjects. First, gait cycle signals of all acquired features are approximated by trigonometric polynomial coefficients. Periodic signals can be approximated by:

$$S(x) = a_0 + \sum_{n=1}^N a_n \cos(nx) + i \sum_{n=1}^N b_n \sin(nx), \quad (11)$$

where a_n and b_n are the polynomial coefficient acquired by DFT. We use these coefficient to form the descriptor for each feature. Such approximation serves as a low-pass filter, where higher frequencies are filtered out and, in the same time, greatly reduces feature size, so it also reduces the dimensionality of features. If acquired feature size is 100 elements, we can safely use $N \approx 10$, which gives approximately 20 coefficients. Gait descriptors of individual features

$$\vec{d}_i = [a_0, \dots, a_{N_i}, b_1, \dots, b_{N_i}], \quad (12)$$

are then stacked together to form a descriptor of the entire gait cycle:

$$\vec{D}_c = [\vec{d}_1, \vec{d}_2, \dots, \vec{d}_{N_f}], \quad (13)$$

where \vec{D}_c is subject's descriptor of c_i th gait cycle and $\vec{d}_1 \cdots \vec{d}_{N_f}$ are feature descriptors of N_f different features.

Acquired descriptors are still too long for further processing. For example, in our case of 64 features each containing 20 coefficients, descriptor length is 1280. Dimensionality is further reduced by PCA to retain approximately 99% of variance, which ends up in approximately 100 PCA coefficients.

Furthermore, all gallery descriptors are processed by LDA to achieve better discrimination between gallery models.

4.3. Distance Based Classification. Now we calculate the distances between each probe descriptor (gait cycle) and all descriptors of all the models in the gallery. Distance between two subjects is defined as

$$D(p, g_m) = f_c(d(\vec{p}_p, \vec{g}_{m_j})), \quad i \in P, j \in Gm, \quad (14)$$

where p and g_m denote probe and gallery subjects, P and G_m number of descriptors (corresponding to gait cycles) for each subject, and $d(\cdot)$ the distance between two descriptors. f_c is a criteria function, denoting which distance to chose, among distances formed by several probe descriptors. Most commonly mean, minimum and median are used. We choose median as it best reduces the importance of deviated distances (outliers) that might result from measurement errors. We then calculate $D(p, g_m)$ for all gallery models to obtain a vector of distance scores:

$$\vec{D}_p = \{D(p, g_1), \dots, D(p, g_M)\}, \quad (15)$$

where M is the number of subjects in the gallery. Since we use Cumulative Match Characteristics (CMC) to represent classification results, the vector is sorted and ranks are assigned to the models based on calculated distances. The model with the smallest distance is chosen as best (rank 1) match.

4.4. Feature Fusion Scheme. Different features have different discriminative abilities. Therefore, it is natural to assume that using these features separately and assigning their influence by weighting could improve classification results. To demonstrate this point, we employ feature fusion scheme [23], where each feature can be seen as a separate classifier and final result is formed by fusing the results of all the classifiers. Such process can additionally help in the case of missing or erratically measured features. For example, in the case of occlusions only a few features (like missing parts of the legs, etc.) are affected and negative effects can be diminished by classification based on the remaining features, which over-vote the problematic ones.

First, we perform distance based classification as described earlier in Section 4.3 for each feature separately. We compose gait descriptors based on single feature and perform classification. PCA is not required in this case since trigonometric coefficients sufficiently diminish the dimensionality to make LDA feasible. Each feature forms a vector of distance scores $\vec{D}_{p,f}$, which is first normalized to interval $[0, 1]$ to remove feature distance bias using min-max norm. Then we combine all the score vectors of all the features to a single fused distance score:

$$\vec{S}_p = \frac{1}{F} \sum_{i=1}^{i=F} (w_i \|\vec{D}_{p,i}\|_{\min-\max}), \quad (16)$$

where F is the number of features and w_i are feature weights. Please note that $\|\cdot\|_{\min-\max}$ denotes vector normalization, which results in normalized vector, rather than vector norm, which results in a scalar value. Finally, the so-obtained distance score vector \vec{S}_p is sorted and ranks are assigned for all gallery models.

In this work we obtain weights experimentally by evaluating the discriminative power of the features on the basis of intra-/interclass feature variance. Class corresponds to a subject. The intraclass feature variance $\sigma_{s,f}^2(X)$ is the variance of all the signal samples (rows of X) of specific feature f for single subject s . Sample $x_i \in X$ is the signal of the feature f during single gait cycle. Interclass feature variance σ_f^2 is the variance measured on all the samples of all subjects for the same feature (see examples on Figure 5). The ratio of average (through subjects) intra class feature variance and inter class variance,

$$r_\sigma = \frac{\overline{\sigma_{s,f}^2}}{\sigma_f^2} \quad (17)$$

is an indicator of feature discrimination power: the smaller the ratio is, the bigger the discrimination power of the feature can be expected. For our experiments, the variances were calculated on training subjects subset.

Undoubtedly, the process of assigning weights could be more sophisticated using some training technique. However, classification performance turned out to be relatively insensitive to small variations in weights, therefore chosen weight assignment is sufficient for demonstrating the effect of feature classifier fusion on classification performance.

4.5. Noise, Occlusions, and Outliers. Due to sensitive nature of skeleton segmentation process, several types of errors caused by noise sensitive video capturing process, poor quality silhouette extraction algorithm, or scene objects occluding recorded subject may occur. We deal with these errors on several different layers of our method.

Most common are small erratic measurements of bone and joint positions, which are due to noisy silhouettes, for example, random artifacts appearing on particular frames of the video, holes between legs get filled in knee or ankle area, and so forth. This type of errors only occurs on a few consecutive frames and then disappears and might later reappear in some other areas. The result of such errors is noisy signals obtained from segmented skeleton. The noise can be effectively handled by spike detection, elimination, and interpolation as described in Section 3.2 and additional filtering by trigonometric polynomial coefficients as described in Section 4.2.

Larger disruptions can be caused by occluding objects in the scene, missing larger parts of silhouettes, body parts, and so forth. When these errors are short-lived, most of their effects are already eliminated by noise handling procedures. On the other hand, longer presence of occluding objects might result in erratic measurements of several features for entire or even several gait cycles. In the case of missing or badly measured features, bad effects are eliminated by feature fusion (Section 4.4), which acts as classifier fusion where single classifier (feature) adds only minor contribution to final score, while most of the score is formed by the rest of the unaffected features. In the cases when entire gait cycles are affected, such cycles appear as outliers in probe/gallery distance calculation process (Section 4.3) and the effects of problematic distances are eliminated by calculating the median of the distances of all available gait cycles.

5. Experimental Results and Discussion

We tested our methods on OU-ISIR gait database [24], more precisely dataset A, which is composed of high quality gait silhouette sequences of 34 subjects from side view, walking on a treadmill with speed variation from 2 km/h to 10 km/h at 1 km/h interval. For each subject and each speed two sequences are provided, one for the gallery and the other for the probe.

In our cross-speed test, we performed several experiments, where gallery subjects belong to one speed and matching probe subjects belong to the other speed. The results are given as rank 1 correct classification rate in Cumulative Match Characteristic (CMC) to enable comparison with other works, as CMC is also mostly used by other authors. Such metric is highly dependant on the size of the gallery and in order to enable fair comparison to other works, the number of subjects must be the same. 25 subject were used for identification and 9 were used for training previously described feature space transformation. Such split was designed in [18] and adopted by other researchers working on speed-invariant gait recognition as a method benchmark.

TABLE 1: Recognition performance (%) results of basic experiments without feature fusion and space transformation for walking speeds. G and P denote the speed group of gallery and probe, respectively.

G/P	2 km/h	3 km/h	4 km/h	5 km/h	6 km/h	7 km/h
2 km/h	84	80	44	24	16	16
3 km/h	36	80	72	28	28	12
4 km/h	44	68	92	84	52	28
5 km/h	40	36	68	100	88	64
6 km/h	16	24	28	68	92	92
7 km/h	28	20	28	56	76	96

TABLE 2: Recognition performance (%) results of experiments with feature fusion and without space transformation for walking speeds.

G/P	2 km/h	3 km/h	4 km/h	5 km/h	6 km/h	7 km/h
2 km/h	88	88	96	72	56	52
3 km/h	68	92	96	84	76	52
4 km/h	72	80	96	92	88	72
5 km/h	56	72	96	100	100	96
6 km/h	56	64	76	96	100	100
7 km/h	36	56	52	80	92	100

TABLE 3: Recognition performance (%) results of experiments without space transformation for running speeds.

G/P	No fusion			Feature fusion		
	8 km/h	9 km/h	10 km/h	8 km/h	9 km/h	10 km/h
8 km/h	96	92	92	96	96	96
9 km/h	92	100	100	100	100	100
10 km/h	76	92	96	92	96	96

The experiments were split to four sets to illustrate the impact of feature fusion and space transformation on recognition results. Additionally, we split the speeds to walking (2 km/h to 7 km/h) and running (8 km/h to 10 km/h), because running is so much different to walking in terms of gait dynamics that it is regarded as different action (in analogy to action recognition field) and the cross-matching is quite difficult.

First, we perform basic method evaluation, without feature fusion and without space transformation. The results in Table 1 are quite modest and rarely reach 90% even when gallery and probes are in the same speed group. It can be noticed that higher speeds yield better results. We assume that this is because higher speeds reveal more specifics (e.g., consider running), intraclass variation is smaller, and also dynamic features are easier (less noisy) for capturing at higher speeds, when subject's silhouettes are more spread at double support phases, more information is revealed.

Next, we perform experiments with previously described feature fusion scheme without space transformation. The results in Table 2 show noticeable improvement. For easier comparison see also test result summary in Figure 7.

Results for higher speeds (i.e., running speeds) with and without feature fusion are given separately in Table 3. These also confirm our high speed observation.

TABLE 4: Recognition performance (%) results of experiments without feature fusion and with space transformation for walking speeds.

G/P	2 km/h	3 km/h	4 km/h	5 km/h	6 km/h	7 km/h
2 km/h	92	84	84	72	44	32
3 km/h	68	88	84	72	60	48
4 km/h	72	92	96	88	88	64
5 km/h	64	76	100	100	96	92
6 km/h	40	60	72	88	100	96
7 km/h	36	36	48	76	96	92

TABLE 5: Recognition performance (%) results of experiments with feature fusion and with space transformation for walking speeds.

G/P	2 km/h	3 km/h	4 km/h	5 km/h	6 km/h	7 km/h
2 km/h	92	96	92	92	60	68
3 km/h	80	96	100	84	76	64
4 km/h	80	92	100	96	96	72
5 km/h	80	92	100	100	96	100
6 km/h	76	92	100	100	100	100
7 km/h	72	60	80	96	100	100

TABLE 6: Recognition performance (%) results of experiments with space transformation for running speeds.

G/P	Space transformation			Space transformation + fusion		
	8 km/h	9 km/h	10 km/h	8 km/h	9 km/h	10 km/h
8 km/h	96	96	96	100	100	100
9 km/h	88	100	100	100	100	100
10 km/h	92	96	96	100	100	100

The results of the next experiments where we use feature space transformation without and with feature fusion are given in Tables 4 and 5. The space transformation again improves recognition performance in both cases (with and without fusion). In the case, where gallery and probes are taken from the same speed (0 km/h speed change) as shown in result summaries in Table 7 and Figure 7, the differences are not so drastic. Nevertheless, space transformation reveals small improvement and together with feature fusion reaches almost 100%. This improvement is due to the effect achieved by removing the means of the whole speed group from specific subject's features, and since only inter class differences remain in the signals, only those are modelled in descriptors.

Finally, the results of space transformation for running are given in Table 6, and in the case of 18 both improvements reach 100% in all the experiments.

Table 7 and Figure 7 show average recognition performance for cross-speed walking and running experiments. Basic results are given in column 1, feature fusion results are given in column 2, space transformation results are given in column 3, and results with both improvements are given in column 4. Also, the average performance for different degree of speed changes (from 0 km/h to 5 km/h) and the performance gains for feature fusion and spatial transformation are given. Feature gain is calculated as a

TABLE 7: Average recognition performance (%) of cross-speed walking and running.

	Basic	Feature	ST	ST + feature	Feature gain	ST gain	ST + feature gain
Walk	53.0	79.1	74.9	88.3	26.1	9.2	35.3
Run	92.9	96.9	95.6	100.0	4.0	3.1	7.1
$\Delta = 0$ km/h	92.9	96.4	95.6	98.7	3.6	2.2	5.8
$\Delta = 1$ km/h	73.2	90.8	89.2	98.0	17.6	7.2	24.8
$\Delta = 2$ km/h	44.0	83.0	79.0	95.0	39.0	12.0	51.0
$\Delta = 3$ km/h	28.7	65.3	61.3	82.0	36.7	16.7	53.4
$\Delta = 4$ km/h	16.0	55.0	42.0	62.0	39.0	7.0	46.0
$\Delta = 5$ km/h	22.0	44.0	34.0	44.0	22.0	0.0	22.0

TABLE 8: Recognition performance (%) comparison to other works handling cross-speed walking gait identification.

Test scenario	Our method	SN [8]	HMM [14]	SVT [18]	HSC [19]	DCM [20]
Small speed change	96	/	84	90	96	98
Large speed change	68	34	/	58	68	82
Whole dataset	88.33	/	/	/	85.67	92.44

difference between feature fusion results (2nd column) and basic results (1st column), while space transformation gain is calculated as a difference between the results of both improvements (column 4) and results with only feature fusion (column 2). Such calculation indicates how much gain does space transformation bring on top of feature fusion. Overall gain (column 7) is calculated as a difference between the results of both improvements (column 4) and basic results (column 1). It can be noticed that performance gain reaches the peak at 3 km/h degree of speed change and then starts falling back down to 22% at the largest degree of speed change 5 km/h. This indicates the deficiency in both improvements, which do not cope well with severe speed changes. Nevertheless, the average performance gain for cross-speed walking recognition is 35%.

5.1. Comparison to Other Works. For cross-speed walking gait recognition authors in [18] designed two gait recognition tests on OU-ISIR-A dataset to enable comparison with other works handling speed changes. We compare our results to the following state-of-the-art gait recognition methods, which all focus on dealing with walking speed change: HMM-based time normalized (HMM) [14], Stride Normalization (SN) [8], Silhouette Volume Transformation (SVT) [18], High-order Shape Configuration (HSC) [19], and Differential Composition Model (DCM) [20]. The results of HMM and SN methods are based on 25 and 24 subjects from other datasets, while SVT, HSC, and DCM are based on the same OU-ISIR-A dataset used also in our experiments. Similar test scenarios are designed for OU-ISIR-A dataset. For small speed change HMM uses 3.3 km/h and 4.5 km/h, while OU-ISIR-A uses similar 3 km/h and 4 km/h speed change. For large speed change SN uses the speed change between 2.5 km/h and 5.8 km/h, which approximately corresponds to 2 km/h and 6 km/h speed change in OU-ISIR-A dataset.

Results in Table 8 show method performance for both previously described gait tests and also the average method performance on the entire OU-ISIR-A dataset (test scenario:

whole dataset). It also gives performance for methods that published these results. It can be seen that our method was outperformed only by DCM method, especially in the scenario with larger speed changes (4 km/h or more). Nevertheless, our method demonstrates state-of-the-art performance by using model based gait features describing gait dynamics, which is greatly affected by walking speed changes and discarding any possible appearance based identification clues that other silhouette based methods benefit from. It can be noticed that no other model based methods can be found among these results, merely because existing model based methods rarely match the performance of nonmodel based techniques even with no covariate factors present. To our best knowledge, our method is also the first model-based method handling walking speed changes and together with the use of dynamic features represents a novel contribution to gait analysis research field.

6. Conclusion

In this paper we presented a skeleton model based gait recognition system using only features that describe gait dynamics. We described solutions for solving specific problems, that is, two-stage feature alignment (image moments based coarse alignment together with distance based fine alignment) that is crucial for successful comparison of time-series features like ours. We addressed a problem of walking-speed variation and proposed feature fusion and space transformation approach that successfully mitigate its negative effects on recognition performance. Moreover, our features can be understood by human (medical, kinesiological) expert and can handle walking speed changes by undemanding training stage that also has a human understandable interpretation. Such property gives our method the perspective for being used also in other fields like medicine, kinesiology, and sports.

We evaluated the performance of proposed methods on OU-ISIR gait database and proved that model based system concentrating on dynamic features only can demonstrate

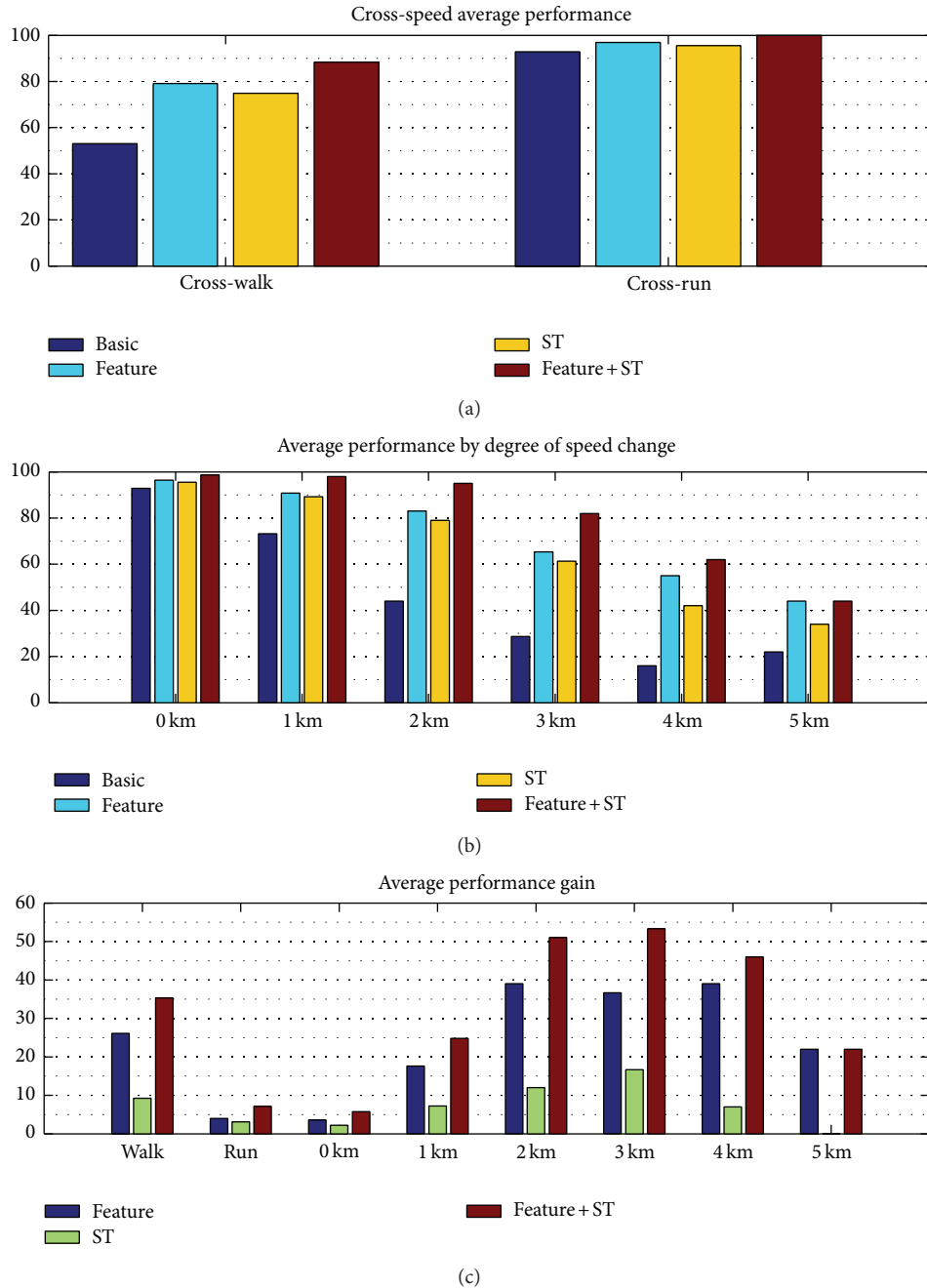


FIGURE 7: Recognition performance (%) results summary: (a) average performance of cross-speed walking and running, (b) average performance by degree of speed change (in km/h), and (c) performance gains for feature fusion and space transformation.

state-of-the-art performance and can easily find its place alongside other appearance based state-of-the-art methods. To the best of our knowledge, our method is the first model-based method handling walking speed changes efficiently, that is, comparable to state-of-the-art results. Although OU-ISIR gait database contains relatively small number of 34 subjects, especially in benchmark form as designed by [18], it provides the broadest range of walking speeds and is up-to-date the most appropriate database for studying walking speed effects on human gait. Moreover, general

recognition ability of similar model-based approaches was already addressed by other authors (e.g., [3]), where correct classification rate of 84% was achieved on 100 subjects at unchanged conditions.

Nevertheless, there are further problems that need to be addressed in the future. First, the problem of time series feature alignment should be circumvented by using a distance metric that is starting point invariant. Furthermore, the performance of larger (4 km/h and up) speed change should be investigated and improved. This could be achieved by more

sophisticated feature selection technique on one hand and on the other by finding stronger models of walking speed spaces, which could also tackle the problem of cross-walker-runner identification.

Conflict of Interests

The authors declare that there is no conflict of interests regarding the publication of this paper.

Acknowledgment

Operation is partly financed by the European Union, European Social Fund.

References

- [1] G. Johansson, "Visual motion perception," *Scientific American*, vol. 232, no. 6, pp. 76–88, 1976.
- [2] G. Ariyanto and M. S. Nixon, "Model-based 3D Gait biometrics," in *Proceedings of the International Joint Conference on Biometrics (IJCB '11)*, pp. 354–359, October 2011.
- [3] J.-H. Yoo and M. S. Nixon, "Automated markerless analysis of human Gait motion for recognition and classification," *ETRI Journal*, vol. 33, no. 2, pp. 259–266, 2011.
- [4] T. Yu and J.-H. Zou, "Automatic human Gait imitation and recognition in 3D from monocular video with an uncalibrated camera," *Mathematical Problems in Engineering*, vol. 2012, Article ID 563864, pp. 1–35, 2012.
- [5] H. Lu, K. N. Plataniotis, and A. N. Venetsanopoulos, "A full-body layered deformable model for automatic model-based Gait recognition," *Eurasip Journal on Advances in Signal Processing*, vol. 2008, Article ID 261317, pp. 1–14, 2008.
- [6] Z. Liu and S. Sarkar, "Simplest representation yet for Gait recognition: averaged silhouette," in *Proceedings of the 17th International Conference on Pattern Recognition (ICPR '04)*, vol. 4, pp. 211–214, August 2004.
- [7] S. Sarkar, P. J. Phillips, Z. Liu, I. R. Vega, P. Grother, and K. W. Bowyer, "The humanID Gait challenge problem: data sets, performance, and analysis," *IEEE Transactions on Pattern Analysis and Machine Intelligence*, vol. 27, no. 2, pp. 162–177, 2005.
- [8] R. Tanawongsuwan and A. Bobick, "Modelling the effects of walking speed on appearance-based Gait recognition," in *Proceedings of the IEEE Computer Society Conference on Computer Vision and Pattern Recognition (CVPR '04)*, pp. II783–II790, July 2004.
- [9] Z. Wang, X. Sun, L. Sun, and Y. Huang, "Manifold adaptive kernel semisupervised discriminant analysis for Gait recognition," *Advances in Mechanical Engineering*, vol. 2013, pp. 1–12, 2013.
- [10] M. Peternel and A. Leonardis, "Visual learning and recognition of a probabilistic spatio-temporal model of cyclic human locomotion," in *Proceedings of the 17th International Conference on Pattern Recognition (ICPR '04)*, pp. 146–149, August 2004.
- [11] W. Stone and M. Skubic, "Capturing habitual, in-home Gait parameter trends using an inexpensive depth camera," in *Proceedings of the International Conference of the IEEE Engineering in Medicine and Biology Society*, pp. 5106–5109, 2012.
- [12] T. Banerjee, J. M. Keller, and M. Skubic, "Resident identification using kinect depth image data and fuzzy clustering techniques," in *Proceedings of the International Conference of the IEEE Engineering in Medicine and Biology Society*, pp. 5102–5105, 2012.
- [13] J. Kovac and P. Peer, "Transformation based Walking speed normalization for Gait recognition," *KSII Transactions on Internet and Information Systems*, vol. 7, no. 11, pp. 2690–2701, 2013.
- [14] Z. Liu and S. Sarkar, "Improved Gait recognition by Gait dynamics normalization," *IEEE Transactions on Pattern Analysis and Machine Intelligence*, vol. 28, no. 6, pp. 863–876, 2006.
- [15] S. Lee, Y. Liu, and R. Collins, "Shape variation-based frieze pattern for robust Gait recognition," in *Proceedings of the IEEE Computer Society Conference on Computer Vision and Pattern Recognition (CVPR '07)*, June 2007.
- [16] A. Veeraraghavan, A. Srivastava, A. K. Roy-Chowdhury, and R. Chellappa, "Rate-invariant recognition of humans and their activities," *IEEE Transactions on Image Processing*, vol. 18, no. 6, pp. 1326–1339, 2009.
- [17] T. Kobayashi and N. Otsu, "Three-way auto-correlation approach to motion recognition," *Pattern Recognition Letters*, vol. 30, no. 3, pp. 212–221, 2009.
- [18] A. Tsuji, Y. Makihara, and Y. Yagi, "Silhouette transformation based on walking speed for Gait identification," in *Proceedings of the IEEE Computer Society Conference on Computer Vision and Pattern Recognition (CVPR '10)*, pp. 717–722, June 2010.
- [19] W. Kusakunniran, Q. Wu, J. Zhang, and H. Li, "Speed-invariant Gait recognition based on procrustes shape analysis using higher-order shape configuration," in *Proceedings of the 18th IEEE International Conference on Image Processing (ICIP '11)*, pp. 545–548, September 2011.
- [20] W. Kusakunniran, Q. Wu, J. Zhang, and H. Li, "Differential composition model," *Systems, Man, and Cybernetics*, vol. 42, no. 6, pp. 1654–1668, 2012.
- [21] L. Zappella, X. Llado, and J. Salvi, *New Trends in Motion Segmentation, Pattern Recognition*, Edited by P.-Y. Yin, InTech, 2009.
- [22] D. A. Winter, *The Biomechanics and Motor Control of Human Movement*, John Wiley & Sons, 1990.
- [23] X. Huang and N. Boulgouris, "Model-based human Gait recognition using fusion of features," in *Proceedings of the International Conference on Acoustics, Speech and Signal Processing*, pp. 1469–1472, 2009.
- [24] Y. Makihara, H. Mannami, A. Tsuji et al., "The OU-ISIR Gait database comprising the Treadmill dataset," *IPSI Transactions on Computer Vision and Applications*, vol. 4, pp. 53–62, 2012.

Research Article

Penalized Maximum Likelihood Algorithm for Positron Emission Tomography by Using Anisotropic Median-Diffusion

Qian He^{1,2} and Lihong Huang^{1,3}

¹ College of Mathematics and Econometrics, Hunan University, Changsha 410082, China

² College of Information Science and Engineering, Hunan City University, Yiyang 413000, China

³ Department of Information and Technology, Hunan Women's University, Changsha 410004, China

Correspondence should be addressed to Qian He; heqian0808@163.com

Received 1 October 2013; Revised 9 December 2013; Accepted 24 December 2013; Published 20 January 2014

Academic Editor: Gelan Yang

Copyright © 2014 Q. He and L. Huang. This is an open access article distributed under the Creative Commons Attribution License, which permits unrestricted use, distribution, and reproduction in any medium, provided the original work is properly cited.

Nowadays, positron emission tomography (PET) is widely used in engineering. In this paper, a novel penalized maximum likelihood (PML) algorithm is presented for improving the quality of PET images. The proposed algorithm fuses an anisotropic median-diffusion (AMD) filter to the maximum-likelihood expectation-maximization (MLEM) algorithm. The fusing algorithm shows its positive effect on image reconstruction and denoising. Experimental results present that the proposed method denoises and reconstructs images with high quality. Furthermore, by comparing with other classical reconstructing algorithms, this novel algorithm shows better performance in the edge preservation.

1. Introduction

PET technology, which has been widely used in neurology, oncology, and new medicine exploitation, is one of the advanced and noninvasive diagnostic techniques in modern nuclear medical. In order to obtain a high quality reconstructed image from clinical projection data with strong noise, an excellent image reconstruction algorithm is indispensable.

The MLEM algorithm is a classic method in PET image reconstruction when the measured data follows Poisson distribution [1]. One problem of this algorithm is the ill-posed problem, which represents that the reconstructed images cannot remove the noise of projection data [2]. Today, an ill-posed image reconstruction problem, such as MLEM, can be transformed into a well-posed one through the use of regularization term. The reconstructed results should be not only content with measured data to some extent but also be consistent with additional regularization term that is independent of those data at the same time. That is usually called PML or Bayesian algorithm. Numerous PML algorithms have been proposed in the past decades [3–10].

Thereinto, Green proposed a Bayesian algorithm, known as the one-step-late (OSL) algorithm [6]. The key of this

algorithm is to find an appropriate energy function, which is defined by Gibbs probability distribution. Unfortunately, the selection of the energy function is difficult. The median root prior (MRP) algorithm [9], firstly proposed by Alenius, is an application of OSL algorithm. This algorithm is good at coping with those images that have locally monotonic structures. However, the images reconstructed by MRP are still noisy because median filter cannot remove Gaussian and Poisson noise effectively, which dominate in PET images [7].

The anisotropic diffusion (AD) filter [11] is a nonlinear partial differential equation (PDE) based on diffusion process. Overcoming the undesirable effects of linear smoothing filter, such as blurring or dislocating the useful edge information of the images, AD has been widely used in image smoothing, image reconstruction and image segmentation [12–15]. The basic idea of AD is adaptively choosing diffusive coefficients in diffusion process so that diffusion is maximal within smooth regions and minimal near the edges.

In order to remove noise and preserve edge information at the same time, image reconstruction based on AD has become the research focus [7, 8, 15, 16]. Yan proposed a PML algorithm [16] that combined MLEM with AD filter (called MELM-PDE) and could obtain acceptable reconstructed

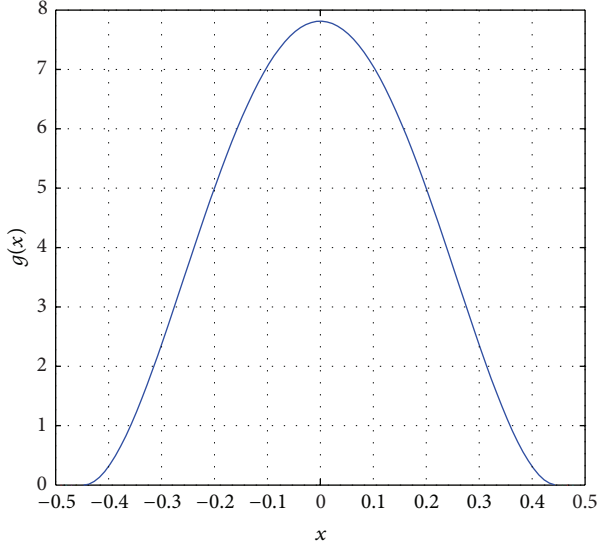


FIGURE 1: The plot of diffusion function with $K = 0.2$.

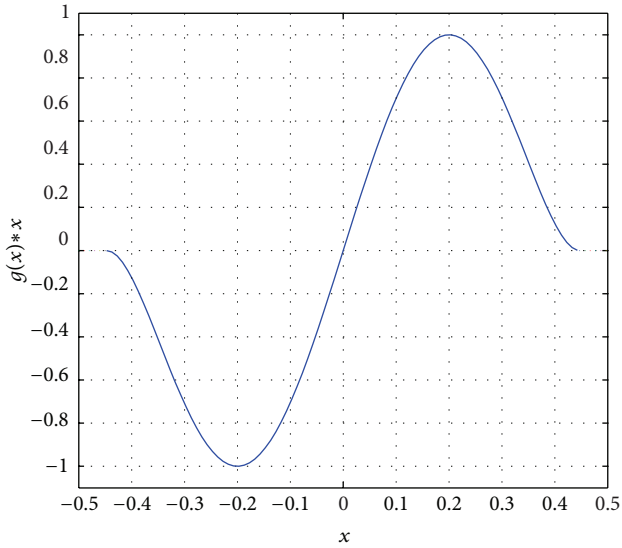


FIGURE 2: The plot of flux function with $K = 0.2$.



FIGURE 3: Modified Shepp-Logan phantom.

results. However, MLEM-PDE cannot remove the isolated noise and preserve edge information accurately due to the defects of P-M diffusion model [15].

In this paper, we proposed a new PML algorithm for PET image reconstruction based on AMD. The proposed algorithm can effectively remove noise while preserving edge information accurately. In Section 2, PET image reconstruction algorithms such as MLEM, OSL, and MRP are introduced. The AMD filter is presented in Section 3. In Section 4, our proposed algorithm is described. Simulation experiments are given in Section 5. Finally, Section 6 is the conclusion.

2. Image Reconstruction Algorithms for PET

In PET, the maximum likelihood (ML) algorithm seeks a solution that makes the measured data most likely to occur and maximizes the conditional probability $p(g | f)$, where g is the measured data and f is the emission image. It is described in the following:

$$\hat{f} = \arg \max_{f \geq 0} L(f),$$

$$L(f) = \log(p(g | f)) \quad (1)$$

$$= \sum_{i=1}^N \left(- \sum_{j=1}^M H_{i,j} f_j + g_i \log \left(\sum_{j=1}^M H_{i,j} f_j \right) \right).$$

In (2), H_{ij} is the probability of photons emitted by pixel j , which can be detected by the detector i , f_j is the number of photons emitted by the pixel j , and g_i is the number of photons captured by the detector i .

In order to solve (1), Shepp and Vardi [1] have proposed the EM algorithm. The iterative formula can be described in the following:

$$f_j^{k+1} = f_j^k \frac{\sum_{i=1}^N H_{ij} (g_i / \sum_{l=1}^M H_{il} f_l^k)}{\sum_{i=1}^N H_{ij}}, \quad (2)$$

where k is the iteration.

Although MLEM algorithm is better than filtered back-projection (FBP) algorithm [17], its convergence rate is extremely slow, and as the iteration number increases, the reconstructed results suffer from noise artifacts. The usual method to solve this problem is to introduce a regularization term, and the objective function is

$$\hat{f} = \arg \max_{f \geq 0} [L(f) + P(f)], \quad (3)$$

where $L(f)$ has been explained above and $P(f)$ is regularization term or penalty term.

The OSL algorithm uses the current image f^k when calculating the value of the derivative of the energy function, and the iterative formula can be defined as [6]

$$f_j^{k+1} = f_j^k \frac{\sum_{i=1}^N H_{ij} (g_i / \sum_{l=1}^M H_{il} f_l^k)}{\sum_{i=1}^N H_{ij} + \beta (\partial / \partial f_j) U(f) |_{f^k}}, \quad (4)$$

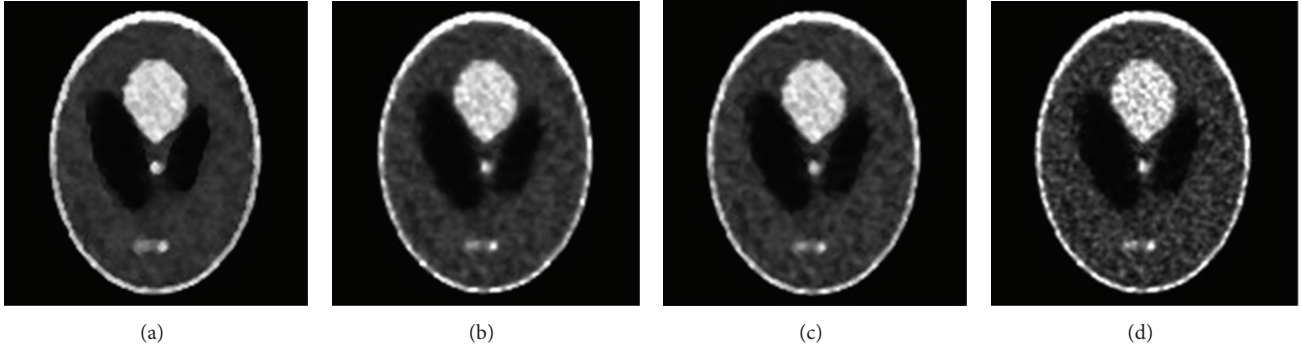


FIGURE 4: The modified Shepp-Logan phantom reconstructed by different algorithms after 50 iterations: (a) MLEM-AMD with $h = 40$ and $K = 1.5$; (b) MLEM-PDE with $h = 40$ and $K = 40$; (c) MRP with $\beta = 0.1$; (d) MLEM.

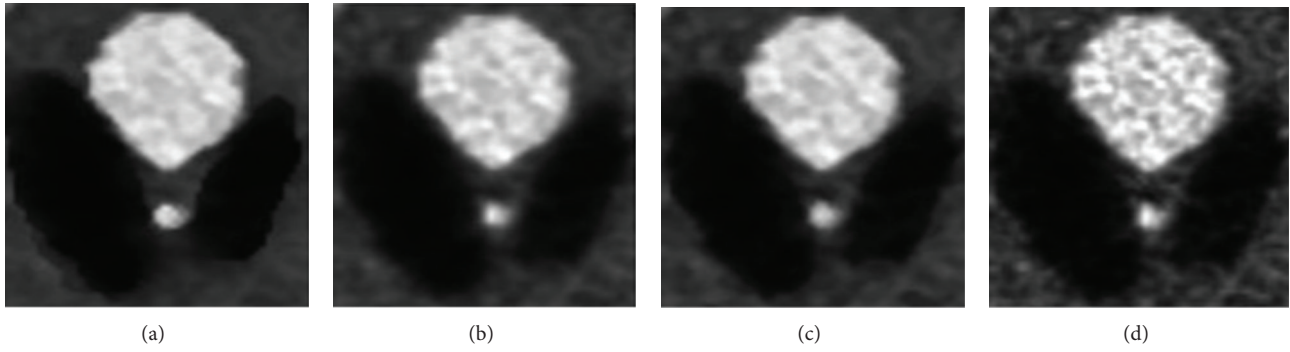


FIGURE 5: The zoomed images of Figure 4: (a) MLEM-AMD; (b) MLEM-PDE; (c) MRP; (d) MLEM.

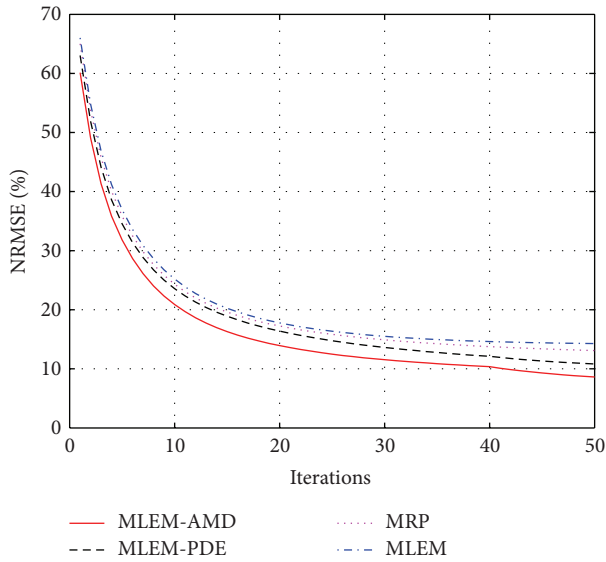


FIGURE 6: The plots of NRMSE along with iterations for different algorithms.

where $U(\cdot)$ is the energy function and β is the Bayes weight of the prior.

The MRP algorithm can be coped with monotonic structures in a neighborhood by comparing the pixel against the

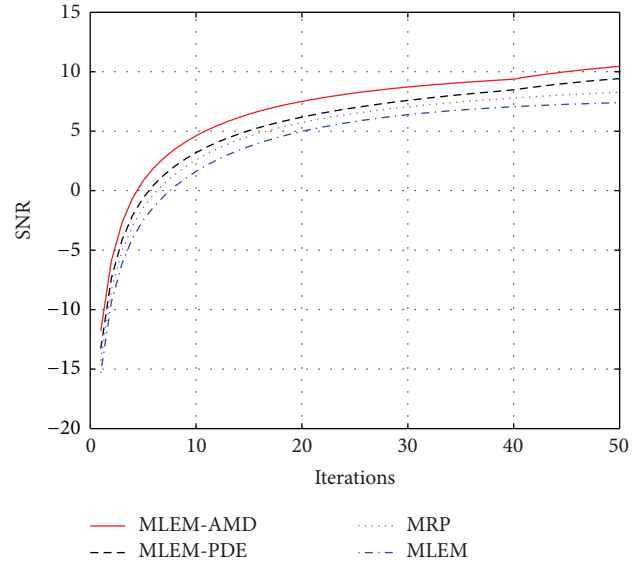


FIGURE 7: The plots of SNR along with iterations for different algorithms.

local median. Edge preservation is an intrinsic characteristic of median filter, and its update equation is [9]

$$f_j^{k+1} = f_j^k \frac{\sum_{i=1}^N H_{ij} (g_i / \sum_{l=1}^M H_{il} f_l^k)}{\sum_{i=1}^N H_{ij} + \beta ((f_j^k - M(f_j^k)) / M(f_j^k))}, \quad (5)$$

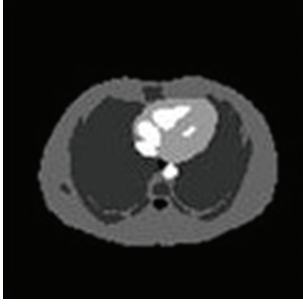


FIGURE 8: Real thorax phantom.

where $M(f_j^k)$ is the median of pixel j within its neighborhood.

3. Anisotropic Median-Diffusion Filter

The AD filter (usually called P-M diffusion model), firstly proposed by Perona and Malik, is a nonlinear filter that purports to remove noise without blurring edges, and the basic equation is [11]

$$\frac{\partial f(x, y, t)}{\partial t} = \text{div} [g(|\nabla f(x, y, t)|) \nabla f(x, y, t)], \quad (6)$$

where t is the time parameter, div is the divergence operator, $f(x, y, 0)$ is the original image, $\nabla f(x, y, t)$ is the gradient of the image at time t , and $g(\cdot)$ is the diffusion coefficient, which is a function of local gradient. This function should be satisfied:

$$\begin{aligned} \lim_{x \rightarrow 0} g(x) &= 1, \\ \lim_{x \rightarrow \infty} g(x) &= 0, \end{aligned} \quad (7)$$

so that the diffusion is more in smooth regions and less near the edges. They put forward the following two diffusion coefficients:

$$\begin{aligned} g_1(x) &= \exp \left[-\left(\frac{x}{K} \right)^2 \right], \\ g_2(x) &= \frac{1}{1 + (x/K)^2}, \end{aligned} \quad (8)$$

where K is a gradient threshold that judges if there is a local edge. Gradient threshold K determines the quality of the filter [18], Perona and Malik suggested using Canny's "noise estimator" [19] to determine K , Torkamani-Azar and Tait used the mean of the absolute gradient as K [20], and Black et al. determined K from the median absolute deviation [21].

Although AD filter can suppress the noise and preserve the edge information to some extent, it cannot preserve the detail edges effectively and accurately [8]. Ling and Bovik proposed AMD filter [22] on the basis of AD filter. This filter

incorporates a median filter into the diffusion step, and the discrete form is defined as

$$\begin{aligned} f_j^{k+1} &= f_j^k + \frac{w}{|N_j|} \sum_{j' \in N_j} (g(|\nabla f_{j,j'}^k|) \nabla f_{j,j'}^k), \\ f_j^{k+1} &= \text{Median}(f_j^k, W), \end{aligned} \quad (9)$$

where $w \in [0, 1]$ controls the rate of diffusion, k is iteration number, f_j is the gray value of pixel j , $|N_j|$ is the number of neighbor at pixel j (usually four directions, north, south, east, and west, resp.), $\nabla f_{j,j'} = f_{j'} - f_j$, W is the window for the median operator (such as a 3×3 square), and the diffusion coefficient $g(\cdot)$ is

$$g(x) = \begin{cases} \frac{25}{16K} \left[1 - \left(\frac{x}{\sqrt{5}K} \right)^2 \right]^2, & |x| \leq \sqrt{5}K, \\ 0, & \text{otherwise.} \end{cases} \quad (10)$$

The flux function $\phi(x)$ is defined as $\phi(x) = g(x) \cdot x$.

The diffusion coefficient and the flux function are presented, respectively, in Figures 1 and 2. These figures together with (9) suggest that diffusion is maximal within smooth regions and stopped near the edges.

In AMD, diffusion process can smooth the regions with small gradient between current pixel and its neighborhood, while regions with large gradient (edge or noise spike) are left unchanged. Noise spike that generated the large gradients will be removed effectively by the median filter subsequently. However, those large gradients generated by the edges will not be affected by the median filter. Thus, low-level noise is smoothed by diffusion, and high-level noise is removed by median filter. In brief, the AD and median filter are always mutually complementary to gradually eliminate noise without blurring the edges [22].

4. Proposed Algorithm

Although MLEM-PDE algorithm is better than classical reconstructing algorithms, the images reconstructed by MLEM-PDE are still noisy because P-M diffusion model is not good enough for the removal of isolated noise and accurate preservation of edges. Therefore, it is natural that a novel diffusion model should be introduced into the MLEM algorithm. In this paper, we proposed a new PML algorithm (called MELM-AMD) by fusing AMD filter to the MLEM algorithm. The discrete form of the proposed algorithm can be defined as follows:

$$f_j^{k+1,h} = f_j^{k,h} \frac{\sum_{i=1}^N H_{ij} (g_i / (\sum_{l=1}^M H_{il} f_l^{k,h}))}{\sum_{i=1}^N H_{ij}}, \quad (11)$$

$$f_j^{k+1,h+1} = f_j^{k+1,h} + \frac{w}{|N_j|} \sum_{j' \in N_j} (g(|\nabla f_{j,j'}^{k+1,h}|) \nabla f_{j,j'}^{k+1,h}), \quad (12)$$

$$f_j^{k+1,h+1} = \text{Median}(f_j^{k+1,h+1}, W), \quad (13)$$

where h is diffusion number and diffusion coefficient $g(\cdot)$ is defined by (10).

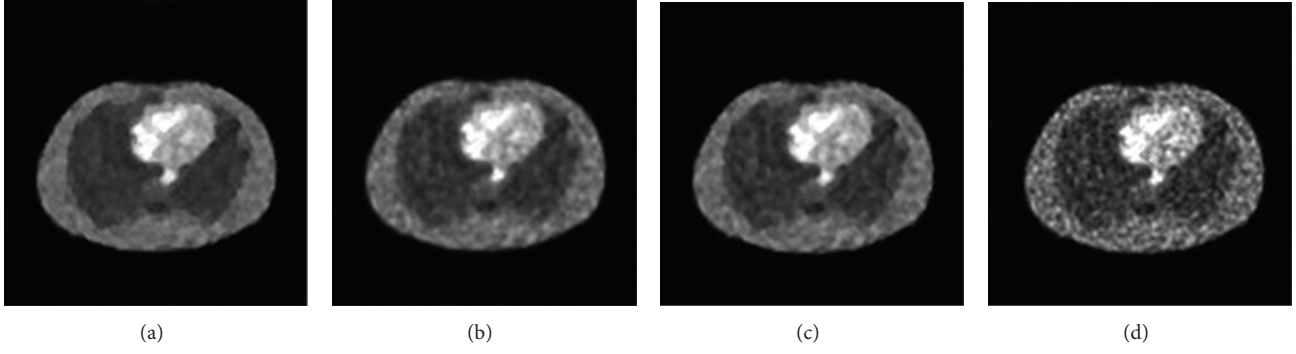


FIGURE 9: The real thorax phantom reconstructed by different algorithms after 50 iterations: (a) MLEM-AMD; (b) MLEM-PDE; (c) MRP; (d) MLEM.

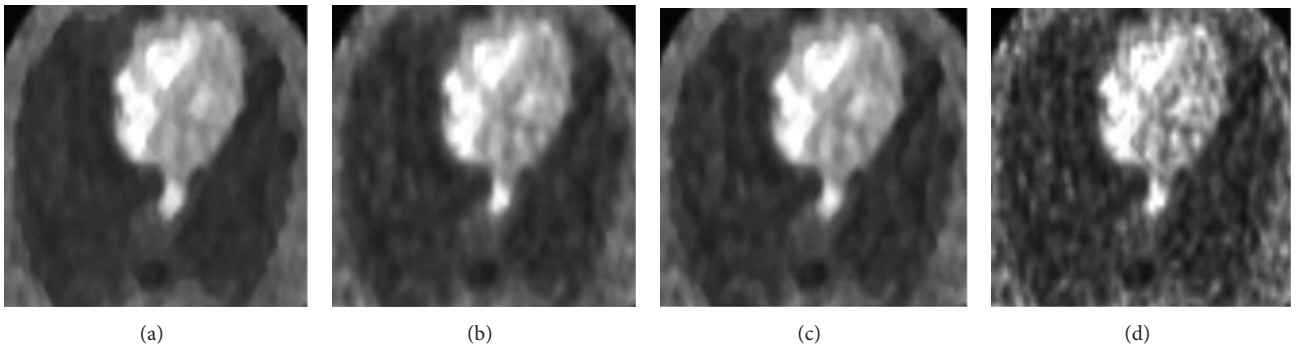


FIGURE 10: The zoomed images of Figure 9: (a) MLEM-AMD; (b) MLEM-PDE; (c) MRP; (d) MLEM.

The proposed algorithm can select appropriate diffusion coefficients adaptively during the diffusion process. At each diffusion step, noise with small gradients will be smoothed by (12), while the large gradients generated by noise spike will be removed effectively by (13). If large gradients generated by edges, the algorithm will not affect them. So, the proposed algorithm can preserve the edges more validly than other methods.

5. Simulation Experiments

In order to examine the effectiveness of the proposed algorithm, we compared the reconstructed image produced by MLEM-AMD algorithm with those brought by different algorithms, such as MLEM, MRP, and MLEM-PDE in computer simulations. These algorithms tested by computer-generated modified Shepp-Logan phantom are shown in Figure 3, and the size of the image phantom is 128×128 pixels. The distribution of projection data has the Poisson characteristics and is assumed to be generated by 128 angular views (averagely distributed in the range of 180 degrees), while each angle has 128 radial bins. The Poisson noise is added into projection data and the number of photons captured by radial bins is about 6×10^5 .

The reconstructed images generated by different algorithms that are shown in Figures 4 and 5 are the zoomed images of Figure 4. From the figures, we can see that the proposed algorithm has well performance of noise

removal and edges preservation especially the thin edges and detailed information. At the same time, we can observe that the MLEM-AMD algorithm overcomes the shortcoming of streak artifacts and the reconstructed image is more similar to the original phantom. In a word, the proposed algorithm is good at producing high quality image with low noise and preserving edge information.

Normalized root-mean-square error (NRMSE) and signal-to-noise ratios (SNR) are used to evaluate quantitatively the performance of the proposed algorithm, which are defined as

$$(1) \text{NRMSE} = \frac{\sum_{i=1}^N \sum_{j=1}^M [f(i, j) - \hat{f}(i, j)]^2}{\sum_{i=1}^N \sum_{j=1}^M [f(i, j)]^2}, \quad (14)$$

where $\hat{f}(i, j)$ and $f(i, j)$ denote the value of pixel (i, j) in reconstructed image and the original image, respectively. The smaller the value of NRMSE is, the better the performance of the algorithm embodies:

$$(2) \text{SNR} = 10 \log_{10} \frac{\sum_{i=1}^N \sum_{j=1}^M (\hat{f}(i, j) - \bar{f})^2}{\sum_{i=1}^N \sum_{j=1}^M (\hat{f}(i, j) - f(i, j))^2}, \quad (15)$$

where $\hat{f}(i, j)$ and $f(i, j)$ have been explained above and \bar{f} is the average grayscale of all pixels in reconstructed image \hat{f} . The better the algorithm is, the bigger the value of SNR is.

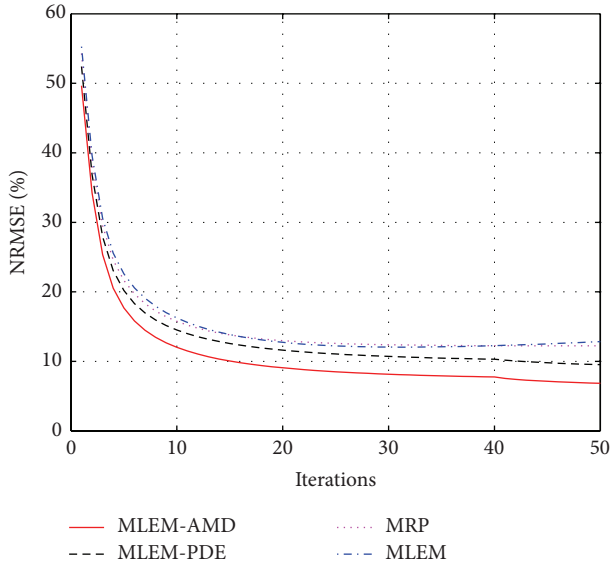


FIGURE 11: The plots of NRMSE along with iterations for different algorithms.

Figure 6 is the plots of NRMSE along with iterations for different algorithms. As it is shown, the NRMSE produced by the proposed algorithm is always smaller than those produced by other algorithms distinctly. The MLEM-AMD algorithm significantly improves the quality of reconstructed image in term of NRMSE. Figure 7 is the plots of SNR along with iterations for different algorithms, and it also proves that the MLEM-AMD algorithm can obtain the better reconstructed image than other algorithms.

Simulated data generated by the real thorax phantom (see Figure 8) is applied to further test the validity of proposed algorithm. The projection data were generated by the method mentioned above, and the number of photons captured by radial bins is about 5.2×10^5 .

The images reconstructed by MLEM-AMD, MLEM-PDE, MRP, and MLEM that are shown in Figures 9 and 10 are the zoomed images of Figure 9. From the figures, we can see that proposed algorithm can also remove noise and preserve edge information effectively.

Figures 11 and 12 are the plot of NRMSE and SNR along with iteration number for different algorithms, respectively. From these quantitative results, it is also obvious that the application of proposed algorithm can obtain better reconstructed image.

6. Conclusion

In this paper, a novel PML algorithm called MLEM-AMD was proposed for improving the quality of reconstructed image, which fuses AMD filter into MLEM. Iterations of the proposed method can be divided into two steps: firstly, reconstruct image with MLEM algorithm; secondly, remove noise with the AMD filter. From simulation experiments in Section 5, we can see that the MLEM-AMD algorithm can remove noise and preserve edge information effectively in PET image reconstruction. In our experiment, MLEM-AMD

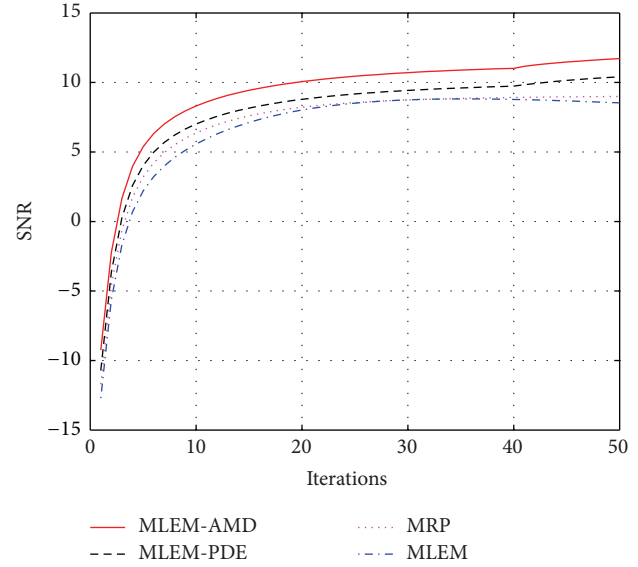


FIGURE 12: The plots of SNR along with iterations for different algorithms.

shows better performance than the classic algorithms, for example, MLEM-PDE, MRP, and MLEM. The reconstructed images by the proposed algorithm show significant improvement in visual quality. In conclusion, the proposed algorithm absorbs the advantage of AMD filter and can reconstruct the images of high quality.

Conflict of Interests

The authors declare that there is no conflict of interests regarding the publication of this paper.

Acknowledgments

The authors would like to thank anonymous reviewers for their helpful work of this paper. This work was supported by Fund Project of Hunan Provincial Education Department no. 12C0573 and Yiyang Municipal Science and Technology Bureau no. 2012JZ50.

References

- [1] L. A. Shepp and Y. Vardi, "Maximum likelihood reconstruction for emission tomography," *IEEE Transactions on Medical Imaging*, vol. 1, no. 2, pp. 113–122, 1982.
- [2] A. Gaitanis, G. Kontaxakis, G. Spyrou, G. Panayiotakis, and G. Tzanakos, "PET image reconstruction: a stopping rule for the MLEM algorithm based on properties of the updating coefficients," *Computerized Medical Imaging and Graphics*, vol. 34, no. 2, pp. 131–141, 2010.
- [3] C.-T. Chen, V. E. Johnson, W. H. Wong, X. Hu, and C. E. Metz, "Bayesian image reconstruction in positron emission tomography," *IEEE Transactions on Nuclear Science*, vol. 37, no. 1, pp. 636–641, 1990.
- [4] S. Somayajula, C. Panagiotou, A. Rangarajan, Q. Li, S. R. Arridge, and R. M. Leahy, "PET image reconstruction using

- information theoretic anatomical priors," *IEEE Transactions on Medical Imaging*, vol. 30, no. 3, pp. 537–549, 2011.
- [5] G. Wang and J. Qi, "Penalized likelihood PET image reconstruction using patch-based edge-preserving regularization," *IEEE Transactions on Medical Imaging*, vol. 31, no. 12, pp. 2194–2204, 2012.
- [6] P. J. Green, "Bayesian reconstructions from emission tomography data using a modified EM algorithm," *IEEE Transactions on Medical Imaging*, vol. 9, no. 1, pp. 84–93, 1990.
- [7] J. H. Yan and J. Yu, "Median-prior tomography reconstruction combined with nonlinear anisotropic diffusion filtering," *Journal of the Optical Society of America A*, vol. 24, no. 4, pp. 1026–1033, 2007.
- [8] Z. G. Gui and J. W. He, "Regularized maximum likelihood algorithm for PET image reconstruction using a detail and edges preserving anisotropic diffusion," *Optik*, vol. 123, no. 6, pp. 507–510, 2012.
- [9] S. Alenius and U. Ruotsalainen, "Bayesian image reconstruction for emission tomography based on median root prior," *European Journal of Nuclear Medicine*, vol. 24, no. 3, pp. 258–265, 1997.
- [10] I.-T. Hsiao, A. Rangarajan, and G. Gindi, "A new convex edge-preserving median prior with applications to tomography," *IEEE Transactions on Medical Imaging*, vol. 22, no. 5, pp. 580–585, 2003.
- [11] P. Perona and J. Malik, "Scale-space and edge detection using anisotropic diffusion," *IEEE Transactions on Pattern Analysis and Machine Intelligence*, vol. 12, no. 7, pp. 629–639, 1990.
- [12] K. Krissian and S. Aja-Fernández, "Noise-driven anisotropic diffusion filtering of MRI," *IEEE Transactions on Image Processing*, vol. 18, no. 10, pp. 2265–2274, 2009.
- [13] D. Kazantsev, S. R. Arridge, S. Pedemonte et al., "An anatomically driven anisotropic diffusion filtering method for 3D SPECT reconstruction," *Physics in Medicine and Biology*, vol. 57, no. 12, pp. 3793–3810, 2012.
- [14] Y. Wu, B. Tracey, P. Natarajan, and J. P. Noonan, "James-Stein type center pixel weights for non-local means image denoising," *IEEE Signal Processing Letters*, vol. 20, no. 4, pp. 411–414, 2013.
- [15] Z. G. Gui, Y. Liu, and J. W. He, "PML algorithm for positron emission tomography combined with nonlocal fuzzy anisotropic diffusion filtering," *IEEE Transactions on Nuclear Science*, vol. 59, no. 5, pp. 1984–1989, 2012.
- [16] J. H. Yan, *Investigation of Positron Emission Tomography Image Reconstruction*, Huazhong University of Science & Technology, Wuhan, China, 2007.
- [17] G. T. Herman, *Image Reconstruction from Projections: the Fundamentals of Computerized Tomography*, Academic Press, New York, NY, USA, 1980.
- [18] C. Tsotsios and M. Petrou, "On the choice of the parameters for anisotropic diffusion in image processing," *Pattern Recognition*, vol. 46, no. 5, pp. 1369–1381, 2013.
- [19] J. Canny, "A computational approach to edge detection," *IEEE Transactions on Pattern Analysis and Machine Intelligence*, vol. 8, no. 6, pp. 679–698, 1986.
- [20] F. Torkamani-Azar and K. E. Tait, "Image recovery using the anisotropic diffusion equation," *IEEE Transactions on Image Processing*, vol. 5, no. 11, pp. 1573–1578, 1996.
- [21] M. J. Black, G. Sapiro, D. H. Marimont, and D. Heeger, "Robust anisotropic diffusion," *IEEE Transactions on Image Processing*, vol. 7, no. 3, pp. 421–432, 1998.
- [22] J. Ling and A. C. Bovik, "Smoothing low-SNR molecular images via anisotropic median-diffusion," *IEEE Transactions on Medical Imaging*, vol. 21, no. 4, pp. 377–384, 2002.

Research Article

Linear Chromatic Adaptation Transform Based on Delaunay Triangulation

Rok Kreslin,¹ Pilar M. Calvo,² Luis G. Corzo,³ and Peter Peer¹

¹ Faculty of Computer and Information Science, University of Ljubljana, Slovenia

² Polytechnical Faculty of San Sebastian, University of the Basque Country (UPV/EHU), Spain

³ Creatio Irizar Group Innovation Center AIE, 20216 Ormaiztegui, Spain

Correspondence should be addressed to Rok Kreslin; rok.kreslin@fri.uni-lj.si

Received 25 September 2013; Revised 13 November 2013; Accepted 2 December 2013; Published 16 January 2014

Academic Editor: Yue Wu

Copyright © 2014 Rok Kreslin et al. This is an open access article distributed under the Creative Commons Attribution License, which permits unrestricted use, distribution, and reproduction in any medium, provided the original work is properly cited.

Computer vision algorithms that use color information require color constant images to operate correctly. Color constancy of the images is usually achieved in two steps: first the illuminant is detected and then image is transformed with the chromatic adaptation transform (CAT). Existing CAT methods use a single transformation matrix for all the colors of the input image. The method proposed in this paper requires multiple corresponding color pairs between source and target illuminants given by patches of the Macbeth color checker. It uses Delaunay triangulation to divide the color gamut of the input image into small triangles. Each color of the input image is associated with the triangle containing the color point and transformed with a full linear model associated with the triangle. Full linear model is used because diagonal models are known to be inaccurate if channel color matching functions do not have narrow peaks. Objective evaluation showed that the proposed method outperforms existing CAT methods by more than 21%; that is, it performs statistically significantly better than other existing methods.

1. Introduction

One of the pillars of color science is the illuminant of the image being treated. Many real-life applications in the field of computer vision require images that are invariant to the illuminant changes. In [1] authors discuss a problem of the fluorescent lamp spectral distribution change over time in their computer vision system for classifying marble plates. Face detectors [2, 3] and face extractors [4] use predefined skin colors to segment the image. These colors accurately present skin tones only on images with standard illumination. Color- and texture-based image search [5] also requires images to be described with illuminant invariant descriptors.

The mechanism of human vision system that takes care of the illuminant invariance is called color constancy [6]. In digital world it is usually modelled as a two-step process consisting of illuminant estimation and image transformation [7]. This paper discusses the second step of the process, that is, image transformation.

Image transformations are done with chromatic adaptation transforms (CATs). The conversion from one illuminant

to a different one has mostly been handled by using single diagonal von Kries-like transformation [8] for all the colors in the gamut of the input image. The main reason for using a single diagonal model is the fact that usually only one corresponding color pair under two different illuminants is known (i.e., source and target illuminants); thus there is not enough information to construct more complex models. But if there are many known corresponding color pairs, there is no need to limit ourselves to one diagonal transformation; instead we can use a higher number of more complex transformations.

Diagonal von Kries like transformations scale color channels independently. Whether or not human color constancy operates in the same way is beyond the scope of this paper. But it has been shown [9, 10] that diagonal von Kries like transformations do not accurately model chromatic adaptation if color channels are not independent of each other; that is, channel color matching functions have wide peaks. Sensor sharpening [11] has been used to derive new color matching functions with narrow peaks but some correlation

between different color channels still remains even after the sharpening process. Full linear transformations can be used to account for the correlation between different color channels.

The method proposed in this paper uses Delaunay triangulation and Macbeth color checker to divide the color gamut of the input image and it constructs one full linear transformation for each triangle of the divided color gamut; that is, each color in the input image is transformed with the matrix of the triangle that contains the color. It is meant to be used primarily as a preprocessing step of other computer vision algorithms operating with color information.

Similar approaches have been used to transform colors from camera color space to device-independent color space. It should be noted that our approach addresses the chromatic adaptation and assumes that colors have already been transformed from camera to device-independent color space. Granger [12] divided color space based on the hue values of reference color points and calculated transformation matrix for each one of the subspaces. Andersen and Hardeberg [13] used patches of the Macbeth color checker to divide color space and associated each subspace with linear transformation that preserves neutral colors and hue planes. Both of the approaches use two-dimensional chromaticity space to find subspace that contains specific color, but actual transformation is done using all three channels of the original color space. Our approach differs from that in [12, 13] by defining a new way of dividing color space using Delaunay triangulation and using chromaticity space both to find subspace and transform color points.

The rest of the paper is organised as follows. Section 2 describes the problem and related work. Section 3 provides the description of the new method. Section 4 gives experimental evaluation of the new method. Finally, conclusions are drawn in Section 5.

2. Problem and Related Work

Chromatic adaptation is the ability of the human visual system to adjust to illumination changes and preserve color appearance of the objects [14]. It allows us to see stable colors of the objects illuminated by a wide range of different illuminations. Chromatic adaptation transforms (CATs) are methods used in digital imaging and color science to model the described mechanism of the human visual system. They provide a means to transform color values under a source illumination into color values under a target illumination.

A standard model to compute transformation from one illumination to another one is diagonal von Kries like adaptation model [8]. If (R, G, B) denotes color value under source illumination, then model states that we can model the same color value under target illumination as

$$\begin{bmatrix} R' \\ G' \\ B' \end{bmatrix} = \begin{bmatrix} c_R & 0 & 0 \\ 0 & c_G & 0 \\ 0 & 0 & c_B \end{bmatrix} \begin{bmatrix} R \\ G \\ B \end{bmatrix}, \quad (1)$$

where c_R , c_G , and c_B represent scaling coefficients for color channels. These scaling coefficients are most often the ratios

of target illumination (R_t, G_t, B_t) and source illumination (R_s, G_s, B_s) ; that is, $c_R = R_t/R_s$, $c_G = G_t/G_s$, and $c_B = B_t/B_s$. However, different CATs differ in the color space in which this scaling takes place.

Obvious choice is the color space in which image is initially described, such as *sRGB* color space. This process is simple as no additional transformations of the color spaces are required. Other commonly used color spaces are derived as linear transformations of the *XYZ* space [15]. The process of deriving these linear transformations of the *XYZ* space is called sensor sharpening [11]. Color matching functions of the derived color spaces tend to have sharper, narrower peaks, thus they support better the von Kries like models. The basic model for transforming color values in derived color spaces is as follows.

- (1) (R, G, B) value is transformed into (X, Y, Z) value.
- (2) (X, Y, Z) value is transformed using

$$\begin{bmatrix} X' \\ Y' \\ Z' \end{bmatrix} = \mathbf{M}^{-1} \cdot \begin{bmatrix} c_R & 0 & 0 \\ 0 & c_G & 0 \\ 0 & 0 & c_B \end{bmatrix} \cdot \mathbf{M} \cdot \begin{bmatrix} X \\ Y \\ Z \end{bmatrix}. \quad (2)$$

- (3) (X', Y', Z') value is transformed back to (R', G', B') value.

Some commonly used transformations of the *XYZ* color space, \mathbf{M} , are as follows.

- (i) *XYZ*: \mathbf{M}_{XYZ} is the identity matrix in (3). This method's performance is poor [16]:

$$\mathbf{M}_{XYZ} = \begin{bmatrix} 1 & 0 & 1 \\ 0 & 1 & 0 \\ 0 & 0 & 1 \end{bmatrix}. \quad (3)$$

- (ii) *Bradford*: a commonly used transformation derived by comparing 58 samples of color wool under illuminants D65 and A [17]. At the beginning this transformation was nonlinear in the blue channel, but this nonlinearity was eliminated later. Consider

$$\mathbf{M}_{Bradford} = \begin{bmatrix} 0.8951 & 0.2664 & -0.1614 \\ -0.7502 & 1.7135 & 0.0367 \\ 0.0389 & -0.0685 & 1.0296 \end{bmatrix}. \quad (4)$$

- (iii) *Sharp*: a widely used newer transformation derived from the Bradford transform [18]. It has more narrow peaks of color basis functions than the Bradford color space; thus it supports better von Kries like model. Consider

$$\mathbf{M}_{Sharp} = \begin{bmatrix} 1.2694 & -0.0988 & -0.1706 \\ -0.8364 & 1.8006 & 0.0357 \\ 0.0297 & -0.0315 & 1.0018 \end{bmatrix}. \quad (5)$$

- (iv) *CMCCAT2000*: simplified *CMCCAT2000* [19] is the successor of the complex *CMCCAT97* transformation [20], which was also derived from the Bradford transformation. *CMCCAT2000* also allows modelling of

the partial adaptation of the observer, but partial adaptation is not considered in this paper because we assume a fully adapted observer. Consider

$$\mathbf{M}_{\text{CMCCAT2000}} = \begin{bmatrix} 0.7982 & 0.3389 & -0.1371 \\ -0.5918 & 1.5512 & 0.0406 \\ 0.0008 & 0.239 & 0.9753 \end{bmatrix}. \quad (6)$$

All of the described transformations use the diagonal von Kries like model to model illuminant change. But it has been shown [9, 10] that diagonal model is not accurate if color channels are correlated. Even after color channels are transformed using sensor sharpening there is still some correlation left. We can model the correlation using full linear model instead of the diagonal model. The reason why usually the full linear model is not used is that there is not enough information available to determine the coefficients, in particular, if we only know the values of the illuminants. But if we have more color correspondence pairs between two illuminations, there is no need to limit our methods to the diagonal model. Instead we can use full linear model that also captures correlations between color channels.

3. Proposed Method

The algorithm proposed in this paper is based on the assumption that color points whose chromaticity values are close together in the color gamut of the source illumination should warp smoothly to a new color gamut of the target illumination. In order to change the illuminant of any color point, the color gamut is divided into smaller regions according to some reference points, and the transformation to be applied to each region is computed. That is, the objective is to obtain the transformation matrix to be applied to each region in the source color gamut. Our method is suitable for controlled applicative environment, because it assumes that both source and target illuminations are known and that the Macbeth color checker is present in the input image, or color values of the patches of the Macbeth color checker captured under the illuminant of the input image are known.

The following subsections explain our transformation between the source and the target color gamut, outline the Delaunay triangulation used to divide the color gamut into smaller regions, and finally describe the proposed CAT method to change the illuminant.

3.1. Calculation of the Transformation Matrices between Different Color Gamuts. The function of transformation to be applied for changing the illuminant can be obtained if some reference points are known in the source color gamut and their transformations in the target color gamut are known as well. We describe these reference points in chromatic rg space. The reason why we are using the chromatic rg model instead of the native RGB model is that we want similar colors, ignoring intensity values, to be transformed with the same transformation matrix.

The following equations system in (7) is the mathematical relation between one chromatic point in the source color

gamut $X(x, y)$ and the target color gamut $U(u, v)$. This relation can be linear, quadratic, cubic, and so forth, depending on the value of k . The quantities a and b are unknown factors that can be solved if several points in the source color gamut and their transformation in the target color gamut are known. Consider

$$u = \sum_k \sum_{i=0}^k a_{(k(k+1)+2i)/2} x^{k-i} y^i, \quad (7)$$

$$v = \sum_k \sum_{i=0}^k b_{(k(k+1)+2i)/2} x^{k-i} y^i.$$

Any point within the source color gamut $X(x, y)$ can be transformed into the corresponding point of the target color gamut $U(u, v)$ by using the relation in (7).

If a linear relation ($k = 1$) is considered, then the system in (7) becomes

$$u = a_0 + a_1 \cdot x + a_2 \cdot y, \quad (8)$$

$$v = b_0 + b_1 \cdot x + b_2 \cdot y$$

or in matrix form

$$\mathbf{U} = \mathbf{A} \cdot \mathbf{Y}, \quad (9)$$

where

$$\mathbf{U} = \begin{bmatrix} u \\ v \end{bmatrix}, \quad (10)$$

$$\mathbf{A} = \begin{bmatrix} a_0 & a_1 & a_2 \\ b_0 & b_1 & b_2 \end{bmatrix}, \quad (11)$$

$$\mathbf{Y} = \begin{bmatrix} 1 \\ x \\ y \end{bmatrix}. \quad (12)$$

In order to calculate the unknown factors in \mathbf{A} : a_j and b_j for $j = 0, 1, 2$ as there are six unknown factors and two equations, it is necessary to know at least three points in the source color gamut and their transformations in the target color gamut. If we had chosen a higher order relation ($k > 1$) more correspondence points would have to be known.

The known three points in the source color gamut $X_l(x_l, y_l)$ for $l = 1, 2, 3$, describe a triangle. They can be arranged in matrix form as

$$\mathbf{S} = \begin{bmatrix} 1 & 1 & 1 \\ x_1 & x_2 & x_3 \\ y_1 & y_2 & y_3 \end{bmatrix}. \quad (13)$$

And the known three points of the transformed triangle in the target color gamut $U_l(u_l, v_l)$, for $l = 1, 2, 3$, can be arranged in matrix form as

$$\mathbf{T} = \begin{bmatrix} u_1 & u_2 & u_3 \\ v_1 & v_2 & v_3 \end{bmatrix}. \quad (14)$$

The equations system to be solved in order to compute the unknown factors in \mathbf{A} is

$$\mathbf{T} = \mathbf{A} \cdot \mathbf{S}. \quad (15)$$

And the solution to this system is

$$\mathbf{A} = \mathbf{T} \cdot \mathbf{S}^{-1}, \quad (16)$$

where \mathbf{S}^{-1} can be computed by means of a singular values decomposition (SVD) [21].

Transformation matrix \mathbf{A} differs from diagonal models used by other CAT methods by also capturing the relations between separate color channels; thus it is more accurate if color channels are correlated.

Once the transformation matrix \mathbf{A} is known, it is possible to transform any point within the triangle defined by the known reference three points in the source color gamut to the target color gamut by using (9). The smaller the triangle in the source color gamut, the more accurate the transformation will be for the points inside the triangle. The transformation is completely accurate when transforming vertices of the triangle, because they have direct mappings from source to target illuminant. So if we reduce the size of the triangle, color points that lie inside it become more similar to the vertices of the triangle which have direct mappings defined. This is the reason why it is desirable to divide the color gamut into the smaller possible triangles according to the reference points known in both color gamuts. The method explained in the following subsection is used to obtain the biggest number of nonoverlapping triangles given a number of reference points.

3.2. Delaunay Triangulation. Delaunay triangulation [22] is a well-known method in the field of mesh generation due to its optimality properties. In the plane or the 2D case, the Delaunay triangulation $\text{Del}(P)$ of a set of n points $P = \{p_i\}$, for $i = 1, \dots, n$ in \mathbb{R}^2 , is a collection of triangles $\text{Tr}(p_j, p_k, p_l)$, such that no point in P is inside the circumcircle of any triangle in $\text{Del}(P)$.

For a set of n points, the number of triangles produced by triangulation depends on the spatial distribution of the points. If b is a number of points forming convex hull of the points, then the number of triangles N is at most

$$N = 2n - 2 - b. \quad (17)$$

Degeneration of N can occur, if all the points lie on the same line. Then there are no triangles defined. But considering the domain of color transformation this is unlikely to happen.

The Delaunay triangulation will be used to divide the color gamut into smaller regions (triangles) according to the reference points known in both color gamuts. We should mention that the resulting triangulation is not unique when four or more points lie on the same circle. Further research will be needed to study the effects of different possible triangulations of the same color points.

3.3. Illuminant Change Method. Once the formula for the transformation matrix for a number of reference points is known and the way to divide the color gamut into smaller triangles has been established, then, in order to perform the illuminant change, the following steps are to be carried out.

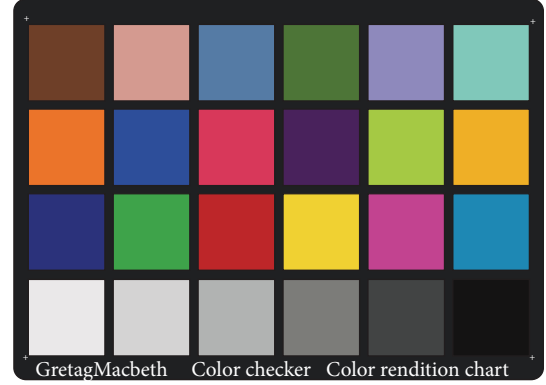


FIGURE 1: Macbeth color checker. Color patches have spectral reflectance intended to mimic those of natural objects such as human skin, foliage, and flowers.

- (1) The Macbeth color checker (Figure 1), present in the input image, is used as the reference to achieve color constancy. Delaunay triangulation is done to divide the original color gamut by using the mean (r, g) values of the 24 patches of the Macbeth color checker. Figure 2 shows triangulations of the color gamut for two different illuminants.
- (2) Once the triangles are defined, the transformation matrix \mathbf{A} of each triangle in the source color gamut is computed using (16). Thus, there are as many matrices \mathbf{A} as triangles.
- (3) For each point of the source color gamut that needs to be transformed, the transformation in the target color gamut is obtained with (9), that is, by applying the transformation matrix \mathbf{A} of the triangle that contains the point. First, RGB color point $C = (R, G, B)$ is converted to rg point $C_{rg} = (r, g)$. Then the triangle containing point C_{rg} is found and the point is transformed using the transformation matrix \mathbf{A} of the triangle containing it, resulting in a new rg point $C'_{rg} = (r', g')$. The new RGB point $C' = (R', G', B')$ is obtained using

$$\begin{aligned} R' &= r' \cdot (R + G + B), \\ G' &= g' \cdot (R + G + B), \end{aligned} \quad (18)$$

$$B' = (1 - r' - g') \cdot (R + G + B),$$

preserving the sum of channel intensities before and after the transformation.

As far as the points in the source color gamut are inside one of the triangles obtained by Delaunay triangulation using the patches of the Macbeth color checker, the resulting transformation using the matrices \mathbf{A} is valid. Nevertheless, the triangles defined by the patches of the Macbeth color checker do not cover the whole rg chromaticity space. Hence, problems appear when transforming a point in the source color gamut that is outside any triangle, as the illuminant is not corrected properly for these points.

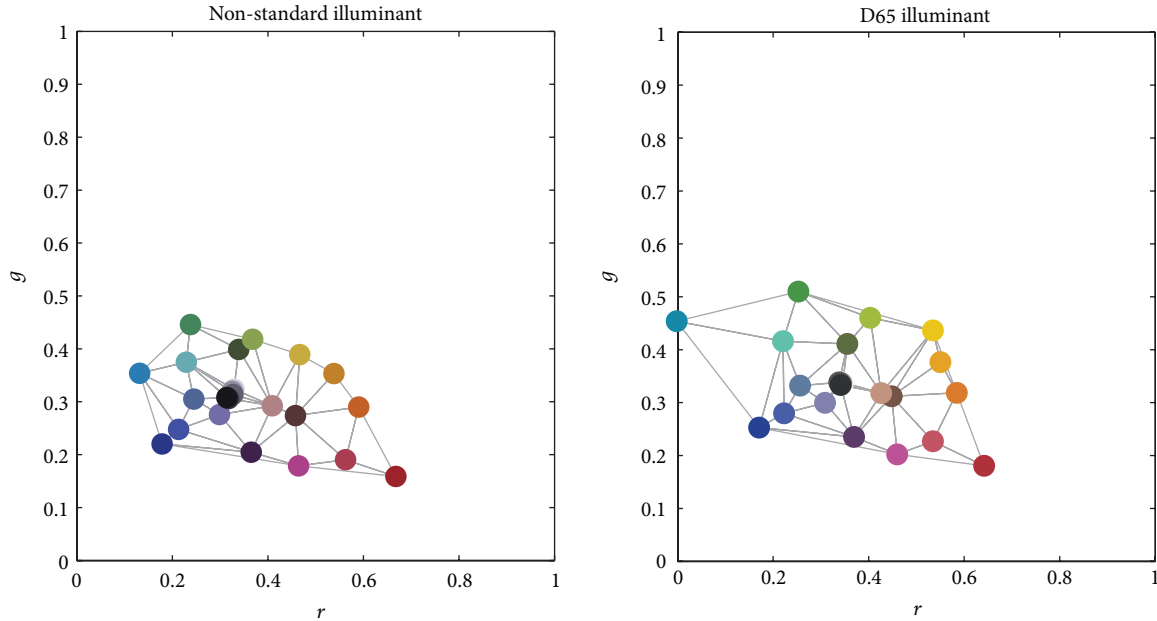


FIGURE 2: Triangulations of the color gamut for two different illuminants. The triangulations are shown in the rg chromaticity space with the point colors being the same as patch colors of the Macbeth color checker captured under the same illuminant.

In order to handle these points outside the triangles defined by the patches of the Macbeth color checker, we consider the vertices of the whole rg chromaticity space as reference points together with the patches of the Macbeth color checker. The vertices of the rg chromaticity space in (r, g) are $(0, 0)$, $(1, 0)$, and $(0, 1)$. Note that point $(1, 1)$ is not the vertex of the rg chromaticity space. By the definition of rg space, sum of both components cannot be greater than one [23]. The transformed points of these vertices for any illuminant are the same points, as the limits of the rg space are fixed and if an overflow occurs the obtained point is saturated to the limit.

The proposed method has one restriction. The triangles defined by the values of the Macbeth color checker under a source illuminant may cross or fold over each other when transformed to a target illuminant. Likewise the transformation of the arbitrary color point within certain triangle under the source illuminant does not guarantee that transformed color point will be contained in the corresponding triangle under the target illuminant. Because of these properties the inverse transformation cannot be defined with our proposed method. However exact inverse transformation is rarely needed in the applicative environment described at the beginning of the paper.

4. Experimental Evaluation

To objectively evaluate the performance of our method, we used color-checker image database [24]. It contains 568 images captured under different artificial and natural illuminations. All the images in the database contain a Macbeth color checker, which is an assumption our method implies. The coordinates of the patches of a Macbeth color checker

are available on the website of the image database [25], from which we also obtained illuminant estimates used by other CAT methods. To speed up evaluation, all transformations were made on the downscaled versions of images (813×541) also available on the website of the image database.

All the images in the database are described in $sRGB$ color space with gamma correction applied. CAT methods assume that linear images are given, so inverse gamma correction was applied to produce linear images [26]:

$$Ch_{lin} = \begin{cases} Ch_{sRGB}, & Ch_{sRGB} \leq 0.04045, \\ \left(\frac{Ch_{sRGB} + 0.055}{1.055} \right)^{2.4}, & Ch_{sRGB} > 0.04045, \end{cases} \quad (19)$$

where Ch_{lin} represents the linearized $sRGB$ value of the color channel $Ch = \{R, G, B\}$.

To evaluate the performance of our method, we transformed the color patches of the Macbeth color checker on each of the 568 images and compared the transformed values with the values of the patches of the Macbeth color checker captured under standard D65 illuminant [27]. To ensure that our method is not in a privileged position compared to other CAT methods we took two precautions as follows.

- (i) The color value of the patch currently being transformed cannot be used when triangulating the source color gamut and calculating transformation matrices. Otherwise it is the part of the transformation matrix.
- (ii) Chromaticity values of the patches in the last row of the Macbeth color checker are very similar. That is the reason why we ignore all the patches of the Macbeth color checker in the last row except the third patch from the left. One could also choose any other patch from the last row.

Performance of our method is evaluated using the following steps.

- (1) Color values of the patches of the Macbeth color checker in the input image are calculated.
- (2) All the color patches from the last row of the Macbeth color checker except the third one from the left are discarded.
- (3) To each of the remaining 19 color patches we apply the following:
 - (a) From the set of color values we temporarily remove the value of the patch currently being transformed.
 - (b) Delaunay triangulation is applied.
 - (c) We find the triangle containing the color value of the patch currently being transformed.
 - (d) We use the transformation matrix of the triangle to transform the patch value.
 - (e) Difference between the transformed value and the reference value of the patch under standard D65 illumination is computed.
- (4) The error of the single image is equal to the mean difference of all the transformed color patches.

Performance of other CAT methods (sRGB, XYZ, Bradford, Sharp, and CMCCAT2000) is evaluated similarly as follows.

- (1) Color values of the patches of the Macbeth color checker in the input image are calculated.
- (2) All the color patches from the last row of the Macbeth color checker except the third one from the left are discarded.
- (3) Color values of the 19 remaining patches are transformed using the CAT method. Differences between the transformed value and the reference value of the patch under standard D65 illumination are computed.
- (4) The error of the single image is equal to the mean difference of all the transformed color patches.

To compute the difference between the values of transformed patches and reference patches, perceptual euclidian distance (PED) is used:

$$\text{PED}(e_t, e_r) = \sqrt{w_R(R_t R_r)^2 + w_G(G_t G_r)^2 + w_B(B_t B_r)^2}, \quad (20)$$

where $e_t = (R_t, G_t, B_t)$ represents normalised transformed values, $e_r = (R_r, G_r, B_r)$ represents normalised reference values, and w_R , w_G , and w_B represent weight coefficients. It was shown that PED with weight coefficients $w_R = 0.26$, $w_G = 0.70$, and $w_B = 0.04$ finds its roots in human vision and correlates significantly higher than any other distance measures [28].

Mean PED errors of different methods are shown in Table 1. Performance of the evaluated methods is similar.

TABLE 1: Comparison of mean PED error of different CAT methods.

Method	PED	Rank
sRGB	0.047	3.
XYZ	0.048	4.
Bradford	0.047	3.
Sharp	0.046	2.
CMCCAT2000	0.046	2.
DT-based	0.038	1.

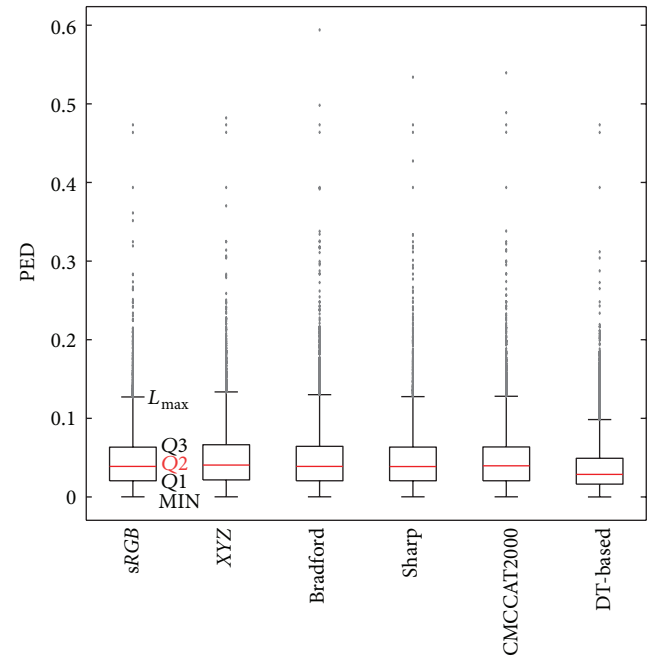


FIGURE 3: Boxplots summarizing PED errors of different CAT methods. First boxplot from the left has labels showing five statistics.

The only method that stands out is our proposed method (DT-based) that has significantly lower mean PED error than the other methods. The second best methods (Sharp and CMCCAT2000) have more than 21% greater mean PED error. This is an encouraging result for the use of the proposed method.

Figure 3 shows box plots of PED errors for different CAT methods. Box plot is a tool for visualisation of the data distribution [7] or in our case a tool for the visualization of the distribution of the PED errors. It visualizes five statistics: minimal error MIN, lower quartile Q1, median error Q2, upper quartile Q3, and limited maximal error LMAX, which is not greater than $Q3 + 1.5(Q3 - Q1)$. Errors greater than LMAX are shown as outliers.

Although the evaluated CAT methods have similar box plots, it can be clearly seen that our proposed method has lower Q1, Q2, Q3, and LMAX (MIN = 0 for all the methods).

TABLE 2: Results of the Mann-Whitney U test comparing median PED errors of different CAT methods.

	<i>sRGB</i>	<i>XYZ</i>	Bradford	Sharp	CMCCAT2000	DT-based
<i>sRGB</i>		0	0	0	0	-1
<i>XYZ</i>	0		0	-1	0	-1
Bradford	0	0		0	0	-1
Sharp	0	1	0		0	-1
CMCCAT2000	0	0	0	0		-1
DT-based	1	1	1	1	1	

A positive value (1) at location (i, j) indicates that the median PED error of the methods i is significantly lower than the median PED error of method j at the 95% confidence level. A negative value (-1) indicates the opposite, and a zero (0) indicates that there is no significant difference between the two methods.

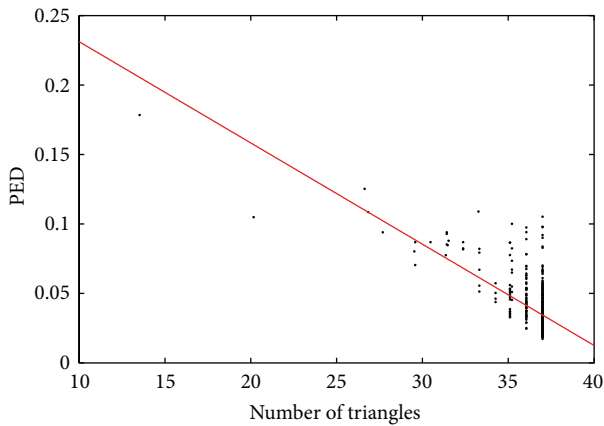


FIGURE 4: Correlation between the number of triangles and PED error. Dots represent mean number of triangles produced by triangulation and mean PED error on every image in the database. Red line is used to quickly visualize linear least-square trend of the data and it is not meant to be an accurate model of the relation.

This tells us that most PED errors of our proposed method are lower than corresponding PED errors produced by other CAT methods.

To verify that our proposed method performs better than other existing methods, we conducted statistical test as suggested in [7]. Mann-Whitney U test [29] is a nonparametric statistical test that does not imply normal distribution of underlying values. It is used to show whether median values of two samples are statistically significantly different or not. Two values are significantly different if, given the confidential level, we can conclude that the observation is not the result of a random process [30].

We compared median PED errors of each pair of evaluated methods and checked if two values are significantly different. Results are presented in Table 2. Median PED errors of methods *sRGB*, *XYZ*, Bradford, Sharp, and CMCCAT2000 are not significantly different, except for the significantly lower error of the Sharp transform compared to the *XYZ* transform. The proposed method has significantly lower median PED error compared to all of the other methods. We

conclude that under the experimental conditions presented in this paper our method significantly outperforms other existing methods.

Surprisingly the *sRGB* method performs similarly to the methods using sensor sharpening. Some authors [11, 15] state that methods based on *RGB* color model do not perform as well as sensor sharpened methods. We showed differently.

Figure 4, showing correlation between the number of triangles produced by triangulation and mean PED error, confirms that the number of triangles has significant influence on the performance of the proposed method. A higher number of triangles imply lower triangle areas in which the transformation matrix more accurately transforms part of the original color gamut. A higher number of known corresponding points between the source and the target color gamut results in more accurate transformation matrices and better method performance.

Figure 5 shows random image from the color-checker image database transformed with conventional *XYZ* method and our proposed method. Original image was shot under artificial light and has strong color cast. Both transformations greatly reduce this color cast when transforming to D65 illuminant. By closer examining image transformed with *XYZ* method (zoom in on the image) you can still see yellow color cast on the ground. On the image transformed with our method this color cast is completely removed.

5. Conclusion

This paper tackles the problem of changing the illuminant of an image and proposes a new method to increase the accuracy of the transform. The proposed method uses Delaunay triangulation and linear transformations in order to transform the input image. The only assumption it relies on is that the color values of the patches of the Macbeth color checker captured under the same illuminant as the input image must be known; that is, the Macbeth color checker must be captured under the same illuminant but not necessarily in the same image.

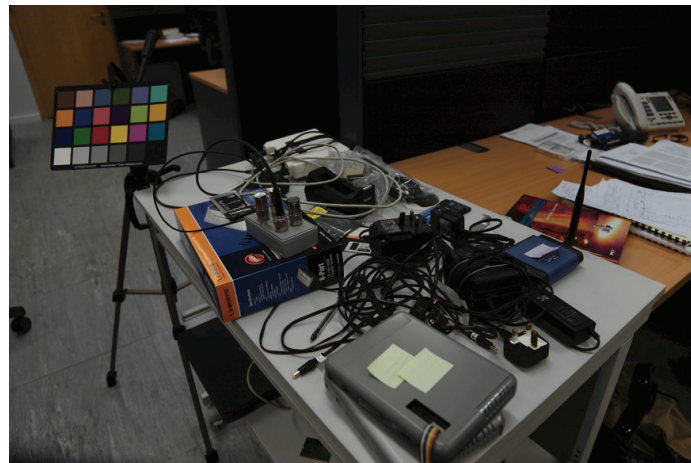
Objective comparison shows that our method performs significantly better than other state-of-the-art methods.



(a)



(b)



(c)

FIGURE 5: Visual comparison of original image (a), image transformed with XYZ transform (b), and image transformed with our method (c). Target illuminant is D65.

Conflict of Interests

The authors declare that there is no conflict of interests regarding the publication of this paper.

Acknowledgment

This work was supported by the Ministry of Science of Republic of Slovenia, Program Computer Vision.

References

- [1] L. G. Corzo, J. A. Peñaranda, and P. Peer, "Estimation of a fluorescent lamp spectral distribution for color image in machine vision," *Machine Vision and Applications*, vol. 16, no. 5, pp. 306–311, 2005.
- [2] J. Kovac, P. Peer, and F. Solina, "Human skin color clustering for face detection," in *EUROCON, Computer As A Tool*, vol. 2, pp. 144–148, 2003.
- [3] S. Liu, W. Fu, W. Zhao, J. Zhou, and Q. Li, "A novel fusion method by static and moving facial capture," *Mathematical Problems in Engineering*, vol. 2013, Article ID 503924, 6 pages, 2013.
- [4] X. Li and X. Cao, "A simple framework for face photo-sketch synthesis," *Mathematical Problems in Engineering*, vol. 2012, Article ID 910719, 19 pages, 2012.
- [5] Y.-K. Chan, M.-H. Tsai, J.-S. Wang, S.-W. Guo, and J.-L. Wu, "Color-texture-based image retrieval system using Gaussian Markov random field model," *Mathematical Problems in Engineering*, vol. 2009, Article ID 410243, 17 pages, 2009.
- [6] M. D. Fairchild, *Color Appearance Models*, John Wiley & Sons, 2005.
- [7] J. van de Weijer, T. Gevers, and A. Gijsenij, "Edge-based color constancy," *IEEE Transactions on Image Processing*, vol. 16, no. 9, pp. 2207–2214, 2007.
- [8] J. von Kries, "Influence of adaptation on the effects produced by luminous stimuli," in *Sources of Color Science*, D. L. MacAdam, Ed., pp. 109–119, MIT Press, Cambridge, Mass, USA, 1970.
- [9] G. West and M. H. Brill, "Necessary and sufficient conditions for Von Kries chromatic adaptation to give color constancy," *Journal of Mathematical Biology*, vol. 15, no. 2, pp. 249–258, 1982.
- [10] D. A. Forsyth, "A novel algorithm for color constancy," *International Journal of Computer Vision*, vol. 5, no. 1, pp. 5–35, 1990.
- [11] K. Barnard, F. Ciurea, and B. Funt, "Sensor sharpening for computational color constancy," *Journal of the Optical Society of America A*, vol. 18, no. 11, pp. 2728–2743, 2001.
- [12] E. M. Granger, "Scanner calibration technique," US Patent 6 134 029, October 17, 2000.
- [13] C. F. Andersen and J. Y. Hardeberg, "Colorimetric characterization of digital cameras preserving hue planes," *Color and Imaging Conference*, vol. 13, no. 1, pp. 141–146, 2005.
- [14] M. Ebner, *Color Constancy*, John Wiley & Sons, New York, NY, USA, 2007.
- [15] S. Süsstrunk, J. Holm, and G. D. Finlayson, "Chromatic adaptation performance of different RGB sensors," in *Proceedings of the IS&T/SPIE Electronic Imaging*, pp. 172–183, January 2001.
- [16] J. A. S. Viggiano, "Comparison of the accuracy of different whitebalancing options as quantified by their color constancy," in *Sensors and Camera Systems For Scientific, Industrial, and Digital Photography Applications*, 2004.
- [17] R. W. G. Hunt and M. R. Pointer, *Metamerism and Colour Constancy*, John Wiley and Sons, 2011.
- [18] G. D. Finlayson and S. Süsstrunk, "Performance of a chromatic adaptation transform based on spectral sharpening," in *Proceedings of the 8th IS and T/SID Color Imaging Conference (CIC '00)*, pp. 49–55, November 2000.
- [19] H. Li, M. Ronnier Luo, B. Rigg, and R. W. G. Hunt, "CMC 2000 chromatic adaptation transform: CMCCAT2000," *Color Research and Application*, vol. 27, no. 1, pp. 49–58, 2002.
- [20] C. Li, M. R. Luo, and B. Rigg, "Simplification of the CMC-CAT97," in *Proceedings of the 8th IS and T/SID Color Imaging Conference (CIC '00)*, pp. 56–60, November 2000.
- [21] A. Ben-Israel and T. N. E. Greville, *Generalized Inverses: Theory and Applications*, Springer, 2003.
- [22] B. Delaunay, "Sur la sphre vide, izvestia akademii nauk sssr," *Otdelenie Matematicheskikh I Estestvennykh Nauk*, vol. 6, no. 7, pp. 793–800, 1934.
- [23] C. Balkenius and B. Johansson, "Finding colored objects in a scene," Tech. Rep., LUCS Minor 12, Lund University Cognitive Science (LUCS), Lund, Sweden, 2007.
- [24] P. V. Gehler, C. Rother, A. Blake, T. Minka, and T. Sharp, "Bayesian color constancy revisited," in *Proceedings of the 26th IEEE Conference on Computer Vision and Pattern Recognition (CVPR' 08)*, June 2008.
- [25] P. Gehler, 2008, Bayesian Color Constancy Revisited, <http://people.kyb.tuebingen.mpg.de/pgehler/colour/index.html>.
- [26] IEC multimedia systems and equipment—colour measurement and management—part 2-1: Colour management—default rgb colour space —srgb, Standard IEC 61966-2-1: 1999.
- [27] D. Pascale, 2006, RGB coordinates of the Macbeth ColorChecker, <http://www.babelcolor.com/download/RGB>.
- [28] A. Gijsenij, T. Gevers, and M. P. Lucassen, "A perceptual comparison of distance measures for color constancy algorithms," in *Proceedings of the European Conference on Computer Vision (ECCV' 08)*, pp. 208–221, 2008.
- [29] H. B. Mann and D. R. Whitney, "On a test of whether one of two random variables is stochastically larger than the other," *The Annals of Mathematical Statistics*, vol. 18, no. 1, pp. 50–60, 1947.
- [30] R. Fisher, *Statistical Methods For Research Workers*, Cosmo study guides, Cosmo Publications, 1925.

Research Article

Minimum Error Thresholding Segmentation Algorithm Based on 3D Grayscale Histogram

Jin Liu,^{1,2} Jianhong Zheng,² Quanhua Tang,¹ and Weidong Jin³

¹ School of Software, Jiangxi Normal University, Nanchang 330022, China

² Department of Computer Application, Faculty of Information Science and Technology, Southwest Jiaotong University, Chengdu 610031, China

³ Department of Electronic & Information Engineering, Faculty of Electrical Engineering, Southwest Jiaotong University, Chengdu 610031, China

Correspondence should be addressed to Quanhua Tang; quanhua3408@163.com

Received 25 October 2013; Revised 5 December 2013; Accepted 9 December 2013; Published 14 January 2014

Academic Editor: Su-Qun Cao

Copyright © 2014 Jin Liu et al. This is an open access article distributed under the Creative Commons Attribution License, which permits unrestricted use, distribution, and reproduction in any medium, provided the original work is properly cited.

Threshold segmentation is a very important technique. The existing threshold algorithms do not work efficiently for noisy grayscale images. This paper proposes a novel algorithm called three-dimensional minimum error thresholding (3D-MET), which is used to solve the problem. The proposed approach is implemented by an optimal threshold discriminant based on the relative entropy theory and the 3D histogram. The histogram is comprised of gray distribution information of pixels and relevant information of neighboring pixels in an image. Moreover, a fast recursive method is proposed to reduce the time complexity of 3D-MET from $O(L^6)$ to $O(L^3)$, where L stands for gray levels. Experimental results demonstrate that the proposed approach can provide superior segmentation performance compared to other methods for gray image segmentation.

1. Introduction

Image segmentation is an essential procedure to analyze the image structure as other processing steps heavily depend on its results, and a wide variety of segmentation techniques have been reported in the last two decades. Some of its applications relate to many fields, such as medical imaging [1, 2], document analysis [3, 4], object recognition [5], and SAR segmentation and quality inspection of materials [6].

Image thresholding based on gray level histogram information is an important technique for image segmentation. Most techniques can be roughly categorized into two groups: global thresholding and local thresholding. The former means the process of a whole image with only one threshold, while the latter means that one separates an image into several subimages and then handles each subimage with a selected threshold. Global thresholding is a nonparametric, unsupervised, and self-adapting method. Although the method appears to be simplistic, it is very important and fundamental with wide applicability [7–9]. The classic global thresholding methods are maximum between-cluster

variance (Otsu) [10], minimum error thresholding (MET) [11], and maximum entropy method [12]. In [11], appropriate thresholds are selected by a minimum error criterion. This criterion is designed to minimize the classification error probability based on the assumption that histograms are governed by a mixture of Gaussian densities. Its essence is to consider image binarization as a Gaussian distribution fitting problem. In [13], a survey over 40 thresholding techniques by Mehmet Sezgin and Bülent Sankur shows that MET is the best performing thresholding algorithm.

Noticeably, all 1D thresholding algorithms only utilize 1D histogram of an image, which only represents the grey-level distribution of the image. Its performance degrades immensely when the difference of grey-level distribution between objects and background is inconspicuous; namely, its segmentation capability significantly degrades when the image is corrupted by strong noise. Therefore many 2D thresholding approaches which employ point pixel information and the local average grey level of the neighbourhood pixels have been proposed in [14–16]. These methods show satisfactory results for Gaussian noise images. However, they

are almost useless if the image is degraded with other types of noise or the mixed noise [17].

Actually, the more information contained in the image can be utilized to obtain a better segmentation. Studies have shown that the mean filter tends to curb the Gaussian noise, and median filter tends to curb the salt-and-pepper noise. Therefore, in this paper we propose a new algorithm called three-dimensional minimum error threshold (3D-MET), which employs point pixel information, the local average grey level, and median gray level of the neighborhood pixels, to cope with the problem of threshold segmentation for mixed noise image. So, here the "3D" refers to 3 parametric dimensions (pixel gray level, area mean gray level, and area median gray level) instead of 3 spacial dimensions, and threshold is applied along each parametric dimension separately. The choice of the thresholds along the three parametric dimensions is made by finding the threshold triplet that globally optimizes a given criterion. The basic idea of the proposed algorithm is to take into consideration more adequately spatial correlation between image pixels and image segmentation so as to reduce the impact of noise.

This paper is organized as follows. In Section 2, the 3D histogram is defined. Section 3 gives a detailed description of the proposed 3D-MET. Section 4 describes the fast recursive method of 3D-MET. The experiment results are discussed in Section 5 and Section 6 gives the concluding remarks of this work.

2. 3D Histogram

Let the pixels of a given image be represented in L gray levels $[0, 1, \dots, L-1]$. The number of pixels at level i is defined by n_i and the total number of pixels by $N = n_1 + n_2 + \dots + n_L$. Now assume the grey level value at coordinate (x, y) in the image is defined by $F(x, y)$. The average gray level and median gray level in $K \times K$ neighborhood of the $F(x, y)$ can be defined by $G(x, y)$ and $H(x, y)$, respectively:

$$G(x, y) = \frac{1}{K \times K} \sum_{i=-(K-1)/2}^{(K-1)/2} \sum_{j=-(K-1)/2}^{(K-1)/2} F(x+i, y+j), \quad (1)$$

$$H(x, y) = \text{Med} \left\{ \sum_{i=-(K-1)/2}^{(K-1)/2} \sum_{j=-(K-1)/2}^{(K-1)/2} F(x+i, y+j) \right\},$$

where K is neighborhood size and usually takes an odd number. Since $0 \leq F(x, y) \leq L-1$, it follows that $0 \leq G(x, y) \leq L-1$, $0 \leq H(x, y) \leq L-1$.

Suppose the frequency of the three-element set (i, j, k) composed of $F(x, y)$, $G(x, y)$, and $H(x, y)$ is f_{ijk} ; then the joint probability density is defined as p_{ijk} :

$$p_{ijk} = \frac{f_{ijk}}{N}, \quad i, j, k = 0, 1, 2, \dots, L-1. \quad (2)$$

The distribution of p_{ijk} can be summarized in a form of 3D histogram. p_{ijk} is defined as the value of one point in 3D histogram, which represents the probability of the (i, j, k) . The domain of the 3D histogram is shown in Figure 1(a).

Assume that the optimal threshold (s, t, q) divided the 3D histogram into eight subblocks, numbered 0 through 7, respectively, as shown in Figures 1(b) and 1(c). Generally, the gray level of pixels within an object and background region is symmetrical. This means that the probability of object and background almost always happens near the main diagonal of 3D histogram, whereas those off-diagonal subblocks contain the distributions of the edges and noise. Therefore, subblocks 0 and 1 denote the background and object, respectively, while the others, numbered 2 through 7, denote edges and noise. Conventionally we can suppose reasonably that object and background regions hold the absolute majority of 3D histogram; that is to say, the probability of off-diagonal subblocks is nearly zero; that is,

$$\sum_B p_{ijk} \approx 0, \quad 0 \leq i, j, k \leq L-1, \quad B = 2, 3, \dots, 7. \quad (3)$$

3. 3D Minimum Error Thresholding (3D-MET)

The 3D histogram defined above can be viewed as an estimate of the probability density function $P'_{i,j,k}$ of the mixture population:

$$P'_{i,j,k} = P_0(s, t, q) p(i, j, k | 0) + P_1(s, t, q) p(i, j, k | 1), \quad (4)$$

where $P_0(s, t, q)$ and $P_1(s, t, q)$ are prior probability of object and background. $p(i, j, k | 0)$ and $p(i, j, k | 1)$ are 3D normally distributed with mean μ_1 , μ_2 , and μ_3 , which satisfy

$$p(i, j, k) = \frac{1}{(2\pi)^{3/2} \sqrt{|\Sigma|}} \times \exp \left[-\frac{1}{2} \begin{pmatrix} i - \mu_1 \\ j - \mu_2 \\ k - \mu_3 \end{pmatrix}^T \Sigma^{-1} \begin{pmatrix} i - \mu_1 \\ j - \mu_2 \\ k - \mu_3 \end{pmatrix} \right], \quad (5)$$

where Σ is the covariance matrix.

Now suppose that we dichotomize the pixels into two classes C_0 and C_1 (background and objects or vice versa) by an optimal threshold (s, t, q) . s , t , and q are the segmentation thresholds corresponding to the original image, the mean filtered image, and the median filtered image, respectively. The probabilities of C_0 and C_1 are given by

$$P_0 = \sum_{i=0}^s \sum_{j=0}^t \sum_{k=0}^q p_{ijk} = P_0(s, t, q), \quad (6)$$

$$P_1 = \sum_{i=s+1}^{l-1} \sum_{j=t+1}^{l-1} \sum_{k=q+1}^{l-1} p_{ijk} = P_1(s, t, q)$$

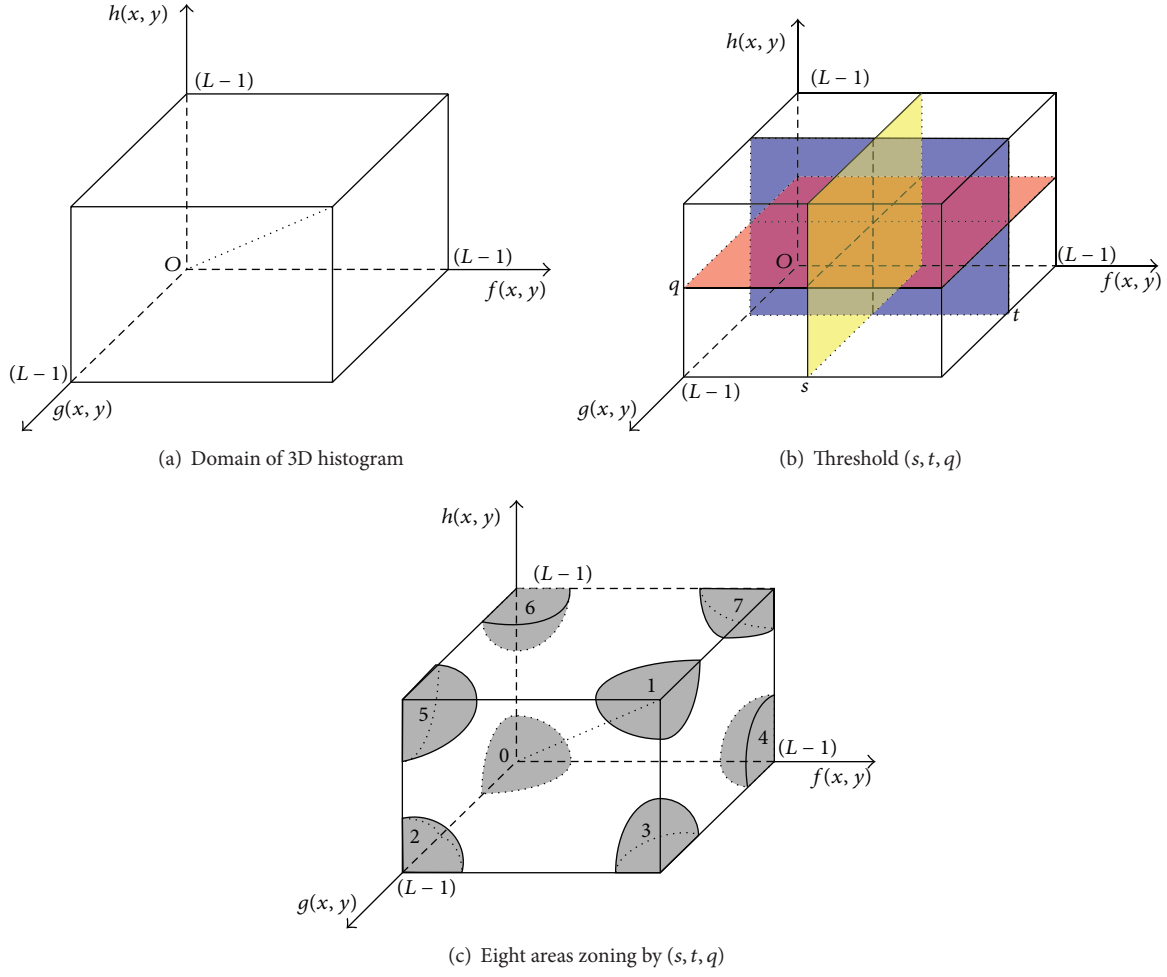


FIGURE 1: Three-dimensional histogram.

and the corresponding class mean levels and variances of C_0 and C_1 are

$$\begin{aligned} \mu_0 &= (\mu_{0i}(s, t, q), \mu_{0j}(s, t, q), \mu_{0k}(s, t, q))^T \\ &= \left(\sum_{i=0}^s \sum_{j=0}^t \sum_{k=0}^q \frac{i p_{ijk}}{P_0}, \sum_{i=0}^s \sum_{j=0}^t \sum_{k=0}^q \frac{j p_{ijk}}{P_0}, \sum_{i=0}^s \sum_{j=0}^t \sum_{k=0}^q \frac{k p_{ijk}}{P_0} \right)^T \end{aligned} \quad (7)$$

$$\begin{aligned} \mu_1 &= (\mu_{1i}(s, t, q), \mu_{1j}(s, t, q), \mu_{1k}(s, t, q))^T \\ &= \left(\sum_{i=s+1}^{L-1} \sum_{j=t+1}^{L-1} \sum_{k=q+1}^{L-1} \frac{i p_{ijk}}{P_1}, \sum_{i=s+1}^{L-1} \sum_{j=t+1}^{L-1} \sum_{k=q+1}^{L-1} \frac{j p_{ijk}}{P_1}, \right. \\ &\quad \left. \sum_{i=s+1}^{L-1} \sum_{j=t+1}^{L-1} \sum_{k=q+1}^{L-1} \frac{k p_{ijk}}{P_1} \right)^T \end{aligned} \quad (8)$$

$$\begin{aligned} \sigma_0^2 &= (\sigma_{0i}^2(s, t, q), \sigma_{0j}^2(s, t, q), \sigma_{0k}^2(s, t, q))^T \\ &= \left(\sum_{i=0}^s \sum_{j=0}^t \sum_{k=0}^q \frac{(i - \mu_{0i})^2 p_{ijk}}{P_0}, \sum_{i=0}^s \sum_{j=0}^t \sum_{k=0}^q \frac{(j - \mu_{0j})^2 p_{ijk}}{P_0}, \right. \\ &\quad \left. \sum_{i=0}^s \sum_{j=0}^t \sum_{k=0}^q \frac{(k - \mu_{0k})^2 p_{ijk}}{P_0} \right)^T \end{aligned} \quad (9)$$

$$\begin{aligned} \sigma_1^2 &= (\sigma_{1i}^2(s, t, q), \sigma_{1j}^2(s, t, q), \sigma_{1k}^2(s, t, q))^T \\ &= \left(\sum_{i=s+1}^{L-1} \sum_{j=t+1}^{L-1} \sum_{k=q+1}^{L-1} \frac{(i - \mu_{1i})^2 p_{ijk}}{P_1}, \right. \\ &\quad \sum_{i=s+1}^{L-1} \sum_{j=t+1}^{L-1} \sum_{k=q+1}^{L-1} \frac{(j - \mu_{1j})^2 p_{ijk}}{P_1}, \\ &\quad \left. \sum_{i=s+1}^{L-1} \sum_{j=t+1}^{L-1} \sum_{k=q+1}^{L-1} \frac{(k - \mu_{1k})^2 p_{ijk}}{P_1} \right)^T \end{aligned} \quad (10)$$

The correlation coefficients of $p(i, j, k | 0)$ and $p(i, j, k | 1)$, respectively, are

$$\rho_0(s, t) = \left(\left(\sum_{i=0}^s \sum_{j=0}^t \sum_{k=0}^q [(i - \mu_{0i}(s, t, q)) \times (j - \mu_{0j}(s, t, q)) p_{ijk}] \right) \times (P_0(s, t, q))^{-1} \right) \times (\sigma_{0i}(s, t, q) \sigma_{0j}(s, t, q))^{-1}, \quad (11)$$

$$\rho_0(s, q) = \left(\left(\sum_{i=0}^s \sum_{j=0}^t \sum_{k=0}^q [(i - \mu_{0i}(s, t, q)) \times (k - \mu_{0k}(s, t, q)) p_{ijk}] \right) \times (P_0(s, t, q))^{-1} \right) \times (\sigma_{0i}(s, t, q) \sigma_{0k}(s, t, q))^{-1}, \quad (12)$$

$$\rho_0(t, q) = \left(\left(\sum_{i=0}^s \sum_{j=0}^t \sum_{k=0}^q [(j - \mu_{0j}(s, t, q)) \times (k - \mu_{0k}(s, t, q)) p_{ijk}] \right) \times (P_0(s, t, q))^{-1} \right) \times (\sigma_{0j}(s, t, q) \sigma_{0k}(s, t, q))^{-1}, \quad (13)$$

$$\rho_1(s, t) = \left(\left(\sum_{i=s+1}^{L-1} \sum_{j=t+1}^{L-1} \sum_{k=q+1}^{L-1} [(i - \mu_{1i}(s, t, q)) \times (j - \mu_{1j}(s, t, q)) p_{ijk}] \right) \times (P_1(s, t, q))^{-1} \right) \times (\sigma_{1i}(s, t, q) \sigma_{1j}(s, t, q))^{-1}, \quad (14)$$

$$\rho_1(s, q) = \left(\left(\sum_{i=s+1}^{L-1} \sum_{j=t+1}^{L-1} \sum_{k=q+1}^{L-1} [(i - \mu_{1i}(s, t, q)) \times (k - \mu_{1k}(s, t, q)) p_{ijk}] \right) \times (P_1(s, t, q))^{-1} \right) \times (\sigma_{1i}(s, t, q) \sigma_{1k}(s, t, q))^{-1}, \quad (15)$$

$$\rho_1(t, q) = \left(\left(\sum_{i=s+1}^{L-1} \sum_{j=t+1}^{L-1} \sum_{k=q+1}^{L-1} [(j - \mu_{1j}(s, t, q)) \times (k - \mu_{1k}(s, t, q)) p_{ijk}] \right) \times (P_1(s, t, q))^{-1} \right) \times (\sigma_{1j}(s, t, q) \sigma_{1k}(s, t, q))^{-1}. \quad (16)$$

The total mean level vector of the 3D histogram is

$$\mu = (\mu_i, \mu_j, \mu_k)^T = \left(\sum_{i=0}^{L-1} \sum_{j=0}^{L-1} \sum_{k=0}^{L-1} i p_{ijk}, \sum_{i=0}^{L-1} \sum_{j=0}^{L-1} \sum_{k=0}^{L-1} j p_{ijk}, \sum_{i=0}^{L-1} \sum_{j=0}^{L-1} \sum_{k=0}^{L-1} k p_{ijk} \right)^T. \quad (17)$$

In the following, we introduce the relative entropy theory proposed in [18], which is used to measure the disparity between two distributions. The smallest value of relative entropy means the least disparity. So, we can use relative entropy to calculate the disparity between 3D histogram p_{ijk} and the mixture probability $P'_{i,j,k}$; that is,

$$R(s, t, q) = \sum_{i=0}^s \sum_{j=0}^t \sum_{k=0}^q p_{ijk} \ln \frac{p_{ijk}}{P_0 p(i, j, k | 0)} + \sum_{i=s+1}^{L-1} \sum_{j=t+1}^{L-1} \sum_{k=q+1}^{L-1} p_{ijk} \ln \frac{p_{ijk}}{P_1 p(i, j, k | 1)}. \quad (18)$$

$R(s, t, q)$ can be simplified and rewritten as $W(s, t, q)$ (see proof of the statement in the appendix), as shown in

$$W(s, t, q) = P_0(s, t, q) \ln \sigma_{0i} \sigma_{0j} \sigma_{0k} + P_1(s, t, q) \ln \sigma_{1i} \sigma_{1j} \sigma_{1k} - P_0(s, t, q) \ln P_0(s, t, q) - P_1(s, t, q) \ln P_1(s, t, q). \quad (19)$$

Equation (19) is the criterion function of the proposed 3D-MET. The value of the threshold (s, t, q) yielding the lowest value of criterion $W(s, t, q)$ will give the best fit model and therefore the optimum minimum error threshold (s^*, t^*, q^*) ; that is,

$$(s^*, t^*, q^*) = \arg \min_{0 \leq s, t, q \leq L-1} W(s, t, q). \quad (20)$$

4. Fast Recursive Implementation of the 3D-MET

The advocated 3D-MET searches the optimum threshold exhaustively in 3D space, and each search has to start

from (0,0,0). It is clear that this exhaustive search for the threshold vector (s^*, t^*, q^*) that satisfies (20) is time consuming. In order to compute the value of each (s, t, q) , its computation time is $O(L^3)$. To find out the lowest value of (s, t, q) , the count of (s, t, q) that we must compute is L^3 . So the total computation time for threshold is $O(L^6)$. In the following we propose a fast recursive method for 3D-MET to reduce its algorithm complexity. The method can be briefly stated as follows.

Step 1. Denote the zeroth-order cumulative moments of the 3D histogram by P_0 , the first-order cumulative moments by X_1, Y_1 , and Z_1 , and second-order cumulative moments by X_2, Y_2 , and Z_2 ; that is,

$$\begin{aligned} P_0 &= \sum_{i=0}^s \sum_{j=0}^t \sum_{k=0}^q p_{ijk}, & X_1 &= \sum_{i=0}^s \sum_{j=0}^t \sum_{k=0}^q i p_{ijk}, \\ Y_1 &= \sum_{i=0}^s \sum_{j=0}^t \sum_{k=0}^q j p_{ijk}, & Z_1 &= \sum_{i=0}^s \sum_{j=0}^t \sum_{k=0}^q k p_{ijk}, \\ X_2 &= \sum_{i=0}^s \sum_{j=0}^t \sum_{k=0}^q i^2 p_{ijk}, & Y_2 &= \sum_{i=0}^s \sum_{j=0}^t \sum_{k=0}^q j^2 p_{ijk}, \\ & & Z_2 &= \sum_{i=0}^s \sum_{j=0}^t \sum_{k=0}^q k^2 p_{ijk}. \end{aligned} \quad (21)$$

Step 2. Represent each component of mean levels and variances in (7) through (10) as a function of $P_0, X_1, Y_1, Z_1, X_2, Y_2$, or Z_2 :

$$\begin{aligned} \mu_{0i}(s, t, q) &= \sum_{i=0}^s \sum_{j=0}^t \sum_{k=0}^q \frac{i p_{ijk}}{P_0} = \frac{X_1}{P_0}, \\ \mu_{0j}(s, t, q) &= \sum_{i=0}^s \sum_{j=0}^t \sum_{k=0}^q \frac{j p_{ijk}}{P_0} = \frac{Y_1}{P_0}, \\ \mu_{0k}(s, t, q) &= \sum_{i=0}^s \sum_{j=0}^t \sum_{k=0}^q \frac{k p_{ijk}}{P_0} = \frac{Z_1}{P_0}, \\ \mu_{1i}(s, t, q) &= \sum_{i=s+1}^{L-1} \sum_{j=t+1}^{L-1} \sum_{k=q+1}^{L-1} \frac{i p_{ijk}}{P_1} \approx \frac{\mu_i - X_1}{1 - P_0}, \\ \mu_{1j}(s, t, q) &= \sum_{i=s+1}^{L-1} \sum_{j=t+1}^{L-1} \sum_{k=q+1}^{L-1} \frac{j p_{ijk}}{P_1} \approx \frac{\mu_j - Y_1}{1 - P_0}, \\ \mu_{1k}(s, t, q) &= \sum_{i=s+1}^{L-1} \sum_{j=t+1}^{L-1} \sum_{k=q+1}^{L-1} \frac{k p_{ijk}}{P_1} \approx \frac{\mu_k - Z_1}{1 - P_0}, \\ \sigma_{0i}^2(s, t, q) &= \sum_{i=0}^s \sum_{j=0}^t \sum_{k=0}^q \frac{(i - \mu_{0i})^2 p_{ijk}}{P_0} \\ &= \sum_{i=0}^s \sum_{j=0}^t \sum_{k=0}^q \frac{i^2 p_{ijk}}{P_0} - \mu_{0i}^2(s, t, q) = \frac{X_2}{P_0} - \left(\frac{X_1}{P_0} \right)^2, \end{aligned}$$

$$\begin{aligned} \sigma_{0j}^2(s, t, q) &= \sum_{i=0}^s \sum_{j=0}^t \sum_{k=0}^q \frac{(j - \mu_{0j})^2 p_{ijk}}{P_0} \\ &= \sum_{i=0}^s \sum_{j=0}^t \sum_{k=0}^q \frac{j^2 p_{ijk}}{P_0} - \mu_{0j}^2(s, t, q) = \frac{Y_2}{P_0} - \left(\frac{Y_1}{P_0} \right)^2, \end{aligned}$$

$$\begin{aligned} \sigma_{0k}^2(s, t, q) &= \sum_{i=0}^s \sum_{j=0}^t \sum_{k=0}^q \frac{(k - \mu_{0k})^2 p_{ijk}}{P_0} \\ &= \sum_{i=0}^s \sum_{j=0}^t \sum_{k=0}^q \frac{k^2 p_{ijk}}{P_0} - \mu_{0k}^2(s, t, q) \\ &= \frac{Z_2}{P_0} - \left(\frac{Z_1}{P_0} \right)^2, \end{aligned}$$

$$\begin{aligned} \sigma_{1i}^2(s, t, q) &= \sum_{i=s+1}^{L-1} \sum_{j=t+1}^{L-1} \sum_{k=q+1}^{L-1} \frac{(i - \mu_{1i})^2 p_{ijk}}{P_1} \\ &= \sum_{i=s+1}^{L-1} \sum_{j=t+1}^{L-1} \sum_{k=q+1}^{L-1} \frac{i^2 p_{ijk}}{P_1} - \mu_{1i}^2(s, t, q) \\ &\approx \frac{X_T - X_2}{1 - P_0} - \left(\frac{\mu_i - X_1}{1 - P_0} \right)^2, \end{aligned}$$

$$\begin{aligned} \sigma_{1j}^2(s, t, q) &= \sum_{i=s+1}^{L-1} \sum_{j=t+1}^{L-1} \sum_{k=q+1}^{L-1} \frac{(j - \mu_{1j})^2 p_{ijk}}{P_1} \\ &= \sum_{i=s+1}^{L-1} \sum_{j=t+1}^{L-1} \sum_{k=q+1}^{L-1} \frac{j^2 p_{ijk}}{P_1} - \mu_{1j}^2(s, t, q) \\ &\approx \frac{Y_T - Y_2}{1 - P_0} - \left(\frac{\mu_j - Y_1}{1 - P_0} \right)^2, \end{aligned}$$

$$\begin{aligned} \sigma_{1k}^2(s, t, q) &= \sum_{i=s+1}^{L-1} \sum_{j=t+1}^{L-1} \sum_{k=q+1}^{L-1} \frac{(k - \mu_{1k})^2 p_{ijk}}{P_1} \\ &= \sum_{i=s+1}^{L-1} \sum_{j=t+1}^{L-1} \sum_{k=q+1}^{L-1} \frac{k^2 p_{ijk}}{P_1} - \mu_{1k}^2(s, t, q) \\ &\approx \frac{Z_T - Z_2}{1 - P_0} - \left(\frac{\mu_k - Z_1}{1 - P_0} \right)^2. \end{aligned} \quad (22)$$

Step 3. Create four lookup tables to eliminate redundant calculation:

$$\begin{aligned} P_0(m, n, r) &= \sum_{i=0}^m \sum_{j=0}^n \sum_{k=0}^r p_{ijk}, & X_2(m, n, r) &= \sum_{i=0}^m \sum_{j=0}^n \sum_{k=0}^r i^2 p_{ijk}, \\ Y_2(m, n, r) &= \sum_{i=0}^m \sum_{j=0}^n \sum_{k=0}^r j^2 p_{ijk}, & Z_2(m, n, r) &= \sum_{i=0}^m \sum_{j=0}^n \sum_{k=0}^r k^2 p_{ijk}. \end{aligned} \quad (23)$$

Step 4. Using the following recursive formula, calculate $P_0(m, n, r)$, $X_2(m, n, r)$, $Y_2(m, n, r)$, and $Z_2(m, n, r)$:

$$\begin{aligned}
P_0(0, 0, 0) &= P_{000}, & P_0(m, 0, 0) &= P_0(m-1, 0, 0) + P_{m00}, \\
P_0(0, n, 0) &= P_0(0, n-1, 0) + P_{0n0}, \\
P_0(0, 0, r) &= P_0(0, 0, r-1) + P_{00r}, \\
P_0(m, n, 0) &= P_0(m-1, t, 0) + P_0(m, n-1, 0) \\
&\quad - P_0(m-1, n-1, 0) + P_{mn0}, \\
P_0(m, 0, r) &= P_0(m-1, 0, r) + P_0(m, 0, r-1) \\
&\quad - P_0(m-1, 0, r-1) + P_{m0r}, \\
P_0(0, n, r) &= P_0(0, n-1, r) + P_0(0, n, r-1) \\
&\quad - P_0(0, n-1, r-1) + P_{0nr}, \\
P_0(m, n, r) &= P_0(m-1, n, r) + P_0(m, n-1, r) \\
&\quad + P_0(m, n, r-1) - P_0(m-1, n-1, r) \\
&\quad - P_0(m, n-1, r-1) - P_0(m-1, n, r-1) \\
&\quad + P_0(m-1, n-1, r-1) + P_{mnr}.
\end{aligned} \tag{24}$$

Using the same argument, we have

$$\begin{aligned}
X_2(m, n, r) &= X_2(m-1, n, r) + X_2(m, n-1, r) \\
&\quad + X_2(m, n, r-1) - X_2(m-1, n-1, r) \\
&\quad - X_2(m, n-1, r-1) - X_2(m-1, n, r-1) \\
&\quad + X_2(m-1, n-1, r-1) + m^2 \times P_{mnr}, \\
Y_2(m, n, r) &= Y_2(m-1, n, r) + Y_2(m, n-1, r) \\
&\quad + Y_2(m, n, r-1) - Y_2(m-1, n-1, r) \\
&\quad - Y_2(m, n-1, r-1) - Y_2(m-1, n, r-1) \\
&\quad + Y_2(m-1, n-1, r-1) + n^2 \times P_{mnr}, \\
Z_2(m, n, r) &= Z_2(m-1, n, r) + Z_2(m, n-1, r) \\
&\quad + Z_2(m, n, r-1) - Z_2(m-1, n-1, r) \\
&\quad - Z_2(m, n-1, r-1) - Z_2(m-1, n, r-1) \\
&\quad + Z_2(m-1, n-1, r-1) + r^2 \times P_{mnr}.
\end{aligned} \tag{25}$$

Step 5. For each recursive result in Step 4, calculate once (19), until finding out the threshold (m, n, r) which minimizes $W(s, t, q)$.

While calculating the probabilities of class occurrence and variances of (s, t, q) in Step 4, the accumulation of frequencies is obtained by summing up only several datum terms. Therefore for each (s, t, q) , the computation complexity is decreased from $O(L^3)$ to $O(L^0)$, and the computation complexity of 3D-MET is decreased from $O(L^6)$ to $O(L^3)$.

5. Experimental Results and Discussion

Experiments are implemented in Visual C++ 6.0 language under a personal computer with microdevices (Intel Core 2 Duo) 1.83 GHz CPU, 1 GRAM in Windows XP system. Test images are two synthetic aperture radar (SAR) images and two license plate images. Performance is compared in segmentation quality and algorithm efficiency. In this section, the experimental results of our algorithm will be compared to 2D Otsu, 2D maximum entropy, and 2D-MET. For comparison purposes, all above algorithms are implemented recursively and the size of the neighborhood window K is set to 3.

5.1. Segmentation Results of Different Noise Images. Figure 2(a) is a SAR image with 2% Gaussian noise, named "SAR1." The 1D histogram of SAR1 is unimodal. The absence of an internal minimum is indicative of a unimodal histogram, which would correspond to a homogeneous image, as shown in Figure 2(b). Figures 2(c) and 2(d) show the segmentation results of 2D Otsu and 2D maximum entropy. Obviously, neither 2D Otsu nor 2D maximum entropy gets meaningful results; namely, the river is not separated from test image. Figure 2(e) is the result of 2D-MET and it shows that the river is separated from the test image successfully, but its visual effect is not good as Figure 2(f). That is to say, 3D-MET obtains the best segmentation performance.

Figure 3(a) shows the other SAR image with 2% Gaussian noise and 2% salt-and-pepper noise. Due to the interference of mixed noise, the 1D histogram of SAR2 shown in Figure 3(b) is approximated as a normal distribution, and there is an extremely small peak near the coordinate origin. The gray distribution between the river and the land of the SAR2 has biggish diversity. For such kind of image, the goal of segmentation is to separate rivers from the image. Figures 3(c) and 3(d) show that neither 2D Otsu method nor 2D maximum entropy separates the river from background. Figure 3(e) is the result of 2D-MET with threshold (102, 93), which separates rivers from background successfully, but it cannot eliminate salt-and-pepper noise. Owing to the utilization of mean levels and median levels of the neighbourhood pixels, 3D-MET gets the best segmentation result. Figure 3(f) shows that 3D-MET not only separates rivers from background successfully but also eliminates the mixed noise effectively.

5.2. Segmentation Results of Images Disturbed by Nonuniform Illumination. Figure 4(a) is a poorly illuminated license plate image, named "License 1." From Figures 4(c) and 4(d), we can see that 2D Otsu and 2D maximum entropy suffered from nonuniform illumination too much to separate the license number from background. Figures 4(e) and 4(f) are the results of 2D-MET and 3D-MET with thresholds (31, 47) and (53, 77, 61), respectively. Obviously, both of them separated the license number from background clearly. But the result of the latter is better than the former.

In order to compare the performance of each thresholding in the mixed interference environment, Figure 5(a)

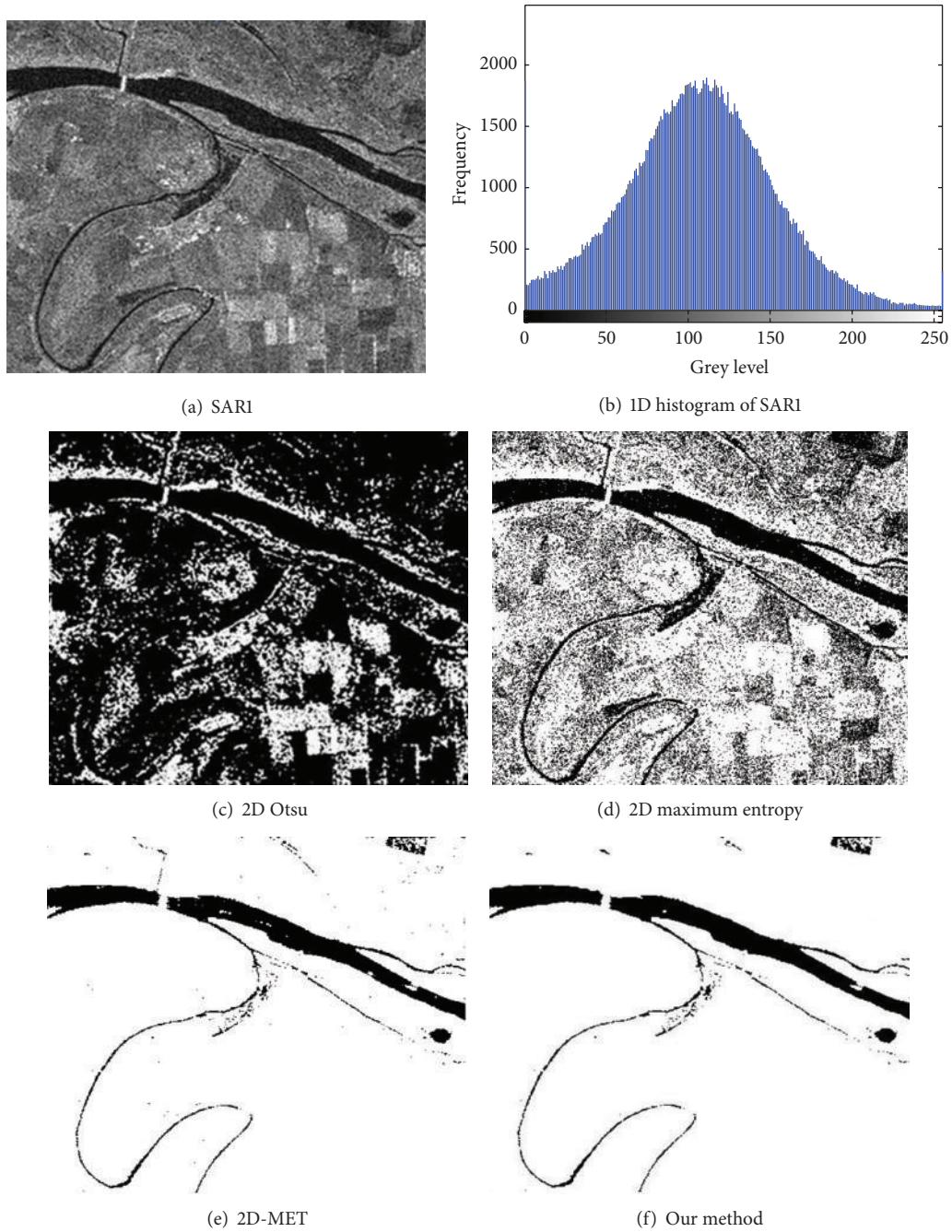


FIGURE 2: The segmented results of SARI.

is the other license plate image influenced by nonuniform illumination and 2% salt-and-pepper noise, named “License 2.” Figure 5(b) is the 1D histogram of License 2. Figure 5(c) shows the worst result of 2D Otsu with threshold (71, 75). The 2D maximum entropy separated the numbers from the license plate, but it cannot effectively curb the noise in the image, as shown in Figure 5(d). Figures 5(e) and 5(f) show the results of 2D-MET and 3D-MET. Both of the METs completely separated the license numbers; moreover, the border of the license plate and the number “5” in the bottom right corner of the image are clearly separated. By comparing

Figures 5(e) and 5(f), it is easy to see that 2D-MET also cannot curb the salt-and-pepper noise and the proposed 3D-MET curbed the noise very well and got the best segmentation performance.

5.3. Evaluation of Segmentation Quality. According to the availability of a segmented image reference, all evaluation criteria can be classified into two categories: supervised or unsupervised evaluation [19]. The 3D-MET proposed in this paper is a nonparametric and unsupervised method, and no reference segmented image is available. Therefore,

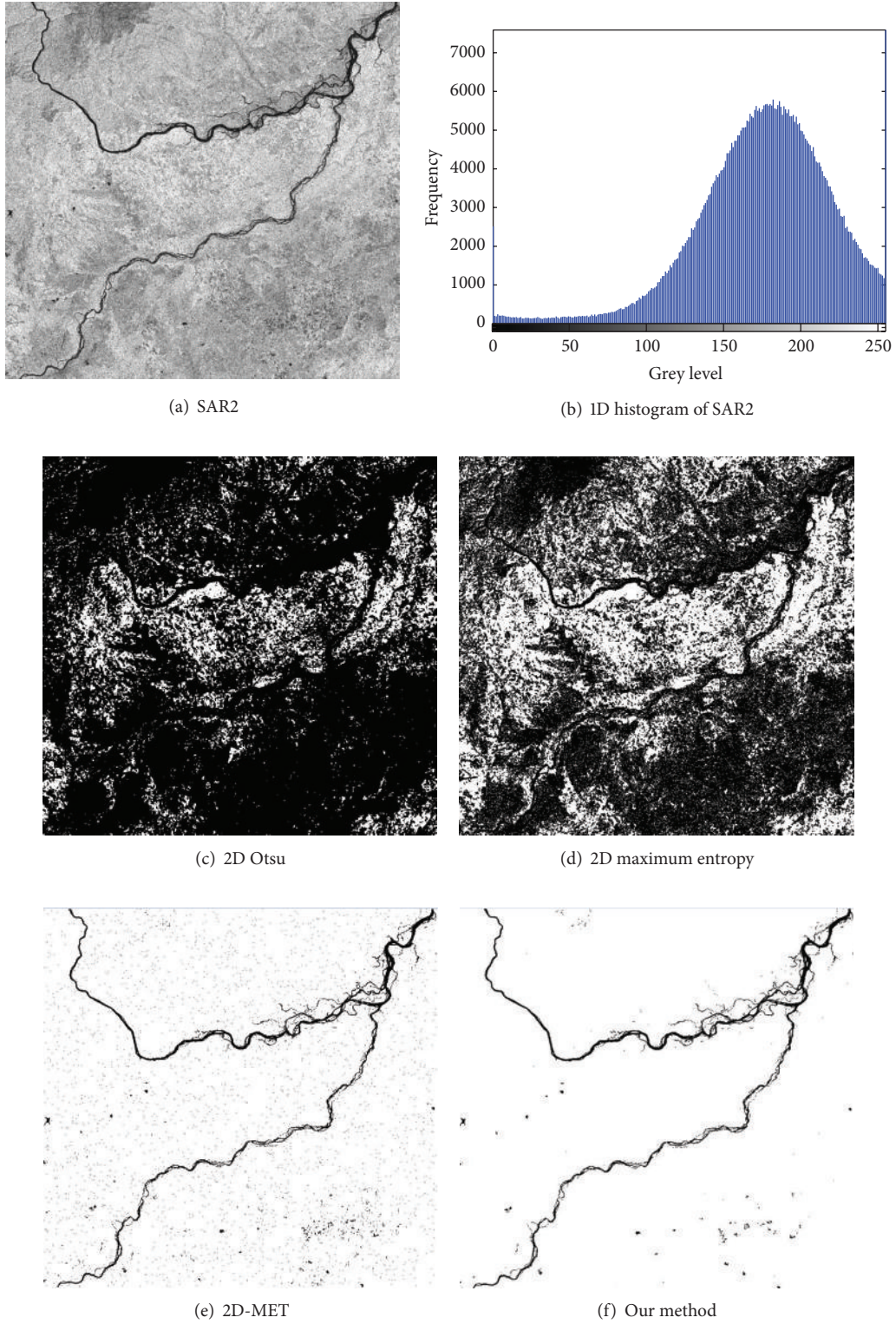


FIGURE 3: The segmented results of SAR2.

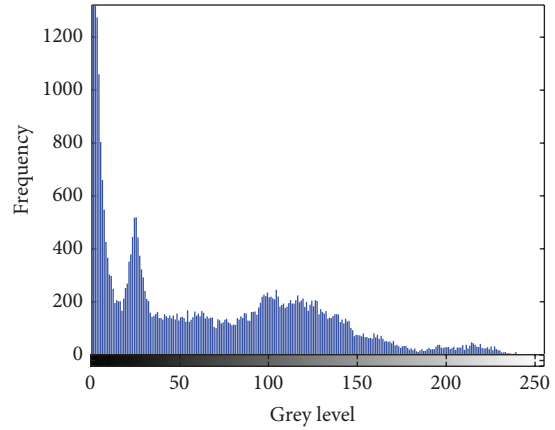
three criteria belonging to unsupervised evaluation are used in this paper: interregion contrast (IRC), intraregion uniformity (IRU), and inter-intra-criterion (IIC). Based on these normalized criteria, the higher their values within 0 and 1, the better the segmentation.

IRC and IRU introduced by Levine and Nazif are defined by the following expressions, respectively [20]:

$$\text{IRC} = \frac{\sum_{R_i} A_i C_i}{\sum_{R_i} A_i},$$



(a) License 1



(b) 1D histogram of License 1



(c) 2D Otsu



(d) 2D maximum entropy



(e) 2D-MET



(f) Our method

FIGURE 4: The segmented results of License 1.

$$IRU = 1 - \frac{2(N-1)}{A(g_{\max} - g_{\min})^2} \sum_{k=1}^N \sum_{i \in R_k} (g_i - m_k)^2. \quad (26)$$

IIC proposed by Rosenberger is the mean of IRC and IRU [21]. By using IIC, it will remove any irresolution during the comparison between two segmentations. The IIC is defined by the following expression:

$$IIC = \frac{IRC + IRU}{2}. \quad (27)$$

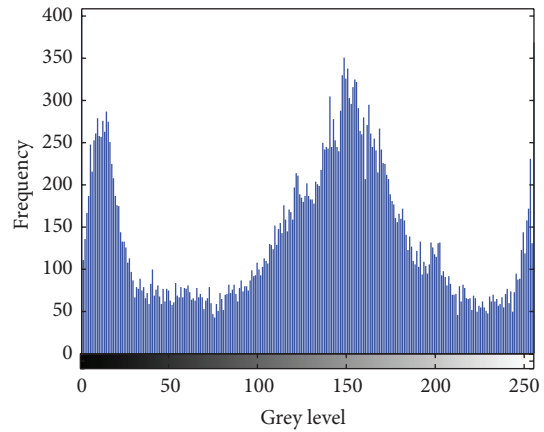
Table 1 summarizes the results of the evaluation criteria obtained with different methods. We can see that the value of IIC is the highest with our method. A visual inspection shows

that the discrimination between the regions is better ensured with our method. In addition, for License 1, the values of IRC and IRU of 2D Otsu are higher than those provided by 2D Maximum entropy, but for License 2 the positions are reversed.

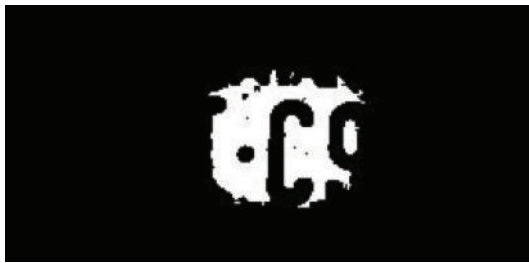
5.4. Comparison of Algorithm Efficiency. In the following we compare the thresholds and computation time of each algorithm for the above four images. In this paper, the resolution of SAR1, SAR2, License 1, and License 2 is 486×411 , 771×740 , 293×250 , and 272×133 , respectively. The gray level of all test images is 256. The detected thresholds and computation time of the algorithms are reported in Table 2. The segmentation performance of the 3D-MET is much better than others, but its recursive search in a 3D



(a) License 2



(b) 1D histogram of License 2



(c) 2D Otsu



(d) 2D maximum entropy



(e) 2D-MET



(f) Our method

FIGURE 5: The segmented results of License 2.

space costs more time than the 2D thresholding, as shown in Table 2. For most applications, the proposed method is competent in practical engineering. And for the large SAR images or remote sensing images, the process takes a longer time and it is not suitable for real-time systems.

Table 3 shows the space cost of 3D-MET in different gray levels. The space size is in relation to the count of the gray level. The recursive implementation of 3D-MET needs to store additional four lookup tables, but this is only a small overhead relative to nowadays' computer memory.

6. Conclusion

Due to the difficulty of the thresholding segmentation of images with mixed noise, we propose a new thresholding

algorithm for image segmentation based on 3D histogram and relative entropy theory. Experimental results show that the proposed approach is valid and successful. The quantitative analysis also shows that the proposed method effectively improves the segmentation capability for mixed noise images. And the proposed method can be applied and extended to other classification applications. In addition, it is interesting to point out the following. Firstly, any single algorithm could not be successful for all image types; the combination of more than one thresholding algorithm is worth a try to obtain the robustness. Secondly, the 3D-MET takes more time to locate the optimal threshold than the 2D thresholding. This problem should be solved by processor upgrading or further improvement of the algorithm.

TABLE 1: Measures of the unsupervised evaluation criteria.

		2D Otsu	2D maximum entropy	2D-MET	3D-MET
SAR1	IRC	0.375	0.43	0.617	0.662
	IRU	0.671	0.715	0.977	0.993
	IIC	0.523	0.573	0.797	0.828
SAR2	IRC	0.358	0.418	0.589	0.671
	IRU	0.629	0.694	0.898	0.989
	IIC	0.494	0.524	0.744	0.83
License 1	IRC	0.427	0.323	0.603	0.615
	IRU	0.751	0.573	0.937	0.991
	IIC	0.589	0.448	0.77	0.803
License 2	IRC	0.311	0.512	0.581	0.631
	IRU	0.341	0.764	0.881	0.988
	IIC	0.336	0.638	0.731	0.81

TABLE 2: Comparison of thresholds and time cost (second).

	2D Otsu		2D maximum entropy		2D-MET		3D-MET	
	Threshold	Time	Threshold	Time	Threshold	Time	Threshold	Time
SAR1	(106, 127)	1.45	(89, 134)	2.18	(45, 68)	2.36	(92, 124, 113)	3.71
SAR2	(166, 202)	3.95	(202, 192)	4.64	(102, 93)	4.46	(109, 102, 152)	9.42
License 1	(103, 217)	0.36	(205, 108)	1.38	(31, 47)	1.41	(53, 77, 61)	2.67
License 2	(71, 75)	0.40	(131, 133)	1.59	(42, 48)	1.68	(63, 57, 91)	3.18

TABLE 3: Space cost (byte).

Grayscale	64	128	256	512	1024
Space cost	5×64^3	5×128^3	5×256^3	5×512^3	5×1024^3

Appendix

The derivation of $W(s, t, q)$ from $R(s, t, q)$ is

$$\begin{aligned}
& \sum_{i=0}^s \sum_{j=0}^t \sum_{k=0}^q p_{ijk} \ln p(i, j, k | 0) \\
&= \sum_{i=0}^s \sum_{j=0}^t \sum_{k=0}^q p_{ijk} \ln \left\{ \frac{1}{(2\pi)^{3/2} \sqrt{|\Sigma|}} \right. \\
&\quad \times \exp \left[-\frac{1}{2} (i - \mu_{0i}, j - \mu_{0j}, k - \mu_{0k}) \right. \\
&\quad \times \Sigma^{-1} (i - \mu_{0i}, j - \mu_{0j}, \\
&\quad \left. \left. k - \mu_{0k}) \right] \right\} \\
&= \sum_{i=0}^s \sum_{j=0}^t \sum_{k=0}^q p_{ijk} \frac{1}{(2\pi)^{3/2} \sqrt{|\Sigma|}} \\
&\quad - \frac{1}{2} \sum_{i=0}^s \sum_{j=0}^t \sum_{k=0}^q p_{ijk} \left[(i - \mu_{0i}, j - \mu_{0j}, k - \mu_{0k}) \right. \\
&\quad \left. \times \Sigma^{-1} (i - \mu_{0i}, j - \mu_{0j}, k - \mu_{0k})^T \right]. \tag{A.1}
\end{aligned}$$

According to (7), (9), and (11)–(13), it follows that

$$\begin{aligned}
& \frac{1}{2} \sum_{i=0}^s \sum_{j=0}^t \sum_{k=0}^q p_{ijk} \left[(i - \mu_{0i}, j - \mu_{0j}, k - \mu_{0k}) \Sigma^{-1} \right. \\
&\quad \left. \times (i - \mu_{0i}, j - \mu_{0j}, k - \mu_{0k})^T \right] \tag{A.2} \\
&= P_0(s, t, q) = P_0.
\end{aligned}$$

Substituting (A.2) into (A.1), we obtain

$$\begin{aligned}
& \sum_{i=0}^s \sum_{j=0}^t \sum_{k=0}^q p_{ijk} \ln p(i, j, k | 0) \\
&= -P_0 \ln \left[(2\pi)^{3/2} \sigma_{0i} \sigma_{0j} \sigma_{0k} \sqrt{|R|} \right] \\
&= -P_0 \ln (2\pi)^{3/2} - P_0 \ln \sigma_{0i} \sigma_{0j} \sigma_{0k} - P_0 \ln \sqrt{|R|} - P_0, \\
& \sum_{i=0}^s \sum_{j=0}^t \sum_{k=0}^q p_{ijk} \ln \frac{p_{ijk}}{p_0 p(i, j, k | 0)} \\
&= \sum_{i=0}^s \sum_{j=0}^t \sum_{k=0}^q p_{ijk} \left[\ln p_{ijk} - \ln P_0 - \ln p(i, j, k | 0) \right]
\end{aligned}$$

$$\begin{aligned}
&= \sum_{i=0}^s \sum_{j=0}^t \sum_{k=0}^q p_{ijk} \ln p_{ijk} - \sum_{i=0}^s \sum_{j=0}^t \sum_{k=0}^q p_{ijk} \ln P_0 \\
&\quad - \sum_{i=0}^s \sum_{j=0}^t \sum_{k=0}^q p_{ijk} \ln p(i, j, k | 0) \\
&= \sum_{i=0}^s \sum_{j=0}^t \sum_{k=0}^q p_{ijk} \ln p_{ijk} - P_0 \ln P_0 + P_0 \ln (2\pi)^{3/2} \\
&\quad + P_0 \ln \sigma_{0i} \sigma_{0j} \sigma_{0k} + P_0 \ln \sqrt{|R|} + P_0.
\end{aligned} \tag{A.3}$$

Using the same argument, according to (8), (10), and (14)–(16), it follows that

$$\begin{aligned}
&\sum_{i=s+1}^{L-1} \sum_{j=t+1}^{L-1} \sum_{k=q+1}^{L-1} p_{ijk} \ln \frac{p_{ijk}}{p_1 p(i, j, k | 1)} \\
&= \sum_{i=s+1}^{L-1} \sum_{j=t+1}^{L-1} \sum_{k=q+1}^{L-1} p_{ijk} [\ln p_{ijk} - \ln P_1(s, t, q) \\
&\quad - \ln p(i, j, k | 1)] \\
&= \sum_{i=s+1}^{L-1} \sum_{j=t+1}^{L-1} \sum_{k=q+1}^{L-1} p_{ijk} \ln p_{ijk} - \sum_{i=s+1}^{L-1} \sum_{j=t+1}^{L-1} \sum_{k=q+1}^{L-1} p_{ijk} \ln P_1 \\
&\quad - \sum_{i=s+1}^{L-1} \sum_{j=t+1}^{L-1} \sum_{k=q+1}^{L-1} p_{ijk} \ln p(i, j, k | 1) \\
&= \sum_{i=s+1}^{L-1} \sum_{j=t+1}^{L-1} \sum_{k=q+1}^{L-1} p_{ijk} \ln p_{ijk} - P_1 \ln P_1 + P_1 \ln (2\pi)^{3/2} \\
&\quad + P_1 \ln \sigma_{1i} \sigma_{1j} \sigma_{1k} + P_1 \ln \sqrt{|R|} + P_1.
\end{aligned} \tag{A.4}$$

Adding (A.4) to (A.3), we have

$$\begin{aligned}
R(s, t, q) &= \sum_{i=0}^s \sum_{j=0}^t \sum_{k=0}^q p_{ijk} \ln p_{ijk} + \sum_{i=s+1}^{L-1} \sum_{j=t+1}^{L-1} \sum_{k=q+1}^{L-1} p_{ijk} \ln p_{ijk} \\
&\quad + P_0 \ln (2\pi)^{3/2} + P_1 \ln (2\pi)^{3/2} + P_0 \ln \sqrt{|R|} \\
&\quad + P_1 \ln \sqrt{|R|} + P_0 + P_1 - P_0 \ln P_0 - P_1 \ln P_1 \\
&\quad + P_0 \ln \sigma_{0j} \sigma_{0k} + P_1 \ln \sigma_{1i} \sigma_{1j} \sigma_{1k}.
\end{aligned} \tag{A.5}$$

Because $R(s, t, q) > 0$, $P_0 \ln (2\pi)^{3/2} + P_1 \ln (2\pi)^{3/2}$ is constant. So, according to (4), we have

$$\begin{aligned}
P_0 + P_1 &= P_0(s, t, q) + P_1(s, t, q) \approx 1, \\
\sum_{i=0}^s \sum_{j=0}^t \sum_{k=0}^q p_{ijk} \ln p_{ijk} &+ \sum_{i=s+1}^{L-1} \sum_{j=t+1}^{L-1} \sum_{k=q+1}^{L-1} p_{ijk} \ln p_{ijk} \\
&\approx \sum_{i=0}^{L-1} \sum_{j=0}^{L-1} \sum_{k=0}^{L-1} p_{ijk} \ln p_{ijk}.
\end{aligned} \tag{A.6}$$

And from the definition of 3D histogram, it is easy to find out that all correlation coefficients in matrix R are functions of the neighborhood size K . Generally, $\rho_{12} = \rho_{13} = \rho_{23} = 1/K$. So $\sqrt{|R|}$ has no relation to the threshold selection and can be viewed as a constant.

Therefore, to minimize $R(s, t, q)$ is equivalent to minimizing the following function:

$$\begin{aligned}
W(s, t, q) &= P_0(s, t, q) \ln \sigma_{0i} \sigma_{0j} \sigma_{0k} + P_1(s, t, q) \ln \sigma_{1i} \sigma_{1j} \sigma_{1k} \\
&\quad - P_0(s, t, q) \ln P_0(s, t, q) \\
&\quad - P_1(s, t, q) \ln P_1(s, t, q).
\end{aligned} \tag{A.7}$$

Conflict of Interests

The authors declare that there is no conflict of interests regarding the publication of this paper.

Acknowledgments

The authors would like to thank the reviewers whose valuable suggestions have improved the quality of the paper. This work was supported by the National Natural Science Foundation of China under Project 61262037 and Project 61134002.

References

- [1] S. Candemir and Y. S. Akgül, "Statistical significance based graph cut regularization for medical image segmentation," *Turkish Journal of Electrical Engineering & Computer Sciences*, vol. 19, no. 6, pp. 957–972, 2011.
- [2] M. Ceylan, Y. Özbay, O. N. Uçan, and E. Yildirim, "A novel method for lung segmentation on chest CT images: complex-valued artificial neural network with complex wavelet transform," *Turkish Journal of Electrical Engineering & Computer Sciences*, vol. 18, no. 4, pp. 613–623, 2010.
- [3] A. M. Vil'kin, I. V. Safonov, and M. A. Egorova, "Bottom-up document segmentation method based on textural features," *Pattern Recognition and Image Analysis*, vol. 21, no. 3, pp. 565–568, 2011.
- [4] K. H. Hsia, S. F. Lien, and J. P. Su, "Fast restoration of warped document image based on text rectangle area segmentation," *Journal of Software*, vol. 8, pp. 1162–1167, 2013.
- [5] P. Nadia and T. Sinisa, "Hough forest random field for object recognition and segmentation," *IEEE Transactions on Pattern Analysis and Machine Intelligence*, vol. 35, pp. 1066–1079, 2013.

- [6] M.-D. Yang, T.-C. Su, N.-F. Pan, and Y.-F. Yang, "Systematic image quality assessment for sewer inspection," *Expert Systems with Applications*, vol. 38, no. 3, pp. 1766–1776, 2011.
- [7] J. J. Ranjani and S. J. Thiruvengadam, "Fast threshold selection algorithm for segmentation of synthetic aperture radar images," *IET Radar, Sonar & Navigation*, vol. 6, no. 8, pp. 788–795, 2012.
- [8] M. K. Quweider, J. D. Scargle, and B. Jackson, "Grey level reduction for segmentation, thresholding and binarisation of images based on optimal partitioning on an interval," *IET Image Processing*, vol. 1, no. 2, pp. 103–111, 2007.
- [9] D. Ahmed, H. Kamal, and D. Moussa, "Fast multilevel thresholding for image segmentation through a multiphase level set method," *Signal Processing*, vol. 93, pp. 139–153, 2013.
- [10] N. Otsu, "A threshold selection method from gray-level histograms," *IEEE Transactions on Systems, Man, and Cybernetics*, vol. 9, no. 1, pp. 62–66, 1979.
- [11] J. Kittler and J. Illingworth, "Minimum error thresholding," *Pattern Recognition*, vol. 19, no. 1, pp. 41–47, 1986.
- [12] J. N. Kapur, P. K. Sahoo, and A. K. C. Wong, "A new method for gray-level picture thresholding using the entropy of the histogram," *Computer Vision, Graphics, & Image Processing*, vol. 29, no. 3, pp. 273–285, 1985.
- [13] M. Sezgin and B. Sankur, "Survey over image thresholding techniques and quantitative performance evaluation," *Journal of Electronic Imaging*, vol. 13, no. 1, pp. 146–168, 2004.
- [14] M.-H. Horng and R.-J. Liou, "Multilevel minimum cross entropy threshold selection based on the firefly algorithm," *Expert Systems with Applications*, vol. 38, no. 12, pp. 14805–14811, 2011.
- [15] A. Nakib, H. Oulhadj, and P. Siarry, "Image histogram thresholding based on multiobjective optimization," *Signal Processing*, vol. 87, no. 11, pp. 2516–2534, 2007.
- [16] P. Gu and Y. Zhang, "Improved 2D Otsu segmentation algorithm for infrared image," *Journal of Image and Graphics*, vol. 16, no. 8, pp. 1424–1428, 2011.
- [17] X. Y. Yan and L. C. Jiao, "Non-local three dimensional Otsu image thresholding segmentation based on anisotropic adaptive Gaussian weighted window," *Journal of Electronics & Information Technology*, vol. 34, pp. 2672–2679, 2012.
- [18] S. Kullback, *Information Theory and Statistics*, Dover, Mineola, NY, USA, 1968.
- [19] S. P. Foliquet and L. Guigues, "Evaluation of image segmentation: state of the art, new criteria and comparison," *Traitement du Signal*, vol. 23, pp. 109–124, 2003.
- [20] M. D. Levine and A. M. Nazif, "Dynamic measurement of computer generated image segmentations," *IEEE Transactions on Pattern Analysis and Machine Intelligence*, vol. 7, no. 2, pp. 155–164, 1985.
- [21] C. Rosenberger, *Mise en oeuvre d'un system adaptatif de segmentation d'image [Ph.D. thesis]*, University of Rennes I, Rennes, France, 1999.

Research Article

A Simple and High Performing Rate Control Initialization Method for H.264 AVC Coding Based on Motion Vector Map and Spatial Complexity at Low Bitrate

Yalin Wu and Sun-Woo Ko

Department of Smart Information Systems, Jeonju University, 303 Cheonjam-ro, Wansan-gu, Jeonju 560-759, Republic of Korea

Correspondence should be addressed to Sun-Woo Ko; godfriend@hanmail.net

Received 13 October 2013; Revised 20 November 2013; Accepted 26 November 2013; Published 8 January 2014

Academic Editor: Gelan Yang

Copyright © 2014 Y. Wu and S.-W. Ko. This is an open access article distributed under the Creative Commons Attribution License, which permits unrestricted use, distribution, and reproduction in any medium, provided the original work is properly cited.

The temporal complexity of video sequences can be characterized by motion vector map which consists of motion vectors of each macroblock (MB). In order to obtain the optimal initial QP (quantization parameter) for the various video sequences which have different spatial and temporal complexities, this paper proposes a simple and high performance initial QP determining method based on motion vector map and temporal complexity to decide an initial QP in given target bit rate. The proposed algorithm produces the reconstructed video sequences with outstanding and stable quality. For any video sequences, the initial QP can be easily determined from matrices by target bit rate and mapped spatial complexity using proposed mapping method. Experimental results show that the proposed algorithm can show more outstanding objective and subjective performance than other conventional determining methods.

1. Introduction

In the last decade, multimedia data has been applied to communication, security, entertainment, and military. Because multimedia data has the problem of large amount of data, it can be hardly stored and transmitted. Video coding can effectively solve the problem. With the development of terminal equipment and communication networks, the video coding standards have been continually established as MPEG-1 [1], MPEG-2 [2], MPEG-4 [3], H.261 [4], H.262, H.263 [5], H.264 [6], and H.265 [7]. Especially, H.264/AVC can be applied for extensive areas such as DVD and VOD over cable and bit streaming video at low bit rate with high quality.

In multimedia communication and transmission, rate control (RC) algorithm plays a crucial role. H.264/AVC includes an RC [8] which can be used to achieve optimal subjective quality given transmission bandwidth limit by regulating the encoding parameters. In RC, the optimal QP has been determined for every frame of video sequence. The large amount of encoded and good perceptual quality can be obtained by reducing the QP. In contrast, the QP increment can reduce the encoded bits and perceptual quality. The mean

absolute difference (MAD) of residual MB can be used to determine the QP for MB. However, the chicken-and-egg dilemma [6] occurs in the process of determining QP. In JVT-G012 [9], the scheme of one-pass RC uses a linear MAD prediction model to solve the chicken-and-egg dilemma. According to the efficiency and simplicity of JVT-G012, the scheme of JVT-G012 has been widely applied in H.264 software and hardware. The algorithm of JVT-G012 includes the process of initialization for RC. In this process, the initial QP is determined for IDR picture in a video sequence. Therefore, the optimal MAD of IDR can be calculated using initial QP. The MAD of next frame is predictable using optimal MAD of IDR. The process of initial QP determination is an important part in RC. The value of initial QP can influence the RC performance. Conventionally, the value of initial QP can be determined according to the number of bits per pixel (BPP) which depends on the target bit rate, frame rate, and image size in JVT-G012. Although the scheme of BPP is easy to implement, it is very rough and imprecise. Generally, video sequence is two-element data which includes spatial and temporal components. According to information theory, the relatively large number of bits is used to represent

the video sequence which has highly complicated spatial and temporal features. In contrast, relatively small amount of bits can encode the low complex video sequence. In the situation of the restricted target bits, a large initial QP is expected for highly complicated video sequence. In spite of reducing the image quality, it is in the limited data range. For the low complex video sequence, a small initial QP is assigned; not only the target bits can be fulfilled but the excellent image quality can be also obtained. Using this idea, it is very important that the scheme of RC initialization is used to consider spatial and temporal complexities of video sequence. In order to complete this target, Wang and Kwong [10] and Wu and Kim [11] proposed the schemes which used the characteristics of video sequences as well as BPP to determine the initial QP. However, their methods do not consider quality balance of reconstructed video sequence and the provided parameters cannot apply any video sequence. The criterion of selecting the sample video sequences has not been provided. In addition, the algorithm of determining optimal initial QP has not been explained either. Moreover, Hu et al. [12] proposed a scheme of computing the initial QP for spatial scalable video coding (SVC). However, this scheme is only applicable to the SVC standard.

In order to solve the existing problems, we propose a simple and high performance method to determine an initial QP in given target bit rate. To obtain the initial QP for any video sequences, it is very important to measure the spatial and temporal complexities of the video sequences. In H.264/AVC [6] standard, the motion vector is proposed as a measure of temporal complexities of video sequences. Primarily, temporal complexities of ten video sequences are analyzed using motion vector and 4 video sequences are screened out as the samples. And then, the spatial complexities of samples are calculated using the rate of number of complex MBs, which are determined by variance of MB, in the IDR. In this paper, an algorithm for determining optimal initial QP is proposed for producing the reconstructed video sequences with high and stable qualities at the encoding bits which are very close to target bit rates within the range of 0.4 to 1.0 Mbps. Subsequently, optimal initial QPs of 4 samples constitute two-dimensional matrices basis of spatial complexity and target bit rate. Moreover, we propose a mapping method to determine the spatial complexity of tested video sequences by the two-dimensional matrices. For any tested video sequence, its optimal initial QP can be chosen from the built matrix using its mapped spatial complexity and target bit rate. Section 2 presents the related method of initialization process of RC. Section 3 interprets the evolution process of proposed method. The results of experiment are shown in Section 4. Finally, Section 5 shows the conclusion of this study.

2. Related Method of Initialization

Algorithm of Rate Control

In this section, we review some initialization methods of RC which are used to decide initial QPs in the recent literatures. The method of JVT-G012 that can automatically

conclude the value of initial QP for the IDR is the most traditional and coarse method. The advantages of JVT-G012 are easy implementation and low computational complexity. In the case of the poor performance hardware of terminal equipment, JVT-G012 is being of extensive usage. Various versions of the reference software of H.264 [7, 13] have adopted JVT-G012. The disadvantage of JVT-G012 is being not accurate enough. The method of JVT-G012 uses only BPP to determine an initial QP as follows:

$$\text{JVTQP} = \begin{cases} 35, & \text{BPP} \geq J_1, \\ 25, & J_1 < \text{BPP} \leq J_2, \\ 20, & J_2 < \text{BPP} \leq J_3, \\ 10, & \text{BPP} > J_3, \end{cases} \quad (1)$$

$$\text{BPP} = \frac{\text{BR}}{\text{FR} \times \text{VS}}, \quad (2)$$

where JVTQP is calculated by the initial QP of initialization process of RC. BPP, which is the bits per pixel, is computed using BR, FR, and VS which represent the target bit rate, the frame rate, and the size of frame in (2). J_1 , J_2 , and J_3 are thresholds. For QCIF video sequences, the thresholds are given as 0.1, 0.3, and 0.6. For CIF video sequences, the thresholds are recommended to be 0.6, 1.4 and 2.4 in JM9.3 [10].

In the method of Wang, the value of initial QP is computed on the basis of BPP and spatial feature. The spatial feature can be computed using entropy information and the dc mode of INTRA 16×16 of the IDR.

Consider

$$\begin{aligned} \text{Entropy} &= - \sum_{i=0}^{L-1} p(i) \log_2 [p(i)], \\ \text{MC} &= \frac{\sum_{k=1}^N \sum_{t=0}^{15} \sum_{j=0}^{15} |M^k(t, j) - M_{\text{dc}}^k|}{1000 \times N}, \end{aligned} \quad (3)$$

where $L - 1$ is maximum gray level value of pixel, $p(i)$ is the probability of gray level i , N is the number of MBs in IDR, $M^k(t, j)$ is used to denote the pixel value at (i, j) of the k th MB, and M_{dc}^k is used to denote the predicted compensation value computed from the dc mode of INTRA 16×16 . Finally, the initial QP can be calculated by (4). Figure 1 shows the relationship of the best initial QP and BPP by News, Foreman, and Mobile. And then (5) can be computed by this relationship:

$$\text{initial QP} = F_1(\text{BPP}) + F_2(\text{Entropy}, \text{MC}), \quad (4)$$

$$F_1(\text{BPP}) = \begin{cases} c1 \cdot \text{BPP} + c2, & \text{BPP} \geq 0.4, \\ c3 \cdot \text{BPP} + c4, & 0.4 > \text{BPP} \geq 0.2, \\ c5 \cdot \text{BPP}^2 + c6 \cdot \text{BPP} + c7, & 0.2 > \text{BPP}, \end{cases} \quad (5)$$

$$F_2 = \max \{ t1 \text{Entropy}^2 + t2 \text{Entropy} + t3, e1 \text{MC}^2 + e2 \text{MC} + e3 \}, \quad (6)$$

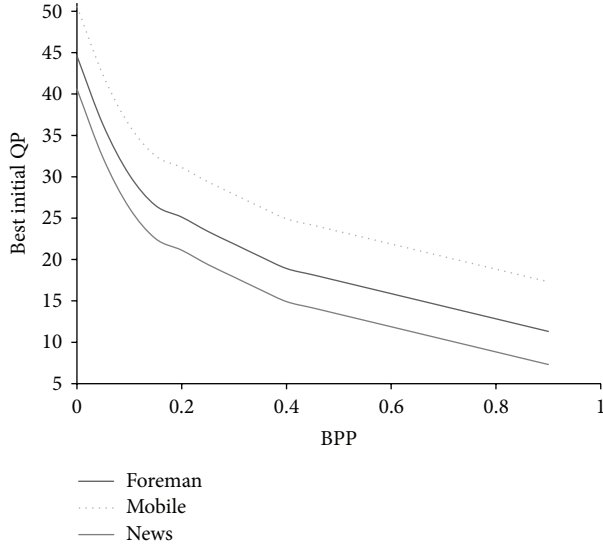


FIGURE 1: Relationship between the best initial QP and BPP according to News, Foreman, and Mobile.

where $\theta = \{c1, c2, c3, c4, c5, c6, c7, t1, t2, t3, e1, e2, e3\}$ can be defined as $\theta = \{-15.21, 25, -30.41, 31, 462.47, -189.86, 44.60, -15.25, 241.81, -944.42, -0.76, 13.59, -49.18\}$ for CIF video sequences. At QCIF video sequences, $\theta = \{-12.67, 24, -25.34, 29, 546.59, -221.55, 46.41, 14.25, -184.76, 595.95, 0.67, -7.23, 18.50\}$. The value of initial QP is computed using (4).

In the scheme of Wu, initial QP is calculated on the basis of BPP, the MAD value of the IDR, and the average MAD value of the 2nd, 3rd, and 4th frames which are encoded using intermode as follows:

$$\text{initial QP} = F_1(\text{BPP}) + F_3(\text{MAD}_I, \text{MAD}_{AP}), \quad (7)$$

$$\begin{aligned} F_3(\text{MAD}_I, \text{MAD}_{AP}) = & p1 \cdot [a \cdot \text{MAD}_I \\ & + (1 - a) \cdot \text{MAD}_{AP}]^2 \\ & + p2 \cdot [a \cdot \text{MAD}_I \\ & + (1 - a) \cdot \text{MAD}_{AP}] + p3, \end{aligned} \quad (8)$$

where the value of a is 0.05 and $\theta = \{c1, c2, c3, c4, c5, c6, c7, p1, p2, p3\}$ can be determined as $\theta = \{-15.21, 25, -30.41, 31, 462.47, -189.86, 44.60, -0.78, 8.48, -10.90\}$ for CIF video sequences and $\theta = \{-12.67, 24, -25.34, 29, 546.59, -221.55, 46.41, 0.36, 1.30, -2.78\}$ for the size of QCIF. The value of initial QP is computed using (7).

The parameters used in the method of Wang and Wu are calculated using three types of tested video sequences. In Wu and Wang, the extracting method of sample video sequences has not been shown. It is difficult to say that they can represent the various spatial and temporal complexities video sequences. Moreover, Wang and Wu have not taken into account the quality consistency of recovered video sequences. Furthermore, the scheme of the best initial QP determination is not explained.

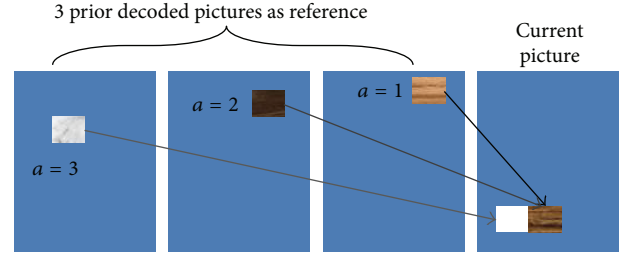


FIGURE 2: The process of ME.

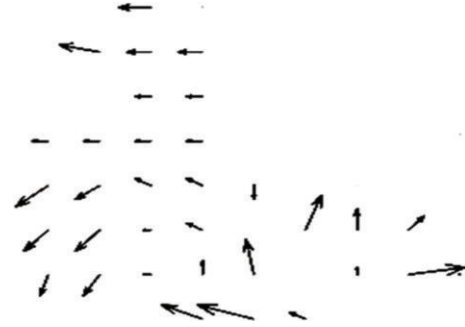


FIGURE 3: Motion vector map.

3. Proposed Initialization Algorithm of Rate Control

3.1. Spatial and Temporal Complexities. In the video sequence, the content of adjacent frames has not any significant difference. In order to save amount of bits, only difference is encoded. For finding difference, most video coding standards support the method named motion estimation (ME) [6]. ME is used to investigate the 16×16 at the objective region in reference frames that closely matches the current MB. ME is improved by H.264/AVC such as variable block size, multiple reference frames, and optimization algorithm. Figure 2 shows the process of ME. Motion vectors are used to compress video by storing the changes to an image from one frame to the next. Figure 3 shows motion vector.

By the number and magnitude of the motion vectors, the temporal complexity of video sequences can be measured and predicted. In H.264/AVC, most frames are encoded using intermode [4–6]. For the video coding performance, the temporal complexity is more important than spatial complexity.

Figure 4 shows the result of motion vector maps for ten different types of sample video sequences [14]. In Figure 4, the ten video sequences can be simply divided into two categories. The Bus, Flower, and Mobile video sequences are classified as a complex case. On the contrary, Foreman, Waterfall, Silent, Paris, Bridge-far, Mother-daughter, and News video sequences are relatively simple case. Complexity means that the number of motion vectors is high and vice versa. In complex videos, Mobile video is captured by fixed camera and its motion vectors exist in each MB. Flower video shows the movement of the objects located at the lower part of the video while Bus video has the movement on the all-region.

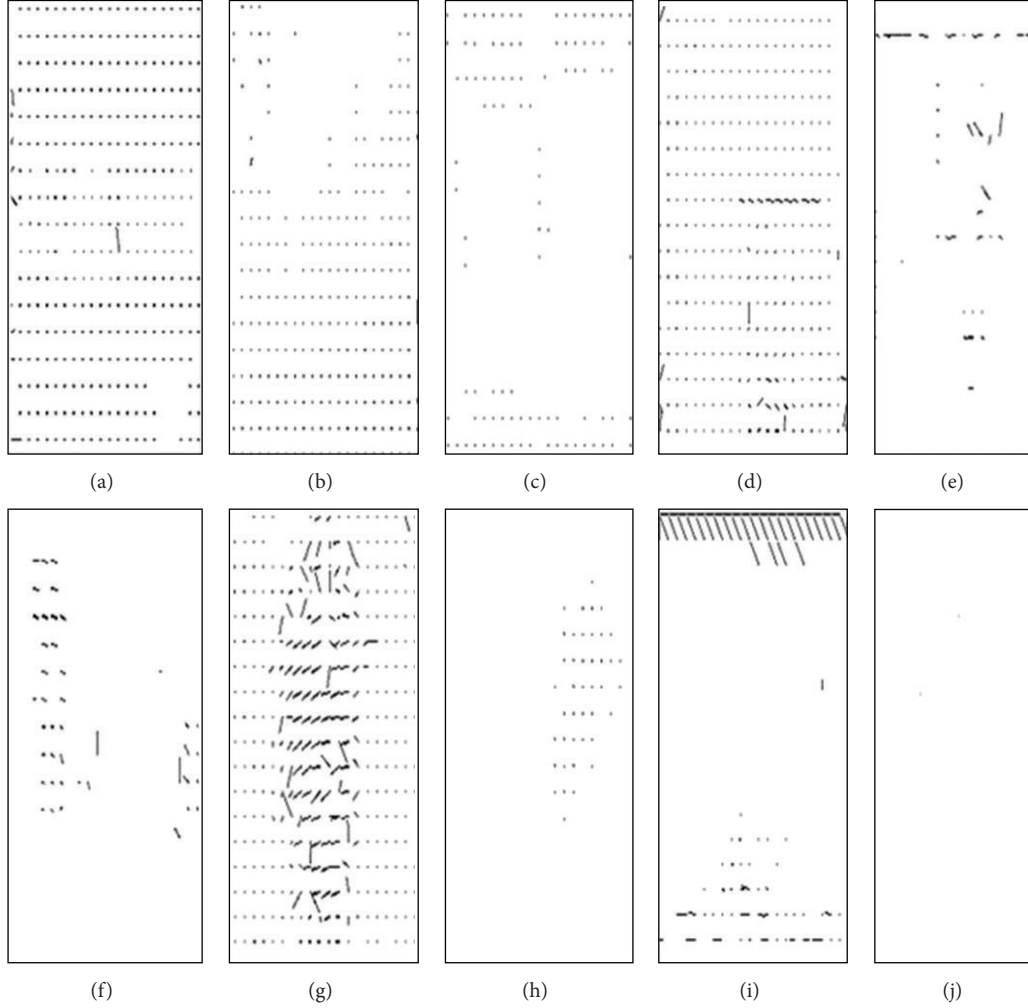


FIGURE 4: Motion vectors obtained from ten video sequences.

In simple videos, Waterfall is a typical case which applies the zoom-out photography technology and Foreman, which is classic interview type, has motion vectors in the middle of the image. Moreover, News, Paris, Mother-daughter, and Silent are also interview style video sequences. According to their motion vectors, various types of video sequences have different patterns. The patterns can be used to distinct typical video sequences. We use 4 video sequences which are Mobile, Flower, Waterfall, and Foreman as the sample video sequence to analyse any video sequences because they have distinctive features.

In proposed initialization algorithm of RC, the value of initial QP is computed based on the spatial and temporal complexities at the given target bit rate. As the sample video sequences are selected, the calculating method of spatial complexity of sample video sequences must be provided.

In H. 264, the smallest encoding unit is MB. MB includes two INTRA prediction modes which are INTRA 16×16 [4] and INTRA 4×4 [4]. Figure 5 shows the INTRA prediction modes. In Figure 5(a), the INTRA 4×4 has 9 prediction modes. In Figure 5(b), the INTRA 16×16 has 4 prediction modes.

Generally, the INTRA 16×16 mode is used in the MBs which are in the homogeneous regions of image. However, the INTRA 4×4 mode is used in the MBs which are in the object and edge parts of image [4]. In Figure 6, the nonhomogeneous MBs have the same value of pixels. The INTRA 16×16 mode is used to process the homogeneous MBs. The reasons to use INTRA 16×16 blocks are to save the computing time and to maintain the image quality. The INTRA 4×4 mode is used to process the non-homogeneous MBs which have the different pixel values. The reason to use INTRA 4×4 blocks is to maintain the quality.

Since the variance of an MB, which includes 256 pixels, is the equal of the total information of the DC and AC coefficients of the MB, the spatial complexity of the MB can be estimated using variance [15].

Consider

$$MB_{\text{var}} = \frac{1}{256} \left(\sum_{i=0}^{15} \sum_{j=0}^{15} [Y(i, j)]^2 - \left[\sum_{i=0}^{15} \sum_{j=0}^{15} Y(i, j) \right]^2 \right), \quad (9)$$

where the variance of MB is computed by MB_{var} and $Y(i, j)$ is value of the pixel which is luminance signal at (i, j) . An MB

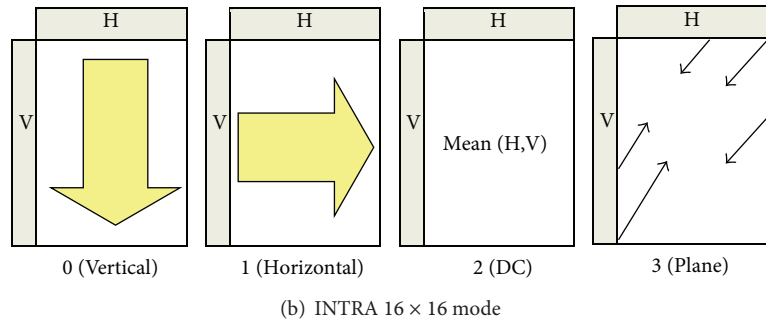
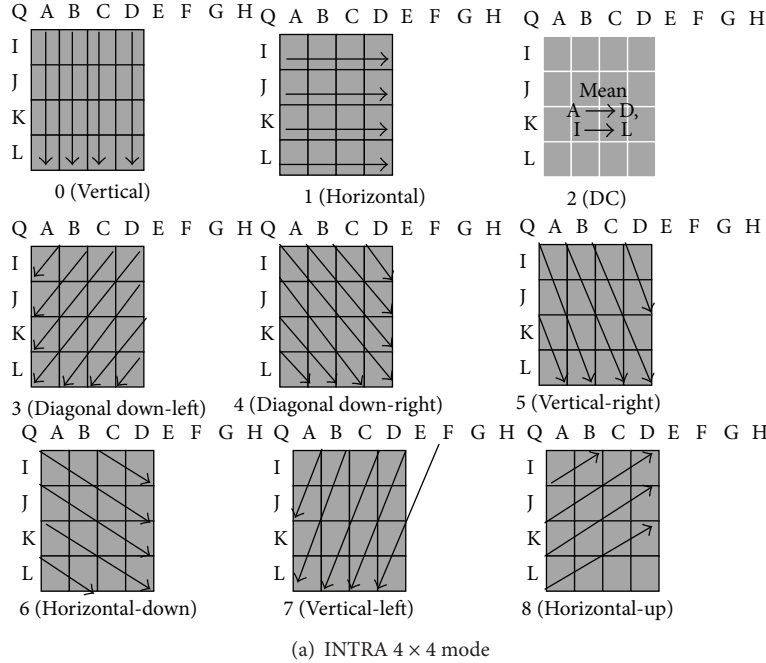


FIGURE 5: INTRA prediction modes.

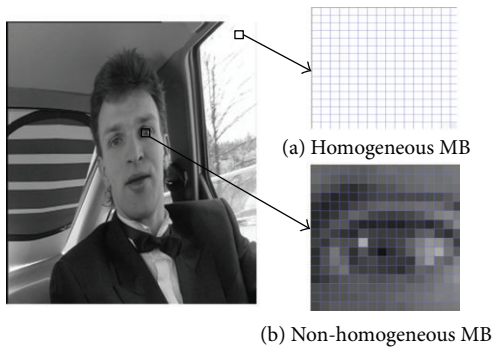


FIGURE 6: Type of MBs.

is classified to be of high or low complexity by threshold of variance as follows:

$$MB_{Complexity} = \begin{cases} \text{high,} & MB_{var} > T, \\ \text{low,} & MB_{var} \leq T, \end{cases} \quad (10)$$

where T is the threshold value defined as 92735 [15]. Figure 7 shows the classification process of MB according to the value of variance. The spatial complexity of the IDR is measured according to the proportion of the number of complex MBs as follows:

$$Frame_{complex} = \frac{MB_{Complex}}{MB_{Frame}} \times 100 (\%), \quad (11)$$

where the $Frame_{complex}$ is the rate of the number of complex MBs in the IDR. $MB_{Complex}$ is the number of the complex MBs of IDR and MB_{Frame} is the total number of the MBs of IDR.

The $Frame_{complex}$ can be a measure of the spatial complexity.

3.2. Proposed Algorithm for Determining the Optimal Initial QP. According to the given target bit rate, the value of initial QP is directly related to the performance of encoding at the H.264/AVC. The performance of encoding can be evaluated using the quality of reconstructed video sequences and total bits. In other words, the objectives are to satisfy target bit rate to ensure the best quality of reconstructed video sequences.

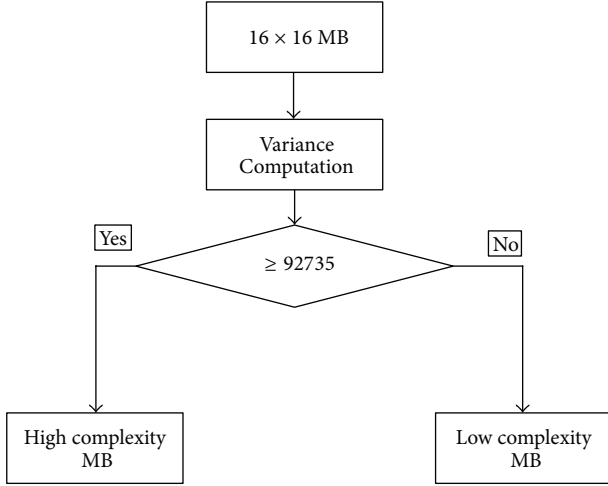


FIGURE 7: Classification process of MB.

And also the stability of reconstructed video sequences is a very important quality measure in multimedia broadcasting and transmission. Thus the optimal initial QP algorithm has the following properties: (1) maximizing PSNR(peak signal-to-noise ratio) that means the best quality of reconstructed video sequences, (2) maximizing stability that is defined as the differences of QPs, and (3) minimizing total real bits under satisfying the target bit rate.

To find out the optimal initial QP, all potential 52 initial QPs are calculated. For each initial QP, the results which include PSNR, real bits of prior 60 frames, and the differences of QPs in a group of pictures (GOP) are recorded at the given target bit rate. So an initial QP, which produces the maximum PSNR and the minimum of real bits under satisfying target bit rate and minimum differences of QPs, is the optimal initial QP. Since the numeric value of real bits is much larger than PSNR and differences of QPs and also PSNR, real bits, and differences of QPs have different dimensions, PSNR, real bits, and differences of QPs are normalized as follows:

$$\overline{\text{PSNR}}_{\text{Initial QP}} = (\text{PSNR}_{\text{Initial QP}} - \text{MIN}_{\text{Initial QP}=0, \dots, 51} (\text{PSNR}_{\text{Initial QP}})) \times (\text{MAX}_{\text{Initial QP}=0, \dots, 51} (\text{PSNR}_{\text{Initial QP}}) - \text{MIN}_{\text{Initial QP}=0, \dots, 51} (\text{PSNR}_{\text{Initial QP}}))^{-1},$$

$$\text{Initial QP} = 0, \dots, 51, \quad (12)$$

$$\overline{\text{BIT}}_{\text{Initial QP}} = (\text{BIT}_{\text{Initial QP}} - \text{MIN}_{\text{Initial QP}=0, \dots, 51} (\text{BIT}_{\text{Initial QP}})) \times (\text{MAX}_{\text{Initial QP}=0, \dots, 51} (\text{BIT}_{\text{Initial QP}}) - \text{MIN}_{\text{Initial QP}=0, \dots, 51} (\text{BIT}_{\text{Initial QP}}))^{-1},$$

$$\text{Initial QP} = 0, \dots, 51, \quad (13)$$

$$\overline{\text{DQP}}_{\text{Initial QP}} = (\text{DQP}_{\text{Initial QP}} - \text{MIN}_{\text{Initial QP}=0, \dots, 51} (\text{DQP}_{\text{Initial QP}})) \times (\text{MAX}_{\text{Initial QP}=0, \dots, 51} (\text{DQP}_{\text{Initial QP}}) - \text{MIN}_{\text{Initial QP}=0, \dots, 51} (\text{DQP}_{\text{Initial QP}}))^{-1},$$

$$\text{Initial QP} = 0, \dots, 51, \quad (14)$$

where $\overline{\text{PSNR}}_{\text{Initial QP}}$, $\overline{\text{BIT}}_{\text{Initial QP}}$, and $\overline{\text{DQP}}_{\text{Initial QP}}$ represent the values of normalized PSNR, real bits, and differences of QPs, respectively. $\text{PSNR}_{\text{Initial QP}}$, $\text{BIT}_{\text{Initial QP}}$, and $\text{DQP}_{\text{Initial QP}}$ are actual unnormalized values. The optimal initial QP is calculated as follow:

$$\text{Optimal Initial QP} = \underset{\text{Initial QP}=0, \dots, 51}{\text{argmin}} \left(\alpha \left(1 - \overline{\text{PSNR}}_{\text{Initial QP}} \right) + \beta \overline{\text{BIT}}_{\text{Initial QP}} + \gamma \overline{\text{DQP}}_{\text{Initial QP}} \right), \quad (15)$$

where Optimal Initial QP is the optimal initial QP, $0 \leq \alpha, \beta, \gamma \leq 1$, and $\alpha + \beta + \gamma = 1$. In our research, the values of α, β, γ are set to 1/3.

3.3. Mapping Method of Spatial Complexity for Generalization. For the video sequences which have the similar complexity, the initial QPs should be similar. A mapping method of spatial complexity is proposed for any tested video sequence. The spatial complexities of selected sample video sequences can be calculated using (11), according to the given target bit rate. For any video sequence, its spatial complexity is computed using (11) too. The spatial complexity of a video sequence can be mapped by selecting the nearest matching spatial complexity from a set of sample proportion spaces as follows:

$$\text{Difference}_i = |\text{SSC}_i - \text{TSC}|, \quad \text{for } i = 1, 2, \dots, 4, \quad (16)$$

where Difference_i is the absolute value of difference between the spatial complexity of i th sample video and a tested one. SSC_i is the i th spatial complexity among 4 sample video sequences. TSC is the spatial complexity of the tested video sequence.

Let *Mapping Sample* denote the sample video that has minimum Difference_i , $i = 1, \dots, 4$.

In Table 1, MSC is the spatial complexity of sample video. Type 1, Type 2, Type 3, and Type 4 are 4 sample video sequences, which are Waterfall, Foreman, Flower, and Mobile, respectively. Table 1 shows that Mobile has the highest spatial complexity and Waterfall has the lowest spatial complexity, which is in agreement with Figure 4. In addition, Table 1 includes 4 groups of the optimal initial QPs which are 4 affiliated sample video sequences at low bit rate, respectively. The initial QP of a test video sequence can be determined by only selecting an element from Table 1 based on *Mapping Sample* and given target bit rate.

TABLE 1: Lookup table for proposed initial QP.

Bit rate	(MSC) Video			
	(32%)	(44%)	(53%)	(90%)
	Type 1	Type 2	Type 3	Type 4
0.4 (Mbps)	30	38	42	45
0.5 (Mbps)	33	32	39	42
0.6 (Mbps)	30	30	36	40
0.7 (Mbps)	28	27	35	36
0.8 (Mbps)	28	25	37	37
0.9 (Mbps)	25	24	34	33
1.0 (Mbps)	25	23	35	32

4. Experimental Results

The proposed algorithm and existing methods, which are JVT-G012 and Wu, are implemented on JM9.3 [13] which is the reference software for H.264. In addition, the experiment uses 7 various CIF (352 × 288) standard video sequences that are Waterfall, Foreman, Flower, Mobile, Bus, City, and Stefen, respectively. In the standard video sequences, Waterfall, Foreman, Flower, and Mobile are selected samples, and Bus, City, and Stefen are used to tested generalized quality of proposed algorithm. According to the proposed scheme which is the spatial complexity calculation and mapping, Mobile is the *Mapping Sample* of Stefen and Bus and City are correspondent to Flower and Foreman, respectively. The experimental conditions are as follows.

- The system platform is Intel (R) Core(TM)2 Duo CPU E7400 2.80 GHZ, 2.00 GB RAM, and the OS is Microsoft Windows XP professional 2002 Service Pack 3.
- JM 9.3 is implemented at the Visual Studio 6.0.
- The profile baselines are used; one GOP has 15 frames which includes that the 1st frame is encoded by intra and others are encoded as interframes; the B-picture is not adopted. The item of “Rate Control Enable” is enabled, the item of “Initial QP” is set to 0, and the target bit rates are limited to range that is from 0.4 to 1.0 (units: Mbps).
- The proposed initial QP is determined using Table 1.
- As for the standard video sequence, the number of frames is 60, the frame rate is 30.

4.1. Objective Evaluation. The three methods which are proposed algorithm, JVT-G012, and Wu are compared in terms of PSNR and the difference of real bits. These indicators of performance can be quantized as follows:

$$\text{PSNR} = 10 \log_{10} \frac{(2^n - 1)^2}{\text{MSE}}, \quad (17)$$

where $\text{MSE} = \sum_{x=0}^{X-1} \sum_{y=0}^{Y-1} (\hat{p}(x, y) - p(x, y))^2$ and \hat{p} is the pixel value of the reconstructed video sequence. p is the original pixel value.

TABLE 2: Comparison of coding performance.

Video sequence	(a) PSNR _{Average} (db)		
	JVT-G012	Wu	Proposed
Waterfall	36.04	35.83	36.12
Foreman	37.78	37.68	37.81
Flower	29.11	29.14	29.16
Mobile	28.12	28.28	28.37
Bus	30.12	30.18	30.24
City	34.72	34.63	34.75
Stefen	31.48	31.46	31.59
Average	32.48	32.46	32.58

Video sequence	(b) ΔR_{total} (bit)		
	JVT-G012	Wu	Proposed
Waterfall	0	-2288	14048
Foreman	0	-2272	2152
Flower	0	62336	69072
Mobile	0	128888	154184
Bus	0	5944	5456
City	0	-1576	-1904
Stefen	0	-1096	24
Total	0	189936	243032

Consider

$$\Delta R = R_{\text{JVT}} - R_{b_{\text{JVT\&TEST}}}, \quad (18)$$

where R_{JVT} is the real bits of the JVT-G012 and $R_{b_{\text{JVT\&TEST}}}$ is the real bits of the algorithms which are proposed method, Wu, and JVT-G012.

Table 2 shows that the simulation results for the average PSNR and the total ΔR , which can be calculated at the range of the target bit from 0.4 to 1.0 Mbps for each video sequence, are indicated by PSNR_{Average} and ΔR_{total} , respectively.

In Table 2(a), the proposed method obtains more better quality performance than JVT-G012 and Wu, although improvement is not obvious. However, ΔR_{total} shows that the proposed algorithm has quite prominent bit rate performance. The proposed method reduces 243032 bits than JVT-G012 in total although each PSNR_{Average} is similar. This illustrates that the reconstructed video of proposed method has minimum actual total bits at the same or similar quality in almost all of simulations except City.

One of the important quality measures of a video is that the quality of each frame should be uniform. The existing methods have not involved this issue. The proposed method has solved this issue by selecting initial QP according to the highest and stablest quality as well as the lowest actual bits in (15). In Table 3, the quality of each frame shows an example of extreme changes. According to the JVT-G012, the value of initial QP is 25 at the target bit rate 0.7 Mbps. The maximum QP is 51 which can generate abominable quality and the minimum QP is 25 which can generate good quality. So the difference between the maximum and minimum of QPs in GOP can be a good measure for the stability of video quality. Figure 8 shows this stability performance

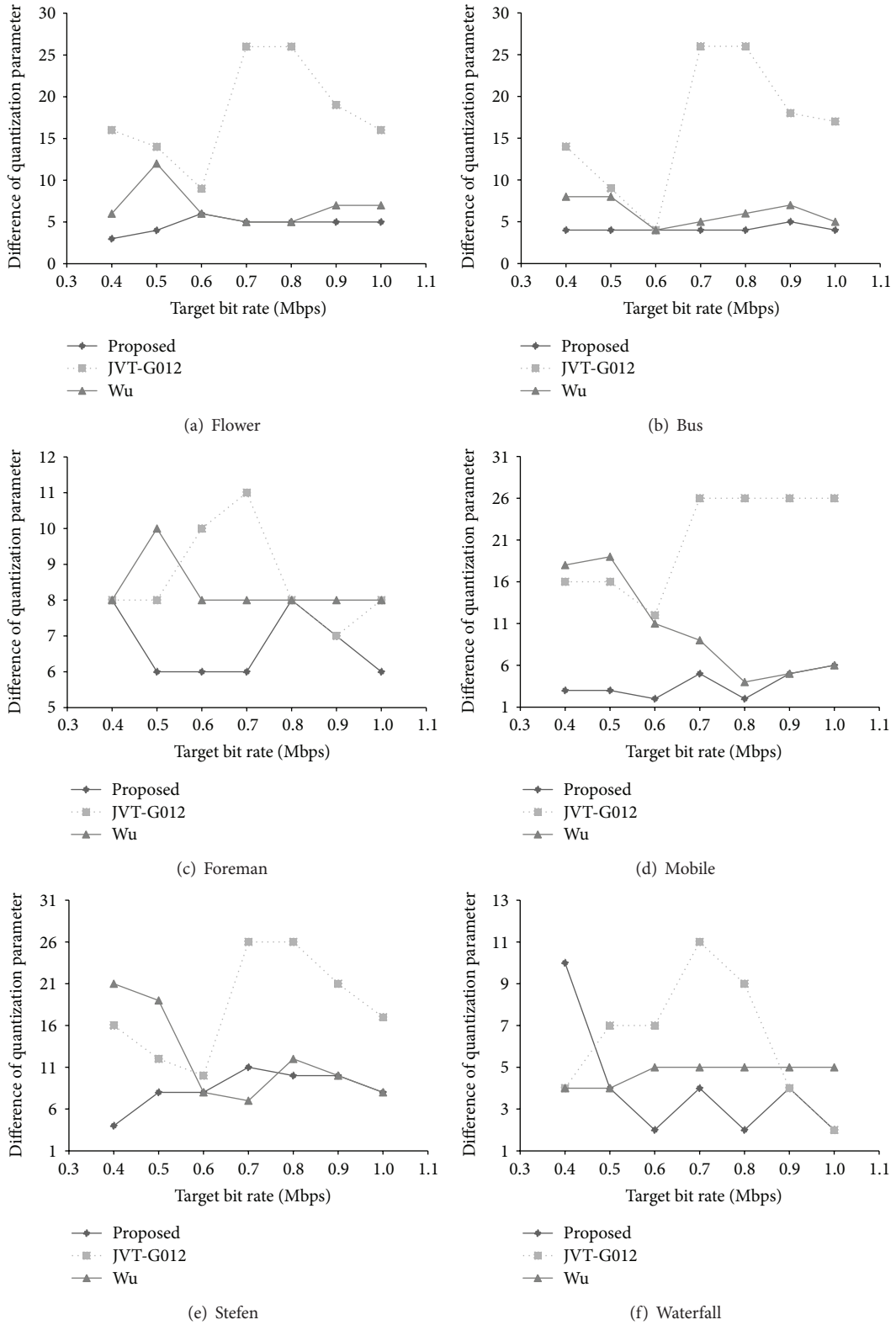


FIGURE 8: Stability performances.

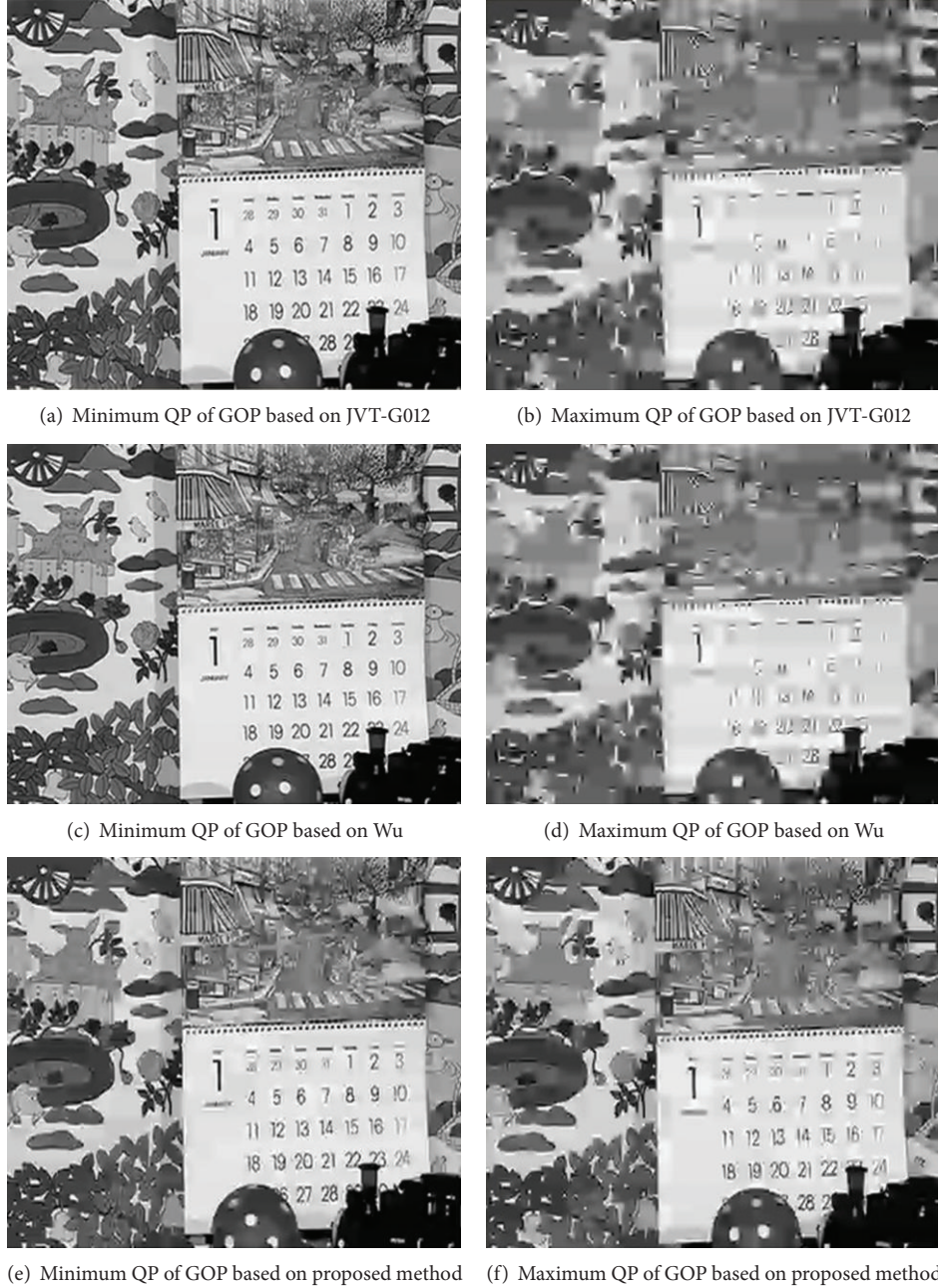


FIGURE 9: Result of subjective evolution.

for proposed method, Wu, and JVT-G012. In Figure 8, the proposed method obtains the lower difference of QPs than others in all the cases.

In fact, PSNR can objectively and effectively assess quality of one frame. However, PSNR is not a perfect measure to evaluate the qualities of video sequences which have multiple frames. In Table 3, although the average PSNR is good, the quality of reconstructed video sequences is very low because the change of frame quality is very high. Extremely high fluctuation of the frame qualities means not only the repetition of fuzzy and vivid images but also video broken phenomenon.

So in order to evaluate video sequences, average PSNR and stability should be considered simultaneously in a GOP.

The quality of video sequences that have high complexity is very sensitive to the value of initial QP at low bit rate. For a given target bit, low initial QP can lead the large bits assignment to the first frame and insufficient bits to the other frames in a GOP to maintain qualities. Therefore, the stability of a reconstructed video sequence is a very important quality performance. Proposed optimal initial QP is determined under consideration of stability in (15). In Figure 8, the proposed method shows better results for all test

TABLE 3: Reconstructed video with extremely changing quality.

Frame number	Bit/frame	QP	Frame PSNR
0	291952	25	38.084
1	95904	25	36.900
2	42176	31	34.305
3	24272	32	32.891
4	17208	34	32.058
5	12504	36	30.613
6	10280	38	30.614
7	8848	40	29.980
8	7776	42	29.338
9	7184	44	28.591
10	6408	46	27.687
11	5720	48	26.682
12	4976	50	25.367
13	4856	51	24.405
14	5432	51	24.615

video sequences at low bitrate. Especially, in high complexity video sequences, the proposed method guarantees excellent results.

4.2. Subjective Evaluation. General video user evaluates video sequences by just looking but not by calculating PSNR or stability. This implies the importance of subjective evaluation. Frankly speaking the relationship between the results of objective evaluation and subjective one is not known. Therefore, it is not easy to convert the difference of objective evaluation results to the differences in subjective evaluation.

In this part, three methods, proposed method, JVT-G012, and Wu, are subjectively evaluated using the objective evaluation results, that is, the maximum and minimum QPs at 0.4 Mbps target bitrate. The Mobile sample video sequence is tested. Figure 9 shows result of this situation.

The average PSNRs of the proposed method, JVT-G012, and Wu are very similar at objective assessment, which are 25.22, 25.03, and 24.83, respectively.

Although Figures 9(a) and 9(c) show better quality than Figure 9(e), all objects in Figure 9(e) are vividly identified at minimum QPs. Although Figures 9(b) and 9(d) are very fuzzy and some details of frame are lost, the quality of Figure 9(f) is excellent compared with Figures 9(b) and 9(d).

In subjective evaluation, we can see also the importance of stability from the gaps in Figures 9(a), 9(b), 9(c), 9(d), 9(e), and 9(f), respectively.

5. Conclusions

In order to obtain the optimal initial QP for the various video sequences which have different spatial and temporal complexities, we propose a simple and high performance initial QP determining method based on motion vector map and temporal complexity to decide an initial QP in given target bit rate. Four sample video sequences are selected according to the temporal complexity which is measured

using motion vectors map, and the spatial complexities of four sample video sequences are computed according to proposed method. For any video sequences, the initial QP can be easily determined from matrices by target bit rate and mapped spatial complexity using proposed mapping method. Experimental results show that the proposed algorithm can obtain more outstanding objective and subjective performance than other conventional determining methods. In the future, one of the further research areas will be the development of quantitative measure for the temporal complexity. The study on temporal complexity will provide a hint to explain or to solve the exceptional case for H.264 AVC coding.

Conflict of Interests

The authors declare that they have no financial or personal relationships with other people or organizations that can inappropriately influence their work; there is no professional or other personal interests of any nature or kind in any product, service, and/or company that could be construed as influencing the position presented in, or the review of, the paper entitled.

References

- [1] MPEG-2: ISO/IEC JTC1/SC29/WG11 and ITU-T, ISO/IEC, 13818-2, Information Technology_Generic Coding of Moving Pictures and Associated Audio Information: Video, ISO/IEC and ITU-T International Standard Draft, 1994.
- [2] ITU-T Rec. H. 264/ISO/IEC, 11496-10, Advanced Video Coding, Final Committee Draft, Document JVT-F100, December 2002.
- [3] H. Kalva, "Standards: the H.264 video coding standard," *IEEE Multimedia*, vol. 13, no. 4, pp. 86–90, 2006.
- [4] T. Wiegand, G. J. Sullivan, G. Bjøntegaard, and A. Luthra, "Overview of the H.264/AVC video coding standard," *IEEE Transactions on Circuits and Systems for Video Technology*, vol. 13, no. 7, pp. 560–576, 2003.
- [5] H. Schwarz, D. Marpe, and T. Wiegand, "Overview of the scalable video coding extension of the H.264/AVC standard," *IEEE Transactions on Circuits and Systems for Video Technology*, vol. 17, no. 9, pp. 1103–1120, 2007.
- [6] G. J. Sullivan and T. Wiegand, "Video compression—from concepts to the H.264/AVC standard," *Proceedings of the IEEE*, vol. 93, no. 1, pp. 18–31, 2005.
- [7] G. J. Sullivan, J. Ohm, H. Woo-Jin, and T. Wiegand, "Overview of the high efficiency video coding (HEVC) standard," *IEEE Transactions on Circuits and Systems for Video Technology*, vol. 22, no. 12, pp. 1649–1668, 2012.
- [8] T. Wiegand, H. Schwarz, A. Joch, F. Kossentini, and G. J. Sullivan, "Rate-constrained coder control and comparison of video coding standards," *IEEE Transactions on Circuits and Systems for Video Technology*, vol. 13, no. 7, pp. 688–703, 2003.
- [9] Z. Chen and K. N. Ngan, "Recent advances in rate control for video coding," *Signal Processing: Image Communication*, vol. 22, no. 1, pp. 19–38, 2007.

- [10] H. Wang and S. Kwong, "Rate-distortion optimization of rate control for h.264 with adaptive initial quantization parameter determination," *IEEE Transactions on Circuits and Systems for Video Technology*, vol. 18, no. 1, pp. 140–144, 2008.
- [11] W. Wu and H. K. Kim, "A novel rate control initialization algorithm for H.264," *IEEE Transactions on Consumer Electronics*, vol. 55, no. 2, pp. 665–669, 2009.
- [12] S. Hu, H. Wang, S. Kwong, and C.-C. J. Kuo, "Novel rate-quantization model-based rate control with adaptive initialization for spatial scalable video coding," *IEEE Transactions on Industrial Electronics*, vol. 59, no. 3, pp. 1673–1684, 2012.
- [13] "JM Reference Software Version 9.3," <http://iphome.hhi.de/suehring/download>.
- [14] "YUV Video Sequences," <http://trace.eas.asu.edu/yuv/index.html>.
- [15] Y.-H. Huang, T.-S. Ou, and H. H. Chen, "Fast decision of block size, prediction mode, and intra block for H.264 intra prediction," *IEEE Transactions on Circuits and Systems for Video Technology*, vol. 20, no. 8, pp. 1122–1132, 2010.

Research Article

The New Mathematical Model of Motion Compensation for Stepped-Frequency Radar Signal

Yun Lin,¹ Xiaochun Xu,¹ Jinfeng Pang,¹ Bin Li,¹ and Ruolin Zhou²

¹ Harbin Engineering University, Room 148, Building 21, NO. 145 Natong Street, Nangang District, Harbin, Heilongjiang 150001, China

² Department of Electrical and Computer Engineering, Western New England University, Springfield, MA, USA

Correspondence should be addressed to Yun Lin; linyun@hrbeu.edu.cn

Received 24 August 2013; Revised 28 November 2013; Accepted 9 December 2013; Published 8 January 2014

Academic Editor: Su-Qun Cao

Copyright © 2014 Yun Lin et al. This is an open access article distributed under the Creative Commons Attribution License, which permits unrestricted use, distribution, and reproduction in any medium, provided the original work is properly cited.

When a stepped-frequency radar is used to obtain the high-resolution range profile (HRRP) of high-speed target, accurate speed estimation and motion compensation must be considered. Therefore, in this paper, a novel mathematical method is presented for estimating the target speed. Firstly, the pulse Doppler method is used to calculate the initial estimation value. Secondly, based on the initial estimation value, the minimum entropy method is used to calculate the coarse estimation value. Finally, based on the coarse estimation value, the minimum l_1 -Norms method is used to calculate the accurate estimation value. The numeric simulation results confirm that this new method is effective and predominant, which has a much higher estimation accuracy in a low SNR and a much larger estimation range of target speed. The final estimation value can be used to well compensate for the influence of target speed on HRRP.

1. Introduction

Stepped-frequency (SF) signal is widely used in the high-resolution radar systems [1–3], because it can be used to get the high-resolution range profile (HRRP) of target. However, SF signal is highly sensitive to targets motion. The radial speed between target and radar contributes influence on phase term, which will lead to severe range-speed coupling [4, 5]. As it is well known, the impact of range-speed coupling is well mitigated through motion compensation. Thus, for noncooperative targets, speed estimation method is very important and necessary. In the literature [6, 7], based on time domain and waveform entropy, two speed estimation methods are presented. However, they have low estimation accuracy and are only effective in a high signal-to-noise ratio (SNR) and low-speed moving targets. In the literature [8], based on SF and pulse Doppler radar signal, an effective algorithm of speed estimation is presented. Simulation results show that this method has a higher estimation accuracy and better antinoise performance. However, it will increase the complexity of radar system. So far, besides these methods mentioned above, many other effective speed estimation

methods have been presented, such as in the literature [9–11]. These methods have gotten much better estimation accuracy. Nevertheless, in common, they have much higher computation complexity and need larger calculation burden; therefore, they are not applicable to use in engineering application. Furthermore, the speed estimation of superspeed moving targets in extremely low SNR is still a key problem for SF signal. And much easier implementation in engineering application also should be taken into account. According to the discussion above, in this paper, a new speed estimation method is proposed. It is a joint speed estimation algorithm, which has a combination of initial, coarse, and accurate estimation process. Simulation experiments have proved that this new method has much higher estimation accuracy and lower calculation burden. Meantime, the effect of HRRP is much better than that used to be for superspeed moving targets in extremely low SNR. Therefore, it can be applied in engineering application.

This paper is organized as follows. Section 1 is the introduction. In Section 2, the mathematic model of SF signal is introduced. In Section 3, the speed estimation algorithm of SF signal is illustrated, and then several comparison experiments

between this new algorithm and traditional algorithm are designed. In Section 4, the conclusions and future work are described in detail.

2. The Mathematical Model of SF Signal

2.1. The Mathematical Model of SF Signal. The SF radar system transmits a series of frames of pulses. Each frame contains a sequence of N pulses with carrier frequencies increasing from pulse to pulse. The carrier frequencies are indicated by $f_n = f_0 + n\Delta f$, where $n = 0, 1, \dots, N-1$, f_0 is the fundamental carrier frequency, and Δf is the frequency step. Thus, the total bandwidth is $B = N\Delta f$. The transmitted SF pulse train during the integration time is described as follows:

$$S_T(t) = \sum_{m=0}^{M-1} \sum_{n=0}^{N-1} \text{rect}\left(\frac{t-t_{m,n}}{T_p}\right) \exp[-j2\pi(f_0 + n\Delta f)t], \quad (1)$$

where

$$\text{rect}\left(\frac{t-t_{m,n}}{T_p}\right) = \begin{cases} 1, & 0 \leq \frac{t-t_{m,n}}{T_p} \leq 1, \\ 0, & \text{otherwise} \end{cases} \quad (2)$$

with $t_{m,n} = mT_f + nT_r$, $m = 0, 1, \dots, M-1$; $n = 0, 1, \dots, N-1$. M is the frame number and N is the pulse number in each frame. $\text{rect}(t)$ is the envelope of the transmitted pulse and is assumed to be normalized to unity during the pulse duration T_p . T_r is the pulse repetition interval and T_f is the frame period. $T_N = NT_r$ is the duration time of SF pulse train, which can be used to represent the processing time required to form the HRRP. The illustration of SF signal is shown in Figure 1.

Suppose that the moving target is composed of a set of P points scatters with backscattering coefficients $A(p)$, with $p = 1, 2, \dots, P$. Therefore, the received signal from a moving target can be expressed in (3) as follows:

$$\begin{aligned} S_R(t) &= \sum_{p=1}^P A(p) S_T[t - \tau_p(t)] \\ &= \sum_{m=0}^{M-1} \sum_{p=1}^P \sum_{n=0}^{N-1} A(p) \text{rect}\left[\frac{t-t_{m,n}-\tau_p(t)}{T_1}\right] \\ &\quad \times \exp[-j2\pi(f_0 + n\Delta f)(t - \tau_p(t))], \end{aligned} \quad (3)$$

where $\tau_p(t)$ is the echo delay of the p th scattering point. In this paper, in order to simplify the analytic process, the acceleration and rotation of target are ignored. Therefore, the $\tau_p(t)$ is shown in

$$\tau_p(t) = \frac{2R_p(t)}{c} = \frac{2[R_p(0) - vt]}{c}, \quad (4)$$

where $R_p(0)$ is the radial distance of p th scatter point to radar at the initial time, v is the radial speed of moving target, and c is the speed of light.

2.2. The Mathematic Analysis of SF Signal in Moving Environment. In general, during each frame period, the change of envelope with the target motion can be neglected. Therefore, after the down conversion and sampling of the SF received-signal, the baseband signal is shown in

$$\begin{aligned} S_D(m, n) &= \sum_{p=1}^P A(p) \exp\left\{j2\pi(f_0 + n\Delta f)\right. \\ &\quad \left. \times \frac{2[R_p(0) - (mT_f + nT_r)v]}{c}\right\} \\ &= \sum_{p=1}^P A(p) \exp\{j2\pi\phi(m, n)\}. \end{aligned} \quad (5)$$

In this paper, the number of points for inverse discrete Fourier transform (IDFT) is N , the HRRP of target can be calculated by (6) with the m th frame SF received signal:

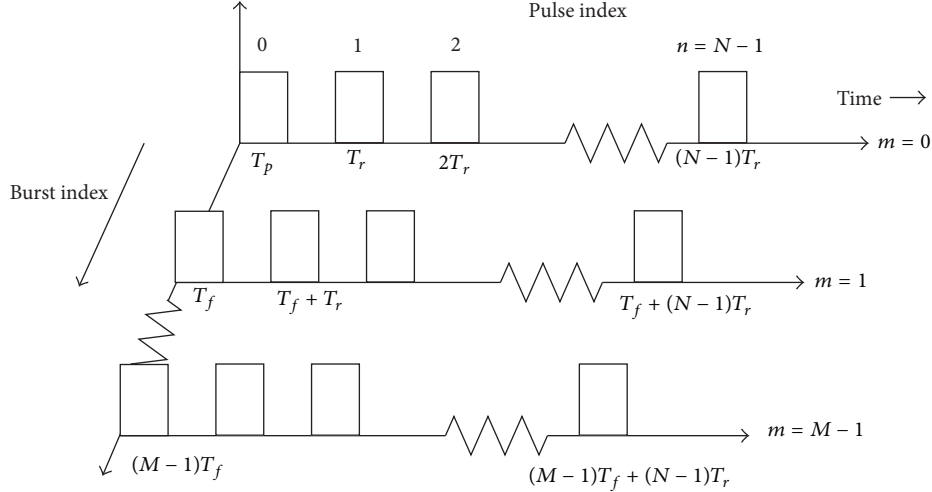
$$\begin{aligned} g(m, i) &= \sum_{n=1}^N S_D(m, n) \exp\left\{j2\pi\frac{in}{N}\right\} \\ &= \sum_{n=1}^N \sum_{p=1}^P A(p) \exp\{j2\pi\phi(m, n)\} \exp\left\{j2\pi\frac{in}{N}\right\}. \end{aligned} \quad (6)$$

Note that the HRRP of target is calculated only by every single frame; therefore, the influence of target motion on HRRP is only embodied in every single frame. In order to simplify the analytic process, suppose $m = 0$. According to (5) and (6), the influence of target motion on HRRP is embodied in the phase $\phi(0, n)$, which is shown in

$$\begin{aligned} \phi(0, n) &= (f_0 + n\Delta f) \frac{2[R_p(0) - vnT_r]}{c} \\ &= \underbrace{\frac{2f_0R_p(0)}{c}}_{\text{const}} + \underbrace{\frac{2nR_p(0)\Delta f}{c}}_{f_R} - \underbrace{\frac{2f_0vT_r n}{c}}_{f_d} - \underbrace{\frac{2v\Delta fT_r n^2}{c}}_{\text{Spread}}. \end{aligned} \quad (7)$$

Equation (7) reveals the special properties of SF signal. For stationary targets, only const and f_R are applicable. The first term represents a constant phase migration, which has no practical influence on HRRP. The second term is produced by the product of frequency. Therefore, the distance between target and radar is converted into the frequency migration, which can be used to calculate the distance between target and radar. In general, the frequency migration can be calculated by IDFT. Furthermore, the range resolution Δr and unambiguous range R_u are, respectively, dependent on frequency resolution and maximum unambiguous frequency of IDFT. The expression for these quantities is described in

$$\Delta r = \frac{c}{2B} = \frac{c}{2N\Delta f}, \quad R_u = \frac{c}{2\Delta f}. \quad (8)$$


 FIGURE 1: Illustration of M frames of SF Signal.

The third term f_d in (7) is a linear phase term (LPT), which represents the Doppler frequency migration due to target motion. The processing of IDFT mistakes the Doppler frequency as a frequency migration due to range and thus results in the shifting of target range from its true range. According to the literature [5] and (8), suppose, in order to perfectly compensate for LPT, that the sustainable error of distance measurement is half of range resolution of SF signal, which is shown as follows:

$$\Delta R = \frac{\Delta r}{2} = \frac{c}{4N\Delta f}. \quad (9)$$

Then, the estimation accuracy of target speed must satisfy

$$|\Delta v|_{\text{LPT}} \leq \frac{c}{2} \left(\frac{\Delta f}{f_0} \right) \left(\frac{1}{T_r} \right) \left(\frac{1}{N\Delta f} \right) = \frac{c}{4f_0NT_r}. \quad (10)$$

The fourth term ‘‘Spread’’ in (7) is a quadratic phase term (QPT), which causes the frequency spread. This phase will disperse target energy into several range bins and lead to several negative effects including the loss of range resolution, range accuracy, and signal-to-noise ratio. According to the literature [5], suppose, in order to perfectly compensate for QPT, the sustainable change of QPT satisfies the following requirement:

$$2\pi \frac{2N\Delta f |\Delta v|_{\text{QPT}} NT_r}{c} \leq \frac{\pi}{2}. \quad (11)$$

Then, the estimation accuracy of target speed must satisfy

$$|\Delta v|_{\text{QPT}} \leq \frac{c}{8N^2\Delta f T_r}. \quad (12)$$

According to the discussion above, the compensation accuracy of LPT is much higher than that of QPT. Therefore, the LPT needs an accurate speed estimation and the QPT only needs a coarse speed estimation. When the target speed is estimated, according to (5) and (7), the LPT and QPT can be eliminated.

TABLE 1: The main parameters of SF radar signal.

f_0	N	Δf	T_1	T_r	M
94 GHz	128	4 MHz	100 ns	20 μ s	96

TABLE 2: The main performance of SF radar signal.

Δr	R_u	$ \Delta v _{\text{LPT}}$	$ \Delta v _{\text{QPT}}$
0.3 m	37.5 m	0.308 m/s	28.610 m/s

In this paper, the main parameters of SF signal are shown in Table 1, and the main performance parameters of SF signal are shown in Table 2.

In this paper, let us suppose that the target speed is constant and takes no account of its own rotation. Meanwhile, the maximum radial length of the target is less than R_u . There are four strong radial scatters which are shown in Figure 2 ($R = 2$ km), and the ratio of normalized scattering intensity (NSI) is 1 : 10 : 6 : 8.

3. The Speed Estimation Algorithm of SF Signal

According to the discussion above, the influence of target motion on HRRP is embodied in the additional LPT and QPT. In order to get better HRRP, firstly, the target speed must be estimated, and then the additional phase terms need to be eliminated. In this paper, based on some traditional mathematic model, a new accurate and fast speed estimation algorithm is proposed.

3.1. The Pulse Doppler Algorithm (PDA). This method is based on pulse Doppler effect; firstly, through IDFT with SF received signal, the Doppler frequency can be calculated, and then the target speed can be calculated by

$$\hat{v}_{\text{IE}} = \frac{2f_0 f_d}{c}. \quad (13)$$

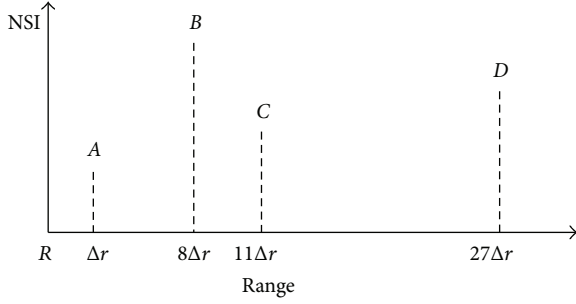


FIGURE 2: The model of target.

According to the IDFT theory, the speed estimation accuracy of PDA is shown in

$$\Delta v_{IE} = \frac{\Delta f_d c}{2f_0} = \frac{c}{2Mf_0 T_r}. \quad (14)$$

In this paper, the accuracy of speed estimation $\Delta \hat{v}_{IE}$ is less than 0.831 m/s, which is only enough to compensate for the QPT. In addition, because of the maximum unambiguous frequency caused by the IDFT, PDA has a great estimation limitation to the interval of target speed, which is shown in (15)

$$v_{\max} = \frac{c}{2f_0 T_r}. \quad (15)$$

Here, $v_{\max} = 79.787$ m/s; therefore, if the target speed goes over v_{\max} , the estimation result will satisfy (16) and cause much greater error:

$$v_{PDA} = \hat{v}_{IE} + kv_{\max} \quad k = 1, 2, \dots \quad (16)$$

Figure 3 indicates the estimation error of PDA in different speed (within an unambiguous rang of speed estimation) and SNR by Monte Carlo experiments; the experiments time is 1000. This simulation experiment indicates that PDA is effective to compensate for QPT in low SNR, but it has a great limitation to v_{\max} .

3.2. The Minimum Entropy Algorithm (MEA). It is well known that the overall target response in the HRRP is changing with the target motion, such as the reduction of peak response, the divergence of scatters, and the blurring effects. According to the theory of image processing, the entropy is a measure of the randomness of an image. The focused images will have a low entropy values. Thus, the mathematical model of entropy can be used as a quality indicator for HRRP. It is defined by

$$H_m = - \sum_{i=0}^{N-1} \hat{g}_m(i) \ln \hat{g}_m(i) \quad \hat{g}_m(i) = \frac{|g(m, i)|}{\sum_{i=0}^{N-1} |g(m, i)|}. \quad (17)$$

According to Formula (6), $g(m, i)$ can be obtained by the IDFT. If the target motion is well compensated, the entropy of HRRP will be minimized. In summary, this method uses the entropy of HRRP as evaluation function to find target speed,

because the estimation value will minimize the entropy of HRRP. Supposing that the speed of target is $V = 2000$ m/s, Figure 4 shows the entropy feature of HRRP in different speed, which proves the effectiveness of MEA. In addition, the MEA is a search process, which needs an initial speed and an effective search algorithm (such as simulated annealing, evolutionary, and genetic algorithm).

Figure 5 indicates the estimation error of MEA with different speed and SNR by Monte Carlo experiments, and the experiments time is also 1000. This simulation experiment proves that, with the SNR decreasing, the estimation accuracy of EMA will rapidly decline, and it can only be used to compensate for QPT in low SNR. However, the EMA has a much bigger interval of speed estimation than that of PDA.

3.3. The Minimum l_1 -Norms Algorithm (MNA). This algorithm needs to transmit two different frames and each frame contains N pulses, which is shown in Figure 6. The first frame is the up frame, the carrier frequency at each pulse increases from f_0 to $f_0 + (N - 1)\Delta f$. The second frame is the down frame, the carrier frequency at each pulse descends from $f_0 + (N - 1)\Delta f$ to f_0 . Therefore, the frequency of n th pulse in up-frame can be calculated by $f_n^1 = f_0 + n\Delta f$ and in down-frame can be calculated by $f_n^2 = f_0 + (N - n - 1)\Delta f$.

According to (5), the n th pulse of received signal can be described as

$$S_D^1(n) = \sum_{p=1}^P A(p) \exp \left\{ j2\pi f_n^1 \frac{2[R_p(0) - vnT_r]}{c} \right\},$$

$$S_D^2(n) = \sum_{p=1}^P A(p) \exp \left\{ j2\pi f_n^2 \frac{2[R_p(0) - v(N+n)T_r]}{c} \right\}. \quad (18)$$

Compensating with a initial speed \hat{v}_{IE} , (18) is converted into the following form:

$$S_{DC}^1(n) = \sum_{p=1}^P A(p) \exp \left\{ j2\pi f_n^1 \frac{2[R_p(0) - \Delta v n T_r]}{c} \right\},$$

$$S_{DC}^2(n) = \sum_{p=1}^P A(p) \exp \left\{ j2\pi f_n^2 \frac{2[R_p(0) - \Delta v (N+n) T_r]}{c} \right\}, \quad (19)$$

where $\Delta v = v - \hat{v}$, $S_{DC}^1(n)$ and $S_{DC}^2(n)$ represent a coarse compensation with the initial target speed. Then, the function of frame error can be defined as l_1 -Norms in

$$R_\varphi(\Delta v) = \frac{1}{N} \sum_{n=0}^{N-1} |S_{DC}^1(n) - S_{DC}^2(n)|, \quad (20)$$

and then it can be further simplified as

$$R_\varphi(\Delta v) = \frac{1}{N} \sum_{n=0}^{N-1} \left| \sin \left[2\pi T_r (f_0 + n\Delta f) (2N - 1 - 2n) \frac{\Delta v}{c} \right] \right|. \quad (21)$$

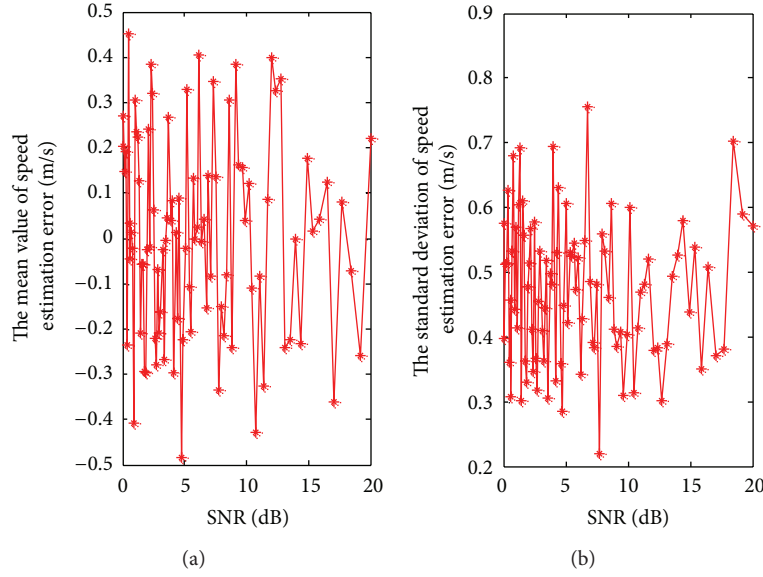


FIGURE 3: The estimation error of PDA.

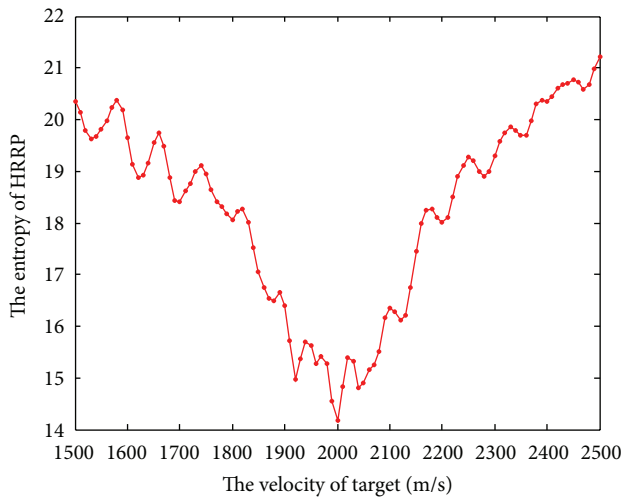


FIGURE 4: The entropy feature of MEA.

According to (21), Δv makes a difference between $S_{DC}^1(n)$ and $S_{DC}^2(n)$ which can be used to estimate target speed. If the target motion is well compensated, then it satisfies $R_\varphi(\Delta v) = 0$. Considering the complexity of target motion and signal environment, the evaluation function of global optimal estimation can be defined as

$$R_\varphi(\hat{v}) = \min \{R_\varphi(\Delta v)\}. \quad (22)$$

Supposing that the speed of target is $V = 2000$ m/s, Figure 7 shows the value of frame error in different speed, which proves the effectiveness of MNA. Therefore, target speed estimation can be performed by searching the minimum peak in Figure 7. Within the searching procedure, the following problems should be considered.

- (1) When the initial estimation value is chosen, wrong searching direction will prolong searching time and increase computation amount.
- (2) In order to get global minimum value as accurate as possible, search step size should be less than the width of the peak. Therefore, the computation amount may be significantly increased.
- (3) Even if the SNR of received signal is high, the curve of evaluation function may also have some local fluctuation nearby the true value. Therefore, if the search algorithm is not very effective, the evaluation function may converge to the local minimum which will cause much higher estimation error.

Figure 8 indicates the estimation error of MNA in different speed and SNR by Monte Carlo experiments; the experiments time is also 1000, and the search step of MNA is 1 m/s. This simulation experiment proves that the estimation accuracy of MNA is very high than that of PDA and MEA, and it can be used to compensate results in LPT in very low SNR.

3.4. The Compound-Estimation Algorithm (CEA). According to the discussion above, in order to overcome the defects of PDA, MEA, and MNA, an improved speed estimation algorithm is presented. It contains three steps including initial estimation, coarse estimation and accurate estimation.

The SF radar system transmits alternately the up frame and the down frame and the received signals are shown in

$$S_D = \begin{bmatrix} S_D(1,1) & S_D(1,2) & \cdots & S_D(1,N) \\ S_D(2,1) & S_D(2,2) & \cdots & S_D(2,N) \\ \vdots & \vdots & \vdots & \vdots \\ S_D(M,1) & S_D(M,2) & \cdots & S_D(M,N) \end{bmatrix}. \quad (23)$$

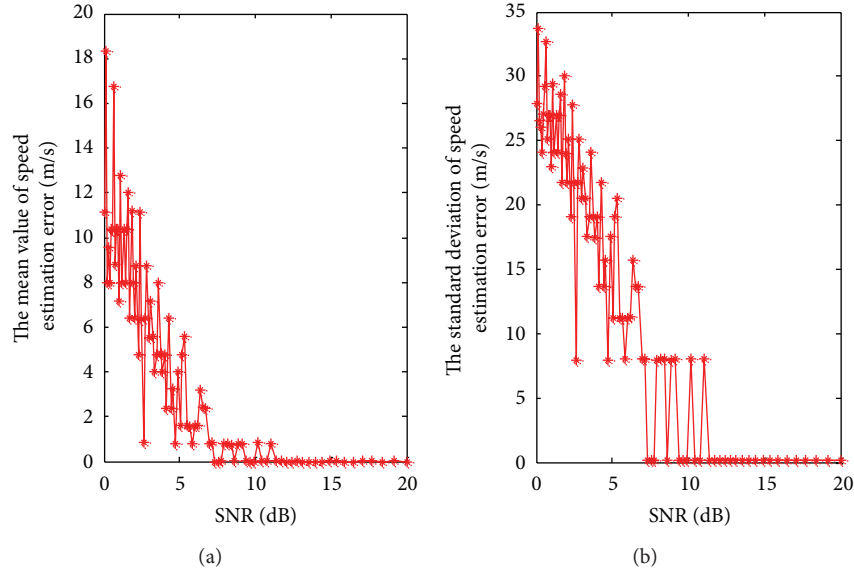


FIGURE 5: The estimation error of MEA.

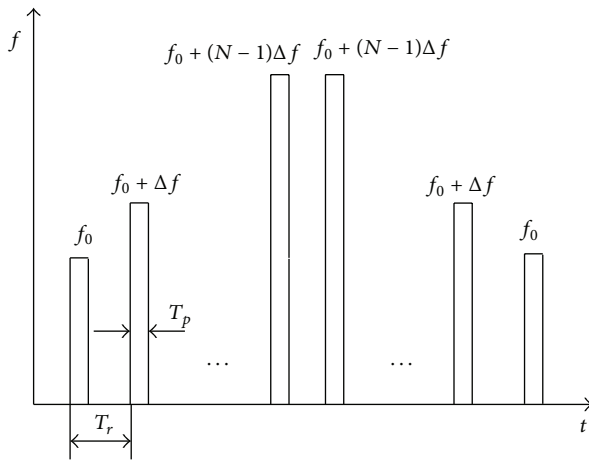


FIGURE 6: The model of the up frame and results in frame.

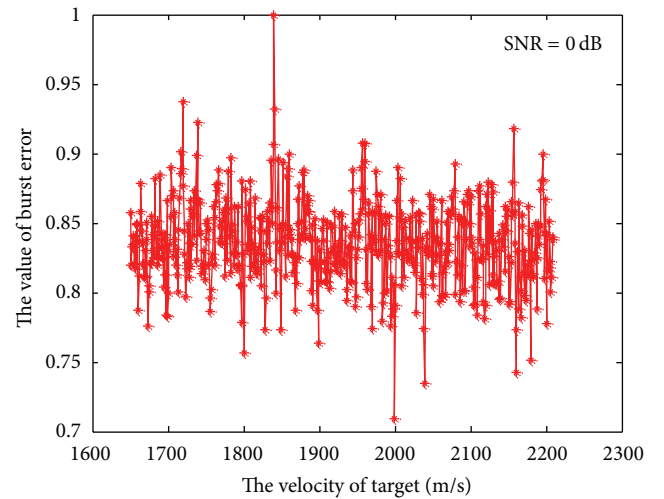


FIGURE 7: The frame error feature of MNA.

The odd row is the up-frame and the even row is the down-frame. The value of $M = 2L$ is even.

3.4.1. The First Step: Initial Estimation (IE) Based on PDA. PDA is used for initial estimation with the first column in (23). The new signal sequence for estimation is shown in

$$\begin{aligned} \mathbf{S}_D^{\text{odd}} &= [S_D(1, 1) \ S_D(3, 1) \ \cdots \ S_D(2L-1, 1)], \\ \mathbf{S}_D^{\text{even}} &= [S_D(2, 1) \ S_D(4, 1) \ \cdots \ S_D(2L, 1)]. \end{aligned} \quad (24)$$

According to the discussion in Section 3.1, the estimation value can be calculated by (13) and (24) with IDFT, and they are defined as $\hat{v}_{IE}^{\text{odd}}$ and $\hat{v}_{IE}^{\text{even}}$. Then, the initial estimation value can be calculated by

$$\hat{v}_{IE} = \frac{\hat{v}_{IE}^{\text{odd}} + \hat{v}_{IE}^{\text{even}}}{2}. \quad (25)$$

In this paper, according to the main parameters of SF signal in Table 1, the initial estimation error is $|\Delta\hat{v}_{IE}| \leq 1.662$ m/s, which is only enough to compensate for the QPT. The maximum unambiguous estimation interval of target speed is $|\hat{v}_{IE}| \leq v_{\max} = 79.787$ m/s. In this paper, suppose that the estimation interval of target speed is $V \in [0, 6000]$ m/s; therefore, according to (16), there are a total of 77 possible estimation values, which are $k = 0, 1, \dots, 76$. Therefore, the MEA is used for expanding the estimation interval of target speed.

3.4.2. The Second Step: Coarse Estimation (CE) Based on MEA. After compensating with initial estimation value, MEA is used for coarse estimation with the first and second row

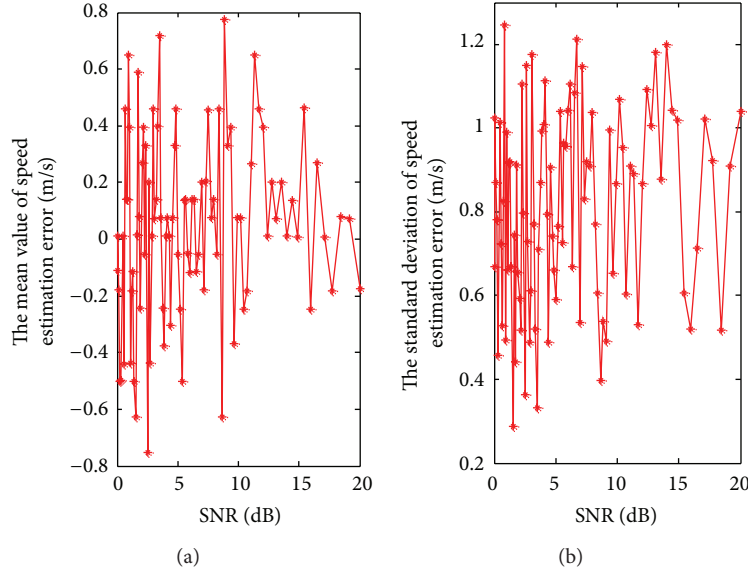


FIGURE 8: The estimation error of MNA.

in (23). The new SF signal sequence for estimation is shown in

$$\begin{aligned} \mathbf{S}_D^1 &= [S(1, 1) \ S(1, 2) \ \cdots \ S(1, N-1)], \\ \mathbf{S}_D^2 &= [S(2, 1) \ S(2, 2) \ \cdots \ S(2, N-1)]. \end{aligned} \quad (26)$$

According to the discussion in Sections 3.1 and 3.2, the coarse estimation values can be calculated by (17) and (26) with these initial estimation values, which are shown as follows:

$$v_{CE}^i = \hat{v}_{IE} + kv_{\max} \quad k = 0, 1, \dots, 76, \quad i = 1, 2. \quad (27)$$

According to these 77 possible values, two coarse estimation values which are defined as \hat{v}_{CE}^i can be calculated, and then the final value of coarse estimation can be calculated by

$$\hat{v}_{CE} = \frac{\hat{v}_{CE}^1 + \hat{v}_{CE}^2}{2}. \quad (28)$$

According to the discussion of MEA method, the possible value of target speed can be determined. However, this coarse estimation value is only enough to compensate for QPT. Therefore, finally, the MNA is used to increase the estimation accuracy of target speed.

3.4.3. The Third Step: Accurate Estimation (AE) Based on MNA. When the coarse estimation value is obtained, the true value of target speed will surely consist in $[\hat{v}_{CE} - \hat{v}_{IE}/2, \hat{v}_{CE} + \hat{v}_{IE}/2]$. Therefore, the final estimation value can be defined as $\hat{v}_{AE} = \hat{v}_{CE} + k\Delta v$, which satisfies $\hat{v}_{AE} \in [\hat{v}_{CE} - \hat{v}_{IE}/2, \hat{v}_{CE} + \hat{v}_{IE}/2]$. According to the discussion in Table 2 and Section 3.3, in order to compensate for the LPT, choosing the search step as $\Delta v = 0.2$ m/s, the MNA is used to calculate the accurate estimation value with (19), (20), and (26), which can be used to compensate for LPT.

Figure 9 indicates the estimation error of CEA in $V \in [0, 6000]$ m/s and $\text{SNR} \in [0, 20]$ dB. It proves that the CEA is effective to compensate for LPT in a much larger estimation interval of target speed and extremely low SNR.

Figures 10 and 13 are the HRRP of a moving target with four different compensation methods. HRRP0 is the HRRP of static target. Figure 10 is the HRRP of a moving target based on PDA. Because of the limitation of estimation interval, the HRRP1 is completely a distortion and cannot identify target. Figure 11 is the HRRP of a moving target based on MEA, and the HRRP2 produces a big range migration beyond an unambiguous range window. In addition, it can be used to identify target. However, because of the limitation of estimation accuracy, the HRRP2 cannot be used for distance measurement. Figure 12 is the HRRP of a moving target based on MNA, and the HRRP3 produces a little migration within an unambiguous range window and also can be used to identify target. The accuracy of distance measurement is much more accurate than that of MEA. Figure 13 is the HRRP of a moving target based on CEA, and the HRRP4 produces the smallest migration within an unambiguous range window and has the highest accuracy of distance measurement; the HRRP4 also can be used to identify target. Therefore, the CEA has the best compensation result for identifying target and distance measurement.

4. Conclusion

In this paper, three different speed estimation models are analyzed in detail. The PDA has an accurate estimation value in low SNR. However, it has a large limitation to estimation interval of target speed, which will make a great estimation error for a high-speed moving target. The MNA has a coarse estimation value in a much larger speed estimation interval. However, it has a large limitation to SNR, and the estimation accuracy is not enough for well compensating the influence

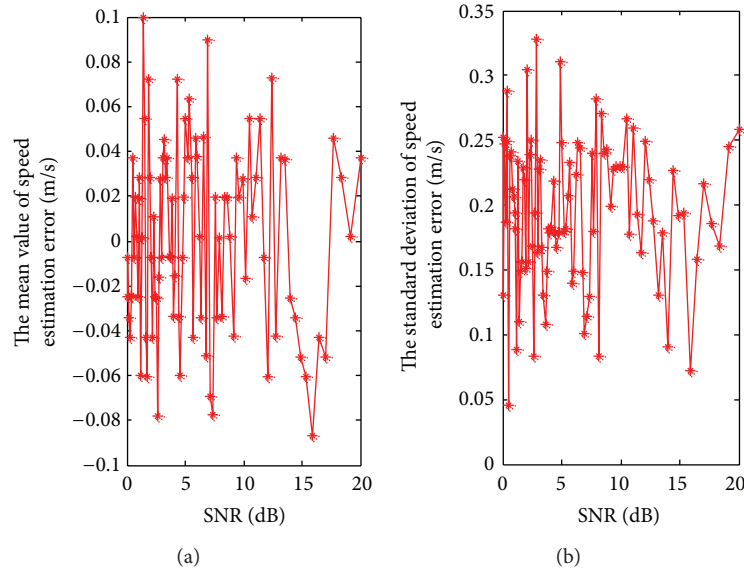


FIGURE 9: The estimation error of CEA.

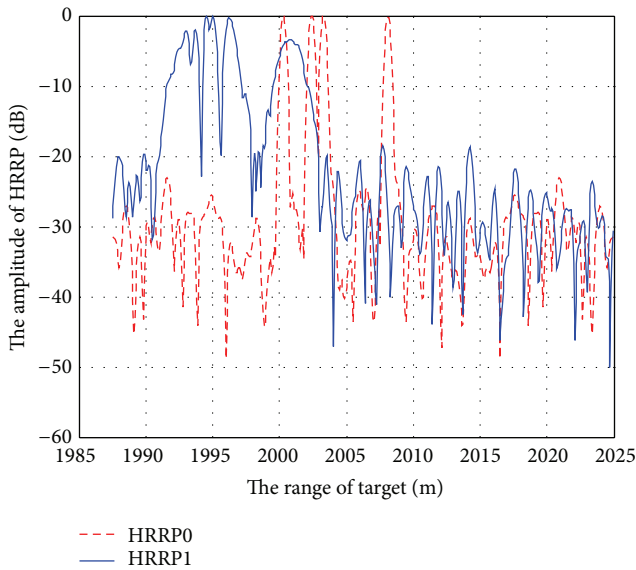


FIGURE 10: The HRRP of SF signal based on PDA.

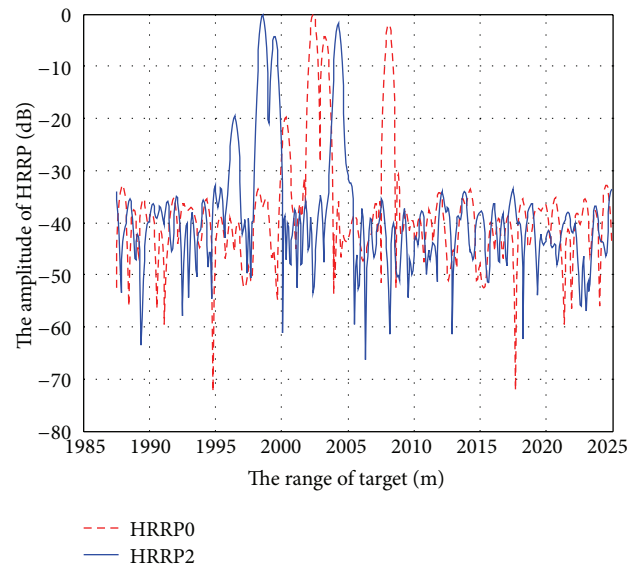


FIGURE 11: The HRRP of SF signal based on MEA.

of target speed on HRRP. The MNA has the best estimation accuracy. However, the local minimum value of frame error function will produce worse estimation accuracy and make a large computation amount.

According to the advantages and defects of PDA, MEA, and MNA, the CEA is presented in this paper. Firstly, according to the main parameters of SF signal, some important performance parameters can be calculated. Secondly, the initial estimation value is obtained by PDA. Thirdly, based on the initial estimation value and the estimation interval of target speed, the MEA is used for the coarse estimation value. Finally, based on the coarse estimation value and the final estimation accuracy, the MNA is used for the accurate

estimation. The theory analysis and simulation results confirm that this new method is effective and predominant, which has a much higher speed estimation accuracy in real-time and a much larger estimation interval of target speed. Furthermore, the influence of super-high speed motion of target on HRRP can be perfectly compensated, and the HRRP can be used to improve the detection, recognition, and distance measurement performance of moving target.

Conflict of Interests

The authors declare that there is no conflict of interests regarding the publication of this paper.

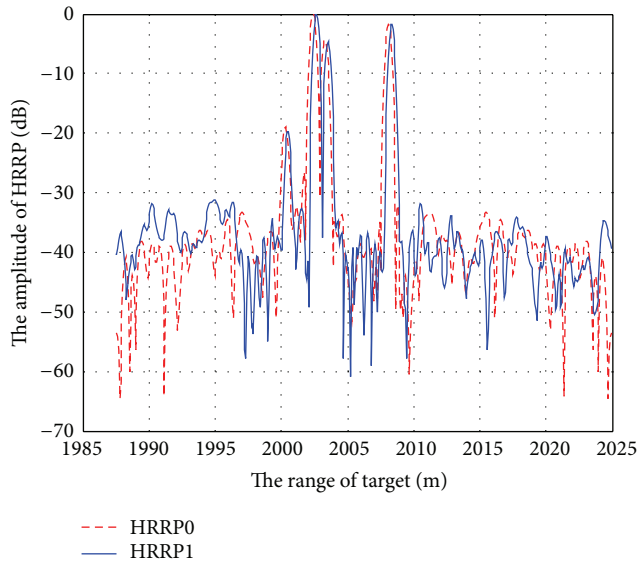


FIGURE 12: The HRRP of SF signal based on MNA.

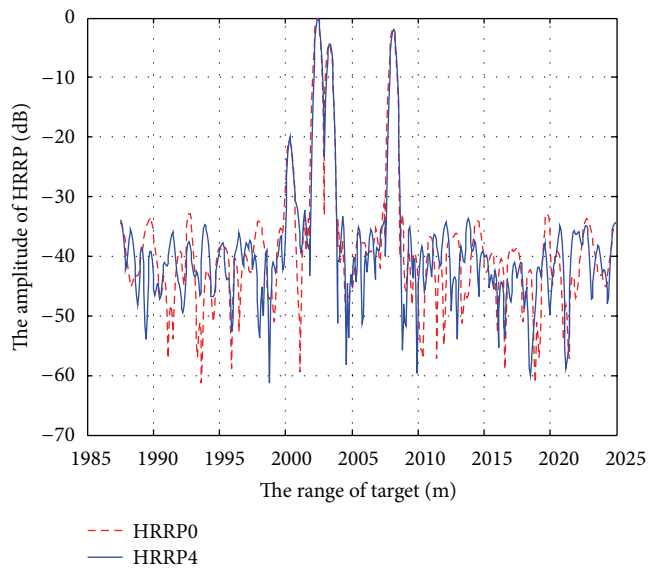


FIGURE 13: The HRRP of SF signal based on CEA.

- [2] T. H. Einstein, "Contrast-optimization-based range-profile autofocus for polarimetric stepped-frequency radar," *IEEE Transactions on Geoscience and Remote Sensing*, vol. 48, no. 4, pp. 2049–2056, 2010.
- [3] B. Pang, D.-H. Dai, S.-Q. Xing et al., "Imaging enhancement of stepped-frequency radar using the sparse reconstruction technique," *Progress in Electromagnetics Research-Pier*, vol. 140, pp. 63–89, 2013.
- [4] S. Chang-gui and L. Xing-guo, "Two-step stretch processing method for MMW high-resolution radar," *Journal of Infrared and Millimeter Waves*, vol. 22, no. 6, pp. 457–460, 2006.
- [5] L. Teng, "Doppler performance analysis of frequency stepped radar signal," *Modern Radar*, vol. 2, pp. 31–37, 1996.
- [6] L. Jing, L. Xing-guo, and W. Wen, "Application of waveform entropy method for motion compensation of MMW Costas frequency hopped radar," *Journal of Infrared and Millimeter Waves*, vol. 22, no. 4, pp. 303–306, 2003.
- [7] J. Liu, X.-G. Li, and Y.-H. Li, "Motion compensation for 1-d range profile of moving target in MMW Costas frequency hopped radar," *Journal of Infrared and Millimeter Waves*, vol. 24, no. 5, pp. 344–347, 2005.
- [8] W. Gui and L. Xing-guo, "Compound approach of measuring speed based on step-frequency and pulse doppler system," *Journal of Infrared and Millimeter Waves*, vol. 27, no. 3, pp. 191–194, 2008.
- [9] F. Berizzi, M. Martorella, A. Cacciamano, and A. Capria, "A contrast-based algorithm for synthetic range-profile motion compensation," *IEEE Transactions on Geoscience and Remote Sensing*, vol. 46, no. 10, pp. 3053–3062, 2008.
- [10] G. Xia, H. Su, and P. Huang, "Velocity compensation methods for LPRF modulated frequency stepped-frequency (MFSF) radar," *Journal of Systems Engineering and Electronics*, vol. 21, no. 5, pp. 746–751, 2010.
- [11] L. Hai-bo and L. Jun-dao, "Target motion compensation algorithm based on keystone transform for wideband pulse doppler radar," *Transactions of Beijing Institute of Technology*, vol. 32, no. 6, pp. 626–631, 2012.

Acknowledgments

This work is supported by the Nation Nature Science Foundation of China no. 61301095 and 61201237, Nature Science Foundation of Heilongjiang Province of China no. QC2012C069, and the Fundamental Research Funds for the Central Universities no. HEUCFZ1129, no. HEUCF130810, and no. HEUCF130817.

References

- [1] D. R. Wehner, "Novel range profile synthesis algorithm for linearly stepped-frequency modulated inversed synthetic aperture radar imaging of remote manoeuvring target," *Let Radar Sonar and Navigation*, vol. 5, no. 4, pp. 496–506, 2011.

Research Article

A Model for Recognizing Key Factors and Applications Thereof to Engineering

Baofeng Shi and Guotai Chi

School of Business Management, Dalian University of Technology, Dalian 116024, China

Correspondence should be addressed to Guotai Chi; chigt@dlut.edu.cn

Received 9 September 2013; Revised 6 November 2013; Accepted 1 December 2013; Published 8 January 2014

Academic Editor: Gelan Yang

Copyright © 2014 B. Shi and G. Chi. This is an open access article distributed under the Creative Commons Attribution License, which permits unrestricted use, distribution, and reproduction in any medium, provided the original work is properly cited.

This paper presents an approach to recognize key factors in data classification. Using collinearity diagnostics to delete the factors of repeated information and Logistic regression significant discriminant to select the factors which can effectively distinguish the two kinds of samples, this paper creates a model for recognizing key factors. The proposed model is demonstrated by using the 2044 observations in financial engineering. The experimental results demonstrate that the 13 indicators such as “marital status,” “net income of borrower,” and “Engel’s coefficient” are the key factors to distinguish the good customers from the bad customers. By analyzing the experimental results, the performance of the proposed model is verified. Moreover, the proposed method is simple and easy to be implemented.

1. Introduction

With the advent of the era of big data, the data classifications exist in fingerprint recognition, facial recognition, customer classification, DNA identification, product category, and so forth. So it has become more and more important for researchers to find the key factors which are capable of effectively distinguishing the data. For this purpose, many mathematical models are explored as the decision support methods to classify the data.

In the literature, there are two main data classification methods. Artificial intelligence method is one of the classification methods for recognizing key factors. Hu et al. proposed an adaptive multilevel kernel machine method for scene classification and experimented on two popular benchmark datasets, which demonstrated that the proposed model outperformed the original spatial PACT [1]. In order to obtain the performance of customer classification models, Finlay compared the performance of several multiple classifiers and found that Error Trimmed Boosting outperformed all other multiple classifiers on UK credit data [2]. Akkoc proposed a three stage hybrid Adaptive Neuro Fuzzy Inference System client classification model, which is based on statistical

techniques and Neuro Fuzzy. The proposed model performs better than the Linear Discriminant Analysis, Logistic Regression Analysis, and Artificial Neural Network (ANN) approaches [3]. By combining the biometric fractal pattern and particle swarm optimization (PSO)-based classifier, a fingerprint recognition model was established [4]. Twala explored the predicted behavior of five classifiers for different types of noise in terms of credit risk prediction accuracy and how such accuracy could be improved by using classifier ensembles. The experimental evaluation showed that the ensemble of classifiers technique has the potential to improve prediction accuracy [5]. Chen studied the classification problem of default customers and nondefault customers by using Support Vector Machines. Experiment demonstrated that the proposed model can effectively recognize the key factors [6].

Statistics and measurement method is another classification tool to solve this problem. Căleanu et al. studied the problems of feature extraction and classifier design in facial recognition by combining a feature extraction technique and a k-NN statistical classifier method. Experimental results showed that the approach enables them to achieve both higher classification accuracy and faster processing time [7]. Compared with conventional models such as multiple

discriminant analysis, logistic regression analysis, and neural networks for the classification problems of bankrupt firms and nonbankrupt firms, Min and Lee proposed the DEA classification model [8]. Shi and Chi studied the customer classification problem by combining correlation analysis and Probit regression. Experiment demonstrated that the proposed model can recognize the key factors which can effectively distinguish the default customers from the nondefault ones [9]. In order to distinguish good customers and bad customers, Hwang et al. established ordered semiparametric Probit customers classification model by substituting ordered semiparametric function for linear regression function [10]. Sun et al. presented a classification method for distinguishing distressed enterprises and nondistressed enterprises based on gray forecasting and pattern recognition. Then the calculating result was classified to judge state of enterprise with the pattern recognition model [11]. Because attribute interactions toward classification were not considered in the classification methods, a new nonlinear classification method with nonadditive measures was proposed. Experimental results showed that applying nonadditive measures on the classic optimization-based models could improve the classification robustness and accuracy by comparing with some popular classification methods [12]. Because the existing model-based approaches are often conceptually and numerically instable for large and complex data sets, Corander et al. considered a Bayesian model-based method for unsupervised classification of discrete valued vectors, which have certain advantages over standard solutions based on latent class models [13].

Although the existing researches have made great progress, there are still some drawbacks. Firstly, the collinearity between factors cannot be excluded in the existing classification researches. Secondly, the existing models include the factors which are unable to effectively distinguish the two types of samples.

The purpose of this paper is to set up a model for recognition key factors, which is based on collinearity diagnostics and Logistic regression significant discriminant. Using a Chinese state-owned commercial bank's 2044 petty loans for farmers, the proposed model is tested by screening the key factors which can effectively distinguish the good customers from the bad ones.

The rest of the paper is structured as follows. We will give the constructing principle of the model for recognition key factors in Section 2. The third part is the construction steps of this model. The fourth part presents the data and the empirical results. Conclusions are given in Section 5.

2. The Constructing Principle of the Model for Recognizing Key Factors

(1) *The Principle of Screening Key Factors.* It is obtained by the bilateral probability P_j of regression coefficient c_j for every factor x_j^i by constructing the Logistic regression model among factors x_j^i and default state y_i of customers (wherein, y_i is equal to 0 denoting the i th customer is a good customer and y_i is equal to 1 denoting the i th customer is

a bad customer). Comparing the bilateral probability P_j with the given critical probability P_0 , it can distinguish whether the factor x_j^i has an obvious effect on default state of customers. By deleting these factors that have no obvious effect on default status, it ensures that the reserved factors can effectively distinguish the bad customers from the good ones.

(2) *The Principle of Eliminating Redundant Information between Factors.* The more redundant factors data system includes, the more disorder the data classification results will be. This paper eliminates the repeated information of the factors by using collinearity diagnostics.

Flowchart of the research methodology is shown in Figure 1.

3. The Recognition Key Factors Model Based on Collinearity Diagnostics and Logistic Regression Significant Discriminant

3.1. *Data Standardization.* There are two kinds of factors in practice. One is called quantitative factors (namely, quantitative indicators) and the other is called qualitative factors (namely, qualitative indicators).

(1) *The Data Standardized of Quantitative Factors.* The quantitative factors include positive factors, negative factors, and interval factors. The positive factors are the factors whose values are the bigger, the better; the negative factors are the factors whose values are the smaller, the better. And the interval factors are the factors whose values are reasonable only when they lie in certain intervals.

Let x_j^i denote the standardization score of the i th observed value of the j th indicator. Let v_{ij} denote the factor data of the i th observed value of the j th indicator. Let n denote the number of observations. The standardization equations of the positive factors and the negative factors are shown as (1) and (2), respectively [12],

$$x_j^i = \frac{v_{ij} - \min_{1 \leq i \leq n} (v_{ij})}{\max_{1 \leq i \leq n} (v_{ij}) - \min_{1 \leq i \leq n} (v_{ij})}, \quad (1)$$

$$x_j^i = \frac{\max_{1 \leq i \leq n} (v_{ij}) - v_{ij}}{\max_{1 \leq i \leq n} (v_{ij}) - \min_{1 \leq i \leq n} (v_{ij})}. \quad (2)$$

Let q_1 denote the left boundary of the ideal interval. Let q_2 denote the right boundary of the ideal interval. The standardization of the interval factors is shown as follows [12]:

$$x_j^i = \begin{cases} 1 - \frac{q_1 - v_{ij}}{\max(q_1 - \min_{1 \leq i \leq n} (v_{ij}), \max_{1 \leq i \leq n} (v_{ij}) - q_2)}, & v_{ij} < q_1 \text{ (a)}, \\ 1 - \frac{v_{ij} - q_2}{\max(q_1 - \min_{1 \leq i \leq n} (v_{ij}), \max_{1 \leq i \leq n} (v_{ij}) - q_2)}, & v_{ij} > q_2 \text{ (b)}, \\ 1, & q_1 \leq v_{ij} \leq q_2 \text{ (c)}. \end{cases} \quad (3)$$

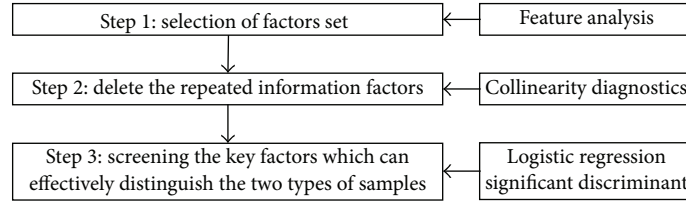


FIGURE 1: Flowchart of the research methodology.

The meanings of the rest of letters in (3) are the same as the letters in (1).

(2) *The Data Standardization of Qualitative Factors.* By rational analysis and expert investigation for qualitative factors, the scoring standard of qualitative factors can be obtained.

3.2. Deleting the Repeated Information Factors Based on Collinearity Diagnostics

(1) The Steps of Collinearity Diagnostics

Step 1 (building regression equation). Let x_j^i denote the standardization score of the i th observed value of the j th factor ($i = 1, \dots, n, j = 1, \dots, m$); then the regression equation of this factor with the rest of the factors is as follows:

$$x_j^i = a_0 + a_1 x_1^i + \dots + a_{j-1} x_{j-1}^i + a_{j+1} x_{j+1}^i + \dots + a_m x_m^i. \quad (4)$$

The estimated values a_i can be obtained by using least squares estimation in (4). Substituting these parameters a_i into (4), the estimated value \hat{x}_j^i of factor x_j^i can be obtained.

Step 2 (calculating the determination coefficient R_j^2). Let \bar{x}_j denote the mean value of the j th indicator. Then

$$\bar{x}_j = \frac{1}{n} \sum_{i=1}^n x_{ij}. \quad (5)$$

Let R_j^2 denote the determination coefficient of the j th indicator. Then

$$R_j^2 = \frac{\sum_{i=1}^n (\hat{x}_{ij} - \bar{x}_j)^2}{\sum_{i=1}^n (x_{ij} - \bar{x}_j)^2}. \quad (6)$$

The economic meanings of (6) are as follows. The bigger determination coefficient R_j^2 is, the stronger the correlation between the j th factor and the rest of factors will be. That is to say, the rest of factors can reflect the j th factor information effectively, and the j th factor should be deleted.

Step 3 (calculating the variance inflation factor VIF). Let VIF_j denote the variance inflation factor of the j th indicator. Then

$$VIF_j = \frac{1}{1 - R_j^2}. \quad (7)$$

The economic meanings of (7) are as follows. The variance inflation factor VIF_j reflects the correlation between the j th factor and the rest of factors in the same feature layer. If the variance inflation factor VIF_j is greater than 10 [14], it indicates that there is a multicollinearity between the j th factor and the rest of factors, and the j th factor should be deleted.

(2) *The Standard of Collinearity Diagnostics Screening.* Factors, reflecting repeated information, constitute a set, and the factors only whose variance inflation factors are smaller than 10 are reserved [14].

3.3. Screening the Key Factors Based on Logistic Regression Significant Discriminant

(1) *The Establishment of Logistic Regression Function.* Let y_i denote the data status of the i th observed value; let y_i equal to 0 denote that the i th observed value belongs to the first kind of sample, for example, good sample; let y_i equal to 1 denote that the i th observed value belongs to the other kind of sample, for example, bad sample. Let a and c_j denote regression coefficients. Let m denote the number of factors. Let x_j^i denote the standardization of the i th observed value of the j th indicator. Let ε_i denote random error. The Logistic multiple linear regression function between data status y_i and factors x_j^i is as follows [14]:

$$\log it (y_i) = a + c_1 x_1^i + c_2 x_2^i + \dots + c_m x_m^i. \quad (8)$$

The function of (8): it is obtained by the bilateral probability P_j of regression coefficient c_j for every factor x_j^i by constructing the Logistic regression function between evaluation factors x_j^i and data state y_i of farmers. Comparing the bilateral probability P_j with the given critical probability P_0 , it can distinguish whether the factors x_j^i have an obvious effect on data state y_i . Deleting these factors that do not have an obvious effect on data status, it ensures that the reserved factors can effectively distinguish bad samples from good ones.

(2) *The Standard of Logistic Regression Significant Discriminant Screening.* As a matter of experience, the threshold probability P_0 equals 0.05 [14].

If $P_j \geq P_0 = 0.05$ [14], accept the assumption that the true value of regression coefficient c_j corresponds to the factor

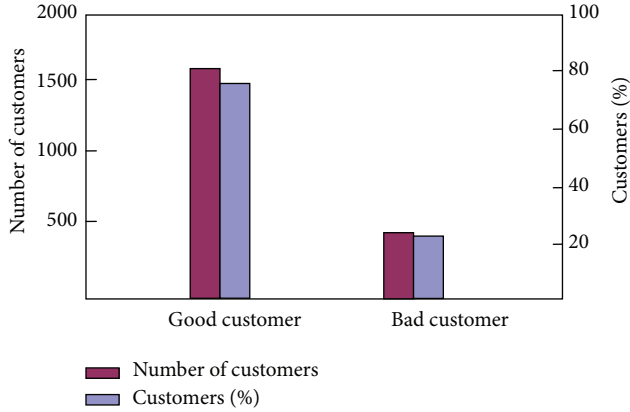


FIGURE 2: The distribution of customers.

x_j^i . It indicates that probability of the true value of regression coefficient c_j being zero is at least 95%. In other words, the factor x_j^i cannot significantly distinguish the data status and it should be deleted.

Conversely, if $P_j < P_0 = 0.05$ [14], refuse the assumption that the true value of regression coefficient c_j corresponds to the factor x_j^i . It indicates that probability of the true value of regression coefficient c_j not being zero is at least 95%. In other words, the factor x_j^i can significantly distinguish the data status and it should be reserved.

4. Empirical Study

4.1. Samples and Data Source

(1) *Samples*. In order to verify the effectiveness of the proposed model, this paper recognizes the key factors which can effectively distinguish the good customers from the bad ones by using a Chinese state-owned commercial bank's 2044 petty loans for farmers [15]. The sample includes 1589 nondefault customers (i.e., good customers) and 455 default customers (i.e., bad customers). The distribution of customers is shown in Figure 2.

(2) *The Establishment of Extensive Factors Set*. According to the available factors from a Chinese national commercial bank [15], this paper selects 68 factors of petty loans for farmers, which includes five feature layers, that is, "basic information," "repayment ability," "repayment willing," "guarantee and joint guarantee," and "macro environment," as shown in Column 1, 2, 5 of Table 1.

At the beginning of screening factors, we removed 18 unavailable factors, such as "credit status of joint guarantor" and "technical support efforts." Other 50 factors are left. The deleted factors are marked with "unavailability delete" in Column 7 of Table 1.

(3) *Data Source*. The data in the first to 50th Row and the first to 2044th Column of Table 2 are from the farmers petty credit loan system of a Chinese national commercial bank

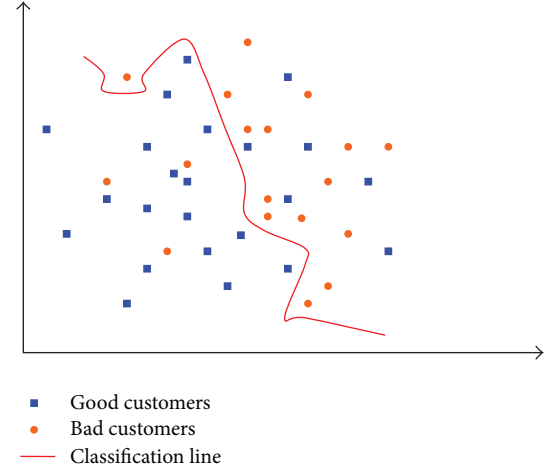


FIGURE 3: The classification demo figure of good customers and bad customers.

headquarter [15]. Since there exists no missing data, we used all data without any adjustment. The default status of each customer is shown in the corresponding Column, the 51st Row of Table 2. The number "1" denotes default customers, and the number "0" denotes nondefault customers.

Next, the key factors which can distinguish the two types of customers effectively will be selected. The classification demo result of good customers and bad customers is shown in Figure 3.

4.2. The Establishment of Recognizing Key Factors Model

4.2.1. The Standardization of Factors Data

(1) *Scoring the Quantify Factors*. It should be pointed out that there are two interval factors in this credit system, that is, "Consumer price index" and "Age". The ideal interval of "Consumer price index" is [101, 105] [12]. Inflation or deflation is nonexistent within this interval. The ideal interval of "Age" is [31, 45] [12]. The repayment ability and repayment willingness of these customers are strong in the interval.

According to the factors type in Column d of Table 2, take the original data of positive factors v_{ij} from Column 1 to 2044 of Table 2 into (1), the original data of negative factors v_{ij} into (2), and the original data of interval factors v_{ij} into (3), and then the standardized data of factors x_j^i are obtained. The results are shown in Column 2045 to 4088 of Table 2.

(2) *Scoring the Qualitative Factors*. The scoring standard of qualitative factors can be obtained by rational analysis, as shown in Column 2 to 6 of Table 3.

According to the factor type in Column d of Table 2, standardized scores of qualitative factors can be obtained in Table 2 based on the scoring criteria of qualitative factors in Table 3. The results are shown in Column 2045 to 4088 of Table 2.

TABLE 1: Extensive factors set.

(1) Feature layers	(2) Factors	(3) References	(4) Screening result	(5) Factors	(6) References	(7) Screening result
Basic information	Loan purpose	[9, 16, 17]	Deleted by collinearity diagnostics	Supporting population	[16, 18]	Deleted by collinearity diagnostics
	Age	[3, 9, 16–25]		Family number/labor force	[16]	
	Value of house owing	[9, 16, 18, 24, 25]	Reserved	Number of members	[18, 24]	Deleted by significance
	Marital status	[3, 9, 16, 17]		Number of labor force	[18, 22]	
	Education background	[3, 9, 16, 17]	Deleted by significance
	Household expenses	[9, 17, 18]		Area ratio of disposable assets	[9, 16]	Unavailability delete
Repayment ability	Expenses/incomes	[16, 19, 20, 22, 23]		Agricultural production incomes	[16, 18, 24]	Deleted by collinearity diagnostics
	Nonagricultural incomes/total incomes	[16, 18, 24]	Reserved	Net agricultural incomes	[16, 18, 24]	Deleted by significance
	Net income of borrower	[16, 18, 24]		Total expenses	[9, 25]	
	Education cost of children each year	[16, 18, 24]	Deleted by significance
	Agricultural production expenses	[9, 16, 17]		Total property	[16]	Unavailability delete
Repayment willingness	Private loans	[9, 16, 17]	Deleted by significance	Loaning records of borrower	[9, 16–18, 22, 24, 25]	Deleted by significance
	Residential stability	[3, 16, 17]	Reserved
	Residential status	[3, 9]		Social reputation status	[16, 17]	Unavailability delete
Guarantee and joint guarantee	Strength of guarantor	[9, 16, 18]	Reserved	Age of guarantor	[9, 16, 18, 25]	Deleted by significance
	Marital status of guarantor	[9, 16–18, 25]	
	Gender of guarantor	[9, 16, 24]	Deleted by significance	Credit status of joint guarantor	[16]	Unavailability delete
Macro environment	Engel's coefficient	[9, 16, 26]		Regional government policy	[9, 18, 25]	Deleted by collinearity diagnostics
	Increasing rate of regional GDP	[9, 16, 26]	Reserved
	Per capita agricultural output value	[17, 23]		Technical support efforts	[9, 18, 24]	Unavailability delete

4.2.2. *Deleting the Repeated Information Factors.* By substituting the standardized data of factors x_j^i in the 2045th and the 4088th Column of Table 2 into (4)–(6), the determination coefficient R_j^2 of all factors is obtained, as shown in the fourth Column of Table 4. By taking the determination coefficient R_j^2 in the fourth Column of Table 4 into (7), the variance inflation factor VIF_i of all factors is obtained, as shown in the fifth Column of Table 4.

According to the standard of collinearity diagnostics screening shown in Section 3.2. (2), if the variance inflation

factor VIF of an indicator is greater than 10, the indicator or factor should be deleted. In this progress, eight factors which reflect repeated information are deleted and 42 factors are reserved. The deleted factors include “Loan purpose,” “House value,” and “Regional government policy,” as shown in the sixth Column of Table 4 marked as “Deleted.”

4.2.3. *Screening the Key Factors*

(1) *The Establishment of Logistic Regression Model.* By substituting the ultimate 42 factors reserved in Table 4 into (8), the

TABLE 2: The original data and standardized data of factors.

(a) No.	(b) Feature layers	(c) Factors	(d) Factor type	Original data of factors v_{ij}				Standardized data of factors x'_j			
				(1) M. Song	(2044) M. Xu	(2045) M. Song	Nondefault customers (3920) D. Liu	(3921) F. Chen	Default customers (4088) M. Xu		
1	Basic information	Loan purpose	Qualitative	3	3	0.600	0.600	0.600	0.600	0.600	0.600
...		
14		House value	Positive	0.130	0.000	0.39	0.33	0.31	0.31	0.29	0.29
15	Repayment ability	Expenses/incomes	Positive	18.989	8.124	1.000	0.887	0.000	0.000	0.123	0.123
...		
31		Expense of family's daily life	Negative	120	8	0.737	0.534	1.000	1.000	0.001	0.001
32	Repayment willingness	Private loans	Qualitative	1.12	0.51	0.014	0.025	0.019	0.019	0.006	0.006
...		
39		Repayment to net income ratio	Negative	35.28	64.84	0.688	1.000	0.991	0.991	0.426	0.426
40	Guarantee and joint guarantee	Strength of guarantor	Positive	0.066	0.009	0.041	0.157	0.347	0.347	0.005	0.005
...		
45		Age of guarantor	Interval	45	36	1.000	0.059	0.094	0.094	1.000	1.000
46	Macro environment	Engel's coefficient	Negative	0.373	0.399	0.892	0.135	0.246	0.246	0.773	0.773
...		
50		Regional government policy	Qualitative	1	3	1.000	0.600	0.000	0.000	0.000	0.000
51	—	Default or not y_i	—	0	1	0	0	1	1	1	1

TABLE 3: The scoring criteria of qualitative factors.

(1) No.	(2) Feature layers	(3) Factors	(4) Options number	(5) Options	(6) Scoring
1			1	Undergraduate and above	1.00
2			2	Junior college	0.90
3	Basic information	Education background	3	High school and technical secondary school	0.60
4			4	Junior high school	0.40
5			5	Primary school	0.20
6			6	Other	0.00
...
70	Guarantee and joint guarantee	Group membership of coguarantee	1	Friendly relations, associating frequently, very familiar, business partners or neighbors	1.00
71			2	Ordinary relations, a little familiar	0.80
72			3	Unknown	0.50

TABLE 4: Collinearity diagnostics of factors.

(1) No.	(2) Feature layers	(3) Factors	(4) Determination coefficient R_j^2	(5) Variance inflation factor (VIF _j)	(6) Screening result of collinearity diagnostics
1		Loan purpose	0.942	17.241	Deleted
2	Basic information	Age	0.091	1.100	Reserved
...	
14		House value	0.928	13.889	Deleted
15		Expenses/incomes	0.731	3.717	Reserved
...	Repayment ability
31		Expense of family's daily life	0.199	1.248	Reserved
32		Private loans	0.063	1.067	Reserved
...	Repayment willingness
39		Repayment to net income ratio	0.497	1.988	Reserved
40		Strength of guarantor	0.456	1.838	Reserved
...	Guarantee and joint guarantee
45		Age of guarantor	0.320	1.471	Reserved
46		Engel's coefficient	0.265	1.361	Reserved
...	Macro environment
50		Regional government policy	0.968	31.250	Deleted

Logistic regression model between data status (i.e., default status) y_i and factors x_j^i is obtained as follows:

$$\log it (y_i) = a + c_1x_1^i + c_2x_2^i + \dots + c_{42}x_{42}^i. \quad (9)$$

The parameter i equals 1, 2, ..., 2044, respectively, in (9). By taking the standardized data of factors x_j^i in Column 2045 to 4088 of Table 2 into (9), the regression coefficients c_j of 42 factors and the corresponding bilateral probability P_j are obtained, as shown in Column four and five of Table 5.

(2) *Recognizing the Key Factors.* Based on the key factors screening standard shown in Section 3.3. (2), if $P_j \geq P_0 = 0.05$, the factor x_j^i cannot significantly distinguish the default status and should be deleted. On the contrary, the factor x_j^i

should be retained. And the threshold probability P_0 equals 0.05 in this paper, as shown in Column 6 of Table 5.

Comparing the critical probability $P_0 = 0.05$ with data in the first Row and the fifth Column of Table 5, the bilateral probability P_1 corresponding to the regression coefficient c_1 of the first factor "Age" is less than the critical probability 0.05; that is, $P_1 = 0.007 < P_0 = 0.05$. It indicates that the factor "Age" can significantly distinguish the default status and should be reserved. The result is marked with "Reserved" in the first Row and the seventh Column of Table 5.

Similarly, comparing the critical probability 0.05 with the other data in the fifth Column of Table 5, the screening results were listed in the corresponding row in the seventh Column of Table 5. The Logistic regression significant discriminant screening deleted 29 factors, such as "Private loans" and "Repayment to net income ratio."

TABLE 5: Screening the key factors based on Logistic regression significant discriminant.

(1) No.	(2) Feature layers	(3) Factors	(4) Regression coefficients c_j	(5) Bilateral probability P_j	(6) Critical probability P_0	(7) Screening result
1	Basic information	Age	-1.827	0.007	0.05	Reserved
...	
11		Number of labor force	2.017	0.405		Deleted
12	Repayment ability	Expenses/incomes	0.079	0.044	0.05	Reserved
...	
26		Expense of family's daily life	-0.328	0.834		Deleted
27	Repayment willingness	Private loans	6.220	0.104	0.05	Deleted
...	
33		Repayment to net income ratio	2.962	0.762		Deleted
34	Guarantee and joint guarantee	Strength of guarantor	-1.973	0.000	0.05	Reserved
...	
38		Age of guarantor	0.264	0.772		Deleted
39	Macro environment	Engel's coefficient	-0.152	0.018	0.05	Reserved
...	
42		CPI	3.211	0.336		Deleted

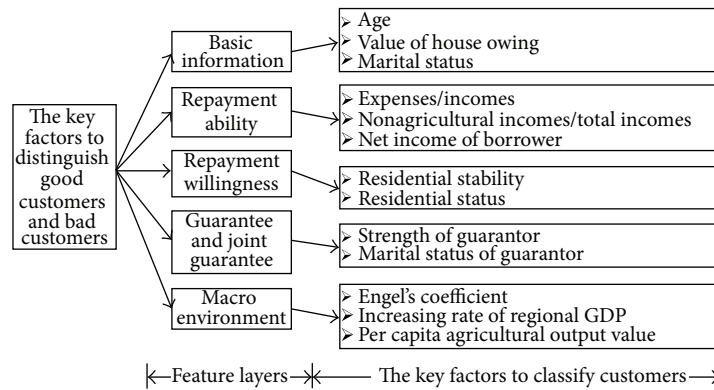


FIGURE 4: The key factors to distinguish good customers and bad customers.

In conclusion, this paper extracts thirteen factors which can effectively distinguish good customers from bad ones, as shown in Figure 4.

5. Conclusion

With the advent of the era of big data, data classification puzzles have emerged in DNA identification, fingerprint recognition, customer classification, facial recognition, and so forth. Recently, recognizing key factor methods and classifier models have been proposed for solving this problem. So it has become more and more important for researchers to find key factors which are capable of effectively distinguishing the data. To do that, many mathematical models are explored as the decision support methods to classify the data.

We propose a model for recognition key factors, which is based on the combination of collinearity diagnostics and logistic regression significant discriminant. To demonstrate

the performance of the proposed model, factors screening tasks were performed by an empirical study of the 2044 observations in financial engineering. Our empirical results show that the proposed model can accurately screen the key factors, which can effectively distinguish the good customers and bad customers. Moreover, the proposed method is simple and easy to be implemented.

The main contribution of this study is as follows: deleting the factors that reflect repeated information by using collinearity diagnostics and recognizing the factors which can effectively distinguish the two kinds of samples by using Logistic regression significant discriminant; this paper established a recognition key factors model for data classification.

Conflict of Interests

The authors declare that there is no conflict of interests regarding the publication of the paper.

Acknowledgments

The research is supported by the National Natural Science Foundation of China (Grant no. 71171031), the Ministry of Education of China as Science and Technology Research Project (Grant no. 2011-10), the China Banking Regulatory Commission as a Risk Management Project of Banking Information Technology (Grant no. 2012-4-005), and the Bank of Dalian as credit rating and loan pricing systems for small business (Grant no. 2012-01). The authors thank the organizations mentioned above.

References

- [1] J. Hu, L. Wang, F. Duan, and P. Guo, "Adaptive multilevel kernel machine for scene classification," *Mathematical Problems in Engineering*, vol. 2013, Article ID 324945, 9 pages, 2013.
- [2] S. Finlay, "Multiple classifier architectures and their application to credit risk assessment," *European Journal of Operational Research*, vol. 210, no. 2, pp. 368–378, 2011.
- [3] S. Akkoc, "An empirical comparison of conventional techniques, neural networks and the three stage hybrid Adaptive Neuro Fuzzy Inference System (ANFIS) model for credit scoring analysis: the case of Turkish credit card data," *European Journal of Operational Research*, vol. 222, no. 1, pp. 168–178, 2012.
- [4] C. Lin, J. Chen, Z. Gaing, and M. Younis, "Combining biometric fractal pattern and particle swarm optimization-based classifier for fingerprint recognition," *Mathematical Problems in Engineering*, vol. 2010, Article ID 328676, 14 pages, 2010.
- [5] B. Twala, "Multiple classifier application to credit risk assessment," *Expert Systems with Applications*, vol. 37, no. 4, pp. 3326–3336, 2010.
- [6] Y. Chen, "Research on evaluation and decision system of small amount loans for farmers based on support vector machines," *Dalian University of Technology*, pp. 22–58, 2011.
- [7] C.-D. Căleanu, X. Mao, G. Pradel, S. Moga, and Y. Xue, "Combined pattern search optimization of feature extraction and classification parameters in facial recognition," *Pattern Recognition Letters*, vol. 32, no. 9, pp. 1250–1255, 2011.
- [8] J. H. Min and Y.-C. Lee, "A practical approach to credit scoring," *Expert Systems with Applications*, vol. 35, no. 4, pp. 1762–1770, 2008.
- [9] B. Shi and G. Chi, "A credit risk evaluation index screening model of petty loans for small private business and its application," *Advances in Information Sciences and Service Sciences*, vol. 5, no. 7, pp. 1116–1124, 2013.
- [10] R.-C. Hwang, H. Chung, and C. K. Chu, "Predicting issuer credit ratings using a semiparametric method," *Journal of Empirical Finance*, vol. 17, no. 1, pp. 120–137, 2010.
- [11] X. Sun, W.-H. Qiu, and B.-J. Tang, "Research about model of early-warning of enterprise crisis based on gray forecasting and pattern recognition," *System Engineering Theory and Practice*, vol. 25, no. 5, pp. 36–42, 2005.
- [12] N. Yan, Z. Chen, Y. Shi, Z. Wang, and G. Huang, "Using non-additive measure for optimization-based nonlinear classification," *American Journal of Operations Research*, vol. 2, no. 3, pp. 364–373, 2012.
- [13] J. Corander, M. Gyllenberg, and T. Koski, "Bayesian unsupervised classification framework based on stochastic partitions of data and a parallel search strategy," *Advances in Data Analysis and Classification*, vol. 3, no. 1, pp. 3–24, 2009.
- [14] A. Rencher and G. Schaalje, *Linear Models in Statistics*, John Wiley & Sons, Hoboken, NJ, USA, 2008.
- [15] Chi Guotai Research Group of Dalian University of Technology, "Credit risks decision and evaluation system of microcredit for farmers for postal savings bank of China," *Dalian University of Technology*, 2011.
- [16] Postal Savings Bank of China, "Merchant credit rating table of Postal Savings Bank of China," *Postal Savings Bank of China*, 2009.
- [17] Construction Bank of China, "Small business customers evaluation approaches of China Construction Bank," *Construction Bank of China*, pp. 1–8, 2007.
- [18] Emei credit cooperatives, *The operating rules and regulationsof micro-credit loans to farmers for Rural Credit Cooperatives of Sichuan Province*, 2013, http://www.emxh.com/article/2007/0803/file_142.html.
- [19] Standard and Poor's Ratings Services, "S&P's study of China's top corporates highlights their significant financial risks," *Standard & Poor's Ratings Services*, pp. 175–199, 2012.
- [20] Moody's Investors Service, "Global credit research," *Moody's Investors Service*, pp. 136–147, 2009.
- [21] Fitch Ratings, "Fitch ratings global corporate finance 2012 transition and default study," *Credit Market Research—Fitch Ratings*, pp. 2–27, 2013.
- [22] Fair Isaac Corporation, "Free FICO Credit Score," Fair Isaac Corporation, 2013, <http://www.myfico.com/Default.aspx>.
- [23] T.-C. Wang and Y.-H. Chen, "Applying rough sets theory to corporate credit ratings," in *Proceedings of the IEEE International Conference on Service Operations and Logistics, and Informatics*, pp. 132–136, June 2006.
- [24] Agricultural Bank of China, "Management of farmers creditrating of Agricultural Bank of China," *Agricultural Bank of China*, 2008.
- [25] Industrial and Commercial Bank of China, "The notice about printing the evaluation method of the small business corporate clients credit rating of China Industrial and Commercial Bank means," *Industrial and Commercial Bank of China*, no. 78, 2005.
- [26] K. Carling, T. Jacobson, J. Lindé, and K. Roszbach, "Corporate credit risk modeling and the macroeconomy," *Journal of Banking and Finance*, vol. 31, no. 3, pp. 845–868, 2007.

Research Article

A Novel Machine Learning Strategy Based on Two-Dimensional Numerical Models in Financial Engineering

Qingzhen Xu

School of Computer Science, South China Normal University, Guangzhou 510631, China

Correspondence should be addressed to Qingzhen Xu; xqz1997@126.com

Received 23 October 2013; Revised 27 November 2013; Accepted 4 December 2013

Academic Editor: Gelan Yang

Copyright © 2013 Qingzhen Xu. This is an open access article distributed under the Creative Commons Attribution License, which permits unrestricted use, distribution, and reproduction in any medium, provided the original work is properly cited.

Machine learning is the most commonly used technique to address larger and more complex tasks by analyzing the most relevant information already present in databases. In order to better predict the future trend of the index, this paper proposes a two-dimensional numerical model for machine learning to simulate major U.S. stock market index and uses a nonlinear implicit finite-difference method to find numerical solutions of the two-dimensional simulation model. The proposed machine learning method uses partial differential equations to predict the stock market and can be extensively used to accelerate large-scale data processing on the history database. The experimental results show that the proposed algorithm reduces the prediction error and improves forecasting precision.

1. Introduction

The operation of securities markets is changing at any time. More and more researchers on the stock market did a lot of research, which hopes to find the run law of the stock market [1]. Machine learning is programming computers to optimize a performance criterion using example data or past experience. However, the operation of the securities market is a very complex system; if you want to find out the operation of the internal laws of the stock market it is very difficult. It is widely acknowledged in machine learning that the performance of a learning algorithm is dependent on both its parameters and the training data.

Machine learning belongs to the field of artificial intelligence. The field's main objects of study are computer algorithms that improve their performance through experience. Machine learning focuses on prediction, based on known properties learned from the training data. In recent years, many scholars at home and abroad have made great contributions to the stock market forecasting in both empirical and theoretical work, which are necessary and sufficient for solving the financial engineering problem. For example, Chang et al. thought that using time series models to forecast stock

index movements and make reasonably accurate predictions has two major drawbacks [1]. They forecasted the Taiwan stock exchange capitalization weighted stock index (TAIEX) by proposing a hybrid adaptive network based fuzzy inference system (ANFIS) model. Chu et al. proposed a dual-factor modified fuzzy time series model, which took stock index and traded volume as forecasting factors to predict stock index [2]. Xu presented a continuous time M/G/1 queue with multiple vacations and server close-down time [3]. Xu and Ma presented a discrete time Geo/G/1 queue with Bernoulli gated service simulation system [4]. Xu et al. proposed a theoretical model, but there was no practical application [5]. He et al. used established theoretical models to calculate cash flow in stock market research in 2011 [6]. However, He et al. can only calculate cash flow of the stock or the stock market but cannot solve the problem of forecasting the stock market [6]. Xu and Liu gave a strategy for forecasting average price and index of stocks using the algorithm of genetics, which applied the knowledge of statistics to choosing item by probability according to stock market, and they forecasted the volatility of Dow Jones Indexes and Standard & Poor's 500 Indexes [7, 8]. However, there was some failure prediction from July 2011 to September 2011 in the decline phase.

However the above research is not accurate in practice stock market. In order to better improve the forecasting accuracy, this paper focuses on improving the theoretical model.

Machine learning algorithms can be organized into a taxonomy based on the desired outcome of the algorithm or the type of input available during training the machine. Our goal of this paper is to use partial differential equations to predict the stock market. In order to study a practical simulation system to guide the investors to invest, this paper proposes a two-dimensional numerical model for machine learning to simulate major US stock market index and uses a heuristic two-dimensional mathematical simulation model with partial differential equations to simulate stock market index. The new machine learning method can be extensively used to accelerate large-scale data processing on the history database. The experimental results show that the proposed algorithm reduces the prediction error and improves forecasting precision.

The rest of this paper is organized as follows. Section 2 presents the model description. Section 3 presents the method of solution. Section 4 presents the simulation results of major U.S. stock market index and finally some conclusions are pointed out and future works are offered in Section 5.

2. Two-Dimensional Numerical Models

In this section, the proposed dimensional numerical models will be discussed. In general, dimensional numerical models in financial engineering can be described as follows.

Definition 1. Assume that x represents the volume, y represents the main index or stock's close price, C_c represents the market activity, τ_b represents the rate of low price to close price, τ_s represents the rate of high price to close price, ε_b represents the low price, ε_s represents the high price, ε_c represents the Tradable Market Capitalization rate, ζ_1 represents the impact factor of low price, and ζ_2 represents the impact factor of high price. The new dimensional numerical models can be formulated as

$$\begin{aligned}\frac{\partial U_b}{\partial t} &= \frac{1}{\tau_b} \nabla \cdot (D_b \nabla U_b) - \xi_1 \varepsilon_b \Gamma_c, \\ \frac{\partial U_s}{\partial t} &= \frac{1}{\tau_s} \nabla \cdot (D_s \nabla U_s) - \xi_2 \varepsilon_s \Gamma_c,\end{aligned}\quad (1)$$

$$C_c \frac{\partial T}{\partial t} = \nabla \cdot (K_{\text{mix}} \nabla T) + \varepsilon_c \Gamma_c (\xi_1 \lambda_c + \xi_2 \lambda_s),$$

in which t represents the time ($t > 0$), Γ_c represents the day turnover rate, λ_c represents the volume of business of high price, and λ_s represents the low price individually, respectively. $\zeta_1 = \varepsilon_b / \varepsilon_s$, $\zeta_2 = \varepsilon_c / \varepsilon_s \varepsilon_b = \sqrt{\varepsilon_{bx}^2 + \varepsilon_{by}^2}$, $\varepsilon_s = \sqrt{\varepsilon_{sx}^2 + \varepsilon_{sy}^2}$, $\varepsilon_b + \varepsilon_s + \varepsilon_c = 1$, $\tau_b, \tau_s \in (0, 1)$.

Definition 2. Assume that U_b represents the Dow Jones Indexes, U_s represents the Standard & Poor's 500 Index, T represents the NASDAQ Composite Index, D_{bx} represents efficient change rate of the low price to volume, D_{by} represents

efficient change rate of the low price to close price, D_{sx} represents efficient change rate of the high price to volume, D_{sy} represents efficient change rate of the high price to close price, K_x represents the impact factor of open price, and K_y represents the impact factor of close price. The related numerical model can be formulated as

$$\begin{aligned}\frac{\partial (C_b \varepsilon_b)}{\partial t} &= \frac{1}{\tau_b} \left[\frac{\partial}{\partial x} \left(D_{bx} \frac{\partial (C_b \varepsilon_{bx})}{\partial x} \right) \right. \\ &\quad \left. + \frac{\partial}{\partial y} \left(D_{by} \frac{\partial (C_b \varepsilon_{by})}{\partial y} \right) \right] - \varepsilon_b \zeta_1 \Gamma_c, \\ \frac{\partial (C_s \varepsilon_s)}{\partial t} &= \frac{1}{\tau_s} \left[\frac{\partial}{\partial x} \left(D_{sx} \frac{\partial (C_s \varepsilon_{sx})}{\partial x} \right) \right. \\ &\quad \left. + \frac{\partial}{\partial y} \left(D_{sy} \frac{\partial (C_s \varepsilon_{sy})}{\partial y} \right) \right] - \varepsilon_s \zeta_2 \Gamma_c, \\ C_c \frac{\partial T}{\partial t} &= \frac{\partial}{\partial x} \left(K_x \frac{\partial T}{\partial x} \right) + \frac{\partial}{\partial y} \left(K_y \frac{\partial T}{\partial y} \right) \\ &\quad + \varepsilon_c \Gamma_c (\zeta_1 \lambda_c + \zeta_2 \lambda_s),\end{aligned}\quad (2)$$

in which ε_{bx} represents the rate of low price's volume to day volume, ε_{by} represents the rate of low price's volume to close price's volume, ε_{sx} represents the rate of high price's volume to day volume, and ε_{sy} represents the rate of high price's volume to close price's volume. $U_s = C_s(x, y, t) \varepsilon_s$, $U_b(x, y, t) = C_b(x, y, t) \varepsilon_a$.

3. Description of the Proposed Algorithm

The solution domain is $[x, y]$, x is the forecast time horizon, and y is the price index range. The solution domain is divided into intervals h_1, h_2 in the direction of the forecast time horizon x , the price index range y . So $x_i = ih_1$ ($h_1 = 1$). $y_j = jh_2$ ($h_2 = 1$), vol_{ij} is the $i \times j$ th unit volume. $(U_b)_{ij}(x_i, y_j)$ is denoted by $(U_b)_{ij}$ and $(U_s)_{ij}(x_i, y_j)$ is denoted by $(U_s)_{ij}$. Considering a uniform grid, the spatial discretization of the solution domain in finite volume ij is then

$$\begin{aligned}& \int_{\text{vol}_{ij}} \nabla \cdot (D_b \nabla U_b) d\text{vol}_{ij} \\ &= \int_{\text{vol}_{ij}} \frac{\partial}{\partial x} \left(D_b \frac{\partial U_b}{\partial x} \right) d\text{vol}_{ij} + \int_{\text{vol}_{ij}} \frac{\partial}{\partial y} \left(D_b \frac{\partial U_b}{\partial y} \right) d\text{vol}_{ij} \\ &= ((D_b)_{(i+(1/2))jk}) ((U_b)_{(i+1)jk} - (U_b)_{ijk}) \\ &\quad - (D_b)_{(i-(1/2))jk} ((U_b)_{ijk} - (U_b)_{(i-1)jk}) \times (h_1)^{-1} \\ &\quad + ((D_b)_{i(j+(1/2))k}) ((U_b)_{i(j+1)k} - (U_b)_{ijk}) \\ &\quad - (D_b)_{i(j-(1/2))k} ((U_b)_{ijk} - (U_b)_{i(j-1)k}) \times (h_2)^{-1}\end{aligned}$$

$$\begin{aligned}
& \int_{\text{vol}_{ij}} \nabla \cdot (D_s \nabla U_s) d\text{vol}_{ij} \\
&= \int_{\text{vol}_{ij}} \frac{\partial}{\partial x} \left(D_s \frac{\partial U_s}{\partial x} \right) d\text{vol}_{ij} + \int_{\text{vol}_{ij}} \frac{\partial}{\partial y} \left(D_s \frac{\partial U_s}{\partial y} \right) d\text{vol}_{ij} \\
&= \left((D_s)_{(i+(1/2))jk} \left((U_s)_{(i+1)jk} - (U_s)_{ijk} \right) \right. \\
&\quad \left. - (D_s)_{(i-(1/2))jk} \left((U_s)_{ijk} - (U_s)_{(i-1)jk} \right) \right) \times (h_1)^{-1} \\
&\quad + \left((D_s)_{i(j+(1/2))k} \left((U_s)_{i(j+1)k} - (U_s)_{ijk} \right) \right. \\
&\quad \left. - (D_s)_{i(j-(1/2))k} \left((U_s)_{ijk} - (U_s)_{i(j-1)k} \right) \right) \times (h_2)^{-1} \\
& \int_{\text{vol}_{ij}} \nabla \cdot (K_{\text{mix}} \nabla T) d\text{vol}_{ij} \\
&= \int_{\text{vol}_{ij}} \frac{\partial}{\partial x} \left(K_{\text{mix}} \frac{\partial T}{\partial x} \right) d\text{vol}_{ij} + \int_{\text{vol}_{ij}} \frac{\partial}{\partial y} \left(K_{\text{mix}} \frac{\partial T}{\partial y} \right) d\text{vol}_{ij} \\
&= \left((K_{\text{mix}})_{(i+(1/2))jk} \left((T)_{(i+1)jk} - (T)_{ijk} \right) \right. \\
&\quad \left. - (K_{\text{mix}})_{(i-(1/2))jk} \left((T)_{ijk} - (T)_{(i-1)jk} \right) \right) \times (h_1)^{-1} \\
&\quad + \left((K_{\text{mix}})_{i(j+(1/2))k} \left((T)_{i(j+1)k} - (T)_{ijk} \right) \right. \\
&\quad \left. - (K_{\text{mix}})_{i(j-(1/2))k} \left((T)_{ijk} - (T)_{i(j-1)k} \right) \right) \times (h_2)^{-1}. \tag{3}
\end{aligned}$$

These results are from the cell volume, vol_{ij} being equal to $h_1 h_2$. The limited efficient change rates are considered. The method is implemented as

$$\begin{aligned}
(D_b)_{(i+(1/2))jk} &= \varepsilon_b (D_b)_{(i-(1/2))jk} + (1 - \varepsilon_b) (D_c)_{(i-(1/2))jk}, \\
(D_b)_{i(j+(1/2))k} &= \varepsilon_b (D_b)_{i(j-(1/2))k} + (1 - \varepsilon_b) (D_c)_{i(j-(1/2))k}, \\
(D_s)_{(i+(1/2))jk} &= \frac{\gamma \cos \theta \sin^2 \alpha d_c (\varepsilon_s)_{(i-(1/2))jk}^{1/3}}{20\eta (\varepsilon_s)_{(i-(1/2))jk}^{1/3}}, \\
(D_s)_{i(j+(1/2))k} &= \frac{\gamma \cos \theta \sin^2 \alpha d_c (\varepsilon_s)_{i(j-(1/2))k}^{1/3}}{20\eta (\varepsilon_s)_{i(j-(1/2))k}^{1/3}}. \tag{4}
\end{aligned}$$

The fully implicit Newton-Krylov (NK) method is based on a first-order forward Euler time integration. In the method we converge the nonlinearities within a time step thus we need a time step index k and a nonlinear iteration index n . The first-order accurate time integration method is

$$\begin{aligned}
& \frac{(U_b)_{ij(k+1)}^n - (U_b)_{ijk}}{\delta} - \left(\frac{\partial}{\partial x} \left((D_b)_{ij(k+1)}^n \frac{\partial (U_b)_{ij(k+1)}^n}{\partial x} \right) \right. \\
&\quad \left. + \frac{\partial}{\partial y} \left((D_b)_{ij(k+1)}^n \frac{\partial (U_b)_{ij(k+1)}^n}{\partial y} \right) \right) \\
&= -(\xi_1)_{ij(k+1)}^n (\varepsilon_c)_{ij(k+1)}^n (\Gamma_c)_{ij(k+1)}^n,
\end{aligned}$$

$$\begin{aligned}
& \frac{(U_s)_{ij(k+1)}^n - (U_s)_{ijk}}{\delta} - \left(\frac{\partial}{\partial x} \left((D_s)_{ij(k+1)}^n \frac{\partial (U_s)_{ij(k+1)}^n}{\partial x} \right) \right. \\
&\quad \left. + \frac{\partial}{\partial y} \left((D_s)_{ij(k+1)}^n \frac{\partial (U_s)_{ij(k+1)}^n}{\partial y} \right) \right) \\
&= -(\xi_2)_{ij(k+1)}^n (\varepsilon_c)_{ij(k+1)}^n (\Gamma_c)_{ij(k+1)}^n, \\
& \frac{(T)_{ij(k+1)}^n - (T)_{ijk}}{\delta} - \left(\frac{\partial}{\partial x} \left((K_{\text{mix}})_{ij(k+1)}^n \frac{\partial (T)_{ij(k+1)}^n}{\partial x} \right) \right. \\
&\quad \left. + \frac{\partial}{\partial y} \left((K_{\text{mix}})_{ij(k+1)}^n \frac{\partial (T)_{ij(k+1)}^n}{\partial y} \right) \right) \\
&= (\varepsilon_c)_{ij(k+1)}^n (\Gamma_c)_{ij(k+1)}^n \left((\xi_1)_{ij(k+1)}^n (\lambda_c)_{ij(k+1)}^n \right. \\
&\quad \left. + (\xi_2)_{ij(k+1)}^n (\lambda_s)_{ij(k+1)}^n \right). \tag{5}
\end{aligned}$$

Concentrating on the solution of the two-dimensional simulation model of major U.S. stock market index, we find that the nonlinear function plays an important role in describing the algorithm and monitor convergence. The nonlinear iteration is implemented with an inexact, matrix-free Newton-Krylov method [9, 10]. By defining the nonlinear functions to differentiate them, we get the discredited equations at each grid cell.

We use F_{ij}^A function to compute Dow Jones Industrial Average (U_b) at segmentation cell i, j , F_{ij}^L function to compute S & P 500 (U_s) at segmentation cell i, j , and F_{ij}^T function to simulate the NASDAQ Composite Index (T) at segmentation cell i, j , which are described as follows:

$$\begin{aligned}
F_{ij}^A &= \int_{\text{vol}_{ij}} \left[\frac{(U_b)_{ij(k+1)}^n - (U_b)_{ijk}}{\delta} \right. \\
&\quad \left. - \left(\frac{\partial}{\partial x} \left((D_b)_{ij(k+1)}^n \frac{\partial (U_b)_{ij(k+1)}^n}{\partial x} \right) \right. \right. \\
&\quad \left. \left. + \frac{\partial}{\partial y} \left((D_b)_{ij(k+1)}^n \frac{\partial (U_b)_{ij(k+1)}^n}{\partial y} \right) \right) \right. \\
&\quad \left. + (\xi_1)_{ij(k+1)}^n (\varepsilon_c)_{ij(k+1)}^n (\Gamma_c)_{ij(k+1)}^n \right] d\text{vol}_{ij}, \tag{6}
\end{aligned}$$

$$\begin{aligned}
F_{ij}^L &= \int_{\text{vol}_{ij}} \left[\frac{(U_s)_{ij(k+1)}^n - (U_s)_{ijk}}{\delta} \right. \\
&\quad \left. - \left(\frac{\partial}{\partial x} \left((D_s)_{ij(k+1)}^n \frac{\partial (U_s)_{ij(k+1)}^n}{\partial x} \right) \right. \right. \\
&\quad \left. \left. + \frac{\partial}{\partial y} \left((D_s)_{ij(k+1)}^n \frac{\partial (U_s)_{ij(k+1)}^n}{\partial y} \right) \right) \right. \\
&\quad \left. + (\xi_2)_{ij(k+1)}^n (\varepsilon_c)_{ij(k+1)}^n (\Gamma_c)_{ij(k+1)}^n \right] d\text{vol}_{ij}, \tag{7}
\end{aligned}$$

$$\begin{aligned}
F_{ij}^T = \int_{\text{vol}_{ij}} & \left[\frac{(T)_{ij(k+1)}^n - (T)_{ijk}}{\delta} \right. \\
& - \left(\frac{\partial}{\partial x} \left((K_{\text{mix}})_{ij(k+1)}^n \frac{\partial (T)_{ij(k+1)}^n}{\partial x} \right) \right. \\
& \quad \left. + \frac{\partial}{\partial y} \left((K_{\text{mix}})_{ij(k+1)}^n \frac{\partial (T)_{ij(k+1)}^n}{\partial y} \right) \right) \quad (8) \\
& - (\varepsilon_c)_{ij(k+1)}^n (\Gamma_c)_{ij(k+1)}^n \\
& \times \left((\xi_1)_{ij(k+1)}^n (\lambda_c)_{ij(k+1)}^n \right. \\
& \quad \left. + (\xi_2)_{ij(k+1)}^n (\lambda_s)_{ij(k+1)}^n \right) \left. \right] d\text{vol}_{ij}.
\end{aligned}$$

4. Machine Learning and Data Mining of Major U.S. Stock Market Index

In this section, we simulate the U.S. stock market. All data are from the United States public securities market information. We apply the above mathematical model to get the future of the U.S. stock market index chart.

4.1. U.S. Stock Market Trend Forecast in One Year. From Figure 1, we know that Dow Jones Index fell all the way down from early September 2011 to November 20, 2011 or so. The Dow Jones index would arrive at the bottom end in November 20, 2011, and be about to usher in a wave of a strong rebound. The rebound starting from November 20, 2011 will continue to April 20, 2012. Dow Jones Index will reach the bottom of 9500 and will rise 30 percent. At April 20, 2012, DJI will arrive at 12269. In 2012 from April 20 to July 20 only, Dow Jones Index will enter a phase of slow decline. The Dow Jones Index would have reached 10830 in July 20. The Dow Jones Index would rise to start a new round just from July 20. This wave of the market rally will continue until December 20. The Dow Jones Index would reach 13000 in December 20. The second rally is twenty percent of the rate of increase. However, it is not very good in the second phase of rising, and especially there would be a small drop from August 20 to October 20.

From Figure 2, we can see that Standard & Poor's 500 index fell all the way down from early September 2011 to November 23, 2011 or so. Standard & Poor's 500 Index would arrive at the bottom end in November 23, 2011, and be about to usher in a wave of a strong rebound. The rebound starting from November 23, 2011 will continue to April 12, 2012. Standard & Poor's 500 will reach the bottom of 1017 in November 23, 2011 around and will rise 30 percent in the next 4 months. At April 12, 2012, Standard & Poor's 500 will arrive at 1325. Standard & Poor's 500 will enter a phase of slow decline from April 12 to July 18 in 2012. Standard & Poor's 500 would reach 1190 in July 18. Standard & Poor's 500 would rise to start a new round just from July 18. This wave of the market rally will continue until December 12. Standard & Poor's 500 would reach 1429 in December 12. The second rally is twenty percent of the rate of increase. However, it is not very good

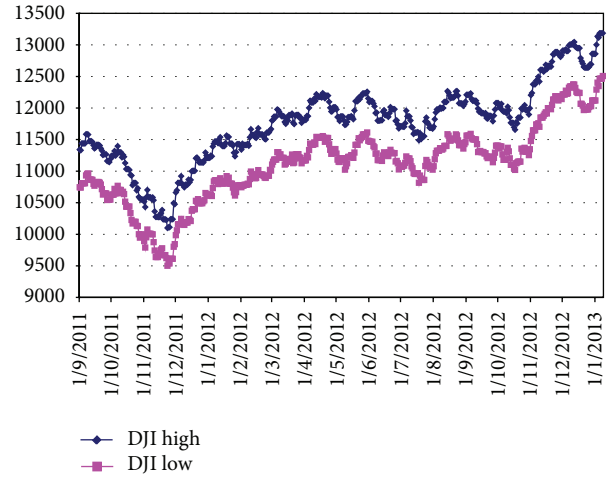


FIGURE 1: Dow Jones Indexes daily forecast chart for one year.

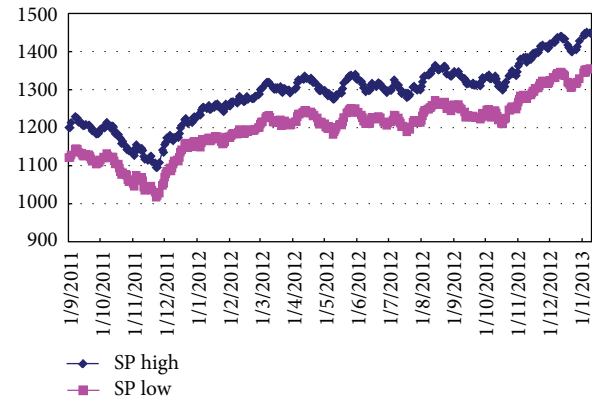


FIGURE 2: Standard & Poor's 500 Index daily forecast chart for one year.

in the second phase of rising, and especially there would be a small drop from August 15 to October 15.

From Figure 3, we find that the NASDAQ index would be sideways trend shocks between 2400 and 2700 from early September 2011 to December 1, 2011 or so. The NASDAQ index would usher in a wave of mad cow market rally from December 1, 2011 to February 13, 2012. The market would rise 29 percent. The NASDAQ index would reach a high of 3145 in mid-February 2012. From mid-February 2012, the NASDAQ index would enter the downward trend. It will reach the bottom of 2574 in June 30, 2012. The NASDAQ index would enter the sideways trend shock from July 1 to October 5 in 2012. During this period, the NASDAQ index would swing between 2600 and 2900. The NASDAQ index would begin a bull market from 2600 as a starting point. The NASDAQ index would reach the high point of 3295 in the end of 2012. There would be 27 percent increase.

4.2. U.S. Stock Market Trend Forecast in Four Years. From Figure 4, we can see that Dow Jones Indexes would arrive at the bottom in the end of November 2011. From the end



FIGURE 3: NASDAQ Index daily forecast chart for one year.

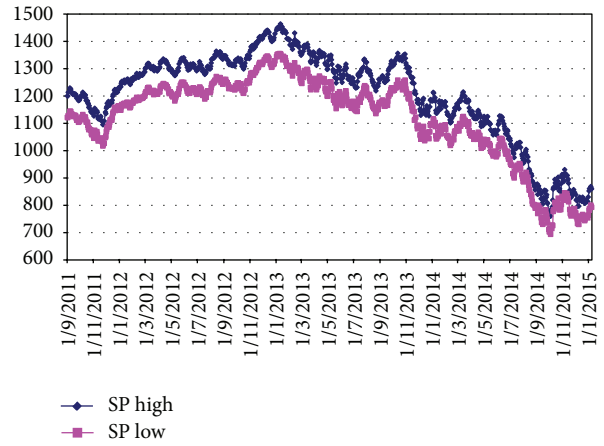


FIGURE 5: Standard & Poor's 500 Index daily forecast chart in four years.

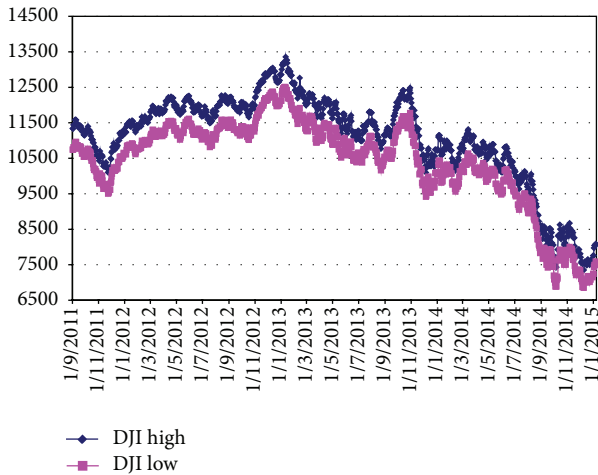


FIGURE 4: Dow Jones Indexes daily forecast chart in four years.

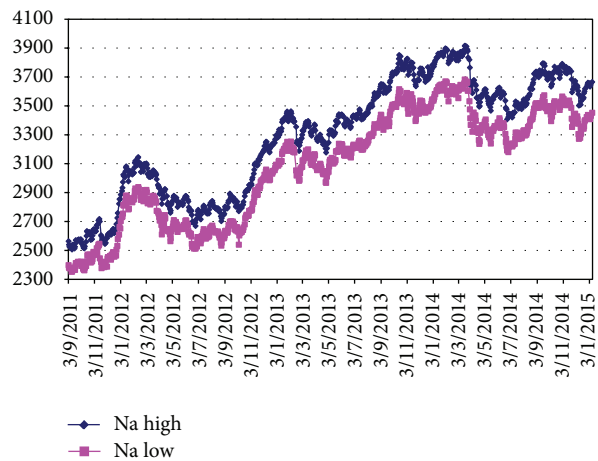


FIGURE 6: NASDAQ Index daily forecast chart in four years.

of November 2011 to early January 2013, Dow Jones Indexes would be a bull market. There would be a forty percent increase during the rising trend. From early January 2013 to early December 2014, Dow Jones Indexes would be a long stock market crash. The decline of the stock market crash would reach fifty percent. It is very terrible, and the stock market crash would be similar with the 2008 financial crisis.

From Figure 5, we know that Standard & Poor's 500 Index would arrive at the bottom in the end of November 2011. From the end of November 2011 to mid-December 2012, Standard & Poor's 500 Index would be a bull market. There would be about forty percent increase during the rising trend. From early January 2013 to the end of October 2014, Standard & Poor's 500 Indexes would be a long stock market crash. The decline of the stock market crash would reach forty-seven percent. The stock market crash would be similar with the 2008 financial crisis. It would be below 700.

From Figure 6, we know that the NASDAQ Index would be a sideways process from early September to December 1 in 2011. The NASDAQ Index would be a bull market rally from December 1, 2011 to February 13, 2012. From February

13, 2012 to April 28, 2012, the NASDAQ Index would be a bear market decline. The NASDAQ Index would be a bottoming process from May 1, 2012 to October 5, 2012. It would be up to 5 months during the bottoming period. The NASDAQ Index would experience a rising market from early October 2012 to the end of January 2013. From early February 2013 to late April 2013, The NASDAQ Index would experience a down market. The NASDAQ Index would experience a longer period of rising prices from early May 2013 to the end of January 2014. From early February 2014 to the end of June 2014, the NASDAQ Index would experience a down market. Then the NASDAQ Index would enter the market downturn. All in all, it would be a rising trend from the end of 2012 to early 2014.

4.3. *Summary of Future Market Trends.* From Figures 1–6, we found that DJI and S&P 500 are highly correlated. The NASDAQ Index would take the independent market. We can conclude the future trend as Table 1.

From Table 1, we can see that NASDAQ trend is different with DJI and S&P 500. We conducted in-depth analysis. When the bear market is coming, the first small-cap stocks

TABLE 1: Different periods with different trends in U.S. stock market index.

Period	DJI	S&P 500	NASDAQ	Conclusion
2011.9.1~2011.11.30	Down	Down	Sideways	NASDAQ are better than DJI and S&P 500
2011.11.30~2013.2.1	Up	Up	First up, second down, again up	NASDAQ would have a complex trend
2011.11.30~2012.2.13	Up	Up	UP	All up
2013.2~2014.12	Stock crash	Stock crash	Sideways	Active in the Nasdaq Capital Market

would go into the bear market faster than large-cap stocks. On the contrary, when the bull market is coming, the first small-cap stocks would go into the bull market faster than large-cap stocks. In the U.S. stock market, the Dow Jones Index comes to the bull market and reaches the top peak, and NASDAQ will enter bear market or that bull market faster than DJI. While most people know that the bull market arrived, small-cap stocks have little chance. Then large-cap stocks rise up and small-cap stocks come to fall. Dow Jones Index is on behalf of big business and NASDAQ Index is on behalf of small business. We can understand the reason of different trends between NASDAQ and DJI.

5. Conclusions

The computational analysis of machine learning algorithms and their performance is a branch of theoretical computer science known as computational learning theory. This paper proposes a two dimensional numerical model for machine learning to simulate major U.S. stock market index and uses a nonlinear implicit finite-difference method to find numerical solutions of the two-dimensional simulation model. The new machine learning method can be extensively used to accelerate large-scale data processing on the history database. We substantially increase the investment rate of return in the securities market investment practice based on the above machine learning result. In the future, we will investigate European stock markets and Asian stock markets. In addition, the proposed machine learning algorithm and two dimensional numerical models will be applied to the more financial fields.

Acknowledgment

The authors gratefully acknowledge the helpful comments and suggestions of the reviewers, which have improved the presentation.

References

- [1] J.-R. Chang, L.-Y. Wei, and C.-H. Cheng, "A hybrid ANFIS model based on AR and volatility for TAIEX forecasting," *Applied Soft Computing Journal*, vol. 11, no. 1, pp. 1388–1395, 2011.
- [2] H.-H. Chu, T.-L. Chen, C.-H. Cheng, and C.-C. Huang, "Fuzzy dual-factor time-series for stock index forecasting," *Expert Systems with Applications*, vol. 36, no. 1, pp. 165–171, 2009.
- [3] Q. Xu, "Continuous time M/G/1 queue with multiple vacations and server close-down time," *Journal of Computational Information Systems*, vol. 3, no. 2, pp. 753–757, 2007.
- [4] Q. Xu and Z. Ma, "Discrete time Geo/G/1 queue with Bernoulli gated service simulation system," *Applied Mathematics and Computation*, vol. 204, no. 1, pp. 37–44, 2008.
- [5] Q. Xu, S. Bao, Z. Ma, and N. Tian, " $M^x/G/1$ queue with multiple vacations," *Stochastic Analysis and Applications*, vol. 25, no. 1, pp. 127–140, 2007.
- [6] C. He, Y. Liu, and Q. Xu, "Research on Chinese stock market's money flow by two-stage model," *Management World*, vol. 2, no. 3, pp. 16–26, 2011.
- [7] Q. Xu, "A new algorithm to forecast Shanghai composite index," *Journal of Information and Computational Science*, vol. 7, no. 12, pp. 2463–2467, 2010.
- [8] Q. Xu and Y. Liu, "A genetic algorithms to forecast American shares price index," *Journal of Information and Computational Science*, vol. 8, no. 8, pp. 1245–1250, 2011.
- [9] P. N. Brown and Y. Saad, "Hybrid Krylov methods for nonlinear systems of equations," *SIAM Journal on Scientific and Statistical Computing*, vol. 11, no. 3, pp. 450–481, 1990.
- [10] D. A. Knoll, W. J. Rider, and G. L. Olson, "An efficient nonlinear solution method for non-equilibrium radiation diffusion," *Journal of Quantitative Spectroscopy & Radiative Transfer*, vol. 63, no. 1, pp. 15–29, 1999.

Research Article

Efficient Interaction Recognition through Positive Action Representation

Tao Hu,¹ Xinyan Zhu,^{1,2} Wei Guo,¹ and Kehua Su²

¹Laboratory for Information Engineering in Surveying, Mapping and Remote Sensing, Wuhan University, Wuhan 430072, China

²School of Computer Science, Wuhan University, Wuhan 430072, China

Correspondence should be addressed to Wei Guo; guowei98032@gmail.com

Received 2 September 2013; Revised 11 November 2013; Accepted 13 November 2013

Academic Editor: Yue Wu

Copyright © 2013 Tao Hu et al. This is an open access article distributed under the Creative Commons Attribution License, which permits unrestricted use, distribution, and reproduction in any medium, provided the original work is properly cited.

This paper proposes a novel approach to decompose two-person interaction into a Positive Action and a Negative Action for more efficient behavior recognition. A Positive Action plays the decisive role in a two-person exchange. Thus, interaction recognition can be simplified to Positive Action-based recognition, focusing on an action representation of just one person. Recently, a new depth sensor has become widely available, the Microsoft Kinect camera, which provides RGB-D data with 3D spatial information for quantitative analysis. However, there are few publicly accessible test datasets using this camera, to assess two-person interaction recognition approaches. Therefore, we created a new dataset with six types of complex human interactions (i.e., named K3HI), including kicking, pointing, punching, pushing, exchanging an object, and shaking hands. Three types of features were extracted for each Positive Action: joint, plane, and velocity features. We used continuous Hidden Markov Models (HMMs) to evaluate the Positive Action-based interaction recognition method and the traditional two-person interaction recognition approach with our test dataset. Experimental results showed that the proposed recognition technique is more accurate than the traditional method, shortens the sample training time, and therefore achieves comprehensive superiority.

1. Introduction

Over the last few decades, human activity analysis has undergone rapid development receiving increasing attention in many fields, such as intelligent surveillance, human-computer interaction, and elder care management [1, 2]. Human activity can be categorized according to complexity as partial body action [3], simple action [4], interaction activity [5, 6], or group activity [7]. Motivated by the activity classes drawn from [5, 6], this paper focuses on two-person interaction recognition of six complex interactions: kicking, pointing, pushing, punching, exchanging an object, and shaking hands.

Much research has been done on two-person interactions [5–10] with respect to the kinds of complex action relationships and human features necessary for recognition. For example, [5] took into account whether one person's hand is above another's shoulder or whether one person's foot is near another's torso. Reference [6] used head-pose, arm-pose, leg-pose, and overall body-pose estimation with both

people for recognition. However, these processes are complex and time consuming and the recognition results might not be as accurate as required for a particular application. This paper proposes a new definition for interactions based on one person's behavior called Positive Action. In this method, one person's action plays the key role in an interaction; thus, two-person interaction recognition can be simplified into Positive Action recognition. This approach is simpler than traditional methods, saves computing time, and improves recognition results.

The recent proliferation of a cheap but effective depth sensor, the Microsoft Kinect [11], has created more opportunities for quantitative analysis of complex human activities. As compared to the traditional video camera, Kinect has the advantage of synchronous acquisition of color and depth images; with the use of depth maps, 3D information about a scene from a particular point of view is easily computed under diverse conditions [12]. This in turn will make behavior detection easier in badly lit or dark places. For example, Figure 1(a) represents a depth image captured by Kinect in

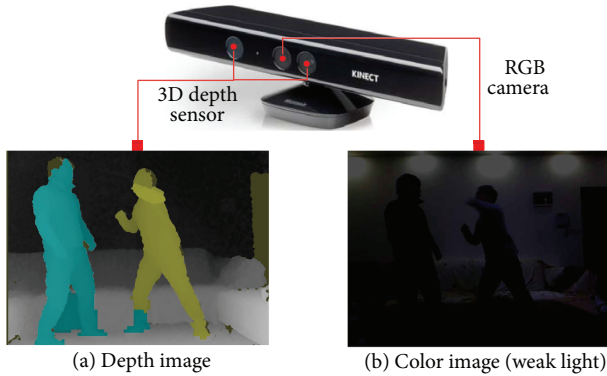


FIGURE 1: RGB-D data captured by Kinect.

weak light, which clearly shows one person punching at another; Figure 1(b) shows a color image of this interaction synchronously captured with the depth image. With a traditional camera, only RGB images as seen in Figure 1(b) are collected, with limited value for surveillance and other applications. Unfortunately, there are few publicly accessible test datasets to assess two-person interaction recognition approaches using the depth sensor. Thus, we created a new dataset for two-person interaction. The first version of this original dataset is available to download on the Internet at http://www.lmars.whu.edu.cn/prof_web/zhuxinyan/DataSetPublish/dataset.html.

The Microsoft Kinect sensor produces a new type of data, RGB-D data, which is an improvement on RGB images for human behavior recognition research. Therefore, many researchers have collected their own data and some of them are publicly accessible on the Internet [13–15]. In [16], Sung et al. produced a dataset including a total of twelve unique activities in five realistic domestic environments: office, kitchen, bedroom, bathroom, and living room. The RGBD-HuDaAct video database [17] collected in a lab environment includes 12 categories of human daily activities: making a phone call, mopping the floor, entering a room, and so forth. The LIRIS human activity dataset contains (gray/RGB/depth) videos showing people performing various activities taken from daily life (discussing, making telephone calls, exchanging an item, etc.); it includes information on not only the action class but also the spatial and temporal positions of objects in the video. However, these datasets only address individual activities and not two-person interactions [18].

Several more-than-one-person datasets were created using Kinect. In [19], the UT Kinect-human detection dataset was created: there are 98 frames with two people appearing in the scene at different depths in a variety of poses, including several simple interactions. In addition, [5] chose eight types of two-person interactions to establish another two-person dataset, including approaching, departing, pushing, kicking, punching, exchanging objects, hugging, and shaking hands. However, this latter dataset is not publicly available on the Internet.

Depth imaging data produced by the Kinect sensor is driving new single and daily activity recognition problem

research. For human activity or behavior representation, the method in [16, 20] detected and recognized different activities through body-pose features, hand position features, and motion information, using the Kinect sensor. In [17], Ni et al. proposed depth-extended feature representation methods to obtain superior recognition performance based on RGBD-HuDaAct datasets. Nowozin and Shotton [21] used skeletal features: joint velocities, joint angles, and joint angle velocities to reduce the latency in recognizing an action.

For human activity or behavior recognition, most efforts use HMM-based approaches. Park and Aggarwal [6] used HMMs for human motion recognition and combined it in a hierarchical way using DBNs (Dynamic Bayesian Networks). Vogler and Metaxas [22] presented parallel HMMs to recognize American sign language based on magnet tracking data, while Wilson and Bobick [23] proposed parametric HMMs to recognize human gestures. HMM-based recognition of more complex sequences is addressed by [24–26]. The method proposed in [24] was able to recognize motion units with optical flow data; in [25], Li proposed a landmark point trajectories-based approach to recognize view-invariant human actions and Chen et al. [26] presented a star skeleton model to recognize a single action and a series of actions.

Presently, there is little human interaction research based on Microsoft Kinect data and few papers report on a complex human activity dataset created to depict two-person interactions [5]. This research concluded that activity recognition represented by geometric relational features based on distance between all pairs of joints outperforms other feature choices. Our proposed approach and test dataset extend this research.

The contribution of this paper is twofold; we developed an efficient approach based on Positive Action representation to recognize two-person interactions and created a new dataset based on the Kinect sensor to test and verify methods. The rest of this paper is organized as follows. Section 2 shows our interaction dataset; Section 3 details the Positive Action definition and feature extraction method; Section 4 presents the Positive Action and the traditional interaction recognition method via HMMs; Section 5 demonstrates experimental results from two different approaches using our test dataset; finally Section 6 concludes this paper and discusses future work.

2. K3HI: Kinect-Based 3D Human Interaction Dataset

We collected two-person interactions using a Microsoft Kinect sensor. All videos were recorded in an indoor room while 15 volunteers performed activities. Each pair of people performed all types of interactions. The dataset has a total of approximately 320 interactions organized into eight categories. The first version of this dataset has been made publicly available to the research community to encourage progress in human action studies based on this new technology (http://www.lmars.whu.edu.cn/prof_web/zhuxinyan/DataSetPublish/dataset.html). Since approaching and departing activities are simple, recognition accuracy for both

interactions was almost 100% [5, 6]; therefore, we choose other types of relatively complex two-person interactions for recognition studies.

The most important data in our dataset is the spatial information (3D coordinates) of the two persons' skeletons. In order to ensure the integrity and continuity of target data, the original RGB images and depth information were ignored when capturing data. An articulated skeleton for each person was extracted using the OpenNI software [27] and Natural Interaction (NITE) Middleware provided by PrimeSense [28]. A skeleton was represented by the 3D positions of 15 joints, including head, neck, left shoulder, right shoulder, left elbow, right elbow, left hand, right hand, torso center, left hip, right hip, left knee, right knee, left foot, and right foot. However, when two persons overlapped, especially in a hugging activity (e.g., see Figure 2), full body tracking of interactions with NITE Middleware might be inaccurate. Bad and lost tracking will seriously affect interaction results, so hugging was not considered in our dataset. At last, six types of two-person interactions were captured, including kicking, punching, pointing, pushing, exchanging an object, and shaking hands. Figure 3 visualizes the collected interaction data as represented in the form of skeletons with different colors representing different actors.

3. Positive Action Representation

3.1. Positive Action Definition. Most existing work about human interactions focuses on two people, considering what kind of action relationship they have and what kind of features should be chosen to best represent an interaction [5, 6, 10–12]. Interactions can be classified into two groups: the first group indicates that one person acts first and the other person gives a responsive action, for example, kicking, pointing, punching, pushing, and so forth; the second group of interactions represents both people performing an almost identical synchronous action, for example, exchanging an object, shaking hands, and so forth. We propose that an interaction can be decomposed into a Positive Action and a Negative Action. For interactions in the first group, the person who acts first, resulting in the other person's reaction, performs a Positive Action. In the second group, since both people's behavior is similar and synchronized, we simply define the action, which moves with greater position changes in the first few frames, as the Positive Action. In all cases, a Negative Action is defined as a reciprocal action corresponding to a Positive Action in a two-person interaction.

After a Positive Action is identified, complex interaction recognition becomes relatively easy. Figures 4(a)–4(f) represent the original two-person interactions which were tested in [6], while Figures 4(a')–4(f') show the simplified results that the complex interactions are reduced into Positive Action-based representations. It can be seen that Positive Actions are discriminated with each other; therefore, only one person's features are taken into account and traditional interaction recognition can be transformed into Positive Action recognition.

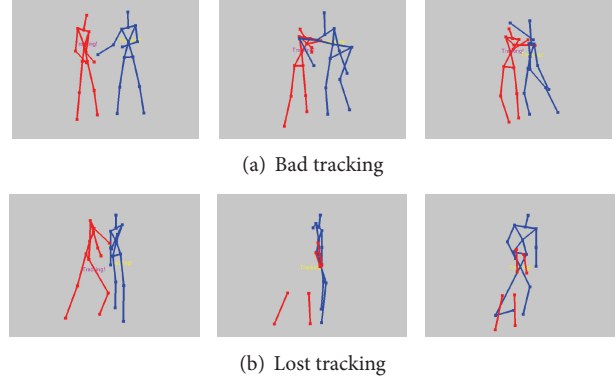


FIGURE 2: Bad tracking and lost tracking for a hugging activity. (a) and (b) show the key process in hugging for two different pairs; the last two images in (a) represent bad tracking of human bodies, and (b) represents lost tracking of bodies.

3.2. Positive Action Extraction. Next, we obtained the Positive Actions in our dataset by means of mathematical analysis, especially for interactions in the first group as defined in Section 3.1. The window size for each interaction was approximately 25 frames. We only kept the first ten frames—since the action changes in the first few frames are enough to distinguish Positive Action and Negative Action. The extraction process for Positive Action is divided into the following three procedures.

(1) *Aligning the Sequence.* For an interaction activity, there are always time or frame length variances when capturing the data. Before discerning a Positive Action, we first select the interactions of the same class to align the sequences. Then, the Dynamic Time Warping (DTW) model is used to align the sequences of the same activity class as mentioned in [29]. For each class, we selected a standard interaction sequence suitable for representation of the interaction process. We computed separately the minimal DTW distance between the remaining interaction sequences and the standard interaction sequence in the same class to find the optimal alignment.

In the DTW process, we express the feature vectors of two different sequences (in the same interaction class) as two time series (or frame series) $S_{T_1}^{(1)}$ and $S_{T_2}^{(2)}$, defined as follows:

$$\begin{aligned} S_{T_1}^{(1)} &= (s_1^{(1)}, s_2^{(1)}, \dots, s_{t_1-1}^{(1)}, s_{t_1}^{(1)}), \\ S_{T_2}^{(2)} &= (s_1^{(2)}, s_2^{(2)}, \dots, s_{t_2-1}^{(2)}, s_{t_2}^{(2)}). \end{aligned} \quad (1)$$

Accordingly, the costs between two series will be lower if they are similar, meaning that if two sequences are well aligned, the minimal DTW distance will be defined as

$$\begin{aligned} D(S_{T_1}^{(1)}, S_{T_2}^{(2)}) \\ = \min \{D(S_{T_1-1}^{(1)}, S_{T_2-1}^{(2)})\}, \end{aligned}$$

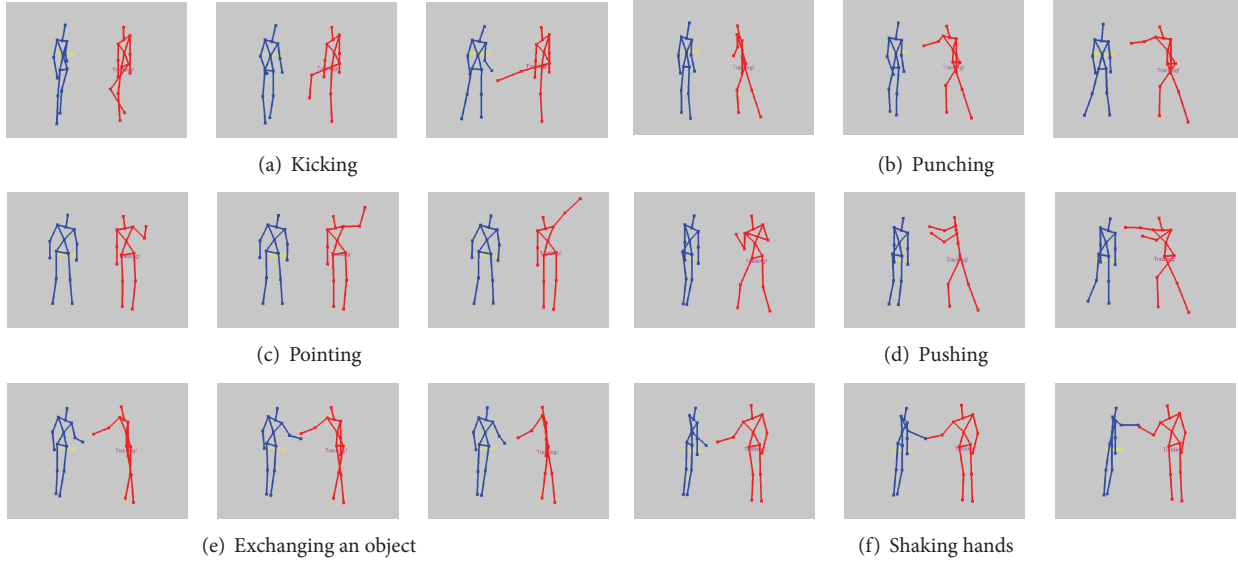


FIGURE 3: Skeleton visualization of interactions in our dataset. Three key poses were selected to represent the process of each interaction: (a) kicking, (b) punching, (c) pointing, (d) pushing, (e) exchanging an object, and (f) shaking hands.

$$D(S_{T_1-1}^{(1)}, S_{T_2}^{(2)}), D(S_{T_1}^{(1)}, S_{T_2-1}^{(2)})\} \\ + d(S_{t_1}^{(1)}, S_{t_2}^{(2)}), \quad (2)$$

where $d(S_{t_1}^{(1)}, S_{t_2}^{(2)})$ is the feature distance at time t_1 and t_2 in two sequences $S_{T_1}^{(1)}$ and $S_{T_2}^{(2)}$.

It is known that there are two persons' 3D joint positions in an activity sequence, represented as

$$\left\{ P_{(i,j)}^{(1)} = \left(x_{(i,j)}^{(1)}, y_{(i,j)}^{(1)}, z_{(i,j)}^{(1)} \right), \right. \\ \left. P_{(i,j)}^{(2)} = \left(x_{(i,j)}^{(2)}, y_{(i,j)}^{(2)}, z_{(i,j)}^{(2)} \right) \right\}, \quad (3)$$

where $P_{(i,j)}^{(1)}$ and $P_{(i,j)}^{(2)}$ are the position set of the first and the second persons, respectively; i and j are the frame index and the joint index. We used the joint positions to characterize the feature in each frame for a distance computation between $S_{T_1}^{(1)}$ and $S_{T_2}^{(2)}$. The distance is described as

$$d(s_{t_1}^{(1)}, s_{t_2}^{(2)}) \\ = \sum_{j=1}^n \left(\left| P_{(t_2,j)}^{(1)} - P_{(t_1,j)}^{(1)} \right|^2 + \left| P_{(t_2,j)}^{(2)} - P_{(t_1,j)}^{(2)} \right|^2 \right), \quad (4)$$

where $|P_{(t_2,j)} - P_{(t_1,j)}|$ indicates the Euclidean distance at time t_1 and time t_2 . Then, we placed the Euclidean distance into formula (4) to obtain the minimal DTW distance, finding the optimal alignment between variable length interaction sequences.

(2) *Computing Key Joint Position Changes.* We selected eight joints as key joints, which represent changes in the body's

motion; these joints include the left and right elbow, left and right hand, left and right knee, and left and right foot.

The position changes of the joints were described by calculating the distances between neighboring frames, defined as follows:

$$D_{(i,i+1)}^j = \left| P_{i+1}^{(j;x,y,z)} - P_i^{(j;x,y,z)} \right|, \quad (5)$$

where $D_{(i,i+1)}^j$ is the Euclidean distance of a key joint j between frame i and $i+1$; $P_i^{(j;x,y,z)}$ indicates the position of joint j at frame i and (x, y, z) are the 3D coordinates.

(3) *Identifying Positive Action.* For actions in the first group which is defined in Section 3.1, it is tougher to extract Positive Action than it is in the second group. According to the benchmark in [30], human reaction time is around 0.2-0.3 s. Our collected data is 15 frames per second. When reaction time is converted into frames, it consists of 3-4 frames. This means that in the first group of interactions when a Positive Action starts, about 3-4 frames later, a corresponding Negative Action occurs.

In our Positive Action definition, because the joint positions in the first two adjacent frames change and conform to the benchmark, we can compare the maximum position changes of both persons' key joints between initial i th and $(i+3)$ th frame of a sequence. The value of i for the standard interaction sequence mentioned in procedure (1) is one. For the other sequences after DTW processing, i will be different value. This is expressed as follows:

$$\text{Positive Action} = \arg \max \left(\max(D_{(i,i+3)}^{(p1;j)}), \max(D_{(i,i+3)}^{(p2;j)}) \right), \quad (6)$$

where $\max(D_{(i,i+3)}^{(p1;j)})$ and $\max(D_{(i,i+3)}^{(p2;j)})$ indicate the maximum position changes of joints for person one and person two

in an interaction; $\max(D_1, D_2)$ indicates that if $D_1 > D_2$, D_1 will represent the Positive Action and D_2 will represent the Negative Action; otherwise, D_2 will be the Positive Action. Figure 6 shows the processing results for Positive Actions, ignoring the Negative Actions. Each action has its own distinct characteristics, including easily confused interactions, such as exchanging an object and shaking hands.

Positive Action extraction is much easier in the second group as compared with the first group. According to the definition of Positive Action for group two, we also use (6); therefore, the person with the maximum $D_{(i,i+3)}^{(p;j)}$ performs the Positive Action.

In order to verify the method which is used to extract Positive Action, we selected the “kicking” action from the first group of interactions and “shaking hands” from the second group and calculated the position changes using (5) for the first 10 frames. Figure 5 shows the results: from Figure 5(a), it can be seen that as person one’s right foot and right knee positions change from the first frame to the third frame, person two’s left and right elbows as well as left and right hands positions also change in the fourth frame. These changes suggest that when person one starts to kick, person two’s upper limbs react milliseconds later so that the first person’s motion belongs to the Positive Action. However, Figure 5(b) does not show any connection between the two behaviors, except that both of their right hands and elbows move in a synchronized fashion. In general, experimental results support our Positive Action extraction method.

The visualization of Positive Actions is shown in Figure 6. Table 1 represents the extraction results for Positive Action with and without DTW for the first group, illustrating that the extraction results for Positive Action have greater accuracy after DTW preprocessing.

3.3. Feature Extraction. After Positive Actions are extracted, we utilize several body-pose features for motion-capture data representation and evaluate these features using our test dataset. One of the biggest challenges when using skeleton joints as a feature is that semantically similar motions may not necessarily be numerically similar [31]. To overcome this, [32] used relational body-pose features as introduced in [31], describing geometric relations between specific joints in a single pose or a short sequence of poses. Relational pose features were used to recognize daily-life activities performed by a single actor in a random forest framework; the features included joint, plane, and velocity features.

(i) Joint Features

Joint Distance. Let $p_{j,t} \in \mathfrak{R}^3$ be the 3D location of joint j in a Positive Action at time $t \in T$. The joint distance feature F_{JoiDis} is defined as the Euclidean distance between two joints at time t and is represented as

$$F_{\text{JoiDis}}^{(j_1, j_2; t)} = |p_{(j_1; t)} - p_{(j_2; t)}|, \quad (7)$$

where j_1 and j_2 are any two joints of a single person ($j_1 \neq j_2$).

Joint Motion. Similar to the joint distance feature, the joint motion feature F_{JoiMot} is defined as the Euclidean distance

TABLE 1: Accuracy of Positive Action extraction.

1st kind of interaction	Kicking	Pointing	Pushing	Punching
Accuracy (without DTW)	93.9%	95.8%	92.3%	90%
Accuracy (with DTW)	98.6%	99.2%	98.5%	97.7%

between joints j_1 at time t_1 and j_2 at time t_2 . It captures Positive Action joint motions and is represented as

$$F_{\text{JoiDis}}^{(j_1, j_2; t_1, t_2)} = |p_{(j_1; t_1)} - p_{(j_2; t_2)}|. \quad (8)$$

(ii) Plane Features

Plane Feature. F_{Plane} captures the geometric relationship between a plane and a joint; F_{Plane} helps to express whether the left hand lies in front of the plane spanned by the right shoulder, left shoulder, or torso. It is defined as

$$F_{\text{Plane}}^{(j_1, j_2, j_3, j_4; t)} = \text{dist}(p_{(j_1; t)}, \langle p_{(j_2; t)}, p_{(j_3; t)}, p_{(j_4; t)} \rangle), \quad (9)$$

where $\langle p_{(j_2; t)}, p_{(j_3; t)}, p_{(j_4; t)} \rangle$ indicates the plane spanned by three other joints j_2 , j_3 , and j_4 . $\text{dist}(p_{(j_1; t)}, \langle \cdot \rangle)$ represents the Euclidean distance from joint j to the plane.

Normal Plane Feature. F_{NorPlane} is similar to a plane feature; it helps to determine if and how far the joint “hand” is raised above the “shoulder”; F_{NorPlane} is defined as follows:

$$F_{\text{NorPlane}}^{(j_1, j_2, j_3, j_4; t)} = \text{dist}(p_{(j_1; t)}, \langle p_{(j_2; t)}, p_{(j_3; t)}, p_{(j_4; t)} \rangle), \quad (10)$$

where j_1 is the joint as in a plane feature and $\langle p_{(j_2; t)}, p_{(j_3; t)}, p_{(j_4; t)} \rangle$ indicates that the plane with normal vector $p_{(j_2; t)} - p_{(j_3; t)}$ passing through $p_{(j_4; t)}$. j_1, j_2, j_3 , and j_4 represents different joints.

(iii) Velocity Features

Velocity Feature. F_{Vel} captures the velocity of one joint along a direction generated by two other joints at time t . F_{Vel} is defined as

$$F_{\text{Vel}}^{(j_1, j_2, j_3; t)} = \frac{v_{j_1; t} \cdot (p_{j_2; t} - p_{j_3; t})}{|p_{j_2; t} - p_{j_3; t}|}, \quad (11)$$

where j_1, j_2 , and j_3 are different joints.

Normal Velocity Feature. F_{NorVel} is similar to a normal plane feature; it captures the velocity of one joint along the direction of the normal vector of the plane generated by three other joints at time t . F_{NorVel} is defined as

$$F_{\text{NorVel}}^{(j_1, j_2, j_3, j_4; t)} = v_{j_1; t} \cdot \hat{n} \langle p_{j_2; t}, p_{j_3; t}, p_{j_4; t} \rangle, \quad (12)$$

where $\hat{n} \langle \cdot \rangle$ is the unit normal vector of the plane represented by $\langle \cdot \rangle$ when j_1, j_2, j_3 , and j_4 are different joints.

4. Positive Action Recognition via HMM

Hidden Markov Models (HMMs) are widely used for modeling time series data. Formally, a HMM can be described

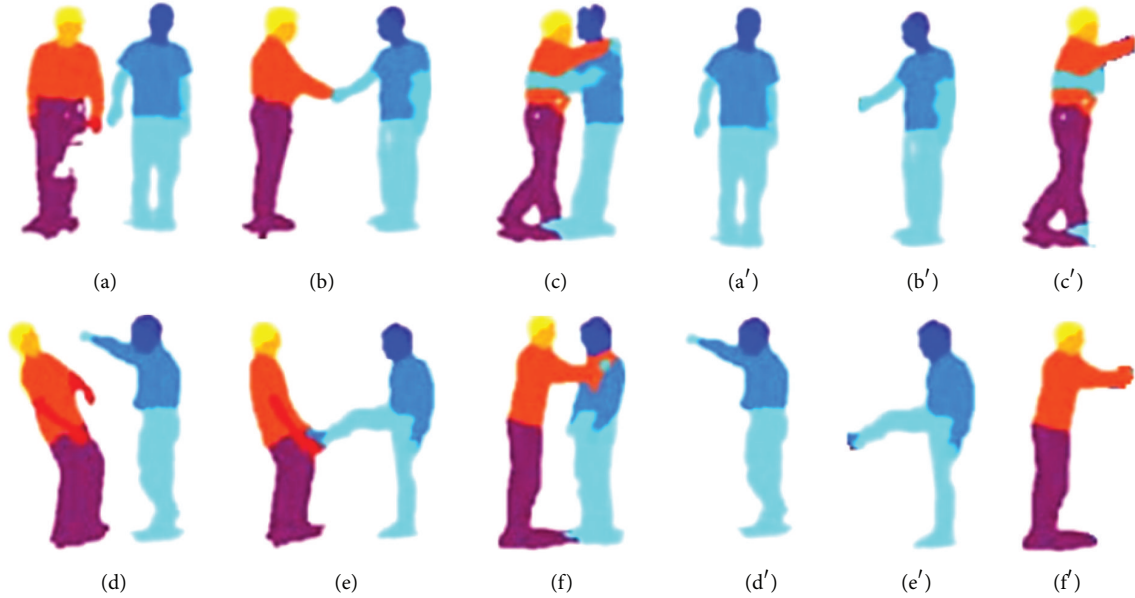


FIGURE 4: A comparison between interactions and Positive Actions. (a)–(f) show the original interaction data in [6] and (a')–(f') are the Positive Actions of one person described in this paper.

as a 5-tuple $\Omega = (\Phi, \Sigma, \pi, \delta, \lambda)$, where Φ are the hidden variables and δ are the transitions probabilities among states; these probabilities, as well as the starting probabilities π , are discrete. Every observation state has a set of possible emissions Σ and discrete/continuous probabilities λ for these emissions. A Gaussian Mixture Model (GMM) is used to represent the observation states for each hidden variable and to compute their probabilities [33]. GMM density is defined as the weighted sum of Gaussian densities.

In the training process, HMM parameters are initialized: we manually decided the observation states' number N and hidden states' number M ; then we divided equally the data sequence into N parts and clustered each part using K -means to establish the GMM. After the HMM parameters are known, the Baum-Welch algorithm, also known as the Forward-Backward algorithm, was used to reevaluate the HMM parameters and to compute the output probability of observation sequence O_i^x (indicating the i th sample sequence of action x). Finally, the sequence probabilities are summed up and HMM parameters are confirmed until we get the maximum value $P(O | \Omega) = \sum P(O_i^x | \Omega_i)$. After training, we have six HMMs for each type of action.

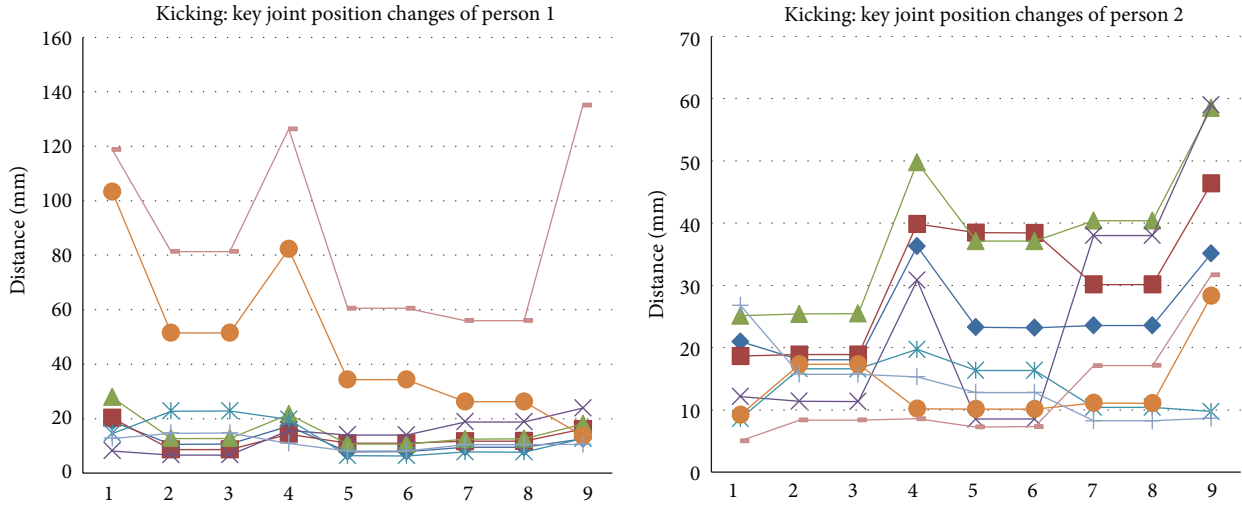
During the recognition process, given the data sequence of unknown action X , the feature vectors are extracted for each frame. Using the Viterbi algorithm, the likelihood $P_i = P(O_i^x | \Omega_i)$ of observation sequence O_i^x is generated. We repeated this procedure based on the six HMMs generated in training process and produced the probabilities p_i ($1 \leq i \leq 6$). Thus, by comparing the values p_i , we obtained the maximum likelihood p_{\max} , which represents the type of interaction.

5. Experimental Results

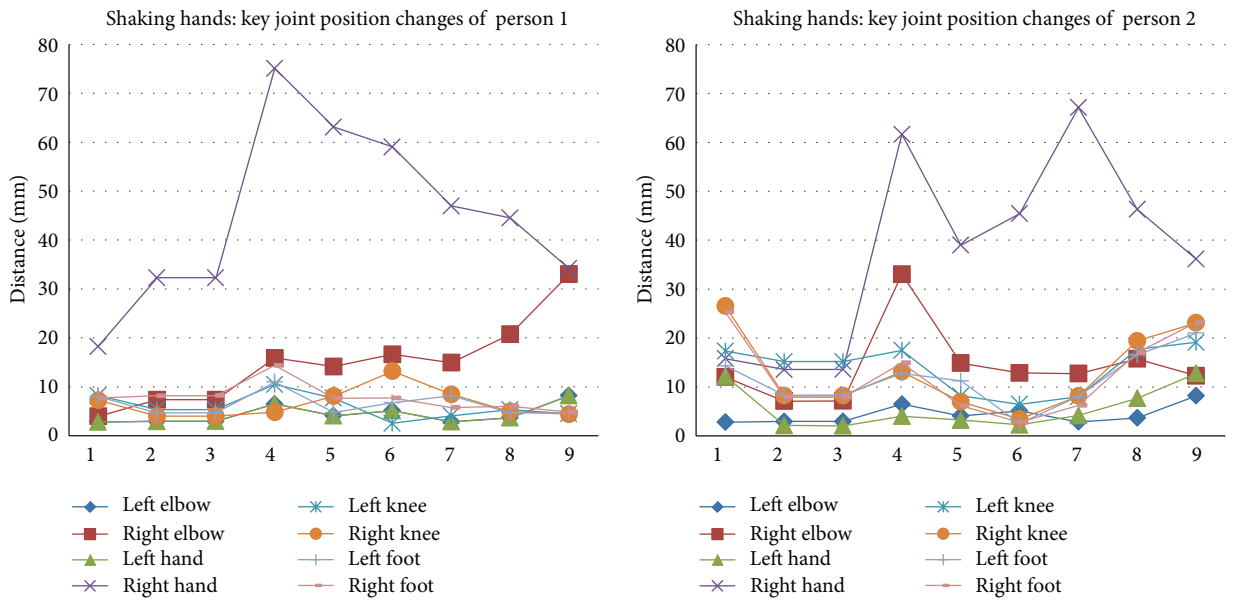
We selected the features extracted from among the Positive Actions identified in Section 3.2 to recognize interactions and used the features extracted from original interaction data as in [5]. Then, we compared and evaluated the recognition results from both approaches. The process for feature extraction and action recognition is illustrated in Figure 7.

In the Positive Action-based interaction approach, features as described in Section 3.3 were classified into three groups: joint features, plane features, and velocity features. In our experiments, we recognized six kinds of Positive Actions for each feature and mixed the features. There are fifteen joints (including 3D coordinates) for each action. Thus, the dimension of F_{JoiDis} is $C_{15}^2 = 105$ for each frame and the F_{JoiMot} was $C_5^2 \times C_T^2$ (T is the total number of frames for each interaction). Considering the larger dimensions of both plane and velocity features, we selected key joints to characterize the features. For plane features, the relationship between the four limbs and main body is critical; therefore, the plane was spanned from seven joints ("head," "neck," "left shoulder," "right shoulder," "torso," "left hip," and "right hip") and eight joints for the target joint. In this way, we created a lower dimension $C_7^3 \times 8$ for each frame. However, the feature dimensions were larger than the training sample number; thus, Principal Component Analysis (PCA) was used to reduce the dimensions.

To classify interactions, evaluation is done with a 4 fold cross-validation: 3 folds are used for training and 1 for testing. Based on the fact that the 3 state HMM performs much better than the 4- and 5 state HMMs in our experiments, we trained a 3 state, continuous HMM with GMM. As expected,



(a) The first group of interaction: kicking



(b) The second group of interaction: shaking hands

FIGURE 5: Key joints position changes in two groups of interactions during the first 10 frames. (a) shows the first group of interaction with “kicking” as an example; (b) shows the second group and takes “shaking hands” as an example.

the transition probabilities and the observation probabilities turned out to be different for different actions. After training, the HMM parameters are known while the Viterbi algorithm was used to find the maximum likelihood category. Table 2 shows the experimental results for each kind of feature representation.

For the traditional two-person relationship-based interaction recognition method (called the old approach in the rest of this paper), three kinds of features referring to [5] were also extracted based on the original captured data (see Figure 3). The training and recognition process was identical with the Positive Action-based (new) method. Figure 8 shows the recognition results in a confusion matrix: (a)–(c) represents the Positive Action-based approach and (d)–(f) for the values

TABLE 2: Interactions recognition results via Positive Action-based representation.

Features	Average accuracy
Raw position	45.2%
Joint distance	76.1%
Joint motion	75.6%
Plane	63.2%
Normal plane	65.3%
Velocity	44.2%
Normal velocity	41.2%

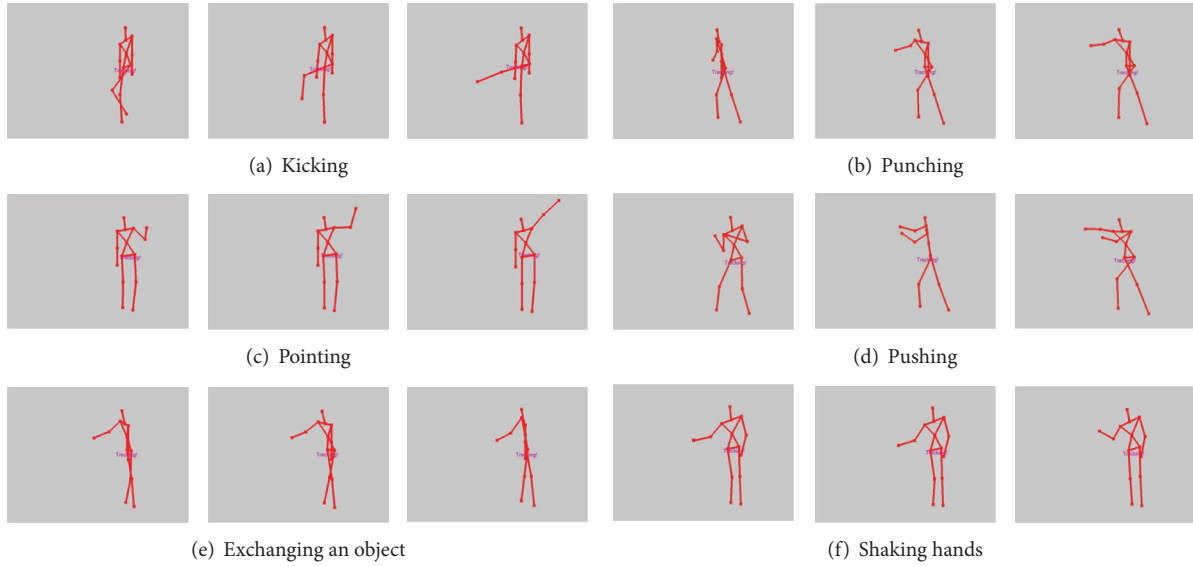


FIGURE 6: Skeletons visualization of Positive Actions. The red skeletons show only Positive Actions in two-person interactions. These are considered as the interaction representation and Negative Actions are ignored in the recognition process.

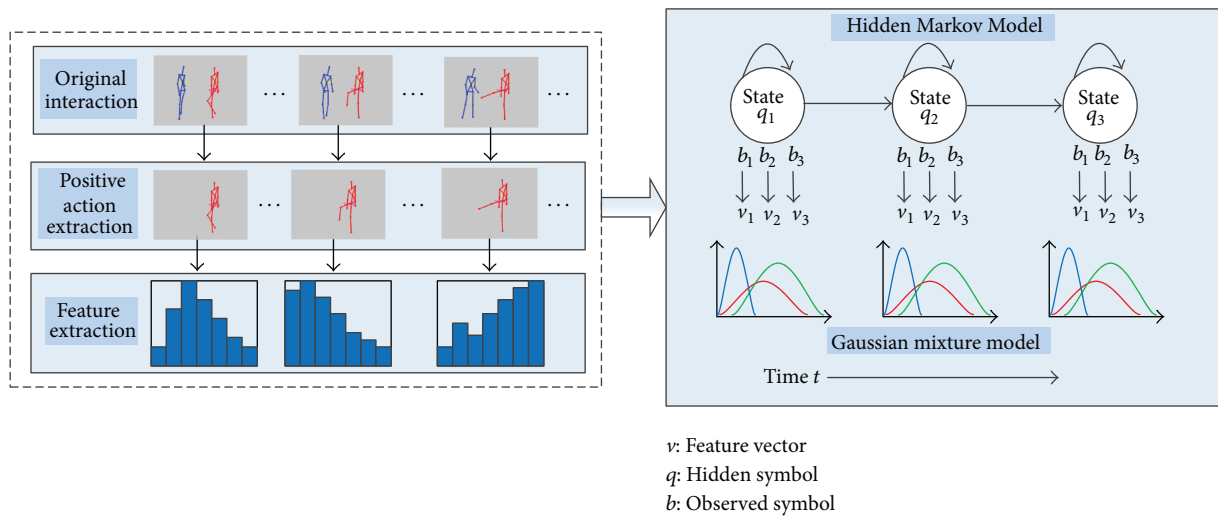


FIGURE 7: Flow of the interaction recognition system.

generated by the old approach. The confusion matrix also compares different kinds of features for recognition: joint features include the joint motion and joint distance features; plane features include the plane and normal plane features; velocity features include the velocity and normal velocity features. The average recognition accuracy for each kind of feature from (a) to (c) is 78.67%, 66.83%, and 55.67%; the average accuracy from (d) to (f) is 70.00%, 61.67%, and 48.67%. Therefore, joint features-based recognition results are better than plane and velocity features, suggesting that geometric relational features based on the distance between joints outperform other feature choices, verifying the conclusions found in [5]. Furthermore, in both the old and new approaches, there exists some confusion between “pointing”

and “punching” and between “exchanging an object” and “shaking hands.” Our results show that these actions are similar, leading to lower recognition accuracy.

Most importantly, the average accuracy for interaction recognition based on Positive Action representation, as proposed in this paper, is 7% greater than two-person relationship-based approaches, especially since geometric relational feature-based recognition is almost 10% greater. There are several reasons for these results. First, a two-person feature representation is more complex than a Positive Action-based representation, creating unstable factors. For example, the “pointing” interaction in normal plane features: the Positive Action-based method only judges whether one person’s “hand” position is higher than its’ own “shoulder”;

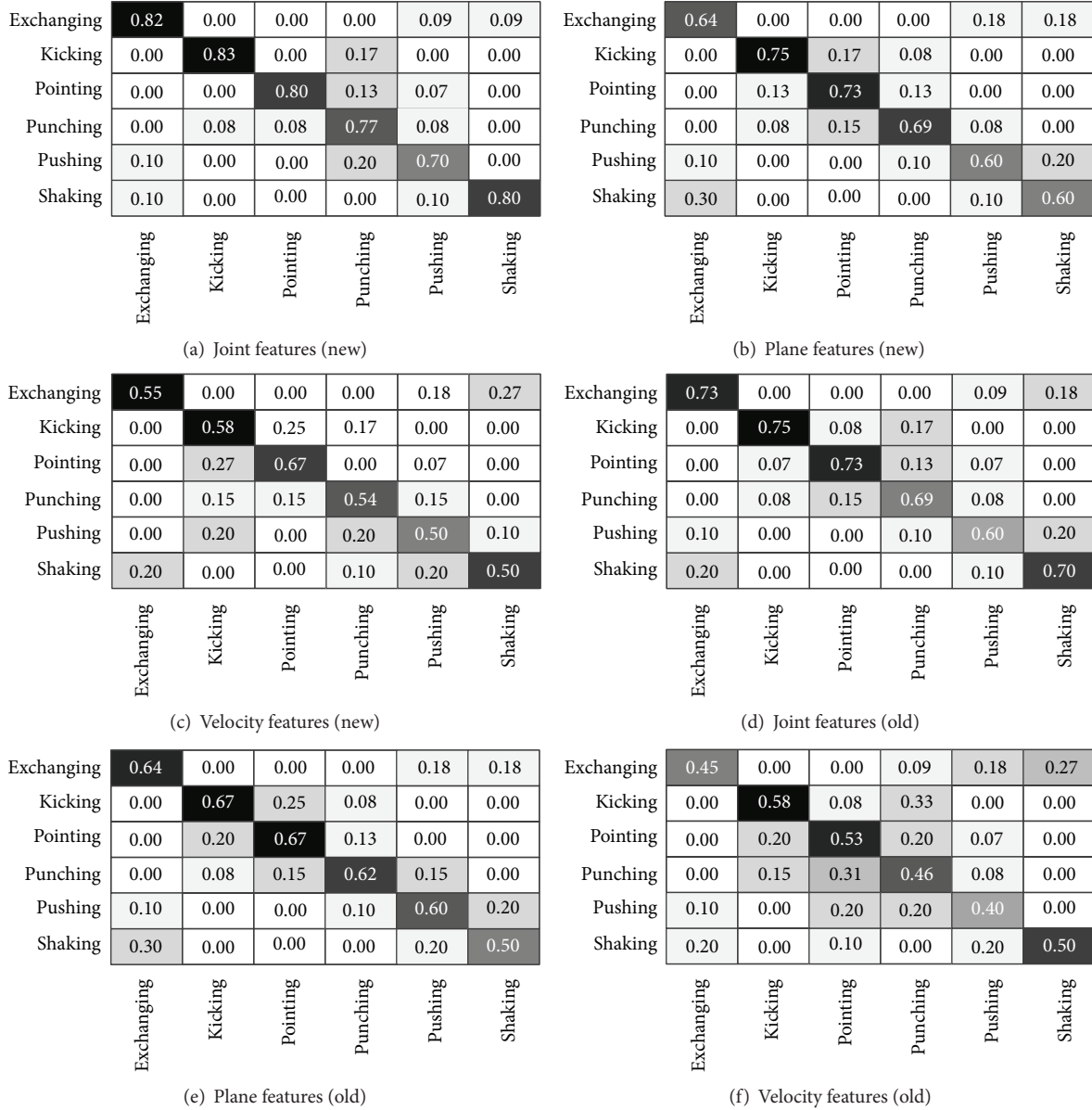


FIGURE 8: Confusion matrix for different features for two approaches. (a)–(c) are the recognition results based on Positive Action representation; (d)–(f) are the results based on old one referred to [5].

however, the old approach as in [5] must judge the spatial relationship for both persons’ shoulders, which will lead to more conditions for recognition; therefore, the Positive Action-based approach needs less training samples than the old approach to get more or less the same recognition accuracy. Second, for the same kind of feature, the Positive Action-based representation method has fewer dimensions than the old approach. The old approach therefore is more sensitive during dimension reduction in the training process; thus, its recognition accuracy will be lower.

To verify the generalizability of our proposed method, we tested the dataset against two more classifiers, including Support Vector Machines (SVMs) and Multiple Instance Learning (MIL). The test features were represented by the

combination of joint distance and joint motion. The results in Table 3 suggest that MIL has better performance than SVMs while the Positive Action-based method is much better than the two-person based method. Therefore, different classifier supports the conclusion that our new method is effective.

In addition to a comparison of the interaction recognition accuracy for both approaches, we also compared time costs and evaluated the training time to arrive at optimal HMM parameters (see Figure 9). The average training time for three kinds of features based on Positive Action representation is 42.47 MS (millisecond), 79.52 MS, and 67.88 MS, while for the old approach referring to [5], the average training time is 63.27 MS, 199.6958 MS and 156.3827 MS.

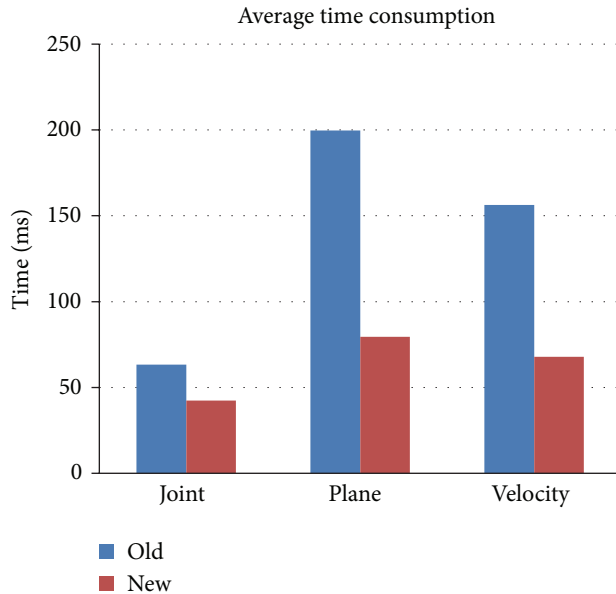


FIGURE 9: Average time cost for training samples. It is the old and new methods that are evaluated according to three kinds of features: joint, plane, and velocity features.

The Positive Action-based representation method consumes less time than the old approach.

In summary, Positive Action-based representation for two-person interaction recognition outperforms the old approach; not only is its recognition accuracy better, but also the time cost for training is less. So, the new method transforms a relatively complex two-person interaction into a simpler Positive Action, making the recognition procedure more cost effective while maintaining or even improving recognition quality. Therefore, the new proposed approach is efficient for interaction recognition.

6. Conclusion

This paper presented a novel approach to recognize relatively complex human interactions: different from many existing interaction recognition methods, we focused our research on single actions which are useful when distinguishing differences between types of interactions. Two-person interaction recognition is transformed into Positive Action-based recognition.

The key contributions of this paper are as follows: (1) we investigated the reciprocal relationships in two-person interaction and proposed a new definition for single person's behavior called Positive Action; (2) two-person interactions were recognized based on Positive Action representation via continuous HMMs; (3) a new test interaction dataset based on Microsoft Kinect camera was created and it is publicly available; our experimental results demonstrate that the proposed method outperforms old approaches based on two-person relationships.

In the future, we plan to find more volunteers to capture more data and extend our interaction dataset to include

TABLE 3: The performance on more classifiers.

Classifier	Positive Action	Two persons
SVMs	81.67%	76.67%
MIL	83.33%	78.33%

additional interaction categories. More importantly, owing to the limitations of human tracking software, such as the NITE Middleware or the Windows SDK for Kinect, there occasionally are some inaccurate tracking results. Therefore, we need to find a better way to track human actions, further improving the recognition accuracy.

Acknowledgments

The authors are grateful to the volunteers for capturing data. This work was supported by the National Natural Science Foundation (41301517), the National 863 Key Program (2013AA122301), the National Key Technology R&D Program (2012BAH35B03), Chinese NSF Creative Research Group project (41023001), the National 973 Program (2011CB707001), the Fundamental Research Funds for the Central Universities (2012619020215), and Doctoral Fund of Ministry of Education (20120141120006).

References

- [1] J. K. Aggarwal and M. S. Ryoo, "Human activity analysis: a review," *ACM Computing Surveys*, vol. 43, no. 3, article 16, 2011.
- [2] R. W. Poppe, "A survey on vision-based human action recognition," *Image and Vision Computing*, vol. 28, no. 6, pp. 976–990, 2010.
- [3] J. Yang, Y. F. Li, K. Wang, Y. Wu, G. Altieri, and M. Scalia, "Mixed signature: an invariant descriptor for 3D motion trajectory perception and recognition," *Mathematical Problems in Engineering*, vol. 2012, Article ID 613939, 29 pages, 2012.
- [4] S. Sadek, A. A. Hamadi, B. Michaelis, and U. Sayed, "Chord-length shape features for human activity recognition," *ISRN Machine Vision*, vol. 2012, Article ID 872131, 9 pages, 2012.
- [5] Y. Kiwon, J. Honorio, D. Chattopadhyay, T. L. Berg, and D. Samaras, "Two-person interaction detection using body-pose features and multiple instance learning," in *Proceedings of the IEEE Computer Society Computer Vision and Pattern Recognition Workshops (CVPRW '12)*, vol. 28, no. 35, pp. 28–35, Providence, RI, USA, June 2012.
- [6] S. Park and J. K. Aggarwal, "A hierarchical Bayesian network for event recognition of human actions and interactions," *Multimedia Systems*, vol. 10, no. 2, pp. 164–179, 2004.
- [7] L. S. Wu, L. M. Xia, and D. Y. Luo, "Survey on human interactive behavior recognition and comprehension," *Computer Applications and Software*, vol. 28, no. 11, pp. 60–63, 2011.
- [8] K. Sato and J. K. Aggarwal, "Tracking and recognizing two-person interactions in outdoor image sequences," in *Proceedings of the IEEE Workshop on Multi-Object Tracking*, pp. 87–94, Vancouver, Canada, 2001.
- [9] S. Park and J. K. Aggarwal, "Recognition of human interaction using multiple features in gray scale images," in *Proceedings of the 15th International Conference on Pattern Recognition*, vol. 1, pp. 51–54, Barcelona, Spain, 2000.

- [10] M. S. Ryoo and J. K. Aggarwal, "Recognition of composite human activities through context-free grammar based representation," in *Proceedings of the IEEE Computer Society Conference on Computer Vision and Pattern Recognition (CVPR '06)*, vol. 2, pp. 1709–1718, New York, NY, USA, June 2006.
- [11] <http://www.microsoft.com/en-us/kinectforwindows/>.
- [12] S. Escalera, "Human behavior analysis from depth maps," in *Articulated Motion and Deformable Objects*, vol. 7378 of *Lecture Notes in Computer Science*, pp. 282–292, Springer, Berlin, Germany, 2012.
- [13] H. Kuehne, H. Jhuang, E. Garrote, T. Poggio, and T. Serre, "HMDB: a large video database for human motion recognition," in *Proceedings of the IEEE International Conference on Computer Vision (ICCV '11)*, pp. 2556–2563, Barcelona, Spain, November 2011.
- [14] M. S. Ryoo and J. K. Aggarwal, "ICPR contest on Semantic Description of Human Activities (SDHA)," UT-Interaction Dataset, 2010.
- [15] A. Patron-Perez, M. Marszalek, I. Reid, and A. Zisserman, "Structured learning of human interactions in TV shows," in *Proceedings of the IEEE Transactions on Pattern Analysis and Machine Intelligence*, vol. 34, no. 12, pp. 2441–2453, December 2012.
- [16] J. Sung, C. Ponce, B. Selman, and A. Saxena, "Human activity detection from RGBD images," in *Proceedings of the AAAI Workshop on Pattern, Activity and Intent Recognition (PAIR '11)*, pp. 47–55, San Francisco, Calif, USA, August 2011.
- [17] B. Ni, G. Wang, and P. Moulin, "RGBD-HuDaAct: a color-depth video database for human daily activity recognition," in *Proceedings of the IEEE International Conference on Computer Vision Workshops (ICCVW '11)*, pp. 1147–1153, Barcelona, Spain, November 2011.
- [18] C. Wolf, J. Mille, E. Lombardi et al., "The LIRIS human activities dataset and the ICPR, 2012 human activities recognition and localization competition," Tech. Rep. RR-LIRIS-2012-004, LIRIS Laboratory, Lyon, France, 2012.
- [19] L. Xia, C.-C. Chen, and J. K. Aggarwal, "Human detection using depth information by Kinect," in *Proceedings of the IEEE Computer Society Conference on Computer Vision and Pattern Recognition Workshops (CVPRW '11)*, pp. 15–22, Colorado Springs, Colo, USA, June 2011.
- [20] S. Z. Masood, C. Ellis, A. Nagaraja, M. F. Tappen, J. J. Laviola, and R. Sukthankar, "Measuring and reducing observational latency when recognizing actions," in *Proceedings of the IEEE International Conference on Computer Vision Workshops (ICCVW '11)*, pp. 422–429, Barcelona, Spain, November 2011.
- [21] S. Nowozin and J. Shotton, "Action points: a representation for low-latency online human action recognition," Tech. Rep., Microsoft Research, 2012.
- [22] C. Vogler and D. Metaxas, "Parallel hidden Markov models for american sign language recognition," in *Proceedings of the 7th IEEE International Conference on Computer Vision (ICCV'99)*, vol. 1, pp. 116–122, Kerkyra, Greece, September 1999.
- [23] A. D. Wilson and A. F. Bobick, "Parametric hidden Markov models for gesture recognition," *IEEE Transactions on Pattern Analysis and Machine Intelligence*, vol. 21, no. 9, pp. 884–900, 1999.
- [24] D. Gehrig, H. Kuehne, A. Woerner, and T. Schultz, "HMM-based human motion recognition with optical flow data," in *Proceedings of the 9th IEEE-RAS International Conference on Humanoid Robots*, pp. 425–430, Paris, France, December 2009.
- [25] X. Li and K. Fukui, "View invariant human action recognition based on factorization and HMMs," *IEICE Transactions on Information and Systems*, vol. 91, no. 7, pp. 1848–1854, 2008.
- [26] H.-S. Chen, H.-T. Chen, Y.-W. Chen, and S.-Y. Lee, "Human action recognition using star skeleton," in *Proceedings of the 4th ACM International Workshop on Video Surveillance and Sensor Networks (VSSN '06)*, pp. 171–178, New York, NY, USA, October 2006.
- [27] <http://www.openni.org/>.
- [28] <http://www.primesense.com/>.
- [29] S. Sempena, N. U. Maulidevi, and P. R. Aryan, "Human action recognition using dynamic time warping," in *Proceedings of the International Conference on Electrical Engineering and Informatics (ICEEI '11)*, pp. 1–5, Bandung, Indonesia, July 2011.
- [30] <http://www.humanbenchmark.com>.
- [31] M. Muller, T. Roder, and M. Clausen, "Efficient content-based retrieval of motion capture data," *ACM Transactions on Graphics*, vol. 24, no. 3, pp. 677–685, 2005.
- [32] A. Yao, J. Gall, G. Fanelli, and L. V. Gool, "Does human action recognition benefit from pose estimation?" in *Proceedings of the British Machine Vision Conference (BMVC '11)*, pp. 67.1–67.11, University of Dundee, Dundee, UK, September 2011.
- [33] B. Poonam, K. Anuj, K. Sumit, S. Akash, and G. Shitij, "Improved hybrid model of HMM/GMM for speech recognition," in *Book 5 Intelligent Technologies and Applications*, Institute of Information Theories and Applications, Sofia, Bulgaria, 2008.

Research Article

Human Walking Pattern Recognition Based on KPCA and SVM with Ground Reflex Pressure Signal

Zhaoqin Peng,¹ Chun Cao,¹ Qiusheng Liu,² and Wentao Pan¹

¹ School of Automation Science and Electrical Engineering, Beihang University, Beijing 100191, China

² School of Mechanical Engineering, Tsinghua University, Beijing 100084, China

Correspondence should be addressed to Zhaoqin Peng; pzqin@126.com

Received 11 August 2013; Accepted 11 September 2013

Academic Editor: Gelan Yang

Copyright © 2013 Zhaoqin Peng et al. This is an open access article distributed under the Creative Commons Attribution License, which permits unrestricted use, distribution, and reproduction in any medium, provided the original work is properly cited.

Algorithms based on the ground reflex pressure (GRF) signal obtained from a pair of sensing shoes for human walking pattern recognition were investigated. The dimensionality reduction algorithms based on principal component analysis (PCA) and kernel principal component analysis (KPCA) for walking pattern data compression were studied in order to obtain higher recognition speed. Classifiers based on support vector machine (SVM), SVM-PCA, and SVM-KPCA were designed, and the classification performances of these three kinds of algorithms were compared using data collected from a person who was wearing the sensing shoes. Experimental results showed that the algorithm fusing SVM and KPCA had better recognition performance than the other two methods. Experimental outcomes also confirmed that the sensing shoes developed in this paper can be employed for automatically recognizing human walking pattern in unlimited environments which demonstrated the potential application in the control of exoskeleton robots.

1. Introduction

In the past decades, many wearable human-assistive robot systems have been developed for the purpose of assisting physically weakened people such as elderly, disabled, and injured people. Many important results have already been achieved. Sankai et al. developed hybrid-assistive limb (HAL) for augmenting power of normal persons [1, 2] and Kazerooni et al. introduced Berkeley Lower Extremity Exoskeleton (BLEEX) for military applications [3, 4]. Yamamoto et al. developed Power Assist Suit to assist nurses lifting heavy patients [5]. Kong and Jeon introduced Exoskeleton for Patients and Old People by Sogang University (EXPOS) for weakened persons [6]. However, there are several factors that limited the general use and commercialization of these devices. In particular, the development of control strategy is challenging [7, 8]. Most of the control strategies adopted in the exoskeleton robots used finite-state machines for gait phase detection. At the hardware level, the mechanical components and sensors used in the prototypes usually

confine the nature of the low-level controllers to particular configurations [7, 8]. The control objective of an exoskeleton robot is to follow up the movements of a healthy wearer, augmenting his/her physical capabilities for specific tasks in a relatively safe way. Human motion intent recognition is one of the key issues of the controller of the exoskeleton robot. This is because these exoskeleton robots must know the wearer's intent so that they can follow the movements of the wearers.

In recent years, many researches were focused on the recognition of human's motion pattern for the purpose of control of exoskeleton robot. Signals for the gait recognition can be obtained by different kinds of sensors. The main information types used are biomechanical signals, electromyographic (EMG) signals, peripheral nervous system signals, and central nervous system signals [8]. During the signals for motion pattern recognition, EMG signals were widely used in the exoskeleton robots. However, noise included in the EMG signals makes it difficult to identify the gait phase of walking exactly. Furthermore, each joint of a human body is actuated with the cooperation of many muscles. Therefore, it

is difficult to identify wear's walking pattern accurately based on the activities of only few muscles.

Consequently, studies on the motion pattern recognition are focused on looking for other signals instead of EMG. Ground reflex pressure (GRF) signal is viable and effective for identifying behavior because human movement and posture are well reflected in foot pressure distribution. Many walking pattern recognition methods based on GRF were studied. Force platform is widely used to analyze human movement. However, the force platform imposes constraints on measurement and is not feasible for measurement of free-living subjects. The present researches tend to focus on daily worn wristwatches, glasses, and shoes where sensors can be embedded into. With embedded sensors, noninvasive detection is available for providing action assistance. Many researchers have developed wearable sensors attached to insoles [9–18].

In many robotic systems, pressure sensors were installed at toe or heel to recognize movements. Most of the methods were based on threshold [9, 15, 16]. Hirata et al. set two representative points to measure GRF on the heel and the toe, and considered the threshold to determine flat foot. However, the recognition accuracy is relatively low. In order to improve the recognition accuracy, many researches focus on the recognition algorithm besides trying to find sensors replacing EMG, and most of the recognition algorithms are based on machine learning. Recognition model was built offline. An algorithm based on support vector machine (SVM) fusing neuromuscular and mechanical signals to continuously recognize a variety of locomotion modes was developed [10]. Walking modes were classified by a classifier based on Bayesian [11]. Different computational approaches have been proposed to support various gait pattern-based applications.

Generally, using more signal acquisition channels could provide more motion information for better performance of walking pattern classification. However, more sensors will definitely increase the complexity of computation and analysis which may lead to slow discrimination response. These issues make walking pattern recognition a difficult task for the control of exoskeleton robot. Therefore, comprehensive analysis between the recognition accuracy and the processing speed should be done. Feature extraction acts as a vital role for pattern recognition. In order to improve the processing speed, some algorithms can be used to compress the data during the process of feature extraction. Principal component analysis (PCA) is a well-known method for feature extraction which can lower dimension [19–23]. By calculating the eigenvectors of the covariance matrix of the original inputs, PCA linearly transforms a high-dimensional input vector into a low-dimensional one whose components are uncorrelated. Although PCA has many advantages, it has many shortcomings, such as its sensitiveness to noise and its limitation to data description. To eliminate these shortcomings, many methods have been proposed to improve PCA algorithm. Among these improved PCA algorithms, kernel-based PCA (KPCA) proposed is a state-of-the-art one as a nonlinear PCA algorithm [24–27]. KPCA utilizes kernel function to gain the random high-order correlation

between input variants and finds the principal components needed through the inner production between input data. KPCA not only can successfully describe the data with Gaussian distribution, but also can describe the data with non-Gaussian distribution. More and more researchers are interested in this field and have carried out some relevant researches.

It is worth noting that stair climbing has not been studied as extensively as gait during the control of exoskeleton robot, although the significance of the prevention of falling on stairs has been well recognized. Startzell et al. [28] reported that more than 1000 individuals over the age of 65 years die in the United States each year as a result of falling on stairs. More recently, Lee and Chou [29] found that older adults had more difficulty in maintaining balance during stair descending than stair ascending. Hayashi and Kiguchi [30] proposed a stability control method based on ZMP on a assistant robot system when go upstairs and downstairs. So that the controller can adopt active stability control strategy during stair ascending to ensure the safety of the wearer. Therefore, in the application of walking assistance for older people, it is very important for the controller of the exoskeleton robot to know whether the wearer is stair descending or stair ascending.

The main purpose of this paper is to apply machine learning approaches to recognize the walking pattern of stair descending or stair ascending from the pattern of walking on a flat surface or standing still using the GRF data. In order to improve both the recognition accuracy and rapidity, data-decreased algorithms based on both PCA and KPCA were studied in this paper. Comparing with the traditional motion recognizing methods based on pressure threshold which are used in most exoskeleton robots, the method proposed in this paper can provide higher recognition accuracy.

This reminder of this paper is organized as follows. Section 2 presented the walking pattern recognizing system with foot pressure sensing shoes. Section 3 illustrates the proposed method. In Section 4, experimental results were shown. Finally, Section 5 summarized this paper.

2. System Description

A pair of foot pressure sensing shoes was developed in this paper. The distribution of the pressure sensors was shown in Figure 1 and the sensors position were listed in Table 1. Pressure sensors are FSR402, which are force-sensitive resistor sensor. FSR402 sensor is a flexible printed circuit with a thickness of 0.5 mm. The more sensors placed, the higher the precision of plantar pressure distribution can be measured. In this system, seven sensors were installed on each insole at seven different positions. These seven points were defined after walking analysis experiments, according to plantar parts traditionally used in researches about gait analysis [31, 32]. A microcontroller (STM32F107VET6) was employed for analog-digital conversion, data processing, and control of data transmission. The wireless transmission module based on ZigBee communication was used for digital data output and input.

TABLE 1: Names of sensing positions.

Position number	Name
1	Great toe
2	Little ball
3	Lateral border
4	Heel
5	Posterior metatarsal
6	Anterior metatarsal
7	Great ball

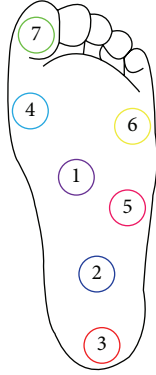


FIGURE 1: Measurement position.

3. Methodologies

The proposed method for recognition of human motion pattern using FRG signals was displayed in Figure 2 which can be divided into two main stages: offline and online stages. The offline stage shown in dashed box involves the processes required for motion pattern recognition model building. The result from the offline stage is a motion pattern recognition model which will be used later in online motion pattern recognition. The process of online motion pattern recognition was shown in a solid box.

3.1. Data Inputs. The first step of the process is to create the training input dataset from the signals that were obtained from the 14 pressure sensors which installed under the sole. The signals are wirelessly transmitted to the PC. The raw data is made up of the pressure of each point at each time step. In addition, every time step is labeled with a value which indicates the current type of motion (such as walking forward on a flat surface, stair descending, or stair ascending):

$$\text{data} = \{p_1^{\text{SR}}, p_2^{\text{SR}}, \dots, p_i^{\text{SR}}, \dots, p_n^{\text{SR}}\}, \quad (1)$$

where SR denotes the sensor sample rate and n is the number of pressure sensor.

3.2. Preprocessing and Segmentation. The signals were filtered by a low-pass filter with a 10 Hz cut-off frequency. In order to prepare the input from the sensor data, the sliding window technique is used to segment the GRF data for continuous classification decision making (Figure 3).

Features that characterized the data signals were extracted from each analysis window. This technique is commonly used for separating time series data into the input vector without losing information. An experiment on the different window length was carried out where it was decided to use a window of 200 ms. Therefore, decisions are made at 200 ms intervals. Processing algorithms were implemented in MATLAB; the processing was performed on a PC with 2 G, 2 GHZ CPU.

3.3. Feature Extraction and Reduction. The performance of the classifier mainly depends on the effective feature extraction method. In this work, five features were calculated from the collected sensor data for training and testing, which are average value, standard deviation, maximum value, minimum value, and difference deviation.

3.3.1. The Principal Analysis Feature Reduction. A commonly used feature reduce method is the principal analysis (PCA), which maps data onto the axes of greatest variance and reduces the number of dimensions. PCA reduces dimensionality by throwing away axes with small variances, ensuring that the data matrix, now projected onto its principal components, loses as little information as possible.

Mathematically, the principal components of a matrix X are calculated from the eigenvectors of X 's covariance matrix C . If x_i is the i th column of X , C was obtained from the following formula:

$$C = \frac{1}{N} \sum_{i=1}^N x_i x_i^T, \quad (2)$$

where N is the number of columns in X . The n th eigenvector of C , v^n , can then be found using the standard eigenvalue of problem

$$\lambda_n v^n = C v^n. \quad (3)$$

There must exist some vector of coefficients α^n that allows v^n to be constructed from X and that allows the n th principal component of X to be calculated:

$$PC_n = v^n \cdot X = \sum_{i=1}^N \alpha_i^n (x_i \cdot X), \quad (4)$$

where α_i^n is the i th component of α^n .

Since PCA is linear transformation, it is relatively quick to compute. However, the PCA algorithm may not be effective in dealing with nonlinear feature boundaries.

In this study, foot pressure detection is formulated as a four-class classification problem. The distribution of foot pressure signals is nonlinear. Therefore, a linear boundary is inappropriate. The input vector should be mapped into a high-dimensional feature space for higher classifying accuracy.

3.3.2. The Kernel Principal Analysis Feature Reduction

(a) Algorithm Principle. The algorithm of KPCA has aroused considerable interest in the fields of pattern recognition and

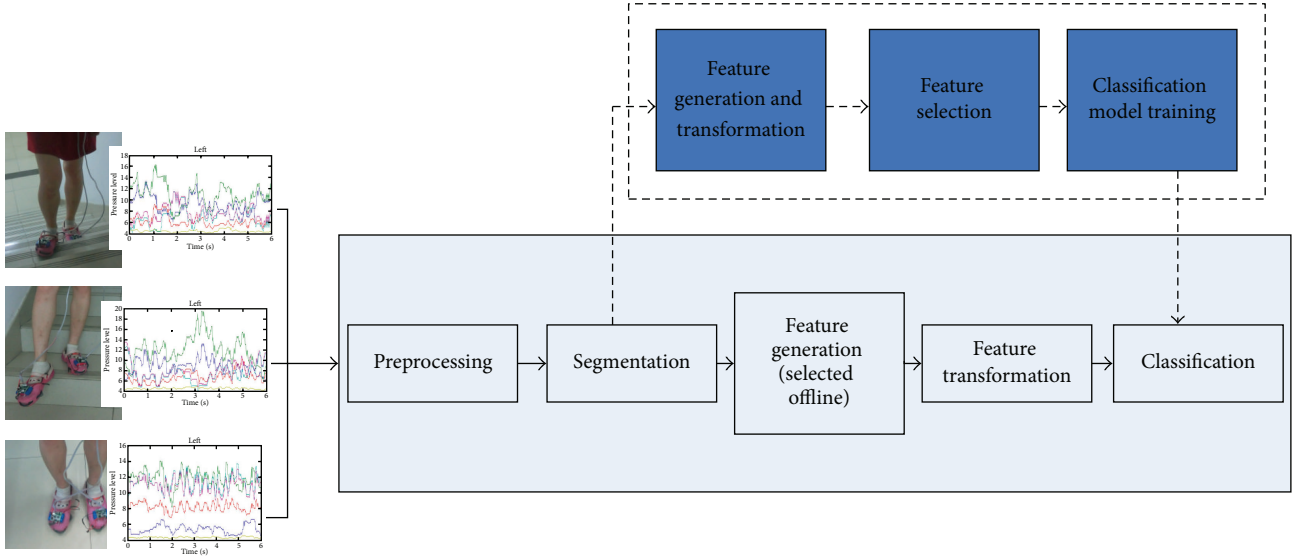


FIGURE 2: The process of human motion pattern recognition.

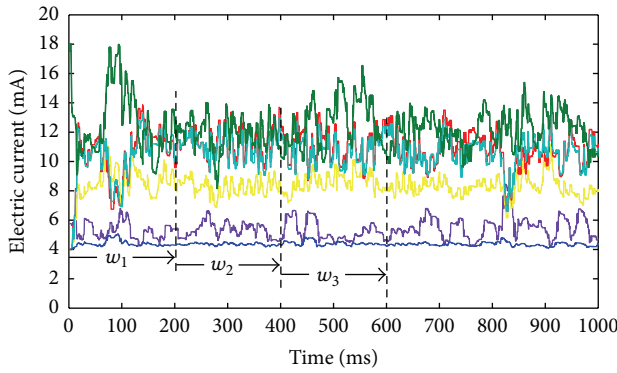


FIGURE 3: Windowing of pressure data in the continuous classifier.

machine learning. Similar to PCA, kernel principal component analysis (KPCA) takes a matrix of data and projects it onto new, reduced principal components. Unlike PCA, however, KPCA accomplishes this mapping through the use of a nonlinear kernel function. The purpose of KPCA is to keep as much information as possible in terms of variance and find directions that have minimal reconstruction error. KPCA has been proven to be more effective than PCA on nonlinear data sets. KPCA maps data to a higher-dimensional feature space and then executes traditional PCA. The nature of KPCA makes it far more adept at representing nonlinear data in a way that can be interpreted linearly.

If the data matrix X is mapped into a higher-dimensional feature space by a kernel Φ , that is, $X \rightarrow \Phi(X)$, then the math describing KPCA is very similar to that of PCA. A covariance matrix can be built as follows:

$$C = \frac{1}{M} \sum_{\mu=1}^M \Phi(x_{\mu}) \Phi(x_{\mu})^T. \quad (5)$$

Then, the eigenvectors are found in the same way as PCA. Constructing the principal components yields:

$$kPC_n = v^n \cdot \Phi(X) = \sum_{i=1}^N \alpha_i^n (\Phi(x_i) \cdot \Phi(X)). \quad (6)$$

Feature extraction with KPCA uses a kernel function defined as $k(x_i, x_j) = \Phi(x_i) \cdot \Phi(x_j)$. A kernel matrix K is then built up from evaluations of this kernel function such that

$$k_{ij} = \Phi(x_i) \cdot \Phi(x_j). \quad (7)$$

To construct K , the vectors x_i for $i = 1, \dots, N$ are examined, centered, and scaled before being fed into the kernel function. Calculation time can be reduced drastically by realizing that K is symmetric and thus $K_{ij} = K_{ji}$. K is then centered in the feature space:

$$K_{ij} = K_{ij} - \frac{1}{N} \sum_{r=1}^N K_{ir} - \frac{1}{N} \sum_{r=1}^N K_{rj} + \frac{1}{N^2} \sum_{r,s=1}^N K_{rs}. \quad (8)$$

Because of the series of relations set up in (3), (4), (6), and (7), the eigenvectors of K must be the coefficient vectors α^m such that

$$\lambda_m \alpha^m = K \alpha^m. \quad (9)$$

Therefore, it follows from (5) and (6) that the m th principal component generated by KPCA can be calculated with the following formula:

$$kPC_m = \sum_{i=1}^N \alpha_i^m K_i, \quad (10)$$

where K_i is the i th row of K . Here, $m = 1, \dots, M$. The value of M is the number of eigenvectors desired to be extracted

from K , and can vary based on the user's needs provided that $M < N$.

The goal of this research was to improve the classification accuracy with a kernel PCA because of the fact that KPCA tends to have better results than PCA with nonlinear data, and experimental results with both PCA and KPCA were illustrated in this paper.

(b) *Kernel Function Selection.* The core ideal of KPCA is to map the input data into a kernel feature space using non-linear mapping and then perform linear PCA in that space. In general, this non-linear mapping is realized by means of a kernel function. It is thus quite obvious that deciding on the form of the kernel function plays a crucial role in KPCA-based methods. Some of the most widely used kernel functions are Gaussian kernel equation (11), polynomial kernel equation (12), and sigmoid kernel equation (13):

$$k_{\sigma}^{\text{Gaussian}}(x, y) = \exp\left(-\frac{\|x - y\|^2}{\sigma^2}\right), \quad (11)$$

$$k_{c,d}^{\text{Polynomial}}(x, y) = (\langle x, y \rangle + c)^d, \quad (12)$$

$$k_{\alpha,\beta}^{\text{Sigmoid}}(x, y) = \tanh(\alpha \langle x, y \rangle + \beta). \quad (13)$$

Once the kernel function was selected, values of multiple free kernel parameters must be determined. Although these kernel functions have been widely used in many applications successfully, they are not the optimal choice for all data sets. Instead of a priori selecting kernel function from a finite set of candidates without explicitly considering the structure of the data, the better way is to estimate it from the data. With a data-dependent kernel function tailored to data under consideration, the performance of KPCA or other kernel-based methods can be improved.

(c) *Number of Principal Components.* One of the crucial steps of the PCA-based and KPCA-based approaches is also determining the number of principal components to keep. The new components we got are within a new dimensional space. By employing only a finite set of eigenvectors in the descending order of eigenvalues, the number of principal components in s_t will be reduced. Therefore, the cumulative contribution rate of the first several components would be expressed as $(1/t) \sum_{i=1}^m s_t(i)$. Usually the contribution rate value is over 95% to characterize the original data.

3.4. Support Vector Machine for Classification. A nonlinear approach, that is, support vector machine (SVM) with a nonlinear kernel, was investigated for walking pattern recognition. Support vector machine (SVM) is based on the foundation of statistical learning theory [33]. It is a powerful classification algorithm with state-of-the-art property. Recently, SVM has been successfully applied to plenty of fields, such as pattern identification, regression analysis, and function approximating [34, 35]. The results give the evidence that this technique cannot only be satisfactory from the theoretical perspective, but also can lead to high accuracy in practical applications. Additional reasons for choosing the

SVM with a nonlinear kernel were as follows: (1) a nonlinear classifier might accurately classify the data when the linear boundaries among classes are difficult to define and (2) the SVM is more computationally efficient than other nonlinear classifiers, such as the ANN.

The basic SVM takes a set of input data and predicts, for each given input, which of two possible classes forms the output, making it a nonprobabilistic binary linear classifier. Given a set of training examples, each marked as belonging to one of two categories, an SVM training algorithm builds a model that assigns new examples into the first category or the other.

By choosing a non-linear mapping, the SVM constructs an optimum separation hyperplane in the higher-dimensional space. To start with, we train a classifier $f(x)$ with a learning algorithm from a set of samples $\{(x_i, y_i), i = 1, 2, \dots, N\}$. y_i is the given label for each training example x_i . We take a linear classification function:

$$f(x) = w^T x + b, \quad (14)$$

where w and b are defined according to

$$\min J(w, \xi) = \frac{1}{2} \|w\|^2 + C \sum_{i=1}^N \xi_i. \quad (15)$$

The parameter C is for controlling the trade-off between the model complexity and empirical risk [15]. In this case, we have to utilize the kernel function to map input vector x to a higher-dimensional space through a nonlinear mapping $\Phi(x)$. Hence, the inner product does not need to be evaluated in the feature space. With the kernel concept $K(x_i, x_j) = \Phi^T(x_i)\Phi(x_j)$, the resulting SVM model can be written as

$$f(x_i) = \sum_{k=1}^{N_s} y_k \alpha_k K(x_i, s_k) + b, \quad (16)$$

where s_k , $k = 1, 2, \dots, N_s$ are support vectors, which are determined during the training process.

So the formula above results in an optimization problem with convex constrains, which is ready to be solved by the interior point method. For the walking pattern recognition issue, we selected the foot pressure signals of the 14 points in Figure 1 as input vectors. Thus, the SVM classifier was enabled to identify four kinds of movements: walking on level ground, standing still, stair descending, and stair ascending.

A multiclass SVM with "one-against-one" structure was used [10]. The applied kernel function was radial basis function (RBF), which was defined as

$$k(x_i, x_j) = \exp\left(-\gamma \|x_i - x_j\|^2\right), \quad \gamma > 0, \quad (17)$$

where x_i and x_j are the feature vectors the of i th and j th classes, respectively, and $\gamma = 1/n$, where n is the dimension of the feature x . During the training procedure, all observed feature vectors x were nonlinearly mapped into a higher-dimensional feature space based on the kernel function in (17). For the k -class classification problem, $k(k-1)/2$ binary classifiers were constructed.



FIGURE 4: Ascending and descending stairs with developed shoes.

3.5. Evaluation and Validation. The performances of the dimensionality reduction algorithms based on both PCA and KPCA were evaluated by experiments data. The data set is partitioned into 2 subsets. One subset is used to train the classifier model, whereas the other subset is used to test the classifier model. The classifier was evaluated by the classification accuracy (CA) which was defined as the percentage of correctly classified observations out of the total number of observations within that class.

The value of CA can be calculated using the following equation:

$$CA = \frac{\text{Number of correctly classified testing data}}{\text{Total number of applied testing data}}. \quad (18)$$

4. Experimentations and Results

4.1. Experimental Protocol. During the experiments, the participant wore a pair of shoes with pressure sensors installed in the sole. Our tests were carried out using a 24-year-old female wearer, 1.66 m tall. Wearer walked at a comfortable speed. With battery power supplied, foot pressure signals were gathered by 14 FSR402 sensors every 40 ms and transmitted virtually through the data processing board to the computer wirelessly. The waveforms of each sensor on both feet were exhibited on the desktop simultaneously for monitoring. The walking pattern recognition procedure was implemented by MATLAB 2010a, running on a PC with 2 G, 2 GHZ CPU.

The raw data on foot pressure distributions for each moving pattern were acquired with the developed foot pressure sensing shoes (Figure 4). Variation of foot pressure for each kind of movement was displayed in Figure 5.

4.2. Experimental Result. There was a total of 4 classes, with a total of 6 binary classifiers for the classifier in each walking pattern. To build each binary classifier, a hyperplane

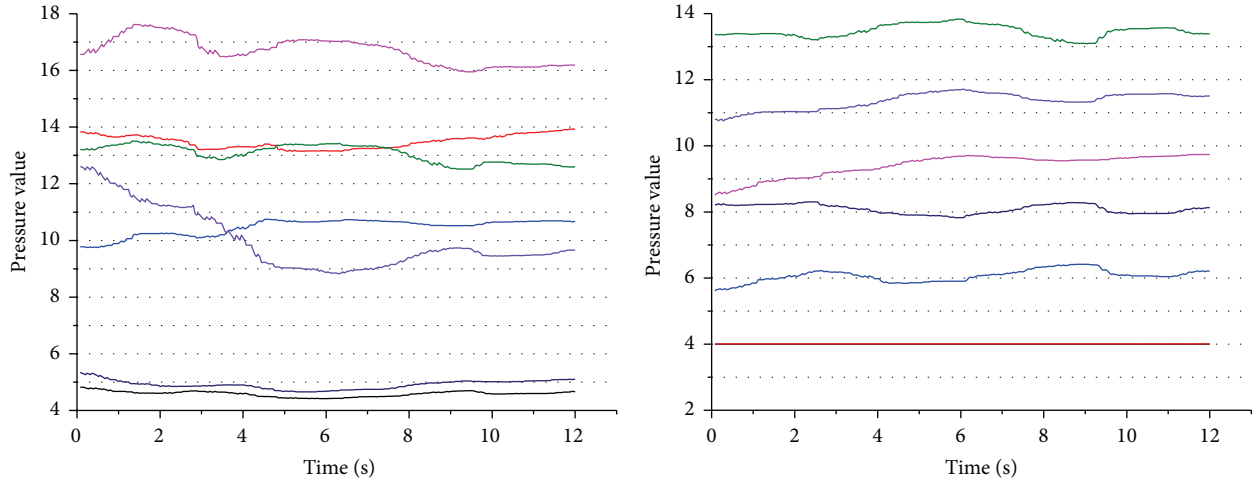
was found by maximizing the boundary margin between two classes and minimizing the training classification errors. Six hyperplanes between any two classes were computed after training. During the testing procedure, each observed feature vector x was nonlinearly transformed and sent to the individual binary classifiers built in the training procedure; therefore, a total of 6 classification decisions were made. A voting strategy was used to make the final decision. The class (mode) with the most votes out of the 6 decisions was considered to be the locomotion mode. If more than one class had the same number of votes, the class (mode) with the smaller class index was chosen as the final decision.

Five internal time-domain parameters were picked up as feature, which are average value, standard deviation, maximum value, minimum value, and difference deviation. Features representing the pressure signal were memorized in matrix and sent to the classifier. Cross-validation was used to train and test the classifier based on SVM. We picked up 630 sets of data samples of each moving pattern; the former 420 are for classifier training and the latter for testing. The training data and training label are used to form the whole training set.

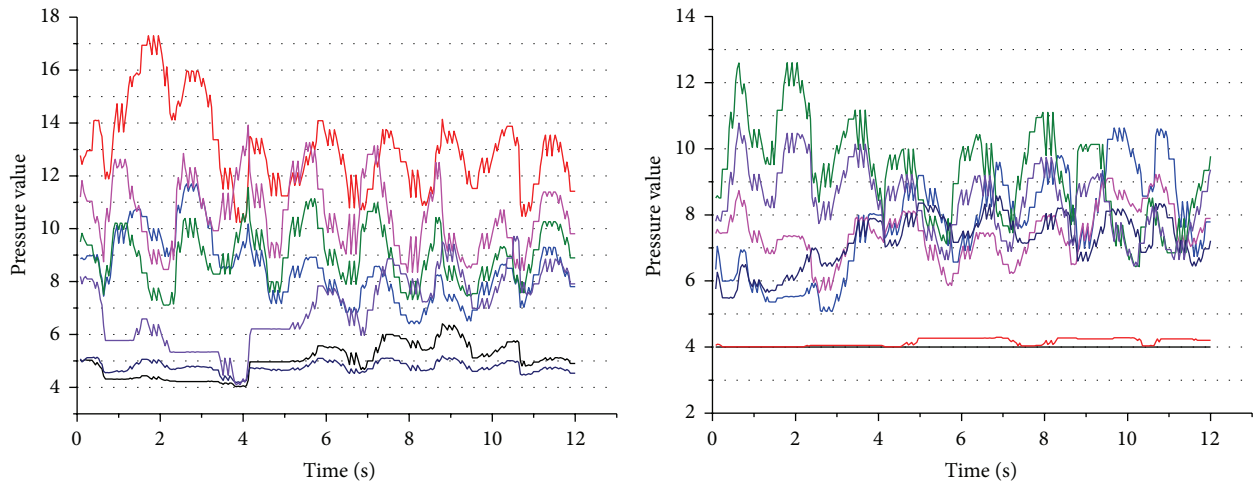
The classification accuracy of SVM, SVM-PCA, and SVM-KPCA was compared in the experiments.

(1) SVM. For the training part, we got an optimal C of 724 and G of 8 by cross-validation. The optimization of these two parameters is done for obtaining a high recognition rate based on current training samples. The RBF (radial basis function) kernel is employed. The cross-validation result (contour map and 3D view) of parameter selection is shown in Figure 6. The accuracy is about 91.96%.

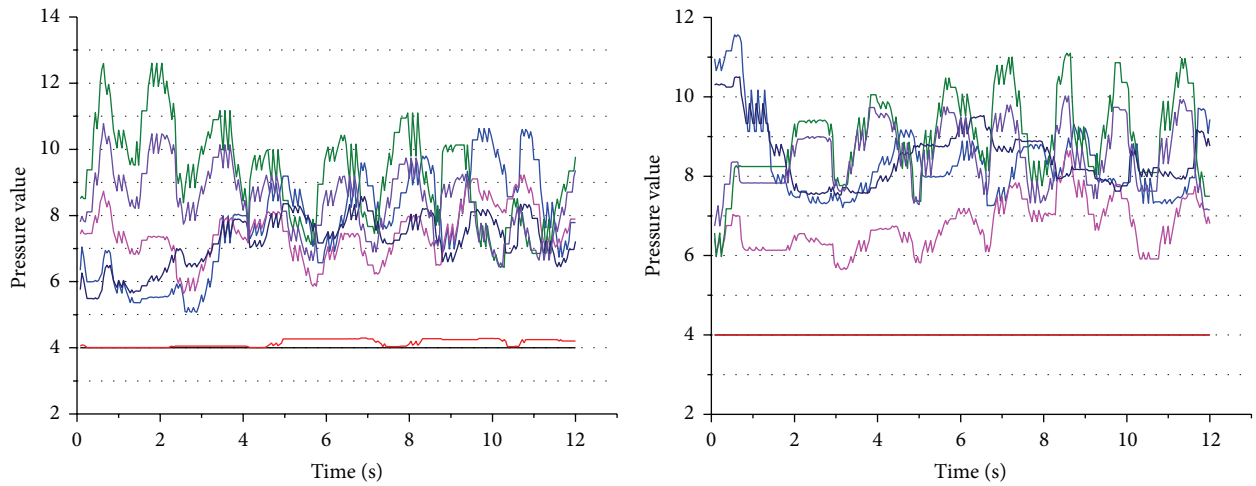
The classification model was applied to predict the output category for testing samples identification. The actual and testing patterns of testing samples were shown in Figure 7.



(a) Foot pressure distribution of standing still



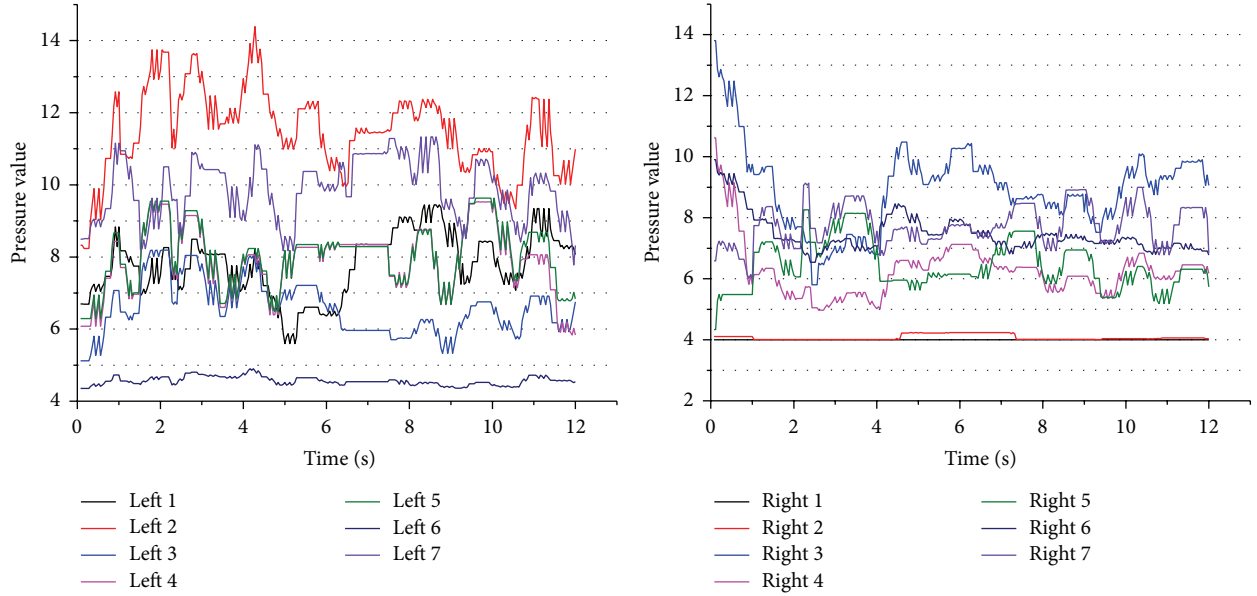
(b) Foot pressure distribution of walking forward



- | | | | |
|----------|----------|-----------|-----------|
| — Left 1 | — Left 5 | — Right 1 | — Right 5 |
| — Left 2 | — Left 6 | — Right 2 | — Right 6 |
| — Left 3 | — Left 7 | — Right 3 | — Right 7 |
| — Left 4 | | — Right 4 | |

(c) Foot pressure distribution of stair ascending

FIGURE 5: Continued.



(d) Foot pressure distribution of stair descending

FIGURE 5: Foot pressure distribution of four walking patterns.

According to Figure 7, we summarize the classification performance results achieved by this SVM classifier. The average accuracy with all seven sensors is at 92.9% for all four kinds of movements and the diagnosis accuracy for each moving pattern is in Table 2.

(2) *SVM-PCA*. Compared with the preset inputs, we sent the input matrix to PCA processing algorithm for dimensionality reduction beforehand. We took the columns of PCs which occupied over 95% information of original data. A few numbers of new input eigenvectors provided sufficient information for foot pressure labeling and walking pattern recognition. The accuracy rate can be obtained when $C = 1024$ and $G = 32$; it reaches as high as 88.7% (Figure 8). The outcome of inputting the new eigenvectors in classifier is shown in Table 3. It could be noted that if a SVM classifier is used, declining recognition rate of moving patterns would be caused by PCA, whereas the classification time with proposed PCA algorithm did have a higher recognition speed, which was only 0.21 seconds. It decreased 0.25 seconds compared to the former classification. The accuracy is about 92.26% which is a little higher than the result of SVM.

(3) *SVM-KPCA*. We also sent the input matrix to KPCA processing algorithm for dimensionality reduction beforehand. Firstly, different kernel functions on the effect of dimensionality reduction were analyzed. In this paper, 3 kinds of typical kernel functions, Gaussian kernel, polynomial kernel, and sigmoid kernel ((11)–(13)), were used to reduce the dimensionality, respectively. KPCA1, KPCA2, and KPCA3, denote Gaussian kernel, polynomial kernel and sigmoid kernel, respectively.

The kernel parameters of different kernel functions were selected after several simulation experiment as follows: $\sigma =$

TABLE 2: Accuracy of different movements with SVM.

Moving pattern	Training accuracy (%)	Testing accuracy (%)
Standing still	100	100
Walking on level	91.2	91.0
Stair ascending	93.1	93.7
Stair descending	90.0	86.7

TABLE 3: Accuracy of different movements with PCA.

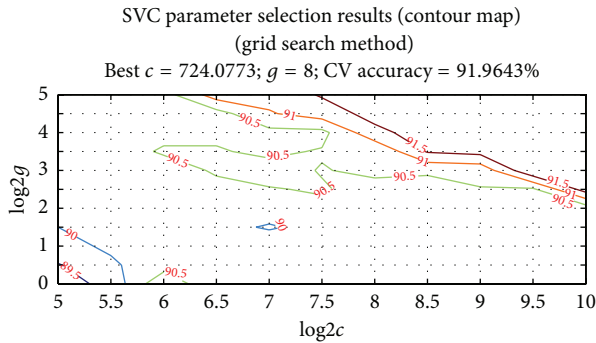
Moving pattern	Training accuracy (%)	Testing accuracy (%)
Standing still	99.8	100
Walking on level	89.3	80.5
Stair ascending	90.8	88.6
Stair descending	89.8	86.2

0.05 for KPCA1, $c = 1$, $d = 4$ for KPCA2, and $\alpha/1000 = 1$, $\beta = -1$ for KPCA3. Comparison of results of the principal cumulative contribution rate of these 3-type KPCA kernel function and PCA was illustrated in Figure 9.

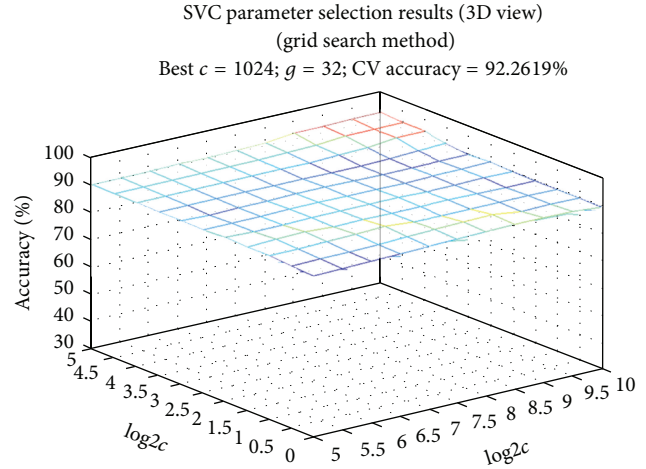
According to the analysis result, we can see that if the selection of the kernel parameters is appropriate, good dimensionality reduction result can be obtained through KPCA algorithm. Algorithm based on KPCA has more excellent feature selection capability compared with PCA.

We also took the columns of PCs which occupied over 95% information of original data. A few numbers of new input eigenvectors were fed to the SVM classifier.

As an example, when polynomial kernel function was used, the accuracy rate can be obtained; it reaches as high as 92.5%. The parameters of SVM are $C = 8$ and $G = 32$, respectively. The error between the predicted data and



(a) Contour map of parameter selection results



(b) 3D view of parameter selection results

FIGURE 6: The cross-validation results of parameter selection of SVM.

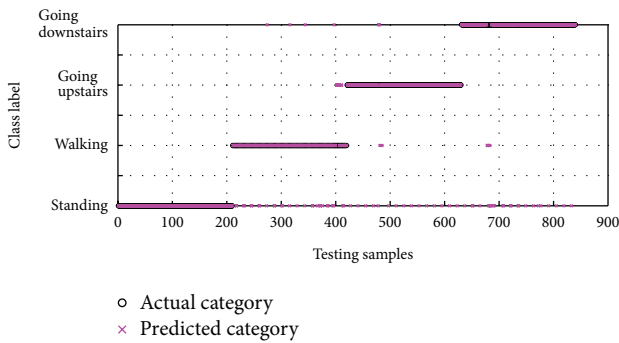


FIGURE 7: Actual and testing patterns of testing samples with SVM.

the original data was shown in Figure 10, and the outcome of inputting the new eigenvectors in classifier is shown in Table 4. The classification time after KPCA2 processing was only 0.22 seconds. The error figure was shown in Figure 10. The values of 0, 1, 2, and 3 labeled standing, walking, upstairs, and downstairs, respectively. The ordinate value of Figure 10 is the difference between the predicted and original value. The difference would be zero if the motion pattern was recognized correctly. For example, for the motion pattern of walking, if the difference value was -1 , it indicated that the walking pattern was recognized as standing. From the experimental result, the recognition error of downstairs was higher than other kinds of motion.

Based on the experimental results, for the same testing data, the recognition of the algorithms based on KPCA with different kernel functions were obviously higher than algorithm based on KPCA. The biggest defect of KPCA over PCA is that more runtime would be required by KPCA algorithm during the training stage because it mapped data to a higher-dimensional space in order to perform PCA. However, the additional time could be taken as a one-time

TABLE 4: Accuracy of different movements with KPCA2.

Moving pattern	Training accuracy (%)	Testing accuracy (%)
Standing still	100	100
Walking on level	86.4	85.7
Stair ascending	92.1	88.8
Stair descending	91.4	90.1

TABLE 5: Comparison of recognition rate with different processing methods.

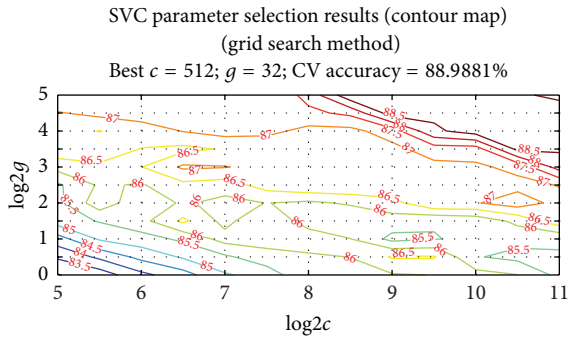
Processing method	SVM	SVM-PCA	SVM-KPCA2
Average recognition accuracy	92.9%	88.7%	91.1%
Data dimension	70	42	42
Running time	0.46 s	0.21 s	0.22 s

cost and has little impact on the recognition speed in online classifying.

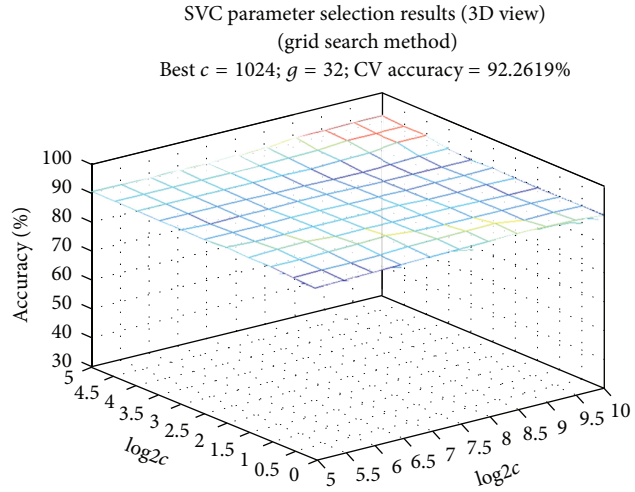
The average recognition accuracy and running time with different processing algorithms were compared in Table 5. From the experimental results, we can see if a SVM classifier is used, the classification speed is much higher with the dimensionality reduction algorithm (PCA, KPCA). The declining recognition rate of walking patterns would be caused by PCA. However, no obvious recognition rate decline was caused by KPCA.

5. Conclusions

This study demonstrated that the foot pressure sensing shoes designed in this paper was able to recognize four walking patterns accurately. The experimental results showed that the classification method fusing SVM and KPCA was superior to the method that only used SVM or fused SVM and PCA. The average recognition accuracy based on KPCA-SVM classifier



(a) Contour map of parameter selection results



(b) 3D view of parameter selection results

FIGURE 8: The cross-validation result of parameter selection of SVM-PCA.

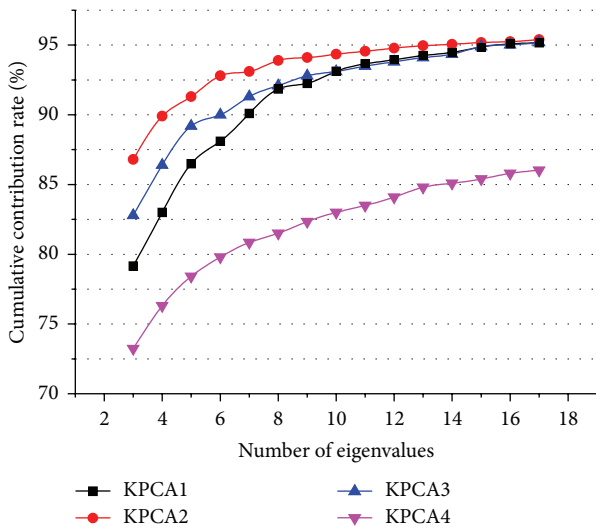


FIGURE 9: The KPCA and PCA processing results of testing samples.

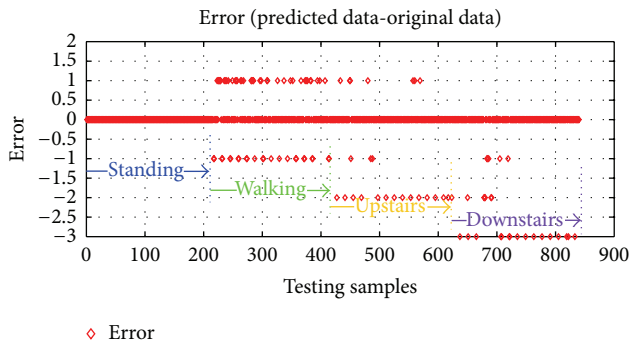


FIGURE 10: The error figure of SVM-KPCA2.

produced 91.1%, and the classifying speed is twice as fast as that SVM classifier. These promising results may help the future controller design of exoskeleton robot.

However, there still exists some drawback of our designed system. The processing speed of microcontroller and ZigBee communication used in the data acquisition mode is limited, which result in lower sampling rate. Higher-speed data acquisition device would be adopted in the future to obtain better recognition accuracy. Furthermore, walking patterns of stair ascending and stair descending were recognized in this study, but in the real control of exoskeleton robot, predicting these two walking pattern in advance is more important for the controller to adopt corresponding stability control strategy. So, researches on the walking pattern predicting algorithm will be studied in our future work and will be discussed in further studies.

Acknowledgments

This research is a general project, Project 61305131 supported by the Natural Science Foundation of China. Special appreciation should be given to the Research Centre of Fluid Power Transmission and Control, Beihang University, for the sake of their selfless help.

References

- [1] T. Hayashi, H. Kawamoto, and Y. Sankai, "Control method of robot suit HAL working as operator's muscle using biological and dynamical information," in *Proceedings of the IEEE/RSJ International Conference on Intelligent Robots and Systems (IROS '05)*, pp. 3063–3068, Alberta, Canada, August 2005.
- [2] A. Tsukahara, R. Kawanishi, Y. Hasegawa, and Y. Sankai, "Sit-to-stand and stand-to-sit transfer support for complete paraplegic patients with robot suit HAL," *Advanced Robotics*, vol. 24, no. 11, pp. 1615–1638, 2010.

- [3] A. B. Zoss, H. Kazerooni, and A. Chu, "Biomechanical design of the Berkeley lower extremity exoskeleton (BLEEX)," *IEEE/ASME Transactions on Mechatronics*, vol. 11, no. 2, pp. 128–138, 2006.
- [4] J. Ghan, R. Steger, and H. Kazerooni, "Control and system identification for the Berkeley lower extremity exoskeleton (BLEEX)," *Advanced Robotics*, vol. 20, no. 9, pp. 989–1014, 2006.
- [5] K. Yamamoto, M. Ishii, H. Noborisaka, and K. Hyodo, "Stand alone wearable power assisting suit—sensing and control systems," in *Proceedings of the IEEE International Workshop on Robot and Human Interactive Communication*, pp. 661–666, Kanagawa, Japan, September 2004.
- [6] K. Kong and D. Jeon, "Design and control of an exoskeleton for the elderly and patients," *IEEE/ASME Transactions on Mechatronics*, vol. 11, no. 4, pp. 428–432, 2006.
- [7] H. Herr, "Exoskeletons and orthoses: classification, design challenges and future directions," *Journal of NeuroEngineering and Rehabilitation*, vol. 6, no. 1, article 21, pp. 1–9, 2009.
- [8] R. Jiménez-Fabián and O. Verlinden, "Review of control algorithms for robotic ankle systems in lower-limb orthoses, prostheses, and exoskeletons," *Medical Engineering and Physics*, vol. 34, no. 4, pp. 397–408, 2012.
- [9] Y. Hirata, T. Iwano, and K. Kosuge, "Control of wearable walking helper on slope based on integration of acceleration and GRF information," in *Proceedings of the IEEE/RSJ International Conference on Intelligent Robots and Systems (IROS '08)*, pp. 3731–3736, Nice, France, September 2008.
- [10] H. Huang, F. Zhang, Z. Dou, L. J. Hargrove, D. R. Rogers, and K. B. Englehart, "Continuous locomotion-mode identification for prosthetic legs based on neuromuscular–mechanical fusion," *IEEE Transactions on Biomedical Engineering*, vol. 58, no. 10, pp. 2867–2875, 2011.
- [11] L. Du, F. Zhang, M. Liu, and H. Huang, "Toward design of an environment-aware adaptive locomotion-mode-recognition system," *IEEE Transactions on Biomedical Engineering*, vol. 59, no. 10, pp. 2716–2725, 2012.
- [12] I. P. I. Pappas, M. R. Popovic, T. Keller, V. Dietz, and M. Morari, "A reliable gait phase detection system," *IEEE Transactions on Neural Systems and Rehabilitation Engineering*, vol. 9, no. 2, pp. 113–125, 2001.
- [13] W. Tao, T. Liu, R. Zheng, and H. Feng, "Gait analysis using wearable sensors," *Sensors*, vol. 12, no. 2, pp. 2255–2283, 2012.
- [14] Z. Wang, M. Jiang, Y. Hu, and H. Li, "An incremental learning method based on probabilistic neural networks and adjustable fuzzy clustering for human activity recognition by using wearable sensors," *IEEE Transactions on Information Technology in Biomedicine*, vol. 16, no. 4, pp. 691–699, 2012.
- [15] P. H. Veltink, C. Liedtke, E. Droog, and H. Kooij, "Ambulatory measurement of ground reaction forces," *IEEE Transactions on Neural Systems and Rehabilitation Engineering*, vol. 13, no. 3, pp. 423–427, 2005.
- [16] C. Liedtke, S. A. W. Fokkenrood, J. T. Menger, H. van der Kooij, and P. H. Veltink, "Evaluation of instrumented shoes for ambulatory assessment of ground reaction forces," *Gait & Posture*, vol. 26, no. 1, pp. 39–47, 2007.
- [17] K. Zhang, M. Sun, D. K. Lester, F. X. Pi-Sunyer, C. N. Boozer, and R. W. Longman, "Assessment of human locomotion by using an insole measurement system and artificial neural networks," *Journal of Biomechanics*, vol. 38, no. 11, pp. 2276–2287, 2005.
- [18] K. Chen and D. Bassett Jr., "The technology of accelerometry-based activity monitors: current and future," *Medicine and Science in Sports and Exercise*, vol. 37, no. 11, pp. S490–S500, 2005.
- [19] G.-W. Wang, C. Zhang, and J. Zhuang, "An application of classifier combination methods in hand gesture recognition," *Mathematical Problems in Engineering*, vol. 2012, Article ID 346951, 17 pages, 2012.
- [20] C. Lin, B. Wang, X. Zhao, and M. Pang, "Optimizing kernel PCA using sparse representation-based classifier for MSTAR SAR image target recognition," *Mathematical Problems in Engineering*, vol. 2013, Article ID 847062, 10 pages, 2013.
- [21] J.-H. Cho, J.-M. Lee, S. W. Choi, D. Lee, and I.-B. Lee, "Fault identification for process monitoring using kernel principal component analysis," *Chemical Engineering Science*, vol. 60, no. 1, pp. 279–288, 2005.
- [22] Y. Wen, Y. Lu, and P. F. Shi, "Handwritten Bangla numeral recognition system and its application to postal automation," *Pattern Recognition*, vol. 40, no. 1, pp. 99–107, 2007.
- [23] X. G. You, D. Zhang, Q. Chen, P. Wang, and Y. Y. Tang, "Face representation by using non-tensor product wavelets," in *Proceedings of the 18th International Conference on Pattern Recognition (ICPR '06)*, pp. 503–506, Hong Kong, August 2006.
- [24] Y. Xu, D. Zhang, Z. Jin, M. Li, and J.-Y. Yang, "A fast kernel-based nonlinear discriminant analysis for multi-class problems," *Pattern Recognition*, vol. 39, no. 6, pp. 1026–1033, 2006.
- [25] G. C. Cawley and N. L. C. Talbot, "Efficient leave-one-out cross-validation of kernel fisher discriminant classifiers," *Pattern Recognition*, vol. 36, no. 11, pp. 2585–2592, 2003.
- [26] K. Hotta, "Local co-occurrence features in subspace obtained by KPCA of local blob visual words for scene classification," *Pattern Recognition*, vol. 45, no. 10, pp. 3687–3694, 2012.
- [27] A. Nowicki, M. Grochowski, and K. Duzinkiewicz, "Data-driven models for fault detection using kernel PCA: a water distribution system case study," *International Journal of Applied Mathematics and Computer Science*, vol. 22, no. 4, pp. 939–949, 2012.
- [28] J. K. Startzell, A. Owens, L. M. Mulfing, and P. R. Cavanagh, "Stair negotiation in older people: a review," *Journal of the American Geriatrics Society*, vol. 48, no. 5, pp. 567–580, 2000.
- [29] H. Lee and L. Chou, "Balance control during stair negotiation in older adults," *Journal of Biomechanics*, vol. 40, no. 11, pp. 2530–2536, 2007.
- [30] Y. Hayashi and K. Kiguchi, "Stairs-ascending/descending assist for a lower-limb power-assist robot considering ZMP," in *Proceedings of the IEEE/RSJ International Conference on Intelligent Robots and Systems (IROS '11)*, pp. 1755–1760, San Francisco, Calif, USA, September 2011.
- [31] C. Sugimoto, M. Tsuji, G. Lopez et al., "Development of a behavior recognition system using wireless wearable information devices," in *Proceedings of the 1st International Symposium on Wireless Pervasive Computing (ISWPC '06)*, pp. 1–5, Phuket, Thailand, January 2006.
- [32] G. Yuan, M. Zhang, Z. Wang, and J. Zhang, "The distribution of foot pressure and its influence factors in Chinese people," *Chinese Journal of Physical Medicine and Rehabilitation*, vol. 26, no. 3, pp. 156–159, 2004.
- [33] F. Pitta, M. Y. Takaki, N. H. Oliveira et al., "Relationship between pulmonary function and physical activity in daily life in patients with COPD," *Respiratory Medicine*, vol. 102, no. 8, pp. 1203–1207, 2008.
- [34] P. Neuhaus and H. Kazerooni, "Industrial-strength human-assisted walking robots," *IEEE Robotics and Automation Magazine*, vol. 8, no. 4, pp. 18–25, 2001.

- [35] A. Zoss, H. Kazerooni, and A. Chu, "On the mechanical design of the Berkeley lower extremity exoskeleton (BLEEX)," in *Proceedings of the IEEE/RSJ International Conference on Intelligent Robots and Systems (IROS '05)*, pp. 3465–3472, Alberta, Canada, August 2005.

Research Article

Subband Adaptive Filtering with l_1 -Norm Constraint for Sparse System Identification

Young-Seok Choi

Department of Electronic Engineering, Gangneung-Wonju National University, Gangneung 210-702, Republic of Korea

Correspondence should be addressed to Young-Seok Choi; yschoi@gwnu.ac.kr

Received 27 September 2013; Revised 26 November 2013; Accepted 26 November 2013

Academic Editor: Yue Wu

Copyright © 2013 Young-Seok Choi. This is an open access article distributed under the Creative Commons Attribution License, which permits unrestricted use, distribution, and reproduction in any medium, provided the original work is properly cited.

This paper presents a new approach of the normalized subband adaptive filter (NSAF) which directly exploits the sparsity condition of an underlying system for sparse system identification. The proposed NSAF integrates a weighted l_1 -norm constraint into the cost function of the NSAF algorithm. To get the optimum solution of the weighted l_1 -norm regularized cost function, a subgradient calculus is employed, resulting in a stochastic gradient based update recursion of the weighted l_1 -norm regularized NSAF. The choice of distinct weighted l_1 -norm regularization leads to two versions of the l_1 -norm regularized NSAF. Numerical results clearly indicate the superior convergence of the l_1 -norm regularized NSAFs over the classical NSAF especially when identifying a sparse system.

1. Introduction

Over the past few decades, the relative simplicity and good performance of the normalized least mean square (NLMS) algorithm have made it a popular tool for adaptive filtering applications. However, its convergence performance is significantly deteriorated in case of correlated input signals [1, 2]. As a popular solution, adaptive filtering in the subband has been recently developed, which is referred to as subband adaptive filter (SAF) [3–7]. Its distinct feature is based on the property that the LMS-type adaptive filters converge faster for white input signals than colored ones [1, 2]. Thus, carrying out a prewhitening on colored input signals, it results in the accelerated convergence compared to the LMS-type adaptive filters. Recently, the use of multiple-constraint optimization criteria into formulation of a cost function has resulted in the normalized SAF (NSAF) with its computational complexity close to that of the NLMS algorithm [6, 7].

In the context of a system identification, the unknown system to be identified is sparse in common scenarios, such as echo paths [8] and digital TV transmission channels [9]. Namely, the unknown system consists of many near-zero coefficients and a small number of large ones. However, the adaptive filtering algorithms suffer from poor convergence

performance in case of identifying the sparse system [8]. Indeed, the capability of the NSAF is faded in a sparse system identification scenario. To deal with this issue, a variety of proportionate adaptive algorithms have been presented for NSAF, which utilize proportionate step sizes to distinct filter taps [10–12]. However, these algorithms have not exploited the sparsity condition of an underlying system.

Recently, motivated by compressive sensing framework [13, 14] and the least absolute shrinkage and selection operator (LASSO) [15], a number of adaptive filtering algorithms which make use of the sparsity condition of an underlying system have been developed [16–20]. The core idea behind this approach is to incorporate the sparsity condition of underlying system by imposing an a sparsity-inducing constraint term. Adding the sparsity constraint using l_0 or l_1 -norm constraint to the cost function makes the least relevant weights of the filter shrink to zeros. However, to the best of the author's knowledge, adaptive filtering in subband which exploits the sparsity condition has not been studied yet.

With regard, this paper presents a novel approach of the sparsity-regularized NSAFs, which incorporates the sparsity condition of the system directly into the cost function via a sparsity-inducing constraint term. This is carried out by regularizing a weighted l_1 -norm of the filter weights estimate

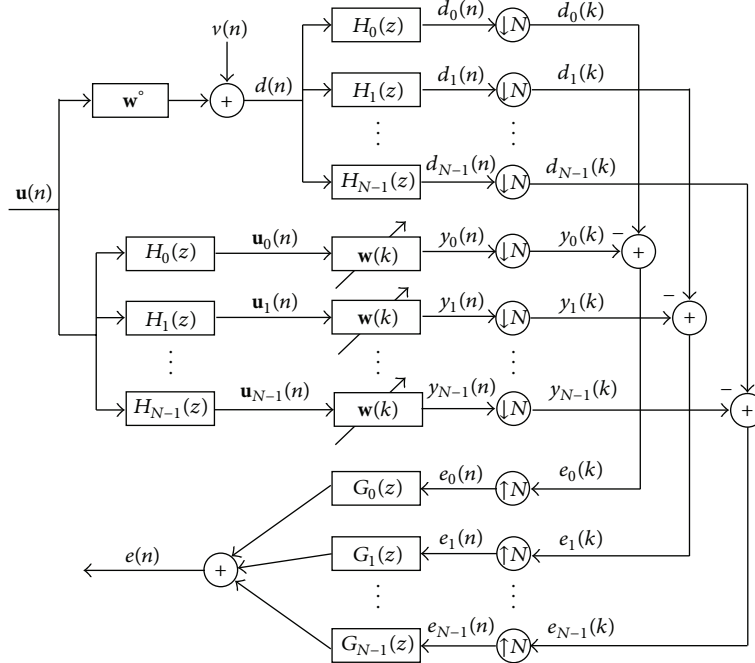


FIGURE 1: Subband structure with the analysis filters and synthesis filters and the subband desired signals, subband filter outputs, and subband error signals.

to the cost function. Considering the two choices of the weighted l_1 -norm regularization, two stochastic gradient-based l_1 -norm regularized NSAF algorithms are derived. First, the l_1 -norm NSAF (l_1 -NSAF) is obtained by utilizing the identity matrix as a weighting matrix. Second, the reweighted l_1 -norm NSAF (l_1 -RNSAF) which uses the current estimate of the system as a weighted l_1 -norm is developed. Through numerical simulations, the resultant sparsity-regularized NSAFs have proven their superiority over the classical NSAFs, especially when the sparsity of the underlying system becomes severe.

The remainder of the paper is organized as follows. Section 2 introduces the classical NSAF, followed by the derivation of the proposed sparsity-regularized NSAFs in Section 3. Section 4 illustrates the computer simulation results and Section 5 concludes this study.

2. Conventional NSAF

Consider a desired signal $d(n)$ that arises from the system identification model

$$d(n) = \mathbf{u}(n) \mathbf{w}^\circ + v(n), \quad (1)$$

where \mathbf{w}° is a column vector for the impulse response of an unknown system that we wish to estimate, $v(n)$ accounts for measurement noise with zero mean and variance σ_v^2 , and $\mathbf{u}(n)$ denotes the $1 \times M$ input vector,

$$\mathbf{u}(n) = [u(n) \ u(n-1) \ \cdots \ u(n-M+1)]. \quad (2)$$

Figure 1 shows the structure of the NSAF, where the desired signal $d(n)$ and input signal $u(n)$ are partitioned into

N subbands by the analysis filters $H_0(z), H_1(z), \dots, H_{N-1}(z)$. The resulting subband signals, $d_i(n)$ and $y_i(n)$ for $i = 0, 1, \dots, N-1$, are critically decimated to a lower sampling rate commensurate with their bandwidth. Here, the variable n to index the original sequences and k to index the decimated sequences are used for all signals. Then, the decimated filter output signal at each subband is defined as $y_{i,D}(k) = \mathbf{u}_i(k) \mathbf{w}(k)$, where $\mathbf{u}_i(k)$ is $1 \times M$ row vector, such that

$$\mathbf{u}_i(k) = [u_i(kN), u_i(kN-1), \dots, u_i(kN-M+1)], \quad (3)$$

and $\mathbf{w}(k) = [w_0(k), w_1(k), \dots, w_{M-1}(k)]^T$ denotes an estimate for \mathbf{w}° with length M . Thus the decimated subband error signal is given by

$$e_{i,D}(k) = d_{i,D}(k) - y_{i,D}(k) = d_{i,D}(k) - \mathbf{u}_i(k) \mathbf{w}(k), \quad (4)$$

where $d_{i,D}(k) = d_i(kN)$ is the decimated desired signal at each subband.

In [6], the authors have formulated the Lagrangian-based multiple-constraint optimization problem, which is formulated as

$$J_{\text{NSAF}}(k) = \|\mathbf{w}(k+1) - \mathbf{w}(k)\|^2 + \sum_{i=0}^{N-1} \lambda_i [d_{i,D}(k) - \mathbf{u}_i(k) \mathbf{w}(k+1)], \quad (5)$$

where λ_i for $i = 0, 1, \dots, N-1$ denote the Lagrange multipliers. Solving the cost function (5), the update recursion of the NSAF algorithm is given by [6, 7]. Consider

$$\mathbf{w}(k+1) = \mathbf{w}(k) + \mu \sum_{i=0}^{N-1} \frac{\mathbf{u}_i^T(k)}{\|\mathbf{u}_i(k)\|^2} e_{i,D}(k), \quad (6)$$

where μ is the step-size parameter.

3. Weighted l_1 -Norm Regularized NSAF

3.1. Derivation of the Proposed Algorithm. To reflect the sparsity condition of the true system, that is, \mathbf{w}° , a weighted l_1 -norm of the filter weight estimate is regularized on the cost function of the NSAF, which is given by

$$J_{l_1\text{-NSAF}}(k) = \|\mathbf{w}(k+1) - \mathbf{w}(k)\|^2 + \sum_{i=0}^{N-1} \lambda_i [d_{i,D}(k) - \mathbf{u}_i(k) \mathbf{w}(k+1)] + \gamma \|\mathbf{\Pi} \mathbf{w}(k+1)\|_1, \quad (7)$$

where $\|\mathbf{\Pi} \mathbf{w}(k+1)\|_1$ accounts for the weighted l_1 -norm of the filter weight vector $\mathbf{w}(k+1)$ and is written as

$$\|\mathbf{\Pi} \mathbf{w}(k+1)\|_1 = \sum_{m=0}^{M-1} \pi_m |w_m(k+1)|, \quad (8)$$

where $\mathbf{\Pi}$ is a $M \times M$ weighting matrix whose diagonal elements are π_m and other elements are equal to zero, and $w_m(k+1)$ denotes the m th tap weight of $\mathbf{w}(k+1)$, for $m = 0, 1, \dots, M-1$. In addition, γ is a positive value parameter which plays a role in compromising the error related term and the weighted l_1 -norm regularization in the right-hand side of (7).

To find the optimal weight vector $\mathbf{w}(k+1)$ which minimizes the cost function (7), the derivative of (7) with respect to $\mathbf{w}(k+1)$ is taken and set to zero. Note that the weighted l_1 -norm regularization term, that is, $\|\mathbf{\Pi} \mathbf{w}(k+1)\|_1$, is not differentiable at any point in case $w_m(k+1) = 0$. To address this issue, a subgradient calculus [21] is carried out.

Thus, taking the derivative of (7) with respect to the weight vector $\mathbf{w}(k+1)$ and letting the derivative be equal to zero, it leads to

$$\mathbf{w}(k+1) = \mathbf{w}(k) + \frac{1}{2} \sum_{i=0}^{N-1} \lambda_i \mathbf{u}_i^T(k) - \frac{\gamma}{2} \nabla_{\mathbf{w}}^s \|\mathbf{\Pi} \mathbf{w}(k+1)\|_1, \quad (9)$$

where $\nabla_{\mathbf{w}}^s f(\cdot)$ denotes a subgradient vector of a function $f(\cdot)$ with respect to $\mathbf{w}(k+1)$. An available subgradient vector $\nabla_{\mathbf{w}}^s \|\mathbf{\Pi} \mathbf{w}(k+1)\|_1$ is obtained as [21]. Consider

$$\nabla_{\mathbf{w}}^s \|\mathbf{\Pi} \mathbf{w}(k+1)\|_1 = \mathbf{\Pi}^T \text{sgn}(\mathbf{\Pi} \mathbf{w}(k+1)) = \mathbf{\Pi} \text{sgn}(\mathbf{w}(k+1)), \quad (10)$$

since $\mathbf{\Pi}$ is assumed as a diagonal matrix with positive-valued elements, where $\text{sgn}(\cdot)$ is a componentwise sign function defined by

$$\text{sgn}(x) = \begin{cases} \frac{x}{|x|}, & x \neq 0 \\ 0, & \text{elsewhere.} \end{cases} \quad (11)$$

Substituting (10) into (9) and assuming $\text{sgn}[\mathbf{w}(k+1)] \approx \text{sgn}[\mathbf{w}(k)]$, it is given by

$$\mathbf{w}(k+1) = \mathbf{w}(k) + \frac{1}{2} \sum_{i=0}^{N-1} \lambda_i \mathbf{u}_i^T(k) - \frac{\gamma}{2} \mathbf{\Pi} \text{sgn}(\mathbf{w}(k)). \quad (12)$$

Substituting (12) into the multiple constraints of the NSAF, that is, $d_{i,D}(k) = \mathbf{u}_i(k) \mathbf{w}(k+1)$, $i = 0, 1, \dots, N-1$ and rewriting as a matrix form, it leads to

$$\mathbf{\Lambda} = 2[\mathbf{U}(k) \mathbf{U}^T(k)]^{-1} \mathbf{e}_D(k) + \gamma[\mathbf{U}(k) \mathbf{U}^T(k)]^{-1} \mathbf{U}(k) \mathbf{\Pi} \text{sgn}(\mathbf{w}(k)), \quad (13)$$

where $\mathbf{\Lambda} = [\lambda_0, \lambda_1, \dots, \lambda_{N-1}]^T$ is the $N \times 1$ Lagrange vector,

$$\mathbf{U}(k) = \begin{bmatrix} \mathbf{u}_0(k) \\ \vdots \\ \mathbf{u}_{N-1}(k) \end{bmatrix}, \quad \mathbf{e}_D(k) = \begin{bmatrix} e_{0,D}(k) \\ \vdots \\ e_{N-1,D}(k) \end{bmatrix}. \quad (14)$$

By neglecting the off-diagonal elements of $\mathbf{U}(k) \mathbf{U}^T(k)$ [6], the components of $\mathbf{\Lambda}$ in (13) can be simplified to

$$\lambda_i = 2 \frac{e_{i,D}(k)}{\|\mathbf{u}_i(k)\|^2} + \gamma \frac{\mathbf{u}_i(k)}{\|\mathbf{u}_i(k)\|^2} \mathbf{\Pi} \text{sgn}(\mathbf{w}(k)), \quad (15)$$

for $i = 0, 1, \dots, N-1$.

Consequently, combining (12) and (15), the update recursion of the sparsity-regularized NSAF is given by

$$\begin{aligned} \mathbf{w}(k+1) &= \mathbf{w}(k) \\ &+ \mu \sum_{i=0}^{N-1} \left[\frac{\mathbf{u}_i^T(k)}{\|\mathbf{u}_i(k)\|^2} e_{i,D}(k) \right. \\ &\quad \left. + \frac{1}{2} \gamma \frac{\mathbf{u}_i(k)}{\|\mathbf{u}_i(k)\|^2} \mathbf{\Pi} \text{sgn}(\mathbf{w}(k)) \mathbf{u}_i^T(k) \right] \\ &- \frac{\mu \gamma}{2} \mathbf{\Pi} \text{sgn}(\mathbf{w}(k)), \end{aligned} \quad (16)$$

where μ is the step-size parameter.

3.2. Determination of the Weighted l_1 -Norm Regularization. Here, by choosing the weighting matrix $\mathbf{\Pi}$, two versions of the sparsity-regularized NSAF are developed. First, the use of the identity matrix as the weighting matrix, that is, $\mathbf{\Pi} = \mathbf{I}_M$, results in the following update recursion:

$$\begin{aligned} \mathbf{w}(k+1) &= \mathbf{w}(k) \\ &+ \mu \sum_{i=0}^{N-1} \left[\frac{\mathbf{u}_i^T(k)}{\|\mathbf{u}_i(k)\|^2} e_{i,D}(k) \right. \\ &\quad \left. + \frac{1}{2} \gamma \frac{\mathbf{u}_i(k)}{\|\mathbf{u}_i(k)\|^2} \text{sgn}(\mathbf{w}(k)) \mathbf{u}_i^T(k) \right] \\ &- \frac{\mu \gamma}{2} \text{sgn}(\mathbf{w}(k)), \end{aligned} \quad (17)$$

which is referred to as the l_1 -norm NSAF (l_1 -NSAF) as an unweighted case. The l_1 -NSAF uniformly attracts the

TABLE I: Computational complexity.

	NSAF	l_1 -NSAF	l_1 -RNSAF
Multiplications	$3M + 3NL$	$6M + 3NL$	$7M + 3NL$
Divisions	1	2	$2 + M/N$

(M : filter length, N : number of subbands, and L : length of the analysis filters and synthesis filters).

tap coefficients of $\mathbf{w}(k)$ to zero. The zero attraction process leads to the improved convergence of the l_1 -NSAF when the majority of entries of a system are zero; that is, a system is sparse.

Second, to approximate the actual sparsity condition of an underlying system, that is, l_0 -norm of the system, the weights of $\mathbf{\Pi}$ are chosen inversely proportional to magnitude of the actual coefficients of the system as given by

$$\pi_m = \begin{cases} \frac{1}{|w_m|}, & w_m \neq 0 \\ \infty, & w_m = 0, \end{cases} \quad (18)$$

where w_m denotes the m th coefficients of the system, that is, \mathbf{w}° . However, since the actual coefficients of the system are unavailable, the estimate of the current filter weights is utilized instead of the actual weights, which is referred to as the reweighting scheme [22], as follows:

$$\pi_m(k) = \frac{1}{|w_m(k)| + \epsilon} \quad \text{for } m = 0, 1, \dots, M-1, \quad (19)$$

where $w_m(k)$ denotes the m th tap weight of the $\mathbf{w}(k)$ and ϵ is a small positive value to avoid singularity when $|w_m(k)| = 0$. Then, the weighting matrix $\mathbf{\Pi}$ consists of the values of $\pi_m(k)$ as the m th diagonal elements and has a time-varying feature. Finally, the update recursion is given by

$$\begin{aligned} \mathbf{w}(k+1) = \mathbf{w}(k) & \\ & + \mu \sum_{i=0}^{N-1} \left[\frac{\mathbf{u}_i^T(k)}{\|\mathbf{u}_i(k)\|^2} e_{i,D}(k) \right. \\ & \quad \left. + \frac{1}{2} \gamma \frac{\bar{\mathbf{u}}_i(k)}{\|\mathbf{u}_i(k)\|^2} \text{sgn}(\mathbf{w}(k)) \mathbf{u}_i^T(k) \right] \\ & - \frac{\mu \gamma \text{sgn}(\mathbf{w}(k))}{2 |\mathbf{w}(k)| + \epsilon}, \end{aligned} \quad (20)$$

where $\bar{\mathbf{u}}_i(k) = \mathbf{u}_i(k) \mathbf{\Pi}$ and the vector division operation in last term accounts for a componentwise division. Then, this recursion is called the reweighted l_1 -norm NSAF (l_1 -RNSAF)

Table 1 lists the number of multiplications and divisions of the NSAF [6], l_1 -NSAF, and l_1 -RNSAF per iteration. As shown in Table 1, the use of l_1 -norm constraint leads to an acceptable increase in computation.

4. Numerical Results

The performance of the proposed sparsity-regularized NSAFs is validated by carrying out computer simulations in a system

identification scenario in which the unknown channel is randomly generated. The lengths of the unknown system are $M = 128$ and 512 in experiments where S of them are nonzero. The nonzero filter weights are positioned randomly and their values are taken from a Gaussian distribution $\mathcal{N}(0, 1/S)$. Here, $S = 4$ is used in the simulations except Figure 5 in which various S values are considered. The adaptive filter and the unknown system are assumed to have the same number of taps. The input signals are obtained by filtering a white, zero-mean, Gaussian random sequence through a first-order system $G(z) = 1/(1-0.9z^{-1})$. The signal-to-noise ratio (SNR) is calculated by

$$\text{SNR} = 10 \log_{10} \left(\frac{E[y^2(n)]}{E[v^2(n)]} \right), \quad (21)$$

where $y(n) = \mathbf{u}(n)\mathbf{w}^\circ$. The measurement noise $v(n)$ is added to $y(n)$ such that SNR = 10, 20, and 30 dB. In order to compare the convergence performance, the normalized mean square deviation (MSD),

$$\text{Normalized MSD} = E \left[\frac{\|\mathbf{w}^\circ - \mathbf{w}(k)\|^2}{\|\mathbf{w}^\circ\|^2} \right], \quad (22)$$

is taken and averaged over 50 independent trials. The cosine-modulated filter banks [23] with the subband number of $N = 4$ are used in the simulations. The prototype filter of length $L = 32$ is used. For comparison purpose, the proportionate NSAF (PNSAF) [12] is considered, which has been developed for sparse system identification. The step-size is set to $\mu = 0.5$ for SAF algorithms except the PNSAF where the step sizes $\mu = 0.6$ (Figure 2) and $\mu = 0.65$ (Figure 6) are chosen to achieve similar steady-state MSD with the l_1 -RNSAF for comparison purpose. For the l_1 -RNSAF, $\epsilon = 0.01$ is chosen. In addition, $\rho = 0.05$ is used for the PNSAF. The γ values are obtained by repeated trials to minimize the steady-state MSD.

Figure 2 shows the normalized MSD curves of the NLMS, NSAF, l_1 -NSAF, and l_1 -RNSAF, in cases of $N = 4$ and SNR = 30 dB. For the l_1 -NSAF and l_1 -RNSAF, $\gamma = 3 \times 10^{-5}$ is chosen. As shown in Figure 2, the not only l_1 -RNSAF outperforms the conventional NLMS, NSAF, PNSAF, and l_1 -NSAF, but also the l_1 -NSAF has better performance than other conventional algorithms, in terms of the convergence rate and the steady-state misalignment.

In Figure 3, to verify the effect of γ on convergence performance, the normalized MSD curves of the l_1 -RNSAF for different γ values are illustrated, in case of $N = 4$ and SNR = 30 dB. For different γ values ($\gamma = 1 \times 10^{-4}$, 1×10^{-5} , 5×10^{-5} , and 1×10^{-6}), the l_1 -RNSAF is not excessively sensitive to γ . The analysis of an optimal γ value remains a future work.

Next, the performance of the proposed l_1 -norm regularized NSAFs is compared to the original NSAF under different SNR conditions. Figure 4 depicts the normalized MSD curves of the NSAF, l_1 -NSAF, and l_1 -RNSAF under SNR = 10 and 20 dB, respectively. The γ value for the l_1 -NSAF and l_1 -RNSAF is set to 5×10^{-5} . It is clear that both the l_1 -NSAF and l_1 -RNSAF are superior to the NSAF under several SNR cases. Furthermore, the l_1 -RNSAF performs well compared to l_1 -NSAF.

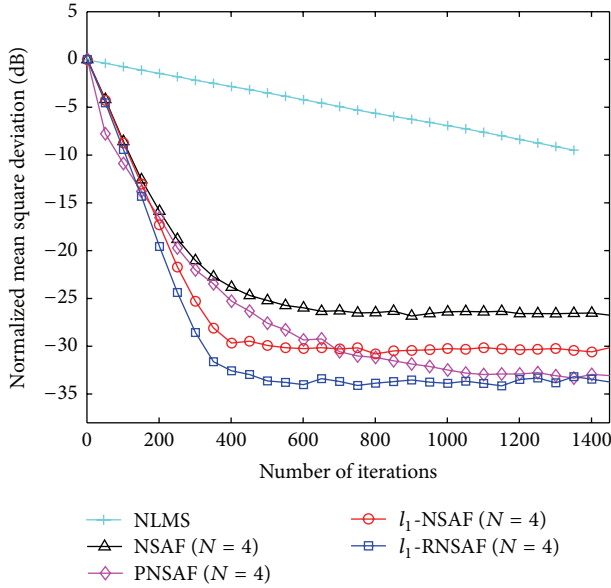


FIGURE 2: Normalized MSD curves of the NLMS, NSAF, PNSAF, l_1 -NSAF, and l_1 -RNSAF ($N = 4$).

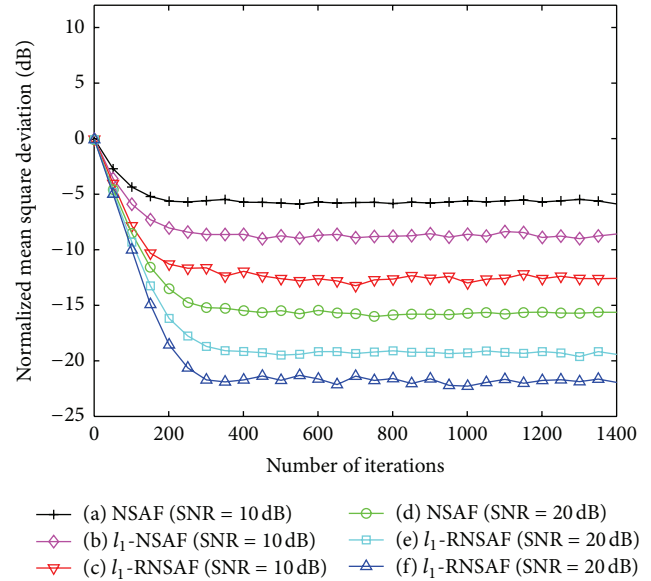


FIGURE 4: Normalized MSD curves of the NSAF, l_1 -NSAF, and l_1 -RNSAF under various SNR conditions (SNR = 10, 20, and 30 dB, $N = 4$).

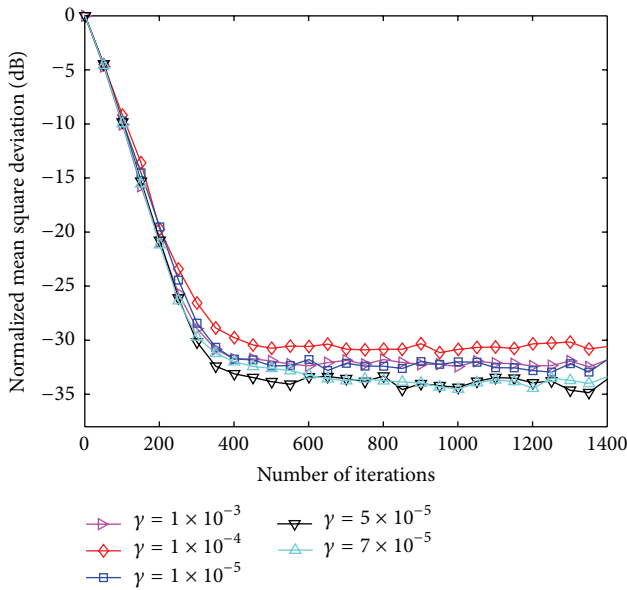


FIGURE 3: Normalized MSD curves of the l_1 -RNSAF for various γ values ($N = 4$).

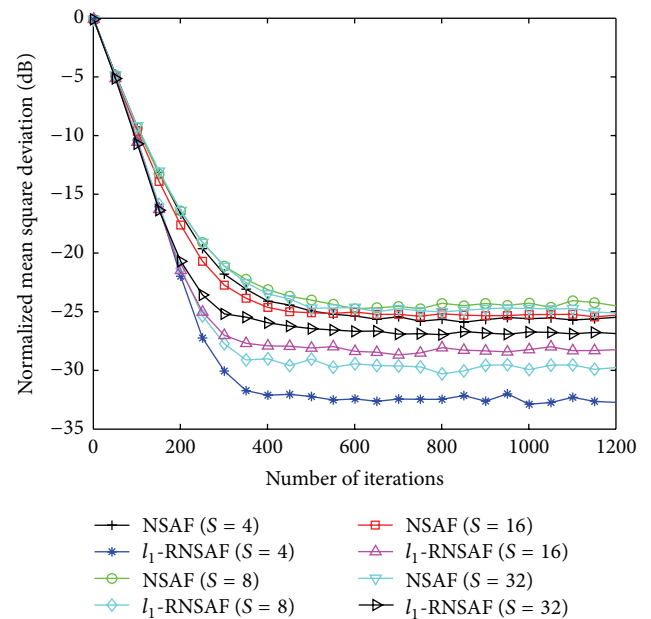


FIGURE 5: Normalized MSD curves of the NSAF and l_1 -RNSAF under various sparsity conditions ($S = 4, 8, 16$, and $32, N = 4$).

In Figure 5, the convergence properties of the NSAF and l_1 -RNSAF are compared under various sparsity conditions of an underlying system. With the same length of the system, that is, $M = 128$, different sparsity conditions ($S = 4, 8, 16$, and 32) are considered under $\text{SNR} = 30$ dB. The value of γ is set to 3×10^{-5} for the l_1 -RNSAF. Figure 5 shows that the NSAF is independent of the sparsity condition. On the other hand, the results indicate that the more sparse the underlying system, the better the l_1 -RNSAF.

The comparison of performance of the NSAF, l_1 -NSAF, and l_1 -RNSAF with a long system, here, the filter length $M =$

512, is presented in Figure 6. For the l_1 -NSAF and l_1 -RNSAF, $\gamma = 5 \times 10^{-5}$ is chosen. A similar result of Figure 2 is observed in Figure 6.

Finally, the tracking capabilities of the algorithms of a sudden change in the system are tested for $N = 4$ and $\text{SNR} = 30$ dB. Figure 7 shows the results when the unknown system is right-shifted for 20 taps. Same value of γ in Figure 2 is used. As can be seen, the l_1 -NSAF and l_1 -RNSAF keep track of weight change without losing the convergence rate nor

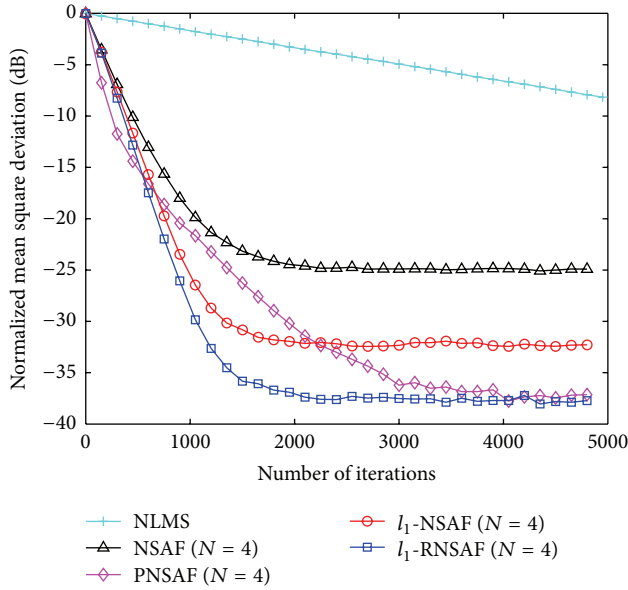


FIGURE 6: Normalized MSD curves of the NLMS, NSAF, PNSAF, l_1 -NSAF, and l_1 -RNSAF for long system of $M = 512$ ($N = 4$).

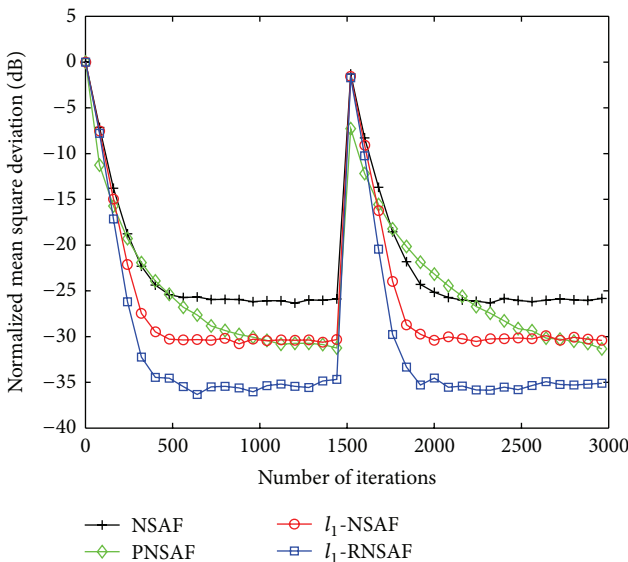


FIGURE 7: Normalized MSD curves of the NSAF, PNSAF, l_1 -NSAF, and l_1 -RNSAF in case of a time-varying unknown system ($N = 4$). The system is right-shifted for 20 taps at 1500 iterations.

the steady-state misalignment compared to the conventional NLMS, NSAF, and PNSAF. To be specific, the l_1 -RNSAF achieves better performance than the l_1 -NSAF in terms of both convergence rate and steady-state misalignment.

5. Conclusion

A new family of the NSAFs which takes into account the sparsity condition of an underlying system has been presented by incorporating a weighted l_1 -norm constraint of

filter weights in the cost function. The update recursion is obtained by employing subgradient calculus on the weighted l_1 -norm constraint term. Subsequently, two sparsity regularized NSAFs, that is, the unweighted l_1 -NSAF and l_1 -RNSAF have been developed. The numerical results indicate that the proposed l_1 -NSAF and l_1 -RNSAF achieve highly improved convergence performance over the conventional algorithms for sparse system identification.

Conflict of Interests

The author declares that there is no conflict of interests regarding the publication of this paper.

Acknowledgment

This research was supported by new faculty research program funded by Gangneung-Wonju National University (2013100162).

References

- [1] S. Haykin, *Adaptive Filter Theory*, Prentice Hall, Upper Saddle River, NJ, USA, 4th edition, 2002.
- [2] A. H. Sayed, *Fundamentals of Adaptive Filtering*, Wiley, New York, NY, USA, 2003.
- [3] A. Gilloire and M. Vetterli, "Adaptive filtering in subbands with critical sampling: analysis, experiments, and application to acoustic echo cancellation," *IEEE Transactions on Signal Processing*, vol. 40, no. 8, pp. 1862–1875, 1992.
- [4] M. De Courville and P. Duhamel, "Adaptive filtering in subbands using a weighted criterion," *IEEE Transactions on Signal Processing*, vol. 46, no. 9, pp. 2359–2371, 1998.
- [5] S. S. Pradhan and V. U. Reddy, "A new approach to subband adaptive filtering," *IEEE Transactions on Signal Processing*, vol. 47, no. 3, pp. 655–664, 1999.
- [6] K. A. Lee and W. S. Gan, "Improving convergence of the NLMS algorithm using constrained subband updates," *IEEE Signal Processing Letters*, vol. 11, no. 9, pp. 736–739, 2004.
- [7] K. A. Lee and W. S. Gan, "Inherent decorrelating and least perturbation properties of the normalized subband adaptive filter," *IEEE Transactions on Signal Processing*, vol. 54, no. 11, pp. 4475–4480, 2006.
- [8] D. L. Duttweiler, "Proportionate normalized least-squares adaptation in echo cancelers," *IEEE Transactions on Speech and Audio Processing*, vol. 8, no. 5, pp. 508–518, 2000.
- [9] W. F. Schreiber, "Advanced television systems for terrestrial broadcasting: some problems and some proposed solutions," *Proceedings of IEEE*, vol. 83, no. 6, pp. 958–981, 1995.
- [10] S. L. Gay, "Efficient, fast converging adaptive filter for network echo cancellation," in *Proceedings of the 32nd Asilomar Conference on Signals, Systems & Computers*, pp. 394–398, November 1998.
- [11] H. Deng and M. Doroslovački, "Improving convergence of the PNLMS algorithm for sparse impulse response identification," *IEEE Signal Processing Letters*, vol. 12, no. 3, pp. 181–184, 2005.
- [12] M. S. E. Abadi, "Proportionate normalized subband adaptive filter algorithms for sparse system identification," *Signal Processing*, vol. 89, no. 7, pp. 1467–1474, 2009.

- [13] D. L. Donoho, "Compressed sensing," *IEEE Transactions on Information Theory*, vol. 52, no. 4, pp. 1289–1306, 2006.
- [14] E. J. Candès, J. Romberg, and T. Tao, "Robust uncertainty principles: exact signal reconstruction from highly incomplete frequency information," *IEEE Transactions on Information Theory*, vol. 52, no. 2, pp. 489–509, 2006.
- [15] R. Tibshirani, "Regression shrinkage and selection via the lasso," *Journal of Royal Statistical Society B*, vol. 58, pp. 267–288, 1996.
- [16] Y. Chen, Y. Gu, and A. O. Hero, "Sparse LMS for system identification," in *Proceedings of the International Conference on Acoustics, Speech, and Signal Process (ICASSP '09)*, pp. 3125–3128, April 2009.
- [17] Y. Gu, J. Jin, and S. Mei, " l_1 norm constraint LMS algorithm for sparse system identification," *IEEE Signal Processing Letters*, vol. 16, no. 9, pp. 774–777, 2009.
- [18] J. Jin, Y. Gu, and S. Mei, "A stochastic gradient approach on compressive sensing signal reconstruction based on adaptive filtering framework," *IEEE Journal on Selected Topics in Signal Processing*, vol. 4, no. 2, pp. 409–420, 2010.
- [19] E. M. Eksioğlu and A. K. Tanc, "RLS algorithm with convex regularization," *IEEE Signal Processing Letters*, vol. 18, no. 8, pp. 470–473, 2011.
- [20] N. Kalouptsidis, G. Mileounis, B. Babadi, and V. Tarokh, "Adaptive algorithms for sparse system identification," *Signal Processing*, vol. 91, no. 8, pp. 1910–1919, 2011.
- [21] D. P. Bertsekas, *Convex Analysis and Optimization*, Athena Scientific, Cambridge, Mass, USA, 2003.
- [22] E. J. Candès, M. B. Wakin, and S. P. Boyd, "Enhancing sparsity by reweighted l_1 minimization," *The Journal of Fourier Analysis and Applications*, vol. 14, no. 5-6, pp. 877–905, 2008.
- [23] P. P. Vaidyanathan, *Multirate Systems and Filterbanks*, Prentice-Hall, Englewood Cliffs, NJ, 1993.

Research Article

Improvement and Simulation of an Autonomous Time Synchronization Algorithm for a Layered Satellite Constellation

Feijiang Huang,^{1,2} Xiaochun Lu,^{2,3} Guangcan Liu,¹ Liping Sun,¹
Wang Sheng,¹ and Yingde Wang¹

¹ Department of Electronics and Communication Engineering, Changsha University, Changsha 410022, China

² Key Laboratory of Precision Navigation and Timing Technology, Chinese Academy of Sciences, Xi'an 710600, China

³ National Time Service Center, Chinese Academy of Sciences, Xi'an 710600, China

Correspondence should be addressed to Feijiang Huang; ccsuhfj@163.com

Received 1 September 2013; Revised 5 November 2013; Accepted 14 November 2013

Academic Editor: Cao Su-Qun

Copyright © 2013 Feijiang Huang et al. This is an open access article distributed under the Creative Commons Attribution License, which permits unrestricted use, distribution, and reproduction in any medium, provided the original work is properly cited.

Autonomous time synchronization for satellite constellations is a key technology to establish a constellation system time without the use of a ground station. The characteristics of satellite visibility time for layered satellite constellations containing geostationary earth orbit (GEO), inclined geosynchronous orbit (IGSO), and medium earth orbit (MEO) satellites are simulated by establishing a visible satellite model. Based on the satellite visible simulation results for a layered constellation, this study investigates the autonomous time synchronization algorithm that corresponds to the layered constellation structure, analyzes the main error of the time synchronization algorithm, and proposes methods to improve the characteristics of satellite movement in the constellation. This study uses an improved two-way time synchronization algorithm for autonomous time synchronization in the GEO-MEO satellite layer of a layered satellite constellation. The simulation results show that in a condition with simulation errors, the time synchronization precision of this improved algorithm can be controlled within 5 ns and used in high-precision autonomous time synchronization between layered satellite constellations.

1. Introduction

With the development of space science and technology, aerospace application systems require improvements in terms of high-precision time frequency, which is used in satellite navigation, space-based integrated information networks, space-based measurement and control, distributed-type satellite systems, and deep space detection. In current aerospace applications, time reference is established on the ground. Thus, most finishing aerospace technical activities of aircraft must be synchronized with corresponding ground stations [1, 2]. This synchronous mode has a number of defects [3]. By contrast, the direct establishment of high-precision time frequency reference within the constellation can enhance the autonomous operational capability of aerospace application systems. Therefore, further studies on related theories and implementation technologies related to autonomous time

synchronization are necessary to improve the precision of autonomous time synchronization of constellations.

Current domestic and international studies on autonomous time synchronization focus on the following aspects: autonomous navigation algorithms for satellite navigation systems, space-based measurement and control, space-based information transport architecture and routing algorithms, distributed satellite systems, new atomic frequency standards, and improved precision of existing time synchronization methods [4–9]. Current studies seldom focus on autonomous time synchronization algorithms and data processing models used in satellite constellations. Based on a simulation of the characteristics of satellite visibility time of a layered satellite constellation, this study focuses on an autonomous time synchronization algorithm and an improvement method that corresponds to its constellation structure. This study uses

the two-way time synchronization algorithm to conduct simulated autonomous time synchronization between different layers of satellites.

2. Satellite Constellation Autonomous Time Synchronization

Satellite constellation autonomous time indicates that given a lack of long-term support from a ground system, the satellite constellation constantly updates the satellite clock parameters introduced by the ground station by using two-way distance measurements between satellites, data exchanges, and an on-board filtering processor to establish and maintain the constellation time [3]. The autonomous navigation ability of a constellation has been studied extensively, specifically under the precondition of malfunction or destruction of the ground measurement and control station. In such a case, the satellite equipment in the constellation can synchronize via intersatellite distance measurements combined with established satellite orbit information. Such measurements ensure precise orbit determination for autonomous operation, time reference maintenance, long-term independent operation of the constellation, reconstruction and repair of the measurement and control station, and enhancement of the antijamming and antidamage ability of the system. Autonomous time synchronization is a key technology for autonomous navigation constellations [4, 10]. Only with autonomous time synchronization can autonomous satellite constellation navigation meet the required level of precision. Thus, autonomous time synchronization and time keeping technology is a major research topic in the field of aerospace application systems.

3. Visual Simulation of a Layered Satellite Constellation

A layered satellite constellation is composed of three types of orbiting satellites, each forming their own layer: geostationary earth orbit (GEO), inclined geosynchronous orbit (IGSO), and medium earth orbit (MEO). Intersatellite physical visibility must be achieved to ensure autonomous time synchronization in a layered satellite constellation. Electromagnetic power requirements must then be met to ensure normal communication during physical visibility. Therefore, considering the visual time modeling and simulation of the layered satellite constellation is essential in studying autonomous time synchronization for layered satellite constellation.

3.1. Mutual-Visual Model of Satellites. Generally speaking, after two satellites rotating around the earth determine their positions in the air at a random time, these satellites can see each other only when both of them are higher than the tangential level on the surface of the earth. The most extreme situation is when two satellites are located at the externally tangential level simultaneously, as shown in Figure 1. Therefore, we can obtain a visual function to depict whether two

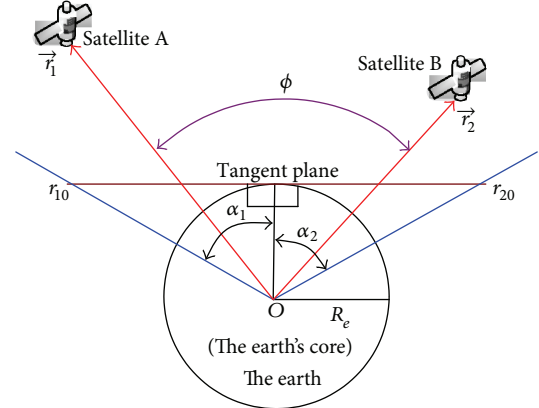


FIGURE 1: Visual calculation model between satellites.

TABLE 1: Comparison of mutual visual conditions for GEO, IGSO, and MEO satellites.

Link types	Percentage of satellite mutual-visual time accounting for simulation cycle
GEO-GEO	100%
GEO-IGSO	100%
GEO-MEO	97.47%
IGSO-MEO	98.55%

satellites are within sight of each other. This visibility function is as follows [11]:

$$\psi = \alpha_1 + \alpha_2 - \phi, \quad (1)$$

where α_1 and α_2 are the limiting angles and ϕ represents an included angle between two position vectors of two satellites that connect to the core of the earth at different positions. The values of α_1 , α_2 , and ϕ are indicated in [11]. When $\psi > 0$, the two satellites can see each other. Otherwise, they have no visual contact.

3.2. Mutual-Visual Simulation Results between Satellite Constellation Layers. Based on the mutual-visual model, the Satellite Tool Kit (STK) software is used to simulate typical visual conditions between satellites at different layers of a layered satellite constellation. The simulated statistical results are presented in Table 1.

Table 1 shows that GEO and IGSO satellites can see each other continuously for 24 hours each day. The visibility time of GEO and MEO satellites accounts for 97.47% of the entire MEO satellite regression cycle and that of IGSO and MEO satellites accounts for 98.55%. Therefore, when the ground station cannot be used, we can conduct autonomous time synchronization by establishing satellite links in high rail among GEO, IGSO, and MEO satellites. The average synchronous time of MEO satellites can account for 98% of the simulation cycle to improve the autonomous time synchronization precision of layered constellations [12].

4. Autonomous Time Synchronization Algorithm for a Layered Satellite Constellation

According to the simulation results, when the ground station cannot be used, the constellation time is established uniformly, mainly through intersatellite mutual autonomous time synchronization. The accurate satellite position cannot be known beforehand, and precise measurement of the propagation path delay of the time signal between satellites is difficult to obtain. Therefore, the autonomous time synchronization algorithm of the constellation should significantly reduce the path propagation delay of the time synchronization signal, and the main measurement should be completed autonomously by the satellites.

4.1. Two-Way Time Synchronization Algorithm. Because the two-way time synchronization algorithm of the satellites does not require the accurate position of the two satellites in advance, the algorithm can offset the influence of the propagation path and other additional delays, which results in precise time synchronization. When the satellites can see each other in the constellation, the two-way time synchronization algorithm can be used directly for intersatellite autonomous time synchronization in the layered satellite constellation. The intersatellite two-way time synchronization principle is shown in Figure 2 [13]. Satellites A and B are installed with radio transmitters and receivers. Both satellites transmit and receive each others time synchronization signals simultaneously. The equation can be expressed as follows:

$$\begin{aligned} T_1 &= \Delta t + t_2 + \tau_{BA} + r_1 + \delta_1, \\ T_2 &= -\Delta t + t_1 + \tau_{AB} + r_2 + \delta_2. \end{aligned} \quad (2)$$

In (2), Δt represents the clock correction of Satellites A and B, T_1 is the time difference between Satellite A transmitting its timing signal and receiving the timing signal transmitted by Satellite B, t_2 indicates the transmitting equipment delay of Satellite B, τ_{BA} indicates the propagation time delay from Satellite B to Satellite A, r_1 stands for the receiving equipment delay of Satellite A, δ_1 indicates other delays, T_2 represents the time difference between Satellite B transmitting its timing signal and receiving the timing signal transmitted by Satellite A, t_1 is the transmitting equipment delay of Satellite A, τ_{AB} indicates the propagation time delay of from Satellite A to Satellite B, r_2 is the receiving equipment delay of Satellite B, and δ_2 indicates other delays.

After solving (2), we can obtain the clock offset Δt of Satellites A and B:

$$\begin{aligned} \Delta t &= \frac{T_1 - T_2}{2} + \frac{t_1 - t_2}{2} + \frac{r_2 - r_1}{2} \\ &\quad + \frac{\tau_{AB} - \tau_{BA}}{2} + \frac{\delta_2 - \delta_1}{2}. \end{aligned} \quad (3)$$

In (3), T_1 and T_2 can be determined by measuring Satellites A and B. t_1 , r_1 , t_2 , and r_2 can each be calibrated in advance according to the satellite transmission signal

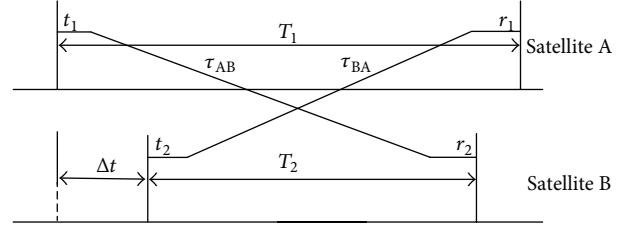


FIGURE 2: Schematic of two-way time synchronization of satellites.

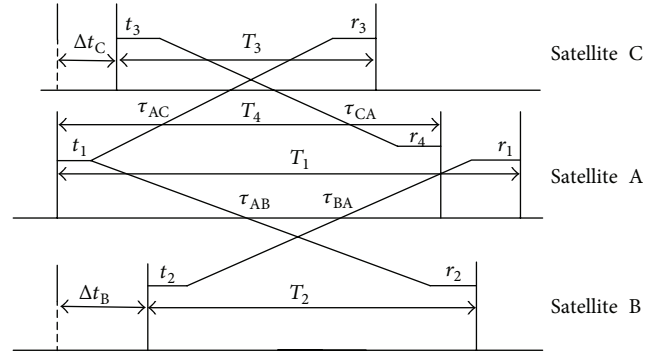
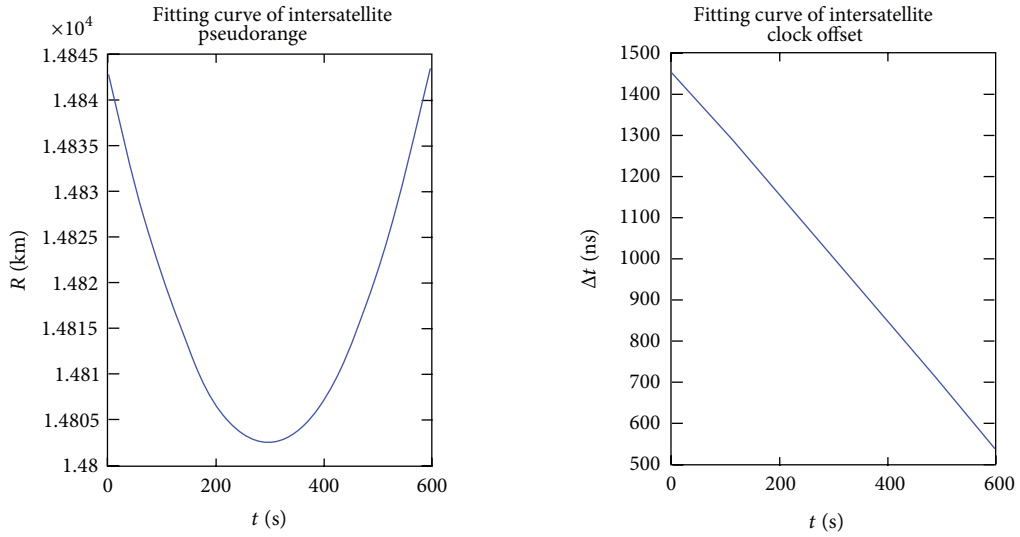


FIGURE 3: Schematic of common view two-way time synchronization.

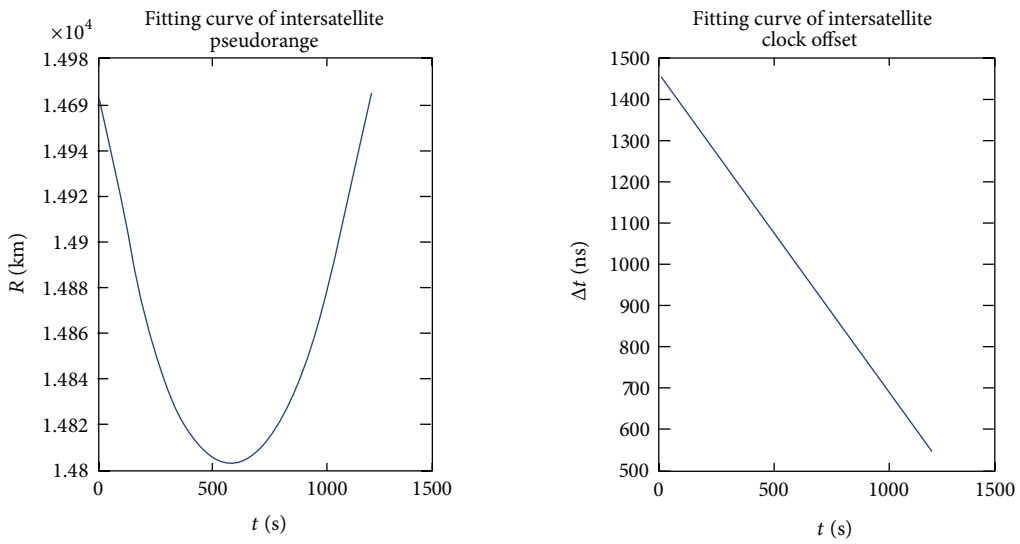
frequency. When the frequencies of the time synchronization signals transmitted by Satellites A and B are close, the link is symmetrical and the propagation delay is approximately equal: $\tau_{AB} = \tau_{BA}$. Meanwhile, ignoring the effects of other delays, we can determine the satellite clock offset.

4.2. Common View Two-Way Time Synchronization Algorithm. If the satellites in a constellation cannot see each other, we cannot directly use the two-way time synchronization algorithm to achieve intersatellite autonomous time synchronization in the layered satellite constellation. Thus, we have to use a public visual satellite to complete the indirect two-way time synchronization, that is, common view two-way time synchronization, as shown in Figure 3. In the figure, Satellite A is a mutual visual satellite assumed to be either GEO or IGSO type. Satellites B and C cannot see each other. When Satellite A transmits the time synchronization signal to Satellites B and C simultaneously and receives the time synchronization signals of the other satellites, according to the principle of two-way time synchronization, the following equations are obtained:

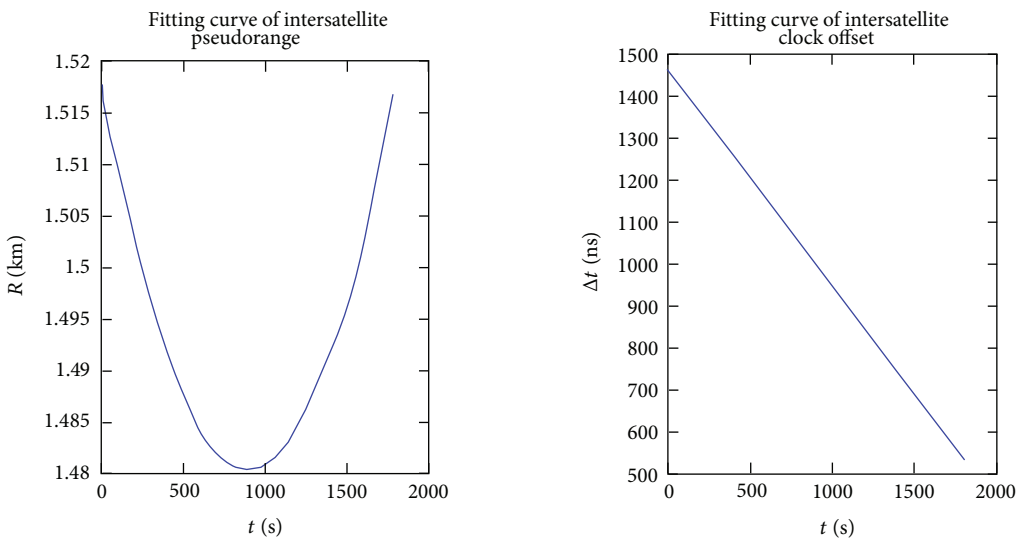
$$\begin{aligned} \Delta t_B &= \frac{T_1 - T_2}{2} + \frac{t_1 - t_2}{2} + \frac{r_2 - r_1}{2} \\ &\quad + \frac{\tau_{AB} - \tau_{BA}}{2} + \frac{\delta_2 - \delta_1}{2} \\ \Delta t_C &= \frac{T_4 - T_3}{2} + \frac{t_1 - t_3}{2} + \frac{r_3 - r_4}{2} \\ &\quad + \frac{\tau_{AC} - \tau_{CA}}{2} + \frac{\delta_3 - \delta_4}{2}. \end{aligned} \quad (4)$$



(a) Fitting results of a 10-minute time synchronization from 23:32:50.000 on June 1, 2008 to 23:42:50.000 on June 1, 2008

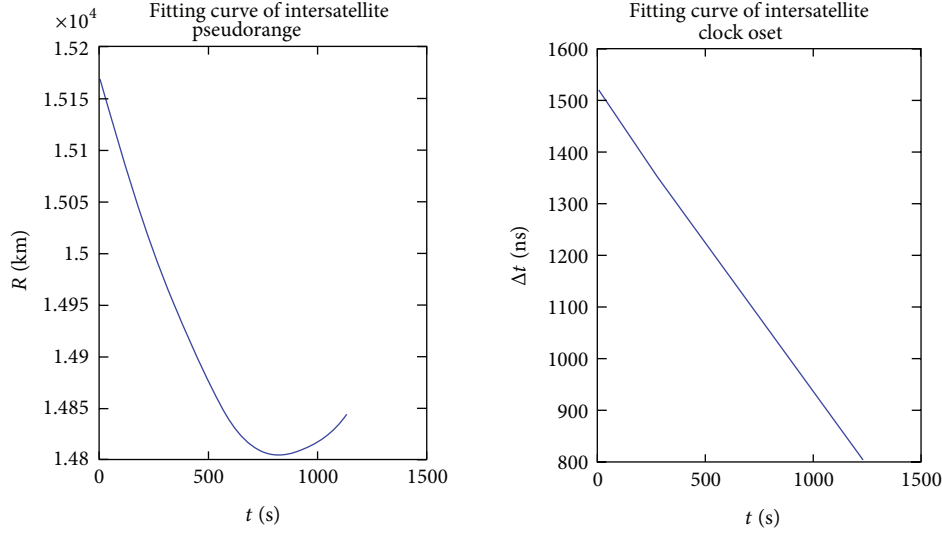


(b) Fitting results of a 20-minute time synchronization from 23:27:50.000 on June 1, 2008 to 23:47:50.000 on June 1, 2008



(c) Fitting results of a 30-minute time synchronization from 23:22:50.000 on June 1, 2008 to 23:52:50.000 on June 1, 2008

FIGURE 4: Continued.



(d) Fitting results of a 20-minute time synchronization from 23:22:50.000 on June 1, 2008 to 23:42:50.000 on June 1, 2008 (asymmetrical)

FIGURE 4: Fitting curves of pseudorange and clock offset between GEO and MEO satellites.

In (4), Δt_B and Δt_C indicate the clock offset between Satellites A and B and between Satellites A and C, respectively. The other parameters have the same meanings as in two-way time synchronization.

After solving (4), we can obtain the clock offset Δt_{BC} of Satellites B and C as follows:

$$\Delta t_{BC} = \frac{T_1 + T_3 - T_2 - T_4}{2} + \frac{t_3 - t_2}{2} + \frac{r_2 + r_4 - r_1 - r_3}{2} + \frac{(\tau_{AB} - \tau_{BA}) - (\tau_{AC} - \tau_{CA})}{2} + \frac{\delta_3 + \delta_1 - \delta_4 - \delta_2}{2}. \quad (5)$$

In (5), the transmission time delay t_1 of mutual visual Satellite A is eliminated. With the receiving channel delay r_4 and r_1 of mutual visual Satellite A are equal, and other delays δ_1 and δ_4 are the same, and the impact on time synchronization of those delay is eliminated. The transmission delays of Satellites B and C (t_2 and t_3) receive delays r_2 and r_3 and can be calibrated in advance according to the satellite transmitting signal frequency. Disregarding other delays and the effects of δ_2 and δ_3 , we can simplify (5) as follows:

$$\Delta t_{BC} = \frac{T_1 + T_3 - T_2 - T_4}{2} + \frac{(\tau_{AB} - \tau_{BA}) - (\tau_{AC} - \tau_{CA})}{2}. \quad (6)$$

Considering $\tau_{AB} = \tau_{BA}$ and $\tau_{AC} = \tau_{CA}$ in (6), we have to determine only the time difference between each transmission timing signal of Satellites A and B and Satellites A and C measured by the satellite itself as well as the receiving timing signal transmitted by another satellite; thus, the clock offset of two satellites that cannot see each other is acquired accurately.

5. Two-Way Time Synchronization Algorithm Improvement and Simulation

5.1. Principle of Improved Two-Way Time Synchronization Algorithm. In the two-way time synchronization algorithm and common view time synchronization algorithm, determining the clock offset of mutually visual and invisible satellites requires taking advantage of the fact that the mutual transmission two-way time synchronization signals have approximately equal propagation delays. However, given the high speed of satellites in the constellation, the paths of the two-way time synchronization signals of the constellation generally do not have equal propagation delays, and the precision of the clock offset obtained by applying the algorithm is reduced. Thus, we have improved this algorithm so that it can be used in unequal delay conditions.

According to the movement characteristics of satellites in the constellation, the time synchronization can be conducted when the intersatellite distance has regular changes. We can use an intersatellite pseudorange fitting polynomial and an intersatellite clock offset polynomial to express the process of two-way time synchronization. The intersatellite pseudorange and clock offset polynomial after fitting are as follows [14]:

$$R = f_1(t), \quad (7)$$

$$\Delta t = f_2(t), \quad (8)$$

where R indicates the pseudo range polynomial and Δt indicates the clock offset polynomial. If we suppose that $df_1(t)/dt = 0$, then we can determine the corresponding time t_3 when the intersatellite pseudo range is at its minimum value R_{\min} , that is, when the calculated intersatellite clock offset and the actual satellite clock offset are at the proximate moment. Substituting t_3 into (8), we can find

TABLE 2: Comparison of least squares fitting results of different time lengths of the GEO and MEO satellites in the same period (on June 1, 2008, the actual clock offset is $1\ \mu\text{s}$).

Period	23:32:50.00 to 23:42:50.00	23:27:50.00 to 23:47:50.00	23:22:50.00 to 23:52:50.00	23:22:50.00 to 23:42:50.00 (asymmetrical)
Pseudorange fitting polynomial	$R = 0.0004620897t^2 - 0.2767866515t + 14843.9503933924$	$R = 0.0004601381t^2 - 0.5525447643t + 14968.4674054507$	$R = 0.0004569549t^2 - 0.8239841380t + 15174.4148791739$	$R = 0.0004594126t^2 - 0.8273193074t + 15175.1192383119$
Pseudorange minimum value moment corresponding to $\rho_{\min}(\text{s})$	299.4944839741193	600.411855223807	901.603341546627	900.4098268430367
Clock offset fitting polynomial	$\Delta t = -1.53961927325t + 1462.39429390793$	$\Delta t = -0.77368332728t + 1464.4655576661$	$\Delta t = -0.51949244881t + 1467.72268747967$	$\Delta t = -0.58308473555t + 1505.84764677203$
Minimum clock offset $\Delta t_{\min}(\text{ns})$	1001.286814148183	999.9369138812618	999.3465597276504	980.8324209975162

the corresponding intersatellite clock offset with minimum error $\Delta t_{\min} = f_2(t_3)$ when the intersatellite pseudo range is at the minimum.

5.2. Improved Two-Way Time Synchronization Algorithm Simulation. To validate the accuracy of the improved two-way time synchronization algorithm, we apply it to the autonomous time synchronization between a GEO satellite (Satellite A) and an MEO satellite (Satellite B). If we assume that the actual clock offset of Satellites A and B is $1\ \mu\text{s}$ prior to synchronization, four sections of dynamic two-way time synchronization data are generated using STK. The equipment delay of the receiver and transmitter on the satellite as well as other delays are neglected. We can obtain the least squares fitting results of the pseudo range and clock offset of GEO and MEO satellites for different time lengths within the same period, as shown in Figure 4 and Table 2.

Figure 4 and Table 2 show that when the synchronization period is basically symmetrical to the moment when the minimum intersatellite range appears, the time synchronization and polynomial fitting are more precise, the fitting error is small, and the error is within the 1 ns to 2 ns. However, when the synchronization period is not symmetrical to the moment when the minimum intersatellite range appears, the time synchronization and polynomial fitting are less precise, the fitting error is large, and the error reaches 20 ns.

The pseudo range of the different time lengths and the clock offset simulation results of the GEO and MEO satellites in the same period show that the clock offset acquired using the improved two-way time synchronization algorithm is significantly close to the actual clock offset, and the improved two-way time synchronization model and algorithm are accurate.

Considering these simulation results, we use the improved two-way time synchronization algorithm for autonomous time synchronization of different layers within the constellation of satellites. The duration of the two-way

synchronization should be basically symmetrical to the distance between the minimum satellite moment to reduce polynomial fitting error and improve time synchronization accuracy.

6. Conclusions

Considering the need for autonomous time synchronization of layered satellite constellations, we adapted a two-way time synchronization algorithm to layered satellite constellations and investigated a common view two-way time synchronization algorithm. The major effects of satellite motion on algorithm error were analyzed. The main measures of the effect of satellite motion on the algorithm were also investigated. Finally, an improved two-way time synchronization algorithm was applied to the autonomous time synchronization of the GEO-MEO satellite layer within a satellite constellation. Simulation results demonstrate that when the synchronization period is basically symmetrical to the moment when the minimum intersatellite range appears, and when least squares fitting pseudo ranges polynomial and clock offset polynomial are used relative to the conditions of the other error factors, the autonomous time synchronization accuracy of the algorithm can be controlled at less than 5 ns. This result may be useful in conducting autonomous high-precision time synchronization in a layered satellite constellation.

Conflict of Interests

The authors declare that there is no conflict of interests.

Acknowledgments

This study was supported by the National Natural Science Foundation of China (nos. 11073022 and 10673011), the Hunan Provincial Natural Science Foundation (no. 11JJ3072),

the Scientific Research Fund of the Hunan Provincial Education Department (nos. 13A115 and 11B015), the Science and Technology Planning Project of Changsha (no. K1008012-11), and the Open Fund for Key Laboratory of Precision Navigation and Timing Technology, National Time Service Center, Chinese Academy of Sciences (no. 2009PNTT07).

References

- [1] H. L. Wu, S. R. Guo, and S. W. Fan, "The realization of two-way time synchronization between the satellite and the ground station in passive satellite navigation system," *GNSS World China*, vol. 6, pp. 36–40, 2003.
- [2] S. S. Tan, "Two-way pseudo range time synchronization for navigation satellite clock," *Engineering Science*, vol. 8, no. 5, pp. 70–74, 2006.
- [3] H. T. Wu, X. H. Li, Y. Hua, X. C. Lu, and X. H. Yang, *Time Foundation of Satellite Navigation System*, chapter 6, Science Press, Beijing, China, 2011.
- [4] P. Shuai, G. J. Qu, and Z. G. Chen, "Studies on autonomous navigation techniques for navigation constellations," *Engineering Science*, vol. 8, pp. 22–30, 2006.
- [5] X. S. Sun, D. Yang, X. Yang, and K. Zhai, "The tracking laws of user satellite tracking TDRS," *Journal of Astronautics*, vol. 25, no. 1, pp. 41–45, 2004.
- [6] J. J. Bai, X. C. Lu, Z. X. Lu, and W. Peng, "A distributed hierarchical routing protocol for Non-GEO satellite networks," in *Proceedings of the International Conference on Parallel Processing Workshops*, vol. 2, pp. 148–154, 2004.
- [7] L. Shi, J. J. He, and S. W. Lu, "Model and simulation of space communication infrastructure," *Journal of System Simulation*, vol. 18, no. 6, pp. 1643–1652, 2006.
- [8] S. J. Zhang and G. R. Duan, "Cooperative control for distributed satellite formation keeping," *Journal of Astronautics*, vol. 32, no. 10, pp. 2140–2145, 2011.
- [9] Z. C. Zhai, "Recent progress in atomic time and frequency," *World Sci-Tech R and D*, vol. 28, no. 3, pp. 63–69, 2006.
- [10] P. Shuai and G. J. Qu, "Time synchronization techniques of the autonomous navigation of navigation constellation," *Journal of Astronautics*, vol. 26, no. 6, pp. 768–772, 2005.
- [11] G. X. Zhang and H. Zhang, *Satellite Mobile Communication System*, chapter 2, Beijing, China, 2001.
- [12] Q. F. Xu, "Satellite constellation of local navigation system," *Engineering of Surveying and Mapping*, vol. 10, no. 1, pp. 1–6, 2001.
- [13] F. J. Huang, X. C. Lu, H. T. Wu, and Y. J. Bian, "Study on autonomous time synchronization method based on intersatellite," *Computer Science*, vol. 35, no. 9, pp. 123–125, 2008.
- [14] F. Huang, X. Lu, H. Wu, and Y. Bian, "An algorithm of dynamic two-way time transfer based on intersatellite range variation," *Geomatics and Information Science of Wuhan University*, vol. 35, no. 1, pp. 13–16, 2010.

Research Article

A Heuristic Feature Selection Approach for Text Categorization by Using Chaos Optimization and Genetic Algorithm

Hao Chen,¹ Wen Jiang,² Canbing Li,³ and Rui Li¹

¹ School of Information Science and Engineering, Hunan University, Changsha 410082, China

² School of Software, Hunan Vocational College of Science and Technology, Changsha 410118, China

³ College of Electrical and Information Engineering, Hunan University, Changsha 410082, China

Correspondence should be addressed to Hao Chen; xschenhao@139.com

Received 10 October 2013; Revised 13 November 2013; Accepted 17 November 2013

Academic Editor: Gelan Yang

Copyright © 2013 Hao Chen et al. This is an open access article distributed under the Creative Commons Attribution License, which permits unrestricted use, distribution, and reproduction in any medium, provided the original work is properly cited.

Due to the era of Big Data and the rapid growth in textual data, text classification becomes one of the key techniques for handling and organizing the text data. Feature selection is the most important step in automatic text categorization. In order to choose a subset of available features by eliminating unnecessary features to the classification task, a novel text categorization algorithm called chaos genetic feature selection optimization is proposed. The proposed algorithm selects the optimal subsets in both empirical and theoretical work in machine learning and presents a general framework for text categorization. Experimental results show that the proposed algorithm simplifies the feature selection process effectively and can obtain higher classification accuracy with a smaller feature set.

1. Introduction

Due to the era of Big Data and the rapid growth in textual data, feature selection (FS) is very important for organizing the data. Feature selection is also called attribute selection. Feature selection is a key step in automatic text categorization and machine learning systems, which automatically assigns the documents to a set of predefined classes based on their textual content. It is well known that feature selection is often used to deal with a high dimensional space of features whose main objective is to simplify a dataset by reducing its dimensionalities and identifying relevant underlying features. In the practical application of machine learning, the number of features which exist irrelevant and interdependent features usually very large. It easily leads to the following consequences. Firstly, there is more time consumption in features analysis and model training when the number of features is increasing. Secondly, it easily leads to “curse of dimensionality” when the number of features is increasing and results in the model becoming more complicated. Feature selection has been widely applied to various fields including

text categorization [1], signal processing [2], data mining [3], machine learning [4], neural networks, and pattern recognition [5].

Given a feature set $X = \{X_1, \dots, X_n\}$ with size n , there exist 2^n possible feature subsets and each feature subset is represented by a binary vector of dimension n . The FS problem is to find a minimal feature subset of size k ($k < n$) while retaining a suitably high accuracy in representing the original features [6]. As redundant features will affect the system classification accuracy and increase the computation time, we should eliminate the features with little information and ignore the redundant features that are strongly correlated. Feature selection can effectively deal with the problem because of its flexibility, computational efficiency, and capacity to handle high dimensional data [7].

In order to choose a subset of available features by eliminating unnecessary features to the categorization task, this paper makes use of FS method, together with machine learning knowledge, and proposes a novel heuristic algorithm for feature selection called chaos genetic feature selection optimization (CGFSO). Chaos is universal phenomenon in

many nonlinear systems that exhibits sensitive dependence on initial conditions and includes infinite unstable periodic motions [8]. Chaotic optimization algorithm (COA) first changes optimized variables into chaotic variables, examines each point in the entire solution space by change rule of chaotic variables, and accepts the better point as the present optimum solution [9]. Then, it takes the present optimum solution as the kernel and goes on searching the optimum solution by affixing a perturbation until the requirements are met. CGFSO algorithm is applied to text features of bag of words model in which a document is considered as a set of words or terms and each position in the input feature vector corresponds to a given term in original document. The proposed algorithm selects the optimal subsets in both empirical and theoretical work in machine learning and presents a general framework for text categorization. Compared with other existing algorithms, the proposed algorithm simplifies the feature selection process effectively and can obtain higher classification accuracy with a smaller feature set.

The rest of this paper is organized as follows. Section 2 discusses on the prior research on feature selection. Section 3 proposes the CGFSO algorithm. Section 4 shows the experimental results and finally some conclusions are pointed out and future works are offered in Section 5.

2. Related Works

In this section we focus our discussion on the prior research on feature selection. Many scholars at home and abroad have made great contributions to the feature selection in both empirical and theoretical work, which are necessary and sufficient for solving the text categorization problem.

In order to achieve minimum classification error, Kanan and Faez [10] presented an improved ant colony optimization algorithm for feature selection in face recognition. Their algorithm can select the optimal feature subset in terms of shortest feature length and the best performance of classifier. Cao et al. [11] further developed this method by learning feature weights in kernel spaces. The proposed algorithm was often done as a data processing step, independent of classifier construction. To address the problem of jointly learning SVM (support vector machine) parameters and kernels, Zhen et al. [12] proposed a method for choosing SVM parameters including the parameters of kernels by minimizing the leave-one-out cross validation error.

Genetic algorithm (GA) is a parallel heuristic intelligent method, which is a popular technology for nonlinear optimization problem. Due to the advantages of GA, GA has been widely used an effective tool for FS in text categorization. Zhu et al. [13] proposed a combined feature subset selection method, called RICGA (Relief immune clonal genetic algorithm) based on the Relief algorithm, immune clonal algorithm, and GA. In the RICGA method, the paper first use Relief to get rid of irrelevant features then apply a modified genetic algorithm to acquire the finally feature subset. In order to extract feature set, Kim et al. [14] applied genetic algorithm to the feature selection problem and proposed a novel genetic algorithm feature selection (GAFS). Muni et al. [15] presented an online feature

selection algorithm using genetic programming (GP). The proposed GP method simultaneously selected a good subset of features and constructed a classifier using the selected features. Waqas et al. [16] focused on multiobjective genetic algorithms for solving feature subset selection. The research showed that independent subsets of features are excellent in accuracy. AlSukker et al. [17] presented a novel modified genetic algorithm based on enhanced population diversity, parents' selection, and improved genetic operators. Practical results indicated the significance of the proposed GA variant in comparison to many other algorithms from the literature on different datasets. Mahrooghy et al. [18] employed filter-based feature selection genetic algorithm (FFSGA) to find an optimal set of features where redundant and irrelevant features are removed. The entropy index fitness function was used to evaluate the feature subsets. The results showed that using the feature selection technique not only improves the equitable threat score by almost 7% at some threshold values for the winter season, but also extremely decreases the dimensionality.

3. Application of CGFSO Algorithm

In this section, we focus our discussion on algorithms that explicitly attempt to select an optimal feature subset. It is usually difficult to obtain an optimal feature subset and has been proven to be NP-hard. Therefore, lots of heuristic algorithms have been used to perform feature selection of training including genetic algorithms, neural networks, and simulated annealing. In order to avoid the combinatorial search problem to find an optimal subset of m features, the most popular feature selection methods is the application of genetic algorithm, which always provide a suboptimal solution.

Although GA has a powerful quality of global search, it is liable to raise the problem of prematurely convergence in the practical application and has low search efficiency in the late evolving period [19]. Chaos movement can nonrepeatedly cover all state in a certain range, according to its own rules [20]. COA shows a promising performance on nonlinear function optimization. However, the local search capability of COA is poor since its heuristic and stochastic properties often suffer from getting stuck in local optima. Thus, this paper takes advantage of the merit of GA and COA and a novel FS algorithm for text categorization; namely, CGFSO is proposed. The experimental results show that the proposed CGFSO finds subsets that result in the best accuracy, while finding compact feature subsets and performing faster than other traditional methods.

3.1. Chaotic Optimization Algorithm. COA is a novel approach of global optimization that has attracted widespread attention in recent years. In the COA, the well-known logistic map is normally described as follows:

$$x_{n+1} = \mu x_n (1 - x_n), \quad (1)$$

where μ is a control parameter, which cannot be bigger than 4, and x is a variable. It is easy to find that (1) is a deterministic dynamic system without any stochastic disturbance. When

$\mu = 4$ ($0 \leq x_0 \leq 1$), the system above is completely in chaos state.

The basic process of chaos optimization algorithm generally includes two major steps. Firstly, define a chaotic sequences generator based on the logistic map. Generate a sequence of chaotic points and map it to a sequence of design points in the original design space. COA has a very sensitive dependence upon its initial condition and parameter. Chaotic sequences have been adopted instead of random sequences and somewhat good results have been shown in many applications. Then, calculate the objective function based on the generated design points, and choose the point with the minimum objective function as the current optimum. Secondly, the current optimum is assumed to be close to the global optimum after certain iterations, and it is viewed as the consult point with a little chaotic perturbation and explores the descent direction along axis directions in order. Repeat the above two steps until some specified convergence criterion is satisfied, then the global optimum is obtained. However, further numerical simulation showed that the method is effective only in small design space.

3.2. Chaos Genetic Feature Selection Optimization. Generally, a text categorization system consists of several essential parts including feature extraction and feature selection [21, 22]. In the feature selection stage can be used with the proposed algorithms to obtain a feature subset that allows the increase of the classification system accuracy and simplicity, and the reduction of the learning efforts. CGFSO is used to explore the space of all subsets of given feature set. The performance of selected feature subsets is measured by invoking an evaluation function with the corresponding reduced feature space and measuring the specified classification result. Firstly, generating a feature subset from the given feature set, then using the evaluation function to evaluate the feature subset. Evaluation results are compared with the stopping criterion, if the result of the evaluation is better than stopping criterion, then CGFSO algorithm automatically stops. Otherwise, CGFSO algorithm continues to produce the next feature subset. Feature subsets elected general also verify its validity.

In CGFSO algorithm, each individual in the population represents a candidate solution to the feature selection problem [23]. The first thing to consider is the algorithm coding problem, and we set the number of features as the length of chromosomes. If the individual (chromosome) a is represented as a string $a_1 a_2 \dots a_i \dots a_n$, each gene a_i corresponds to the i th feature. If $a_i = 1$, it means that the corresponding feature is selected. If $a_i = 0$, it indicates that the i th feature is ignored.

The solution quality in terms of classification accuracy is evaluated by classifying the training data sets using the selected features. Classification accuracy and feature cost are the two key factors used to design a fitness function. The test accuracy measures the number of examples that are correctly classified. Thus, the individual who has high classification accuracy and low total feature cost produces a high fitness value. The individual with high fitness value has high probability to be selected to the next generation. A solution obtaining higher accuracy and with fewer features

will get a greater quality function value. Therefore, the fitness function can be defined as follows:

$$f(x) = \sqrt{\text{Precision}(x)^2 + \text{Recall}(x)^2} - \lambda \times \frac{\delta(x) \times \cos t(x)}{\text{Precision}(x) + \text{Recall}(x) + 1} + \cos t_{\max}, \quad (2)$$

where $\text{Precision}(x)$ is the test precision ratio, $\text{Recall}(x)$ is the test recall ratio, $\cos t(x)$ is the sum of measurement costs of the feature subset represented by x , and λ ($0 \leq \lambda \leq 1$) is the adjustment coefficient. $\cos t_{\max}$ is an upper bound on the costs of candidate solutions. In this case, $\cos t_{\max}$ is simply the sum of the costs associated with all of the features. $\delta(x) = 1$ indicates that feature x is selected; otherwise, $\delta(x) = 0$ indicates that feature x is ignored.

The main steps of the CGFSO algorithm can be summarized as follows.

Step 1. Give the population size $PopSize$, the crossover probabilities p_c , the mutation probabilities p_m , and the termination generation G_m . Then randomly initialize the initial population $P(k)$, and set evolution generation $k = 0$.

Step 2. Evaluate the fitness of initial population $P(k)$ according to objective function.

Step 3. Select $PopSize/5$ individuals with larger fitness to the next generation population $P(k+1)$.

Step 4. Perform the crossover operation for $P(k)$ to generate $Q(k)$.

Step 5. Perform logistic chaotic mutation for the population $Q(k)$ to generate the population $L(k)$.

Step 6. Compute individual fitness after logistic chaotic mutation. If the fitness value after mutation is larger than the old one, then substitute the old one with it, and obtain the next generation population $P(k+1) = Q(k) \cup L(k)$.

Step 7. $k = k + 1$; if stopping conditions are satisfied, the algorithm ends, and then output the best feature subset; otherwise, go back to Step 2 until the maximum evolution iterations are completed.

4. Experimental Results

In this section, a series of simulation experiments were conducted to show the effectiveness and superiority of the CGFSO algorithm for text categorization problems. In order to provide an overview on the base accuracy of the classifiers, the Reuters collection was taken in our experiments. We use Reuters-21567 that are 5213 documents in training set and 2016 documents in test set and adopt the top ten classes. Experimental platform use Dell computer with CPU Xeon 3.06 GHz (24P8122) and 2 GB of RAM. We implement the proposed CGFSO algorithm and other two FS methods such as GA and SVM; that is, the parameters of CGFSO and GA are set as follows: the size of the population is 100, the maximum

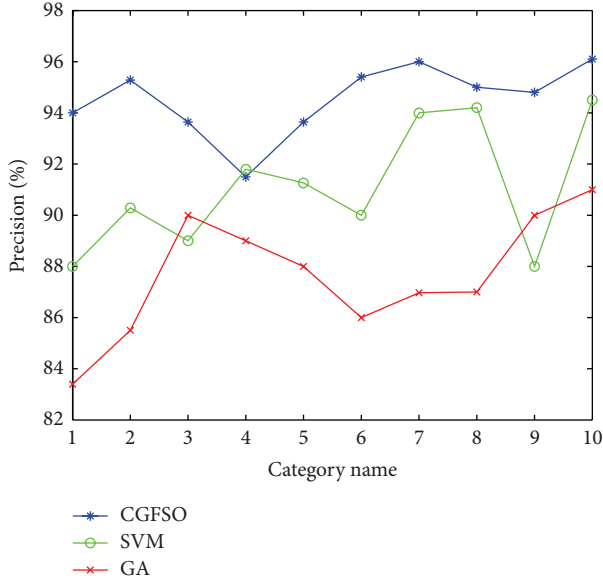


FIGURE 1: The precision of the three feature selection algorithms.

number of generations is 500, crossover probability is 0.7, and mutation probability is 0.2. Since the experimental result depend on the population randomly generated by the CGFSO and GA algorithms, so we have performed 20 simulations on each data set.

4.1. Precision and Recall. In most text categorization, the performance of feature selection techniques is particularly important. Several norms such as precision and recall are often used to evaluate the performance of feature selection algorithm. Precision is defined as the ratio of correct topic cases to the total predicted topic cases. Recall is defined as the proportion of the correct topic cases to the total cases. Precision and recall are defined as follows.

Definition 1. Assume that TP_i represents the number of test documents correctly classified under i th category (C_i) and FP_i denotes the number of test documents incorrectly classified C_i ; then classification precision can be formulated as

$$\text{Precision}(i) = \frac{TP_i}{TP_i + FP_i}. \quad (3)$$

Definition 2. Assume that TP_i represents the number of test documents correctly classified under i th category (C_i), and FN_i is the number of test documents incorrectly classified under other categories; these probabilities may be estimated in terms of the contingency table for C_i ; then classification recall can be formulated as

$$\text{Recall}(i) = \frac{TP_i}{TP_i + FN_i}. \quad (4)$$

4.2. Simulation Experiment. To analyse the performance of the feature selection algorithms, we will show the results obtained using the proposed approach. Figures 1-5 show the

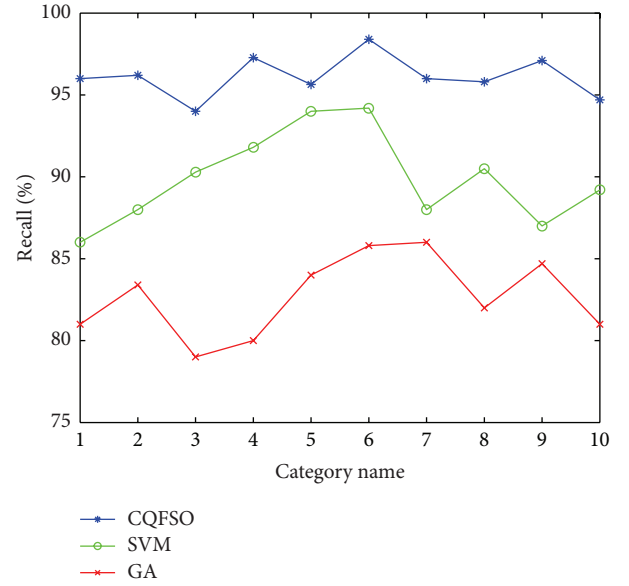


FIGURE 2: The recall of the three feature selection algorithms.

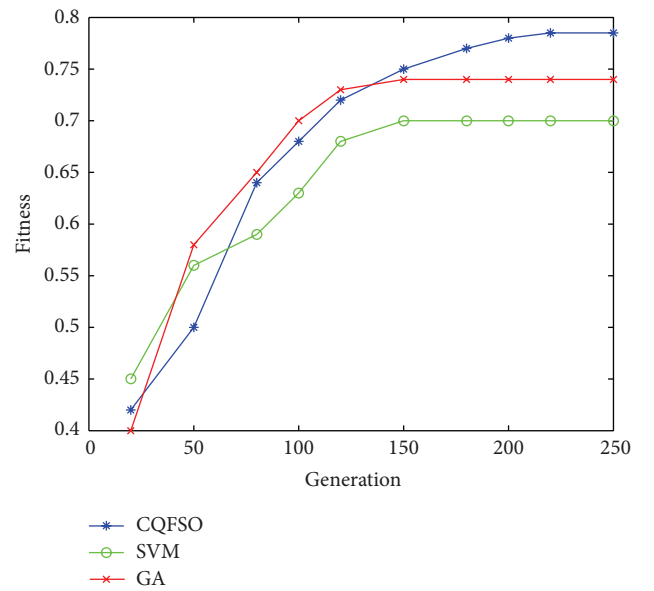


FIGURE 3: The fitness value of the three feature selection algorithms.

performance of our proposed method against the GA and SVM for the ten most frequent categories with respect to classification accuracy. Figure 1 is the precision of GA, SVM, and CGFSO with different categories. Figure 2 shows the recall of the GA, SVM, and CGFSO. Figure 3 shows the average fitness in the solutions obtained by the algorithms GA, SVM, and CGFSO. Figure 4 is the precision of GA, SVM, and CGFSO with different number of features. Figure 5 is the recall of GA, SVM, and CGFSO with different number of features.

From the experimental result in Figure 1, it can be seen that the precision of CGFSO is the highest in most cases and its maximum value is close to 96%. However, the precision

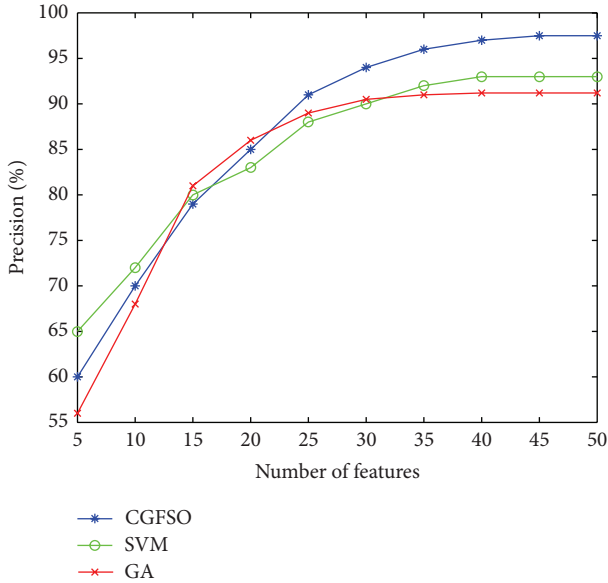


FIGURE 4: The precision of algorithms with different number of features.

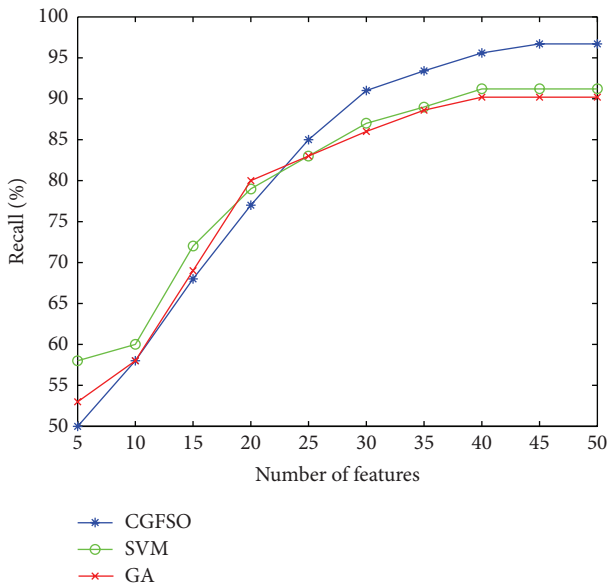


FIGURE 5: The recall of algorithms with different number of features.

of GA is relatively minimal and its minimum value is close to 83.1%. From the experimental results in Figure 2, it can be seen that CGFSO is significantly better than the other two algorithms in the aspect of recall. The maximum recall of CGFSO is close to 98%. However, the recall of GA is relatively minimal and its minimum value is close to 78.5%. From the experimental results in Figures 1 and 2, we can easily see that CGFSO algorithm can obtain better performance with a smaller feature set than other two algorithms, especially in the aspect of recall.

From the experimental results in Figure 3, the average fitness of CGFSO is the highest in most cases and its

maximum value is close to 0.78. The performance of SVM and GA is relatively close. Because CGFSO effectively combines the advantages of chaos optimization algorithm and genetic algorithm, and effectively expands the range of feasible solution. When a gradual increase is in the number of features, the precision and recall of the three feature selection algorithms are gradually increased. As can be seen from Figures 4 and 5, the overall performance of CGFSO is significantly superior to GA and SVM. It is worth noting that our approach has the least number of support vectors compared with other feature selection approaches.

It can be seen from the experimental results that CGFSO learning process effectively and efficiently reduces the complexity of the system in the feature selection stage.

5. Conclusions

Due to the era of Big Data and the rapid growth in textual data, text classification has become a way to process and organize the text data. In order to achieve the goal of this paper, we designed a new text classification algorithm based on genetic algorithm and chaotic optimization algorithm. The experimental results show that the CQFSO yields the best result of these three methods. The experiment also demonstrated that the CQFSO yields better accuracy even with a large data set since it achieved better performance with the lower number of features. In the future, we will design a new heuristic feature selection algorithm, apply it to text classification field, and will involve experiments with other kinds of datasets.

Acknowledgment

This work is partially supported by the National Science Foundation of China under Grant nos. 61370226 and 61272546.

References

- [1] M. H. Aghdam, N. Ghasem-Aghaee, and M. E. Basiri, "Application of ant colony optimization for feature selection in text categorization," in *Proceedings of the IEEE Congress on Evolutionary Computation (CEC '08)*, pp. 2867–2873, IEEE Press, Hong Kong, June 2008.
- [2] T. W. Liao, "Feature extraction and selection from acoustic emission signals with an application in grinding wheel condition monitoring," *Engineering Applications of Artificial Intelligence*, vol. 23, no. 1, pp. 74–84, 2010.
- [3] P. E. N. Lutu and A. P. Engelbrecht, "A decision rule-based method for feature selection in predictive data mining," *Expert Systems with Applications*, vol. 37, no. 1, pp. 602–609, 2010.
- [4] S. Nemati, M. E. Basiri, N. Ghasem-Aghaee, and M. H. Aghdam, "A novel ACO-GA hybrid algorithm for feature selection in protein function prediction," *Expert Systems with Applications*, vol. 36, no. 10, pp. 12086–12094, 2009.
- [5] S. M. Awaidah and S. A. Mahmoud, "A multiple feature/resolution scheme to Arabic (Indian) numerals recognition using hidden Markov models," *Signal Processing*, vol. 89, no. 6, pp. 1176–1184, 2009.

- [6] S.-W. Lin, K.-C. Ying, S.-C. Chen, and Z.-J. Lee, "Particle swarm optimization for parameter determination and feature selection of support vector machines," *Expert Systems with Applications*, vol. 35, no. 4, pp. 1817–1824, 2008.
- [7] T. Peters, D. W. Bulger, T.-H. Loi, J. Y. H. Yang, and D. Ma, "Two-step cross-entropy feature selection for microarrays-power through complementarity," *IEEE/ACM Transactions on Computational Biology and Bioinformatics*, vol. 8, no. 4, pp. 1148–1151, 2011.
- [8] H.-J. Lu, H.-M. Zhang, and L.-H. Ma, "New optimization algorithm based on chaos," *Journal of Zhejiang University SCIENCE A*, vol. 7, no. 4, pp. 539–542, 2006.
- [9] C.-G. Fei and Z.-Z. Han, "A novel chaotic optimization algorithm and its applications," *Journal of Harbin Institute of Technology*, vol. 17, no. 2, pp. 254–258, 2010.
- [10] H. R. Kanan and K. Faez, "An improved feature selection method based on ant colony optimization (ACO) evaluated on face recognition system," *Applied Mathematics and Computation*, vol. 205, no. 2, pp. 716–725, 2008.
- [11] B. Cao, D. Shen, J.-T. Sun, Q. Yang, and Z. Chen, "Feature selection in a kernel space," in *Proceedings of the 24th International Conference on Machine Learning (ICML '07)*, pp. 121–128, June 2007.
- [12] Z. Zhen, X. Zeng, H. Wang, and L. Han, "A global evaluation criterion for feature selection in text categorization using Kullback-Leibler divergence," in *Proceedings of the International Conference of Soft Computing and Pattern Recognition (SoCPaR '11)*, pp. 440–445, October 2011.
- [13] Y. Zhu, X. Shan, and J. Guo, "Modified genetic algorithm based feature subset selection in intrusion detection system," in *Proceedings of the IEEE International Symposium on Communications and Information Technology (ISCIT '05)*, pp. 10–13, IEEE Computer Society, Wuhan China, October 2005.
- [14] H.-D. Kim, C.-H. Park, H.-C. Yang, and K.-B. Sim, "Genetic algorithm based feature selection method development for pattern recognition," in *SICE-ICASE International Joint Conference*, pp. 1020–1025, October 2006.
- [15] D. P. Muni, N. R. Pal, and J. Das, "Genetic programming for simultaneous feature selection and classifier design," *IEEE Transactions on Systems, Man, and Cybernetics, Part B*, vol. 36, no. 1, pp. 106–117, 2006.
- [16] K. Waqas, R. Baig, and S. Ali, "Feature subset selection using multi-objective genetic algorithms," in *Proceedings of the 13th IEEE International Multitopic Conference (INMIC '09)*, pp. 1–6, December 2009.
- [17] A. AlSukker, R. N. Khushaba, and A. Al-Ani, "Enhancing the diversity of genetic algorithm for improved feature selection," in *Proceedings of the IEEE International Conference on Systems, Man and Cybernetics (SMC '10)*, pp. 1325–1331, October 2010.
- [18] M. Mahrooghy, H. Y. Nicolas, G. A. Valentine, A. James, and Y. Shantia, "On the use of the genetic algorithm filter-based feature selection technique for satellite precipitation estimation," *IEEE Geoscience and Remote Sensing Letters*, vol. 9, no. 5, pp. 963–967, 2012.
- [19] M. E. ElAlami, "A filter model for feature subset selection based on genetic algorithm," *Knowledge-Based Systems*, vol. 22, no. 5, pp. 356–362, 2009.
- [20] S. Han, W. Pedrycz, and C. Han, "Nonlinear channel blind equalization using hybrid genetic algorithm with simulated annealing," *Mathematical and Computer Modelling*, vol. 41, no. 6-7, pp. 697–709, 2005.
- [21] H. Kim, P. Rowland, and H. Park, "Dimension reduction in text classification with support vector machines," *Journal of Machine Learning Research*, vol. 6, pp. 37–53, 2005.
- [22] E. S. Correa, M. T. A. Steiner, A. A. Freitas, and C. Carnieri, "A genetic algorithm for solving a capacitated p -median problem," *Numerical Algorithms*, vol. 35, no. 2–4, pp. 373–388, 2004.
- [23] I.-S. Oh, J.-S. Lee, and B.-R. Moon, "Hybrid genetic algorithms for feature selection," *IEEE Transactions on Pattern Analysis and Machine Intelligence*, vol. 26, no. 11, pp. 1424–1437, 2004.

Research Article

Unsupervised Optimal Discriminant Vector Based Feature Selection Method

Su-Qun Cao^{1,2} and Jonathan H. Manton²

¹ Faculty of Mechanical Engineering, Huaiyin Institute of Technology, Huai'an 223003, China

² Department of Electrical and Electronic Engineering, University of Melbourne, Victoria, VIC 3010, Australia

Correspondence should be addressed to Su-Qun Cao; caosuqun@hyit.edu.cn

Received 22 July 2013; Accepted 21 September 2013

Academic Editor: Baochang Zhang

Copyright © 2013 S.-Q. Cao and J. H. Manton. This is an open access article distributed under the Creative Commons Attribution License, which permits unrestricted use, distribution, and reproduction in any medium, provided the original work is properly cited.

An efficient unsupervised feature selection method based on unsupervised optimal discriminant vector is developed to find the important features without using class labels. Features are ranked according to the feature importance measurement based on unsupervised optimal discriminant vector in the following steps. First, fuzzy Fisher criterion is adopted as objective function to derive the optimal discriminant vector in unsupervised pattern. Second, the feature importance measurement based on elements of unsupervised optimal discriminant vector is defined to determine the importance of each feature. The features with little importance measurement are removed from the feature subset. Experiments on UCI dataset and fault diagnosis are carried out to show that the proposed method is very efficient and able to deliver reliable results.

1. Introduction

Feature selection (FS) has become an active research topic in the area of pattern recognition, machine learning, data mining, intelligent fault diagnosis, and so forth. It is performed to choose a subset of the original features by removing redundant and noisy features from high-dimensional datasets in order to reduce computational cost, increase the classification accuracy, and improve result comprehensibility.

In the supervised FS algorithms, since class labels are available in supervised learning, various feature subsets are evaluated using some function of prediction accuracy to select only those features which are related to or lead to the decision classes of the data under consideration. There are numerous supervised feature selection methods [1–7] such as Fisher criterion [1, 2], Relief [3], and Relief-F [4].

However, for many existing datasets, class labels are often unknown or incomplete because large amounts of data make it difficult for humans to manually label the categories of each instance. Moreover, human labeling is expensive and subjective. Thus, it indicates the significance of unsupervised dimensionality reduction. Principal component analysis (PCA) [8] is often used in unsupervised pattern. However,

PCA creates new features or principal components which are functions of original features. It is difficult to obtain intuitive understanding of the data using the new features only. Some unsupervised feature selection methods [8–14] have been proposed such as SUD [9]. SUD, which is a sequential backward selection algorithm to determine the relative importance of variables for Unsupervised Data, uses entropy similarity measurement to determine the importance of features with respect to the underlying clusters.

It is known to us that the famous Fisher criterion which can derive optimal discriminant vector is commonly used to realize feature dimension reduction in supervised pattern. In the unsupervised pattern, how to overcome the lack of the class information to realize feature selection is a worthy topic.

2. An Overview of Optimal Discriminant Vector

Fisher criterion is a discriminant criterion function that was first proposed by Fisher. It is based on the between-class scatter and the within-class scatter. By maximizing this criterion, one can obtain an optimal discriminant vector.

After the sample is projected to this vector, the within-class scatter is minimized and the between-class scatter is maximized [15].

Given c pattern classes $X^{(i)} = [x_i^1, x_i^2, \dots, x_i^{N_i}]$ in the pattern set which contains N d -dimensional patterns, where $i = 1, 2, \dots, c$, N_i is the number of all the patterns in the i th class; thus, $N = N_1 + N_2 + \dots + N_c$. Fisher criterion is defined as follows:

$$J_{FC}(\omega) = \frac{\omega^T S_b \omega}{\omega^T S_w \omega}, \quad (1)$$

where S_b is the between-class scatter matrix denoted by

$$S_b = \sum_{i=1}^c \frac{N_i}{N} (m_i - \bar{x})(m_i - \bar{x})^T, \quad (2)$$

and S_w is the within-class scatter matrix denoted by

$$S_w = \frac{1}{N} \sum_{i=1}^c \sum_{j=1}^{N_i} (x_j^i - m_i)(x_j^i - m_i)^T, \quad (3)$$

where m_i denotes the mean of the i th class, and \bar{x} denotes the mean of all the patterns in the pattern set.

In order to seek an optimal discriminant vector ω by maximizing the Fisher criterion, the optimal discriminant vector ω^* can be obtained by solving the following eigen-system equation:

$$S_w^{-1} S_b \omega^* = \lambda \omega^*, \quad (4)$$

where λ is diagonal and consists of the corresponding eigenvalues. When the inverse of S_w exists, ω^* can be obtained by the maximum eigenvalue of $S_w^{-1} S_b$.

3. Unsupervised Optimal Discriminant Vector Based Feature Selection Method

Fisher criterion mentioned above can only be used in supervised pattern. This means that traditional optimal discriminant vector cannot be calculated directly by the unlabeled samples. Cao et al. [16] introduce fuzzy theory into Fisher criterion and define fuzzy Fisher criterion. Maximizing this criterion cannot only realize clustering but also obtain optimal discriminant vector.

Suppose that the membership function $u_{ij} \in [0, 1]$ with $\sum_{i=1}^c u_{ij} = 1$ for all j and the fuzzy index $m > 1$ is a given real value, where u_{ij} denotes the degree of the j th d -dimensional pattern belonging to the i th class; we can define the following fuzzy within-class scatter matrix S_{fw} :

$$S_{fw} = \sum_{i=1}^c \sum_{j=1}^N u_{ij}^m (x_j - m_i)(x_j - m_i)^T \quad (5)$$

and the following fuzzy between-class scatter matrix S_{fb} :

$$S_{fb} = \sum_{i=1}^c \sum_{j=1}^N u_{ij}^m (m_i - \bar{x})(m_i - \bar{x})^T. \quad (6)$$

Thus, we can derive fuzzy Fisher criterion as follows:

$$J_{FFC} = \frac{\omega^T S_{fb} \omega}{\omega^T S_{fw} \omega}. \quad (7)$$

It is obvious that maximizing J_{FFC} directly in (7) is not a trivial task due to the existence of its denominator. However, we can reasonably relax this problem by applying the following Lagrange multipliers; λ and β_j ($j = 1, 2, \dots, n$) together with the constraint $\sum_{i=1}^c u_{ij} = 1$ to (7):

$$F = \omega^T S_{fb} \omega - \lambda \omega^T S_{fw} \omega + \sum_{j=1}^N \beta_j \left(\sum_{i=1}^c u_{ij} - 1 \right). \quad (8)$$

Setting $\partial F / \partial \omega$ to be zero, we have

$$S_{fw}^{-1} S_{fb} \omega = \lambda \omega, \quad (9)$$

where ω is the eigenvector belonging to the largest eigenvalue λ of $S_{fw}^{-1} S_{fb}$.

Setting $\partial F / \partial m_i$ to be zero, we have

$$m_i = \frac{\sum_{j=1}^N u_{ij}^m (x_j - (1/\lambda) \bar{x})}{\sum_{j=1}^N u_{ij}^m (1 - (1/\lambda))}. \quad (10)$$

Here, m_i is a local maximum of F [17] proved in Appendix.

Setting $\partial F / \partial u_{ij}$ to be zero, we have

$$u_{ij} = \frac{(\omega^T (x_j - m_i)(x_j - m_i)^T \omega - (1/\lambda) \omega^T (m_i - \bar{x})(m_i - \bar{x})^T \omega)^{-1/(m-1)}}{\sum_{k=1}^c (\omega^T (x_j - m_k)(x_j - m_k)^T \omega - (1/\lambda) \omega^T (m_k - \bar{x})(m_k - \bar{x})^T \omega)^{-1/(m-1)}}. \quad (11)$$

When (11) is used, as stated previously, u_{ij} should satisfy $u_{ij} \in [0, 1]$; hence, in order to satisfy this constraint, we let $u_{ij} = 1$ and $u_{i'j} = 0$ for all $i' \neq i$, if

$$\omega^T (x_j - m_i)(x_j - m_i)^T \omega \leq \frac{1}{\lambda} \omega^T (m_i - \bar{x})(m_i - \bar{x})^T \omega. \quad (12)$$

With the above discussion, we can obtain the optimal discriminant vector ω in unsupervised pattern and then do feature selection based on ω . Now, let us illustrate this by the following experiment on 2-dimensional artificial dataset.

Figure 1 contains 168 2-dimensional samples. Through maximizing fuzzy Fisher criterion, we can obtain 2-class clustering result shown as red points and blue points, respectively, and can also get the vector $\omega = (\omega_1, \omega_2)' = (0.4562, -0.8899)'$ shown as a line in Figure 2. We project all samples to x -axis and y -axis. It is obvious that projective points in x -axis from different class are overlapping while those in y -axis are separated well. It means that Y feature is more important than X feature for leading to the decision classes. This is consistent with $|\omega_2| > |\omega_1|$ which gives us a revelation that we can apply the vector ω for feature selection.

Suppose $\omega = (\omega_1, \omega_2, \dots, \omega_d)'$; we define f_k as the k single feature importance measurement for comparison:

$$f_k = \frac{|\omega_k|}{\sum_{k=1}^d |\omega_k|}. \quad (13)$$

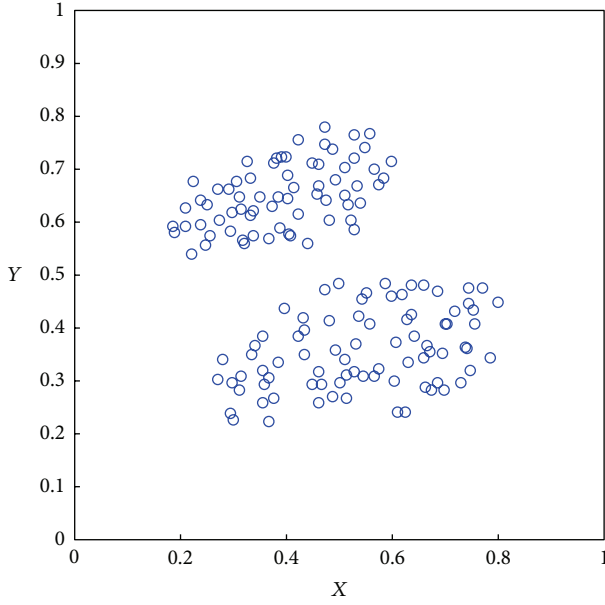
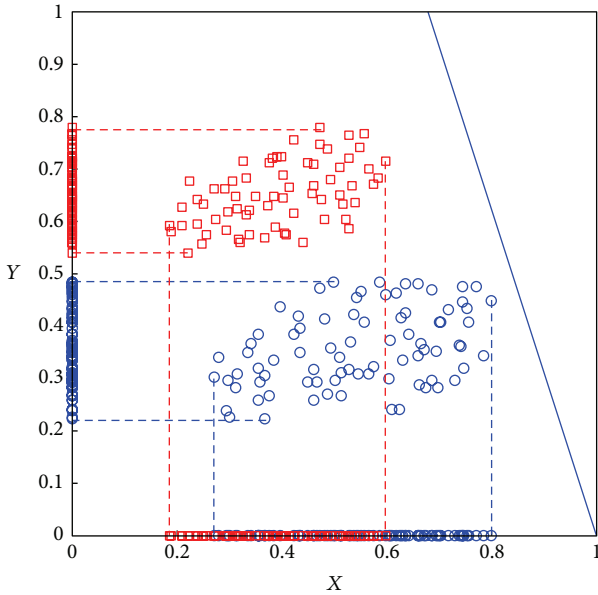


FIGURE 1: 2-dimensional artificial dataset.


 FIGURE 2: The clustering result based on fuzzy Fisher criterion (the solid line is the optimal discriminant vector ω).

To the above artificial dataset, $f_1 = 0.3389$ is the importance measurement of X feature and $f_2 = 0.6611$ is the importance measurement of Y feature.

Proposed Method

Step 1. Set the given threshold ε or the number of iterations α ; initialize $U = [\mu_{ij}]_{c \times N}$ and $m = (m_1, m_2, \dots, m_c)$ using K -means.

Step 2. Compute S_{fw}, S_{fb} using (5), (6), respectively.

Step 3. Compute the largest eigenvalue λ and the corresponding ω using (9).

Step 4. Update m_i and μ_{ij} using (10), (11), and (12), respectively.

Step 5. Compute J_{FFC} .

Step 6. If $J_{\text{FFC}} < \varepsilon$ or the number of iterations $\geq \alpha$, go to Step 7; otherwise go to Step 2.

Step 7. Compute the feature importance measurements which are normalized as f_k . Then sort f_k by the descending order.

Step 8. Set the feature importance threshold θ .

Step 9. Find a feature subset size d_θ which is a minimize number making $\sum_{k=1}^{d_\theta} f_k$ no less than the threshold θ .

Step 10. Choose d_θ features corresponding to the sorted f_k in the descending order, that is, f_k ($k = 1, 2, \dots, d_\theta$), as the selected features and then terminate.

Different feature importance threshold θ leads to different feature subset size. In Step 7 of proposed method, features have already been sorted by the descending order. If the feature subset size d_θ is given from the start, we can simply select the first d_θ features. But if d_θ is not given, we can use θ to determine the feature subset size. The bigger θ is, the larger d_θ is. The recommended range of θ is from 0.8 to 0.95.

4. Experimental Results

4.1. Feature Selection on UCI Dataset Wine. In this experiment, the benchmarking UCI dataset *Wine* [18] was chosen to test the feature selection effectiveness of SUD, Relief-F and our method. We use the following Rand index [19] to evaluate the clustering performance of the dimension reduction data:

$$\text{Rand}(P_1, P_2) = \frac{a + b}{n \times (n - 1) / 2}, \quad (14)$$

where P_1, P_2 denote the clustering results for the original dataset without noise and the corresponding noisy dataset, a denotes the number of any two patterns in the original dataset belonging to the same cluster in P_1, P_2 , b denotes the number of any two patterns in the original dataset belonging to two different clusters in P_1, P_2 , and n is the number of all patterns in the original dataset. Obviously, $\text{Rand}(P_1, P_2) \in [0, 1]$. And $\text{Rand}(P_1, P_2) = 1$ when P_1 is the same as P_2 . The smaller $\text{Rand}(P_1, P_2)$, the bigger the difference between P_1 and P_2 . In other words, the corresponding algorithm has less robust capability in this case.

Table 1 illustrates the basic information of the dataset. We choose 130 samples which belong to class 1 and class 2 as testing dataset. The parameters for the proposed method are set as follows:

$$\varepsilon = 0.001, \quad \alpha = 20, \quad \theta = 0.90. \quad (15)$$

TABLE 1: Class distribution and features of *Wine* dataset.

Class	Number of samples	Features	
		Number	Name
Class 1	59	1	Alcohol
Class 2	71	2	Malic acid
Class 3	48	3	Ash
		4	Alcalinity of ash
		5	Magnesium
		6	Total phenols
		7	Flavanoids
		8	Nonflavanoid phenols
		9	Proanthocyanins
		10	Color intensity
		11	Hue
		12	OD280/OD315 of diluted wines
		13	Proline

TABLE 2: The feature importance measurement of *Wine* dataset.

Number	Number of features	The feature importance measurement f_k	$\sum_{k=1}^{d_\theta} f_k$
1	3	0.3180	0.3180
2	1	0.2709	0.5889
3	12	0.1793	0.7682
4	7	0.0520	0.8202
5	8	0.0445	0.8647
6	11	0.0364	0.9011
7	10	0.0301	0.9312
8	9	0.0243	0.9555
9	4	0.0241	0.9796
10	6	0.0088	0.9884
11	2	0.0057	0.9941
12	5	0.0049	0.9990
13	13	0.0009	0.9999

Table 2 lists the importance measurement of every feature computed by the proposed method. Due to the threshold θ , 6 features will be selected from original features. Figure 3 shows the Rand index values corresponding to the number of features using SUD, Relief-F and our method.

From Figure 3, we can easily find that data selected features by the proposed method have the best clustering result among these three algorithms.

4.2. Feature Selection for Fault Diagnosis. The steel plates faults dataset used in this experiment was donated by Semeion, Research Center of Sciences of Communication, Via Sersale 117, Rome, Italy [20, 21]. It classifies steel plates' faults into 7 different types: Pastry, Z_Scratch, K_Scratch, Stains, Dirtiness, Bumps, and Other_Faults. The dataset

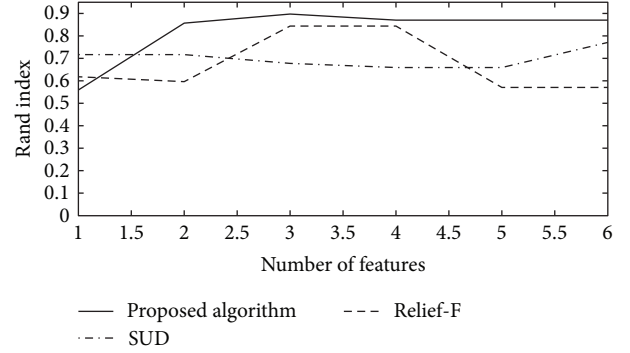


FIGURE 3: Rand index values corresponding to the number of features.

TABLE 3: Class distribution and features of steel plates dataset.

Class	Number of samples	Features	
		Number	Name
Pastry	158	1	X_Minimum
Z_Scratch	190	2	X_Maximum
K_Scratch	391	3	Y_Minimum
Stains	72	4	Y_Maximum
Dirtiness	55	5	Pixels_Areas
Bumps	402	6	X_Perimeter
Other_Faults	673	7	Y_Perimeter
		8	Sum_of_Luminosity
		9	Minimum_of_Luminosity
		10	Maximum_of_Luminosity
		11	Length_of_Conveyer
		12	TypeOfSteel_A300
		13	TypeOfSteel_A400
		14	Steel_Plate_Thickness
		15	Edges_Index
		16	Empty_Index
		17	Square_Index
		18	Outside_X_Index
		19	Edges_X_Index
		20	Edges_Y_Index
		21	Outside_Global_Index
		22	LogOfAreas
		23	Log_X_Index
		24	Log_Y_Index
		25	Orientation_Index
		26	Luminosity_Index
		27	SigmoidOfAreas

includes 1941 samples and every sample owns 27 independent features.

Table 3 shows class distribution and list of features. We choose 348 samples which belong to Pastry and Z_Scratch

TABLE 4: The feature importance measurement of steel plates dataset.

Number	Number of features	The feature importance measurement f_k	$\sum_{k=1}^{d_\theta} f_k$
1	19	0.2191	0.2191
2	15	0.1339	0.353
3	16	0.1283	0.4831
4	17	0.0777	0.559
5	13	0.0676	0.6266
6	12	0.0676	0.6942
7	20	0.0577	0.7519
8	27	0.0548	0.8067
9	21	0.051	0.8577
10	24	0.0343	0.892
11	22	0.0341	0.9261
12	23	0.0247	0.9508
13	25	0.0099	0.9607
14	2	0.0075	0.9682
15	1	0.0074	0.9756
16	26	0.007	0.9826
17	7	0.0044	0.987
18	6	0.0033	0.9903
19	4	0.0029	0.9932
20	3	0.0029	0.9961
21	14	0.0021	0.9982
22	9	0.001	0.9992
23	10	0.0005	0.9997
24	18	0.0001	0.9998
25	5	0.0001	0.9999
26	11	0	0.9999
27	8	0	0.9999

faults as testing dataset. The parameters for the proposed method are set as the previous experiment.

Table 4 lists the importance measurement of every feature computed by the proposed method. Due to the threshold θ , 11 features will be selected from original features. Figure 4 shows the Rand index values corresponding to the number of features using SUD, Relief-F, and our method.

Figure 4 shows that the proposed method is able to find the important features. It also shows that the performance of the proposed method without using class labels is very close to and sometimes better than that of SUD or Relief-F which ranks the original features using the class labels.

5. Conclusions

An efficient unsupervised feature selection method based on unsupervised optimal discriminant vector is developed to find the important features without using class labels. It adopts fuzzy Fisher criterion to derive the optimal discriminant vector in unsupervised pattern. It defines the single feature importance measurement based on unsupervised

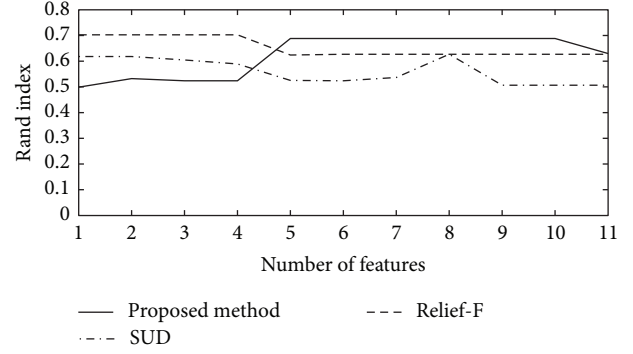


FIGURE 4: Rand Index values corresponding to the number of features.

optimal discriminant vector to determine the importance of every feature. Two experiments on *Wine* dataset and fault diagnosis were carried out to show that the proposed method is able to find important features and is a reliable and efficient feature selection methodology compared to SUD and Relief-F. In the future, we will research how to introduce kernel techniques to the proposed method to enhance its applicability.

Appendix

Proof of (10)

According to [22], we have

$$\frac{\partial (\omega^T S_{fb} \omega)}{\partial m_i} = 2\omega \omega^T \sum_{j=1}^N u_{ij}^m (m_i - \bar{x}),$$

$$\frac{\partial (\omega^T S_{fw} \omega)}{\partial m_i} = -2\omega \omega^T \sum_{j=1}^N u_{ij}^m (x_j - m_i),$$

$$\frac{\partial F}{\partial m_i} = 2\omega \omega^T \sum_{j=1}^N u_{ij}^m (m_i - \bar{x}) + 2\lambda \omega \omega^T \sum_{j=1}^N u_{ij}^m (x_j - m_i) = 0. \quad (\text{A.1})$$

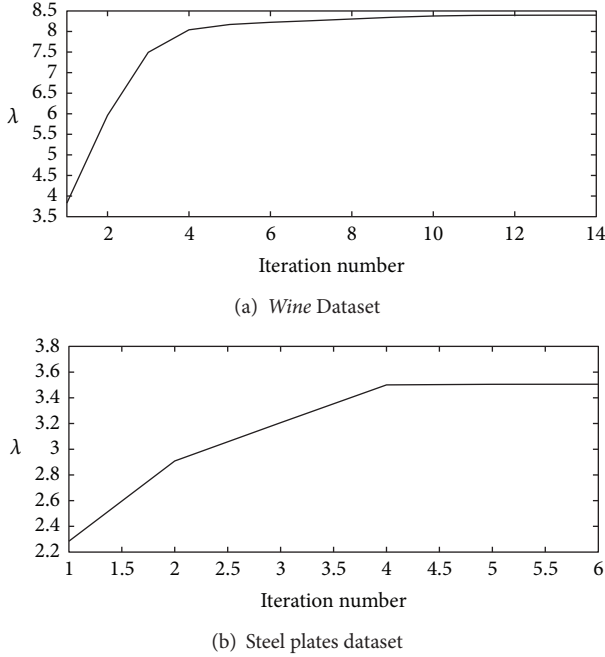
Premultiply by ω^T on both sides,

$$\omega^T \omega \omega^T \sum_{j=1}^N u_{ij}^m (m_i - \bar{x}) + \lambda \omega^T \omega \omega^T \sum_{j=1}^N u_{ij}^m (x_j - m_i) = 0, \quad (\text{A.2})$$

$$\omega^T \left(\sum_{j=1}^N u_{ij}^m (m_i - \bar{x}) + \lambda \sum_{j=1}^N u_{ij}^m (x_j - m_i) \right) = 0. \quad (\text{A.3})$$

We cannot solve m_i from the above equation. But it is obvious that the following equation is the particular solution of (A.3):

$$\sum_{j=1}^N u_{ij}^m (m_i - \bar{x}) + \lambda \sum_{j=1}^N u_{ij}^m (x_j - m_i) = 0, \quad (\text{A.4})$$

FIGURE 5: The λ curve.

that is,

$$m_i = \frac{\sum_{j=1}^N u_{ij}^m (x_j - (1/\lambda)\bar{x})}{\sum_{j=1}^N u_{ij}^m (1 - (1/\lambda))}. \quad (\text{A.5})$$

Now we proof that (A.5) is a local maximum of F .

We find

$$\begin{aligned} \frac{\partial^2 F}{\partial m_i^2} &= 2\omega\omega^T \sum_{j=1}^N u_{ij}^m - 2\lambda\omega\omega^T \sum_{j=1}^N u_{ij}^m \\ &= 2(1 - \lambda)\omega\omega^T \sum_{j=1}^N u_{ij}^m. \end{aligned} \quad (\text{A.6})$$

As $\omega\omega^T$ is positive semidefinite matrix, we have

$$\omega\omega^T > 0. \quad (\text{A.7})$$

And it is obvious that

$$\sum_{j=1}^N u_{ij}^m > 0. \quad (\text{A.8})$$

We track λ value in the experiments shown in Figure 5 and give the empirical evidence to proof $\lambda > 1$.

Thus,

$$\frac{\partial^2 F}{\partial m_i^2} = 2(1 - \lambda)\omega\omega^T \sum_{j=1}^N u_{ij}^m < 0. \quad (\text{A.9})$$

According to [23], (A.5) is the local maximum of F .

Conflict of Interests

The authors declare that they have no conflict of interests.

Acknowledgments

This work is supported by the Major Program of the Natural Science Foundation of the Jiangsu Higher Education Institutions of China (11KJA460001, 13KJA460001), China Spark Program (2013GA690404) Technology Innovation Project of Science and Technology Enterprises at Jiangsu Province in China (BC2012429), the Open Project from the Key Laboratory of Digital Manufacture Technology at Jiangsu Province in China (HGDML-1005), Huaian Science and Technique Program in China (HAG2010062), Huaian 533 Talents Project, Huaian International Science and Technology Cooperation Project (HG201309), Qing Lan Project of Jiangsu Province, and Jiangsu Overseas Research & Training Program for University Prominent Young & Middle-Aged Teachers and Presidents, China.

References

- [1] R. A. Fisher, "The use of multiple measurements in taxonomic problems," *Annals of Eugenics*, vol. 7, pp. 178–188, 1936.
- [2] J. Kittler, "On the discriminant Vector method of feature selection," *IEEE Transactions on Computers*, vol. 26, no. 6, pp. 604–606, 1977.
- [3] K. Kira and L. A. Rendell, "The feature selection problem: traditional methods and a new algorithm," in *Proceedings of the 10th National Conference on Artificial Intelligence*, pp. 129–134, July 1992.
- [4] I. Kononenko, "Estimating attributes: analysis and extension of RELIEF," *Proceedings of the European Conference on Machine Learning*, pp. 171–182, 1994.
- [5] L. Yu and H. Liu, "Efficiently handling feature redundancy in high-dimensional data," in *Proceedings of the 9th ACM SIGKDD International Conference on Knowledge Discovery and Data Mining*, pp. 685–690, August 2003.
- [6] G. V. Lashkia and L. Anthony, "Relevant, irredundant feature selection and noisy example elimination," *IEEE Transactions on Systems, Man, and Cybernetics B*, vol. 34, no. 2, pp. 888–897, 2004.
- [7] Q. Gu, Z. Li, and J. Han, "Generalized fisher score for feature selection," in *Proceedings of the 27th Conference on Uncertainty in Artificial Intelligence (UAI '11)*, pp. 266–273, Barcelona, Spain, July 2011.
- [8] A. R. Webb, *Statistical Pattern Recognition*, John Wiley & Sons, New York, NY, USA, 2nd edition, 2002.
- [9] M. Dash, H. Liu, and J. Yao, "Dimensionality reduction of unsupervised data," in *Proceedings of the 9th IEEE International Conference on Tools with Artificial Intelligence*, pp. 532–539, November 1997.
- [10] J. Basak, R. K. De, and S. K. Pal, "Unsupervised feature selection using a neuro-fuzzy approach," *Pattern Recognition Letters*, vol. 19, no. 11, pp. 997–1006, 1998.
- [11] P. Mitra, C. A. Murthy, and S. K. Pal, "Unsupervised feature selection using feature similarity," *IEEE Transactions on Pattern Analysis and Machine Intelligence*, vol. 24, no. 3, pp. 301–312, 2002.

- [12] M. Dash, K. Choi, P. Scheuermann, and H. Liu, "Feature selection for clustering—a filter solution," in *Proceedings of the 2nd IEEE International Conference on Data Mining*, pp. 115–122, December 2002.
- [13] S. Y. M. Shi and P. N. Suganthan, "Unsupervised similarity-based feature selection using heuristic Hopfield neural networks," in *Proceedings of the International Joint Conference on Neural Networks*, vol. 3, pp. 1838–1843, July 2003.
- [14] J. G. Dy and C. E. Brodley, "Feature selection for unsupervised learning," *Journal of Machine Learning Research*, vol. 5, pp. 845–889, 2004.
- [15] S. Z. Li and A. K. Jain, *Encyclopedia of Biometrics*, Springer, 2009.
- [16] S.-Q. Cao, S.-T. Wang, X.-F. Chen, Z.-P. Xie, and Z.-H. Deng, "Fuzzy fisher criterion based semi-fuzzy clustering algorithm," *Journal of Electronics & Information Technology*, vol. 30, no. 9, pp. 2162–2165, 2008.
- [17] X.-B. Zhi and J.-L. Fan, "Fuzzy fisher criterion based adaptive dimension reduction fuzzy clustering algorithm," *Journal of Electronics & Information Technology*, vol. 31, no. 11, pp. 2653–2658, 2009.
- [18] C. L. Blake and C. J. Merz, "UCI repository of machine learning databases," Department of Information and Computer Science, University of California, Irvine, Calif, USA, 1998, <http://archive.ics.uci.edu/ml/>.
- [19] W. Rand, "Objective criteria for the evaluation of clustering methods," *Journal of the American Statistical Association*, vol. 66, no. 336, pp. 846–850, 1971.
- [20] Center for Machine Learning and Intelligent Systems, the University of California, Irvine, Calif, USA, 2011, <http://archive.ics.uci.edu/ml/datasets/Steel+Plates+Faults>.
- [21] M. Buscema, S. Terzi, and W. Tastle, "A new meta-classifier," in *Proceedings of the Annual North American Fuzzy Information Processing Society Conference (NAFIPS' 10)*, pp. 1–7, IEEE Press, Toronto, Canada, July 2010.
- [22] J. H. Manton, "Differential calculus, tensor products and the importance of notation," 2013, <http://arxiv.org/abs/1208.0197>.
- [23] J. Wilde, *Unconstrained Optimization*, 2011, http://www.econ.brown.edu/students/Takeshi_Suzuki/Math_Camp_2011/Unconstrained_Optimization-2011.pdf.

Research Article

Video Shot Boundary Recognition Based on Adaptive Locality Preserving Projections

Yongliang Xiao,^{1,2} Limin Xia,¹ Shaoping Zhu,² Dazu Huang,² and Jianquan Xie²

¹ School of Information Science and Engineering, Central South University, Changsha 410083, China

² Department of Information Management, Hunan University of Finance and Economics, Changsha 410205, China

Correspondence should be addressed to Limin Xia; xlm@mail.csu.edu.cn

Received 7 August 2013; Revised 25 September 2013; Accepted 10 October 2013

Academic Editor: SunQun Cao

Copyright © 2013 Yongliang Xiao et al. This is an open access article distributed under the Creative Commons Attribution License, which permits unrestricted use, distribution, and reproduction in any medium, provided the original work is properly cited.

A novel video shot boundary recognition method is proposed, which includes two stages of video feature extraction and shot boundary recognition. Firstly, we use adaptive locality preserving projections (ALPP) to extract video feature. Unlike locality preserving projections, we define the discriminating similarity with mode prior probabilities and adaptive neighborhood selection strategy which make ALPP more suitable to preserve the local structure and label information of the original data. Secondly, we use an optimized multiple kernel support vector machine to classify video frames into boundary and nonboundary frames, in which the weights of different types of kernels are optimized with an ant colony optimization method. Experimental results show the effectiveness of our method.

1. Introduction

Video shot boundary recognition is a fundamental process towards video summarization and analysis. There are many boundary recognition methods already presented [1, 2]. Common method to recognize shot boundary is comparing the difference of two adjacent frames with a threshold. In paper [3], the abrupt shot boundary is detected based on an adaptive threshold and gradual transition boundary is detected with a set of standard templates. Warhade et al. [4] detected shot boundary with cross-correlation coefficient, stationary wavelet transform, and combination of local. Thakar and Hadia [5] proposed a new gradual shot detection method in which the threshold can be adaptively determined based on the total information change of video frames. Huo et al. [6] used a statistical model according to the video frame differences to determine the adaptive threshold. In paper [7], the threshold is automatically determined according to the magnitude of color differences quantification. Warhade et al. [8] first extracted structure features from each video frame by using dual-tree complex wavelet transform and then decided the shot boundary based on the spatial domain similarity. In order to reduce the computation, Gao and Ma [9] used color

histogram and mutual information to measure the difference between frames, and then the corner distribution of frames is utilized to exclude most of the false boundaries.

The main disadvantage of these methods is susceptible to the effect of thresholds, which can make a mistake for some complicated long gradual shots. To resolve this problem, people see the video shot recognition as a categorization task. In paper [10], a fuzzy logic method is used to detect shot boundary. This method contains two processing modes, where one is dedicated to detection of abrupt shot and the other for detection of gradual shot. In paper [11], the video feature including HSV (hue, saturation, value), edge orientation, and texture feature is obtained, and then the Kohonen self-organized network is used to recognize shot boundary. Huang et al. [12] classified video frames with a radial basis function neural network. Mohanta et al. [13] used a multilayer perception network to classify video frames based on local features matrix. To improve the recognition performance, Li et al. [14] first removed some frames from the original video which were clearly not shot boundaries, then used a novel SIFT key point matching algorithm to detect shot boundary. Zhao et al. [15] used context feature vector and Tabu-SVM to recognize shot boundary. In paper [16],

the proposed approach first detected general shot boundary with Fisher criterion and then classified the cut and gradual shot with SVM. In order to improve the effect of SVM, Zhao et al. [17] optimized the parameters of SVM with particle swarm method. In addition, Lankinen and Kamarainen [18] detected shot boundary using a visual bag-of-words approach. Donate and Liu [19] extracted salient features from a video sequence and tracked them over time to estimate shot boundaries. Li and Chen [20] recognized shot boundary with macroblock type information which can save a lot of computation cost.

In this paper, we present a novel method to improve the shot boundary recognition accuracy. Firstly, based on the analysis of LPP, we present an adaptive LPP to extract more useful and discriminating features. Secondly, we recognize shot boundary with an optimized multiple kernel support vector machine.

The rest of this paper is organized as follows. Section 2 abstracts the theoretical fundamentals about LPP. In Section 3, we extract the video feature with improved LPP. Section 4 uses an optimized multiple kernel SVM to recognize shot boundary. Some experiments are used to evaluate the presented method in Section 5 and all the paper is concluded in Section 6.

2. Theoretical Fundamentals

2.1. Locality Preserving Projection. Locality preserving projection (LPP) is a dimensionality reduction method which can be explained by the graph theory [21]. Assume there is m -dimensional data point set $X = [x_1, x_2, \dots, x_n]$; we try to find a project matrix A to project these data point into a low-dimensional subspace, and the projection can be expressed as $y_i = A^T x_i$.

The objective function of LPP is as follows:

$$\min \sum_{ij} \|y_i - y_j\|^2 S_{ij}, \quad (1)$$

where the weight matrix S can be defined as follows:

$$S_{ij} = \begin{cases} 1 & \text{if } x_i \text{ is among } K \text{ nearest neighbors of } x_j \\ & \text{or } x_j \text{ is among } K \text{ nearest neighbors of } x_i \\ 0 & \text{else.} \end{cases} \quad (2)$$

Then, the objective function of LPP can be converted into the following minimization problem:

$$\begin{aligned} \min_A \quad & \text{tr}\{A^T X L X^T A\} \\ \text{s.t.} \quad & A^T X D X^T A = 1, \end{aligned} \quad (3)$$

where $D_{ij} = \sum_j W_{ij}$ is a diagonal matrix and $L = D - S$ is a Laplacian matrix.

Lastly, the project matrix A can be obtained by solving a generalized eigenvalue problem as follows:

$$X L X^T A = \lambda X D X^T A. \quad (4)$$

Let the column vectors a_1, a_2, \dots, a_d be the solutions of (4), ordered according to their eigenvalues, $\lambda_1, \lambda_2, \dots, \lambda_d$; we can define the following transformation form:

$$x_i \longrightarrow y_i = A^T x_i, \quad A = [a_1, a_2, \dots, a_d]. \quad (5)$$

2.2. Weight Definition. In the LPP, the weight between two points is defined to be a simple either 1 or 0 or heat kernel, which cannot reflect the class information. Given $X = [x_1, x_2, \dots, x_n]$, let C_i and $N(x_i)$ be the label and k the nearest neighbors of the point x_i , Li et al. [22] presented an orthogonal discriminating projection (ODP), in which the weight S_{ij} between two points is defined as follows:

$$S_{ij} = \begin{cases} \exp\left(-\frac{d^2(x_i, x_j)}{\beta}\right) & \text{if } x_i \in N(x_j), x_j \in N(x_i), C_i = C_j \\ \exp\left(-\frac{d^2(x_i, x_j)}{\beta}\right) \left(1 - \exp\left(-\frac{d^2(x_i, x_j)}{\beta}\right)\right) & \text{if } x_i \in N(x_j), x_j \in N(x_i), C_i \neq C_j \\ 0 & \text{otherwise,} \end{cases} \quad (6)$$

where $d(x_i, x_j)$ denote the geodesic distance between points x_i and x_j , and β is a parameter which is used as a regular.

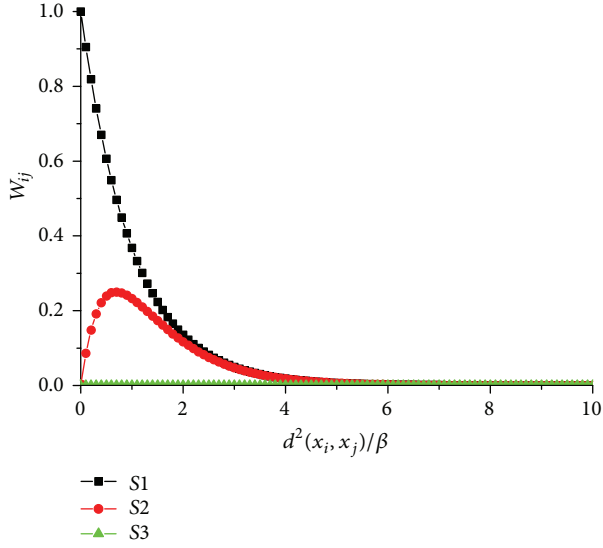
Figure 1 shows that the typical plot of S_{ij} is a function of $d^2(x_i, x_j)/\beta$, where $S_1 = \exp(-d^2(x_i, x_j)/\beta)$, $S_2 = \exp(-d^2(x_i, x_j)/\beta)(1 - \exp(-d^2(x_i, x_j)/\beta))$, $S_3 = 0$.

From Figure 1 we find that S_{ij} is not a monotonically decreasing function of $d^2(x_i, x_j)/\beta$, which is due to the fact that S_2 is a nonmonotonic function. When $0 < d^2(x_i, x_j)/\beta < 0.71$, S_{ij} is monotonically increasing. In the actual applications, S_{ij} should decrease with the increase of $d^2(x_i, x_j)/\beta$. Zhang et al. [23] proposed a modified ODP (MODP) with correlation coefficient $\|(x_i - \bar{x}_i)(x_j - \bar{x}_j)\| / \|(x_i - \bar{x}_i)\| \cdot \|(x_j - \bar{x}_j)\|$ between x_i and x_j .

Obviously, the above definitions about S_{ij} consider only the space structure and not the manifold structure. Meanwhile, the presented k nearest neighbors do not reflect the real information of manifold structure.

3. Video Feature Reduction

In this section, we extract more discriminating video features from the original color, shape, and texture feature. Firstly, we propose an improved LPP. We adaptively select the k nearest neighbors of each point and introduce the model information into the new weight similarity which can make the weight be a monotonically decreasing function of distance. The major merit of ALPP is preserving the local structure and label information of original data. Then we use ALPP to extract more discriminating video features for shot boundary recognition.


 FIGURE 1: Type plot of S_{ij} as a function of $d^2(x_i, x_j)/\beta$.

3.1. Mode Detection. In order to preserve the mode information of data points, we use median-shift method relied on computing the median of local neighborhoods instead of the mean to detect mode. Considering that the median of a set is a point in the set, the method is more robust than mean-shift method. Most importantly, the median-shift method is not a nonparametric method that does not require a prior knowledge of the number of clusters nor does it place any limitations on the shape of the clusters. The process of mode detection is as follows [24].

Suppose we are given a set $S = \{s_1, \dots, s_n\}$, $s_i \in R^d$, $d > 1$; define the Tukey depth of a point to be

$$\text{DEPTH}(s_i) = \min [v^T s_i : v \in R^d, \|v\| = 1], \quad (7)$$

where the Tukey depth of a point is the minimum of its depth along any projection vector v .

Firstly, the median of S is an element with maximal depth

$$\text{MEDIAN}(S) = \max_{s_i \in S} \left(\sum_{v_k \in V} \text{DEPTH}(s_i^T v_k) \right). \quad (8)$$

Then we seek the mode with the median-shift algorithms. For each point we wish to ascend in the direction of the positive gradient of the underlying probability density function. We define the median-shift for point c in set P as

$$c' = \text{MEDIAN}(p \in P \mid \|p - c\| \leq r), \quad (9)$$

where r is a bandwidth parameter. Since c' uses necessarily a point in the dataset, there is no need for multiple iterations in this step. After one iteration all points are linked and we can only go through the list of discovered medians to find a mode. The results of this step are a set of modes representing clusters.

Next, we proceed by iteratively working on the reduced set of modes, replacing the median calculation by weighted median calculation until convergence, where weights are

the number of points mapped to the given mode. The weights are taken into account during the calculation of the depth of each point in the next iteration by modifying the definitions as follows:

$$\text{RANK}(s_i) = \sum_{s_j < s_i} \text{Weight}(s_j) \quad (10)$$

and defining $W = \sum_{s_j} \text{Weight}(s_j)$ as the total weights in the neighborhood of s_i , then

$$\text{DEPTH}(s_i) = \min(\text{RANK}(s_i), W - \text{RANK}(s_i)). \quad (11)$$

Finally, in case of data clustering, and not only mode detection, we map each data point to its closest mode. Let M_i be the model of the point x_i , and let M be the set of M_i mode; we can obtain

$$M = \{M_1, M_2, \dots, M_M\}, \quad (12)$$

where $M_m = \{x_j \mid x_j \in M \wedge \text{model}(x_j) = m\}$.

3.2. Adaptive Neighborhood Selection. Considering the unchangeable k neighborhood not reflecting the mode information of manifold structure, we apply an adaptive strategy to select the neighborhood of each point.

Firstly, we define the manifold adjusted length of line segment

$$L(x_i, x_j) = \begin{cases} \rho^{d(x_i, x_j)} - 1 & x_i \text{ and } x_j \text{ are neighboring points} \\ \text{infinite else,} & \end{cases} \quad (13)$$

where $d(x_i, x_j)$ is the Euclidean distance between x_i and x_j and ρ is a flexing factor. Obviously, this formulation can be utilized to describe the global consistency. In addition, the length of line segment between two points can be elongated or shortened by adjusting the flexing factor ρ [25].

Then, let data points be the nodes of graph $G = (V; E)$ and let $p \in V^l$ be a path of length $l = |p| - 1$ connecting the nodes p_1 and $p_{|p|}$ in which $(p_k, p_{k+1}) \in E$, $1 \leq k \leq |p|$. Let P_{ij} denote the set of all paths connecting nodes x_i and x_j ; the manifold distance metric between two points is defined as follows:

$$D(x_i, x_j) = \min_{p \in P_{ij}} \sum_{k=1}^{|p|-1} L(p_k, p_{k+1}), \quad (14)$$

where $L(a, b)$ denotes the manifold adjusted length of line segment.

Next, the average manifold distance of point x_i is defined as follows:

$$\text{MS}(x_i) = \frac{1}{N_m} \sum_{M_i = M_j} D(x_i, x_j), \quad (15)$$

where N_m is the total number which meets the conditions $M_i = M_j$.

Lastly, the adaptive neighborhood of point x_i is constructed as

$$N'(x_i) = \{x \mid D(x_i, x_j) < MS(x_i) \wedge M_i = M_j\} \quad (16)$$

which shows that the neighborhood of point x_i is adaptively built with the points where the distance is shorter than the average distance.

The major merit of the adaptive neighborhood selection method can be summarized as follows.

- (1) The manifold distance metric can measure the geodesic distance along the manifold, which can elongate the distance among data points in different regions of high density and simultaneously shorten that in the same region of high density.
- (2) The neighborhood of each point is different from others, which is decided by the local density of the origin space. When the local density of x_i is lower, the neighborhood is higher and vice versa.

3.3. Improve Weight Definition. In order to resolve the problem which is described in Section 2.2, we improve the weight definition between two points x_i and x_j as follows:

$$S_{ij} = \begin{cases} \exp\left(-\frac{d^2(x_i, x_j)}{\beta_1}\right) & \text{if } x_i \in N'(x_j), x_j \in N'(x_i), C_i = C_j \\ \exp\left(-\frac{d^2(x_i, x_j)}{\beta_1}\right) \exp\left(-\frac{d^2(x_i, x_j)}{\beta_2}\right) & \text{if } x_i \in N'(x_j), x_j \in N'(x_i), C_i \neq C_j \\ 0 & \text{otherwise,} \end{cases} \quad (17)$$

where $d(x_i, x_j)$ denotes the distance between points x_i and x_j , β_1 and β_2 are the regular parameters, and C_i is the label of the point x_i for definition of $N'(x_i)$ please refer to (16).

Figure 2 shows that the typical plot of S_{ij} is a function of $d^2(x_i, x_j)/\beta$, $\beta = \beta_1 = \beta_2$, where $S_1 = \exp(-d^2(x_i, x_j)/\beta_1)$, $S_2 = \exp(-d^2(x_i, x_j)/\beta_1) \exp(-d^2(x_i, x_j)/\beta_2)$, and $S_3 = 0$.

Similar to paper [26], let $\exp(-d^2(x_i, x_j)/\beta_1)$ be the local weight, and let $\exp(-d^2(x_i, x_j)/\beta_2)$ be the intermode discriminating weight. The new weight definition can be viewed as the local weight and discriminating weight. It means that the discriminating similarity reflects both the local neighborhood structure of model and label information of the data set.

The properties and the corresponding advantages of the improved weight definition can be summarized as follows.

- (1) The improved weight definition make use of the label information and model information to preserve the manifold information, which is very important for classification.
- (2) Since the value of $\exp(-d^2(x_i, x_j)/\beta_2)$ ranges from 0 to 1, no matter how far the two points are, the intermode similarity can be limited in certain ranges.

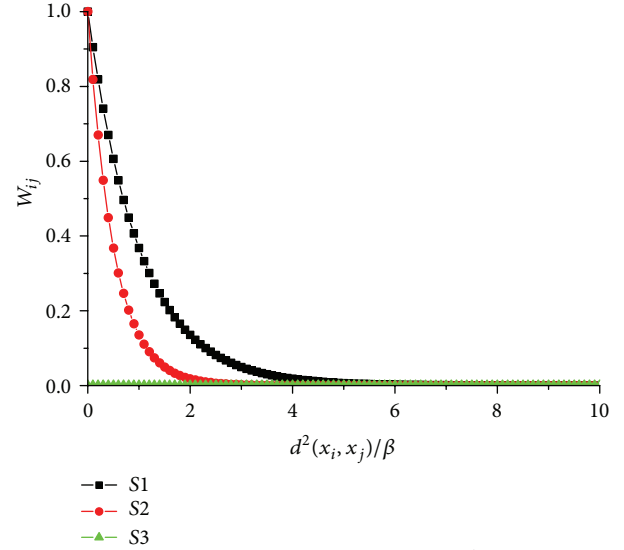


FIGURE 2: Type plot of S_{ij} as a function of $d^2(x_i, x_j)/\beta$.

- (3) With the decrease of the geodesic distance, $\exp(-d^2(x_i, x_j)/\beta_2)$ is a decrease, which means that two near points from different modes have a smaller similarity.
- (4) Note that S_1 and S_2 always decrease when x_i and x_j are far apart and they increase when x_i and x_j are close. Thus, S_{ij} is a monotonically decreasing function of $d^2(x_i, x_j)/\beta$.
- (5) The use of mode prior probabilities makes the newly designed discriminating similarity S_{ij} more suitable for perverting the local structure information of original data.

3.4. Video Feature Reduction. In order to enhance the discriminating information for shot boundary recognition, we hope to combine the label information and model information to improve the discriminating ability and preserve the local neighborhood structure of the original data.

Due to introducing the similarity matrix S , we define the local scatter matrix as follows [23]:

$$\begin{aligned} J_L(A) &= \sum_{i=1}^n \sum_{j=1}^n S_{ij} (y_i - y_j) (y_i - y_j)^T \\ &= \sum_{i=1}^n \sum_{j=1}^n S_{ij} (A^T x_i - A^T x_j) (A^T x_i - A^T x_j)^T \\ &= A^T S_L A, \end{aligned} \quad (18)$$

where $S_L = \sum_{i=1}^n \sum_{j=1}^n S_{ij} (x_i - x_j) (x_i - x_j)^T = XLX^T$, $L = M - S$, $M_{ii} = \sum_j S_{ij}$.

Then we define the nonlocal scatter matrix as follows:

$$\begin{aligned} J_N(A) &= \sum_{i=1}^n \sum_{j=1}^n (1 - S_{ij}) (y_i - y_j) (y_i - y_j)^T \\ &= \sum_{i=1}^n \sum_{j=1}^n (1 - S_{ij}) (A^T x_i - A^T x_j) (A^T x_i - A^T x_j)^T \end{aligned}$$

$$\begin{aligned}
&= A^T (S^T - S^N) A \\
&= A^T S_N A,
\end{aligned} \tag{19}$$

where $S_T = \sum_{i=1}^n \sum_{j=1}^n (x_i - x_j)(x_i - x_j)^T$, $S_N = S_T - S_L$.

Lastly, the objective function of the improved LPP can be expressed as follows:

$$\begin{aligned}
&\arg \max_A J(A) = \arg \max A^T ((1 - \alpha) S_T - \alpha S_L) A \\
&\text{s.t.} \quad A^T A = I,
\end{aligned} \tag{20}$$

where α is an adjustable factor.

So we can find that A consists of the eigenvectors associated with d top eigenvalues of the following eigen-equation:

$$((1 - \alpha) S_T - \alpha S_L) a = \lambda a. \tag{21}$$

The algorithmic procedure of video feature extraction is stated below.

- (1) Extract original video feature including the color, shape and texture feature.
- (2) Perform PCA projection. In order to make the matrix XX^T become nonsingular, we project the dataset into a PCA subspace with a transformation matrix.
- (3) Define the similarity matrix. For each point x_i , compute the similarity $W_{ij} = \exp(-d^2(x_i, x_j)/\beta_1)$, if x_j is the adaptive neighbors of x_i and $c_i = c_j$, and compute the similarity $W_{ij} = \exp(-d^2(x_i, x_j)/\beta_1) \exp(-d^2(x_i, x_j)/\beta_2)$, if x_j is the adaptive neighbors of x_i and $c_i \neq c_j$.
- (4) Compute the diagonal matrix M and Laplacian matrix L and then compute the top d eigenvalues and its corresponding eigenvectors based on (20).
- (5) Perform the ALPP transformation. Let A be an optimal projection matrix; we can project the new data into low dimensionality with

$$Y = A^T X. \tag{22}$$

4. Shot Boundary Recognition

The process of shot boundary detection includes two steps. Firstly, we extract the video features using ALPP method. Secondly, we detect shot boundary using an optimized MKSVM.

4.1. Multiple Kernel SVM. Support vector machines are a family of pattern classification algorithms which is based on the idea of structural risk minimization rather than empirical risk minimization [27]. However, it is often unclear what the most suitable kernel for the task at hand is. Recently, the multiple kernel learning theory has been used for training different kernels by jointly optimizing both the coefficients

of the classifiers and the weights of the kernels which have a more excellent effectiveness for object recognition than SVM [28]. In this paper, we combine several possible kernels to improve the precision of shot boundary recognition.

Let $d = [d_1, d_2, \dots, d_M]^T$ be a vector of weights for the mixture of kernels. A multiple kernel is the combination of the M basis kernels K_m

$$\begin{aligned}
K(x_i, x_j) &= \sum_{m=1}^M d_m K_m(x_i, x_j) \\
&\text{s.t.} \quad d_m \geq 0
\end{aligned} \tag{23}$$

$$\sum_{m=1}^M d_m = 1.$$

Assume there are a data set $D = \{x_i, z_i\}_{i=1}^m$ of labeled examples, where $x_i \in X$ is the input vector and $z_i \in \{-1, 1\}$.

According to paper [29], the primal form of multiple kernel support vector machine (MK SVM) is thus formulated as the following optimization problem:

$$\begin{aligned}
\min_{d, b, \xi} J(d) &= \frac{1}{2} \sum_{m=1}^M \frac{1}{d_m} \|f_m\|^2 + C \sum_{i=1}^l \xi_i \\
&\text{s.t.} \quad y_i \sum_{m=1}^n f_m(x_i) + y_i b \geq 1 - \xi_i \\
&\quad \xi_i \geq 0, \quad \forall i \\
&\quad \sum_{m=1}^M d_m = 1, \quad d_m \geq 0, \quad \forall m.
\end{aligned} \tag{24}$$

Similar to the SVM, with the constraint on d_m , the above minimization problem can thus be transformed into the following dual problem:

$$\begin{aligned}
&\max_{\alpha} \sum_{i=1}^n \alpha_i - \frac{1}{2} \sum_{i,j=1}^n \alpha_i \alpha_j y_i y_j \sum_{m=1}^M d_m k(x_i, x_j) \\
&\text{s.t.} \quad \sum_{i=1}^n y_i \alpha_i = 0, \quad \forall i = 1, \dots, n \\
&\quad 0 \leq \alpha_i \leq C, \quad \sum_{m=1}^M d_m = 1, \quad d_m \geq 0.
\end{aligned} \tag{25}$$

For the test input x , the decision function of MK SVM can be computed as

$$F_{\text{MKL}}(x) = \text{sign} \left(\sum_{m=1}^M d_m K_m(x, x) a_m + b \right). \tag{26}$$

4.2. Ant Colony Optimization Method. Ant colony optimization method (ACO) is an optimizing method inspired by the foraging behavior of ant colonies [30]. When ants walk between their nest and a food source, they mark the paths with special kind of chemical termed pheromone, and

the shorter paths can attract more and more pheromone [31]. In the method, an ant determines its transfer direction according to the amount of pheromone in each path. Firstly, every ant constructs an edge from a start vertex to an end vertex. Then when all ants reach the end vertex, the edges are marked with a pheromone quantity. Thus the colony can converge to the shortest path [32]. In this paper, we apply the ant colony optimization method to solve the weights optimized problem in MKSVM.

Let $P_{ij}^k(t)$ be the proximity which an ant k transfer from element i to j at iteration t . $P_{ij}^k(t)$ can be defined as

$$P_{ij}^k(t) = \begin{cases} \frac{\tau_{ij}^\alpha(i-1)\eta_{ij}^\beta}{\sum_{z \in V_k(x)} \tau_{ij}^\alpha(i-1)\eta_{ij}^\beta} & \text{if } z \in V_k(x) \\ 0 & \text{else,} \end{cases} \quad (27)$$

where $V_k(x)$ is the element which has not been unvisited. τ_{ij} is the pheromone quantity of path (i, j) , η_{ij} is a heuristic measure of moving element i to element j , α , and β are two parameters that control the relative importance of the information heuristics and exception heuristics factor, respectively.

The amount of p all m ants pheromone trail on a path deposited step by step. After time m , the pheromone quantity $\tau_{ij}(t)$ associated with an edge joining element i and j is updated according to the following formula:

$$\tau_{ij}(t+m) = (1-\rho)\tau_{ij}(t-1) + \sum_{k=1}^n \Delta\tau_{ij}^k(t), \quad (28)$$

where ρ is a pheromone evaporation loss coefficient and $\Delta\tau_{ij}^k(t)$ is the pheromone quantity deposited at iteration i by ant k on an edge joining element i and j . The $\Delta\tau_{ij}^k(t)$ is usually defined as

$$\Delta\tau_{ij}^k(i) = \begin{cases} \frac{Q}{L_k} & \text{if } w_{ij} \in T_k(I) \\ 0 & \text{else,} \end{cases} \quad (29)$$

where Q is a constant and L_k is the cost function of k th ant.

For the process of ant colony optimization method please refer to paper [33].

4.3. Shot Boundary Recognition. The process of shot boundary recognition includes the following stages. Firstly, we extract the original feature. Then we reduce the video feature with improved LPP. Lastly, we classify the frame into boundary frame with the optimized MKSVM classifier based on ACO method.

The algorithm of video boundary recognition is described as follows.

- (1) Extract original video feature which includes colors, shape, and texture feature.
- (2) Reduce video feature with improved LPP.

- (3) Define input vector $[(y_{i-k} - y_i), \dots, (y_{i+k} - y_i)]$, where y_i is the video feature vector and i is i th frame of video.
- (4) Label the boundary frames (+1) and nonboundary frame (-1) and build training sample set.
- (5) Initialize the parameters of ACO. Let time $t = 0$, interactive times $I_t = 0$. Set the maximum iterative times $I_t(\max)$ and let initial pheromone $\tau_{xy} = c$ and $\Delta\tau_{xy}(0) = 0$.
- (6) Update I_t by $I_t = I_{t+1}$ and choose the ant element j , as its transform direction according to function (27).
- (7) Update the taboo table pointer. Move the ant to the selected new element and add the element into ant taboo table.
- (8) If all elements of the set have been fully traversed, go to step 7 or else go to the next step.
- (9) Recalculate the pheromone of each path, if $I_t < I_t(\max)$, go to step 6, or else save the weights $d = [d_1, d_2, \dots, d_M]$.
- (10) Classify the video frame into boundary frame based on the following rule:

$$F_{\text{MKL}}(x) = \text{sign} \left(\sum_{i=1}^n \sum_{m=1}^M d_m K_m(x_i, x) a_i + b \right). \quad (30)$$

5. Experiments and Analysis

In this section we present some experiments to validate the proposed approach. Firstly, we investigate the performance of the proposed ALPP method for video feature extraction experiment. Then we recognize shot boundary with the proposed method. The video database includes movie, news, sports, documentary, and MTV. The reason of selecting this type video is that news videos have many long abrupt shots, MTV has fast changes of scenes, sport have fast camera movements and zooming in, movie includes many gradual shots. Some shot samples are shown in Figure 3. For evaluation, we use the common figures of merit of the algorithm standard precision and recall [34]

$$\begin{aligned} \text{Precision} &= \frac{\#(\text{Boundaries correctly detected})}{\#(\text{Total boundaries detected})}, \\ \text{Recall} &= \frac{\#(\text{Boundaries correctly detected})}{\#(\text{Total ground truth boundaries})}. \end{aligned} \quad (31)$$

5.1. Video Feature Exaction Experiment. In order to testify the effectiveness of the adaptive LPP (ALPP), we extract video feature with ODP, MODP, and ALPP method. For convenience of comparison, we use the same method in paper [35] to detect shot boundary. In the experiment, original video feature is built on color feature, shape feature, and texture feature. Then ODP, MODP, and ALPP method, are used to extract video feature with $\alpha = 0.5$ and $\gamma = 0.6$. In the ODP and MODP methods we adopt k nearest neighbor



FIGURE 3: Some shot samples.

TABLE 1: Comparison results between ODP, MODP, and ALPP.

Methods	OPP	MODP	ALPP
Precision	83.7	86.1	89.6
Recall	85.5	87.8	90.4

criterion to define the adjacency matrix, in which the k set to 10. The results of performance comparison by using ODP, MODP, and ALPP are shown in Table 1.

From Table 1, we can find that ALPP obtains comparable recognition performance to LPP and ODP with the same shot boundary detect method. In ALPP method, the improved weight definition combines the label information and model information with adaptive nearest neighbor select strategy, which is very important to reflect the data information truthfully. The experiment shows that ALPP has more useful and discriminating ability to extract video feature than others.

5.2. Shot Boundary Recognition Experiment. In order to investigate the performance of the proposed method, we recognize different video shots, especially for gradual shots. The system performance is compared with the multilayer perception network method (MPN method) [36]. We use the original video feature and set the parameters α and γ to be the same as before. In the proposed method, we use polynomial kernel, radial basis kernel and linear kernel to build MKSVM and set $d = 3$, $\sigma^2 = 0.005$, $\alpha = 1$, $\beta = 5$, $\rho = 0.5$, and $Q = 100$. The experimental results are summarized in Figure 4.

From Figure 4, we found that the above methods can detect not only abrupt cuts but also gradual shots very well, but the proposed method achieves more desired performance than the MPN method for shot boundary recognition. The average precision and recall of the proposed method is up to 94.1% and 91.7%, which is higher by 3.5% and 3.1% than the MPN method, respectively. These results demonstrate that the proposed method is a good tool for shot boundary recognition by using the optimized MKSVM.

5.3. Discussion. Two experiments for different type video have been systematically performed, and so now we can conclude the following.

- (1) We improve the effect of shot boundary detection in two stages. In the feature extract stage, we use ALPP to extract more useful and discriminating video

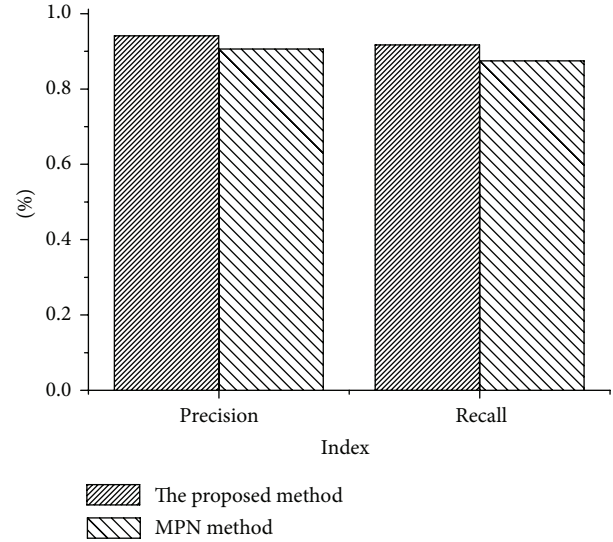


FIGURE 4: Comparison of two recognition methods.

feature. In the shot boundary detection stage, we use optimized MKSVM obtaining more remarkably boundary detection accuracy.

- (2) For feature extraction, the proposed ALPP performed better than LPP and ODP. This is because the former makes use of the label information and model information with adaptive nearest neighbor select strategy. At the same time, the improved weight definition can guarantee that two near points from different modes have a smaller similarity.
- (3) Compared with the MPN method, the proposed method can yield better performance on shot boundary recognition. It owes much to the optimized MKSVM, in which the parameters are optimized by the ant colony method. It should be noted that there are some false detection results in the above methods, which may be due to the existence of irregular object movement and the small content change between consecutive frames.

6. Conclusion

In this paper, we present a new video shot boundary recognition method, which focuses on two key problems: extracting more useful and discriminating feature and improving

the accuracy of shot boundary classifier. The major contributions of the paper are to propose an optimized locality preserving present method with model detection and optimized neighbor selection strategy. Meanwhile, an optimized shot boundary classifier based on MKSVM is designed with the ant colony optimization method. Experiments demonstrate that the proposed method is outstanding. The future work is to optimize the other parameters of MKSVM to achieve more desired result.

Conflict of Interests

The authors declare that there is no conflict of interests regarding the publication of this paper.

Acknowledgments

This project is supported by the Postdoctoral Science Foundation of Central South University, Scientific Research Fund of Hunan University of Finance and Economics under Grant (no. K201205), the Construct Program of the Key Discipline in Hunan Province, Hunan Province Education and Science Issue “Performance Evaluation for College Teacher Based on Adaptive Learning” (no. XJK013CGD083), and the Research Foundation of Science & Technology Office of Hunan Province under Grant (no. 2012GK3064).

References

- [1] G. Y. Wang, H. Z. Kou, and T. Li, “News video shot boundary detection by automated threshold,” *Computer Engineering and Design*, vol. 32, no. 5, pp. 1734–1737, 2011.
- [2] M. B. A. Vila, Q. Xu, M. Feixas, and M. Sbert, “Tsallis entropy-based information measures for shot boundary detection and keyframe selection,” *Signal, Image and Video Processing*, vol. 7, no. 3, pp. 507–520, 2013.
- [3] F. Liu, Y. W. Guo, and K. Y. Yin, “Shot boundary detection using adaptive threshold and fourier fitting,” *Journal of Software*, vol. 23, no. 2, pp. 105–114, 2012.
- [4] K. K. Warhade, S. N. Merchant, and U. B. Desai, “Shot boundary detection in the presence of fire flicker and explosion using stationary wavelet transform,” *Signal, Image and Video Processing*, vol. 5, no. 4, pp. 507–515, 2011.
- [5] V. B. Thakar and S. K. Hadia, “An adaptive novel feature based approach for automatic video shot boundary detection,” in *Proceedings of the International Conference on Intelligent Systems and Signal Processing*, pp. 145–149, Gujarat, India, March 2013.
- [6] Y. Huo, P. Z. Zhang, and Y. F. Wang, “Adaptive threshold based video shot boundary detection framework,” in *Proceedings of the International Conference on Image Analysis and Signal Processing*, pp. 1–5, Hangzhou, China, November 2012.
- [7] Y. Feng, S.-L. Luo, L.-P. Wang, and L.-M. Pan, “A new method of adaptive shot boundary detection,” *Transaction of Beijing Institute of Technology*, vol. 30, no. 1, pp. 100–104, 2010.
- [8] K. K. Warhade, S. N. Merchant, and U. B. Desai, “Shot boundary detection in the presence of illumination and motion,” *Signal, Image and Video Processing*, vol. 7, no. 3, pp. 581–592, 2013.
- [9] G. G. Gao and H. D. Ma, “To accelerate shot boundary detection by reducing detection region and scope,” *Multimedia Tools and Applications*, 2012.
- [10] H. Fang, J. Jiang, and Y. Feng, “A fuzzy logic approach for detection of video shot boundaries,” *Pattern Recognition*, vol. 39, no. 11, pp. 2092–2100, 2006.
- [11] L. Qun, W. Jiang, and Y. Wu, “Approach of shot-boundary detection based on multi-feature fusion,” *Computer Engineering and Applications*, vol. 46, no. 13, pp. 171–174, 2010.
- [12] Z.-W. Huang, W. W. Y. Ng, P. P. K. Chan, J. Li, and D. S. Yeung, “Video shot boundary detection using RBFNN minimizing the L-GEM,” in *Proceedings of the International Conference on Machine Learning and Cybernetics (ICMLC '10)*, pp. 2156–2160, Qingdao, China, July 2010.
- [13] P. P. Mohanta, S. K. Saha, and B. Chanda, “A model-based shot boundary detection technique using frame transition parameters,” *IEEE Transactions on Multimedia*, vol. 14, no. 1, pp. 223–233, 2012.
- [14] J. Li, Y. Ding, Y. Shi, and W. Li, “A divide-and-rule scheme for shot boundary detection based on SIFT,” *International Journal of Digital Content Technology and Its Applications*, vol. 4, no. 3, pp. 202–214, 2010.
- [15] L. Zhao, X. M. Sun, B. J. Shang, and J. G. Wu, “A shot boundary detection method based on context vector and Tabu-SVM,” *Journal of Computational Information Systems*, vol. 8, no. 16, pp. 6817–6824, 2012.
- [16] C. Zhang and W. Q. Wang, “A robust and efficient shot boundary detection approach based on fisher criterion,” in *Proceedings of the 20th ACM International Conference on Multimedia*, pp. 701–704, Nara, Japan, October 2012.
- [17] L. Zhao, X. Sun, and M. Zhang, “A shot boundary detection method based on PSO-SVM,” *Applied Mechanics and Materials*, vol. 130–134, pp. 3821–3825, 2012.
- [18] J. Lankinen and J. K. Kamarainen, “Video shot boundary detection using visual bag-of-words,” in *Proceedings of the International Conference on Computer Vision Theory and Applications*, pp. 788–791, Barcelona, Spain, February 2013.
- [19] A. Donate and X. Liu, “Shot boundary detection in videos using robust three-dimensional tracking,” in *Proceedings of the IEEE Computer Society Conference on Computer Vision and Pattern Recognition Workshops (CVPRW '10)*, pp. 64–69, San Francisco, Calif, USA, June 2010.
- [20] X. J. Li and P. Chen, “The application of fast and effective shot boundary detection algorithm in mechanical engineering,” *Advanced Materials Research*, vol. 681, no. 1, pp. 121–125, 2013.
- [21] X. F. He and P. Niyogi, “Locality preserving projections,” in *Proceedings of the Neural Information Processing Systems*, pp. 153–160, Vancouver, Canada, 2003.
- [22] B. Li, C. Wang, and D.-S. Huang, “Supervised feature extraction based on orthogonal discriminant projection,” *Neurocomputing*, vol. 73, no. 1–3, pp. 191–196, 2009.
- [23] S. W. Zhang, Y. K. Lei, Y. H. Wu, and J. A. Yang, “Modified orthogonal discriminant projection for classification,” *Neurocomputing*, vol. 74, no. 17, pp. 3690–3694, 2011.
- [24] L. Shapira, S. Avidan, and A. Shamir, “Mode-detection via median-shift,” in *Proceedings of the 12th International Conference on Computer Vision (ICCV '09)*, pp. 1909–1916, Kyoto, Japan, October 2009.
- [25] X. Y. Pan and H. Chen, “Multi-agent evolutionary clustering algorithm based on manifold distance,” in *Proceedings of the 8th International Conference on Computational Intelligence and Security*, pp. 123–127, Guangzhou, China, November 2012.
- [26] W. K. Wong and H. T. Zhao, “Supervised optimal locality preserving projection,” *Pattern Recognition*, vol. 45, no. 1, pp. 186–197, 2012.

- [27] C. Cortes and V. Vapnik, "Support-vector networks," *Machine Learning*, vol. 20, no. 3, pp. 273–297, 1995.
- [28] D. Tuia, G. Camps-Valls, G. Matasci, and M. Kanevski, "Learning relevant image features with multiple-kernel classification," *IEEE Transactions on Geoscience and Remote Sensing*, vol. 48, no. 10, pp. 3780–3791, 2010.
- [29] S. Sonnenburg, G. Rätsch, C. Schäfer, and B. Schölkopf, "Large scale multiple kernel learning," *Journal of Machine Learning Research*, vol. 7, no. 1, pp. 1531–1565, 2006.
- [30] A. Hogenboom, F. Frasinca, and U. Kaymak, "Ant colony optimization for RDF chain queries for decision support," *Expert Systems with Applications*, vol. 40, no. 5, pp. 1555–1563, 2013.
- [31] M. Shen, W. N. Chen, J. Zhang, H. S. H. Chung, and O. Kaynak, "Optimal selection of parameters for nonuniform embedding of chaotic time series using ant colony optimization," *IEEE Transactions on Cybernetics*, vol. 43, no. 2, pp. 790–802, 2013.
- [32] K. S. Yoo and S. Y. Han, "A modified ant colony optimization algorithm for dynamic topology optimization," *Computers and Structures*, vol. 123, no. 2, pp. 68–78, 2013.
- [33] L. Lei, "Text categorization using SVM with exponent weighted ACO," in *Proceedings of the 31st Chinese Control Conference*, pp. 3763–3768, Hefei, China, July 2012.
- [34] J. Yuan, H. Wang, L. Xiao et al., "A formal study of shot boundary detection," *IEEE Transactions on Circuits and Systems for Video Technology*, vol. 17, no. 2, pp. 168–186, 2007.
- [35] H. Zhang, A. Kankanhalli, and S. W. Smoliar, "Automatic partitioning of full-motion video," *Multimedia Systems*, vol. 1, no. 1, pp. 10–28, 1993.
- [36] P. P. Mohanta, S. K. Saha, and B. Chanda, "A model-based shot boundary detection technique using frame transition parameters," *IEEE Transactions on Multimedia*, vol. 14, no. 1, pp. 223–233, 2012.

Research Article

Active Semisupervised Clustering Algorithm with Label Propagation for Imbalanced and Multidensity Datasets

Mingwei Leng,¹ Jianjun Cheng,¹ Jinjin Wang,¹ Zhengquan Zhang,²
Hanhai Zhou,¹ and Xiaoyun Chen¹

¹ School of Information Science and Engineering, Lanzhou University, Lanzhou 730000, China

² Gansu Computing Center, Lanzhou 730000, China

Correspondence should be addressed to Xiaoyun Chen; chenxy@lzu.edu.cn

Received 27 August 2013; Revised 11 October 2013; Accepted 13 October 2013

Academic Editor: Gelan Yang

Copyright © 2013 Mingwei Leng et al. This is an open access article distributed under the Creative Commons Attribution License, which permits unrestricted use, distribution, and reproduction in any medium, provided the original work is properly cited.

The accuracy of most of the existing semisupervised clustering algorithms based on small size of labeled dataset is low when dealing with multidensity and imbalanced datasets, and labeling data is quite expensive and time consuming in many real-world applications. This paper focuses on active data selection and semisupervised clustering algorithm in multidensity and imbalanced datasets and proposes an active semisupervised clustering algorithm. The proposed algorithm uses an active mechanism for data selection to minimize the amount of labeled data, and it utilizes multithreshold to expand labeled datasets on multidensity and imbalanced datasets. Three standard datasets and one synthetic dataset are used to demonstrate the proposed algorithm, and the experimental results show that the proposed semisupervised clustering algorithm has a higher accuracy and a more stable performance in comparison to other clustering and semisupervised clustering algorithms, especially when the datasets are multidensity and imbalanced.

1. Introduction

Semisupervised clustering algorithm has been studied recently as a method for improving the performance of clustering algorithm, and it allows the human expert to incorporate domain knowledge into the process of clustering and thus guides it to get better results. The use of domain knowledge in clustering task is motivated by the fact that the priori knowledge for some data objects can be obtained in many applications, the priori knowledge can be the labels of the data objects or the relationships between data objects. The “must-link” and “cannot-link” constraints capture relationships among data objects. Labeled objects could be used in clustering algorithms to help determine the groups and get more meaningful results. Most of the existing semisupervised clustering algorithms can be divided into three categories: method based on labeled data [1–9], pairwise constraints method [10–16], and fuzzy semisupervised method [17–22].

Semisupervised clustering algorithms based on labeled data utilized the label information to improve the performance of clustering. Semisupervised k-means clustering

algorithm is a popular semisupervised clustering method [1–4]. Basu et al. exploited labeled data to generate initial seed clusters [1]. Bilenko et al. proposed a principled probabilistic framework based on hidden markov random fields for semisupervised clustering and presented HMRF-KMEANS based on EM and hidden markov random fields framework [2]. Leng et al. used labeled data to initialize the process of k-means clustering and obtained the similarity threshold of clusters based on the label information; they also utilized similarity threshold to guide k-means clustering algorithm [3]. Dang et al. presented a novel initialization method by propagating the labels of labeled data to more unlabeled data [4]. Zhong used deterministic annealing to expand three semisupervised clustering methods seeded clustering, constrained clustering, and feedback clustering, and their performances were compared with real text datasets [5]. Semisupervised density-based clustering is another kind of popular semisupervised clustering method [6, 7]. Lelis and Sander exploited labeled data to find values for ϵ . They gave a fixed value of MinPts and used the minimum spanning tree (MST) to partition dataset [6]. Böhm and Plant expanded

the clusters starting at all labeled objects simultaneously and proposed a semisupervised hierarchical clustering algorithm [7]. Guan et al. proposed an asymmetric similarity measure for two different documents and a new semisupervised clustering algorithm by expanding affinity propagation [8]. Shiga and Mamitsuka combined soft spectral clustering and label propagation and proposed a semisupervised clustering algorithm by learning locally informative data from multiple graphs [9].

The concepts of two basic pairwise constraints were defined by Wagstaff et al. [10]; they made the insertion of domain knowledge into the clustering (k -means in this case) process, and the pairwise constraints were given as the must-link and cannot-link. Reference [11] divided the pairwise constraints method into instance-level semisupervised clustering [10, 12, 13] and space-level semisupervised clustering [11, 14–16]. Wagstaff et al. viewed the pairwise constraints as instance-level constraints in the process of clustering and proposed the semisupervised clustering algorithm COP-KMeans [10]. Ruiz et al. proposed a semisupervised clustering algorithm called C-DBSCAN [12], which built a set of initial local clusters by partitioning data space into denser subspaces and cannot-link constraints, then merged density-connected local clusters and enforced the must-link constraints, finally, C-DBSCAN merged adjacent neighborhoods in a bottom-up fashion and enforced the remaining cannot-link constraints. Wang and Davidson combined spectral clustering and pairwise constraints in a principled and flexible manner [13]. They used a user-specified threshold to lower-bound how well the given constraints were satisfied, instead of trying to satisfy every given constraint, and they proposed a flexible and generalized framework for constrained spectral clustering. Instance-level semisupervised clustering method introduces pairwise constraints into clustering only and does not utilize the priori knowledge with the highest degree. Space-level semisupervised clustering not only makes use of constraints but also employs the space information provided by the constraints to adjust the process of clustering.

Fuzzy clustering model adopts membership to show the results of clustering, and membership grades are used as probabilities that each data object belongs to every class. In order to improve the performance of fuzzy clustering, the priori knowledge has been applied into it, and most of them used the priori knowledge to modify the objective function. Labeled data [17–19] and pairwise constraints [20–22] are two principal forms of priori knowledge in the fuzzy semisupervised clustering. Pedrycz and Waletzky improved the performance of clustering algorithm by using the information provided by labeled patterns to aid the process of clustering [17]. Bouchachia and Pedrycz utilized the information provided by labeled data to modify the objective function of fuzzy c -means [18]. Gao et al. proposed a fuzzy semisupervised clustering algorithm based on distance, which guided the process of clustering by using background information provided by labeled data and optimized the objective function by adding the label information into it [19]. Grira et al. added the information of pairwise constraints into the process of updating memberships and proposed a fuzzy semisupervised clustering algorithm based on pairwise constraints,

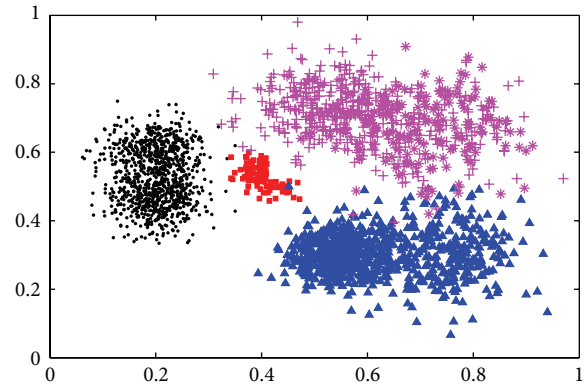


FIGURE 1: An imbalanced and multidensity dataset which contains 4 clusters.

which guided the process of solving membership matrix [20]. Pedrycz et al. used pairwise constraints information to optimize fuzzy c -means by adding an optimization step into the iteration process [21]. Yan et al. proposed fuzzy semisupervised coclustering algorithm for document by using the pairwise constraints to guide the process of constructing it [22].

Most of the semisupervised clustering algorithms assume that the labeled dataset or pairwise constraints are given. In practice, getting the priori knowledge is very expensive and time consuming. In addition, if the size of labeled dataset is too small in the process of constructing semisupervised clustering based on labeled data, some clusters may have no labeled data in imbalanced dataset, and then the data in those clusters will be assigned to other clusters forcibly. For example, the dataset shown in Figure 1 contains four clusters (these clusters are labeled with shapes “·”, “■”, “▲”, and “*”, resp.). The size of cluster “■” is much less than that of the rest of the clusters. If the labeled data are randomly selected from the whole dataset, the data objects in cluster “■” are very difficult to be selected. If cluster “■” has no labeled data, then most of the semisupervised clustering algorithms will miss the cluster “■”. How to select data from imbalanced dataset to guarantee that each cluster has more than one data that can be selected is one work of this paper. One of the solutions to this problem is to adopt active learning method to guide the process of selecting data points, which aims to cover as many clusters as possible.

The active learning method, which aims to achieve high accuracy using labeled data as few as possible, selects informative data actively and labels them by oracle. The active learning method can minimize the cost of obtaining labeled data points greatly without compromising the performance of clustering algorithm, and this is very attractive and valuable in real-world applications.

Perhaps the simplest and most commonly used active learning technique is uncertainty sampling [23], and least confident strategy, margin sampling, and entropy are the most popular uncertainty sampling strategies. Since the most likely label sequence can be efficiently computed using dynamic programming, least confident strategy has been

popular with statistical sequence models in information extraction tasks [24, 25]. However, the least confident strategy only considers information about the most probable label, and it discards information about the remaining label distribution, whereas margin sampling was proposed to correct for a shortcoming in least confident strategy by incorporating the second most likely label [26]. Entropy may be the most popular uncertainty sampling strategy, and it is easily applied to more complex structured instances, such as sequences [25] and trees [27]. Scheffer and Wrobel presented an active learning algorithm to reduce the required data labeling effort and increase the quality of the learning model by selecting “difficult” unlabeled samples [28].

Although most of the active learning strategies are applied into classification tasks, in the recent years, active learning is also introduced into clustering [29–35]. Mallapragada et al. selected constraints through using a min-max criterion to improve the performance of semisupervised clustering algorithms by selecting most uncertain data [29]. The uncertainty sampling technique selects the data objects which lie in the boundaries of clusters, and they are not “representative” of other data in the same cluster. Since knowing their labels is unlikely to improve the performance of the clustering algorithm as a whole, the “representative” method was proposed to solve this problem [30, 31]. Nguyen and Smeulders selected the most representative samples to avoid repeatedly labeling samples in the same cluster [30]. Vu et al. selected useful examples according to a min-max approach to determine the set of labeled data [31]. Active learning technique was also introduced into semisupervised clustering based on pairwise constraints [32–35]. Zhao et al. selected informative document pairs for obtaining user feedback by using active learning approach and incorporated instance-level constraints to guide the clustering process in DBSCAN [32]. Grira et al. defined an active mechanism for the selection of candidate constraints to minimize the amount of constraints required [33]. Wang and Davidson presented an active query strategy based on maximum expected error reduction and a constrained spectral clustering algorithm that can handle both hard and soft constraints [34]. Huang et al. conducted a preliminary clustering process to estimate the true clustering assignments and chose informative document pairs by means of learning the intermediate cluster structure [35].

Most of the existing active learning algorithms are pool-based or stream-based, and they are mainly applied in supervised learning. Although active learning is introduced into semisupervised clustering, the performances of these clustering algorithms are unsatisfying when dealing with the imbalanced and multidensity datasets. The most uncertain data lies on the boundaries of clusters, and it is not “representative” of other data in the same cluster. So knowing its label is unlikely to improve the performance of the clustering algorithm as a whole. This paper selects the data with max density from each cluster which is the result of MST clustering.

Since the dataset is imbalanced, the distribution of labeled data in a given dataset is not the same as the whole data space, and a data point and its k -nearest labeled data may not be

in the same cluster, which leads to the result that most of the existing semisupervised learning algorithms cannot work well, especially when the size of labeled dataset is very small. However, in the whole data space, the label of a data point should be the same as that of most of its k -nearest neighbors. The proposed semisupervised clustering algorithm with label propagation is based on this idea. It expands the labeled dataset by labeling k -nearest neighbors of labeled dataset based on a threshold. Once an unlabeled data is labeled, it should be added into labeled dataset. If the difference of density between clusters is large in multidensity datasets, the expanding process cannot use the same threshold, and the threshold should be generated automatically according to the density of each cluster to which the labeled data point belongs. A new active semisupervised clustering algorithm, called active semisupervised clustering algorithm for imbalanced and multidensity datasets, is proposed based on the facts previously described. The presented algorithm tries to ensure that the selected data can cover as many clusters as possible in a given imbalanced and multidensity dataset. Those selected data are labeled by oracle, and they are viewed as the initial set of labeled data in the process of semisupervised clustering. The proposed algorithm expands the labeled dataset by propagating labels according to expanded threshold obtained automatically based on the character of each cluster which is obtained by running MST clustering algorithm. The proposed clustering algorithm mainly has the following two advantages in comparison with other semisupervised clustering methods.

- (1) The proposed semisupervised clustering method utilizes MST clustering to select data points actively so as to avoid labeling data in the same cluster repeatedly. If we need m labeled data objects, we partition the given dataset into m clusters by using MST clustering and select actively only one data from each cluster. This method can reduce the number of labeled data points greatly without compromising the performance of clustering, and the selected data can cover as many clusters as possible.
- (2) The proposed clustering algorithm achieves label propagation by using labeled data to expand their k -nearest neighbors according to the criterion that is automatically obtained based on the density of the cluster to which the labeled data point belongs, and the expanding model only requires one parameter.

The rest of this paper is organized as follows. Section 2 gives the proposed semisupervised clustering algorithm. In Section 3, three datasets from UCI Machine Learning Repository and one synthetic dataset are used to demonstrate the proposed algorithm. We summarize our work in Section 4.

2. Active Semisupervised Clustering for Imbalanced and Multidensity Datasets

The k -nearest neighbors algorithm is most often used for classification, and it gives the label of an unlabeled data by comparing it to the first k most similar objects in the

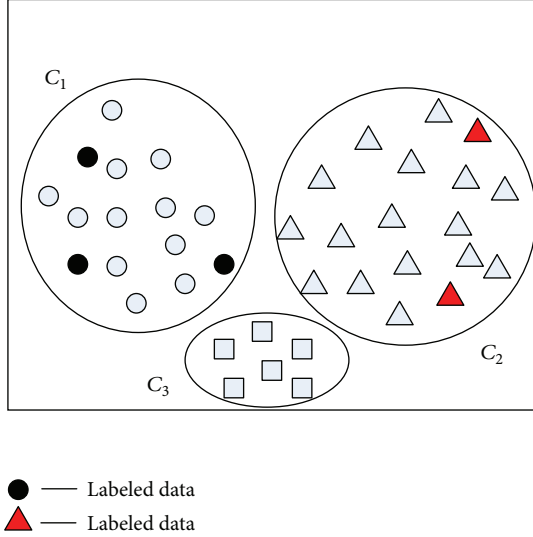


FIGURE 2: Low accuracy of KNN on an imbalanced dataset.

training set. Given a dataset $D = D_l \cup D_u$, where D_l is the labeled dataset and D_u is the unlabeled dataset, the k -nearest neighbors algorithm labels an unlabeled data y with the most frequent label among its k -nearest labeled neighbors. The label of an unlabeled data is given as follows:

$$y^l = \operatorname{argmax}_l \sum_{x \in \text{KNN}(y, D_l)} [x^l == l], \quad (1)$$

where y^l and x^l are the labels of the data objects y and x , respectively, and the meaning of $\text{KNN}(y, D_l)$ is defined as given in Definition 1.

Definition 1. $\text{KNN}(x, C)$. Given one cluster C and one data object $x \in C$, $\text{KNN}(x, C)$ is the set of k -nearest neighbors of x in C .

Each classification algorithm requires enough labeled data to achieve high classification accuracy. However, labeling data is quite expensive and time consuming in many real-world applications, and we can get a very small size of labeled dataset. For instance, there are 3 classes in Figure 2, and D_l contains 5 data objects (3 data objects in C_1 , 2 data objects in C_2 , and no data objects in C_3). The size of labeled dataset is very small compared with the whole dataset; suppose that we let $k = 1$ for k -nearest neighbors algorithm and use it to label the unlabeled data. All unlabeled data objects in C_3 and four unlabeled data objects in C_2 are assigned to C_1 .

There are two problems for most of classifications and semisupervised clustering algorithms like k -nearest neighbors that lead those unlabeled data to wrong class when the size of labeled dataset is too small.

- (1) The first one is that the whole dataset is imbalanced and the size of labeled dataset is too small, and using random method to select labeled data cannot guarantee that each class has more than one data object to be selected.

- (2) The second is that the class label of some unlabeled data and that of its k -nearest labeled neighbors are not the same.

An active semisupervised clustering algorithm with label propagation for imbalanced and multidensity datasets is proposed to solve the previously mentioned problems. It uses MST clustering to partition the given dataset into clusters and selects one data object from each cluster as labeled data. This method for data selection can guarantee that the selected data can cover as many clusters as possible. Although the k -nearest labeled neighbors of each data in C_3 are not in C_3 , the k -nearest neighbors are in C_3 (if $k \leq 4$). Since k -nearest neighbors of each data in C_3 are unlabeled, k -nearest neighbors algorithm has to find the nearest labeled neighbor from C_1 and C_2 . The proposed algorithm selects more important data objects as labeled data and expands its label to its neighbors.

Some definitions are given as follows in order to describe the proposed active semisupervised clustering algorithm.

Definition 2. $\text{dis_KNN}(x, y, C)$. Given one cluster C , one data object $x \in C$, and $y \in \text{KNN}(x, C)$, $\text{dis_KNN}(x, y, C)$ is the distance between x and y .

Definition 3. $k_avgdis(C)$. Given one cluster C , $k_avgdis(C)$ is defined as follows:

$$k_avgdis(C) = \frac{\sum_{x \in C} \max \text{dis_KNN}(x, y, C)}{|C|}, \quad (2)$$

where $|C|$ is the number of data in cluster C .

Definition 4. $\text{density}(x, C)$. Given one cluster C and a data object $x \in C$, $\text{density}(x, C)$ is defined as follows:

$$\text{density}(x, C) = \frac{1}{\max \text{dis_KNN}(x, y, C)}. \quad (3)$$

The proposed active semisupervised clustering process can be divided into two algorithms: active data selection algorithm (Algorithm 1) and semisupervised clustering algorithm with label propagation (Algorithm 2). Algorithm 1 selects important data which do not lie in the boundaries of clusters and outputs those selected data after labeling them. Algorithm 2 expands the labeled datasets by propagating themselves labels to their neighbors.

If the dataset is imbalanced and we select small number of data points from this kind of datasets randomly, then there exist some clusters which have no data to be selected. Using these selected data as the labeled data to guide the process of clustering, the data objects in clusters which have no data being selected are assigned to other clusters forcibly. Thus, decreases the accuracy of semisupervised clustering algorithm, and the clustering results are unsatisfying. In order to make the selected data cover as many clusters as possible, an active mechanism of selecting data points is presented. It partitions a given dataset into m clusters by using MST clustering algorithm; here, m is the number of the data objects which will be selected, and only one data

```

(1) Let  $m = |D| \times p$ ,  $m$  is the number of data points
    to be selected,  $|D|$  is the size of dataset  $D$ .
(2) Use Prime method to construct MST of  $D$ .
(3) Foreach  $edge$  in MST do
(4)   Compute edge's inconsistent value  $f$ .
(5) End Foreach
(6) Sort all  $edges$  in descending order according to  $f$ .
(7) Insert the sorted edges into a list:  $edgesLst$ .
(8) Foreach  $edge$  in  $edgesLst$  do
(9)   Delete  $edge$  from MST
(10)  Check the number of partitions in MST,  $num$ 
(11)  If  $num == m$  then
(12)    Generate  $num$  clusters  $T_1, T_2, \dots, T_m$  from MST
(13)    Break
(14)  End If
(15) End Foreach
(16) Foreach cluster  $T$  in  $T_1, T_2, \dots, T_m$  do
(17)  Compute density of each point in  $T$ 
(18)  Select one data with max density and add it to  $D_l$ 
(19) End Foreach
(20) Query oracle about labels of data in  $D_l$ .
(21) Return  $T_1, T_2, \dots, T_m$  and  $D_l$ .

```

ALGORITHM 1: Selecting data by using MST clustering algorithm (*SelectDataPoint* (D, p)).

```

(1) Input the value of  $k$ .
(2) SelectDataPoint ( $D, p$ ).
(3) Suppose that the number of different labels in  $D_l$  is  $p$ .
(4) Merge  $T_1, T_2, \dots, T_m$  into  $C_1, C_2, \dots, C_p$  according
    to labels of data in  $D_l$ .
(5) Foreach cluster  $C$  in  $C_1, C_2, \dots, C_p$  do
(6)   Foreach data point  $x$  in  $C$  do
(7)     Compute the KNN ( $x, C$ )
(8)   End Foreach
(9)   Compute  $k\_avgdis(C)$ s
(10) End Foreach
(11) Foreach cluster  $C$  in  $C_1, C_2, \dots, C_p$  do
(12)   $Expend(C, k\_avgdis(C), D_l)$ 
(13) End Foreach
(14) Label the rest unlabeled data according to KNN rule.
(15) Output the clustering results.

```

ALGORITHM 2: Semisupervised clustering algorithm with label propagation.

point is chosen in each cluster. Since only one data point in each cluster is selected, each of selected data should be the better representations of corresponding cluster, and the centers of clusters and the data with maximum density are two better representation of each cluster. This paper utilizes the method of label propagation to achieve a high accuracy of semisupervised clustering algorithm, and the data objects with maximum densities are chosen by us and are labeled by oracle. The details of selecting data points are shown in Algorithm 1.

Algorithm 1 has two parameters D and p . D is the dataset which will be clustered, and p is the percent of the selected data in D . Algorithm 1 uses the MST clustering to

partition D into m clusters, and the value of m is larger than or equal to the real number of clusters in the dataset D . MST clustering algorithm used in Algorithm 1 is proposed by Zahn [36]. In the process of labeling the data, we should select the certain data objects which do not lie in the boundaries of clusters. Since the selected data are "representative" of other data in the same cluster, their labels are easy to be labeled, and this can reduce the required data labeling effort and increase the quality of the labeled data. The proposed semisupervised clustering algorithm requires very small number of labeled data, and even some cluster has only one data to be selected as labeled data. The data with max density in one cluster is easier to be labeled compared

```

(1) Get all the labeled data which belong to  $C$  from  $D_l$ .
(2) Let  $D_C^l$  denote these labeled data.
(3) Foreach  $x$  in  $D_C^l$  do
(4)   Compute density of data  $x$ ,  $density(x, C)$ 
(5) End Foreach
(6)   Sort  $D_C^l$  in descending order according to data
      density
(7) While ( $D_C^l$  is not null)
(8)   Take out the first data  $x$  from  $D_C^l$ 
(9)   Compute  $KNN(x, C)$ 
(10)  Foreach  $y$  in  $KNN(x, C)$  do
(11)   If  $dis\_KNN(x, y, C) \leq avgdis$ 
(12)     $y^l \leftarrow x^l$ 
(13)   Insert  $y$  into  $D_C^l$ , and add  $y$  into  $D_l$ 
(14)  End If
(15) End Foreach
(16) Delete  $x$  from  $D_C^l$ 
(17) End while
(18) Return  $D_l$ 

```

ALGORITHM 3: $Expend(C, k_avgdis(C), D_l)$.

with the rest of data, so Algorithm 1 selects the data with max density in each cluster and labels them by querying the oracle about labels of the selected data.

How to use small number of labeled data to achieve a higher accuracy of clustering algorithm is a challenging work, especially when the dataset is imbalanced and multidensity. The semisupervised clustering algorithms should use the character of labeled dataset to guide their clustering process. In this paper, firstly, the clustering results of MST are merged according to the label of its labeled data (each cluster has and only has one labeled data). Since the density of each cluster is not unique and the densities of clusters may be different, we should not use the same expanding threshold when utilizing the method of label propagation to expand the labeled dataset. Secondly, the expanding threshold of each cluster should be obtained based on its density automatically, and it is used to expand the labeled dataset in one cluster. Finally, the rest of unlabeled data are assigned with the most frequent label among its k -nearest labeled neighbors. More detailed information is given in Algorithm 2.

The k in step 1 of Algorithm 2 is the parameter of k -nearest neighbors. Step 2 uses Algorithm 1 to select m data points. Since the value of m is not less than that of p and if m is larger than p , then some clusters in T_1, T_2, \dots, T_m are in the same cluster. Algorithm 2 can be divided into three stages. Firstly, Step 4 merges the clusters which should be in the same cluster into one. x_i and x_j are two data points in D_l , and x_i^l and x_j^l are the labels of them, respectively. If $x_i^l == x_j^l$, then Step 4 merges T_i and T_j into one. Secondly, different clusters may have different densities in multidensity datasets, which leads to the result that the process of label expanding cannot adopt the same expanding threshold on the whole data space when the difference of density between clusters is very large. It should adopt different expanding threshold according to its density of the cluster to which

it belongs. Step 9 computes the expanding threshold for each cluster. In each cluster C_i ($1 \leq i \leq p$), the labeled data which are in C_i expand their labels to their k -nearest neighbors based on the threshold which is obtained in C_i automatically, and function $Expend(C, k_avgdis(C), D_l)$ uses the expanding threshold $k_avgdis(C)$ to expand the labeled dataset D_l by propagating the labels of labeled data in cluster C , and the expanding process is given as Algorithm 3. Steps 5 to 13 complete the process of label propagating. Thirdly, since we use the expanding threshold $k_avgdis(C)$ in the process of label propagation, then part of unlabeled data in cluster C is not be labeled. We should label these unlabeled data after the ending of label propagation and use the k -nearest neighbors rule to deal with the rest of unlabeled data.

Algorithm 3 expands the labeled data in cluster C by using the mechanism of label propagation. In cluster C , we find out the k -nearest neighbors in C for each data x in C . In cluster C , $k_avgdis(C)$ is used as the expanding threshold, which is necessary in multidensity dataset. Steps 10 to 15 utilize $k_avgdis(C)$ as the threshold to expand the labeled data in cluster C . Firstly, we take out one labeled data x which has not been used to expand its label to $KNN(x, C)$ in C . For any data point y in $KNN(x, C)$, if and only if $dis_KNN(x, y, C)$ is less than $k_avgdis(C)$, the label of x is assigned to y . After dealing with $KNN(x, C)$, it takes another labeled data which has not been used to expand its k -nearest neighbors in C and uses the same method to label its k -nearest neighbors. If all of the labeled data in C have been used to label their k -nearest neighbors, Algorithm 3 returns the D_l as the result.

3. Experimental Results and Discussion

We use three standard datasets from UCI Machine Learning Repository [37]—IRIS, Wine, and Ecoli—and one synthetic dataset which is imbalanced and multidensity to demonstrate

the performance of the proposed algorithm. The Euclidean metric is employed to compute the distances between data objects. In order to prove that the proposed method has the ability of dealing with the imbalanced and multidensity datasets, we construct three imbalanced datasets by deleting data objects from IRIS, Wine, and Ecoli. Since the priori knowledge is given as the labeled data, we compare the proposed algorithm with SSDBSCAN and Constrained-Kmeans. We use the clustering accuracy to evaluate the clustering results. The notion of clustering accuracy (CA) of a dataset D is defined as follows:

$$CA = \frac{|D'|}{|D|} \times 100\%, \quad (4)$$

where $|D|$ is the size of the unlabeled dataset D and $|D'|$ is the number of labeled data which are labeled correctly by clustering algorithms in D .

3.1. Standard Datasets. This subsection demonstrates the performance of the proposed semisupervised clustering algorithm in three UCI datasets: IRIS, Wine, and Ecoli. In order to test that the proposed algorithm has a higher accuracy compared with SSDBSCAN and Constrained-Kmeans in imbalanced and multidensity datasets, three datasets are constructed by deleting part of data from some clusters of IRIS, Wine, and Ecoli.

3.1.1. IRIS Dataset. The IRIS dataset, which contains 150 data objects, is perhaps the most well-known dataset in pattern recognition and data mining literature. IRIS contains 3 clusters of 50 data objects each. We turn IRIS into imbalanced and multidensity dataset by deleting 20 data objects from the second cluster randomly, and let modified IRIS denote this dataset. Since IRIS contains only 150 data objects, we select 2, 3, 4, 5, 6, 7, 8, 9, and 10 percents of the dataset from IRIS and the modified IRIS to be labeled datasets, respectively, and view the rest of the data as the unlabeled datasets. The experimental results are shown in Figures 3 and 4.

Figure 3 shows the experimental results of the 3 algorithms which run on the IRIS dataset. Figure 3 shows that the proposed algorithm has a higher accuracy compared with the SSDBSCAN and Constrained-Kmeans. In addition, the proposed algorithm is more stable than SSDBSCAN and Constrained-Kmeans, especially when the size of labeled dataset is very small. The proposed algorithm can reach stable state when selecting more than 3% of all data (there are only 4 labeled data). The accuracy of Constrained-Kmeans is very low when selecting 3% and 4% of all data, just because there is one cluster which has no data being selected, Constrained-Kmeans partitions IRIS dataset into 2 clusters forcibly, and SSDBSCAN has the same problem. The method of labeled data selection is based on MST clustering, and the experimental results show that the accuracy of clustering can be improved highly when using 4 labeled data to guide the process of clustering.

Figure 4 displays the experimental results of algorithms running on the modified IRIS dataset. The proposed algorithm has a much higher accuracy and more stable state

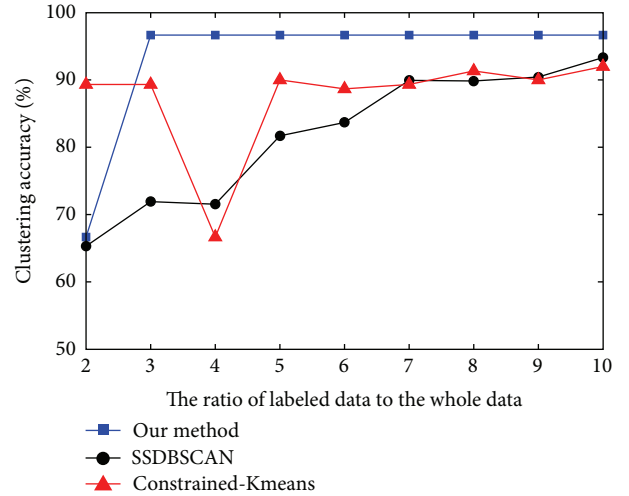


FIGURE 3: Clustering accuracy (%) obtained with the proposed algorithm and other algorithms on IRIS.

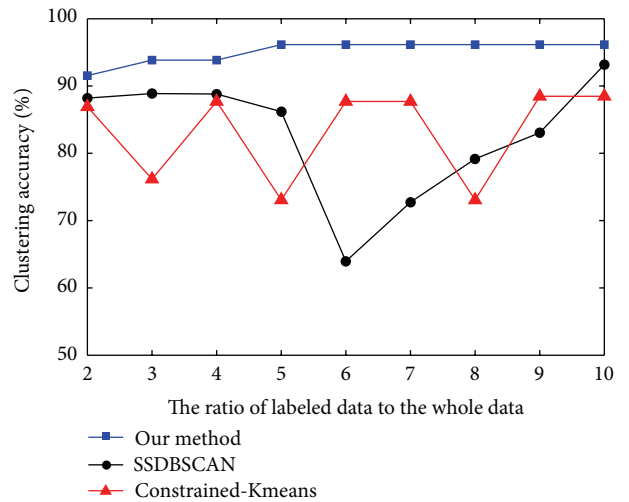


FIGURE 4: Clustering accuracy (%) obtained with the proposed algorithm and other algorithms on modified IRIS.

than SSDBSCAN and Constrained-Kmeans. When IRIS is modified to be imbalanced and multidensity, the labeled data which is selected by using random method cannot cover all clusters, which makes some clusters assigned to other clusters in force, and this is reflected in SSDBSCAN and Constrained-Kmeans, especially in Constrained-Kmeans. But the accuracy of the proposed algorithm is little influenced. The accuracy of the proposed algorithm reaches 93.8% when selecting 3% of all data, and the presented algorithm can reach stable state when selecting more than 7 labeled data.

3.1.2. Wine Dataset. Wine dataset contains 178 data objects, and these data can be assigned to 3 clusters whose sizes are 59, 71, and 48, respectively. We adapt the same method to turn Wine dataset into an imbalanced and multidensity dataset by removing 25 data objects from the first cluster randomly, and let modified Wine denote this dataset. We select 2, 3, 4, 5,

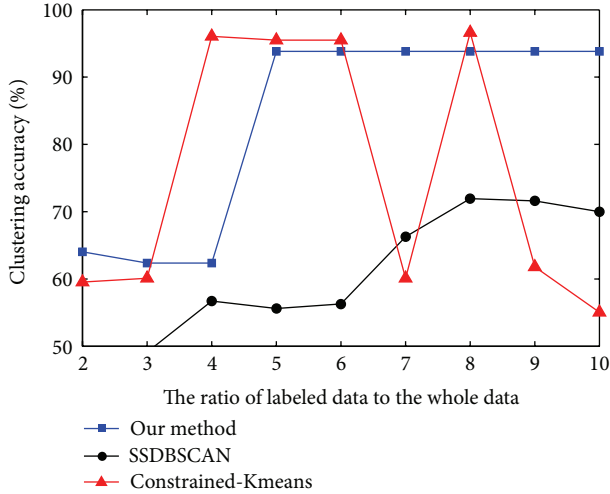


FIGURE 5: Clustering accuracy (%) obtained with the proposed algorithm and other algorithms on Wine.

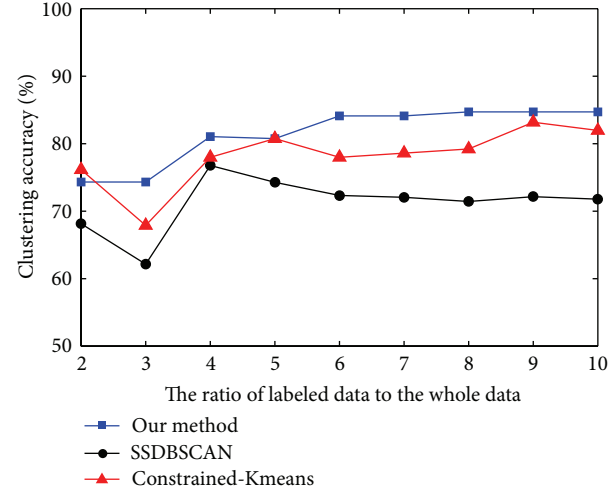


FIGURE 7: Clustering accuracy (%) obtained with the proposed algorithm and other algorithms on Ecoli.

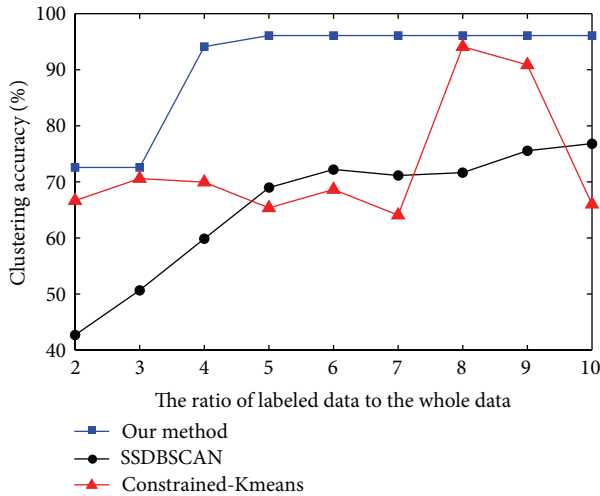


FIGURE 6: Clustering accuracy (%) obtained with the proposed algorithm and other algorithms on modified Wine.

6, 7, 8, 9, and 10 percents of the dataset from Wine and the modified Wine to be labeled datasets, respectively, and view the rest of the data as unlabeled datasets. Figures 5 and 6 show the changes of accuracy of the three algorithms.

Figure 5 shows that the proposed algorithm has a more stable state than SSDBSCAN and Constrained-Kmeans, and the accuracy of the proposed algorithm is much higher than that of Constrained-Kmeans. The proposed algorithm can reach stable state when selecting more than 5% of all data (there are only 9 labeled data). Since SSDBSCAN and Constrained-Kmeans use random method to select labeled datasets, there exists some cluster that has no data that can be selected as labeled data, and their accuracy fluctuates along with the change of percent of labeled data and this is also shown in Figure 5.

Figure 6 shows that the accuracy of Constrained-Kmeans and SSDBSCAN fluctuates much larger than that of the

proposed method, and the proposed algorithm reaches a stable state when selecting only 5% of all data. When we select more than 4% of all data as the labeled data actively, the accuracy of the proposed method is 94.1%, and when the percent is more than 5, the accuracy is 96.1%. When the labeled data cover all clusters, Constrained-Kmeans has a high clustering accuracy which is close to that of the proposed method. But, in the 9 labeled datasets, only two labeled datasets cover all clusters, and the rest 7 labeled datasets miss some cluster. The accuracy of Constrained-Kmeans is less than 80% on the 7 labeled datasets. The accuracy of SSDBSCAN is less than 80% on all the labeled datasets.

3.1.3. Ecoli Dataset. The Ecoli dataset, which contains 336 data objects, has 8 clusters. The sizes of the 8 clusters are 143, 77, 52, 35, 20, 5, 2, and 2, respectively.

Since the data objects of the last three clusters are less than 6 and they can be viewed as noises, in the experiment, we delete these data. We select 2, 3, 4, 5, 6, 7, 8, 9, and 10 percents of the dataset from Ecoli dataset, respectively. The experimental results are shown in Figure 7. The results are similar to those in Figures 4 and 6. Figure 7 shows that the proposed algorithm has a much higher accuracy and more stable state than SSDBSCAN and Constrained-Kmeans. The accuracy of Constrained-Kmeans and SSDBSCAN fluctuates along with the difference of labeled data.

3.2. Synthetic Dataset. In this subsection, we generate 2500 data objects which have two attributes and are viewed as imbalanced and multidensity datasets, and these data can be partitioned into 4 clusters whose sizes are 1000, 100, 800, and 600, respectively. These data are shown in Figure 1. Ten subsets were selected from this synthetic dataset to demonstrate the three algorithms, and the ratios of them to the whole dataset are 1, 2, 3, 4, 5, 6, 7, 8, 9, and 10 percents, respectively. The experimental results are shown in Figure 8.

The accuracy of Constrained-Kmeans and SSDBSCAN depends on the labeled data seriously. Although we select

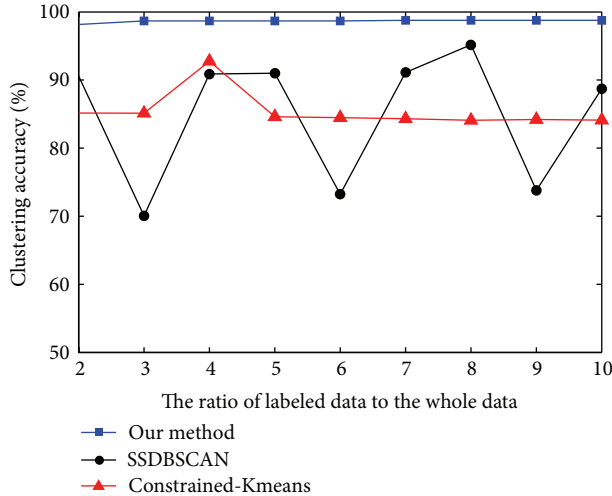


FIGURE 8: Clustering accuracy (%) obtained with the proposed algorithm and other algorithms on Synthetic.

10% of all data, the second cluster has no one data that can be selected as the labeled data, and, in the clustering results, the data objects in the second cluster have to be assigned to other clusters, and this phenomenon manifests in the clustering results of SSDBSCAN. In addition, even if Constrained-Kmeans selects labeled data from all of the clusters, it assigns some data objects from the rest of the three clusters to the second cluster, and this is the reason why the accuracy of Constrained-Kmeans is not improved as the percent of labeled data increases. Figure 8 also shows that the proposed algorithm has a much higher accuracy compared with SSDBSCAN and Constrained-Kmeans. The accuracy of the proposed algorithm exceeds 98% on the 10 subsets.

4. Conclusion

A new active semisupervised clustering algorithm is proposed which actively selects informative data by dealing with the clustering results of MST. Labeling these data and using them to label their k -nearest neighbors are based on an adaptive threshold. The experimental results show that the proposed semisupervised clustering can reach a stable state which only requires very small size of labeled dataset. However, the accuracy of the proposed semisupervised clustering is much lower in the dataset in which clusters overlap each other than that in the dataset in which the boundaries between clusters are not very vague. In the future, we plan to extend this work to the dataset in which clusters overlap each other. We will work on the data selection strategy in an active manner and the method of label propagation in the imbalanced and multidensity datasets in which clusters overlap each other.

Acknowledgments

This paper is supported by the Fundamental Research Funds for the Central Universities (Izujbky-2012-212) and is partially supported by the IBM 2010 X10 Innovation Awards Project.

References

- [1] S. Basu, A. Banerjee, and R. J. Mooney, "Semi-supervised clustering by seeding," in *Proceedings of the 19th International Conference on Machine Learning (ICML '02)*, pp. 27–34, 2002.
- [2] M. Bilenko, S. Basu, and R. J. Mooney, "A probabilistic framework for semi-supervised clustering," in *Proceedings of the 10th ACM SIGKDD International Conference on Knowledge Discovery and Data Mining (KDD '04)*, pp. 59–68, August 2004.
- [3] M. Leng, X. Chen, and L. Li, "K-means clustering algorithm based on semi-supervised learning," *Journal of Computational Information Systems*, vol. 4, no. 5, pp. 2007–2013, 2008.
- [4] Y. Dang, Z. Xuan, L. Rong, and M. Liu, "A novel initialization method for semi-supervised clustering," in *Proceedings of the 4th International Conference on Knowledge Science, Engineering and Management*, pp. 317–328, 2010.
- [5] S. Zhong, "Semi-supervised model-based document clustering: a comparative study," *Machine Learning*, vol. 65, no. 1, pp. 3–29, 2006.
- [6] L. Leis and J. Sander, "Semi-supervised density-based clustering," in *Proceedings of the 9th IEEE International Conference on Data Mining (ICDM '09)*, pp. 842–847, December 2009.
- [7] C. Böhm and C. Plant, "HISSCLU: a hierarchical density-based method for semi-supervised clustering," in *Proceedings of the 11th International Conference on Extending Database Technology (EDBT '08)*, pp. 440–451, March 2008.
- [8] R. Guan, X. Shi, M. Marchese, C. Yang, and Y. Liang, "Text clustering with seeds affinity propagation," *IEEE Transactions on Knowledge and Data Engineering*, vol. 23, no. 4, pp. 627–637, 2011.
- [9] M. Shiga and H. Mamitsuka, "Efficient semi-supervised learning on locally informative multiple graphs," *Pattern Recognition*, vol. 45, no. 3, pp. 1035–1049, 2012.
- [10] K. Wagstaff, C. Cardie, S. Rogers, and S. Schroedel, "Constrained k-means clustering with background knowledge," in *Proceedings of the 18th International Conference on Machine Learning (ICML '01)*, pp. 77–84, 2001.
- [11] D. Klein, S. Kamvar, and C. Manning, "From instance-level constraints to space-level constraints: making the most of prior knowledge in data clustering," in *Proceedings of the 19th International Conference on Machine Learning (ICML '02)*, pp. 307–314, 2002.
- [12] C. Ruiz, M. Spiliopoulou, and E. Menasalvas, "Density-based semi-supervised clustering," *Data Mining and Knowledge Discovery*, vol. 21, no. 3, pp. 345–370, 2010.
- [13] X. Wang and I. Davidson, "Flexible constrained spectral clustering," in *Proceedings of the 16th ACM SIGKDD International Conference on Knowledge Discovery and Data Mining (KDD '10)*, pp. 563–572, July 2010.
- [14] I. S. Dhillon, Y. Guan, and B. Kulis, "Weighted graph cuts without eigenvectors a multilevel approach," *IEEE Transactions on Pattern Analysis and Machine Intelligence*, vol. 29, no. 11, pp. 1944–1957, 2007.
- [15] Z. Lu and M. Á. Carreira-Perpiñán, "Constrained spectral clustering through affinity propagation," in *Proceedings of the 26th IEEE Conference on Computer Vision and Pattern Recognition (CVPR '08)*, pp. 1–8, June 2008.
- [16] C. Alzate and J. A. K. Suykens, "A regularized formulation for spectral clustering with pairwise constraints," in *Proceedings of the International Joint Conference on Neural Networks (IJCNN '09)*, pp. 141–148, June 2009.

- [17] W. Pedrycz and J. Waletzky, "Fuzzy clustering with partial supervision," *IEEE Transactions on Systems, Man, and Cybernetics B*, vol. 27, no. 5, pp. 787–795, 1997.
- [18] A. Bouchachia and W. Pedrycz, "A semi-supervised clustering algorithm for data exploration," in *Proceedings of the 10th International Fuzzy Systems Association World Congress Conference on Fuzzy Sets and Systems*, pp. 328–337, 2003.
- [19] J. Gao, P.-N. Tan, and H. Cheng, "Semi-supervised clustering with partial background information," in *Proceedings of the 6th SIAM International Conference on Data Mining (SDM '06)*, pp. 489–493, 2006.
- [20] N. Grira, M. Crucianu, and N. Boujemaa, "Semi-supervised fuzzy clustering with pairwise-constrained competitive agglomeration," in *Proceedings of the 14th IEEE International Conference on Fuzzy Systems*, pp. 867–872, May 2005.
- [21] W. Pedrycz, V. Loia, and S. Senatore, "P-FCM: a proximity-based fuzzy clustering," *Fuzzy Sets and Systems*, vol. 148, no. 1, pp. 21–41, 2004.
- [22] Y. Yan, L. Chen, and W.-C. Tjhi, "Fuzzy semi-supervised co-clustering for text documents," *Fuzzy Sets and Systems*, vol. 215, pp. 74–89, 2013.
- [23] D. Lewis and W. Gale, "A sequential algorithm for training text classifiers," in *Proceedings of the ACM SIGIR Conference on Research and Development in Information Retrieval*, pp. 3–12, 1994.
- [24] A. Culotta and A. McCallum, "Reducing labeling effort for structured prediction tasks," in *Proceedings of the 20th National Conference on Artificial Intelligence and the 17th Innovative Applications of Artificial Intelligence Conference (AAAI '05)*, pp. 746–751, July 2005.
- [25] B. Settles and M. Craven, "An analysis of active learning strategies for sequence labeling tasks," in *Proceedings of the Conference on Empirical Methods in Natural Language Processing (EMNLP '08)*, pp. 1069–1078, 2008.
- [26] T. Scheffer, C. Decomain, and S. Wrobel, "Active hidden markov models for information extraction," in *Proceedings of the International Conference on Advances in Intelligent Data Analysis (CAIDA '01)*, pp. 309–318, 2001.
- [27] R. Hwa, "Sample selection for statistical parsing," *Computational Linguistics*, vol. 30, no. 3, pp. 253–276, 2004.
- [28] T. Scheffer and S. Wrobel, "Active learning of partially hidden markov models," in *Proceedings of ECML/PKDD Workshop on Instance Selection*, 2001.
- [29] P. K. Mallapragada, R. Jin, and A. K. Jain, "Active query selection for semi-supervised clustering," in *Proceedings of the 19th International Conference on Pattern Recognition (ICPR '08)*, pp. 1–4, December 2008.
- [30] H. T. Nguyen and A. Smeulders, "Active learning using pre-clustering," in *Proceedings of the 21st International Conference on Machine Learning (ICML '04)*, pp. 623–630, July 2004.
- [31] V.-V. Vu, N. Labroche, and B. Bouchon-Meunier, "Active learning for semi-supervised K-means clustering," in *Proceedings of the 22nd International Conference on Tools with Artificial Intelligence (ICTAI '10)*, pp. 12–15, October 2010.
- [32] W. Zhao, Q. He, H. Ma, and Z. Shi, "Effective semi-supervised document clustering via active learning with instance-level constraints," *Knowledge and Information Systems*, vol. 30, no. 3, pp. 569–587, 2012.
- [33] N. Grira, M. Crucianu, and N. Boujemaa, "Active semi-supervised fuzzy clustering," *Pattern Recognition*, vol. 41, no. 5, pp. 1834–1844, 2008.
- [34] X. Wang and I. Davidson, "Active spectral clustering," in *Proceedings of the 10th IEEE International Conference on Data Mining (ICDM '10)*, pp. 561–568, December 2010.
- [35] R. Huang, W. Lam, and Z. Zhang, "Active learning of constraints for semi-supervised text clustering," in *Proceedings of the 7th SIAM International Conference on Data Mining (SDM '07)*, pp. 113–124, April 2007.
- [36] C. T. Zahn, "Graph-theoretical methods for detecting and describing gestalt clusters," *IEEE Transactions on Computers*, vol. 20, no. 1, pp. 68–86, 1971.
- [37] Uci datasets, <http://archive.ics.uci.edu/ml/datasets.html>.

Research Article

Application of Fuzzy Set Theory to Quantitative Analysis of Correctness of the Mathematical Model Based on the ADI Method during Solidification

Xiaofeng Niu,¹ Guanqian Wang,¹ Wei Liang,¹ Hua Hou,²
Hongxia Wang,¹ and Jinshan Zhang¹

¹ College of Materials Science and Engineering, Taiyuan University of Technology, Taiyuan 030024, China

² College of Materials Science and Engineering, North University of China, Taiyuan 030051, China

Correspondence should be addressed to Wei Liang; liangweiyut001@126.com

Received 20 July 2013; Revised 21 October 2013; Accepted 24 October 2013

Academic Editor: SunQun Cao

Copyright © 2013 Xiaofeng Niu et al. This is an open access article distributed under the Creative Commons Attribution License, which permits unrestricted use, distribution, and reproduction in any medium, provided the original work is properly cited.

The explicit finite difference (EFD) method is used to calculate the casting temperature field during the solidification process. Because of its limited time step, the computational efficiency of the EFD method is lower than that of the alternating direction implicit (ADI) method. A model based on the equivalent specific heat method and the ADI method that improves computational efficiency is established. The error of temperature field simulation comes from model simplification, the acceptable hypotheses and calculation errors caused by different time steps, and the different mesh numbers that are involved in the process of numerical simulation. This paper quantitatively analyzes the degree of similarity between simulated and experimental results by the hamming distance (HD). For a thick-walled position, the time step influences the simulation results of the temperature field and the number of casting meshes has little influence on the simulation results of temperature field. For a thin-walled position, the time step has minimal influence on the simulation results of the temperature field and the number of casting meshes has a larger influence on the simulation results of temperature field.

1. Introduction

The 3D heat transfer equation of the temperature field during the solidification process is as follows [1–3]:

$$\rho c_p \frac{\partial T}{\partial t} = \lambda \left(\frac{\partial^2 T}{\partial x^2} + \frac{\partial^2 T}{\partial y^2} + \frac{\partial^2 T}{\partial z^2} \right) + \dot{Q}, \quad (1)$$

$$\dot{Q} = \rho Q \frac{\partial f_s}{\partial t}, \quad (2)$$

where T is the temperature, t is the time, ρ is the average density of the liquid phase and the solid phase, c_p is the specific heat, λ is the convectional parameter, \dot{Q} is the inner heat source, and Q is the latent heat, f_s is the solid phase fraction.

The energy conservation equation is usually solved by the EFD method, and computational efficiency is lower due to its limited time step [4–6].

The critical time step Δt in the EFD method can be taken as follows [6–8]:

$$\Delta t \leq \frac{\rho c_p}{[2 \cdot \lambda \cdot (1/\Delta x^2 + 1/\Delta y^2 + 1/\Delta z^2)]}, \quad (3)$$

where Δx , Δy , and Δz are the mesh sizes in the X , Y , and Z directions, respectively.

In this study, the equivalent specific heat method is adopted to describe the latent heat and the high-order ADI method that is fourth order in space and second order in time. This high-order mathematical model is based on the equivalent specific heat method, and the high-order ADI method is more accurate than the EFD method [7–12].

The error of temperature field simulation comes from model simplification, the acceptable hypotheses and calculation errors of the different time steps, and the different mesh numbers involved in the process of numerical simulation.

TABLE I: Truncation errors.

Method	Truncation errors
This new high-order mathematical model	Fourth order in space and second order in time
The EFD method	Second order in space and first order in time

The degree of similarity between the simulation and the experimental results is quantitatively analyzed using the hamming distance [13–15].

2. Mathematical Model

The energy conservation equation can be given as the following:

$$\rho c_p \frac{\partial T}{\partial t} = \lambda \left(\frac{\partial^2 T}{\partial x^2} + \frac{\partial^2 T}{\partial y^2} + \frac{\partial^2 T}{\partial z^2} \right) + \rho Q \frac{\partial f_s}{\partial t}, \quad (4)$$

$$f_s = \frac{(T_L - T)}{(T_L - T_S)},$$

where T_L is the temperature of the liquid phase and T_S is the temperature of the solid phase. With the equivalent specific heat method [8]:

$$\rho c_p' \frac{\partial T}{\partial t} = \lambda \left(\frac{\partial^2 T}{\partial x^2} + \frac{\partial^2 T}{\partial y^2} + \frac{\partial^2 T}{\partial z^2} \right), \quad (5)$$

$$c_p' = \begin{cases} c_p & T \geq T_L \\ c_p - Q \frac{\partial f_s}{\partial t} & T_L > T \geq T_S \\ c_p & T < T_S. \end{cases}$$

The discretization equations of this high-order mathematical model based on the equivalent specific heat method and the high-order ADI method can be given as the following:

$$\left[1 + \left[\frac{\Delta x^2}{12} - \frac{k\Delta t}{2} \right] \delta_x^2 \right] T_{ijk}^{**}$$

$$= \left[1 + \left[\frac{\Delta x^2}{12} + \frac{k\Delta t}{2} \right] \delta_x^2 \right] \left[1 + \left[\frac{\Delta y^2}{12} + \frac{k\Delta t}{2} \right] \delta_y^2 \right]$$

$$\times \left[1 + \left[\frac{\Delta z^2}{12} + \frac{k\Delta t}{2} \right] \delta_z^2 \right] T_{ijk}^n, \quad (6)$$

$$\left[1 + \left[\frac{\Delta y^2}{12} - \frac{k\Delta t}{2} \right] \delta_y^2 \right] T_{ijk}^* = T_{ijk}^{**},$$

$$\left[1 + \left[\frac{\Delta z^2}{12} - \frac{k\Delta t}{2} \right] \delta_z^2 \right] T_{ijk}^{n+1} = T_{ijk}^*,$$

where $k = (\lambda/\rho c_p')$; δ_x^2 , δ_y^2 , and δ_z^2 are the second-order central difference operators.

Finally, T_{ijk}^{n+1} can be obtained from (6). Each step has a tridiagonal system of equations that can be quickly calculated using the Thomas algorithm [16].

The calculation speed of this high-order mathematical model is faster because it is unconditionally stable. Table 1

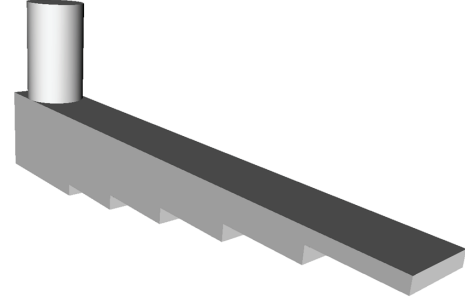


FIGURE 1: 3D model.

shows that this high-order mathematical model is more accurate than the EFD method.

Because the figure analysis cannot be used for quantitative analysis, the fuzzy mathematical theory is introduced [15–19]. The fuzzy set A of the universe of discourse U , $U = \{t_1, t_2, t_3, \dots, t_n\}$, with a generic element of U denoted by t_i , is a set of ordered pairs $\{(t_1, A(t_1)), (t_2, A(t_2)), \dots, (t_n, A(t_n))\}$, where $A(t_i)$ is the membership function of the fuzzy set A , $A(t_i) : U \rightarrow [0, 1]$, and $A(t_i)$ indicates the grade of membership of t_i in A . Similar expression for the fuzzy set B is readily understood with obvious notation.

In this study, t_i represents time nodes; $A(t_i) = (T_{At_i}/T_\infty)$ and $B_{(1or2)}(t_i) = (T_{B(1or2)t_i}/T_\infty)$ are two membership functions; T_{At_i} is the experimentally derived temperature; $T_{B(1or2)t_i}$ is the temperature obtained by simulation; and T_∞ denotes the “typical” temperature [19–21].

According to the HD, the degree of similarity between sets A and B can be evaluated by the function $N(A, B)$:

$$N(A, B) = 1 - \left(\frac{1}{n} \right) \sum_{i=1}^n |A(t_i) - B(t_i)|. \quad (7)$$

Equation (7) is used to quantitatively analyze the degree of similarity between the simulation results and the experimental results.

3. Experimental Results and Discussion

The 3D model is shown in Figure 1; the geometric figure of the casting is shown in Figure 2; the casting mould is 200 mm × 100 mm × 100 mm; the pouring speed is 0.35 m/s; and the pouring temperature is 670°C. The necessary physical parameters are shown in Table 2. The size of the mesh is 1.0 mm × 1.0 mm × 1.0 mm and the number of meshes is 2,000,000.

All of the thermocouples are connected by coaxial cables to a data logger and interfaced with a computer. The temperature data are automatically acquired. A schematic representation of the experimental setup, which is connected

TABLE 2: Physical parameters of casting and mold.

Material	Latent heat (kJ/kg)	Density (kg/m ³)	Specific heat (kJ/kg·K)	Solidus temperature (°C)	Liquidus temperature (°C)
AlSi ₉ Cu ₃	471	2596–2750	0.83–0.97	504	585
Sand	—	2780	0.54–1.00	—	—

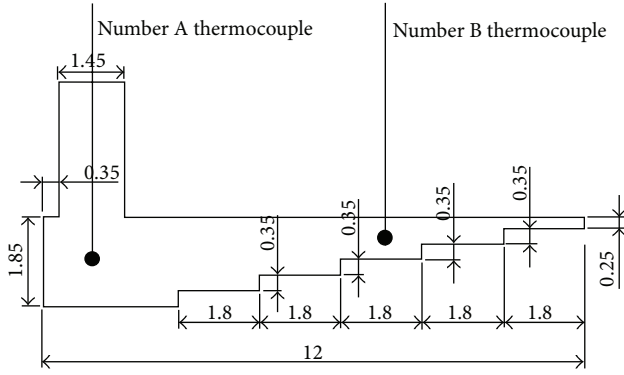


FIGURE 2: Schematic diagram of the experimental setup (cm).

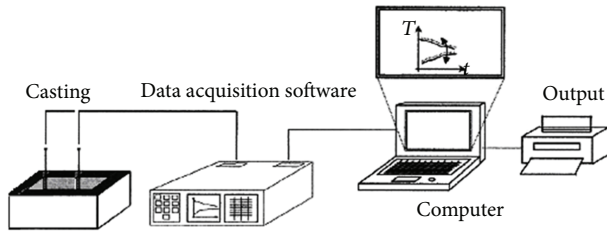


FIGURE 3: Schematic representation of the experimental setup connected to the data acquisition and analysis system.

to the data acquisition and analysis system, is shown in Figure 3. The experimental results are shown in Figure 4.

3.1. Temperature Simulation of Point A. In this section, the high-order mathematical model, which is based on the equivalent specific heat method and the high-order ADI method, is used to compute the energy conservation equation. First, the number of casting meshes is 124031 and this number remains constant. The different time steps ($\Delta t = 0.000026$ s, $20\Delta t = 0.00052$ s, and $200\Delta t = 0.0052$ s) are adopted to compute the temperature simulation of point A. Second, the time step is $20\Delta t$ and this remains constant. The different mesh numbers (6825, 124031, and 672963) are adopted to compute the temperature simulation of point A. The hamming distance can be used to evaluate the degrees of similarity between the simulation results and the experimental results. The figure analysis is shown in Figure 5.

Let U be the universe of discourse, $U = \{t_1 = 0.0$ s, $t_2 = 0.2$ s, $t_3 = 0.4$ s, $t_4 = 0.6$ s, \dots , $t_{10} = 1.8$ s}, with a generic element of U denoted by t_i ; $T_\infty = 671^\circ\text{C}$ denotes “typical” temperature; $A(t_i) = (T_{At_i}/T_\infty)$ and $B(t_i) = (T_{Bt_i}/T_\infty)$ are two membership functions; T_{At_i} represents a temperature measured from the experimental method, and T_{Bt_i} represents

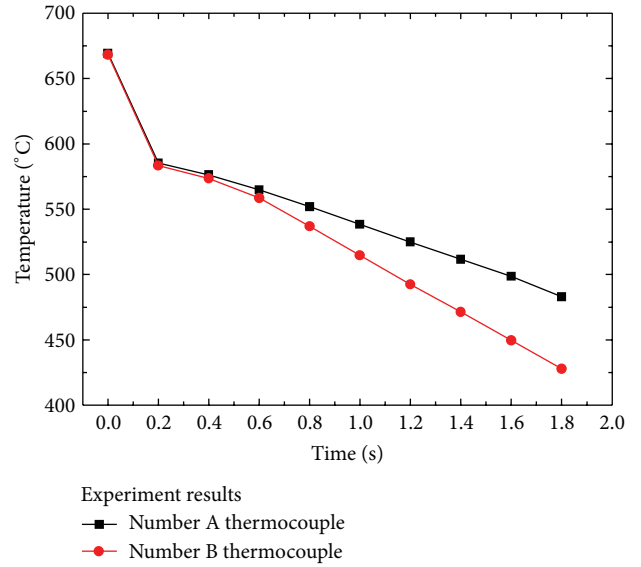


FIGURE 4: Experimental results.

the temperature derived from the simulation method. These include the different time steps and the different mesh numbers.

The fuzzy set A can be described as follows:

$$\begin{aligned}
 A = \left\{ \left(t_1, \left(\frac{669.2}{671} \right) \right), \left(t_2, \left(\frac{585.4}{671} \right) \right), \right. \\
 \left. \left(t_3, \left(\frac{576.2}{671} \right) \right), \left(t_4, \left(\frac{564.8}{671} \right) \right), \right. \\
 \left. \left(t_5, \left(\frac{551.9}{671} \right) \right), \left(t_6, \left(\frac{538.4}{671} \right) \right), \right. \\
 \left. \left(t_7, \left(\frac{525.0}{671} \right) \right), \left(t_8, \left(\frac{511.6}{671} \right) \right), \right. \\
 \left. \left(t_9, \left(\frac{498.7}{671} \right) \right), \left(t_{10}, \left(\frac{483.0}{671} \right) \right) \right\}.
 \end{aligned} \quad (8)$$

The mesh number remains constant.

- (1) The time step is Δt and the number of casting meshes is 124031. The fuzzy set B can be described as follows:

$$\begin{aligned}
 B_1 = \left\{ \left(t_1, \left(\frac{669.5}{671} \right) \right), \left(t_2, \left(\frac{585.6}{671} \right) \right), \right. \\
 \left. \left(t_3, \left(\frac{577.0}{671} \right) \right), \left(t_4, \left(\frac{566.7}{671} \right) \right), \right.
 \end{aligned}$$

$$\left. \begin{aligned} & \left(t_5, \left(\frac{555.3}{671} \right) \right), \left(t_6, \left(\frac{539.8}{671} \right) \right), \\ & \left(t_7, \left(\frac{526.9}{671} \right) \right), \left(t_8, \left(\frac{512.9}{671} \right) \right), \\ & \left(t_9, \left(\frac{499.9}{671} \right) \right), \left(t_{10}, \left(\frac{485.1}{671} \right) \right) \end{aligned} \right\}. \quad (9)$$

According to (7), the degree of similarity between sets A and B can be evaluated:

$$\begin{aligned} N(A, B_1) &= 1 - \left(\frac{1}{10} \right) \sum_{i=1}^{10} |A(t_i) - B(t_i)| \\ &= 0.997839. \end{aligned} \quad (10)$$

(2) The time step is $20\Delta t$ and the number of casting meshes is 124031. The fuzzy set B can be described as follows:

$$\begin{aligned} B_2 &= \left\{ \left(t_1, \left(\frac{669.8}{671} \right) \right), \left(t_2, \left(\frac{590.7}{671} \right) \right), \right. \\ & \left(t_3, \left(\frac{583.3}{671} \right) \right), \left(t_4, \left(\frac{573.2}{671} \right) \right), \\ & \left(t_5, \left(\frac{560.8}{671} \right) \right), \left(t_6, \left(\frac{548.9}{671} \right) \right), \\ & \left(t_7, \left(\frac{534.7}{671} \right) \right), \left(t_8, \left(\frac{520.5}{671} \right) \right), \\ & \left. \left(t_9, \left(\frac{508.1}{671} \right) \right), \left(t_{10}, \left(\frac{490.3}{671} \right) \right) \right\}. \end{aligned} \quad (11)$$

According to (7), the degree of similarity between sets A and B can be evaluated:

$$\begin{aligned} N(A, B_2) &= 1 - \left(\frac{1}{10} \right) \sum_{i=1}^{10} |A(t_i) - B(t_i)| \\ &= 0.988659. \end{aligned} \quad (12)$$

(3) The time step is $200\Delta t$ and the number of casting meshes is 124031. The fuzzy set B can be described as follows:

$$\begin{aligned} B_3 &= \left\{ \left(t_1, \left(\frac{669.9}{671} \right) \right), \left(t_2, \left(\frac{607.8}{671} \right) \right), \right. \\ & \left(t_3, \left(\frac{599.1}{671} \right) \right), \left(t_4, \left(\frac{590.5}{671} \right) \right), \\ & \left(t_5, \left(\frac{580.3}{671} \right) \right), \left(t_6, \left(\frac{570.2}{671} \right) \right), \\ & \left(t_7, \left(\frac{556.9}{671} \right) \right), \left(t_8, \left(\frac{545.3}{671} \right) \right), \\ & \left. \left(t_9, \left(\frac{533.2}{671} \right) \right), \left(t_{10}, \left(\frac{523.0}{671} \right) \right) \right\}. \end{aligned} \quad (13)$$

According to (7), the degree of similarity between sets A and B can be evaluated:

$$\begin{aligned} N(A, B_3) &= 1 - \left(\frac{1}{10} \right) \sum_{i=1}^{10} |A(t_i) - B(t_i)| \\ &= 0.959463. \end{aligned} \quad (14)$$

The time step remains constant.

(1) The time step is $20\Delta t$ and the number of casting meshes is 6825. The fuzzy set B can be described as follows:

$$\begin{aligned} B_4 &= \left\{ \left(t_1, \left(\frac{669.9}{671} \right) \right), \left(t_2, \left(\frac{592.7}{671} \right) \right), \right. \\ & \left(t_3, \left(\frac{584.3}{671} \right) \right), \left(t_4, \left(\frac{575.5}{671} \right) \right), \\ & \left(t_5, \left(\frac{562.8}{671} \right) \right), \left(t_6, \left(\frac{549.9}{671} \right) \right), \\ & \left(t_7, \left(\frac{537.7}{671} \right) \right), \left(t_8, \left(\frac{521.5}{671} \right) \right), \\ & \left. \left(t_9, \left(\frac{510.1}{671} \right) \right), \left(t_{10}, \left(\frac{492.3}{671} \right) \right) \right\}. \end{aligned} \quad (15)$$

According to (7), the degree of similarity between sets A and B can be evaluated:

$$\begin{aligned} N(A, B_4) &= 1 - \left(\frac{1}{10} \right) \sum_{i=1}^{10} |A(t_i) - B(t_i)| \\ &= 0.986140. \end{aligned} \quad (16)$$

(2) The time step is $20\Delta t$ and the number of casting meshes is 672963. The fuzzy set B can be described as follows:

$$\begin{aligned} B_5 &= \left\{ \left(t_1, \left(\frac{669.1}{671} \right) \right), \left(t_2, \left(\frac{586.9}{671} \right) \right), \right. \\ & \left(t_3, \left(\frac{578.9}{671} \right) \right), \left(t_4, \left(\frac{567.7}{671} \right) \right), \\ & \left(t_5, \left(\frac{555.7}{671} \right) \right), \left(t_6, \left(\frac{542.5}{671} \right) \right), \\ & \left(t_7, \left(\frac{527.9}{671} \right) \right), \left(t_8, \left(\frac{514.9}{671} \right) \right), \\ & \left. \left(t_9, \left(\frac{502.1}{671} \right) \right), \left(t_{10}, \left(\frac{485.7}{671} \right) \right) \right\}. \end{aligned} \quad (17)$$

According to (7), the degree of similarity between sets A and B can be evaluated:

$$\begin{aligned} N(A, B_5) &= 1 - \left(\frac{1}{10} \right) \sum_{i=1}^{10} |A(t_i) - B(t_i)| \\ &= 0.995946. \end{aligned} \quad (18)$$

TABLE 3: The comparison results of calculation time.

Method	The number of casting meshes	Calculation time/second
The EFD method	124031	2579
This new high-order mathematical model (the time step is $5\Delta t$)	124031	1742
This new high-order mathematical model (the time step is $20\Delta t$)	124031	253

The hardware environment: microcomputer.

The error of temperature field simulation comes from model simplification, the acceptable hypotheses and calculation errors that can be caused by the different time steps, and the different mesh numbers that are involved in the process of numerical simulation. Because the heat transfer model is based on the energy conservation equation (see (1)) and the governing equations (6), the loss of accuracy comes from calculation error that can be caused by the different time steps and the different mesh numbers.

The conclusions of the analysis and computations can be described as follows.

- (1) The number of casting meshes remains constant and the different time steps are adopted to compute the temperature simulation, with great changes in the degrees of similarity between the simulation results and the experimental results:

$$\begin{aligned} (N(A, B_1) = 0.997839, N(A, B_2) \\ = 0.988659, N(A, B_3) = 0.959463). \end{aligned} \quad (19)$$

- (2) The time step remains constant and the different mesh numbers are adopted to compute the temperature simulation, with the degrees of similarity between the simulation results and the experimental results changing slightly:

$$\begin{aligned} (N(A, B_4) = 0.986140, N(A, B_2) \\ = 0.988659, N(A, B_5) = 0.995946). \end{aligned} \quad (20)$$

In short, this high-order mathematical model is based on the equivalent specific heat method and the high-order ADI method, which can be used to calculate the temperature field. For the thick-walled position (see point A), the time step has a large influence on the simulation results of the temperature field and the number of casting meshes has little influence on the simulation results of temperature field.

In Figure 5, for the thick-walled position, the same conclusions hold: (a) the number of casting meshes remains constant and the changes of the time steps change the simulation results of the temperature field; (b) the time step remains constant and change in the mesh numbers brings little change in the simulation results of the temperature field. These are given to illustrate the validity of the analysis method that uses the hamming distance.

The simulation results and the experimental results can only be qualitatively analyzed by the figure analysis. For the first time, this study analyzes the hamming distance to quantitatively ascertain the degree of similarity between

the simulation results and the experimental results. The quantitative analysis is based on hamming distance and it is more accurate than qualitative analysis based on the figure analysis.

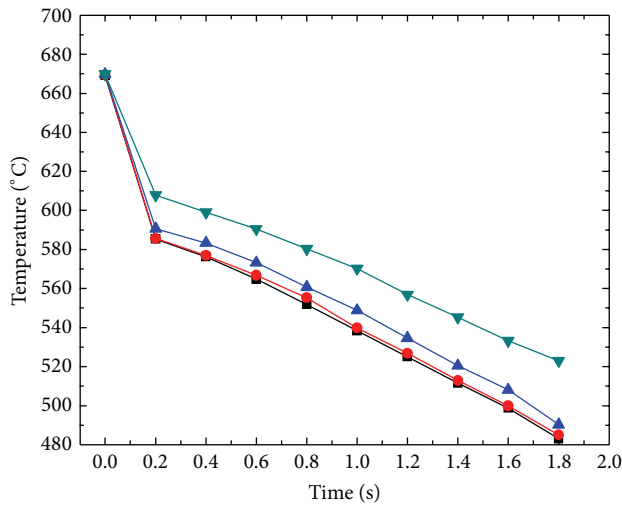
3.2. Temperature Simulation of Point B. The analysis method is similar and its steps are as follows. First, the number of casting meshes is 124031 and this number remains constant. The different time steps ($\Delta t = 0.000026$ s, $20\Delta t = 0.00052$ s, and $200\Delta t = 0.0052$ s) are adopted to compute the temperature simulation of point B. Second, the time step is $20\Delta t$ and this remains constant. The different mesh numbers (6825, 124031, and 672963) are adopted to compute the temperature simulation of point B. The hamming distance can evaluate the degrees of similarity between the simulation results and the experimental results. Figure 6 illustrates the validity of the analysis method of the hamming distance.

The conclusions are that for the thin-walled position (see point B); the time step has little influence on the simulation results of the temperature field and the number of casting meshes has a large influence on the simulation results of the temperature field.

This high-order mathematical model, which is based on the equivalent specific heat method and the high-order ADI method, is superior to the explicit finite difference method. In this section, the number of casting meshes remains constant and the calculation time between the explicit finite difference method and the high-order mathematical model is shown in Table 3.

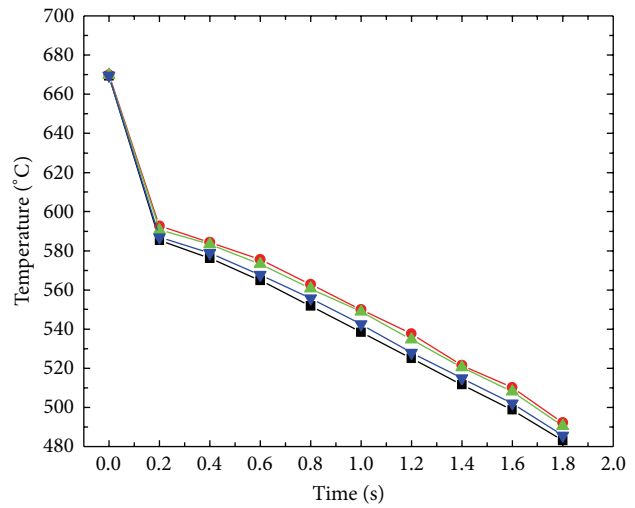
4. Conclusions

- (1) The high-order mathematical model based on the equivalent specific heat method and the high-order ADI method can be used to effectively compute the temperature simulation. Because this mathematical model is unconditionally stable, the different time steps can be chosen with quick calculation.
- (2) For the first time, this paper demonstrates how the analysis method of the hamming distance can be used to quantitatively analyze the degree of similarity between the simulation results of the temperature field and the experimental results of the temperature field.
- (3) For the thick-walled position (see point A), the time step has a large influence on the simulation results of the temperature field and the number of casting meshes has little influence on the simulation results of the temperature field. For the thin-walled position



Number A thermocouple
 ■ Experiment results
 ● The time step is 0.00026 s
 ▲ The time step is 0.00052 s
 ▼ The time step is 0.0052 s
 The number of casting meshes is 124031.

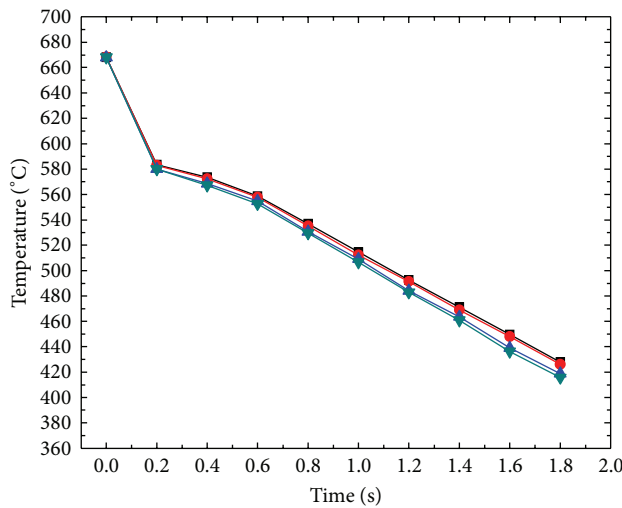
(a) The mesh number remains constant



Number A thermocouple
 ■ Experiment results
 ● The number of casting meshes is 6825
 ▲ The number of casting meshes is 124031
 ▼ The number of casting meshes is 672963
 The time step is 0.00052 s.

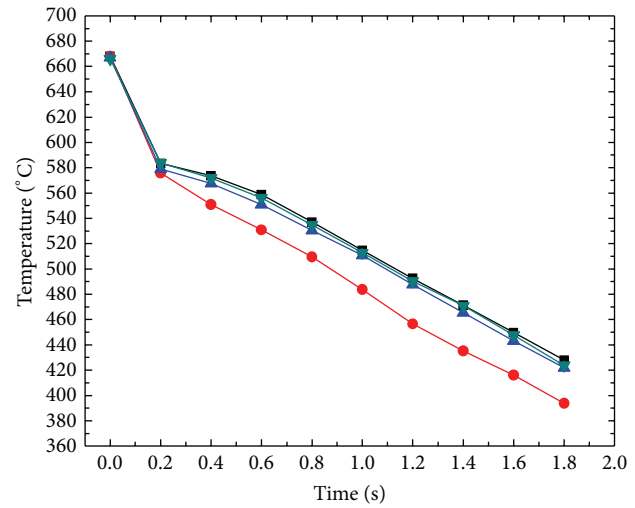
(b) The time step remains constant

FIGURE 5: Comparison results.



Number B thermocouple
 ■ Experiment results
 ● The time step is 0.00026 s
 ▲ The time step is 0.00052 s
 ▼ The time step is 0.0052 s
 The number of casting meshes is 124031.

(a) The mesh number remains constant



Number B thermocouple
 ■ Experiment results
 ● The number of casting meshes is 6825
 ▲ The number of casting meshes is 124031
 ▼ The number of casting meshes is 672963
 The time step is 0.00052 s.

(b) The time step remains constant

FIGURE 6: Comparison results.

(see point B), the time step has little influence on the simulation results of the temperature field and the number of casting meshes has a sizable influence on the simulation results of the temperature field.

Acknowledgment

This research is financially supported by the National Natural Science Foundation of China (Grant nos. 51304145 and 51301118).

References

- [1] D.-C. Tsai and W.-S. Hwang, "Numerical simulation of solidification morphologies of Cu-0.6Cr casting alloy using modified cellular automaton model," *Transactions of Nonferrous Metals Society of China*, vol. 20, no. 6, pp. 1072–1077, 2010.
- [2] Y. Chen, Y.-H. Zhao, and H. Hou, "Numerical simulation for thermal flow filling process casting," *Transactions of Nonferrous Metals Society of China*, vol. 16, pp. 214–218, 2010.
- [3] X.-F. Niu, W. Liang, Y.-H. Zhao et al., "New algorithm for solving 3D incompressible viscous equations based on projection method," *Transactions of Nonferrous Metals Society of China*, vol. 21, no. 8, pp. 1826–1832, 2011.
- [4] T. R. Vijayaram, S. Sulaiman, A. M. S. Hamouda, and M. H. M. Ahmad, "Numerical simulation of casting solidification in permanent metallic molds," *Journal of Materials Processing Technology*, vol. 178, no. 1–3, pp. 29–33, 2006.
- [5] X. Niu, W. Liang, Y. Zhao, and H. Hou, "A new implicit finite difference algorithm of thermal melt flow in filling process based on projection method," *Journal of Computational and Theoretical Nanoscience*, vol. 9, pp. 1–5, 2012.
- [6] J.-J. Droux, "Three-dimensional numerical simulation of solidification by an improved explicit scheme," *Computer Methods in Applied Mechanics and Engineering*, vol. 85, no. 1, pp. 57–74, 1991.
- [7] Y.-F. Chiu, Y.-L. Tsai, and W.-S. Hwang, "Mathematical modeling for the solidification heat-transfer phenomena during the reflow process of lead-tin alloy solder joint in electronics packaging," *Applied Mathematical Modelling*, vol. 27, no. 7, pp. 565–579, 2003.
- [8] H. Hou, *Studies on Numerical Simulation for Liquid-Metal Filling and Solidification during Casting Process*, Saitama Institute of Technology, Saitama, Japan, 2005.
- [9] X. P. Zhang, S. M. Xiong, and Q. Y. Xu, "Numerical methods to improve the computational efficiency of solidification simulation for the investment casting process," *Journal of Materials Processing Technology*, vol. 173, no. 1, pp. 70–74, 2006.
- [10] W. Y. Liao, "A high-order ADI finite difference scheme for a 3D reaction-diffusion equation with neumann boundary condition," *Numerical Methods for Partial Differential Equations*, vol. 29, no. 3, pp. 778–798, 2013.
- [11] S. Karaa and J. Zhang, "High order ADI method for solving unsteady convection-diffusion problems," *Journal of Computational Physics*, vol. 198, no. 1, pp. 1–9, 2004.
- [12] Y.-B. Ge, Z.-F. Tian, and W.-Q. Wu, "A high-order alternating direction implicit method for solving the high dimensional heat equations," *Journal of University of Shanghai for Science and Technology*, vol. 29, no. 1, pp. 55–58, 2007.
- [13] L. A. Zadeh, "Fuzzy sets," *Information and Control*, vol. 8, no. 3, pp. 338–353, 1965.
- [14] R. Scozzafava and B. Vantaggi, "Fuzzy inclusion and similarity through coherent conditional probability," *Fuzzy Sets and Systems*, vol. 160, no. 3, pp. 292–305, 2009.
- [15] C.-Y. Zhang and H.-Y. Fu, "Similarity measures on three kinds of fuzzy sets," *Pattern Recognition Letters*, vol. 27, no. 12, pp. 1307–1317, 2006.
- [16] F.-P. Tan, "A modified Thomas algorithm and its error estimation," in *Proceedings of the 14th Conference of International Linear Algebra Society*, pp. 261–264, 2007.
- [17] Y. Li, D. L. Olson, and Z. Qin, "Similarity measures between intuitionistic fuzzy (vague) sets: a comparative analysis," *Pattern Recognition Letters*, vol. 28, no. 2, pp. 278–285, 2007.
- [18] S. Raha, A. Hossain, and S. Ghosh, "Similarity based approximate reasoning: fuzzy control," *Journal of Applied Logic*, vol. 6, no. 1, pp. 47–71, 2008.
- [19] S.-H. Wei and S.-M. Chen, "A new approach for fuzzy risk analysis based on similarity measures of generalized fuzzy numbers," *Expert Systems with Applications*, vol. 36, no. 1, pp. 589–598, 2009.
- [20] Z. Xu, S. Shang, W. Qian, and W. Shu, "A method for fuzzy risk analysis based on the new similarity of trapezoidal fuzzy numbers," *Expert Systems with Applications*, vol. 37, no. 3, pp. 1920–1927, 2010.
- [21] J. Z. C. Lai, E. Y. T. Juan, and F. J. C. Lai, "Rough clustering using generalized fuzzy clustering algorithm," *Pattern Recognition*, vol. 46, no. 9, pp. 2538–2547, 2013.

Research Article

Tensorial Kernel Principal Component Analysis for Action Recognition

Cong Liu, Xu Wei-sheng, and Wu Qi-di

School of Electrical and Information Engineering, Tongji University, Shanghai 201804, China

Correspondence should be addressed to Cong Liu; 1210482congliu@tongji.edu.cn

Received 25 July 2013; Accepted 30 August 2013

Academic Editor: Gelan Yang

Copyright © 2013 Cong Liu et al. This is an open access article distributed under the Creative Commons Attribution License, which permits unrestricted use, distribution, and reproduction in any medium, provided the original work is properly cited.

We propose the Tensorial Kernel Principal Component Analysis (TKPCA) for dimensionality reduction and feature extraction from tensor objects, which extends the conventional Principal Component Analysis (PCA) in two perspectives: working directly with multidimensional data (tensors) in their native state and generalizing an existing linear technique to its nonlinear version by applying the kernel trick. Our method aims to remedy the shortcomings of multilinear subspace learning (tensorial PCA) developed recently in modelling the nonlinear manifold of tensor objects and brings together the desirable properties of kernel methods and tensor decompositions for significant performance gain when the data are multidimensional and nonlinear dependencies do exist. Our approach begins by formulating TKPCA as an optimization problem. Then, we develop a kernel function based on Grassmann Manifold that can directly take tensorial representation as parameters instead of traditional vectorized representation. Furthermore, a TKPCA-based tensor object recognition is also proposed for application of the action recognition. Experiments with real action datasets show that the proposed method is insensitive to both noise and occlusion and performs well compared with state-of-the-art algorithms.

1. Introduction

Recent years have witnessed a dramatic increase in the quantity of multidimensional data which are so large and complex that it becomes difficult to process them using traditional data processing applications. Hence, there is a growing need for the development and application of feature extraction and dimensionality reduction to analyze multidimensional data.

Tensor provides a natural and efficient way to describe such multidimensional data. The entries of tensor are addressed by more than two indices. The number of indices defines the order of the tensor, and each index defines one of the so-called “modes.” In reality, there are a lot of data that can be formed by tensor. For example, two order tensors include gray level images in computer vision and pattern recognition [1–4], multichannel EEG signals in biomedical engineering [5–7]. Three-order tensors include diffusion tensor imaging (DTI) in brain research [8], hyperspectral cube in remote sensing [9], silhouette sequences in gait analysis [10], and gray video sequences in action recognition [11, 12]. There are also multidimensional signals that can be formed in more

than three-order tensor in the application of color video sequences surveillance, social network analysis [13], and so forth. Figure 1 shows two examples of 3-order tensor for a silhouette sequence and a reconstructed fiber tracts of human brain measured by DTI. The hypothesis behind DTI is that the bundles of fiber tracts make the water diffuse asymmetrically and DTI derives tract directional information from 3-order tensors describing this anisotropy.

Principal Component Analysis (PCA) [14] is one of the most important techniques in the class of unsupervised learning algorithms which linearly transforms a number of possibly correlated variables into uncorrelated features called *principal components* (PCs). The transformation is performed to find directions of maximal variation. Normally, only a few principal components can account for most of the variation in the original dataset. However, PCA is not suitable to discover nonlinear relationships among the original variables. To overcome this limitation, Schölkopf et al. [15] originally proposed Kernel Principal Component Analysis (KPCA) [15] which performs PCA in a Reproducing Kernel Hilbert Space (RKHS) rather than in the input space. In principle, the

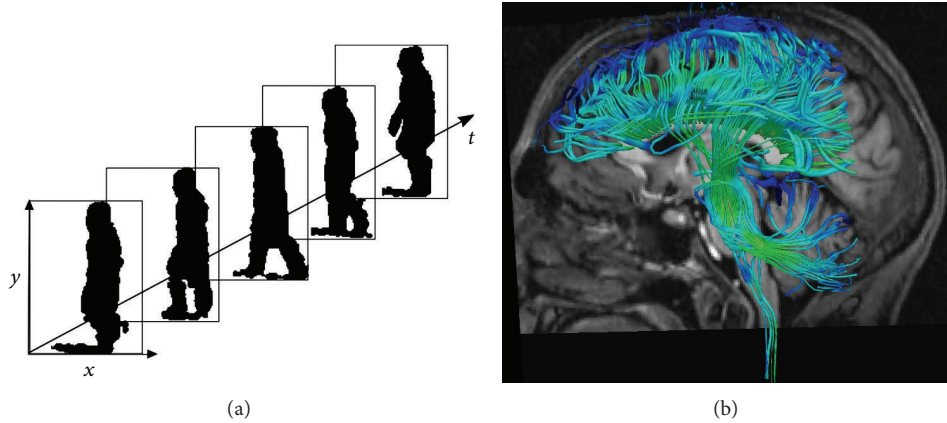


FIGURE 1: Two examples of 3-order tensor: (a) a gait silhouette sequences with the column, row, and time mode; (b) a diffusion tensor imaging (DTI) scan of fiber tracts in human brain which derives tract directional information from 3-order tensors that describe anisotropic diffusion of water.

kernel methods nonlinearly map a set of training samples to a higher dimensional RKHS where conventional linear PCA is performed, with the resulting subspaces being nonlinear with regards to the original input space. In practice, the mapping is performed implicitly via the *kernel trick* [15], where an appropriately chosen kernel function is used to evaluate dot products of mapped input space vectors without having to explicitly carry out the mapping.

As a classical dimensionality reduction method, PCA and KPCA have been widely used in extracting feature from tensor objects. However, before feeding tensorial data to PCA or KPCA, the tensors have to be typically transformed into long vectors by concatenating the tensor entry-wise. This will present several problems. Firstly, the integral structure of tensor is disintegrated; therefore, the information correlated with surrounding entries could be lost. Secondly, the vectorized representation lies in a very high dimensional space, which will bring the *Curse of Dimensionality dilemma* [16]. Thirdly, only sparse data are available in many application areas such as web document classification, face recognition, and disease classification based on gene expression profiling; consequently, the *small sample size (SSS)* problem [17, 18] is inevitable there.

Due to the challenges above, recently, interests have grown in multilinear subspace learning (hereinafter referred to as *tensorial PCA*) that reduces dimensionality of multidimensional data directly from their tensorial representations. Initiated by the pioneer work of Yang et al. [3], a two dimensional PCA (2DPCA) algorithm is proposed. This algorithm solves for a linear transformation that projects an image to a low dimensional matrix while maximizing the variance measure. It works directly on image matrices, but there is only one linear transformation in the 2-mode. Thus, the image data are projected in the 2-mode (the row mode) only, while the projection in the 1-mode (the column mode) is ignored. A more general algorithm named the generalized PCA (GPCA) is introduced in [1], which takes into account the spatial correlation between the image pixels in neighborhood and applies double linear

transforms to both the left and right sides of input image matrices. However, it is formulated for matrices only. Later, the work of multilinear PCA (MPCA) [19] generalizes GPCA to work for tensors of any order, where the objective is to find a *core tensor* (see Section 2.2) that captures most of the original tensorial input variations. In [20], two robust MPCA (RMPCA) algorithms are proposed, where iterative algorithms are derived on the basis of Lagrange multipliers to deal with sample outliers and intrasample outliers. In [21], the nonnegative MPCA (NMPCA) extends MPCA to constrain the projection matrices to be nonnegative. NMPCA preserves the nonnegativity of the original tensor samples that is important when the underlying data have physical or psychological interpretation. RMPCA and NMPCA can be considered as an extension of MPCA. Although the above algorithms exploit tensorial structure for subspace learning, they are formulated on the multilinear projection of tensor to tensor only. Moreover, there exists a different projection scheme that projects tensor to vector. The tensor rank-one decomposition (TROD) algorithm introduced in [22] is one example. This algorithm looks for a second-order projection that projects an image to a low dimensional vector while minimizing a least square (reconstruction) error measure. Nonetheless, the input data are not centered before learning and the work is formulated only for matrices. Later, an uncorrelated MPCA (UMPCA) algorithm is proposed in [23] and adopted in [24], which extracts uncorrelated multilinear features through tensor to vector projection while capturing most of the variation in the original data input.

Although tensorial PCA methods achieve better performance than naive PCA, there remain several shortcomings in them. Firstly, the nonconvex optimality criterion and the suboptimal iterative solver, used by tensorial PCA, do not have any guarantee of global optimality of the solution found. Secondly, the objective of most tensorial PCA algorithms is to find the most expressive core tensor for each input tensor. Therefore, the disadvantage arising in this way is that more storage is required to represent the core tensor compared with the scalar representation used in PCA or KPCA. Last but not

TABLE 1: Comparison between several PCA Algorithms.

Method	Linear/nonlinear	Vector-based/tensor-based
PCA	Linear	Vector-based
KPCA	Nonlinear	Vector-based
Tensorial PCA	Linear	Tensor-based
TKPCA	Nonlinear	Tensor-based

important, none of the above methods takes into account the nonlinear relationships among the tensorial data. In other words, the tensorial PCA algorithms are multilinear method that neglects the higher-order statistics existed between neighborhood. However, it is well known that the object appearances lie on a nonlinear low-dimensional manifold in applications such as action recognition and face recognition where pose or illumination variations exist. Tensorial PCA methods cannot effectively model such nonlinearity, and this prevents them from higher recognition accuracy.

1.1. TKPCA. Motivated by the above drawbacks, in this paper, we propose a *Tensorial Kernel Principal Component Analysis* (TKPCA) to extend the conventional PCA to its kernelized tensor counterpart. TKPCA aims to overcome the drawbacks in traditional PCA and MPCA and brings together the desirable properties of kernel methods and tensor decompositions (see Section 2.1) for significant performance gain when the data are multidimensional and nonlinear dependencies do exist. Table 1 gives connections and differences with other PCA techniques. To the best of our knowledge, this is the first study that addresses the TKPCA problem.

Our approach begins by formulating TKPCA as an optimization problem. Unlike traditional PCA, the *Covariance Matrix* cannot be formed directly from tensorial data. We thus derive the TKPCA in a support vector machine (SVM) fashion, which leads to a convex optimization and fits into the *primal-dual framework* [16]. The primal problem can be solved by dual representation through kernel trick which is based on the Mercer theorem related to positive definite kernels [25]. Subsequently, a kernel function with tensorial inputs (*tensorial kernel*) can be plugged into the dual solution, which takes the nonlinear structure of tensorial representation into account. Furthermore, we design a novel tensorial kernel based on Grassmann Manifold and the positive definiteness which is also proved.

The benefits of the TKPCA can be summarized as follows.

- (i) Tensor representation of multidimensional data reduces the SSS problem and the Curse of Dimensionality phenomenon, facilitating a precise classification performance even for low number of training samples and complex data structure.
- (ii) Kernel method remedies the shortcoming of tensorial PCA in modelling the nonlinear manifold of tensor objects.
- (iii) TKPCA is equivalent to performing a standard KPCA except that the parameters of kernel function are in natural tensor representations, and in general, KPCA achieves higher compression rate (CR) than

tensorial PCA. Therefore, TKPCA offers better CR performance.

- (iv) TKPCA is insensitive to environmental variations and more robust to noise. This is because the Grassmann based kernel function compares similarity between subspaces that are low dimensional approximation of original data and the approximation can “fill in” the missing data. Moreover, the kernel is derived with the geodesic distance on the Grassmann manifold other than the Euclidean distance. Therefore, the TKPCA is expected to capture the topological structure underlying tensor dataset.
- (v) TKPCA is a convex optimization problem which means that any local minimum must also be global. Therefore, TKPCA do not suffer from the issue of local minima as tensorial PCA.

The main contributions of this paper include the following.

- (i) A new TKPCA is introduced for nonlinear dimensionality reduction and feature extraction from tensor object, by encoding the structured information embedded in the tensorial data into the kernels framework.
- (ii) A novel tensorial kernel function is proposed based on Grassmann kernel which can directly measure the similarity between tensorial inputs. Furthermore, the strict positive definiteness proof of proposed kernel function is given.
- (iii) A recognition system is developed for action recognition by selecting more discriminative features after TKPCA projection.

The rest of this paper is organized as follows. Section 2 introduces basic notations, kernel methods concepts, and the notion of multilinear projection for dimensionality reduction. In Section 3, the problem of TKPCA is formulated. Then, the detailed algorithm is summarized and discussed in detail. Moreover, a TKPCA-based tensor object recognition is proposed for application of action recognition. Section 4 lists experiments on action recognition and compares performance against state-of-the-art algorithm. We also assess the noise robustness and investigate sensitivity against occlusion and misalignment. Finally, Section 5 summarizes the major findings of this work.

2. Background and Notation

This section firstly reviews the notations and some basic multilinear operations that are necessary in defining our TKPCA. Then, a multilinear projection is introduced for dimensionality reduction and feature extraction from tensor object. We provide the conceptual foundations of kernel methods in the last part.

2.1. Notations and Basic Multilinear Algebra. Following the notation conventions in multilinear algebra, pattern recognition, and adaptive learning literature [26–29], vectors

TABLE 2: List of important notations.

Notation	Description
\mathcal{X}_m	The m th input tensor sample, $m = 1, \dots, M$
\mathcal{Y}_m	The projection of \mathcal{X}_m on $\{U^{(n)}\}_{n=1}^N$
y	The projection on eigenvector
$\mathcal{A}_{(n)}$	The mode- n matricization of \mathcal{A}
$\mathcal{X}_{m(n)}$	The mode- n matricization of m th tensor sample
$\text{vec}(\mathcal{A})$	The vectorization of \mathcal{A}
$\mathbf{U}^{(n)}$	The n th projection matrix
$\mathbf{U}_{\mathcal{X}}^{(n)}$	The orthonormal base matrix of $\mathcal{X}_{(n)}$
\mathcal{K}	The Gram or Kernel Matrix
M	The number of training samples
N	The order of a tensor object, the number of indices/modes
P	The n -mode dimensionality in the projected space or the number of dominant eigenvectors
Q	The number of most discriminative components of y
$\phi(\cdot)$	The map from vector to RKHS
$\phi(\cdot)$	The map from tensor to HSF

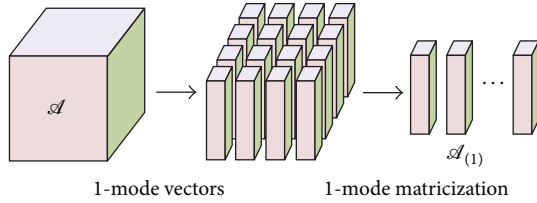


FIGURE 2: Visual illustration of the 1-mode unfolding of a third-order tensor.

are denoted by lowercase boldface letters, for example, \mathbf{x} ; matrices by uppercase boldface, for example, \mathbf{X} ; and tensors by calligraphic letters, for example, \mathcal{X} . Their elements are denoted with indices in parentheses. Indices are denoted by lowercase letters, spanning the range from 1 to the uppercase letter of the index, for example, $n = 1, 2, 3, \dots, N$. In addressing part of a vector/matrix/tensor, “:” denotes the full range of the respective index, and $n_1 : n_2$ denotes indices ranging from n_1 to n_2 . In this paper, only real-valued data are considered. Table 2 summarizes the important symbols used in this paper for quick reference.

An N th-order tensor is denoted as $\mathcal{A} \in \mathbb{R}^{I_1 \times I_2 \times \dots \times I_N}$, which is addressed by N indices i_n , $n = 1, \dots, N$, with each i_n addressing the n -mode of \mathcal{A} .

The n -mode vectors of \mathcal{A} are defined as the I_n dimensional vectors obtained from \mathcal{A} by varying its index i_n while keeping all the other indices fixed. The mode- n matricization of \mathcal{A} is denoted as

$$\mathcal{A}_{(n)} \in \mathbb{R}^{I_n \times (I_1 \times \dots \times I_{n-1} \times I_{n+1} \times \dots \times I_N)}, \quad (1)$$

where the column vectors of $\mathcal{A}_{(n)}$ are the n -mode vectors of \mathcal{A} . Figure 2 illustrates the 1-mode (column mode) matricization of a third-order tensor.

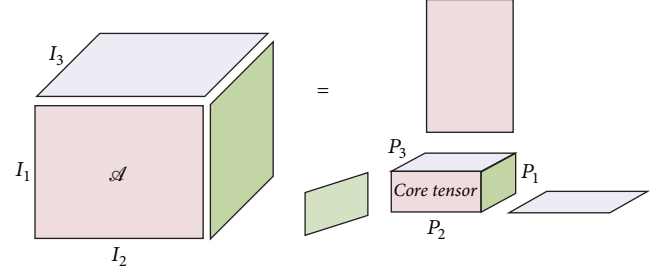


FIGURE 3: The illustration of HOSVD scheme.

The n -mode product of a tensor \mathcal{A} by a matrix $\mathbf{U} \in \mathbb{R}^{j_n \times i_n}$, denoted by $\mathcal{A} \times_n \mathbf{U}$, is a tensor defined with entries:

$$\begin{aligned} (\mathcal{A} \times_n \mathbf{U})(i_1, \dots, i_n - 1, j_n, i_n + 1, i_N) \\ = \sum_{i_n} \mathcal{A}(i_1, \dots, i_N) \cdot \mathbf{U}(j_n, i_n). \end{aligned} \quad (2)$$

The two most commonly used tensor decompositions are Tucker and CANDECOMP/PARAFAC (CP). Both of which can be regarded as higher-order generalizations of the matrix Singular Value Decomposition (SVD). Let $\mathcal{A} \in \mathbb{R}^{I_1 \times I_2 \times \dots \times I_N}$ denote an N th-order tensor; then, Tucker decomposition is defined as follows:

$$\mathcal{A} = \mathcal{S} \times_1 \mathbf{U}^{(1)} \times_2 \mathbf{U}^{(2)} \dots \times_N \mathbf{U}^{(N)}, \quad (3)$$

where $\mathcal{S} \in \mathbb{R}^{P_1 \times P_2 \times \dots \times P_N}$, with $P_n < I_n$ denotes the core tensor and $\mathbf{U}^{(n)} \in \mathbb{R}^{I_n \times P_n}$. When all $\{\mathbf{U}^{(n)}\}_{n=1}^N$ are orthonormal and the core tensor is all orthogonal, this model is called High Order Singular Value Decomposition (HOSVD) [30]; see Figure 3. When all factor matrices have the same number of components and the core tensor is superdiagonal, Tucker model is simplified to CP model. In general, CP model is considered to be a multilinear low rank approximation, while Tucker model is regarded as a multilinear subspace approximation.

The distance between tensors \mathcal{A} and \mathcal{B} can be measured by the Frobenius norm [31], $\text{dist}(\mathcal{A}, \mathcal{B}) = \|\mathcal{A} - \mathcal{B}\|_F$. Although this is a tensor-based measure, it is equivalent to a distance measure of corresponding vector representations. Let $\text{vec}(\mathcal{A})$ be the vector representation (vectorization) of \mathcal{A} ; then, $\text{dist}(\mathcal{A}, \mathcal{B}) = \|\text{vec}(\mathcal{A}) - \text{vec}(\mathcal{B})\|_2$. This implies that the distance between two tensors equals to the Euclidean distance between their vectorized representations.

2.2. Multilinear Principal Component Analysis. An N th-order tensor \mathcal{X} resides in the tensor (multilinear) space $\mathbb{R}^{I_1} \otimes \mathbb{R}^{I_2} \otimes \mathbb{R}^{I_N}$, where $\mathbb{R}^{I_1}, \dots, \mathbb{R}^{I_2}, \mathbb{R}^{I_N}$ are the N vector (linear) spaces. For typical image and video tensor objects, although the corresponding tensor space is of high dimensionality, tensor objects typically are embedded in a lower dimensional tensor subspace (or manifold), in analogy to the (vectorized) face image embedding problem where vector image inputs reside in a low-dimensional subspace of the original input space [15]. Thus, it is possible to find a tensor subspace that

captures most of the variation in the input tensor objects, and it can be used to extract features for recognition and classification applications. To achieve this objective, let us assume that a set of M tensor objects $\{\mathcal{X}_m\}_{m=1}^M$ is available for training. Each tensor object $\mathcal{X}_m \in \mathbb{R}^{I_1 \times I_2 \times \dots \times I_N}$ has values in a tensor space $\mathbb{R}^{I_1} \otimes \mathbb{R}^{I_2} \otimes \dots \otimes \mathbb{R}^{I_N}$, where I_n is the n -mode dimension of the tensor. The objective of *Multilinear Principal Component Analysis of Tensors* (MPCA) [19] is to find a multilinear transformation $\{\mathbf{U}^{(n)} \in \mathbb{R}^{I_n \times P_n}\}_{n=1}^N$ that maps the original tensor space $\mathbb{R}^{I_1} \otimes \mathbb{R}^{I_2} \otimes \dots \otimes \mathbb{R}^{I_N}$ into a tensor subspace $\mathbb{R}^{P_1} \otimes \mathbb{R}^{P_2} \otimes \dots \otimes \mathbb{R}^{P_N}$, with $P_n < I_n$, that is, $\mathcal{Y}_m = \mathcal{X}_m \times_1 \mathbf{U}^{(1)T} \times_2 \mathbf{U}^{(2)T} \dots \times_N \mathbf{U}^{(N)T}$, such that $\{\mathcal{Y}_m \in \mathbb{R}^{P_1} \otimes \mathbb{R}^{P_2} \otimes \dots \otimes \mathbb{R}^{P_N}\}_{m=1}^M$ captures most of the variations observed in the original tensor objects, assuming that these variations are measured by the total tensor scatter: $\sum_{m=1}^M \|\mathcal{X}_m - \bar{\mathcal{X}}\|_F^2$, where $\bar{\mathcal{X}}$ is the empirical mean. In other words, the MPCA objective is the determination of the N projection matrices that maximize the total tensor scatter.

However, there is no known optimal solution which allows for the simultaneous optimization of the N projection matrices. Instead of global optimization, [19] propose a suboptimal iterative solution.

2.3. Kernel Methods. Kernel methods [25] have gained considerable popularity during the last few decades, providing attractive solutions to a variety of problems. The strategy adopted is to embed the data into a space where the patterns can be discovered as linear relations. This will be done in a modular fashion: the first module that performs a nonlinear mapping into *RKHS* or *feature space* implicitly through a kernel function and the second module that is a specific learning algorithm in a dual form designed to discover linear relations in the feature space. The basic assumption is that the obtained feature space reflects nonlinear structure of input data. Hence, the only information that is required is the similarity measure in the feature space, which leads us to avoid explicitly having to know the nonlinear mapping function. Instead, the similarity measure of two data points in the feature space, that is, an inner product, should be appropriately defined by a reproducing kernel formulated in the input space, which is called a *kernel trick*.

The main ingredients of kernel methods are elucidated through kernel PCA, given a set of centered observations $\{\mathbf{x}_m\}_{m=1}^M \in \mathbb{R}^I$ independent and identically distributed (i.i.d.) according to the generator $p(\mathbf{x})$. PCA optimally chooses a subspace that captures most of the variance of the data. The first principal component is defined as $y_m = \mathbf{w}^T \mathbf{x}_m$, where the weight \mathbf{w} can be estimated as the leading eigenvector of sample covariance matrix $\mathbf{C} = (1/M) \sum_{m=1}^M \mathbf{x}_m \mathbf{x}_m^T$, satisfying $\lambda \mathbf{w} = \mathbf{C} \mathbf{w}$ which implies that \mathbf{w} can be also expressed as a linear combination of the training samples, that is, $\mathbf{w} = \sum_{m=1}^M \alpha_m \mathbf{x}_m$. Thus, the *dual* representation of PCA is $M \lambda \alpha = \mathcal{K} \alpha$ with $\mathcal{K}(i, j) = \langle \mathbf{x}_i, \mathbf{x}_j \rangle$, referred to *Kernel Matrix* that consist of inner products between all pairs of training samples. After estimation of α by diagonalizing \mathcal{K} , the first principal component of test sample \mathbf{x}' is obtained

by $y' = \mathbf{w}^T \mathbf{x}' = \sum_{m=1}^M \alpha_m \langle \mathbf{x}_m, \mathbf{x}' \rangle$. Note that, for the dual representation of PCA, all information from training samples is given by the Kernel Matrix \mathcal{K} . This matrix acts as an information bottleneck, as all the information is available to a kernel algorithm.

let us consider an embedding or map $\phi : \mathbb{R}^I \rightarrow F$, where F refer to feature space which could have an arbitrarily large dimensionality. The pairwise inner products in feature space can be computed efficiently directly from the original data items using a kernel function $k(\mathbf{x}_i, \mathbf{x}_j) = \langle \phi(\mathbf{x}_i), \phi(\mathbf{x}_j) \rangle$. Hence, the Kernel Matrix \mathcal{K} can be computed without explicit knowledge of $\phi(\cdot)$. Finally, the first principle component of test sample embedded into feature space $\phi(\mathbf{x}')$ is computed by $\sum_{m=1}^M \alpha_m k(\mathbf{x}_m, \mathbf{x}') = \sum_{m=1}^M \alpha_m \langle \phi(\mathbf{x}_m), \phi(\mathbf{x}') \rangle$.

3. Kernel Principal Component Analysis of Tensor Objects

In this section, we propose a novel unsupervised learning method, called Tensorial Kernel Principal Component Analysis (TKPCA), for nonlinear dimensionality reduction and feature extraction from tensor objects. Unlike conventional PCA, there is no closed-form formula for Covariance Matrix of tensorial data. Therefore, our approach begins by formulating TKPCA as an optimization problem. Then, we develop a kernel function that can directly take tensorial data as parameters other than vectorial ones. Moreover, the detailed algorithm is summarized and discussed. A TKPCA-based tensor object recognition is also proposed for application of action recognition.

3.1. TKPCA as an Optimization Problem. As we have seen in Section 2.3, the KPCA is classically derived by constructing the Covariance Matrix explicitly. However, in statistics and probability theory, the Covariance Matrix is a matrix of covariance between elements of a random *vector*. This means that, before feeding tensors into Covariance Matrix, we have to transform them into vectors firstly, which conflicts with our purpose of this paper. To solve this difficulty, we derive TKPCA as an optimization problem. In this way, the explicit construction of Covariance Matrix is bypassed. Note that there is a number of other ways to derive the PCA [14], and a Generalized Covariance Matrix (GCM) [32] concept also provides an alternative solution from other perspective.

Given is a set of centered tensorial observations $\{\mathcal{X}_m\}_{m=1}^M \in \mathbb{R}^{I_1 \times I_2 \times \dots \times I_N}$, i.i.d., according to the generator $p(\mathcal{X})$ and a nonlinear mapping $\phi : \mathbb{R}^{I_1 \times I_2 \times \dots \times I_N} \rightarrow HSF$, where *HSF* refer to a space of multilinear functions corresponding the infinite dimensional tensors which could have an arbitrarily large dimensionality (see Section 3.2), to the objective is to optimally choose a subspace that captures most of the variance from tensorial samples. The starting point is to define projection onto weight w as

$$y_m = \mathbf{w}_m^T \phi(\mathcal{X}_m). \quad (4)$$

Recall that, while least squares support vector machine classifiers (LS-SVM) have a natural link with *kernel Fisher*

discriminant analysis (minimizing the within class scatter around targets +1 and -1), for TKPCA, we can take the interpretation of a one-class modeling problem with zero target value around which one maximizes the variance. Let us now reformulate the TKPCA problem as follows:

$$\max_{\mathbf{w}} \sum_{m=1}^M [0 - \mathbf{w}^T (\phi(\mathcal{X}_m))]^2, \quad (5)$$

where zero is considered as a single target value. For Kernel Fisher discriminant analysis one aims at minimizing the within scatter around the targets, while for TKPCA analysis one is interested in finding the direction(s) for which the variance is maximal. This interpretation leads to the following primal optimization problem

$$\max_{\mathbf{w}, y} J_p(\mathbf{w}, y) = \frac{\gamma}{2} \sum_{m=1}^M y_m^2 - \frac{1}{2} \mathbf{w}^T \mathbf{w}, \quad (6)$$

where $\gamma \in \mathbb{R}^+$. Equation (6) maximizes the empirical variance of y_m around value 0 while keeping the norm of the corresponding parameter \mathbf{w} small by the regularization term $-(1/2)\mathbf{w}^T \mathbf{w}$. one can also include a bias term; see [33].

The Lagrangian corresponding to (6) is

$$\mathcal{L}(\mathbf{w}, y; \boldsymbol{\alpha}) = \frac{\gamma}{2} \sum_{m=1}^M y_m^2 - \sum_{m=1}^M \alpha_m (y_m - \mathbf{w}^T \phi(\mathbf{n})) - \frac{1}{2} \mathbf{w}^T \mathbf{w}, \quad (7)$$

with conditions for optimality given by

$$\begin{aligned} \frac{\partial \mathcal{L}}{\partial \mathbf{w}} = 0 &\longrightarrow \mathbf{w} = \sum_{m=1}^M \alpha_m \phi(\mathcal{X}_m), \\ \frac{\partial \mathcal{L}}{\partial y_m} = 0 &\longrightarrow \alpha_m = \gamma y_m, \quad m = 1, \dots, M, \\ \frac{\partial \mathcal{L}}{\partial \mathbf{a}_m} = 0 &\longrightarrow y_m = \mathbf{w}^T \phi(\mathcal{X}_m), \quad m = 1, \dots, M. \end{aligned} \quad (8)$$

By eliminating the primal variables \mathbf{w} and y , one obtains $(1/r)\boldsymbol{\alpha}(m) - \sum_{m=1}^M \boldsymbol{\alpha}(m)\phi(\mathcal{X}_m)^T \phi(\mathcal{X}_m) = 0$, for $m = 1, \dots, M$. This is an eigenvalue decomposition that can be present in matrix formulation as

$$\mathcal{H} \boldsymbol{\alpha} = \lambda \boldsymbol{\alpha}, \quad (9)$$

where $\lambda = 1/\gamma$, $\boldsymbol{\alpha} \equiv [\alpha_1, \dots, \alpha_M]^T$, and \mathcal{H} is the centered Kernel Matrix defined entry-wise by

$$\mathcal{H}(i, j) = \langle \phi(\mathcal{X}_i), \phi(\mathcal{X}_j) \rangle = k(\mathcal{X}_i, \mathcal{X}_j), \quad (10)$$

$$i, j = 1, \dots, M,$$

where $\mathcal{X}_i, \mathcal{X}_j \in \{\mathcal{X}_m\}_{m=1}^M$.

The optimal solution to the formulated problem is obtained by selecting the eigenvectors corresponding to the first P largest eigenvalues, where P is a slight abuse of the

notation which, however, simplifies the description. For test sample \mathcal{X}' , the first projection becomes

$$\begin{aligned} y' &= \mathbf{w}^T \phi(\mathcal{X}') = \sum_{m=1}^M \boldsymbol{\alpha}(m) \langle \phi(\mathcal{X}_m), \phi(\mathcal{X}') \rangle \\ &= \sum_{m=1}^M \boldsymbol{\alpha}(m) k(\mathcal{X}_m, \mathcal{X}'), \end{aligned} \quad (11)$$

where $\boldsymbol{\alpha} \equiv [\alpha_1, \dots, \alpha_M]^T$ is the first eigenvector of Kernel Matrix (9). For computing the kernel functions in (10) and (11), we present a *tensorial kernel* function in next section, which can directly take tensorial data as parameters other than vectorial ones.

3.2. RKHS Induced by Multilinear Functions. Kernel should be constructed from input space in a way that the high-dimensional feature space implicated by kernel function reflects the underlying structure of data in original input space. Although a number of kernels have been designed for tensorial objects, few approaches exploit the underlying structure of tensorial space. Recently, Signoretto et al. [34] generalized RKHS to adapt to multilinear functions, which allows a reproducing kernel to exploit algebraic geometry of tensorial space. In principle, the idea of Signoretto et al. is to propose a *tensorial kernel* that can directly take tensorial data as parameters other than vectorial ones. After that, the tensorial kernel is plugged into prime-dual framework to learn the structural information embodied in the tensors.

Let RKHS be $(\mathcal{H}, \langle \cdot, \cdot \rangle)$ equipped with some inner product.

A bounded (continuous) multilinear function on RKHSs denoted by $\psi : \mathcal{H}_1 \times \mathcal{H}_2 \times \dots \times \mathcal{H}_p \rightarrow \mathbb{R}$ is said to be *Hilbert-Schmidt* if it satisfies some constraints. The ensemble of such well behaved Hilbert-Schmidt functions equipped with the inner product $\langle \psi, \psi' \rangle$ forms a Hilbert Space denoted by HSF, which is a space of multilinear functions corresponding the infinite dimensional tensors. Using boldface ϕ denoting the map from tensor object to multilinear function space, we have $\phi : \mathbb{R}^{I_1 \times I_2 \times \dots \times I_N} \rightarrow \text{HSF}$ and define $k : \mathbb{R}^{I_1 \times I_2 \times \dots \times I_N} \times \mathbb{R}^{I_1 \times I_2 \times \dots \times I_N} \rightarrow \mathbb{R}$ by

$$k(\mathcal{X}_i, \mathcal{X}_j) := \langle \phi(\mathcal{X}_i), \phi(\mathcal{X}_j) \rangle_{\text{HSF}}. \quad (12)$$

According to the theory of [34], for N-order tensors $\mathcal{X}_i, \mathcal{X}_j$, a kernel function, exploiting structural properties possessed by the given tensorial representations, can be stated as N product kernel:

$$k(\mathcal{X}_i, \mathcal{X}_j) = \prod_{n=1}^N k(\mathcal{X}_{i(n)}, \mathcal{X}_{j(n)}), \quad (13)$$

where $k(\mathcal{X}_i, \mathcal{X}_j)$ denotes *tensorial kernel*, $k(\mathcal{X}_{i(n)}, \mathcal{X}_{j(n)})$ is *nth factor kernel* of tensorial kernel, and $\mathcal{X}_{i(n)}$ and $\mathcal{X}_{j(n)}$ is the mode- n matricization of \mathcal{X}_i and \mathcal{X}_j , respectively. Equation (13) implies that the similarity measure induced by the kernel function between two tensor objects can be represented as product of factor kernels which measure similarity between mode- n matricization of two tensors.

3.3. Factor Kernel on Grassmann Manifold. The factor kernel represents a similarity measure between two matrices obtained by mode- n matricization of two tensors. In [34], Signoretto et al. adopt Chordal distance as metric to measure such similarity that lead to an ad hoc approach to obtain tensorial kernel. This inconsistency can cause complications and weak guarantees. In our approach, the factor kernel is build from Grassmann kernel by a number of simple operations, resulting in a simpler and better-understood formulation. Note that our factor kernel differs from the result of Signoretto et al.

The fixed dimensional linear subspaces form a non-Euclidean and curved Riemannian manifold known as *Grassmann manifold*, allowing the subspaces to be represented as points on it. In TKPCA, such low dimensional subspaces is used to approximate the mode- n matricization of tensors. The benefits of using subspaces are two-fold: (a) comparing two subspaces is cheaper than comparing two n matricizations of tensor directly when they are very large, for example, too many frames per video, and (b) it is more robust to noise since the subspace can “fill in” the missing pictures.

Given a $I_n \times (I_1 \times \dots \times I_{n-1} \times I_{n+1} \times \dots \times I_N)$ mode- n matricizations $\mathcal{X}_{(n)}$ of rank r , we can represent it as a subspace (and hence as a point on a Grassmann manifold) through any orthogonalisation procedure like SVD. More specifically, let $\mathcal{X}_{(n)} = \mathbf{U}_{\mathcal{X}}^{(n)} \mathbf{D}_{\mathcal{X}}^{(n)} \mathbf{V}_{\mathcal{X}}^{(n)T}$, where the $I_n \times r$ orthonormal matrix $\mathbf{U}_{\mathcal{X}}^{(n)}$ represents an optimised subspace of order r (in the mean square sense) for $\mathcal{X}_{(n)}$ and can be seen as a point on Grassmann manifold $G(r, I_n)$, which is the set of r -dimensional linear subspaces of the \mathbb{R}^{I_n} . The Riemannian distance between two subspaces is the length of the shortest geodesic connecting the two points on the Grassmann manifold. Among many different distances, a few of them can be induced to form a positive definite kernel, and the *Projection metric* is the one.

The Projection metric can be understood by associating a point span $\text{span}(\mathbf{U}_{\mathcal{X}}^{(n)}) \in G(r, I_n)$ with its projection matrix $\mathbf{U}_{\mathcal{X}}^{(n)} \mathbf{U}_{\mathcal{X}}^{(n)T}$ by an embedding:

$$\phi : G(r, I_n) \longrightarrow \mathbb{R}^{I_n \times I_n}, \quad \text{span}(\mathbf{U}_{\mathcal{X}}^{(n)}) \longrightarrow \mathbf{U}_{\mathcal{X}}^{(n)} \mathbf{U}_{\mathcal{X}}^{(n)T}. \quad (14)$$

The image $\phi(G)$ is the set of rank r orthogonal projection matrices. This map is in fact an isometric embedding [35], and the projection metric is simply a Euclidean distance in $\mathbb{R}^{I_n \times I_n}$. The corresponding innerproduct of the space is $\text{tr}[(\mathbf{U}_{\mathcal{X}_i}^{(n)} \mathbf{U}_{\mathcal{X}_i}^{(n)T})(\mathbf{U}_{\mathcal{X}_j}^{(n)} \mathbf{U}_{\mathcal{X}_j}^{(n)T})] = \|\mathbf{U}_{\mathcal{X}_i}^{(n)T} \mathbf{U}_{\mathcal{X}_j}^{(n)}\|_F^2$, and therefore, the *projection kernel*

$$k(\mathbf{U}_{\mathcal{X}_i}^{(n)}, \mathbf{U}_{\mathcal{X}_j}^{(n)}) = \|\mathbf{U}_{\mathcal{X}_i}^{(n)T} \mathbf{U}_{\mathcal{X}_j}^{(n)}\|_F^2 \quad (15)$$

is a Grassmann kernel.

Motivated by classic Gaussian kernel $k(x, y) = \exp(-1/2\sigma^2\|x - y\|_2^2)$, we propose a novel factor kernel based on projection kernel (15), and by Theorem 1, it is provable positive definiteness as required by *Mercer's Theorem* [36].

Theorem 1. Let adjustable parameter $\sigma \in \mathbb{R}^+$; the function that exploit metric on Grassmann manifolds

$$k(\mathcal{X}_{i(n)}, \mathcal{X}_{j(n)}) = \exp\left(-\frac{\|\mathbf{U}_{\mathcal{X}_i}^{(n)} \mathbf{U}_{\mathcal{X}_i}^{(n)T} - \mathbf{U}_{\mathcal{X}_j}^{(n)} \mathbf{U}_{\mathcal{X}_j}^{(n)T}\|_F^2}{2\sigma^2}\right) \quad (16)$$

is positive definite kernel function.

Proof. We first verify that the Projection kernel (15) is positive definite kernel function.

The positive definiteness of Projection kernel follows from the properties of the Frobenius norm. For all $\mathbf{U}_{\mathcal{X}_i}^{(n)}, \mathbf{U}_{\mathcal{X}_j}^{(n)} \in \mathcal{S}$, and $c_i, c_j \in \mathbb{R}$, we have

$$\begin{aligned} \sum_{ij} c_i c_j \|\mathbf{U}_{\mathcal{X}_i}^{(n)T} \mathbf{U}_{\mathcal{X}_j}^{(n)}\|_F^2 &= \sum_{ij} c_i c_j \text{tr}(\mathbf{U}_{\mathcal{X}_i}^{(n)} \mathbf{U}_{\mathcal{X}_i}^{(n)T} \mathbf{U}_{\mathcal{X}_j}^{(n)} \mathbf{U}_{\mathcal{X}_j}^{(n)T}) \\ &= \text{tr}\left(\sum_i c_i \mathbf{U}_{\mathcal{X}_i}^{(n)} \mathbf{U}_{\mathcal{X}_i}^{(n)T}\right)^2 \\ &= \left\|\sum_i c_i \mathbf{U}_{\mathcal{X}_i}^{(n)} \mathbf{U}_{\mathcal{X}_i}^{(n)T}\right\|_F^2 \geq 0. \end{aligned} \quad (17)$$

Next, we use Projection kernel as a footstone to build the more complex factor kernel.

The exponential function can be arbitrarily closely approximated by polynomials with positive coefficients and hence is a limit of kernels. Since the positive definiteness property is closed under taking pointwise limits,

$$k(\mathcal{X}_{i(n)}, \mathcal{X}_{j(n)}) = \exp\left(\frac{k(\mathbf{U}_{\mathcal{X}_i}^{(n)}, \mathbf{U}_{\mathcal{X}_j}^{(n)})}{\sigma^2}\right) \quad (18)$$

is a positive definite kernel function for $\sigma \in \mathbb{R}^+$.

Assuming kernel (18) corresponds to a feature map $\phi(\cdot)$, normalising this kernel corresponds to the feature map

$$\mathbf{U}_{\mathcal{X}_i}^{(n)} \longrightarrow \phi(\mathbf{U}_{\mathcal{X}_i}^{(n)}) \longrightarrow \frac{\phi(\mathbf{U}_{\mathcal{X}_i}^{(n)})}{\|\phi(\mathbf{U}_{\mathcal{X}_i}^{(n)})\|}. \quad (19)$$

Hence, we can express the normalised kernel \hat{k} in terms of $k(\mathcal{X}_{i(n)}, \mathcal{X}_{j(n)})$ as follows:

$$\begin{aligned} \hat{k}(\mathbf{U}_{\mathcal{X}_i}^{(n)}, \mathbf{U}_{\mathcal{X}_j}^{(n)}) &= \left\langle \frac{\phi(\mathbf{U}_{\mathcal{X}_i}^{(n)})}{\|\phi(\mathbf{U}_{\mathcal{X}_i}^{(n)})\|}, \frac{\phi(\mathbf{U}_{\mathcal{X}_j}^{(n)})}{\|\phi(\mathbf{U}_{\mathcal{X}_j}^{(n)})\|} \right\rangle \\ &= \frac{k(\mathbf{U}_{\mathcal{X}_i}^{(n)}, \mathbf{U}_{\mathcal{X}_j}^{(n)})}{\sqrt{k(\mathbf{U}_{\mathcal{X}_i}^{(n)}, \mathbf{U}_{\mathcal{X}_i}^{(n)}) k(\mathbf{U}_{\mathcal{X}_j}^{(n)}, \mathbf{U}_{\mathcal{X}_j}^{(n)})}}, \end{aligned} \quad (20)$$

where the \hat{k} is a valid kernel because it was derived from the feature map (19).

Now, we can normalise the kernel (18) to obtain (16):

$$\begin{aligned}
& \frac{\exp\left(\left(k\left(\mathbf{U}_{\mathcal{X}_i}^{(n)}, \mathbf{U}_{\mathcal{X}_j}^{(n)}\right)\right)/\sigma^2\right)}{\sqrt{\exp\left(\left(k\left(\mathbf{U}_{\mathcal{X}_i}^{(n)}, \mathbf{U}_{\mathcal{X}_i}^{(n)}\right)\right)/\sigma^2\right)\exp\left(\left(k\left(\mathbf{U}_{\mathcal{X}_j}^{(n)}, \mathbf{U}_{\mathcal{X}_j}^{(n)}\right)\right)/\sigma^2\right)}} \\
&= \exp\left(\left(\frac{\left\|\mathbf{U}_{\mathcal{X}_i}^{(n)T} \mathbf{U}_{\mathcal{X}_j}^{(n)T}\right\|_F^2}{\sigma^2} - \frac{\left\|\mathbf{U}_{\mathcal{X}_i}^{(n)T} \mathbf{U}_{\mathcal{X}_i}^{(n)T}\right\|_F^2}{2\sigma^2} - \frac{\left\|\mathbf{U}_{\mathcal{X}_j}^{(n)T} \mathbf{U}_{\mathcal{X}_j}^{(n)T}\right\|_F^2}{2\sigma^2}\right)\right) \\
&= \exp\left(\frac{\operatorname{tr}\left(2\mathbf{U}_{\mathcal{X}_i}^{(n)}\mathbf{U}_{\mathcal{X}_i}^{(n)T}\mathbf{U}_{\mathcal{X}_j}^{(n)}\mathbf{U}_{\mathcal{X}_j}^{(n)T} - \mathbf{U}_{\mathcal{X}_i}^{(n)}\mathbf{U}_{\mathcal{X}_i}^{(n)T}\mathbf{U}_{\mathcal{X}_i}^{(n)}\mathbf{U}_{\mathcal{X}_i}^{(n)T} - \mathbf{U}_{\mathcal{X}_j}^{(n)}\mathbf{U}_{\mathcal{X}_j}^{(n)T}\mathbf{U}_{\mathcal{X}_j}^{(n)}\mathbf{U}_{\mathcal{X}_j}^{(n)T}\right)}{2\sigma^2}\right)} \\
&= \exp\left(\frac{\operatorname{tr}\left(\left(\mathbf{U}_{\mathcal{X}_i}^{(n)}\mathbf{U}_{\mathcal{X}_i}^{(n)T}\right)^2 - 2\mathbf{U}_{\mathcal{X}_i}^{(n)}\mathbf{U}_{\mathcal{X}_i}^{(n)T}\mathbf{U}_{\mathcal{X}_j}^{(n)}\mathbf{U}_{\mathcal{X}_j}^{(n)T} + \left(\mathbf{U}_{\mathcal{X}_j}^{(n)}\mathbf{U}_{\mathcal{X}_j}^{(n)T}\right)^2\right)}{2\sigma^2}\right) \\
&= \exp\left(\frac{\operatorname{tr}\left(\mathbf{U}_{\mathcal{X}_i}^{(n)}\mathbf{U}_{\mathcal{X}_i}^{(n)T} - \mathbf{U}_{\mathcal{X}_j}^{(n)}\mathbf{U}_{\mathcal{X}_j}^{(n)T}\right)^2}{2\sigma^2}\right) \\
&= \exp\left(\frac{\operatorname{tr}\left(\left(\mathbf{U}_{\mathcal{X}_i}^{(n)}\mathbf{U}_{\mathcal{X}_i}^{(n)T} - \mathbf{U}_{\mathcal{X}_j}^{(n)}\mathbf{U}_{\mathcal{X}_j}^{(n)T}\right)^T \left(\mathbf{U}_{\mathcal{X}_i}^{(n)}\mathbf{U}_{\mathcal{X}_i}^{(n)T} - \mathbf{U}_{\mathcal{X}_j}^{(n)}\mathbf{U}_{\mathcal{X}_j}^{(n)T}\right)\right)}{2\sigma^2}\right) \\
&= \exp\left(\frac{\left\|\mathbf{U}_{\mathcal{X}_i}^{(n)}\mathbf{U}_{\mathcal{X}_i}^{(n)T} - \mathbf{U}_{\mathcal{X}_j}^{(n)}\mathbf{U}_{\mathcal{X}_j}^{(n)T}\right\|_F^2}{2\sigma^2}\right). \tag{21}
\end{aligned}$$

□

Finally, substituting (16) in (13), the tensorial kernel based on projection kernel can be represented as

$$\begin{aligned}
k(\mathcal{X}_i, \mathcal{X}_j) &= \prod_{n=1}^N k(\mathcal{X}_{i(n)}, \mathcal{X}_{j(n)}) \\
&= \prod_{n=1}^N \exp\left(-\frac{\left\|\mathbf{U}_{\mathcal{X}_i}^{(n)}\mathbf{U}_{\mathcal{X}_i}^{(n)T} - \mathbf{U}_{\mathcal{X}_j}^{(n)}\mathbf{U}_{\mathcal{X}_j}^{(n)T}\right\|_F^2}{2\sigma^2}\right). \tag{22}
\end{aligned}$$

Furthermore, the positive definiteness of (22) comes from the *closure properties of kernels*: a product of valid kernels is still a kernel [25].

We are now ready to summarize the basic steps for performing a TKPCA with the tensorial kernel, given a set of observation $\{\mathcal{X}_m\}_{m=1}^M \in \mathbb{R}^{I_1 \times I_2 \times \dots \times I_N}$, i.i.d., according to the generator $p(\mathcal{X})$ and $\mathcal{X}_i, \mathcal{X}_j \in \{\mathcal{X}_m\}_{m=1}^M$. For test sample \mathcal{X}' , the pseudo code is summarized in Algorithm 1.

3.4. Properties of TKPCA. Before we proceed to the next section, the following observation is essential.

TKPCA can be seen to arise from a space of multilinear functionals which are, loosely speaking, infinite dimensional tensors. Therefore, TKPCA is equivalent to performing a standard KPCA in the RKHS of multilinear functions except that the parameters of kernel function are in natural tensor

representations. Furthermore, it can be shown that all the properties associated with the KPCA are still valid for the TKPCA. That is, (a) the dominant eigenvector directions optimally retain most of the variance, (b) the MSE (mean square error) in approximating a point in RKHS in terms of the P dominant eigenvectors is minimal, with respect to any other P directions, (c) projections onto the eigenvectors are uncorrelated, and (d) the entropy (under Gaussian assumption) is maximized.

TKPCA Algorithm has the same computational complexity as KPCA provided that the evaluation of kernel function is of complexity $O(1)$. The most time-consuming step is eigendecomposition of \mathcal{K} with complexity $O(M^3)$. When taking into account the evaluation of kernel function, the complexity of computing $\mathbf{U}_{\mathcal{X}_m}^{(n)}$ by any standard SVD algorithm requires $O((I_1 \times \dots \times I_{n-1} \times I_{n+1} \times \dots \times I_N)^3)$ operations. Note that the computational complexity of TKPCA does not grow with the dimensionality of the feature space that we are implicitly working in.

TKPCA compresses each tensor sample of size $\mathbb{R}^{I_1 \times I_2 \times \dots \times I_N}$ to P scalars, where P denotes the first P largest eigenvalues, while $\mathbb{R}^{P_1 \times P_2 \times \dots \times P_N}$ are needed to represent a tensor object in the tensorial PCA solutions. Thus, the compression ratio (CR) is a major advantage that TKPCA enjoys over other solutions, such as MPCA [19], 2DPCA [3], and GPCA [1].

There are several reasons behind the motivation of deriving the factor kernel with Gaussian kernel. Firstly, the Gaussian kernel is the most widely used nonlinear kernel and has been extensively studied in neighbouring fields. Secondly, there is no theoretical method for determining a kernel function. In the absence of expert knowledge, the Gaussian kernel makes a good default nonlinear kernel. Thirdly, the isotropic property of Gaussian kernel endows final tensorial kernel with intrinsic rotation-invariant, which is a desire feature that can be used in applications such as face recognition and action recognition.

Just like choosing kernel, there is no prior knowledge for setting the parameter σ which controls the flexibility of the kernel. Generally speaking, small values of σ allow classifiers to fit any labels, hence risking overfitting. In such cases, the Kernel Matrix becomes close to the identity matrix. On the other hand, large values of σ gradually reduce the kernel to a constant function, making it impossible to learn any nontrivial classifier. The feature space has infinite-dimension for every value of σ , but for large values, the weight decays very fast on the higher-order features. In other words, although the rank of the kernel matrix will be full, for all practical purposes, the data lie in a low-dimensional subspace of the feature space. For a full coverage of choosing kernel and parameters, please refer [37–39].

The PCA and Linear Discriminant Analysis (LDA) are two of the most commonly used subspace techniques. PCA produces an expressive subspace for object representation, while LDA produces a discriminating subspace. For the purpose of classification, LDA is generally believed to be superior to PCA when enough training samples per class are available [40]. However, when the number of available

(1) **Tensorial Kernel Function** $k(\mathcal{X}_i, \mathcal{X}_j)$:
(2) **for** $n = 1$ to N **do**
(3) Compute orthonormal bases $\mathbf{U}_{\mathcal{X}_i}^{(n)} \mathbf{U}_{\mathcal{X}_j}^{(n)}$ from SVD: $\mathcal{X}_{i(n)} = \mathbf{U}_{\mathcal{X}_i}^{(n)} \mathbf{D}_{\mathcal{X}_i}^{(n)} \mathbf{V}_{\mathcal{X}_i}^{(n)T}$,
 $\mathcal{X}_{j(n)} = \mathbf{U}_{\mathcal{X}_j}^{(n)} \mathbf{D}_{\mathcal{X}_j}^{(n)} \mathbf{V}_{\mathcal{X}_j}^{(n)T}$.
(4) Compute $k(\mathcal{X}_i, \mathcal{X}_j)$ by (22).
(5) **TKPCA**:
(6) *Step 1. (Initialization)*:
(7) Center the input samples by subtracting empirical mean: $(1/M) \sum_{m=1}^M \mathcal{X}_m$.
(8) *Step 2. (Training)*:
(9) **for** $i = 1$ to M **do**
(10) **for** $j = 1$ to M **do**
(11) **if** $i \neq j$ **then**
(12) Compute the Kernel Matrix (10): $\mathcal{K}(i, j) = k(\mathcal{X}_i, \mathcal{X}_j)$.
(13) Compute the P dominant eigenvectors α_p by eign-decomposition \mathcal{K} (9).
(14) *Step 3. (Projection)*:
(15) For test sample \mathcal{X}' , compute the P projections onto each one of the dominant eigenvectors (11),
 $y_p \equiv \langle \mathbf{w}, \phi(\mathcal{X}') \rangle = \sum_{m=1}^M \alpha_p(m) k(\mathcal{X}_m, \mathcal{X}'), p = 1, \dots, P$.

ALGORITHM 1: TKPCA: Kernel Principal Component Analysis of tensor objects.

training samples per class is small, the situation considered in this paper, experimental analysis indicates that PCA outperforms LDA [41, 42].

3.5. TKPCA-Based Tensor Object Recognition. After a projection by TKPCA, a new *feature vector* is obtained for each tensor object. The classification tasks on tensor objects are reduced to classification tasks in vector spaces. More precisely, for any query tensor object \mathcal{X} , the projection $\mathbf{y} \in \mathbb{R}^P$ on P most dominant eigenvectors is obtained. Similarly, the gallery set containing data samples with labels is also represented by vectors. Then, any classification methods can be employed to label query.

However, as we have seen above, TKPCA maximizes not only the within-class variation but also the between-class variation. This is due to the fact that the TKPCA works as an unsupervised technique without considering the class label. To overcome this limitation, a feature selection strategy is proposed to select eigenvectors for a more discriminative subspace. The strategy works according to the criterion that is based on the maximization of the following ratio [43]:

$$J = \frac{\sum_{c=1}^C N_c (\bar{\mathbf{y}}_c - \bar{\mathbf{y}})^2}{\sum_{m=1}^M (\mathbf{y}_m - \bar{\mathbf{y}}_{c_m})^2}, \quad (23)$$

where C is the number of classes, M is the number of samples in the gallery set, N_c is the number of samples for class c , and c_m is the class label for the m th gallery sample \mathcal{X}_m . \mathbf{y} is the feature vector of \mathcal{X}_m in the projected nonlinear subspace. The mean feature vector $\bar{\mathbf{y}} = (1/M) \sum_m \mathbf{y}_m$, and class mean feature vector $\bar{\mathbf{y}}_c = (1/N_c) \sum_{m, c_m=c} \mathbf{y}_m$. For the eigenvector selection, only the first Q most discriminative components of \mathbf{y}_q are kept for classification, with Q determined empirically or cross-validated.

Upon the extraction of the proper set of features, a classifier such as Nearest Neighbor Classifier, Bayesian Classifier,

Neural Network, and Support Vector Machine can be applied to recognize the objects. Here, we use a Nearest Neighbor Classifier for classification. The distance between two arbitrary feature vectors is defined by $d(\mathcal{X}_i, \mathcal{X}_j) = \sum_{p=1}^P \|\mathbf{y}_i^p - \mathbf{y}_j^p\|$, where the norm denotes the Euclidean distance between the two feature vectors. Such a simple classifier is selected to study the performance mainly contributed by the TKPCA-based feature extraction algorithm although better classifiers can be investigated.

4. Experiments

This section illustrates the efficacy of TKPCA in tensor object recognition, by applying it to the emerging application of Action Recognition [44] and comparing its performance against state-of-the-art algorithm. We also assess the noise robustness of the proposed approach and investigate sensitivity against occlusion and misalignment.

The action recognition is the process of labeling videos containing human motion with action labels. We will test our method on two action datasets: the KTH human motion dataset [45] and the Ballet dataset [46]. The proposed TKPCA-Based Tensor Object Recognition in Section 3.4 treats each action video as a 3rd-order tensor sample with the spatial row space, column space, and the time space accounting for the 3 modes. The whole dataset will be a 4th-order tensor, with the addition of the sample space.

4.1. KTH Dataset. The KTH human motion data set [45] contains six types of human actions walking, jogging, running, boxing, hand waving, and hand clapping performed several times by 25 subjects in four scenarios: outdoors, outdoors with scale variation, outdoors with different clothes, and indoors. See Figure 4 for sample frames. We first run an automatic pre processing step to track and stabilise the video sequences so that all of the figures appear in the center of the

TABLE 3: Recognition accuracy (in %) for the KTH action recognition dataset.

	STW	BoW-MKL	TCCA	DCCA	TKPCA
Walking	88	100	88	82	97
Jogging	90	80	75	53	98
Running	99	68	77	88	97
Boxing	98	97	92	98	100
Handclapping	100	99	100	86	96
Handwaving	97	99	88	93	100
Total	95	90	87	83	98

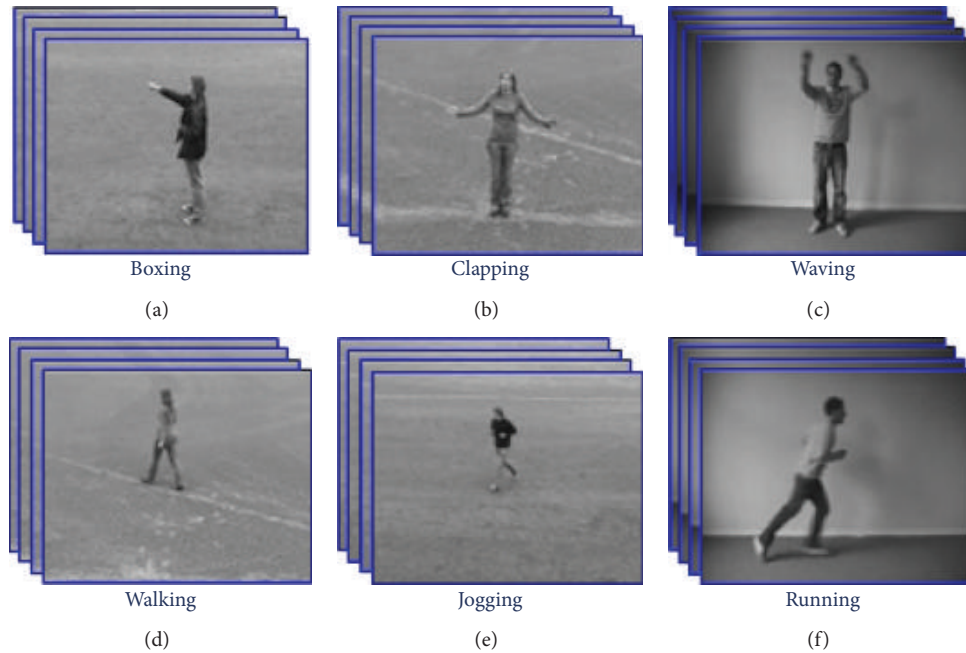


FIGURE 4: The KTH action dataset.

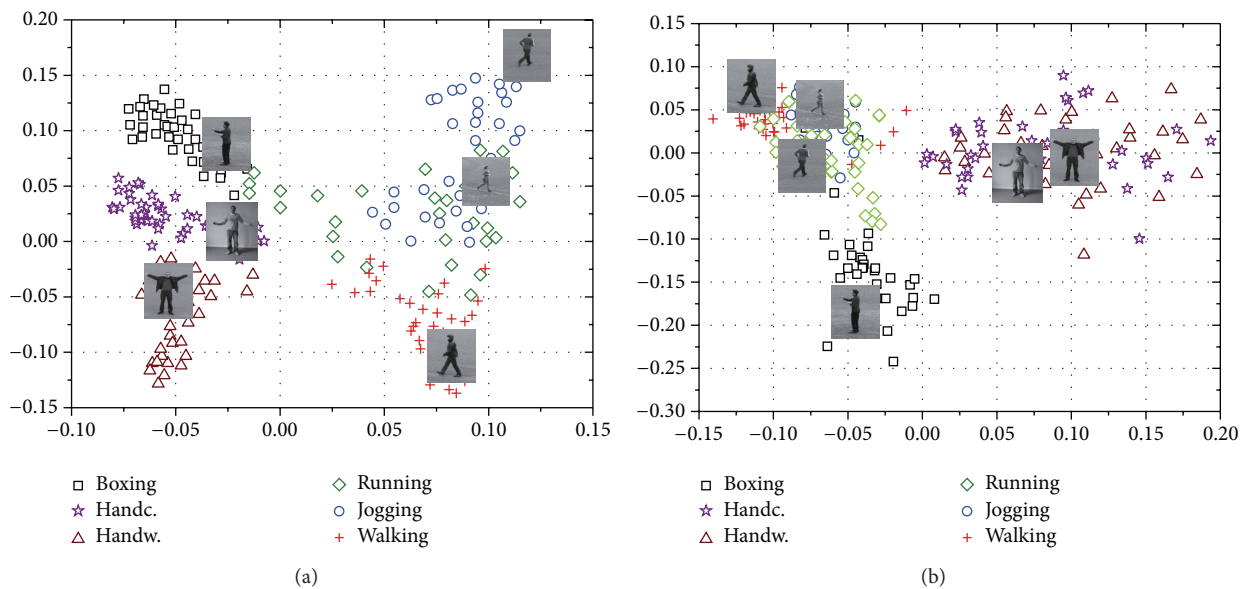


FIGURE 5: Visualization of samples of KTH action recognition dataset in the first two dimensional subspace: (a) represents TKPCA using a tensor kernel; (b) represents KPCA using a Gaussian kernel performed on the vectorization of tensors. Observe that the features obtained by TKPCA are more discriminative than KPCA features.



FIGURE 6: Confusion matrix (in %) for the TKPCA (a) and MPCA (b) methods on the KTH action recognition dataset using LOO protocol.



FIGURE 7: Some example frames from an instructional ballet DVD.

LR hand opening	81.50	2.50	2.50	0.00	3.00	5.00	0.00	5.50
RL hand opening	0.00	100.00	0.00	0.00	0.00	0.00	0.00	0.00
Standing hand opening	0.00	0.00	87.88	4.55	0.00	6.06	0.00	1.52
Leg swinging	3.57	0.00	0.00	85.71	3.57	3.57	0.00	3.57
Jumping	4.55	4.55	9.09	13.14	50.54	0.00	13.60	4.55
Turing	0.00	0.00	5.82	0.00	0.00	94.18	0.00	0.00
Hopping	0.00	2.33	17.23	2.33	2.33	0.00	71.14	4.65
Standing still	6.00	0.00	27.50	11.00	0.00	10.00	0.00	45.50
	LR hand opening	RL hand opening	Standing hand opening	Leg swinging	Jumping	Turing	Hopping	Standing still

FIGURE 8: Confusion matrix (in %) for the TKPCA method on the Ballet dataset.

TABLE 4: Recognition accuracy (in %) along its standard deviation for the Ballet dataset.

Method	Recognition accuracy
KPCA	85.08 ± 1.8
TPM	78.05 ± 2.9
TCCA	77.63 ± 2.9

field of view. All videos were resized to $32 \times 32 \times 32$. In order to have a standard length of 32 frames per video, the middle 32 frames were used.

As this paper focuses on kernelizing Principal Component Analysis for tensor objects, the conventional Kernel Principal Component Analysis using a Gaussian kernel performed on vectorization of tensor $\text{vec}(\mathcal{X})$ should be compared with our new approach TKPCA first. However, for each action video, the dimensionality of vectorized tensor is up to $32768 (32^3)$ which prevents KPCA from computing CPs efficiently. Thus, a reduced-order model [47] is adopted in KPCA. The kernel parameter σ is optimized by methods of cross-validation for both TKPCA and KPCA. The test samples are projected onto the feature subspace to obtain the discriminative features as shown in Figure 5. Observe that TKPCA outperforms KPCA with respect to the discriminative ability, and six classes are well separated even in two dimensional space.

In order to test the TKPCA's ability to capture nonlinear structure of input data, we conduct another experiment to compare TKPCA with the multilinear PCA (MPCA) [19]. Figure 6 illustrates the confusion matrices of TKPCA and MPCA. The confusion matrix is a specific table layout to see if the recognizer is confusing two classes in which rows correspond to the ground truth, and columns correspond to the classification results. It can be seen that TKPCA

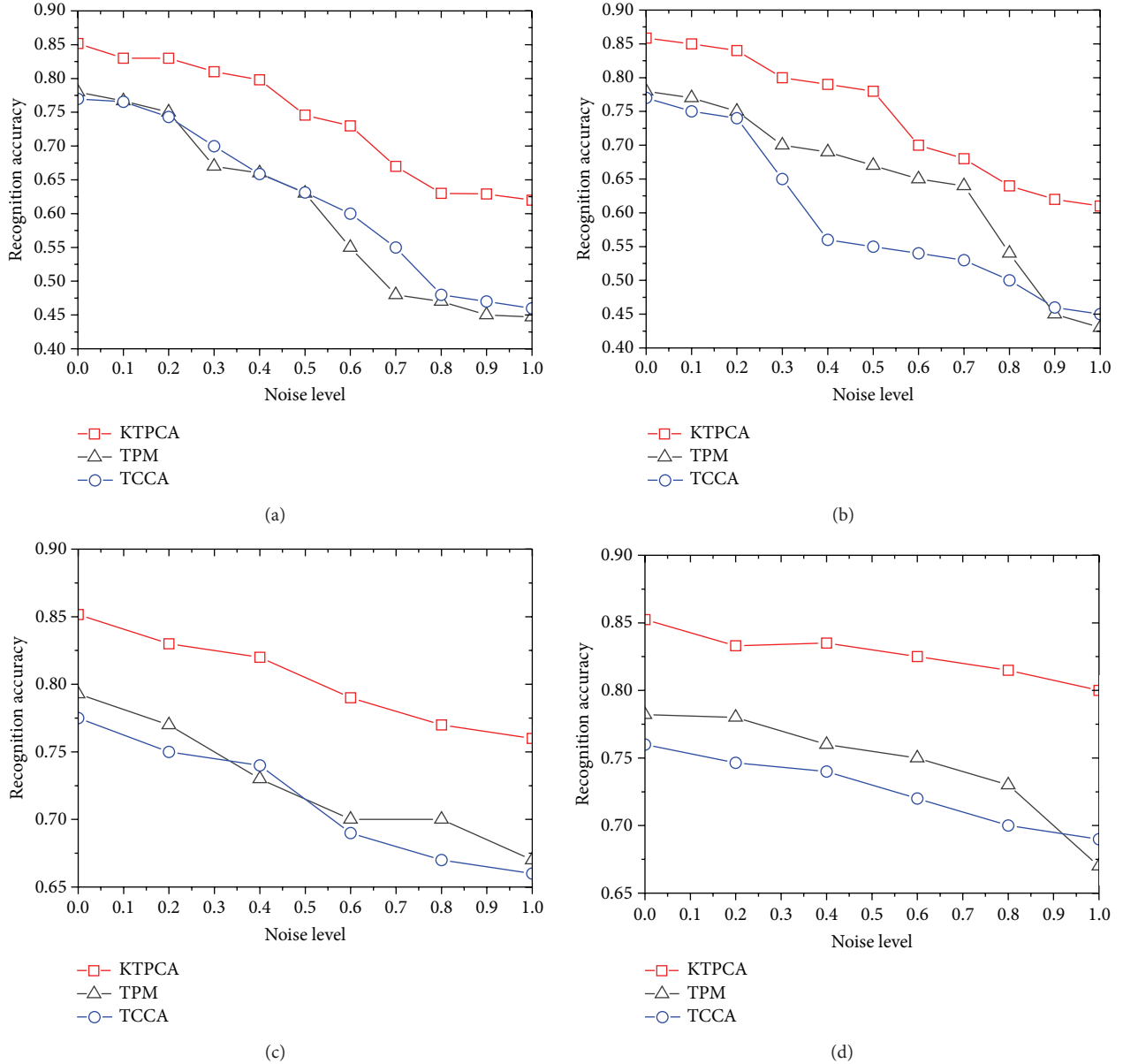


FIGURE 9: Noise resilience analysis: (a) noisy (additive Gaussian) query and clean training set; (b) query and training are both noisy (additive Gaussian); (c) noisy (sparse spikes) query and clean training set; (d) query and training are both noisy (sparse spikes).

achieves average accuracy of 98%, while MPCA achieves 84%, and the confusion of TKPCA only appears among boxing, hand clapping, and hand waving, which is consistent with our intuition that these actions are easily confused. The superiority of TKPCA over MPCA indicates that nonlinear structures of video volumes captured by tensorial kernel significantly improve the discriminative performance.

Next, the proposed TKPCA algorithms are compared against the state-of-the-art action recognition algorithms. We compared TKPCA against spatial-temporal words (STW) [48] and bag of words model in conjunction with multiple kernel learning (BoW-MKL) [49, 50]. In STW, a video sequence is represented by a set of spatial-temporal words, extracted from space-time interest points. The algorithm

then utilises latent topic models such as the probabilistic latent semantic analysis [51] to learn the probability distributions of the spatial-temporal words. BoW-MKL exploits global spatial-temporal distribution of interest points by extracting holistic features from clouds of interest points accumulated over multiple temporal scales. Then, extracted features are fused using MKL. We also compared TKPCA against Tensor Canonical Correlation Analysis (TCCA) [11] and Discriminative Canonical Correlation Analysis (DCCA) [11]. TCCA is an extension of canonical correlation analysis (a principled tool to inspect linear relations between two sets of vectors) to tensor spaces and measures video-to-video tensors in a way similar to our method. DCCA implements a linear discriminant function that maximizes the canonical

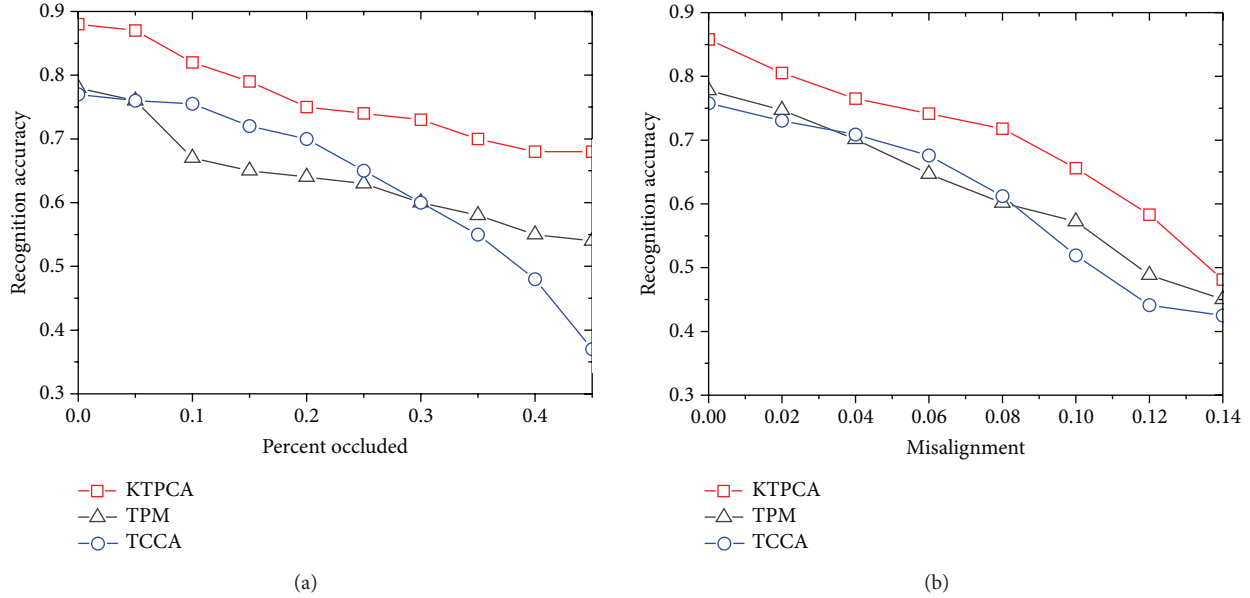


FIGURE 10: Sensitivity analysis to occlusion and misalignment: (a) occlusion; (b) misalignment.

correlations of within-class sets and minimizes the canonical correlations of between-class sets. To facilitate comparison with prior work, we followed the leave-one-out (LOO) cross validation protocol used in STW [48] and TCCA [11].

Looking at the results in Table 3, the first thing to note is that no algorithm is universally the best. In terms of top classification rates, STW, BoW-MKL, and our method are, respectively, best for two of the six actions. However, when our method is better, it is typically by a larger amount, and this is reflected in the higher overall average classification rate of 98% versus 95% for STW and 90% for BoW-MKL.

4.2. Ballet Dataset. The Ballet dataset contains 44 real video sequences of 8 actions collected from an instructional ballet DVD. The dataset consists of 8 complex motion patterns performed by three subjects. The actions include “left-to-right hand opening”, “right-to-left hand opening”, “standing hand opening”, “leg swinging”, “jumping”, “turning”, “hopping”, and “standing still”. Figure 7 shows samples. This dataset has a uniform background and fair illumination and therefore minimises the effect of variations in illumination and background. Yet, at the same time, it is very challenging due to the significant within-class variations in terms of speed, spatial and temporal scale, clothing, and movement. Available samples of each action were randomly split into training and testing sets (the number of actions in both training and testing sets were fairly even). The process of random splitting was repeated ten times, and the average classification accuracy was record. All video sequences were uniformly resized to $50 \times 50 \times 50$. In order to have a standard length of 50 frames per video sequences, the middle 50 frames were used.

For the sake of comparison between tensor based methods, TKPCA algorithm is contrasted with the Tensor as a point on a Product Manifold (TPM) [12] and Tensor

Canonical Correlation Analysis (TCCA) [11]. TPM maps a video tensor to a point on a product manifold and the geodesic distance on a product manifold, is computed for tensor classification. Table 4 shows that the TKPCA algorithm obtains the highest accuracy and outperforms state-of-the-art tensor based methods of TPM and TCCA significantly. The confusion matrix of the proposed TKPCA method is shown in Figure 8. Our performance on this dataset is not as good as the previous ones, which might be because of the complexity of actions in this dataset and significant within-class variations.

4.3. Sensitivity Analysis

4.3.1. Sensitivity to Noise. In addition to the above, to assert robustness to noise we add two types of noise, to the clean Ballet dataset. We compare TKPCA, TPM and TCCA in case of additive Gaussian noise and sparse noise spikes. The noise process in the case of additive Gaussian noise is $N(0, p\sigma_i)$, added to i th frame with σ_i , the standard deviation of the frames and $p \in [0, 1]$. In case of spike noise, we randomly add values drawn from the normal process, $N(0, p\sigma_i)$, to randomly choose time points of each video sequences. The number of noisy time points is no more than 5% of the length of the time-series, spread uniformly over the full time-span. Figure 9 depicts TKPCA, TPM, and TCCA recognition accuracies in presence of different levels of noise. Figure 9 indicates that TKPCA outperforms others, the advantage of which is becoming obvious as the noise level grows. This could be due to our underlying kernel function build on the Grassmann kernel which is more robust to noise since the subspace points on Grassmann Manifold can fill in the missing pictures.

4.3.2. Sensitivity to Occlusion. An important aspect of the proposed approach relates to the sensitivity against occlusion.

We assess the performance at various levels of occlusion in Ballet dataset, from 1.56% up to 45%, by replacing a set of randomly located square blocks of size 4×4 in the query frames with a blank block. The location of occlusion is randomly chosen for each query frame and is unknown to the system. The training frames do not contain occlusions. Figure 10(a) shows the recognition rates of TKPCA, TPM, and TCCA. The proposed TKPCA method significantly outperforms the other two methods in almost all levels of occlusion. Up to 40 percent occlusion, the performance of TKPCA has dropped roughly by 20 percentage points. The proposed TKPCA method has better captured the nonlinear intrinsic geometry and is hence more robust to the missing parts.

4.3.3. Sensitivity to Misalignment. The temporal and spatial misalignment could deteriorate the performance of an action recogniser drastically. In this part, we only consider spatial misalignment and assess and contrast the sensitivity of TKPCA algorithm as compared to TPM and TCCA on Ballet dataset. To this end, we have introduced random displacements to the frames of query videos and measured the accuracy for various amounts of displacements. Figure 10(a) shows the result. The horizontal axis here demonstrates the degree of misalignment. Figure 10(a) reveals that all studied algorithms are sensitive to misalignment. The larger the displacement, the lower would be the recognition accuracy. This is mainly due to the tensorial representation of video highly depending on the relationships that are fragile to misalignment.

5. Conclusion

In this paper, we present a new TKPCA algorithm for dimensionality reduction and feature extraction from tensor objects, such as 2D/3D images and video sequences. TKPCA determines a subspace of lower dimensionality that captures most of the nonlinear variation present in the original tensorial representation. A novel tensorial kernel, which can directly measure the similarity between tensorial inputs, is also proposed based on Grassmann kernel to capture the topological structure underlying tensor dataset. Furthermore, the strict positive definiteness proof of proposed kernel function is given. Experimental results show that the TKPCA remedies the shortcoming of tensorial PCA in modelling the nonlinear manifold of tensor objects and reduces the SSS and Curse of Dimensionality problem. Furthermore, it achieves more compression rate and is robust to both noise and occlusion. To the best of our knowledge, the problem of TKPCA has not been considered in the existing literatures.

Finally, there are still some aspects of TKPCA that deserve further study. For example, TKPCA is essentially *batch* optimization problem, with all training tensor data being available in advance. Such assumption is unsuitable for large-scale data sets and thus unadapted for real-time applications [47]. Therefore, for applications like video surveillance [52] or social networks analysis [53], an online scheme of TKPCA is expected.

Conflict of Interests

The authors declare no conflict of interests.

References

- [1] J. Ye, R. Janardan, and Q. Li, "Gpca: an efficient dimension reduction scheme for image compression and retrieval," in *Proceedings of the 10th ACM SIGKDD International Conference on Knowledge Discovery and Data Mining*, pp. 354–363, August 2004.
- [2] D. Zhang and Z.-H. Zhou, "(2D)2 PCA: Two-directional two-dimensional PCA for efficient face representation and recognition," *Neurocomputing*, vol. 69, no. 1–3, pp. 224–231, 2005.
- [3] J. Yang, D. Zhang, A. F. Frangi, and J.-Y. Yang, "Two-dimensional PCA: a new approach to appearance-based face representation and recognition," *IEEE Transactions on Pattern Analysis and Machine Intelligence*, vol. 26, no. 1, pp. 131–137, 2004.
- [4] C. Ding and J. Ye, "2-dimensional singular value decomposition for 2d maps and images," in *Proceedings of the SIAM International Conference on Data Mining*, pp. 32–43, 2005.
- [5] F. Cong, I. Kalyakin, A.-H. Phan et al., "Benefits of multi-domain feature of mismatch negativity extracted by non-negative tensor factorization from eeg collected by low-density array," *International Journal of Neural Systems*, vol. 22, no. 6, 2012.
- [6] M. Kwon, J. S. Kang, and M. Lee, "Emotion classification in movie clips based on 3d fuzzy gist and eeg signal analysis," in *Proceedings of the International Winter Workshop on Brain-Computer Interface (BCI '13)*, pp. 67–68, 2013.
- [7] J. Ye, T. Li, T. Xiong, and R. Janardan, "Using uncorrelated discriminant analysis for tissue classification with gene expression data," *IEEE/ACM Transactions on Computational Biology and Bioinformatics*, vol. 1, no. 4, pp. 181–190, 2004.
- [8] B. Bosch, E. M. Arenaza-Urquijo, L. Rami et al., "Multiple DTI index analysis in normal aging, amnesic MCI and AD. Relationship with neuropsychological performance," *Neurobiology of Aging*, vol. 33, no. 1, pp. 61–74, 2012.
- [9] N. Renard and S. Bourennane, "Dimensionality reduction based on tensor modeling for classification methods," *IEEE Transactions on Geoscience and Remote Sensing*, vol. 47, no. 4, pp. 1123–1131, 2009.
- [10] M. W. Whittle, *Gait Analysis: An Introduction*, Butterworth-Heinemann, 2006.
- [11] T.-K. Kim and R. Cipolla, "Canonical correlation analysis of video volume tensors for action categorization and detection," *IEEE Transactions on Pattern Analysis and Machine Intelligence*, vol. 31, no. 8, pp. 1415–1428, 2009.
- [12] Y. M. Lui, J. R. Beveridge, and M. Kirby, "Action classification on product manifolds," in *Proceedings of the IEEE Computer Society Conference on Computer Vision and Pattern Recognition (CVPR '10)*, pp. 833–839, June 2010.
- [13] J. Sun, D. Tao, S. Papadimitriou, P. S. Yu, and C. Faloutsos, "Incremental tensor analysis: theory and applications," *ACM Transactions on Knowledge Discovery from Data*, vol. 2, no. 3, article 11, 2008.
- [14] I. Jolliffe, *Principal Component Analysis*, Wiley Online Library, 2005.
- [15] B. Schölkopf, A. Smola, and K.-R. Müller, "Nonlinear component analysis as a kernel eigenvalue problem," *Neural Computation*, vol. 10, no. 5, pp. 1299–1319, 1998.

- [16] C. M. Bishop and N. M. Nasrabadi, *Pattern Recognition and Machine Learning*, vol. 1, Springer, New York, NY, USA, 2006.
- [17] X. He, D. Cai, and P. Niyogi, "Tensor subspace analysis," in *Advances in Neural Information Processing Systems*, pp. 499–506, 2005.
- [18] D. Tao, X. Li, W. Hu, S. Maybank, and X. Wu, "Supervised tensor learning," in *Proceedings of the 5th IEEE International Conference on Data Mining (ICDM '05)*, pp. 450–457, November 2005.
- [19] H. Lu, K. N. Plataniotis, and A. N. Venetsanopoulos, "MPCA: Multilinear principal component analysis of tensor objects," *IEEE Transactions on Neural Networks*, vol. 19, no. 1, pp. 18–39, 2008.
- [20] K. Inoue, K. Hara, and K. Urahama, "Robust multilinear principal component analysis," in *Proceedings of the 12th International Conference on Computer Vision (ICCV '09)*, pp. 591–597, October 2009.
- [21] Y. Panagakis, C. Kotropoulos, and G. R. Arce, "Non-negative multilinear principal component analysis of auditory temporal modulations for music genre classification," *IEEE Transactions on Audio, Speech and Language Processing*, vol. 18, no. 3, pp. 576–588, 2010.
- [22] A. Shashua and A. Levin, "Linear image coding for regression and classification using the tensor-rank principle," in *Proceedings of the IEEE Computer Society Conference on Computer Vision and Pattern Recognition (CVPR '01)*, vol. 1, pp. 142–149, December 2001.
- [23] D. Li, K. Huang, H. Zhang, and L. Zhang, "Umpca based feature extraction for ecg," in *Advances in Neural Networks*, pp. 383–390, Springer, 2013.
- [24] H. Lu, K. N. K. Plataniotis, and A. N. Venetsanopoulos, "Uncorrelated multilinear principal component analysis for unsupervised multilinear subspace learning," *IEEE transactions on Neural Networks*, vol. 20, no. 11, pp. 1820–1836, 2009.
- [25] J. Shawe-Taylor and N. Cristianini, *Kernel Methods for Pattern Analysis*, Cambridge university press, 2004.
- [26] E. Kofidis and P. A. Regalia, "On the best rank-1 approximation of higher-order supersymmetric tensors," *SIAM Journal on Matrix Analysis and Applications*, vol. 23, no. 3, pp. 863–884, 2002.
- [27] L. de Lathauwer, B. de Moor, and J. Vandewalle, "A multilinear singular value decomposition," *SIAM Journal on Matrix Analysis and Applications*, vol. 21, no. 4, pp. 1253–1278, 2000.
- [28] B. W. Bader and T. G. Kolda, "Algorithm 862: Matlab tensor classes for fast algorithm prototyping," *ACM Transactions on Mathematical Software*, vol. 32, no. 4, pp. 635–653, 2006.
- [29] M. Ding, Z. Tian, and H. Xu, "Adaptive kernel principal component analysis," *Signal Processing*, vol. 90, no. 5, pp. 1542–1553, 2010.
- [30] Q. Zhao, C. F. Caiafa, D. P. Mandic et al., "Multilinear subspace regression: an orthogonal tensor decomposition approach," in *Advances in Neural Information Processing Systems*, pp. 1269–1277, 2011.
- [31] S. Yan, D. Xu, Q. Yang, L. Zhang, X. Tang, and H.-J. Zhang, "Multilinear discriminant analysis for face recognition," *IEEE Transactions on Image Processing*, vol. 16, no. 1, pp. 212–220, 2007.
- [32] S. Shan, B. Cao, Y. Su, L. Qing, X. Chen, and W. Gao, "Unified principal component analysis with generalized covariance matrix for face recognition," in *Proceedings of the 26th IEEE Conference on Computer Vision and Pattern Recognition (CVPR '08)*, pp. 1–7, June 2008.
- [33] J. A. K. Suykens, T. van Gestel, J. Vandewalle, and B. de Moor, "A support vector machine formulation to PCA analysis and its kernel version," *IEEE Transactions on Neural Networks*, vol. 14, no. 2, pp. 447–450, 2003.
- [34] M. Signoretto, L. de Lathauwer, and J. A. K. Suykens, "A kernel-based framework to tensorial data analysis," *Neural Networks*, vol. 24, no. 8, pp. 861–874, 2011.
- [35] Y. Chikuse, *Statistics on Special Manifolds*, vol. 174, Springer, 2003.
- [36] S. Theodoridis, K. Nos, and K. M. Bas, *Pattern Recognition*, Elsevier, 4th edition, 2009.
- [37] G. C. Cawley and N. L. C. Talbot, "Preventing over-fitting during model selection via bayesian regularisation of the hyperparameters," *The Journal of Machine Learning Research*, vol. 8, pp. 841–861, 2007.
- [38] G. C. Cawley and N. L. C. Talbot, "On over-fitting in model selection and subsequent selection bias in performance evaluation," *The Journal of Machine Learning Research*, vol. 99, pp. 2079–2107, 2010.
- [39] C. Lampert, *Kernel Methods in Computer Vision*, vol. 4, Now Publishers, 2009.
- [40] J. Lu, K. N. Plataniotis, and A. N. Venetsanopoulos, "Face recognition using LDA-based algorithms," *IEEE Transactions on Neural Networks*, vol. 14, no. 1, pp. 195–200, 2003.
- [41] A. M. Martinez and A. C. Kak, "PCA versus LDA," *IEEE Transactions on Pattern Analysis and Machine Intelligence*, vol. 23, no. 2, pp. 228–233, 2001.
- [42] G. Shakhnarovich and B. Moghaddam, "Face recognition in subspaces," in *Handbook of Face Recognition*, pp. 19–49, Springer, 2011.
- [43] J. Wang, K. N. Plataniotis, and A. N. Venetsanopoulos, "Selecting discriminant eigenfaces for face recognition," *Pattern Recognition Letters*, vol. 26, no. 10, pp. 1470–1482, 2005.
- [44] R. Poppe, "A survey on vision-based human action recognition," *Image and Vision Computing*, vol. 28, no. 6, pp. 976–990, 2010.
- [45] C. Schüldt, I. Laptev, and B. Caputo, "Recognizing human actions: a local SVM approach," in *Proceedings of the 17th International Conference on Pattern Recognition (ICPR '04)*, pp. 32–36, August 2004.
- [46] Y. Wang and G. Mori, "Human action recognition by semilattent topic models," *IEEE Transactions on Pattern Analysis and Machine Intelligence*, vol. 31, no. 10, pp. 1762–1774, 2009.
- [47] P. Honeine, "Online kernel principal component analysis: a reduced-order model," *IEEE Transactions on Pattern Analysis and Machine Intelligence*, vol. 34, no. 9, pp. 1814–1826, 2012.
- [48] J. C. Niebles, H. Wang, and L. Fei-Fei, "Unsupervised learning of human action categories using spatial-temporal words," *International Journal of Computer Vision*, vol. 79, no. 3, pp. 299–318, 2008.
- [49] F. R. Bach, G. R. G. Lanckriet, and M. I. Jordan, "Multiple kernel learning, conic duality, and the SMO algorithm," in *Proceedings of the 21st International Conference on Machine Learning*, p. 6, July 2004.
- [50] M. Bregonzio, T. Xiang, and S. Gong, "Fusing appearance and distribution information of interest points for action recognition," *Pattern Recognition*, vol. 45, no. 3, pp. 1220–1234, 2012.
- [51] T. Hofmann, "Probabilistic latent semantic indexing," in *Proceedings of the 22nd Annual International ACM SIGIR Conference on Research and Development in Information Retrieval*, pp. 50–57, 1999.

- [52] D. A. Ross, J. Lim, R.-S. Lin, and M.-H. Yang, "Incremental learning for robust visual tracking," *International Journal of Computer Vision*, vol. 77, no. 1-3, pp. 125-141, 2008.
- [53] J. Wen, X. Gao, Y. Yuan, D. Tao, and J. Li, "Incremental tensor biased discriminant analysis: a new color-based visual tracking method," *Neurocomputing*, vol. 73, no. 4-6, pp. 827-839, 2010.

Research Article

An Initial Value Calibration Method for the Wheel Force Transducer Based on Memetic Optimization Framework

Guoyu Lin,¹ Weigong Zhang,¹ Fan Yang,¹ Han Pang,² and Dong Wang¹

¹ School of Instrument Science and Engineering, Southeast University, China

² School of Mechanical and Electrical Engineering, China University of Petroleum, China

Correspondence should be addressed to Guoyu Lin; andrew.lin@seu.edu.cn

Received 21 August 2013; Revised 2 October 2013; Accepted 10 October 2013

Academic Editor: Gelan Yang

Copyright © 2013 Guoyu Lin et al. This is an open access article distributed under the Creative Commons Attribution License, which permits unrestricted use, distribution, and reproduction in any medium, provided the original work is properly cited.

Some initial values of the wheel force transducer (WFT) change after being mounted in the vehicle. The traditional static calibration is inadequate to fully obtain these initial values. Aiming to this problem, an online initial value calibration method is proposed. The method does not require any additional calibration equipment or manual operation and just requires the vehicle mounted with the WFT to be driven on a flat road with constant speed. In this way, an initial value mode is constructed and then converted to an optimization problem. To solve this problem and acquire the right initial value, an improved Memetic framework based on particle swarm optimization (PSO) and Levenberg-Marquardt (LM) is adopted. To verify the effect of the proposed method, the real WFT data is used and the comparative test is carried out. The experiment result shows that the proposed method is superior to the traditional one and can improve the measurement accuracy effectively.

1. Introduction

When the vehicle is moving on the road, three-dimensional forces and three-dimensional torques are applied to the wheel, which is longitudinal force F_x , lateral force F_y , vertical force F_z , heeling moment M_x , twist torque M_y , and aligning torque M_z , respectively. The schematic diagram of wheel force is shown in Figure 1, where $O_w X_w Y_w Z_w$ is the wheel coordinate and its origin is the wheel center. The interaction between the vehicle and ground can be represented by the wheel force; therefore, sensing the forces/torque of wheel dynamically has been an important component of vehicle for the research of body vibration, suspension, and wheel dynamics as well as the performance matching of vehicle transmission and braking system [1–3].

Wheel force transducer (WFT) is a tool which can measure the wheel force effectively. For the increasing importance of wheel force, some world famous manufacturers in the automobile test field, including MTS Corporation, Michigan, Scientific Corporation, and Kistler Corporation, and so forth, have been devoted to the research of the WFT and have developed some WFT products. These WFT products have been used in many vehicle test fields and acquired acceptable

performance. However, these WFT products are expensive and their detail technology information are not publicly available due to commercial reasons. These factors not only impede the popularization and application of the WFT, but also slow down the further development of the WFT. Southeast University has been devoted to research of the WFT for over ten years and developed some prototype, as shown in Figure 2, and published some papers in the field of static calibration, decoupling across dimension, and structure analysis [4–6]. However, there are still some inadequacies that need to be improved.

Essentially, the WFT is a multiple dimensional force sensor. The calibration is very important for the WFT because it is used to acquire the mathematical model between input and output of the sensor and affects the measurement accuracy directly. Thus, many scholars have focused on the research of calibration of multiple dimensional force sensor and proposed that a calibration platform is a good device for sensor calibration [7–10]. However, for the WFT, there are three initial values to be solved which are α_0 , F_{CG0} , F_{AE0} , where α_0 is the initial installation angle of the WFT and F_{CG0} and F_{AE0} are the output of B_{CG} bridge and B_{AE} bridge of the WFT. Because of bolt force and wheel weight, these initial

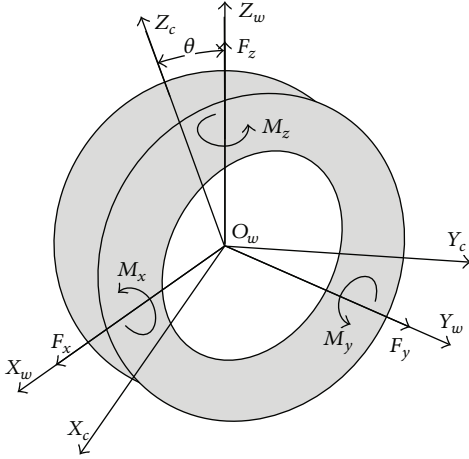


FIGURE 1: The diagram of six-dimensional forces of wheel.

values change after the sensor being bolted in the wheel and then installed in the vehicle. This is quite different from other multiple dimensional force sensors, like wrist force sensor and so on. Therefore, the classical static calibration method is inadequate to acquire the initial value of the WFT.

To handle the problem, the researchers proposed some methods. A traditional way to estimate the initial installation angle α_0 of the WFT is shown in Figure 3, which is presented by Zhang [11]. If no longitudinal force F_x is applied to the sensor, when the output of B_{AE} bridge reaches its maximum in a signal period, the rotating angle of the WFT can be considered as the initial angle α_0 . Based on it, Zhang proposes the scene can be simulated by pushing the vehicle to move slowly and manually. However, this method has two disadvantages: (1) pushing the vehicle to move manually is not suitable for large and heavy vehicles, (2) in the circumstance, the condition of non- F_x is not established in real application. Therefore, by adopting the method, the error exists inevitable. Liu et al. proposed a weighing on-vehicle calibration method for the WFT as shown in Figure 4 [12]. The vehicle is lifted with a jack. Then the specific two beams of the WFT's elastic body are rotated to a horizontal position, successively, and the output of B_{CG} bridge and B_{AE} bridge are considered as F_{CG0} and F_{AE0} . This method achieves good effect in real application; however judging the horizontal position manually will cause error and the whole process is tedious.

The two methods shown above actually belong to an online calibration method. Now, in multiple dimensional force sensor fields, some researchers have focused on the online calibration and proposed some practical methods. Wang proposed an autostatic calibration method where the force sensor that is exerted with a known mass weight is rotating, and then the force exerted on the force sensor by the weight is computed to acquire the calibration matrix [13]. Kourosh presents a novel approach for the calibration of the force/torque sensors of space robots based on the dynamic effects of the wrench (force and torque) applied on a payload with known mass properties [14]. Kim and Sun introduce an effective shape-from-motion method to

calculate the calibration matrix which refers to the fact that the shape of the force sensor can be recovered by knowing the theoretical rank of the shape and applying arbitrary motion to the force [15, 16]. Nevertheless, these online calibration methods are not applicable to the WFT, for example, a known mass weight cannot be exerted on a rolling wheel for safety reasons.

From the related work review, it is clear that the existing methods are time-consuming, and the solved initial value is not correct enough, which results in the inaccuracy of measurement. Therefore, in the paper, an online initial value calibration method is put forward. The rest of the paper is organized as follows. In Section 2, we introduce the WFT's structure used in the paper. In Section 3, the details of the proposed method are elaborated by introducing the initial value mode and showing how to exploit the Memetic algorithm to get the initial value of the WFT. To illustrate the efficiency of the proposed method, in Section 4 we analyze the experimental results on real sampled datasets. Finally, we draw conclusions in the last section of the paper and discuss future work on this topic.

2. The Overall Structure of the Adopted WFT

The WFT depicted in the paper is developed by Southeast University and can measure two forces and one torque which is longitudinal force F_x , lateral force F_y , and twist torque M_y . The overall structure of the exploited 3-axis WFT is shown in Figure 5(a). It is composed of the elastic body, reforming rims, intermediate flange, sample module, and transfer module. The wheel rims are reformed to connect with the elastic body by bolt, and the intermediate flange is used to protect bridge circuit in the elastic body from water and dirt. The sample module is used to sample the wheel force and rotation angle. Then it sends them to the transfer module by wireless module. It connects to the elastic body by intermediate flange and rotates with the rolling wheel. The transfer module connects to the sample module by the bearing and does not rotate with the rolling wheel. It can receive the data from the sample module by wireless module too, and it can forward the data to the data acquisition devices by CAN bus. The electrical flowchart is show in Figure 5(b).

Figure 6 depicts the mechanical structure of the 3-axis WFT's elastomer. According to the requirement of axial structure size of the wheel, the eight spoke structure is exploited. The elastic body consists of an inner ring, an outer ring, and eight elastic beams. The eight elastic beams are labeled as A-H and distributed uniformly between the inner ring and the outer ring. $O_c X_c Y_c Z_c$ is the elastomer coordinate where the CG-beam coincides with X_c axis and the AE-beams coincides with Z_c axis. Resistance strain gauges R1-R16 are placed in the elastic beam to sense its deformation caused by the wheel force. R5 and R6 in C-Beam and R13 and R14 in G-Beam are connected to form the B_{CG} bridge to measure the force applied along Y_c axis. R1 and R2 in A-Beam and R9 and R10 in E-Beam are connected to form the B_{AE} bridge to measure the force applied along Z_c axis. Other strain gauges in B-Beam, D-Beam, F-Beam, and H-Beam are

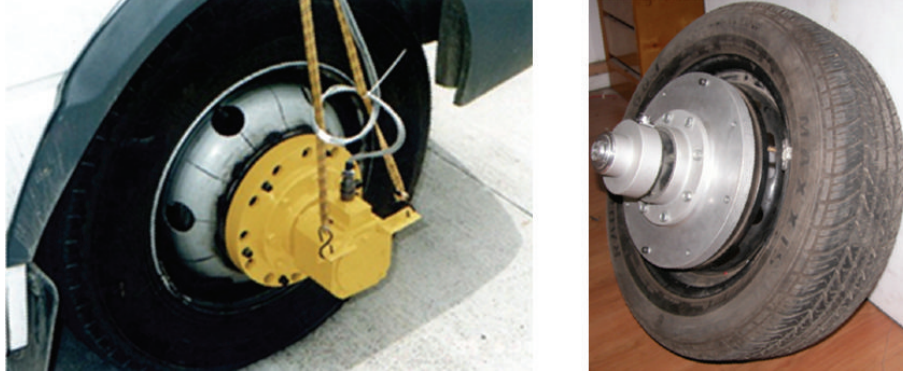


FIGURE 2: The WFT prototypes developed by Southeast University.

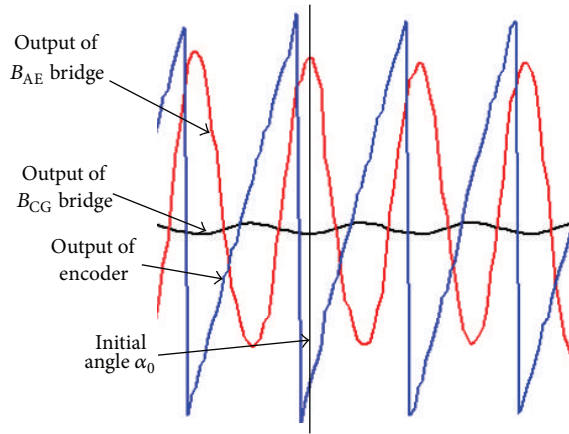


FIGURE 3: The outputs of the WFT.

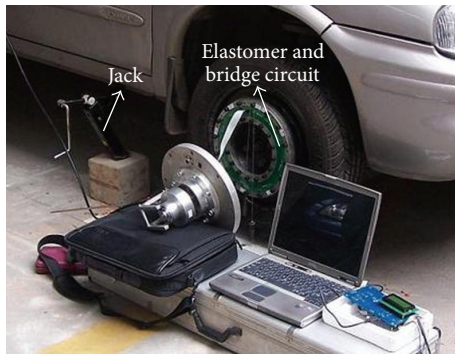


FIGURE 4: The weighing on-vehicle calibration method.

connected to form the B_{BDFH} bridge to measure the torque applied around Y_c axis.

3. Initial Value Calibration Method

3.1. Initial Value Mode. As shown in Figure 6, $O_cX_cY_cZ_c$ is the elastomer coordinate and it rotates with the wheel. The C-G beam is coincident with X_c axis and the A-E beams is coincident with Z_c axis. So the outputs of the three

bridges are all represented in $O_cX_cY_cZ_c$. However, the wheel force is represented in $O_wX_wY_wZ_w$. The relationship between $O_cX_cY_cZ_c$ and $O_wX_wY_wZ_w$ is shown in Figure 1. When the wheel is rolling, $O_cX_cY_cZ_c$ rotates around the Y_w axis, and the rotation angle between $O_cX_cY_cZ_c$ and $O_wX_wY_wZ_w$ is denoted as θ . Furthermore, the outputs of three bridges are sampled by AD converter, and the wheel force/torque is represented in unit KN or KN·m. Therefore, according to the principle of the WFT, a transformation should be carried out to acquire the wheel force from the outputs of three bridges, which is shown below. Consider

$$\begin{bmatrix} F_x \\ F_z \\ M_y \end{bmatrix} = \begin{bmatrix} \cos \theta & \sin \theta & 0 \\ -\sin \theta & \cos \theta & 0 \\ 0 & 0 & 1 \end{bmatrix} \begin{bmatrix} f^1(vF_{CG}) - F_{CG0} \\ f^2(vF_{AE}) - F_{AE0} \\ f^3(vF_{BDFH}) - F_{BDFH0} \end{bmatrix}, \quad (1)$$

where $f^1()$, $f^2()$, and $f^3()$ are the transformation functions which convert the output of bridge (AD value) to force/torque (unit: KN/KN·m). These functions can be obtained by static calibration. vF_{CG} , vF_{AE} , and vF_{BDFH} are the output of B_{CG} bridge, B_{AE} bridge, and B_{BDFH} bridge, respectively, and F_{CG0} , F_{AE0} , and F_{BDFH0} are the initial value of B_{CG} bridge, B_{AE} bridge, and B_{BDFH} bridge in KN, respectively.

It is noticed that θ reflects the relative angle between $O_cX_cY_cZ_c$ and $O_wX_wY_wZ_w$, so it cannot be measured directly. In order to solve the problem, an absolute encoder is adopted to measure the rotation angle of $O_cX_cY_cZ_c$ and its output is denoted as α . When $O_cX_cY_cZ_c$ coincides with $O_wX_wY_wZ_w$, the encoder's output is α_0 . Then (1) can be converted to (2) as shown below:

$$\begin{bmatrix} F_x \\ F_z \\ M_y \end{bmatrix} = \begin{bmatrix} \cos(\alpha - \alpha_0) & \sin(\alpha - \alpha_0) & 0 \\ -\sin(\alpha - \alpha_0) & \cos(\alpha - \alpha_0) & 0 \\ 0 & 0 & 1 \end{bmatrix} \times \begin{bmatrix} f^1(vF_{CG}) - F_{CG0} \\ f^2(vF_{AE}) - F_{AE0} \\ f^3(vF_{BDFH}) - F_{BDFH0} \end{bmatrix}. \quad (2)$$

In (2), there are four initial values to be solved which are α_0 , F_{CG0} , F_{AE0} , and F_{BDFH0} . As shown in Section 1, these initial values change after installation. Therefore, they cannot be

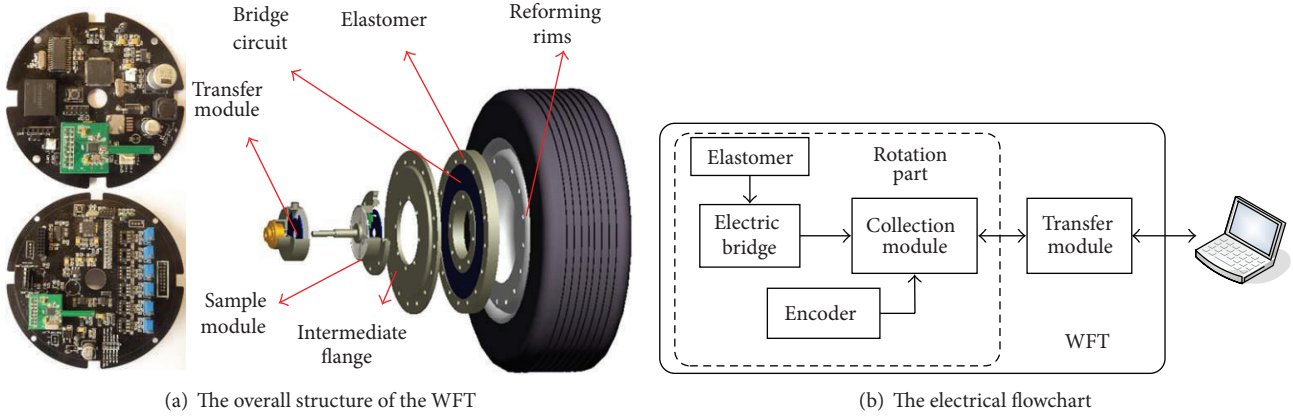


FIGURE 5: Diagram of the adopted 3-axis WFT's structure.

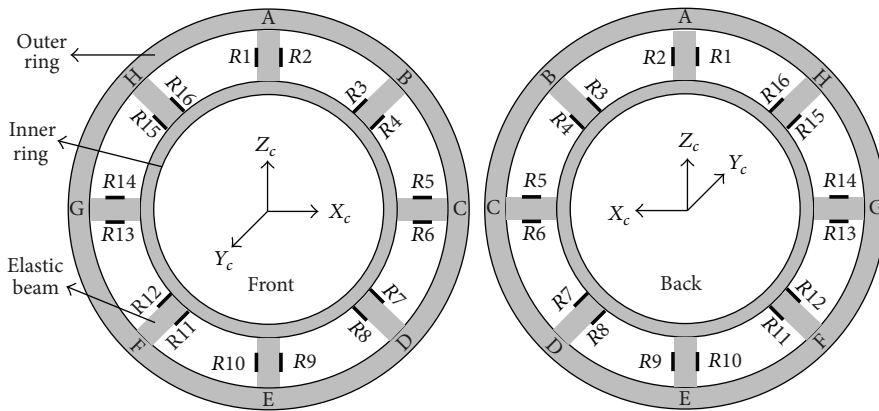


FIGURE 6: The diagram of the WFT elastic body.

obtained by traditional static calibration method. Consider the following.

- (1) For $O_w X_w Y_w Z_w$ is a coordinate in concept, it is hard to judge whether $O_c X_c Y_c Z_c$ coincides with $O_w X_w Y_w Z_w$. Aiming manually is an intuitive approach; however, the elastic body is covered by the intermediate flange as shown in the Figure 5, so aiming manually will cause inevitable error.
- (2) When the WFT is installed in the wheel, the output of B_{BDFH} bridge can be considered as initial value F_{BDFH0} if the vehicle is static.
- (3) The method shown in (2) is not suitable for F_{CG0} and F_{AE0} . When vehicle is static, the component force of vehicle weight is applied to the B_{CG} bridge and B_{AE} bridge, then their output depends on vehicle weight and angle θ . Therefore, measuring initial value F_{CG0} and F_{AE0} correctly is difficult too.

From the description above, it is clear that initial values α_0 , F_{CG0} , and F_{AE0} cannot be measured directly. Unfaithful initial values will result in the inaccurate longitudinal force F_x and vertical force F_z ; therefore how to solve the initial value calibration problem to acquire α_0 , F_{CG0} , and F_{AE0} with high accuracy is an important work.

According to (2), (3) is obtained as

$$\begin{aligned}
 F_x &= \cos(\alpha - \alpha_0) (f^1(vF_{CG}) - F_{CG0}) \\
 &\quad + \sin(\alpha - \alpha_0) (f^2(vF_{AE}) - F_{AE0}), \\
 F_z &= -\sin(\alpha - \alpha_0) (f^2(vF_{CG}) - F_{CG0}) \\
 &\quad + \cos(\alpha - \alpha_0) (f^1(vF_{AE}) - F_{AE0}).
 \end{aligned} \tag{3}$$

In (3), α , F_{CG} , F_{AE} , $f^1(\cdot)$, and $f^2(\cdot)$ can be acquired from the WFT's output and static calibration, and $w = (\alpha_0, F_{CG0}, F_{AE0})$ are the variables to be solved. Because the value of F_x and F_z is unknown, it is difficult to solve the transcendental equations. Intuitively, if the unknowns F_x and F_z can be removed from (3) by some ways, it is possible to solve the transcendental equations and acquire the initial values. This idea is the basis of the proposed method.

Assuming there is a scene where the longitudinal force applied to the wheel remains unchanged and α_{ki} , F_{CGki} , and

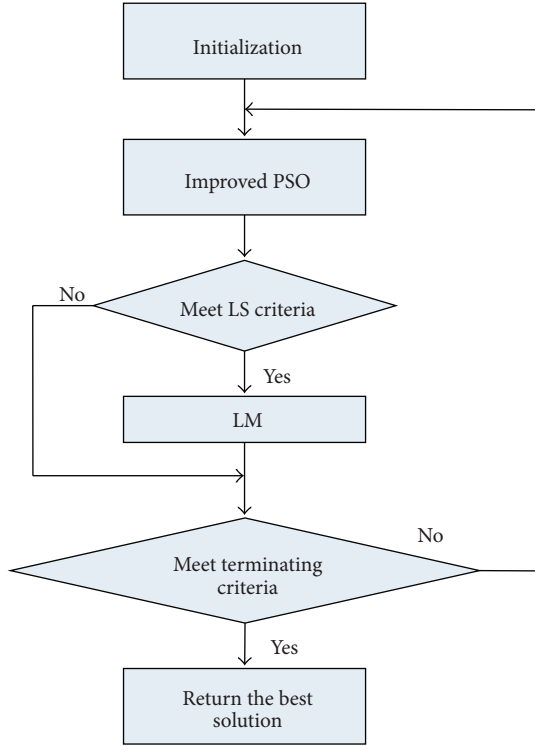


FIGURE 7: The flowchart of the proposed IMAPL.

F_{AEki} are the output of the WFT. Then the following equation can be obtained:

$$\begin{aligned}
 F_{xi} - F_{xj} = & -\sin(\alpha_i - \alpha_0) (f^1(vF_{CGi}) - F_{CG0}) \\
 & + \cos(\alpha_i - \alpha_0) (f^2(vF_{AEi}) - F_{AE0}) \\
 & + \sin(\alpha_j - \alpha_0) (f^1(vF_{CGj}) - F_{CG0}) \\
 & - \cos(\alpha_j - \alpha_0) (f^2(vF_{AEj}) - F_{AE0}) = 0.
 \end{aligned} \quad (4)$$

In (4), i is not equal to j . For the longitudinal force is constant in the whole process; therefore we can get the following equations:

$$\begin{aligned}
 F_{x2} - F_{x1} &= 0 \\
 &\vdots \\
 F_{xi} - F_{x1} &= 0 \\
 F_{xi} - F_{x2} &= 0 \\
 &\vdots \\
 F_{xi} - F_{xi-1} &= 0 \\
 &\vdots \\
 F_{xN} - F_{xN-1} &= 0,
 \end{aligned} \quad (5)$$

where N is the total number of sampled data. Equation (5) is a nonlinear transcendental equation which can be solved by Newton iteration method.

Thus, if we can find a scene where the longitudinal force applied to the wheel is a constant, the unknown variables w can be acquired by solving (5). However, the scene does not exist in reality. Here some similar scenes in real are considered where the longitudinal force applied approximately to the wheel is relatively stable and remains unchanged, for example, the car moves with a constant speed on a flat road. In these real scenes, because of the measurement noise and nonperfect flat road, $\{F_{xi} - F_{xj}\}$ is not exactly equal to 0, then the unknown initial variables w cannot be solved correctly by (5). It is clear that with the correct initial variables, the difference between F_{xi} and F_{xj} is small enough. Therefore, to recover the unknown variables w from the sampled data, we convert the problem of solving (5) to the following optimization minimization problem:

$$w^* = \arg \min_w \left(\frac{\left(\sum_{i,j=1}^N |F_{xi}(w) - F_{xj}(w)| \right)}{N} \right). \quad (6)$$

As long as the optimization problem is solved, the optimal w^* can be acquired and then the initial value α_0 , F_{CG0} and F_{AE0} are obtained.

3.2. Optimization by the Memetic Algorithm. Generally, the sampled dataset is large and the noise is inevitably involved. Thus, an efficient and robust optimization method is required to solve the optimization problem, as shown in (6).

In recent years, the Memetic Algorithm (MA) gradually becomes a research hotspot in evolutionary computing and achieves good effect in many applications [17–20]. In the standard flowchart of MA, a local search (LS) strategy is executed after crossover and mutation operations. By using LS strategy to exploit the local fitness landscape, the slow convergence of EA to locate high quality solutions improves. However, the LS strategy takes effect on individuals selected by EA every generation, which means the MA places too much emphasis on exploitation. This operation will change the balance of exploration and exploitation and weaker the fast convergence capability of EA. To solve the problem, an improved MA based on PSO and LM (IMAPL) is presented, which aims to balance exploration and exploitation. The characteristics of IMAPL are

- (1) LM algorithm is adopted as the LS strategy;
- (2) as one promising EA, an improved PSO algorithm based on immune clone strategy is adopted [21]. The clone and immune operators are integrated into PSO to further improve the exploration capability and diversity;
- (3) unlike the classical MA, in IMAPL, LS strategy is isolated from the EA, and LM is adopted to exploit the local fitness landscape only if PSO is considered to have found a promising solution based on LS criteria.

The algorithm flowchart is shown in Figure 7. In the algorithmic framework, there are two criteria. The first one

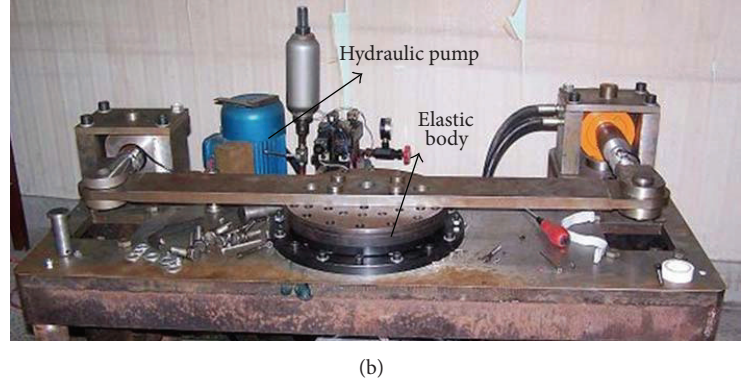
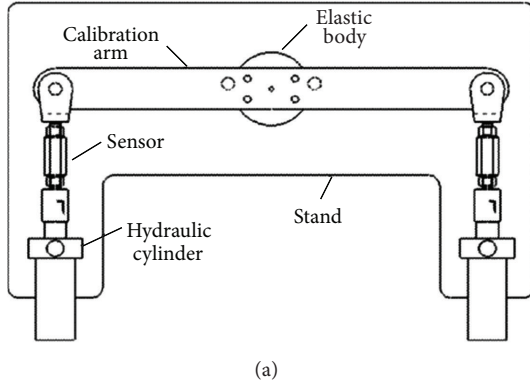


FIGURE 8: The static calibration platform.

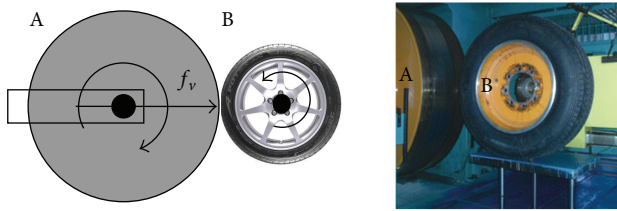


FIGURE 9: The schematic diagram of VDTs.

is the LS criterion which is used to decide whether or not to exploit LM. The other one is the terminating criterion which is used to decide whether or not to terminate the algorithm. LS criteria is a key part of IMAPL. Let $P_g(t)$ and $P_g(t-1)$ denote the global best position of all particles in t th and $(t-1)$ th iterations in the improved PSO algorithm. In LS criteria, if the ratio of the absolute distance between $P_g(t-1)$ and $P_g(t)$ to $P_g(t-1)$ is less than a predetermined threshold T_g , then it is not wise to apply LM to improve $P_g(t)$ since it may lead to the same local optimum. Terminating criteria is simple, it is that when the iteration number reaches a predetermined number T_c or the fitness function is less than a predetermined threshold T_e .

4. Experiments

In the experiments, one type of WFT developed by Southeast University is adopted. It is designed for Chevrolet Sail vehicle, and its measuring range is from 0 kN to 14 kN. Before the experiment, a static calibration is carried out to acquire the transformation function $f^1(\cdot)$, $f^2(\cdot)$, and $f^3(\cdot)$, which is shown in (1). As shown in Figure 8, a static calibration platform based on hydraulics is adopted.

Because it is difficult to verify the effect of the proposed initial value calibration method in real vehicle test, a road wheel test-bed with force feedback is adopted. In this paper, the adopted road wheel test-bed is produced by MTS in 1986 and it is called Vehicle Dynamics Test System (abbreviated as VDTs). For security reasons, the physical map of VDTs cannot be public. Figure 9 shows the schematic diagram and the similar equipment. As shown in Figure 9, the main part

TABLE 1: Three groups of force and speed in initial value calculation.

	Test 1	Test 2	Test 3
Applied force (kN)	13	8	4
Rotating speed (rpm)	20	30	40

of VDTs is composed of driving wheel A and driven wheel B. The wheel A can drive the wheel B to rotate and apply a force f_v to the wheel B along a horizontal direction simultaneously. The WFT is bolted on the wheel B. For the WFT, the force f_v applied to the wheel A can be considered as the longitudinal force F_x . It is good for us that the force f_v can be feedback and measured by VDTs; therefore it can be used to compare with F_x solved by the WFT. It should be noted that the solved F_x is not exactly equal to the force f_v . It is because the WFT and the feedback sensor are mounted in different wheels, and f_v is not exactly along the X -axis of $O_w X_w Y_w Z_w$. Nevertheless, by the error between f_v and F_x solved by the WFT, the performance of the presented method can be evaluated.

4.1. Initial Value Calibration by Means of VDTs. By means of VDTs, it is easy to set up the scenes where the longitudinal force F_x applied to the wheel can be regarded as a constant. Firstly, a constant force f_v is applied to the wheel B by the wheel A. Secondly the wheel A rotates with constant speed for several seconds, and the data is sampled. The two steps repeat for several times with different force and different speed. It is noticed that because the significant vibration is generated when VDTs runs with high speed, the feedback force will also vibrate obviously. Therefore, the low speed is selected here. In the experiments, three different force and speed are adopted, as shown in Table 1.

From the three groups of sampled data, some good and stable data are selected to construct three datasets separately. The three datasets are substituted in (7) which is derived from (6) to calculate the initial value. Consider

$$w^* = \arg \min_w \left(\frac{\left(\sum_{k=1}^3 \sum_{i,j=1}^{N_k} |F_{xi}(w) - F_{xj}(w)| \right)}{\sum_{k=1}^3 N_k} \right), \quad (7)$$

where N_k ($k = 1, 2, 3$) is the number of each dataset.

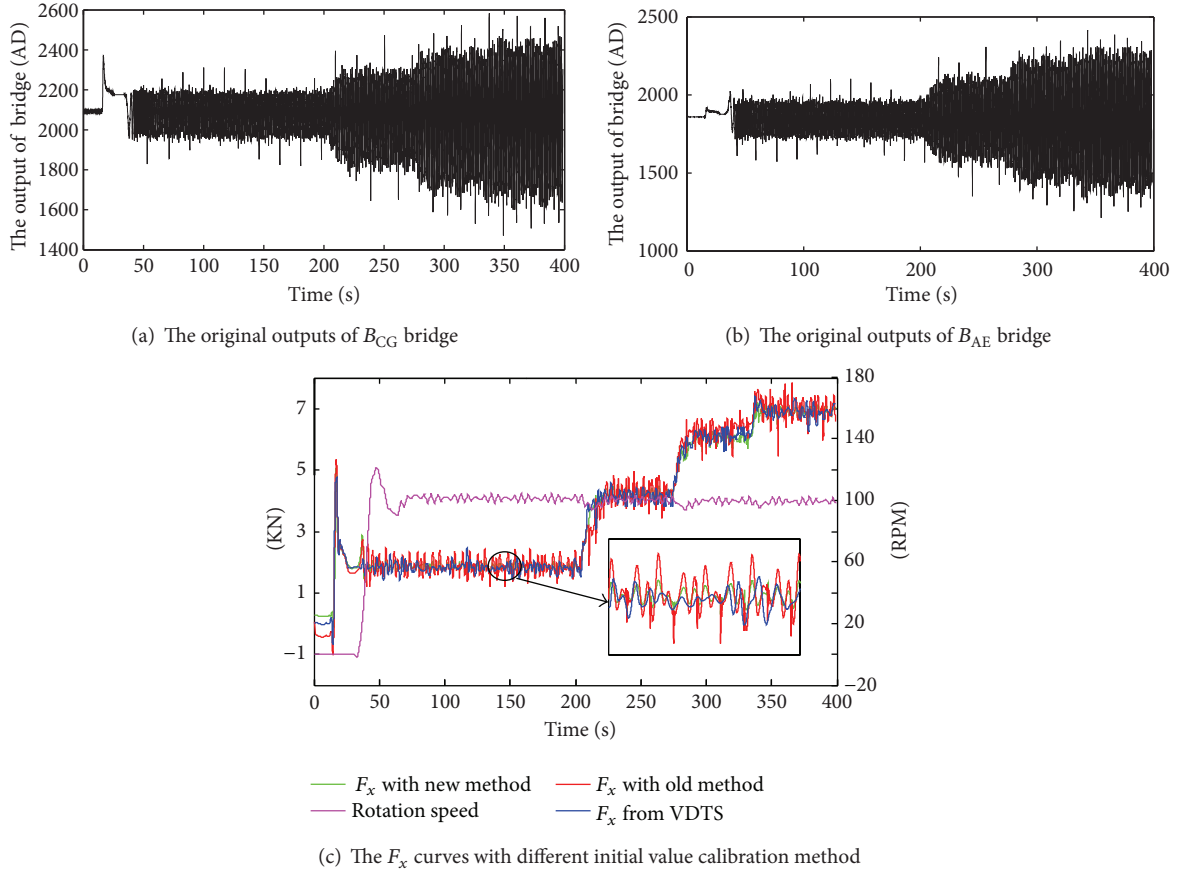


FIGURE 10: The curve of the dynamic test 1.

To solve (7), IMAPL described in Section 3.2 is exploited, and some thresholds are defined in advance. Set $T_g = 10\%$, $T_c = 200$, and $T_e = 2\% \times 14 \text{ KN}$ (14 KN is the maximum measuring range of the adopted WFT). After the optimization, the initial value is acquired as follows, $\alpha_0 = 238.4^\circ$, $F_{CG0} = 242\text{N}$, and $F_{AE0} = 203\text{N}$.

For comparison, the traditional methods are used. Because the dynamic test environment is different from real vehicle, some methods to obtain initial value described in Section 2 cannot be used in VDTs. Here the initial values obtained by traditional methods are denoted as $\{\alpha'_0, F'_{CG0}, F'_{AE0}\}$. In this experiment, the output of B_{CG} bridge and B_{AE} bridge when the WFT is not mounted in the wheel is taken as F'_{CG0} and F'_{AE0} . This operation is a common method to obtain the initial value for other type sensors. For initial value α'_0 , the method proposed by Weigong Zhang is used. To simulate the scene proposed in this method, the wheel B is driven to rotate manually instead of being driven by the wheel A. The initial values $\{\alpha'_0, F'_{CG0}, F'_{AE0}\}$ acquired are 232.6° , 113N , and 102N .

It is noticed that the error between α_0 and α'_0 is relative small. This is because that when the wheel B is driven to rotate manually, the external force applied to the WFT is small enough which meets the principle of Zhang's method. Meanwhile, the error between F_{CG0} and F'_{CG0} , F_{AE0} and F'_{AE0} is large.

4.2. *Dynamic Test by Means of VDTs.* In dynamic test, different force and speed are selected which is as follows.

- (1) Dynamic test 1. The force f_v applied to the wheel B is set to about 1.8KN, 4.1KN, 6.1KN, and 6.9KN, successively, with the constant rotating speed which is about 102 RPM.
- (2) Dynamic test 2. The force f_v applied to the wheel B is set to about 2KN, 4KN, 5.9KN, 8KN, 4.8KN, 2.2KN, and 0.4KN, successively, with the constant rotating speed which is about 118 RPM.
- (3) Dynamic test 3. The force f_v applied to the wheel B is set to about 2.3 KN, 4.2 KN, 6.1 KN, 7.3 KN, and 5.4 KN, successively, with two different rotating speeds which are about 72 RPM and 142 RPM.

The original outputs of B_{CG} bridge in three dynamic tests are shown in Figures 10(a), 11(a), and 12(a) separately, and the original outputs of B_{AE} bridge are shown in Figures 10(b), 11(b), and 12(b). The force f_v , the solved F_x by different initial value calibration method, and the rotation speed in three dynamic tests are shown in Figures 10(c), 11(c), and 12(c), respectively. For evaluating the performance of the proposed initial value calibration method, the dynamic errors (absolute maximum error and average error) are exploited.

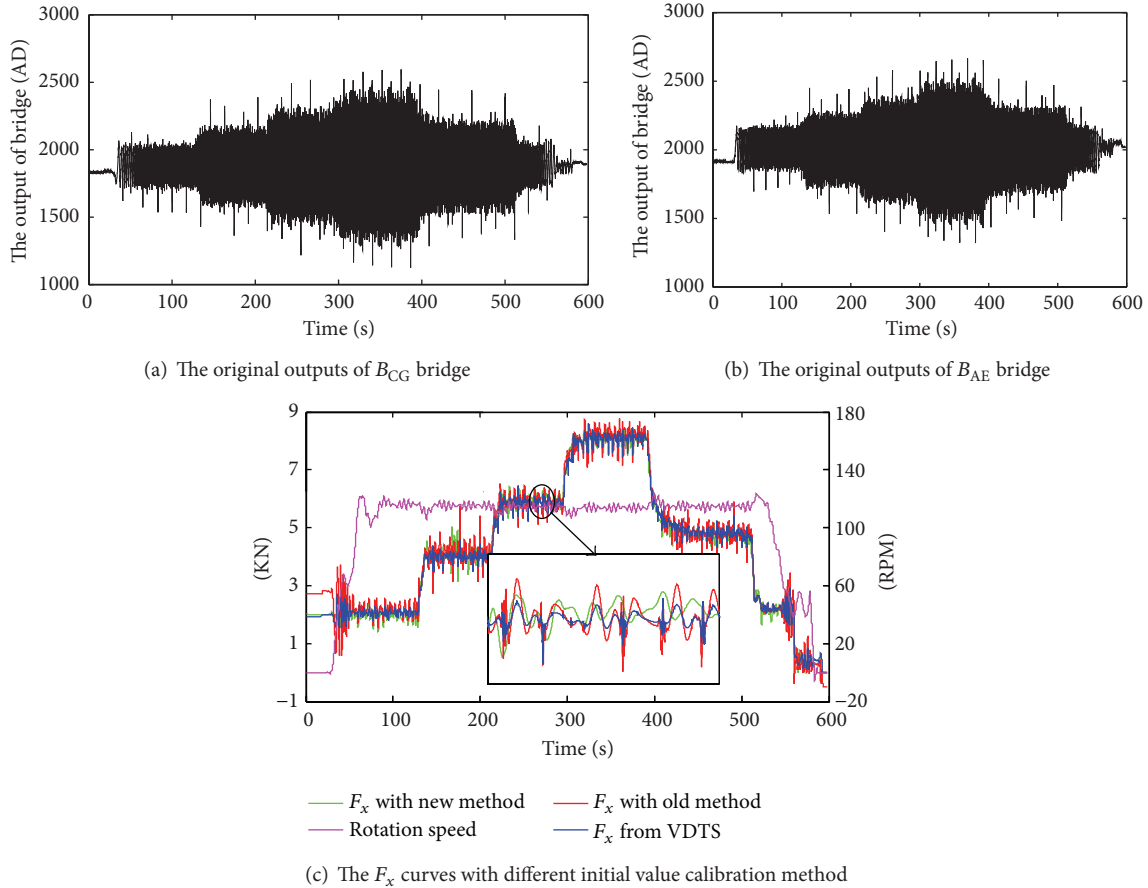


FIGURE 11: The curve of the dynamic test 2.

TABLE 2: The comparison of measuring accuracy based on absolute maximum error (unit: KN).

	Dynamic test 1	Dynamic test 2	Dynamic test 3
The proposed method	1.03	1.13	0.87
The traditional method	1.18	1.38	1.29

TABLE 3: The comparison of measuring accuracy based on average error (unit: KN).

	Dynamic test 1	Dynamic test 2	Dynamic test 3
The proposed method	0.13	0.12	0.15
The traditional method	0.31	0.27	0.42

The dynamic errors of the two initial value calibration methods in three dynamic tests are shown in Tables 2 and 3.

From these figures, it can be seen that the longitudinal force F_x with two different initial value method are all closed to the applied force f_v . Compared with the traditional method in these dynamic tests, it is obvious that the proposed method brings the better solutions than the traditional method.

The absolute maximum errors of the proposed method and that of the old method are all between 10% and 15%, and the ratio of the former to the latter is about 70%~80% which means the absolute maximum errors caused by the two methods are close. From Figure 10 to Figure 12 it can be seen that the maximum error mainly happened at the moment when the wheel A just touches and detaches the wheel B or the time that the wheel begins to rotate or stop. At this moment, the vibration is generated which causes the large change of the output of the WFT regardless of which method is adopted. At the same time, the average errors of the proposed method and that of the old method decrease a lot which are less than 3%, and the ratio of the former to the latter is less than 40%, which means the new method comes with higher accuracy than the previous method with the average errors.

From the analysis of the dynamic test, it is obvious that the proposed initial value calibration method can acquire more accuracy initial value and achieve better performance than the old method.

5. Conclusions

In order to increase the measuring accuracy of the WFT, a new dynamic and online method to resolve the initial values of the WFT is presented in this paper. Without any additional

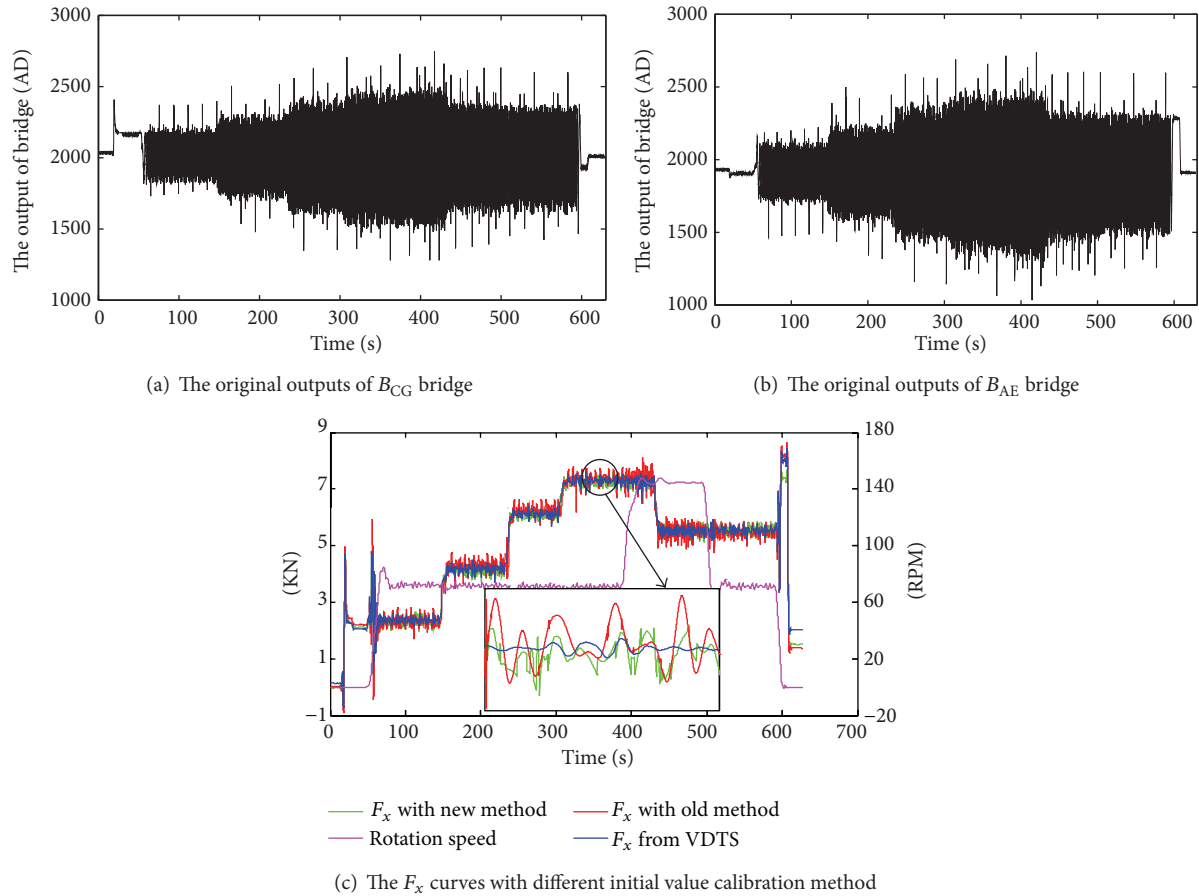


FIGURE 12: The curve of the dynamic test 3.

calibration equipment or manual operation, this method only requires the vehicle mounted with the WFT to be driven on a flat road with constant speed. The theoretical derivation and operation method are introduced. The contrast experiments on the wheel test-bed illustrate its advantage compared to the old ways. With the new method, the initial values are obtained with more accuracy and more convenience, and the measurement accuracy of the WFT is explicitly improved.

Conflict of Interests

The authors declare no conflict of interests.

Acknowledgment

This work is supported by National Natural Science Foundation of China (Grant no. 51305078).

References

[1] M. Corno, M. Gerard, M. Verhaegen, and E. Holweg, “Hybrid ABS control using force measurement,” *IEEE Transactions on Control Systems Technology*, vol. 20, no. 5, pp. 1223–1235, 2012.

[2] X. Zhang, N. Feng, and W. Zhang, “Experimental research on the abs performance based on the wheel forces measured by

roadway test,” *China Mechanical Engineering*, vol. 19, no. 6, pp. 751–755, 2008.

[3] W. Cho, J. Yoon, S. Yim, B. Koo, and K. Yi, “Estimation of tire forces for application to vehicle stability control,” *IEEE Transactions on Vehicular Technology*, vol. 59, no. 2, pp. 638–649, 2010.

[4] Y. Wang, W. Zhang, and H. Wang, “Application of wavelet method with nonlinear threshold control in vehicle wheel force signal denoising,” in *Proceedings of the 4th International Conference on Intelligent Computation Technology and Automation (ICICTA '11)*, pp. 957–960, Shenzhen, China, March 2011.

[5] G. F. Liu, W. G. Zhang, and Z. G. Li, “Research on static decoupling for multi dimensional wheel force transducer,” *Instrument Technique and Sensor*, vol. 7, pp. 15–18, 2006.

[6] Y. Zhou, W. Zhang, G. Liu, and Z. Li, “Research and development on the vehicle roadway test system based on a new six-component wheel force transducer,” *China Mechanical Engineering*, vol. 18, no. 20, pp. 2510–2514, 2007.

[7] K. Guo, W. Chen, Y. Ji, and J. Li, “Study and design of static calibration system for 6-D force sensor based on virtual instrument technology,” in *Proceedings of the 10th International Conference on Electronic Measurement and Instruments (ICEMI '11)*, pp. 81–84, Chengdu, China, August 2011.

[8] H.-M. Zheng, Z.-S. Liu, and Y. Wang, “Study on the method of dynamic characteristic calibration of the 6-axis wrist force sensor for robot,” *Acta Metrologica Sinica*, vol. 26, no. 1, pp. 43–85, 2005.

- [9] R. Sargeant, L. D. Seneviratne, and K. Althoefer, "A 2-axis optical force-torque fingertip sensor for dexterous grasping using linear polarizers," *IEEE Transactions on Instrumentation and Measurement*, vol. 61, no. 12, pp. 3363–3377, 2012.
- [10] J. C. Liu, Y. G. Li, L. Xie, and J. Liu, "Research on static performance calibration system for multi-axis force sensor based on virtual instrument," *Transducer and Micro System Technologies*, vol. 29, no. 11, pp. 86–89, 2011.
- [11] W. G. Zhang, "Study on multi-component wheel force measurement technology," *Journal of Jiangsu University*, vol. 25, no. 1, pp. 25–28, 2004.
- [12] G. F. Liu, S. G. Li, and W. G. Zhang, "Design of acquisition system of weighing calibration equipment for wheel force transducer," *Measurement & Control Technology*, vol. 26, no. 10, pp. 18–20, 2007.
- [13] J. Wang, L. Jiang, and H. Liu, "Auto static calibration of multi-axis force sensor based on triaxial accelerometer," *Chinese Journal of Scientific Instrument*, vol. 29, no. 2, pp. 432–435, 2008.
- [14] K. Parsa and F. Aghili, "Adaptive observer for the calibration of the force-moment sensor of a space robot," in *Proceedings of the IEEE International Conference on Robotics and Automation (ICRA '06)*, pp. 1667–1673, Orlando, Fla, USA, May 2006.
- [15] K. Kim, Y. Sun, R. M. Voyles, and B. J. Nelson, "Calibration of multi-axis MEMS force sensors using the shape-from-motion method," *IEEE Sensors Journal*, vol. 7, no. 3, pp. 344–351, 2007.
- [16] Y. Sun, K. Kim, R. M. Voyles, and B. J. Nelson, "Calibration of multi-axis MEMS force sensors using the shape from motion method," in *Proceedings of the IEEE International Conference on Robotics and Automation (ICRA '06)*, pp. 269–274, Orlando, Fla, USA, May 2006.
- [17] Y. S. Ong and A. J. Keane, "Meta-Lamarckian learning in memetic algorithms," *IEEE Transactions on Evolutionary Computation*, vol. 8, no. 2, pp. 99–110, 2004.
- [18] F. Neri and C. Cotta, "Memetic algorithms and memetic computing optimization: a literature review," *Swarm and Evolutionary Computation*, vol. 2, pp. 1–14, 2012.
- [19] Y. K. Richard, R. L. Fung, and Z. B. Jiang, "A memetic algorithm for the open capacitated arc routing problem," *Transportation Research Part E*, vol. 50, pp. 53–67, 2013.
- [20] S. A. Ludwig, "Memetic algorithms applied to the optimization of workflow compositions," *Swarm and Evolutionary Computation*, vol. 10, pp. 31–40, 2013.
- [21] G. Lin, X. Chen, and W. Zhang, "Robust lane detection algorithm based on multiple information fusion and optimizations," *Journal of Southeast University (Natural Science Edition)*, vol. 40, no. 4, pp. 771–777, 2010.

Research Article

Application of Global Optimization Methods for Feature Selection and Machine Learning

Shaohua Wu,¹ Yong Hu,¹ Wei Wang,¹ Xinyong Feng,¹ and Wanneng Shu²

¹ College of Electronics and Information Engineering, Sichuan University, Chengdu 610064, China

² College of Computer Science, South-Central University for Nationalities, Wuhan 430074, China

Correspondence should be addressed to Xinyong Feng; xinyong_feng@sohu.com

Received 2 September 2013; Revised 12 October 2013; Accepted 14 October 2013

Academic Editor: Gelan Yang

Copyright © 2013 Shaohua Wu et al. This is an open access article distributed under the Creative Commons Attribution License, which permits unrestricted use, distribution, and reproduction in any medium, provided the original work is properly cited.

The feature selection process constitutes a commonly encountered problem of global combinatorial optimization. The process reduces the number of features by removing irrelevant and redundant data. This paper proposed a novel immune clonal genetic algorithm based on immune clonal algorithm designed to solve the feature selection problem. The proposed algorithm has more exploration and exploitation abilities due to the clonal selection theory, and each antibody in the search space specifies a subset of the possible features. Experimental results show that the proposed algorithm simplifies the feature selection process effectively and obtains higher classification accuracy than other feature selection algorithms.

1. Introduction

With the explosive development of massive data, it is difficult to analyze and extract high level knowledge from data. The increasing trend of high-dimensional data collection and problem representation calls for the use of feature selection in many machine learning tasks [1]. Machine learning is the most commonly used technique to address larger and more complex tasks by analyzing the most relevant information already present in databases [2]. Machine learning is programming computers to optimize a performance criterion using example data or past experience. The selection of relevant features and elimination of irrelevant ones are the key problems in machine learning that have become an open issue in the field of machine learning [3]. Feature selection (FS) is frequently used as a preprocessing step to machine learning that chooses a subset of features from the original set of features forming patterns in a training dataset. In recent years, feature selection has been successfully applied in classification problem, such as data mining applications, information retrieval processing, and pattern classification. FS has recently become an area of intense interests and research.

Feature selection is a preprocessing technique for effective data analysis in the emerging field of data mining which is aimed at choosing a subset of original features so that

the feature space is optimally reduced according to the predetermined targets [4]. Feature selection is one of the most important means which can influence the classification accuracy rate and improve the predictive accuracy of algorithms by reducing the dimensionality, removing irrelevant features, and reducing the amount of data needed for the learning process [5, 6]. FS has been an important field of research and development since 1970's and proven to be effective in removing irrelevant features, reducing the cost of feature measurement and dimensionality, increasing classifier efficiency and classification accuracy rate, and enhancing comprehensibility of learned results.

Both theoretical analysis and empirical evidence show that irrelevant and redundant features affecting the speed and accuracy of learning algorithms and thus should be eliminated as well. An efficient and robust feature selection approach including genetic algorithms (GA) and immune clone algorithm (ICA) can eliminate noisy, irrelevant, and redundant data that have been tried out for feature selection.

In order to find a subset of features that are most relevant to the classification task, this paper makes use of FS technique, together with machine learning knowledge, and proposes a novel optimization algorithm for feature selection called immune clonal genetic feature selection algorithm (ICGFSA). We describe the feature selection for selection

of optimal subsets in both empirical and theoretical work in machine learning, and we present a general framework that we use to compare different algorithms. Experimental results show that the proposed algorithm simplifies the feature selection process effectively and either obtains higher classification accuracy or uses fewer features than other feature selection algorithms.

The structure of the rest of the paper is organized as follows. A brief survey is given in Section 2. We study the classification accuracy and formalize it as a mathematical optimization model in Section 3. Section 4 explains the details of the ICGFSA. Several experiments conducted to evaluate the effectiveness of the proposed approach are presented in Section 5. Finally, Section 6 concludes the paper and discusses some future research directions.

2. Related Works

In this section, we focus our discussion on the prior research on feature selection and machine learning. There has been substantial work on feature selection for selection of optimal subsets from the original dataset, which are necessary and sufficient for solving the classification problem.

Extreme learning machine (ELM) is a new learning algorithm for Single Layer Feed-forward Neural network (SLFN) whose learning speed is faster than traditional feed-forward network learning algorithm like back propagation algorithm while obtaining better generalization performance [7]. Support vector machines (SVM) is a very popular machine learning method used in many applications, such as classification. It finds the maximum margin hyperplane between two classes using the training data and applying an optimization technique [8]. SVM has shown good generalization performance on many classification problems.

Genetic algorithm has been proven to be very effective solution in a great variety of approximately optimum search problems. Recently, Huang and Wang proposed a genetic algorithm to simultaneously optimize the parameters and input feature subset of support vector machine (SVM) without loss of accuracy in classification problems [9]. In [10], a hybrid genetic algorithm is adopted to find a subset of features that are most relevant to the classification task. Two stages of optimization are involved. The inner and outer optimizations cooperate with each other and achieve the high global predictive accuracy as well as the high local search efficiency. Reference [11] proposed and investigated the use of a genetic algorithm method for simultaneously aiming at a higher accuracy level for the software effort estimates.

To further settle the feature selection problems, Mr. Liu et al. proposed an improved feature selection (IFS) method by integrating MSPSO, SVM with F -score method [12]. Reference [13] proposed a new evolutionary algorithm called Intelligent Dynamic Swarm (IDS), that is, a modified Particle Swarm Optimization. To evaluate the classification accuracy of IT-IN and remaining four feature selection algorithms, Naive Bayes, SVM, and ELM classifiers are used for ten UCI repository datasets. Deisy et al. proposed IT-IN performs better than the existing above algorithms in terms of number of features [14].

The feature selection process constitutes a commonly encountered problem of global combinatorial optimization. Chuang et al. presented a novel optimization algorithm called catfish binary particle swarm optimization, in which the so-called catfish effect is applied to improve the performance of binary particle swarm optimization [15]. Reference [16] proposed a new information gain and divergence-based feature selection method for statistical machine learning-based text categorization without relying on more complex dependence models. Han et al. study employs feature selection (FS) techniques, such as mutual-information-based filter and genetic algorithm-based wrapper, to help search for the important sensors in data driven chiller FDD applications, so as to improve FDD performance while saving initial sensor cost.

3. Classification Accuracy and F -Score

In this section, the proposed feature selection model will be discussed. In general, feature selection problem can be described as follows.

Definition 1. Assume that $TR = \{D, F, C\}$ represents a training dataset with m features or attributes and n instances, $D = \{o_1, \dots, o_j, \dots, o_n\}$ denotes the instances, $F = \{f_1, \dots, f_i, \dots, f_m\}$ denotes feature space of D constructed from m features, which gives an optimal performance for the classifier, and $C = \{c_1, \dots, c_i, \dots, c_k\}$ represents the set of classes where instances are tagged.

Definition 2. Assume that $o_j = (v_{j1}, \dots, v_{jm})$ represents a value vector of features, where v_{ji} is the value of o_j corresponding to the feature f_i , $o_j \in D$.

The feature selection approaches are used to generate a feature subset F based on the relevance and feature interaction of data samples. The main goal of classification learning is to characterize the relationship between F and C . Assume that F_1 is the subset of already-selected features, F_2 is the subset of unselected features, and $F = F_1 \cup F_2$, $F_1 \cap F_2 = \phi$. Therefore, any optimal feature subset obtained by selection algorithms should preserve the existing relationship between F and C hidden in the dataset.

The best subset of features is selected by evaluating a number of predefined criteria, such as classification accuracy and F -score. In order to evaluate the classification accuracy rate, the specific equation on classification accuracy is defined as follows.

Definition 3. Assume that S is the set of data items to be classified and sc is the class of the item s . If $\text{classify}(s)$ returns the classification accuracy rates of s , then classification accuracy can be formulated as

$$\text{acc}(S) = \frac{\sum_{i=1}^{|S|} \text{ass}(s_i)}{|S|}, \quad s_i \in S, \quad (1)$$

$$\text{ass}(s) = \begin{cases} 1, & \text{classify}(s) = sc, \\ 0, & \text{otherwise,} \end{cases}$$

where $|S|$ represents the number of elements in the collection S , $s \in S$.

F -score is an effective approach which measures the discrimination of two sets of real numbers. The larger the F -score is, the more this feature is discriminative.

Definition 4. Given training vectors X_k . If the number of the j th dataset is n_j , then the F -score of the i th feature is defined as

$$F(s_i) = \frac{\sum_{j=1}^m (\bar{x}_{i,j} - \bar{x}_i)^2}{\sum_{j=1}^m (1/(n_j + 1)) \sum_{k=1}^{n_j} (x_{i,j}^k - x_{i,j})^2}, \quad (2)$$

where \bar{x}_i , $\bar{x}_{i,j}$ are the average of the i th feature of the whole dataset and the j th dataset, respectively; $x_{i,j}^k$ is the i th feature of the k th instance in the j th dataset; m is the number of datasets. $k = 1, 2, \dots, m$ and $j = 1, 2, \dots, l$.

4. Heuristic Feature Selection Algorithm

In this section, we focus our discussion on algorithms that explicitly attempt to select an optimal feature subset. Finding an optimal feature subset is usually difficult, and feature selection for selection of optimal subsets has been shown to be NP-hard. Therefore, a number of heuristic algorithms have been used to perform feature selection of training and testing data, such as genetic algorithms, particle swarm optimization, neural networks, and simulated annealing.

Genetic algorithms have been proven as an intelligent optimization algorithm that can find the optimal solution to a problem in the sense of probability in a random manner [17]. However, standard genetic algorithms have some weaknesses, such as premature convergence and poor local search ability. On the other hand, some other heuristic algorithms, such as particle swarm optimization, simulated annealing, and clonal selection algorithm usually have powerful local search ability.

4.1. Basic Idea. In order to obtain the higher classification accuracy rate and higher efficiency of standard genetic algorithms, some hybrid GA for feature selection have been developed by combining the powerful global search ability of GA with some efficient local search heuristic algorithms. In this paper, a novel immune clonal genetic algorithm based on immune clonal algorithm, called ICGFSA, is designed to solve the feature selection problem. Immune clone algorithm is a simulation of the immune system which has the ability to identify the bacteria and designed diversity, and its search target has certain dispersion and independence. ICA can effectively maintain the diversity between populations of antibodies but also accelerate the global convergence speed [18]. The ICGFSA algorithm has more exploration and exploitation abilities due to the clonal selection theory that an antibody has the possibility to clone some similar antibodies in the solution space with each antibody in the search space specifying a subset of the possible features. The experimental results show the superiority of the ICGFSA in terms of the prediction accuracy with smaller subset of features. The overall scheme of the proposed algorithm framework is outlined in Figure 1.

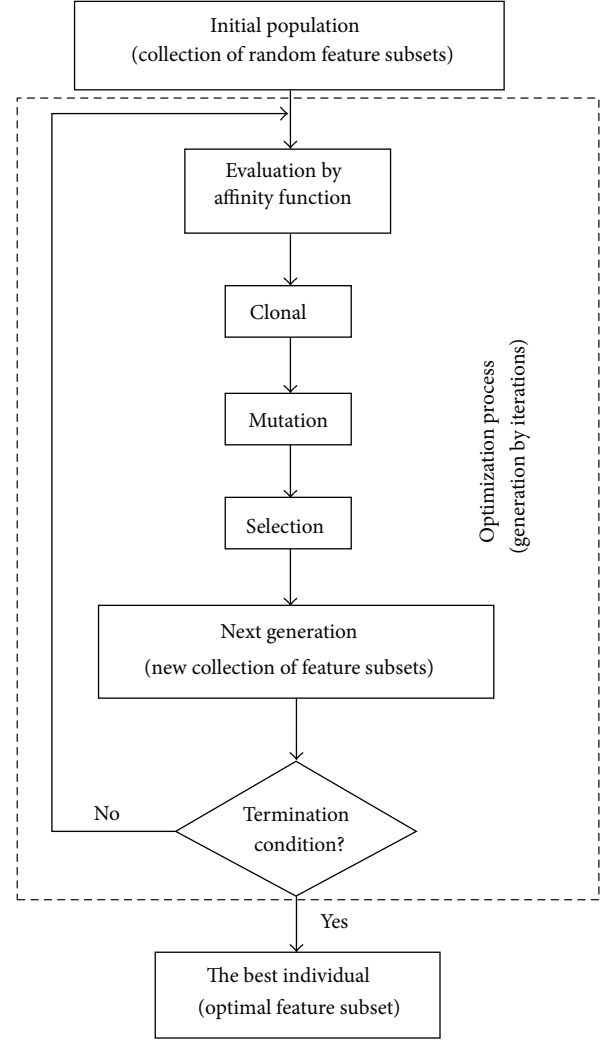


FIGURE 1: Feature selection by ICGFSA algorithm.

4.2. Encoding. In the ICGFSA algorithm, each antibody in the population represents a candidate solution to the feature selection problem. The algorithm uses the binary coding method that “1” means “selected” and “0” means “unselected” [19]. Therefore, the chromosomes represents by a string of binary digits of zeros and ones and each gene in chromosome corresponds to a feature.

4.3. Affinity Function. We design an affinity function that combines classification accuracy rate with F -score, which is the evaluation criterion for the feature selection. The affinity function is defined as follows:

$$\text{affinity}(i) = \lambda_1 \times \text{ass}(s_i) + \lambda_2 \times \frac{1}{|S|} \times \frac{\sum_{j=1}^{|S|} F(\text{FS}(s_j))}{\sum_{j=1}^{|S|} F(s_j)}. \quad (3)$$

In which, $\text{FS}(s_j)$ is equal to the instance of feature i when feature i is selected, otherwise $\text{FS}(s_j)$ is equal to 0, $\lambda_1 + \lambda_2 = 1$.

TABLE 1: Description of dataset.

No.	Datasets	Instances	Features	Classes
1	Liver	345	6	2
2	WDBC	569	30	2
3	Soybean	685	35	19
4	Glass	214	9	6
5	Wine	178	13	3
6	PDF	800	213	2

4.4. Basic Operation. In this section focuses on the three main operations of ICGFSA, including clonal, mutation, and selection. Mutation operation will take the binary mutation operation in standard genetic algorithm [20].

Clonal is essentially the larger antibody affinity for a certain scale replication. Clone size is calculated as follows:

$$\text{size}(i) = \left\lceil \frac{|D|}{|F|} \times \frac{\text{affinity}(i)}{\sum_{j=1}^N \text{affinity}(i)} \right\rceil. \quad (4)$$

In which, $|D|$ and $|F|$ are the number of elements in the set D and F , respectively. N represents the number of antibodies in the population.

The basic idea of selection operation is as follows. Firstly, select the n highest affinity antibodies and generate a number of clones for them. Secondly, antibodies that have been selected directly are retained to the next generation [21].

5. Experimental Results and Discussion

5.1. Parameter Setting. In this section, in order to investigate the effectiveness and superiority of the ICGFSA algorithm for classification problems, the same conditions were used to compare with other feature selection methods such as GA and SVM; that is, the parameters of ICGFSA and GA are set as follows: population size is 50, maximum generations is 500, crossover probability is 0.7, and mutation probability is 0.2. For each dataset we have performed 50 simulations, since the test results depend on the population randomly generated by the ICGFSA algorithm.

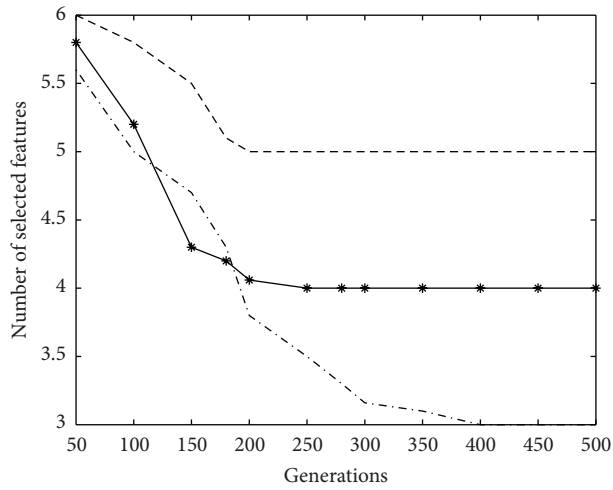
5.2. Benchmark Datasets. To evaluate the performance of ICGFSA algorithms, the following benchmark datasets are selected for simulation experiments: Liver, WDBC, Soybean, Glass, and Wine. These datasets were obtained from the UCI machine learning repository [22] and most of them are frequently used in a comprehensive testing. They suit for feature selection methods under different conditions. Furthermore, to evaluate the algorithms for real Internet data, we also use malicious PDF file datasets from Virus Total [23]. Table 1 is given some general information about these datasets, such as instances, features, and classes.

5.3. Experimental Results. Figure 2 is the number of selected features with different generations in benchmark datasets using ICGFSA, GA, and SVM, respectively. As seen from Figure 2, it can be observed that the number of selected features is decreased with the number of generations increasing,

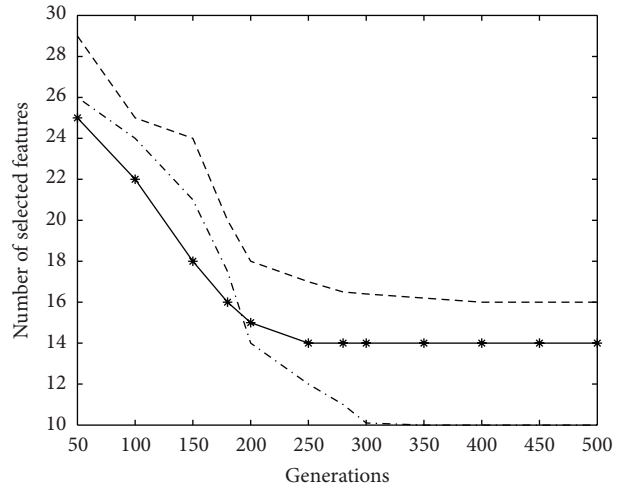
and ICGFSA can converge to the optimal subsets of required number features since it is the stochastic search algorithms. In the Liver dataset, the number of features selected keeps decreasing, while the number of iterations keeps increasing, until ICGFSA obtained nearly 90% classification accuracy, which indicates that a good feature selection algorithm not only decreases the number of features, but also selects features relevant for improving classification accuracy. It can be observed from Figure 3(b) that when the number of iterations increases beyond certain value (say 300), the performance will no longer be improved. In the Wine dataset, there are several critical points (153, 198, 297, etc.) where the trend has been shifted or changed sharply. In the Soybean and Glass datasets, three algorithms have the best performances and significant improvements in the number of selection features.

We carried out extensive experiments to verify the ICGFSA algorithm. The running times that find the best subset of required numbers of features and number of selected features in benchmark datasets using ICGFSA, GA, and SVM are recorded in Table 2. It can be observed from Table 2 that ICGFSA algorithm can achieve significant feature reduction that selects only a small portion from the original features which better than the other two algorithms. ICGFSA is more effective than GA and SVM and, moreover, produces improvements of conventional feature selection algorithms over SVM which is known to give the best classification accuracy. From the experimental results we can obviously see that ICGFSA has the least feature number and clonal selection operations can greatly enforce the local searching ability and make the algorithm fast enough to reach its optimum, which indicates ICGFSA has the ability to break through the local optimal solution when applied to large-scale feature selection problems. It can be concluded that the ICGFSA is relatively simple and can effectively reduce the computational complexity of implementation process.

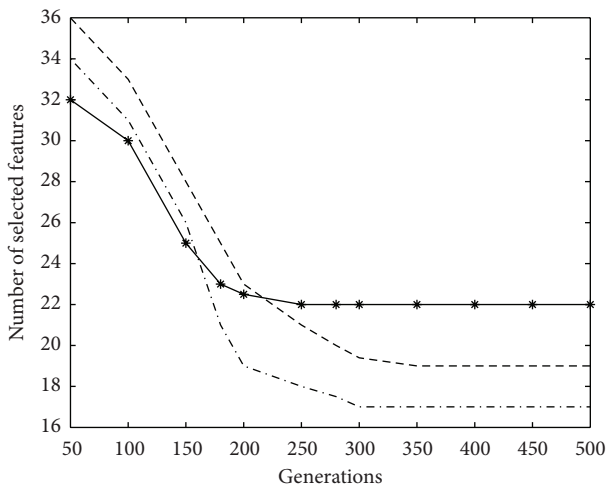
Finally, we inspect the classification accuracy for the proposed algorithm. Figure 3 shows the global best classification accuracies with different generations in benchmark datasets using ICGFSA, GA, and SVM, respectively. In the Liver dataset, the global best classification accuracy of ICGFSA is 88.69%. However, the global best classification accuracy of GA and SVM are only 85.12% and 87.54%, respectively. In the WDBC dataset, the global best classification accuracy of ICGFSA is 84.89%. However, the global best classification accuracy of GA and SVM is only 79.36% and 84.72%, respectively. In the Soybean dataset, the global best classification accuracy of ICGFSA and SVM is 84.96% and 84.94%, respectively. However, the global best classification accuracy of GA is only 77.68%. In the Glass dataset, the global best classification accuracy of ICGFSA is 87.96%. However, the global best classification accuracy of GA and SVM is only 84.17% and 86.35%, respectively. In the Wine dataset, the ICGFSA obtained 94.8% classification accuracy before reaching the maximum number of iterations. In the PDF dataset, the global best classification accuracy of ICGFSA and SVM is 94.16% and 93.97%, respectively. However, the global best classification accuracy of GA is only 92.14%. ICGFSA method is consistently more effective than GA and SVM methods on six datasets.



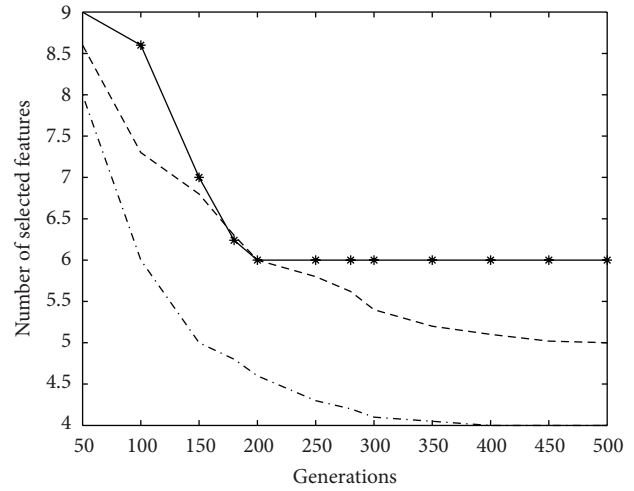
(a) Liver dataset



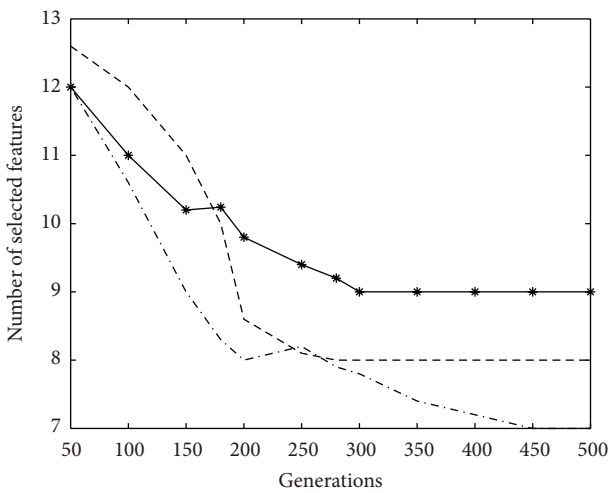
(b) WDBC dataset



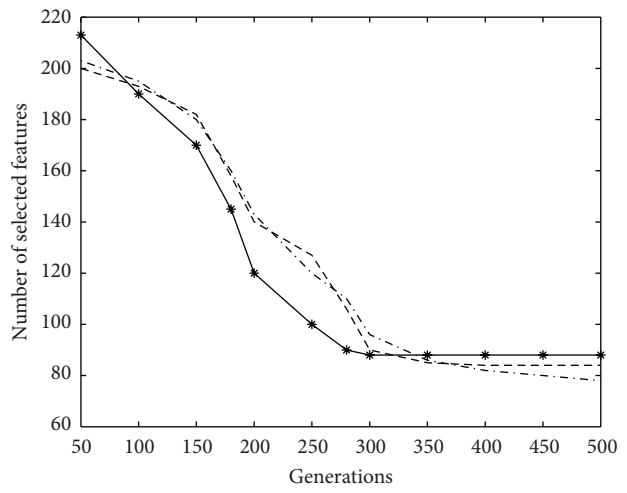
(c) Soybean dataset



(d) Glass dataset



(e) Wine dataset

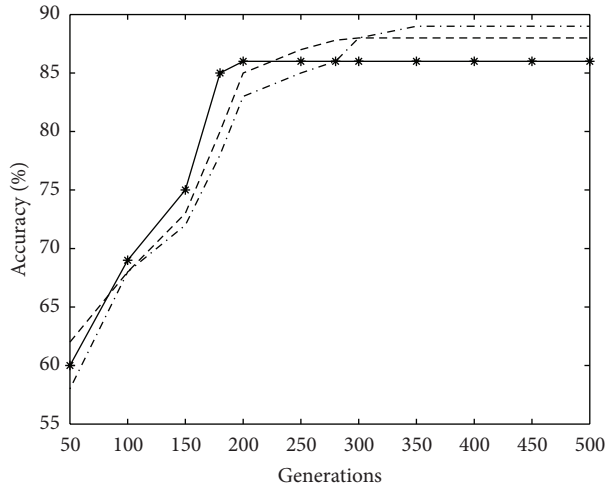


(f) PDF dataset

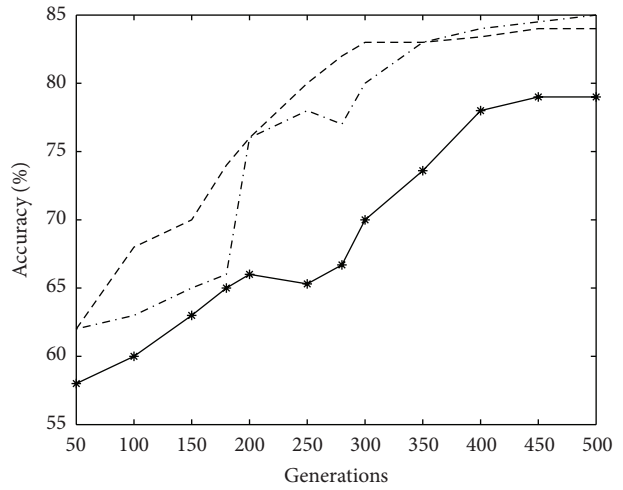
--- ICGFSA
 —●— GA
 --- SVM

--- ICGFSA
 —●— GA
 --- SVM

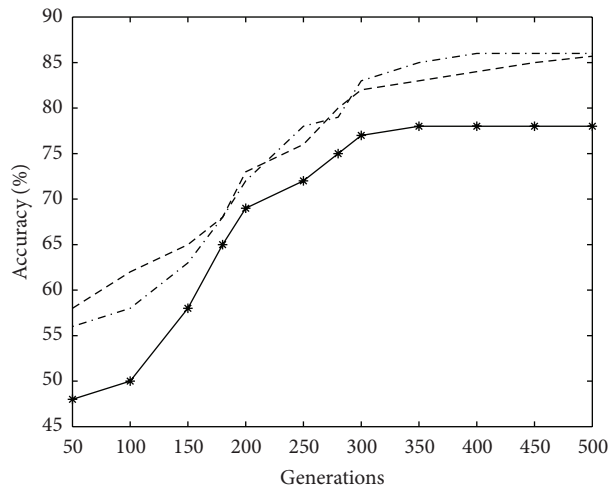
FIGURE 2: Number of selected features with different generations in benchmark datasets.



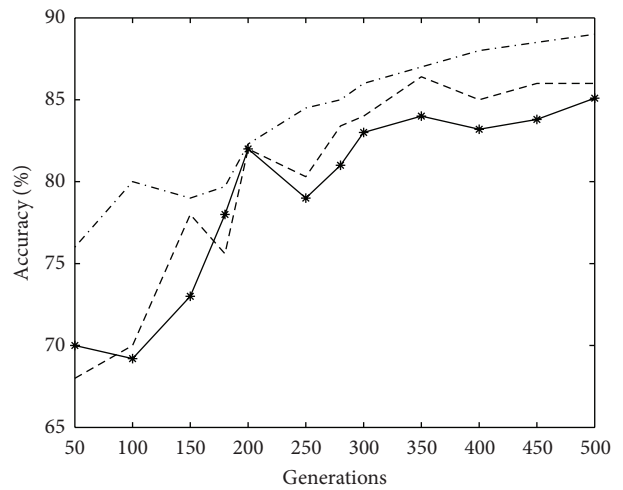
(a) Liver dataset



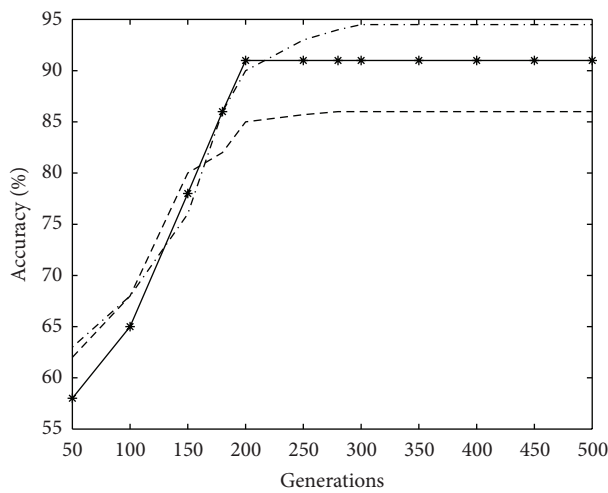
(b) WDBC dataset



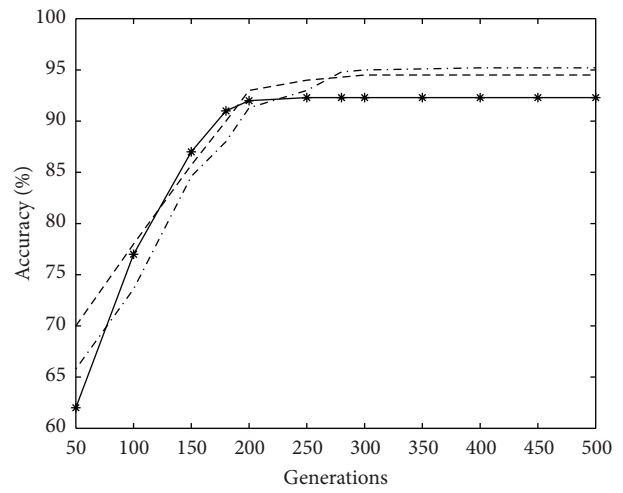
(c) Soybean dataset



(d) Glass dataset



(e) Wine dataset



(f) PDF dataset

--- ICGFSA
 —●— GA
 - - - SVM

--- ICGFSA
 —●— GA
 - - - SVM

FIGURE 3: Global classification accuracies with different generations in benchmark datasets.

TABLE 2: Running time and number of selected features for three feature selection algorithms.

Datasets	Running time (seconds)			Number of selected features		
	ICGFSA	GA	SVM	ICGFSA	GA	SVM
Liver	12.3	11.1	11.2	3	4	5
WDBC	12.6	12.9	13.1	10	14	16
Soybean	13.2	14.7	14.9	17	22	19
Glass	11.8	12.3	11.7	4	6	5
Wine	9.6	10.8	9.5	7	9	8
PDF	830.1	832.5	822	78	89	83

The numerical results and statistical analysis show that the proposed ICGFSA algorithm performs significantly better than the other two algorithms in terms of running time and higher classification accuracy. ICGFSA can reduce the feature vocabulary with best performance in accuracy. It can be concluded that an effective feature selection algorithm is helpful in reducing the computational complexity of analyzing dataset. As long as the chosen features contain enough feature classification information, higher classification accuracy can be achieved.

6. Conclusions

Machine learning is a science of the artificial intelligence. The field's main objectives of study are computer algorithms that improve their performance through experience. In this paper, the main work in machine learning field is on methods for handling datasets containing large amounts of irrelevant attributes. For the high dimensionality of feature space and the large amounts of irrelevant feature, we propose a new feature selection method base on genetic algorithm and immune clonal algorithm. In the future, ICGFSA algorithm will be applied to more datasets for testing performance.

Acknowledgments

This research work was supported by the Hubei Key Laboratory of Intelligent Wireless Communications (Grant no. IWC2012007) and the Special Fund for Basic Scientific Research of Central Colleges, South-Central University for Nationalities (Grant no. CZY11005).

References

- [1] T. Peters, D. W. Bulger, T.-H. Loi, J. Y. H. Yang, and D. Ma, "Two-step cross-entropy feature selection for microarrays-power through complementarity," *IEEE/ACM Transactions on Computational Biology and Bioinformatics*, vol. 8, no. 4, pp. 1148–1151, 2011.
- [2] W.-C. Yeh, "A two-stage discrete particle swarm optimization for the problem of multiple multi-level redundancy allocation in series systems," *Expert Systems with Applications*, vol. 36, no. 5, pp. 9192–9200, 2009.
- [3] L.-Y. Chuang, H.-W. Chang, C.-J. Tu, and C.-H. Yang, "Improved binary PSO for feature selection using gene expression data," *Computational Biology and Chemistry*, vol. 32, no. 1, pp. 29–37, 2008.
- [4] B. Hammer and K. Gersmann, "A note on the universal approximation capability of support vector machines," *Neural Processing Letters*, vol. 17, no. 1, pp. 43–53, 2003.
- [5] L. Yu and H. Liu, "Efficient feature selection via analysis of relevance and redundancy," *Journal of Machine Learning Research*, vol. 5, pp. 1205–1224, 2004.
- [6] G. Qu, S. Hariri, and M. Yousif, "A new dependency and correlation analysis for features," *IEEE Transactions on Knowledge and Data Engineering*, vol. 17, no. 9, pp. 1199–1206, 2005.
- [7] G.-B. Huang, Q.-Y. Zhu, and C.-K. Siew, "Extreme learning machine: theory and applications," *Neurocomputing*, vol. 70, no. 1–3, pp. 489–501, 2006.
- [8] J. G. Dy, C. E. Brodley, A. Kak, L. S. Broderick, and A. M. Aisen, "Unsupervised feature selection applied to content-based retrieval of lung images," *IEEE Transactions on Pattern Analysis and Machine Intelligence*, vol. 25, no. 3, pp. 373–378, 2003.
- [9] C.-L. Huang and C.-J. Wang, "A GA-based feature selection and parameters optimization for support vector machines," *Expert Systems with Applications*, vol. 31, no. 2, pp. 231–240, 2006.
- [10] J. Huang, Y. Cai, and X. Xu, "A hybrid genetic algorithm for feature selection wrapper based on mutual information," *Pattern Recognition Letters*, vol. 28, no. 13, pp. 1825–1844, 2007.
- [11] A. L. I. Oliveira, P. L. Braga, R. M. F. Lima, and M. L. Cornélio, "GA-based method for feature selection and parameters optimization for machine learning regression applied to software effort estimation," *Information and Software Technology*, vol. 52, no. 11, pp. 1155–1166, 2010.
- [12] Y. Liu, G. Wang, H. Chen, H. Dong, X. Zhu, and S. Wang, "An improved particle swarm optimization for feature selection," *Journal of Bionic Engineering*, vol. 8, no. 2, pp. 191–200, 2011.
- [13] C. Bae, W.-C. Yeh, Y. Y. Chung, and S.-L. Liu, "Feature selection with Intelligent Dynamic Swarm and rough set," *Expert Systems with Applications*, vol. 37, no. 10, pp. 7026–7032, 2010.
- [14] C. Deisy, S. Baskar, N. Ramraj, J. S. Koori, and P. Jeevanandam, "A novel information theoretic-interact algorithm (IT-IN) for feature selection using three machine learning algorithms," *Expert Systems with Applications*, vol. 37, no. 12, pp. 7589–7597, 2010.
- [15] L.-Y. Chuang, S.-W. Tsai, and C.-H. Yang, "Improved binary particle swarm optimization using catfish effect for feature selection," *Expert Systems with Applications*, vol. 38, no. 10, pp. 12699–12707, 2011.
- [16] C. Lee and G. G. Lee, "Information gain and divergence-based feature selection for machine learning-based text categorization," *Information Processing and Management*, vol. 42, no. 1, pp. 155–165, 2006.

- [17] J. Huang, Y. Cai, and X. Xu, "A hybrid genetic algorithm for feature selection wrapper based on mutual information," *Pattern Recognition Letters*, vol. 28, no. 13, pp. 1825–1844, 2007.
- [18] L. N. De Castro and F. J. Von Zuben, "Learning and optimization using the clonal selection principle," *IEEE Transactions on Evolutionary Computation*, vol. 6, no. 3, pp. 239–251, 2002.
- [19] H. Han, B. Gu, T. Wang, and Z. R. Li, "Important sensors for chiller fault detection and diagnosis (FDD) from the perspective of feature selection and machine learning," *International Journal of Refrigeration*, vol. 34, no. 2, pp. 586–599, 2011.
- [20] P. Kumsawat, K. Attakitmongkol, and A. Srikaew, "A new approach for optimization in image watermarking by using genetic algorithms," *IEEE Transactions on Signal Processing*, vol. 53, no. 12, pp. 4707–4719, 2005.
- [21] R. Meiri and J. Zahavi, "Using simulated annealing to optimize the feature selection problem in marketing applications," *European Journal of Operational Research*, vol. 171, no. 3, pp. 842–858, 2006.
- [22] C. L. Blake and C. J. Merz, "UCI repository of machine learning databases," Department of Information and Computer Science, University of California, Irvine, Calif, USA, 1998, <http://www.ics.uci.edu/mllearn/MLRepository.html>.
- [23] VirusTotal: <http://www.virustotal.com>.

Research Article

An Efficient Web Usage Mining Approach Using Chaos Optimization and Particle Swarm Optimization Algorithm Based on Optimal Feedback Model

Lu Dai,¹ Wei Wang,² and Wanneng Shu³

¹ Computer School, Hubei University of Technology, Wuhan 430068, China

² College of Electronics and Information Engineering, Sichuan University, Chengdu 610064, China

³ College of Computer Science, South-Central University for Nationalities, Wuhan 430074, China

Correspondence should be addressed to Wei Wang; ww0830@gmail.com

Received 22 July 2013; Revised 18 August 2013; Accepted 21 August 2013

Academic Editor: Baochang Zhang

Copyright © 2013 Lu Dai et al. This is an open access article distributed under the Creative Commons Attribution License, which permits unrestricted use, distribution, and reproduction in any medium, provided the original work is properly cited.

The dynamic nature of information resources as well as the continuous changes in the information demands of the users has made it very difficult to provide effective methods for data mining and document ranking. This paper proposes an efficient particle swarm chaos optimization mining algorithm based on chaos optimization and particle swarm optimization by using feedback model of user to provide a listing of best-matching webpages for user. The proposed algorithm starts with an initial population of many particles moving around in a D -dimensional search space where each particle vector corresponds to a potential solution of the underlying problem, which is formed by subsets of webpages. Experimental results show that our approach significantly outperforms other algorithms in the aspects of response time, execution time, precision, and recall.

1. Introduction

With the rapid development in Internet technology, the number of webpages and the volume of information content have led to an explosion in the amount of available information. While there may be some webpages that are more relevant, popular, or authoritative than others, web users look forward to easily, search the most interesting and significant website by specifying relevant keywords [1]. When a user enters a query into a search engine by using keywords, the engine will provide a list of best-matching webpages according to its criteria [2]. It becomes increasingly important to help user find useful information more easily and quickly.

It is well known that web search is one of the most universal and influential applications on the Internet. Web search engines can support users on a wide variety of topics across a comprehensive range of websites [3]. In order to achieve the typical massive content collections rapid response to a specific query form, web mining technology appears in the technical background and social environment [4]. Web

mining is a comprehensive data mining method that uses data mining techniques from web-related resources and extracts interesting behavior, useful patterns and implicit information, involving web technology, data mining, computational linguistics, artificial intelligence, machine learning and other fields.

Web mining can be viewed as the extraction of structure from an unlabeled, semistructured data set containing the characteristics of users and information [5]. Web mining is divided into web content mining and web usage mining. Web content mining is mining the web page content and the background of transactional database and obtaining useful knowledge from the web document and the description of the content information regarding the websites [6]. Web usage mining is done by mining the appropriate website log files and related data to discover frequent browsing patterns based on clickstream data analysis.

A number of novel optimization methods have been proposed to optimize the web usage evaluation function. The conventional web mining approach makes a type of relevance

ranking, whereby a webpage may be relevant to a topic or theme. Taking into account the amount of available information, the processing essentially requires adequate approaches suitable for extracting only the relevant, sometimes hidden, knowledge as the final result of the problem under consideration. A heuristic intelligent mining approach can be derived using particle swarm optimization (PSO) for addressing the web mining.

This paper focuses on feedback model of user by using chaos optimization and particle swarm optimization to help user find useful information as fast as possible. The dynamic feature of web information as well as the continuous changes in the information demands of the users has made it very difficult to provide efficient and effective approaches for data mining techniques. To realize the goal of searching useful information effectively and efficiently, we have developed an efficient particle swarm chaos optimization mining algorithm (PSCOMA) based on chaos optimization and particle swarm optimization by using feedback model of user to provide a list of best-matching webpages for user. We compare our approach with PSO, PCS, and HITS algorithms, and, as far as we know, it is currently the best method for the problem considered. Experimental results show that our approach significantly outperforms other algorithms in most cases.

The remainder of the paper is organized as follows. A brief survey is given in Section 2. We study the user's feedback behavior and formalize it as a mathematical optimization model in Section 3. Section 4 explains the details of the PSCOMA. Section 5 discusses the experimental results and compares them with other Web mining algorithms. Finally, Section 6 concludes the paper and discusses some future research directions.

2. Related Works

In this section, we focus our discussion on the prior research on web mining. The web mining is a very important problem and has attracted much attention of many researchers.

Drs. Yin and Guo proposed a new formulation for the website structure optimization (WSO) problem based on a comprehensive survey of existing works and practice considerations [7]. In [8], the greedy-add algorithm with backtracking was introduced for obtaining the initial solution, and a better solution is sought through VNS as well as tabu search. Dr. Chen et al. presented a page clipping synthesis (PCS) search method to extract relevant paragraphs from other web search results [9]. Spink et al. reported the results of a major study examining the overlap among four major web search engines for results retrieved for the same queries [10]. In [11], proposed hybrid algorithm makes use of the strong global search ability of particle swarm optimization and the strong local search ability of tabu search to obtain high quality solutions in web mining. Herrera et al. presented a study about the impact of using several features extracted from the document collection and query logs on the task of automatically identifying the users' goals behind their queries [12]. Ling and Van Schaik reported findings from two experiments that explored the influence of font type and line length on a range of performance and

subjective measures [13]. Moawad et al. proposed a new multiagent system based approach for personalizing the web search results. The proposed approach introduces a model to build a user profile from initial and basic information and maintain it through implicit user feedback to establish a complete, dynamic, and up-to-date user profile [14]. Zhang and Dong proposed a novel effective approach to exploit the relationships among users, queries and resources based on the search engine's log [15].

The rank value indicates the importance of a particular page. A hyperlink to a page counts as a vote of support. Link analysis is a method for determining which pages are good for particular topics based on both the quantity and quality of links pointing to that document. PageRank is a link analysis algorithm, named after Larry Page and used by the Google Internet search engine, that assigns a numerical weighting to each element of a hyperlinked set of documents [16]. hyperlink-induced topic search (HITS) is a link analysis algorithm that developed by Jon Kleinberg. HITS provides a new method of searching the web that returns a list of the most valuable sites on a given topic, plus a list of sites that index the subject. In [17], a comparison among the rankings of results for identical queries retrieved from several search engines is made. The method was based only on the set of URLs that appear in the answer sets of the engines being compared.

3. Optimal Feedback Model

In this section, we design the optimal feedback model of users for the evaluation of the weight of webpage. The explicit feedback is the one in which the user is asked to fill up a feedback form after he has obtained searching results [18]. Since the user's feedback behavior reflects the user's preferences, we need to monitor the response of the user to the search results presented before him. Here is the general definition of the problem.

Definition 1. Assume that $FU = \{V, T, L, M, R\}$ represents the feedback model of user, $V = \{v_1, v_2, \dots, v_i, \dots, v_N\}$ denotes the order that user browses the webpages, $T = \{t_1, t_2, \dots, t_i, \dots, t_N\}$ denotes the time in which the user browses the webpages, $L = \{l_1, l_2, \dots, l_i, \dots, l_N\}$ denotes the clicks of the webpages, $M = \{m_1, m_2, \dots, m_i, \dots, m_N\}$ denotes the behavior that the user evaluates the webpages and $R = \{r_1, r_2, \dots, r_i, \dots, r_N\}$ denotes the user's behavior in responding to the webpages.

If v_i is the k th webpage visited by the user, then the value of v_i is set k . If the i th webpage is not browse by the user at all before the next query is submitted, then we set $v_i = 0$, and the corresponding value of t_i is set 0. One of the mostly used measures for evaluating the web usage is the number of clicks needed for accessing the target webpage [19, 20]. The click frequency can be easily derived by scanning the user sessions, and the initial value of l_i is 0; if the user clicks the v_i one time, then set $l_i = l_i + 1$. M indicates the level of importance that webpage holds for the specified query; according to the rules and strategies for evaluation of difference, the value of m_i is not the same, $i = 1, 2, 3$. The initial value of r_i is 0; if the

user participates in the discussion of the i th webpage, then the value of r_i is set 1.

When the feedback model of the user is complete, we propose to define the weight w_i of the i th webpage.

Definition 2. Assume that w_i represents the weight of the i th webpage; w_i represents the importance of the i th webpage and can be formulated as

$$w_i = \lambda_1 \times \frac{1}{v_i + 1} + \lambda_2 \times \frac{t_i}{t_{\max}^i} + \lambda_3 \times l_i + \lambda_4 \times m_i + \lambda_5 \times r_i, \quad (1)$$

where t_{\max}^i denotes the maximum time that the user is expected to spend examining the i th webpage, in which $\sum_{i=1}^5 \lambda_i = 1$, λ_i represents each of the five factors of the feedback vector. According to the user's preferences and practice considerations, the user can set different values for each of the five factors in the feedback vector. From (1), it is not difficult to see that the more time the user spent in browsing through the documents, the more important they must be for him. If the user evaluates the documents or responding to them, they must be having the significance for the user. Therefore, this paper combines of the above five components by simply taking their weighted sum and gives the overall importance of webpages.

4. The Application of PSCOMA

4.1. Particle Swarm Optimization and Chaos Optimization. Particle swarm optimization is an evolutionary computation technique based on swarm intelligence optimization algorithm inspired by the social behavior of birds flocking for food, which was first introduced to optimize various continuous functions by Kennedy and Eberhart. It is computationally effective, has fast convergence, and is easier to implement when compared with other mathematical and evolutionary algorithms while only a few parameters need to be adjusted.

Chaos is a universal phenomenon in many nonlinear systems. Chaos optimization can escape from local minima more easily compared with other stochastic optimization algorithms that escape from local minimum by accepting some wrong solutions according to a certain probability [21]. Chaos optimization can be within a certain range according to their own laws without repetition through all states. Recently, chaos optimization and PSO have been combined in different application fields for different purposes. Some of the works have intended to show the chaotic behaviors in PSO process [22].

4.2. The Basic Idea of PSCOMA. This paper proposes an efficient particle swarm chaos optimization mining algorithm that attempts to balance exploration and exploitation. The PSCOMA makes full use of the strong global search ability of PSO and the strong local search ability of chaos optimization to obtain high quality solution. PSCOMA uses the properties of ergodicity, stochastic property, and regularity of chaos to lead particles exploration.

The webpages that have higher weight are selected to compose an initial population that is then analyzed by PSCOMA. The basic idea of PSCOMA is as follows. The proposed algorithm starts with an initial population of N particles moving around in a D -dimensional search space where each particle vector corresponds to a potential solution of the underlying problem, which is formed by subsets of webpages, starting from the webpages with higher weight that have a high probability of being different from each other. We let the i th particle at the t th iteration be used to evaluate the quality of the particle and represent candidate solution, denoted by $x_t^i = (x_t^{i,1}, x_t^{i,2}, \dots, x_t^{i,D})$, representing a possible solution. The PSCOMA operates using a fitness function that considers the weight of a webpage. Then, all of the particles repeatedly move until a termination condition is satisfied. During each iteration, the particle individual best and swarm's best positions are determined. The particle adjusts its position based on the individual experience and swarm's intelligence. Each particle is further updated using a chaos optimization algorithm. Once the PSCOMA has been run, the best particle individual constitutes the subset of webpages to be returned to the user. When the algorithm terminates, the best particle is returned as a solution.

4.3. Fitness Function. Each particle is assigned a fitness value indicating the merit of the particle. Since all the particles represent candidate feasible solutions, we use (1) to assign a fitness value to each particle.

Definition 3. Assume that w_i represents the weight of the i th webpage that corresponds to a particle, x_t^i denotes the i th particle at the t th iteration, the fitness function of particle x_t^i is given by

$$f(x_t^i) = e^{w_i}. \quad (2)$$

4.4. Formulation of the Movement of the Particle. During the search process, the particle successively adjusts its position and updates its velocity toward the global optimum using two "best" values: p_{best} and g_{best} . The p_{best} represents the best position encountered by itself denoted as $p_{i,j} = (p_{i,1}, p_{i,2}, \dots, p_{i,D})$. The g_{best} represents the best position encountered by any particle in the population denoted as

$$p_g = (p_{g,1}, p_{g,2}, \dots, p_{g,D}). \quad (3)$$

After finding these two best values, the particle updates its velocity and position at the next iteration are calculated according to the following equations:

$$v_{i,j}(t+1) = wv_{i,j}(t) + c_1r_1 [p_{\text{best}_{i,j}}(t) - x_{i,j}(t)] \quad (4)$$

$$+ c_2r_2 [g_{\text{best}_i}(t) - x_{i,j}(t)],$$

$$x_{i,j}(t+1) = x_{i,j}(t) + v_{i,j}(t+1), \quad (5)$$

where c_1 and c_2 are cognitive coefficients, r_1 and r_2 are random real numbers drawn from the interval $(0, 1)$, w is called inertia weight, $0 \leq c_1, c_2 \leq 2$, $0.8 \leq w_1, w_2 \leq 1.2$, and

$$r \in \{r_1, r_2\}, \quad r \sim U(0, 1), \quad j = 1, 2, \dots, D. \quad (6)$$

During the search process for optimum values, it is possible for a particle to escape its search space in any of the dimensions. In each iteration process, when the fitness value of each particle tends to converge or local optimum, it will lead to inertia weight increase; while the fitness value of each particle scattered, it will be easy to make the inertia weight decreases. Therefore, in order to maintain the value of inertia weight range in a reasonable range, (4) should make proper adjustments to the specific implementation is as follows:

$$v_{i,j}(t+1) = w' v_{i,j}(t) + c_1 r_1 [p_{\text{best},j}(t) - x_{i,j}(t)] + c_2 r_2 [g_{\text{best}_i}(t) - x_{i,j}(t)],$$

$$w' = \begin{cases} w_{\max} - \frac{w \times (f - f_{\min})}{f_{\max} - f_{\min}}, & f \leq \bar{f}, \\ w_{\min} + \frac{w \times (f - f_{\min})}{f_{\max} - f_{\min}}, & f > \bar{f}. \end{cases} \quad (7)$$

4.5. Chaotic Local Search in PSO. PSCOMA uses chaotic local search methods during the search process; namely, the chaotic map is used to control the value of parameters in the velocity updating equation. The specific implementations are as follows.

Step 1. Each of the individual x_t^i maps to the interval $[0, 1]$, namely,

$$s_t^j = \frac{x_t^j - x_{\min,j}}{x_t^j - x_{\max,j}}, \quad (8)$$

where $x_{\min,j}$ and $x_{\max,j}$ are, respectively, the lower and upper bounds of the j th dimensional variable, $t = 0, i = 1, 2, \dots, n, j = 1, 2, \dots, D$.

Step 2. Use the logistic equation for chaotic iteration so as to get chaotic gene series:

$$s_{t+1}^j = 4 \times s_t^j \times (1 - s_t^j), \quad j = 1, 2, \dots, D. \quad (9)$$

Step 3. Convert the chaos variables s_{t+1}^j into decision variables x_{t+1}^j :

$$x_{t+1}^j = x_{\min,j} + s_{t+1}^j (x_{\max,j} - x_{\min,j}), \quad j = 1, 2, \dots, D. \quad (10)$$

Step 4. Evaluate the new solution on the basis of decision variables x_{t+1}^j . If the new solution is better than the initial solution, the new solution will be as an optimization result of chaos. Otherwise, go to Step 2, $t = t + 1$.

4.6. The Process of PSCOMA. The process of PSCOMA consists of the following seven steps.

Step 1. Data preparation: training, validation, and test sets are represented, respectively.

Step 2. Particle initialization and PSCOMA parameters setting: the webpages that have higher weight are selected to compose an initial population, which N particles moves around in a D -dimensional search space. Set the PSCOMA parameters including the number of iterations MG , the number of particles N , particle dimension D , inertia weight, cognitive coefficients, and $t = 0$.

Step 3. Randomly generate the position and velocity of particles.

Step 4. Evaluate the fitness of each particle and store the current position of each particle and the adaptation degree of each particle in p_{best} and store the best individual fitness value of the position and fitness value of p_{best} in g_{best} .

Step 5. Update the velocity and position of each particle using (4) and (5).

Step 6. Perform the following chaotic local search for the best particles in population and update its p_{best} and g_{best} .

Step 6.1. Each of the individual x_t^i maps to the interval $[0, 1]$; namely,

$$s_t^j = \frac{x_t^j - x_{\min,j}}{x_t^j - x_{\max,j}}, \quad i = 1, 2, \dots, n, \quad j = 1, 2, \dots, D. \quad (11)$$

Step 6.2. Use the logistic equation for chaotic iteration, so as to get chaotic gene series:

$$s_{t+1}^j = 4 \times s_t^j \times (1 - s_t^j), \quad j = 1, 2, \dots, D. \quad (12)$$

Step 6.3. Convert the chaos variables s_{t+1}^j into decision variables x_{t+1}^j :

$$x_{t+1}^j = x_{\min,j} + s_{t+1}^j (x_{\max,j} - x_{\min,j}), \quad j = 1, 2, \dots, D. \quad (13)$$

Step 6.4. Evaluate the new solution on the basis of decision variables x_{t+1}^j . If fitness of the the new individual is larger than the old one, then the new individual (solution) will be an optimization result of chaos. Otherwise, return Step 6.2.

Step 7. Stop condition checking: if $t > MG$, end the training and testing procedure, otherwise go to Step 2 to begin the next iteration, $t = t + 1$.

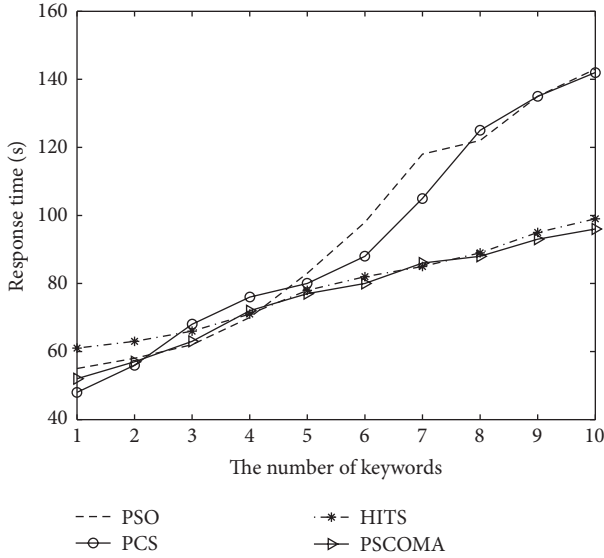


FIGURE 1: The response time in different number of keywords ($m = 10000$).

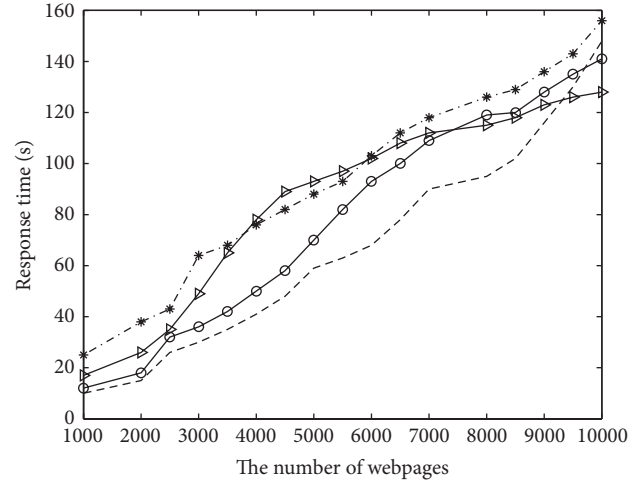


FIGURE 3: The response time in different number of webpages ($n = 5$).

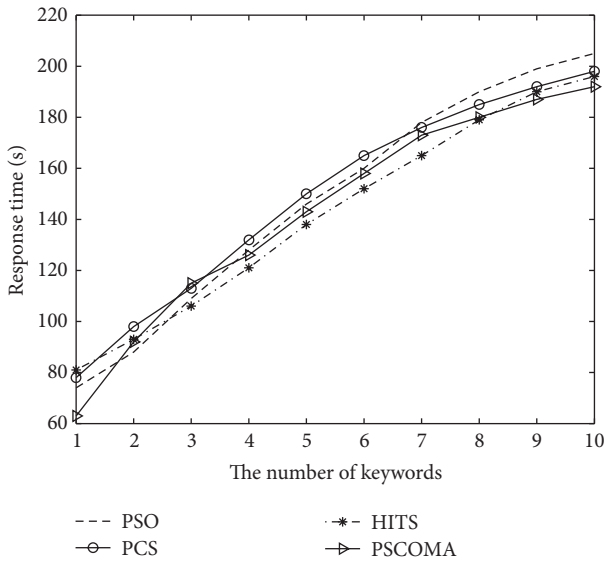


FIGURE 2: The response time in different number of keywords ($m = 20000$).

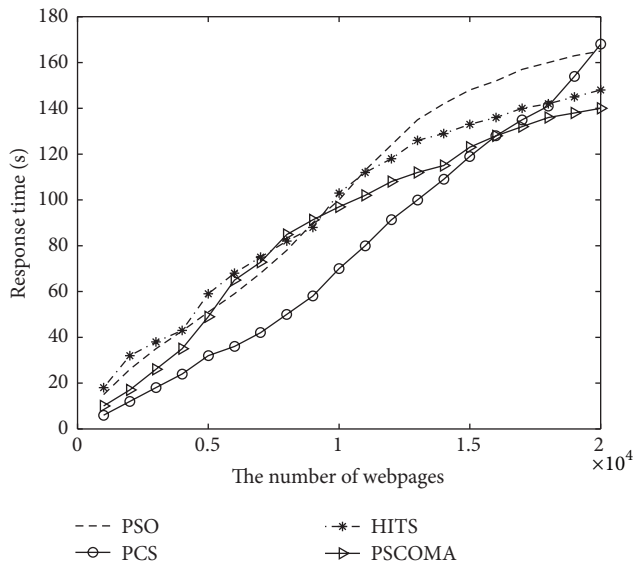


FIGURE 4: The response time in different number of webpages ($n = 6$).

5. Simulation Experiment and Result Analysis

In this section, we present the experimental results which include the algorithm parameter configuration and comparative performances with other algorithms. The platform for conducting the experiments are a PC with Intel Core 2 Duo CPU E6300 processor, 1.86 GHz. All programs are coded in C# language under a Windows NT platform. The numerical results are the means of outcomes from 50 independent runs of the algorithms.

The experimental results compare the PSCOMA with several typical web mining algorithms including the PSO, PCS, and HITS algorithms. We experimented with a few queries

on six popular search engines, namely, AltaVista, Netscape, Excite, Google, Direct Hit, and Yahoo. We denote the number of webpages and keywords in m and n . This paper will be compared from the important aspects of web search such as response time, execution time, precision and recall. Heuristic algorithms have different configuration parameters, which may affect the results. In order to reflect the fairness of algorithms, this paper will take the same configuration

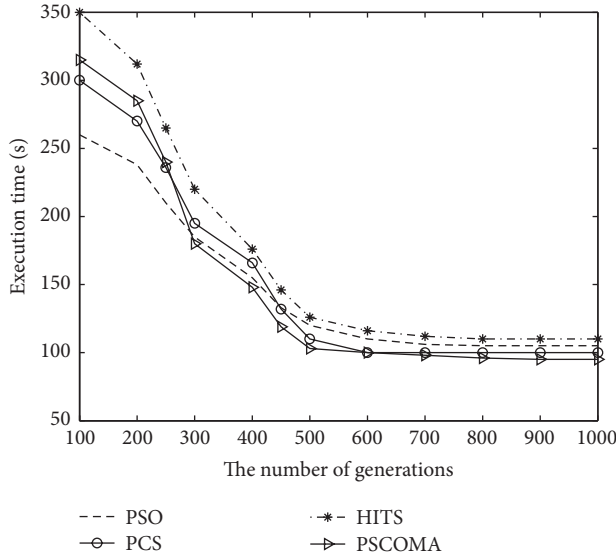


FIGURE 5: The execution time in different number of generations ($m = 10000, n = 5$).

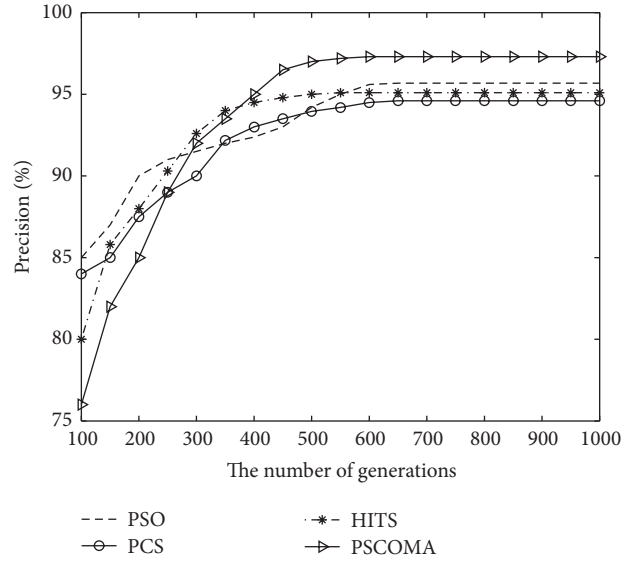


FIGURE 7: The precision in different number of generations ($m = 10000, n = 5$).

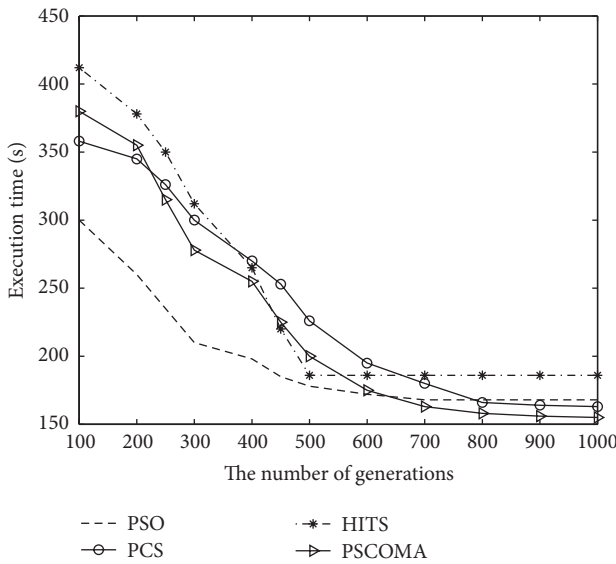


FIGURE 6: The execution time in different number of generations ($m = 20000, n = 6$).

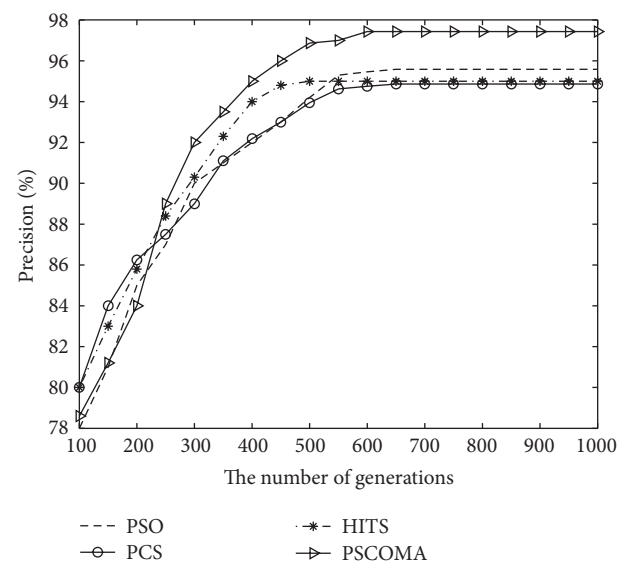


FIGURE 8: The precision in different number of generations ($m = 20000, n = 6$).

parameters in [11]. The specific configuration parameters are as follows:

$$\begin{aligned} N = 40, \quad MG = 1000, \quad r_1 = r_2 = 1, \quad c_1 = c_2 = 2, \\ w_{\max} = 1, \quad w_{\min} = 0.3. \end{aligned} \quad (14)$$

Figures 1 and 2 show the experimental results of the response time in different number of keywords. Figures 3 and 4 show the experimental results of the response time in different number of keywords. Figures 5 and 6 show the execution time in different number of generations. Figures 7 and 8 show the precision in different number of generations. Figures 9 and 10 show the recall in different number of

generations. Figure 11 shows the contrast curve of recall and precision.

As we can see from Figures 1–11, the proposed algorithm PSCOMA outperforms PSO, PCS, and HITS algorithms. In the aspect of response time, PSCOMA is faster than PCS and PSO by 28.6%, indicating that PSCOMA has fast response speed. When increasing the number of keywords, the response time curve of PSCOMA shows to be the most stable. In the aspect of execution time, PSCOMA spends the least time than other algorithms. In addition, when the number of webpages or keywords continually increases, PSCOMA increases the magnitude is the smallest. The simulation results illustrate that the response time and execution

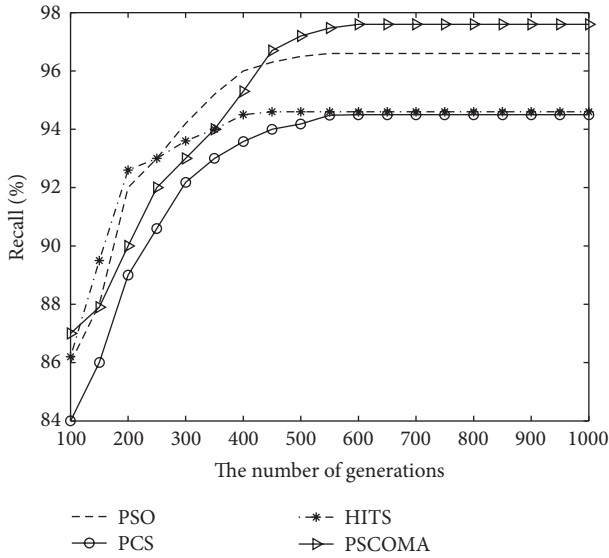


FIGURE 9: The recall in different number of generations ($m = 10000$, $n = 5$).

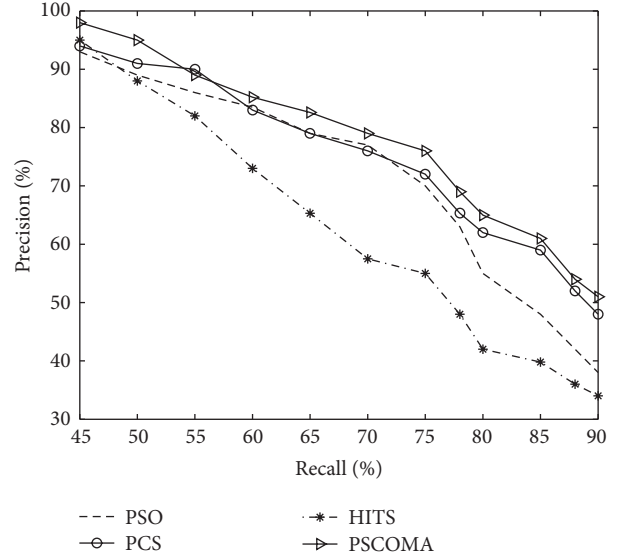


FIGURE 11: The contrast curve of recall and precision ($m = 20000$, $n = 6$).

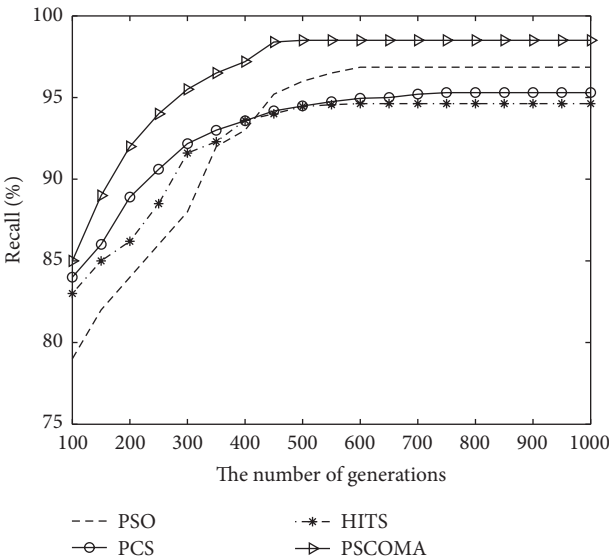


FIGURE 10: The recall in different number of generations ($m = 20000$, $n = 6$).

time of the proposed algorithm are better than those obtained by others. In the aspects of precision and recall, the precision and recall of PSCOMA have performed the best, where the highest precision is close to 97.2% and the highest recall rate is close to 97.8%.

From the experimental results in the aspects of response time, execution time, precision, and recall, we can conclude that PSCOMA is more satisfactory than the PSO, PCS, and HITS algorithms.

6. Conclusions

To prevent the user from being overwhelmed by a large number of redundant and useless or uninteresting information, approaches are needed to provide for data mining. In this paper, we have presented a survey on web mining involving chaos optimization and particle swarm optimization. This paper is the first full use of the strong global search ability of PSO and the strong local search ability of chaos optimization for solving web search and has gained a higher quality solution in the aspects of response time, execution time, precision, and recall. In the future, we will extend the PSCOMA algorithm to other domains of data mining and investigate the possibility of reaching closer optimum by improving chaotic local search.

Acknowledgments

This research work was supported by the Hubei Key Laboratory of Intelligent Wireless Communications (Grant no. IWC2012007) and the Special Fund for Basic Scientific Research of Central Colleges, South-Central University for Nationalities (Grant no. CZY11005). The authors gratefully acknowledge the helpful comments and suggestions of the reviewers, which have improved the presentation.

References

- [1] N. Gandal, "The dynamics of competition in the internet search engine market," *International Journal of Industrial Organization*, vol. 19, no. 7, pp. 1103–1117, 2001.
- [2] Y. Shang and L. Li, "Precision evaluation of search engines," *World Wide Web: Internet and Web Information Systems*, vol. 5, pp. 159–173, 2002.
- [3] M. M. Sufyan Beg and C. P. Ravikumar, "Measuring the Quality of Web Search Results," in *Proceedings of the 6th Joint Conference*

- on *Information Sciences (JCIS '02)*, pp. 324–328, Durham, NC, USA, March 2002.
- [4] M. R. Morris, J. Teevan, and S. Bush, “Enhancing collaborative web search with personalization: groupization, smart splitting, and group hit-highlighting,” in *Proceedings of the ACM Conference on Computer Supported Cooperative Work (CSCW '08)*, pp. 481–484, San Diego, Calif, USA, November 2008.
- [5] J. Sun, H. Zeng, H. Liu, Y. Lu, and Z. Chen, “CubeSVD: a novel approach to personalized web search,” in *Proceedings of the 14th International WorldWide Web Conference*, pp. 382–390, Chiba, Japan, 2005.
- [6] A. Mahmood, “Dynamic replication of web contents,” *Science in China, Series F*, vol. 50, no. 6, pp. 811–830, 2007.
- [7] P.-Y. Yin and Y.-M. Guo, “Optimization of multi-criteria website structure based on enhanced tabu search and web usage mining,” *Applied Mathematics and Computation*, vol. 219, pp. 11082–11095, 2013.
- [8] N. Turajlić and S. Nešković, “Variable Neighborhood Search and Tabu Search for the Web Service Selection Problem,” *Electronic Notes in Discrete Mathematics*, vol. 39, pp. 177–184, 2012.
- [9] L.-C. Chen, C.-J. Luh, and C. Jou, “Generating page clippings from web search results using a dynamically terminated genetic algorithm,” *Information Systems*, vol. 30, no. 4, pp. 299–316, 2005.
- [10] A. Spink, B. J. Jansen, C. Blakely, and S. Koshman, “A study of results overlap and uniqueness among major Web search engines,” *Information Processing and Management*, vol. 42, no. 5, pp. 1379–1391, 2006.
- [11] A. Mahmood, “Replicating web contents using a hybrid particle swarm optimization,” *Information Processing and Management*, vol. 46, no. 2, pp. 170–179, 2010.
- [12] M. R. Herrera, E. S. de Moura, M. Cristo, T. P. Silva, and A. S. da Silva, “Exploring features for the automatic identification of user goals in web search,” *Information Processing and Management*, vol. 46, no. 2, pp. 131–142, 2010.
- [13] J. Ling and P. Van Schaik, “The influence of font type and line length on visual search and information retrieval in web pages,” *International Journal of Human Computer Studies*, vol. 64, no. 5, pp. 395–404, 2006.
- [14] I. F. Moawad, H. Talha, E. Hosny et al., “Agent-based web search personalization approach using dynamic user profile,” *Egyptian Informatics Journal*, vol. 13, pp. 191–198, 2012.
- [15] D. Zhang and Y. Dong, “A novel Web usage mining approach for search engines,” *Computer Networks*, vol. 39, no. 3, pp. 303–310, 2002.
- [16] A. H. Keyhanipour, M. Piroozmand, and K. Badie, “A GP-adaptive web ranking discovery framework based on combinative content and context features,” *Journal of Informetrics*, vol. 3, no. 1, pp. 78–89, 2009.
- [17] J. Bar-Ilan, “Comparing rankings of search results on the Web,” *Information Processing and Management*, vol. 41, no. 6, pp. 1511–1519, 2005.
- [18] Y. Lv, L. Sun, J. Zhang, J.-Y. Nie, W. Chen, and W. Zhang, “An iterative implicit feedback approach to personalized search,” in *Proceedings of the 21st International Conference on Computational Linguistics and 44th Annual Meeting of the Association for Computational Linguistics (COLING/ACL '06)*, pp. 585–592, Sydney, Australia, July 2006.
- [19] C.-C. Lin, “Optimal Web site reorganization considering information overload and search depth,” *European Journal of Operational Research*, vol. 173, no. 3, pp. 839–848, 2006.
- [20] H. Qahri Saremi, B. Abedin, and A. Meimand Kermani, “Website structure improvement: quadratic assignment problem approach and ant colony meta-heuristic technique,” *Applied Mathematics and Computation*, vol. 195, no. 1, pp. 285–298, 2008.
- [21] C.-G. Fei and Z.-Z. Han, “A novel chaotic optimization algorithm and its applications,” *Journal of Harbin Institute of Technology (New Series)*, vol. 17, no. 2, pp. 254–258, 2010.
- [22] B. Alatas and E. Akin, “Chaotically encoded particle swarm optimization algorithm and its applications,” *Chaos, Solitons and Fractals*, vol. 41, no. 2, pp. 939–950, 2009.

Research Article

Low-Complexity Compression Algorithm for Hyperspectral Images Based on Distributed Source Coding

Yongjian Nian,¹ Mi He,² and Jianwei Wan¹

¹ College of Electronic Science and Engineering, National University of Defense Technology, Changsha, Hunan 410073, China

² School of Biomedical Engineering, Third Military Medical University and Chongqing University, Chongqing 400038, China

Correspondence should be addressed to Yongjian Nian; yongjian_nian@163.com

Received 17 July 2013; Revised 20 August 2013; Accepted 20 August 2013

Academic Editor: Gelan Yang

Copyright © 2013 Yongjian Nian et al. This is an open access article distributed under the Creative Commons Attribution License, which permits unrestricted use, distribution, and reproduction in any medium, provided the original work is properly cited.

A low-complexity compression algorithm for hyperspectral images based on distributed source coding (DSC) is proposed in this paper. The proposed distributed compression algorithm can realize both lossless and lossy compression, which is implemented by performing scalar quantization strategy on the original hyperspectral images followed by distributed lossless compression. Multilinear regression model is introduced for distributed lossless compression in order to improve the quality of side information. Optimal quantized step is determined according to the restriction of the correct DSC decoding, which makes the proposed algorithm achieve near lossless compression. Moreover, an effective rate distortion algorithm is introduced for the proposed algorithm to achieve low bit rate. Experimental results show that the compression performance of the proposed algorithm is competitive with that of the state-of-the-art compression algorithms for hyperspectral images.

1. Introduction

Hyperspectral images compression has received more and more attention in the field of remote sensing. Different from panchromatic images, hyperspectral images are three-dimensional data cube. The spectral resolution of hyperspectral images has achieved nanometer grade, which is widely used in geological survey, environment observing, and military scout. With the incessant increase of the spectral and spatial resolution, the data volume of hyperspectral images expands rapidly, which brings heavy pressure for storage and transmission of hyperspectral images. With respect to the onboard hyperspectral images compression, there is a serious contradiction between data acquirement and transmission. Lossless compression may preserve the image information perfectly with a very low compression ratio, while lossy compression may generate images at different quality levels according to the practical requirements. Therefore, it is necessary to develop an efficient algorithm for onboard hyperspectral images compression, which can realize both lossless and lossy compression.

Onboard compression systems exhibit limited storage memory, computational capacity, and power consumption. Such systems prefer compression algorithms that have an excellent compression performance, a low complexity, and resiliency against errors that are caused by a bad channel environment. The most classical lossy compression methods for hyperspectral images are of a three-dimensional approach, in which some transform (e.g., a wavelet transform, discrete cosine transform, or Karhunen-Loeve transform) is used for spectral decorrelation followed by a two-dimensional transform for spatial decorrelation [1–3]. Although this method and other methods can achieve good performance, their complexity is too high and the memory requirement is too large to be implemented onboard. In general, lossless compression algorithms for hyperspectral images are based on spectral linear prediction. Magli also introduced Kalman filter to implement the spectral linear prediction [4]. Tang et al. introduced ground classification to improve the lossless compression performance [5], which has high encoder complexity and poor error resilience. Distributed source coding (DSC) has received increased attention in the past few years

and has provided separate encoding and joint decoding, which moves the computational complexity from the encoder to the decoder, thus meeting the requirements of onboard compression [6, 7]. The basis of distributed lossless compression is the Slepian-Wolf theory [8], while that of distributed lossy compression is the Wyner-Ziv theory [9]. Compression algorithms based on DSC can be carried out by means of binary error-correcting codes or multilevel coset codes. At present, some DSC compression algorithms have been proposed gradually. For the aspect of binary error-correcting codes, Pan et al. proposed a low-complexity DSC algorithm based on the discrete cosine transform; the experimental results demonstrated that the performance of the proposed algorithm is comparable to that of the distributed algorithm, that is, based on informed quantization [10]. Tang et al. proposed a distributed lossy compression algorithm based on spectral prediction and wavelet transform that computed the syndrome of each bitplane by using LDPC (low density parity check) code, the difficulty of which lies in estimating the correlation between bitplanes quickly and accurately [11]. Cheung et al. studied the problems of correlation estimation subject to complexity constraints and its impact on coding efficiency [12]. The resulting model-based approach for lossy compression of hyperspectral images achieved both accurate estimation results and good compression performance. For the aspect of multilevel coset codes, Magli et al. proposed s-DSC and v-DSC [13]. On the basis of s-DSC, Abrardo et al. proposed DSC-based lossless compression algorithms, called A1, A2, and A3, providing both low complexity and error resilience [14]. Abrardo et al. also proposed a DSC lossy compression algorithm based on informed quantization, which provides competitive lossy compression performance [15]. Nian et al. proposed a lossless and near lossless compression algorithm based on DSC, which only obtains excellent compression performance at high bit rate [16, 17]. At present, although the distributed compression algorithm has low encoder complexity, its compression performance is lower than that of traditional classical algorithms. Furthermore, existed distributed compression algorithm can only realize lossless compression. In order to satisfy the different quality requirements of onboard hyperspectral images, this paper presents a low-complexity compression algorithm for hyperspectral images based on DSC, which can perform both lossless and lossy compression. Experimental results demonstrate the effectiveness of the proposed algorithm, making it suitable for onboard compression.

This paper is organized as follows: Section 2 describes the proposed distributed lossless compression; Section 3 presents the proposed distributed lossy compression algorithm of hyperspectral images; experimental results are demonstrated in Section 4; and the conclusions are given in Section 5.

2. Distributed Lossless Compression

2.1. Introduction of DSC. DSC introduces the coset partitioning manner to realize lossless compression. The data space is divided into a great deal of subsets with no intersection between arbitrary two subsets, and each pixel must belong

to one of the subsets. Let Ω be the data space, which is divided into several subsets with the number of Z , and the aforementioned description can be expressed as

$$\begin{aligned}\Omega &= C_1 \cup C_2 \cdots \cup C_z, \\ C_i \cap C_j &= \Phi (i \neq j),\end{aligned}\tag{1}$$

where Φ is an empty aggregate. DSC encoder realizes data compression only by means of binary error-correcting codes or multilevel coset codes. Binary error-correcting codes demonstrate excellent performance by decomposing the source into a series of bitplanes and compressing each bitplane with Turbo, LDPC, Trellis, or other channel codes. Because binary error-correcting codes neglect the correlation between bitplanes, the compression performance is not satisfactory. Generally, the compression performance of multilevel coset codes is better than that of binary error-correcting codes with a much lower complexity [13]. Suppose the source is represented on n bits; then the multilevel coset codes adopt the principle of (n, k) linear codes, partitioning the set of 2^n possible values into 2^r ($r = n - k$) cosets with 2^k elements in each coset, and the Euclidian distance between the adjacent elements of each coset is 2^r . A Slepian-Wolf encoder only needs to transmit the label of the coset to which each pixel belongs to the decoder; the decoder then employs the correlated side information to reconstruct the pixel in the corresponding coset indexed by the received coset label.

2.2. Distributed Lossless Compression. A DSC encoder can compress each source only when an exact knowledge of the correlation is available at the encoder. However, in many practical applications, correlation information may not be available beforehand. Therefore, it is necessary to establish an efficient correlation model subject to the complexity constraints to construct high-quality side information. As we know, the spectral curves of hyperspectral images are nonlinear, and thus, a nonlinear model is suitable for the correlation estimation of hyperspectral images. Unfortunately, nonlinear model of hyperspectral images is difficult to be established. Because the current band is typically correlated with a few previous bands, multilinear regression model can be introduced to construct the high-quality side information of the current band. For the algorithm proposed in this paper, each band of the hyperspectral images is divided into nonoverlapping blocks with a size of $N \times N$. Each block is processed independently, which offers several advantages: first, it can adapt to the local spatial features of a hyperspectral image; second, it can provide error resilience; and finally, it can be easily parallelized. Let $x_{k,i,j}$ denote the pixel of the current block in i th line, j th pixel, and k th band, with $k = 1, 2, \dots, L$ and $i, j = 1, 2, \dots, N$. The pixel $x_{k,i,j}$ is predicted linearly from the decoded pixels $x_{k-1,i,j}, x_{k-2,i,j}, \dots, x_{k-P,i,j}$ of the previous blocks to make the constructed side information as similar as possible to $x_{k,i,j}$ with respect to the standard of minimum mean-squared error. Let μ_k be the average value of the current block, and let μ_{k-l} ($l = 1, 2, \dots, P$) be the average

value of the colocated block in the l th band. The constructed side information of the current block is then expressed as

$$\widehat{x}_{k,i,j} = \sum_{l=1}^P \alpha_l (x_{k-l,i,j} - \mu_{k-l}) + \mu_k, \quad i, j = 1, 2, \dots, N, \quad (2)$$

where $\alpha_k = [\alpha_1, \alpha_2, \dots, \alpha_P]^T$ are the prediction coefficients minimizing the energy of the prediction errors which can be written as

$$(\mathbf{A}\alpha_k - \mathbf{B})^T (\mathbf{A}\alpha_k - \mathbf{B}), \quad (3)$$

where

$$\mathbf{A} = \begin{bmatrix} x_{k-1,1,1} - \mu_{k-1} & \cdots & x_{k-P,1,1} - \mu_{k-P} \\ \vdots & \ddots & \vdots \\ x_{k-1,N,N} - \mu_{k-1} & \cdots & x_{k-P,N,N} - \mu_{k-P} \end{bmatrix}, \quad (4)$$

$$\mathbf{B} = \begin{bmatrix} x_{k,1,1} - \mu_k \\ \vdots \\ x_{k,N,N} - \mu_k \end{bmatrix}.$$

The optimal α_k can be computed as follows:

$$\alpha_k = \begin{bmatrix} r_{k-1,k-1} & \cdots & r_{k-P,k-1} \\ \vdots & \ddots & \vdots \\ r_{k-1,k-P} & \cdots & r_{k-P,k-P} \end{bmatrix}^{-1} \begin{bmatrix} r_{k,k-1} \\ \vdots \\ r_{k,k-P} \end{bmatrix}, \quad (5)$$

where

$$r_{k,k-l} = \sum_{i=1}^N \sum_{j=1}^N (x_{k,i,j} - \mu_k)(x_{k-l,i,j} - \mu_{k-l}). \quad (6)$$

The corresponding errors are written as

$$e_{k,i,j} = x_{k,i,j} - \widehat{x}_{k,i,j}. \quad (7)$$

It should be noted that the correct reconstruction can be obtained only when the Euclidian distance between the adjacent elements in the same coset is twice as large as the maximum absolute error, which can be expressed as

$$2^{r-1} > \max_{i,j=1,2,\dots,N} (|e_{k,i,j}|). \quad (8)$$

Hence, the corresponding rate of the block is given as

$$r = \left\lceil \log_2 \left(\max_{i,j=1,2,\dots,N} (|e_{k,i,j}|) \right) \right\rceil + 2. \quad (9)$$

3. Distributed Lossy Compression

3.1. Scalar Quantization Strategy. Compared with distributed lossless compression, distributed lossy compression employs quantization strategy to quantize the original hyperspectral images followed by distributed lossless compression, which can introduce distortion for the original hyperspectral images. Therefore, the performance of quantization strategy is crucial for distributed lossy compression. In order to keep

the encoder low complexity, practical scalar quantization manner is performed on each block. Let q_k denote the quantizer step size of the current block in the k th band. The quantized values of the current block and its side information are given as

$$y_{k,i,j} = \text{round} \left(\frac{x_{k,i,j}}{q_k} \right), \quad \bar{y}_{k,i,j} = \text{round} \left(\frac{\widehat{x}_{k,i,j}}{q_k} \right). \quad (10)$$

Let $\widehat{x}_{k,i,j}$ be the reconstructed value of $x_{k,i,j}$, and $\widehat{\mu}_k$ is the average value of the corresponding reconstructed block in the k th band. The side information of the current block is constructed by the reconstructed version of the corresponding blocks in the previous bands, which is written as

$$\bar{x}_{k,i,j} = \sum_{l=1}^P \widehat{\alpha}_l (\widehat{x}_{k-l,i,j} - \widehat{\mu}_{k-l}) + \widehat{\mu}_k, \quad (11)$$

where $\widehat{\alpha}_k (\widehat{\alpha}_1, \widehat{\alpha}_2, \dots, \widehat{\alpha}_P)$ are the quantized versions of α_k . As aforementioned, in order to ensure the correct reconstruction, the following condition must be satisfied:

$$|y_{k,i,j} - \bar{y}_{k,i,j}| < 2^{R_k-1}; \quad (12)$$

thus, the optimal quantized step can be computed as follows:

$$q_k = \left\lceil \frac{\max_{i,j=1,2,\dots,N} |\bar{e}_{k,i,j}|}{2^{R_k-1}} \right\rceil + c, \quad (13)$$

where

$$\bar{e}_{k,i,j} = x_{k,i,j} - \bar{x}_{k,i,j} \quad (14)$$

and c is a positive integer. For most blocks, the value of c equals one. If any block fails to satisfy (12), the value of c is to add one every time until (12) is satisfied. The final output bit rate can be computed as

$$R_k = \left\lceil \log_2 \left[\frac{\max_{i,j=1,2,\dots,N} |\bar{e}_{k,i,j}|}{q_k - c} \right] \right\rceil + 1. \quad (15)$$

It should be noted that the quantization strategy introduces no loss for the original hyperspectral images when $q_k = 1$; in this case, the distributed lossy compression algorithm turns to the distributed lossless compression algorithm.

3.2. Rate Distortion for Low Bit-Rate Compression. As can be seen from (9), the minimum value of the coding rate is 2; in other words, the bit rate acquired by the above quantization algorithm cannot be lower than 2, which can be regarded as a near lossless compression. In order to achieve low bit-rate compression, we perform an effective rate-distortion (RD) algorithm on the proposed compression algorithm to obtain the low bit rate. For a certain block, if its energy of prediction errors is low, which means that the prediction performance of this block is perfect, the encoding process of this block may be neglected, otherwise, the encoding process must be executed

[18]. This working manner provides an appropriate tradeoff between the distortion introduced by neglecting the encoding process and the corresponding rate saving. In practice, the energy of the prediction errors of the block which is shown as (16) is used to determine whether the block should be neglected:

$$D = \sum_{i=1}^N \sum_{j=1}^N e_{k,i,j}^2. \quad (16)$$

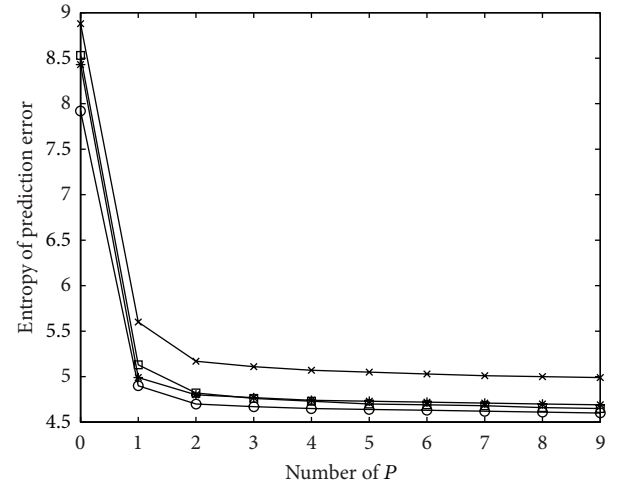
If the distortion D is higher than the threshold, which means that the prediction error has too much energy, neglecting the encoding process will result in a poor compression performance. On the contrary, if D is below the threshold, neglecting the encoding process of this block will have limited impact on the compression performance. In this situation, the prediction errors of this block are set to be zero and only the predictor parameters are written in the encoding stream. By setting different values of the threshold, we can change the output bit-rate flexibly.

4. Results and Discussion

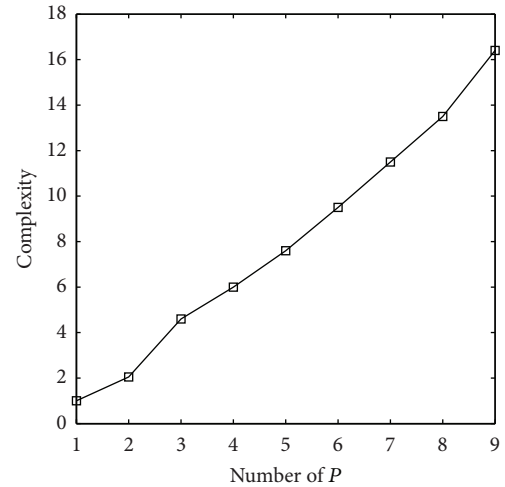
Hyperspectral images acquired by the AVIRIS sensor in 1997 were employed in our experiments. AVIRIS was devised by the JPL (jet propulsion laboratory) of NASA (National Aeronautics and Space Administration, USA), and it covers the 0.41–2.5 μm spectrum range in 10 nm bands. This instrument contains four spectrometers that are flown at a 20 km altitude with a 17 m spatial resolution. The four scenes are Cuprite, Jasper Ridge, Lunar Lake, and Low Altitude, which are widely used for compression testing and the evaluation of hyperspectral images. The radiance data of the above four scenes were represented in 16 bits; each image has 512 lines, 224 bands, and 512 pixels/line. In this paper, the four scenes with image size of $256 \times 256 \times 224$ are used in our experiment.

The proposed algorithm can realize both lossless and lossy compression. We first evaluated the lossless compression performance of the proposed algorithm with several existed classical algorithms. In general, the multiband linear prediction model is expected to improve the quality of side information; however, it also increases the computational complexity. Therefore, a reasonable number P should be typically selected that guarantees both a high quality for the constructed side information and a low complexity for the multilinear regression model. Figure 1 shows the prediction performance and the computational complexity with various values of P , where $P = 0$ refers to the average entropy over all the bands for each scene. As shown in Figure 1, the multilinear regression model using two previous bands provides both high prediction performance and low computational complexity. Note that as the number of P increases, the computational complexity increases rapidly while the prediction gain tends to decrease because bands further away from the current band in the wavelength domain are less correlated. Therefore, the optimal number of P is selected to be 2.

For the proposed algorithm, the block size is also influential for the compression performance. We use bpppb (bit per



(a) Comparison of the entropy of prediction error



(b) Comparison of the complexity

FIGURE 1: Prediction performance and complexity with various P values.

pixel per band) to measure the lossless compression performance. Figure 2 gives the lossless compression performance with different block size ($N = 8, 16, 32, 64, 128, 256$). It can be seen that the best compression performance is obtained when $N = 16$. With the increase of the N number, the compression performance decreases rapidly. For the proposed algorithm, small block can make full use of the spatial correlation, which is beneficial to achieve better compression performance. However, small block size also introduces large additive information, such as predictive coefficients and average value of corresponding block. Although large block introduces little additive information, it cannot make full use of the spatial correlation, which leads to a bad compression performance.

The proposed distributed lossless compression algorithm is compared with several classical algorithms, such as JPEG-LS, 3D CALIC [19], KSP (kalman spectral prediction)

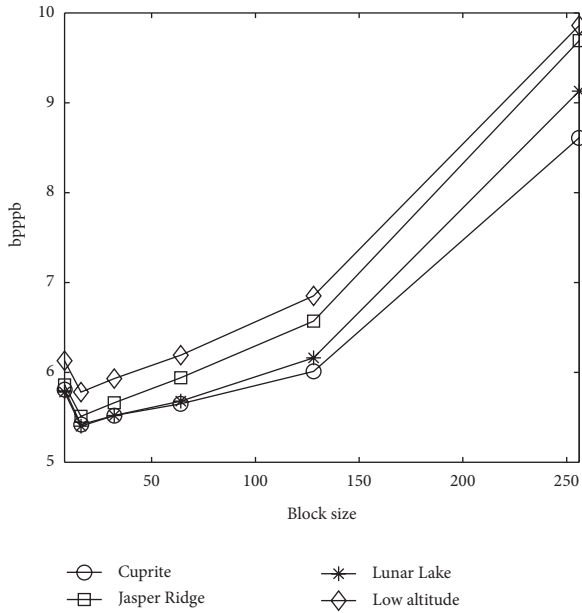


FIGURE 2: Lossless compression performance with different block size.

[4], LUT (look-up table) [20], s-DSC [13], and A1 [14], which are shown in Table 1. JPEG-LS is an excellent lossless compression standard. 3D CALIC, KSP, and LUT are three traditional classical algorithms. s-DSC and A1 are two classical distributed lossless compression algorithms. As can be seen, JPEG-LS performs poorly due to the lack of spectral correlation elimination. LUT has the highest compression performance, and KSP also has the excellent performance by using Kalman filter to eliminate the spectral correlation. The performance of 3D CALIC is much better than JPEG-LS but worse than KSP. s-DSC is only better than JPEG-LS, and A1 is much better than s-DSC. The performance of the proposed algorithm (DSC-lossless) is slightly better than A1. However, there is also a gap between the proposed algorithm and the above two traditional algorithms.

The complexity of the proposed algorithms has been compared with that of existing algorithms, which are reported in Table 2 and are normalized with respect to the complexity of JPEG-LS. As can be seen, LUT is slightly more complex than JPEG-LS; 3D CALIC and KSP are both more complex than JPEG-LS. Because only LSBs are transmitted without any entropy coding of the predictive errors, the proposed DSC-Lossless has very low encoder complexity, even lower than JPEG-LS, while providing better compression performance than the other two distributed lossless compression algorithms. Despite that the complexity of s-DSC is significantly small, which is slightly higher than DSC-lossless, the performance of s-DSC is much worse than DSC-lossless.

In this paper, we use bpppb and signal to noise ratio (SNR) to measure the lossy compression performance. Figure 3 gives the comparison of lossy compression performance of various algorithms with different bit rate, where DSC-lossy is the proposed algorithm and the other algorithms are the classical algorithms for hyperspectral images compression. JPEG2000

TABLE 1: Comparison of lossless compression performance of various algorithms.

	Cuprite	Jasper Ridge	Lunar Lake
JPEG-LS	7.62	8.16	7.55
3D CALIC	5.18	5.14	5.19
KSP	4.88	4.95	4.89
LUT	4.65	4.95	4.71
s-DSC	6.08	6.25	6.23
A1	5.50	5.60	5.51
DSC-lossless	5.42	5.51	5.40

TABLE 2: Comparison of complexity of various algorithms.

Algorithm	Complexity
JPEG-LS	1
LUT	1.14
3D CALIC	28.4
KSP	25.2
s-DSC	0.89
DSC-lossless	0.78

is an excellent compression standard which is primary used for still image compression. DWT-JPEG2000 is also a popular compression algorithm which removes spectral redundancy by using a 9-7 biorthogonal wavelet transform followed by JPEG2000 for spatial compression. Similar with DWT-JPEG2000, KLT-JPEG2000 removes spectral redundancy by using KLT transform followed by JPEG2000 for spatial compression. For the hyperspectral images compression, it is very important to remove its spectral correlation. As can be seen from Figure 3, despite JPEG2000 has the perfect compression performance for still images, its compression performance for hyperspectral images is the worst because it do not remove the spectral correlation. KLT-JPEG2000 has the best compression performance due to the excellent performance of removing spectral correlation. Note that because the filter coefficients of DWT are fixed, its performance of removing spectral correlation is moderate. DWT-JPEG2000 employs DWT to remove the spectral correlation, and the performance of DWT-JPEG2000 is better than that of JPEG2000 while worse than that of KLT-JPEG2000. It should be noted that the performance of the proposed DSC-lossy is comparative to that of DWT-JPEG2000. The performance of DSC-lossy is worse than that of DWT-JPEG2000 at low bit rate while better than that of DWT-JPEG2000 at high bit rate; this is because that the multilinear regression model has serious error accumulation at low bit rate, while at high bit rate this disadvantage can be neglected.

In terms of encoder complexity, the results are reported in Table 3 and normalized with respect to the complexity of JPEG2000. The complexity of KLT-JPEG2000 is the highest, although KLT-JPEG2000 provides the best compression performance. DWT-JPEG2000 has the modest complexity, which is faster than that of KLT-JPEG2000 but lower than that of JPEG2000, but there is a performance gap with KLT-JPEG2000. The proposed algorithm has similar

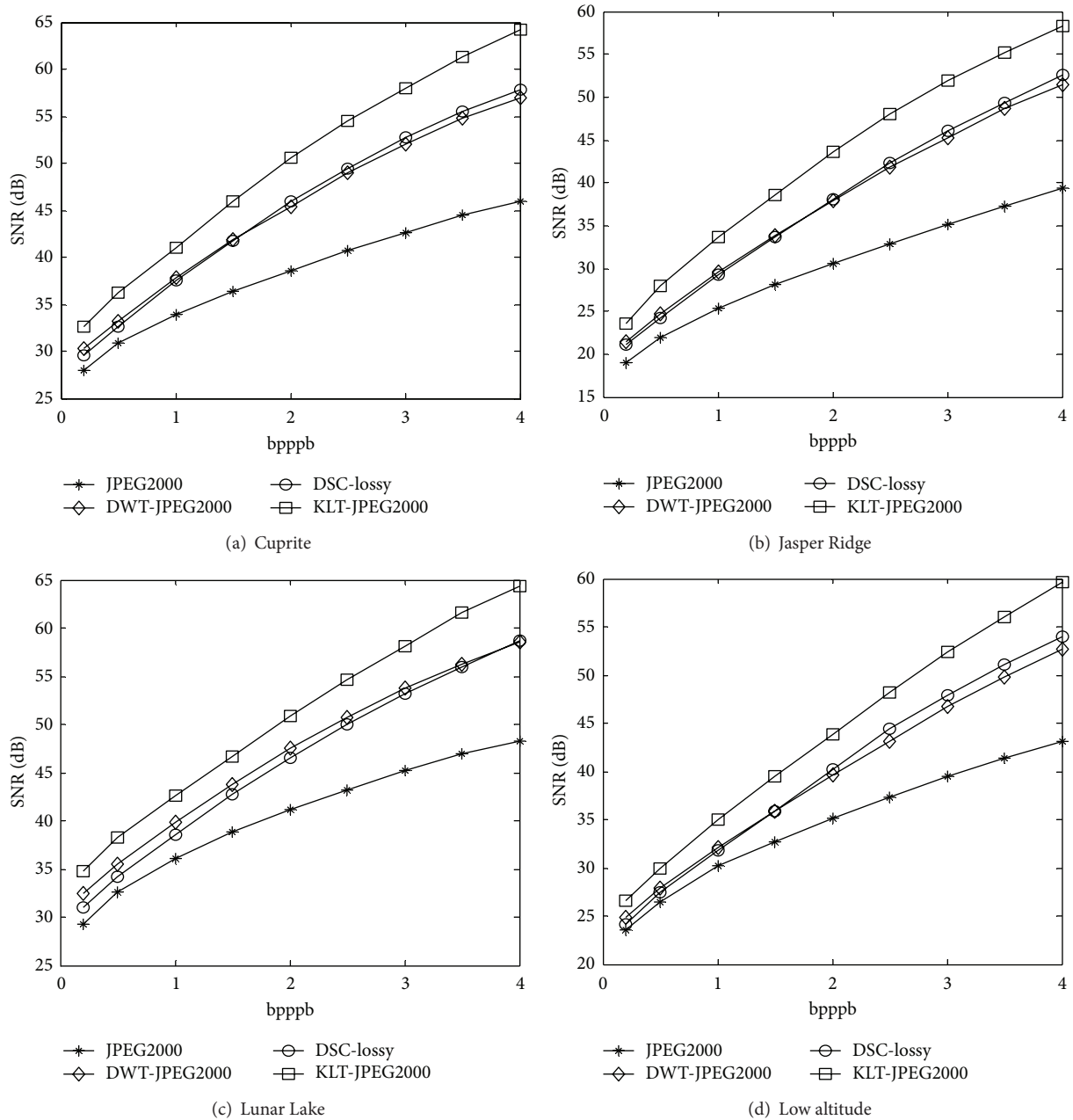


FIGURE 3: Comparison of RD performance of various algorithms.

TABLE 3: Comparison of encoder complexity of various algorithms.

Algorithm	Complexity
JPEG2000	1
DWT-JPEG2000	1.78
KLT-JPEG2000	4.12
DSC-lossy	0.96

compression performance with DWT-JPEG2000, but its encoder complexity is the lowest. Furthermore, the proposed algorithm can be easily parallelized by having encoding

blocks compressed at the same time, which is suitable for the implementation on an FPGA (field-programmable gate array).

5. Conclusion

Although existing classical algorithms can provide excellent compression performance for hyperspectral images, they are not suitable for onboard compression due to the high encoder complexity and poor error resilience. This paper proposes a low-complexity compression algorithm for hyperspectral images based on distributed source coding. Multilinear

regression model is introduced to improve the compression performance of distributed lossless compression algorithm, and optimal scalar quantization is proposed to perform distributed lossy compression. In order to achieve low bit-rate compression, an effective rate-distortion algorithm is also performed on the proposed distributed lossy algorithm. Experimental results show that the proposed algorithm has competitive compression performance and low encoder complexity, making it suitable for onboard compression. In order to further improve the performance of the proposed algorithm at low bit rate, powerful RD algorithm should be paid more attention.

Conflict of Interests

The authors have no conflict of interests to disclose.

Acknowledgment

This work was supported by the National Natural Science Foundation of China (nos. 41201363 and 61101183).

References

- [1] I. Blanes and J. Serra-Sagrista, "Pairwise orthogonal transform for spectral image coding," *IEEE Transactions on Geoscience and Remote Sensing*, vol. 49, no. 3, pp. 961–972, 2011.
- [2] B. Penna, T. Tillo, E. Magli, and G. Olmo, "Transform coding techniques for lossy hyperspectral data compression," *IEEE Transactions on Geoscience and Remote Sensing*, vol. 45, no. 5, pp. 1408–1421, 2007.
- [3] X. Tang, S. Cho, and W. A. Pearlman, "3D set partitioning coding methods in hyperspectral image compression," in *Proceedings of the International Conference on Image Processing (ICIP '03)*, pp. 239–242, Barcelona, Spain, September 2003.
- [4] E. Magli, "Multiband lossless compression of hyperspectral images," *IEEE Transactions on Geoscience and Remote Sensing*, vol. 47, no. 4, pp. 1168–1178, 2009.
- [5] Y. Tang, Q. Xin, G. Li, and J.-W. Wan, "Lossless compression of hyperspectral images based on contents," *Optics and Precision Engineering*, vol. 20, no. 3, pp. 668–674, 2012.
- [6] S. S. Pradhan and K. Ramchandran, "Distributed source coding using syndromes (DISCUS): design and construction," *IEEE Transactions on Information Theory*, vol. 49, no. 3, pp. 626–643, 2003.
- [7] Z. Xiong, A. D. Liveris, and S. Cheng, "Distributed source coding for sensor networks," *IEEE Signal Processing Magazine*, vol. 21, no. 5, pp. 80–94, 2004.
- [8] D. Slepian and J. K. Wolf, "Noiseless coding of correlated information sources," *IEEE Transactions on Information Theory*, vol. 19, no. 4, pp. 471–480, 1973.
- [9] A. D. Wyner and J. Ziv, "The rate-distortion function for source coding with side information at the decoder," *IEEE Transactions on Information Theory*, vol. 22, no. 1, pp. 1–10, 1976.
- [10] X. Pan, R. Liu, and X. Lv, "Low-complexity compression method for hyperspectral images based on distributed source coding," *IEEE Geoscience and Remote Sensing Letters*, vol. 9, no. 2, pp. 224–227, 2012.
- [11] C. Tang, N.-M. Cheung, A. Ortega, and C. S. Raghavendra, "Efficient inter-band prediction and wavelet based compression for hyperspectral imagery: a distributed source coding approach," in *Proceedings of the Data Compression Conference*, pp. 437–446, Snowbird, Utah, March 2005.
- [12] N.-M. Cheung, H. Wang, and A. Ortega, "Sampling-based correlation estimation for distributed source coding under rate and complexity constraints," *IEEE Transactions on Image Processing*, vol. 17, no. 11, pp. 2122–2137, 2008.
- [13] E. Magli, M. Barni, A. Abrardo, and M. Grangetto, "Distributed source coding techniques for lossless compression of hyperspectral images," *EURASIP Journal on Advances in Signal Processing*, vol. 2007, Article ID 45493, 13 pages, 2007.
- [14] A. Abrardo, M. Barni, E. Magli, and F. Nencini, "Error-resilient and low-complexity onboard lossless compression of hyperspectral images by means of distributed source coding," *IEEE Transactions on Geoscience and Remote Sensing*, vol. 48, no. 4, pp. 1892–1904, 2010.
- [15] A. Abrardo, M. Barni, and E. Magli, "Low-complexity lossy compression of hyperspectral images via informed quantization," in *Proceedings of the 17th IEEE International Conference on Image Processing (ICIP '10)*, pp. 505–508, Hong Kong, September 2010.
- [16] Y. J. Nian, Q. Xin, Y. Tang, and J. W. Wan, "Distributed lossless compression of hyperspectral images based on multi-band prediction," *Optics and Precision Engineering*, vol. 20, no. 4, pp. 906–912, 2012.
- [17] Y. J. Nian, J. W. Wan, Y. Tang, and B. Chen, "Near lossless compression of hyperspectral images based on distributed source coding," *Science China Information Sciences*, vol. 55, no. 11, pp. 2646–2655, 2012.
- [18] A. Abrardo, M. Barni, and E. Magli, "Low-complexity predictive lossy compression of hyperspectral and ultraspectral images," in *Proceedings of the 36th IEEE International Conference on Acoustics, Speech, and Signal Processing (ICASSP '11)*, pp. 797–800, Prague, Czech Republic, May 2011.
- [19] X. Wu and N. Memon, "Context-based lossless interband compression: extending CALIC," *IEEE Transactions on Image Processing*, vol. 9, no. 6, pp. 994–1001, 2000.
- [20] J. Mielikainen, "Lossless compression of hyperspectral images using lookup tables," *IEEE Signal Processing Letters*, vol. 13, no. 3, pp. 157–160, 2006.

Research Article

A Novel Fusion Method by Static and Moving Facial Capture

Shuai Liu,^{1,2} Weina Fu,^{1,3} Wenshuo Zhao,¹ Jiantao Zhou,¹ and Qianzhong Li²

¹ College of Computer Science, Inner Mongolia University, Hohhot 010012, China

² School of Physical Science and Technology, Inner Mongolia University, Hohhot 010012, China

³ Department of Computer Science and Technology, Hohhot University of Nationalities, Hohhot 010012, China

Correspondence should be addressed to Shuai Liu; cs.liushuai@imu.edu.cn

Received 27 June 2013; Accepted 21 August 2013

Academic Editor: Su-Qun Cao

Copyright © 2013 Shuai Liu et al. This is an open access article distributed under the Creative Commons Attribution License, which permits unrestricted use, distribution, and reproduction in any medium, provided the original work is properly cited.

For many years, face recognition has been one of the most important domains in pattern recognition. Nowadays, face recognition is more required to be used in video actually. So moving facial capture must be studied firstly because of performance requirement. Since classic facial capture method is not so suitable in a moving environment, in this paper, we present a novel facial capture method in a moving environment. Firstly, continuous frames are extracted from detecting videos by similar characteristics. Then, we present an algorithm to extract the moving object and restructure background. Meanwhile, with analysis of skin color in both moving and static areas, we use the classic faces capture method to catch all faces. Finally, experimental results show that this method has better robustness and accuracy.

1. Background

Today is the era of electronic public security, which uses electronic equipment and network in human security. So identity verification becomes the most important area in electronic social security. Meanwhile, face recognition becomes one of the most widely used biometric identification technologies because of its positive features such as being direct, friendly, convenient, difficult to counterfeit, and cost-effective [1]. Moreover, face recognition also has a wide range in biometric authentication, video surveillance, social security, and other application areas [2]. Generally, face recognition can be divided into three steps: (1) facial detection and segmentation from scene, (2) capture of facial feature, and (3) matching and recognition of human face [3].

Facial detection and capture is the first step in face recognition method. Detecting and tracking faces rapidly from frames in video is the basis of face recognition. Then, recognition will process when an image makes for identification.

However, there are many problems in face detection, like how to use information of facial time and space, how to overcome low resolution ratio and huge range of mutative scale, and how to recognize faces with intense transformation or

a hidden facial part. These are the emphases in studies nowadays [4]. Meantime, facial detection and capture in video need high quality in recognition time sometimes [5]. Thus, it needs low computational cost. So we have to use simpler model with higher accuracy. So, statistical models are used widely in facial detection today [6, 7].

In recent years, neural network, Support Vector Machine (SVM), and AdaBoost are the widest statistical models in facial detection and capture [8]. Thereinto, AdaBoost is used widely in dynamical detection for its fast speed and well stability [9]. Meantime, AdaBoost is also used in other classificatory areas just like classification of music and protein [10, 11]. Besides, AdaBoost is used in other biometric authentications like iris recognition and facial recognition [12].

Though AdaBoost is widely used, it has obvious deficiencies. The first deficiency is its less robustness with transformation of illumination and expression. Secondly, it cannot detect deflecting faces. So, in this paper, we ameliorate AdaBoost by moving object capture [13]; that is, we detect a moving object by using AdaBoost for a tiny time range. Admittedly, facial moving speed is slow. So, frames with tiny time range can be extracted by similar characteristics. We determine relevance of frames by area comparison of moving objects.

Meantime, we determine face when area ratio of facial image is registration more than a threshold. Then, with capture of moving object with restructured background, we analyze skin color in moving area and use it in static area. In this way, all faces are detected and extracted no matter whether these faces are front or deflecting.

The remainder of the paper is organized as follows. We present and analyze our method in Section 2. Then, we present a novel fusion algorithm in Section 3. Moreover, we experiment some data with this novel algorithm and classic AdaBoost algorithm in Section 4. Finally, Section 5 summarizes the main results of the paper.

2. Theory of Methods

There are many expressions of color set in computers and they form different color space. RGB, HLS, YCbCr, and YIQ are the widest used today. Admittedly, skin set gives expression to different cluster features when it is in different color spaces. Researchers discover that skin set shows better clustering results in HLS and YCbCr [14]. Generic terms of YCbCr are called YUV [5]. Y expresses luminance and U, V express chrominance signals.

Since Duan presents her hierarchical method of skin color for color spaces [15], we can analyze distribution of skin color in YIQ and YUV. Then, we use threshold of i and θ to detect skin colors where i is i th component of YIQ and θ is phase angle of YUV. So formula of θ is shown in

$$\theta = \tan^{-1} \left(\frac{|V|}{|U|} \right). \quad (1)$$

We revolve the component of chromatic aberration of YUV to form YIQ. So I contains color information from Orange to Ching and Q contains Green to Magenta. Then, skin tone is between Red and Yellow, and θ is basic in domain [100, 150].

In this paper, we use $\theta \in [100, 150]$ and $I \in [20, 90]$. Then we use (2) to transform YUV and YIQ to RGB:

$$\begin{pmatrix} Y \\ U \\ V \end{pmatrix} = \begin{pmatrix} 0.299 & 0.587 & 0.114 \\ -0.147 & -0.289 & 0.436 \\ 0.615 & -0.515 & -0.100 \end{pmatrix} \begin{pmatrix} R \\ G \\ B \end{pmatrix}, \quad (2)$$

$$\begin{pmatrix} Y \\ I \\ Q \end{pmatrix} = \begin{pmatrix} 0.299 & 0.587 & 0.114 \\ 0.596 & -0.274 & -0.322 \\ 0.211 & -0.523 & 0.312 \end{pmatrix} \begin{pmatrix} R \\ G \\ B \end{pmatrix}.$$

Then, in order to increase speed of facial detection, we fuse skin color detection into face detection after transformation. We extract a frame as original image and detect possible skin color area. Moreover, we crop following images by using skin space model. Then, we cascade connect weak classifiers to strong classifiers. We have (3) to show a weak classifier $h_j(x)$ with feature f_j . In (3), θ_j is clustering threshold of minimum error in training samples and p_j expresses direction of inequality:

$$h_j(x) = \begin{cases} 1, & \text{if } p_j f_j < p_j \theta_j, \\ 0, & \text{otherwise.} \end{cases} \quad (3)$$

In this way, we drop those weak classifiers whose clustering rate less than 50%. Then, in order to enhance accuracy of facial capture, we enhance weight for them with better performance and reduce weight for them with worse performance. Computation of weight is shown in

$$w_{1,i} = \begin{cases} \frac{1}{2m}, & x_i \text{ is negative sample, } m \text{ is the number} \\ & \text{of negative samples,} \\ \frac{1}{2l}, & x_i \text{ is positive sample, } l \text{ is the number} \\ & \text{of positive samples,} \end{cases} \quad (4)$$

$$w_{t,i} = \frac{w_{t,i}}{\sum_{j=1}^n w_{t,j}}, \quad w_{t,i} \in (0, 1) \text{ is probability distribution,} \quad (5)$$

$$h_t = h_k, \quad \text{whose } \varepsilon_k = \min \left\{ \varepsilon_j \mid \varepsilon_j = \sum_i w_t |h_j(x_i) - y_i| \right\}, \quad (6)$$

$$w_{t+1,i} = w_{t,i} \beta_t^{1-e_i}, \quad \text{where } \beta_t = \frac{\varepsilon_t}{1-\varepsilon_t}, \quad (7)$$

$$e_i = \begin{cases} 0, & \text{where } x_i \text{ classify right,} \\ 1, & \text{where } x_i \text{ classify wrong,} \end{cases}$$

$$h(x) = \begin{cases} 1 & \sum_{t=1}^T a_t h_t(x) \geq \frac{1}{2} \sum_{t=1}^T a_t, \quad a_t = \log \frac{1}{\beta_t}, \\ 0 & \text{otherwise.} \end{cases} \quad (8)$$

Equation (4) is initialization of weight, and (5) is normalization of weight. Equation (6) is classifier h_t , which has minimum error rate ε_t for all classifiers h_j of feature j with weight w_t . Equation (7) shows transformation of all weights. Equation (8) presents the strong classifier, which is composed by T weak classifier.

3. A Novel Fusion Algorithm with Background Restructured

In this paper, we restructure background by (9). Without background, we compute function G to express difference of two next frames and function B to express whether there is a moving object in it. Then, applying $I_n(x)$ as pixel gray of foreframe and $T_n(x)$ as threshold, we consider a pixel z is moving when it fits in (10). In this way, we can find all background points by training. Figure 1 is a flow chart of background training. Consider

$$G_{i,i-1}(x, y) = |X_i(x, y) - X_{i-1}(x, y)|,$$

$$B_{i,i-1}(x, y) = \begin{cases} 1, & \text{if } G_{i,i-1}(x, y) \geq \text{threshold,} \\ 0, & \text{otherwise,} \end{cases} \quad (9)$$

$$\begin{aligned} |I_n(x) - I_{n-1}(x)| &> T_n(x), \\ |I_n(x) - I_{n-2}(x)| &> T_n(x). \end{aligned} \quad (10)$$

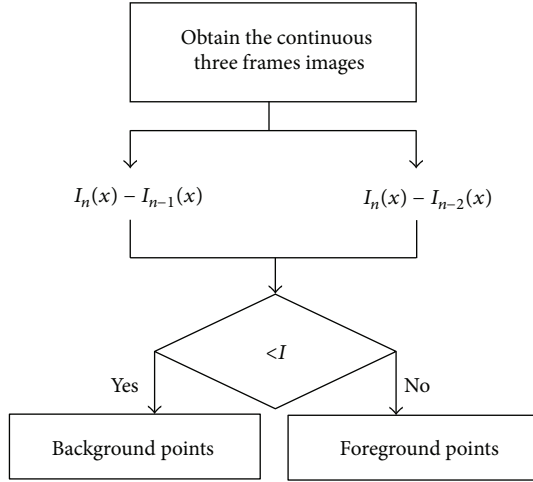


FIGURE 1: Restructure background with training.

After background restructure, we detect facial area from some continuous frames by (8) with skin color detection. We know (8) process well with front faces. Then, based on faces detected by (8), we search moving object around them. We trust a moving object is a face where registration rate of moving object and facial area is more than a threshold and its color belongs to skin color space. The novel fusion method can extract some deflecting faces, which cannot be found by a classic method.

The following steps are presented to show the novel fusion method.

Step 1. When the video plays, catch three continuous frames as original frames from video. Otherwise go to Step 8.

Step 2. If background is not complete, restructure it one time.

Step 3. Extract skin area with skin model and morphological operation.

Step 4. Extract detected areas from corresponding positions of original images, and then these areas are processed to connected rectangle or oval regions.

Step 5. Use (8) to detect faces.

Step 6. Detect moving faces from nearest facial area.

Step 7. Stamp results and go to Step 1.

Step 8. Procedure finished.

We have Figure 2 to show the flow chart of the novel fusion method.

4. Experimental Result and Its Analysis

In this paper, we validate our method from a video, which contains both single face frames and multifaces frames. We

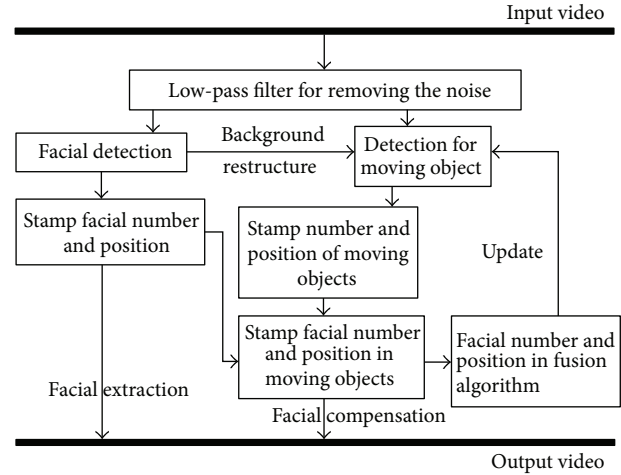


FIGURE 2: Flow chart of our fusion extraction method.

process classic facial capture method and our method to detected faces. Then comparisons of time and rate are shown.

4.1. Single Face Detection. In frame sequence of the video, the face is moving with different kinds. In this paper, we extract the face image by using front, side, up, down, lean, and shaded face. As we know, classic method cannot detect faces when they are not frontal and can only detect a part of faces when they are shaded. Oppositely, the fusion method can detect faces accurately. We put them in Figure 3. Figures from upper two rows are capture result for classic method and figures from bottom two rows are for fusion method.

4.2. Multifaces Capture. In Section 4.1, we choose faces with different kinds and detect them in Figure 4. Figures from upper two rows are capture result for classic method and figures from bottom two rows are presented for fusion method.

4.3. Analysis of Experimental Result. We have (11) to define mean computational time of every image. With fames of single face, it costs 177.502 ms by using classic method and 127.887 ms by this fusion method. Moreover, it costs 229.631 ms by classic method and 153.963 ms by this fusion method with frames of multifaces (two faces in each image). Then, we have Table 1 to show these results. In Table 1, we find the same problem of these two methods is that it costs much time when detection fails. It is because we need to search the whole frame in this condition. Consider the following:

$$T = \frac{\sum_{i=1}^n T_i}{n} \tag{11}$$

Then, we have (12) to define detection accuracy of every image. In (12), N_c is frame number with correct detection and N_t is total frame number. With fames of single face, the accuracy is 72.0% by using classic method and 96.8% by this fusion method. Moreover, the accuracy is 60.5% by classic method and 89.6% by this fusion method with frames

TABLE 1: Performance comparison between a single PC and cloud platform.

Mean detection time	Single face (success)	Single face (fail)	Multifaces (success)	Multifaces (fail)
Classic method	156.392	231.791	178.812	303.626
Mean time (ms)		177.502		229.631
The novel fusion method	126.120	181.354	147.948	205.335
Mean time (ms)		127.887		153.963



FIGURE 3: Comparison of single face capture between two methods.

TABLE 2: Comparison of the face detection accuracy between two methods.

	Classic method	The novel fusion method
Single face	72.0%	96.8%
Multifaces	60.5%	89.6%

of multifaces (two faces in each image). We have Table 2 to show these results. In Table 2, we find accuracy of the fusion method is better than the classic one. We check fail frames of these two methods and find that the classic method shows more negative than the fusion one when deflection of faces is

large. The classic method cannot detect all deflecting faces, but the fusion one can detect most of them. Consider the following:

$$R = \frac{N_c}{N_t}. \quad (12)$$

5. Conclusions

In this paper, by fused skin color model, facial detection method, and moving object capture algorithm, we present a fusion facial detection method. This method takes full



FIGURE 4: Comparison of multifaces detection between two methods.

advantage of information in continuous frames of the detecting video and shows that it is positive in facial detection. Furthermore, we reach that the fusion method has well detecting effect when expressions and facial gestures change greatly. This fusion method remedies deficiencies of the classic method. Finally, we validate our method by using lots of experimental results. The experimental results indicate that the fusion method makes a good effect where faces are moving variously.

The deficiency of this method is that detecting accuracy is low when faces move quickly. In fact, the quickly moving faces lead to error of moving facial judgment. It is because the threshold of two continuous frames is too large that our method treats them as two faces.

Acknowledgments

This work is supported by Grants Programs of Higher-Level Talents of Inner Mongolia University (nos. 125126, 115117), Scientific Projects of Higher School of Inner Mongolia (NJZY13004), National Natural Science Foundation of China (nos. 61261019, 61262082), Key Project of Chinese Ministry

of Education (no. 212025), and Inner Mongolia Science Foundation for Distinguished Young Scholars (2012JQ03). The authors wish to thank the anonymous reviewers for their helpful comments in reviewing this paper.

References

- [1] Y. Yan and Y.-J. Zhang, “State-of-the-art on video-based face recognition,” *Chinese Journal of Computers*, vol. 32, no. 5, pp. 878–886, 2009.
- [2] F. Pan, X. Wang, and B. Xiao, “Study on fast face detection of color image,” *Chinese Journal of Scientific Instrument*, vol. 25, no. 5, pp. 561–564, 2004.
- [3] W. Zhao, R. Chellappa, P. J. Phillips, and A. Rosenfeld, “Face recognition: a literature survey,” *ACM Computing Surveys*, vol. 35, no. 4, pp. 399–458, 2003.
- [4] I. Dryden and K. V. Mardia, *The Statistical Analysis of Shape*, Wiley, London, UK, 1998.
- [5] P. N. Belhumeur, J. P. Hespanha, and D. J. Kriegman, “Eigenfaces vs. fisherfaces: recognition using class specific linear projection,” *IEEE Transactions on Pattern Analysis and Machine Intelligence*, vol. 19, no. 7, pp. 711–720, 1997.

- [6] D. B. Graham and N. M. Allinson, "Characterising virtual eigensignatures for general purpose face recognition," *Face Recognition*, vol. 163, pp. 446–456, 1998.
- [7] K. W. Bowyer, K. Chang, and P. Flynn, "A survey of approaches and challenges in 3D and multi-modal 3D + 2D face recognition," *Computer Vision and Image Understanding*, vol. 101, no. 1, pp. 1–15, 2006.
- [8] S. Zhou and R. Chellappa, "Beyond a single still image: face recognition from multiple still images and videos," in *Face Processing: Advanced Modeling and Methods*, Academic Press, New York, NY, USA, 2005.
- [9] J. Bergstra, N. Casagrande, D. Erhan, D. Eck, and B. Kégl, "Aggregate features and ADABOOST for music classification," *Machine Learning*, vol. 65, no. 2-3, pp. 473–484, 2006.
- [10] X. Jiang, R. Wei, Y. Zhao, and T. Zhang, "Using Chou's pseudo amino acid composition based on approximate entropy and an ensemble of AdaBoost classifiers to predict protein subnuclear location," *Amino Acids*, vol. 34, no. 4, pp. 669–675, 2008.
- [11] C. W. Hsieh, H. H. Hsu, and T. W. Pai, "Protein crystallization prediction with AdaBoost," *International Journal of Data Mining and Bioinformatics*, vol. 7, no. 2, pp. 214–227, 2013.
- [12] Q. Wang, X. Zhang, M. Li, X. Dong, Q. Zhou, and Y. Yin, "Adaboost and multi-orientation 2D Gabor-based noisy iris recognition," *Pattern Recognition Letters*, vol. 33, no. 8, pp. 978–983, 2012.
- [13] W. Fu, Z. Xu, S. Liu, X. Wang, and H. Ke, "The capture of moving object in video image," *Journal of Multimedia*, vol. 6, no. 6, pp. 518–525, 2011.
- [14] Z. Jin, Z. Lou, J. Yang, and Q. Sun, "Face detection using template matching and skin-color information," *Neurocomputing*, vol. 70, no. 4–6, pp. 794–800, 2007.
- [15] L. Duan, W. Gao, G. Cui, and H. Zhang, "A hierarchical method for nude image filtering," *Journal of Computer-Aided Design & Computer Graphics*, vol. 14, no. 5, pp. 404–409, 2002.

Research Article

A Virtual Channels Scheduling Algorithm with Broad Applicability Based on Movable Boundary

Ye Tian, Qingfan Li, Yongxin Feng, and Xiaoling Gao

School of Information Science and Engineering, Shenyang Ligong University, ShenYang 110159, China

Correspondence should be addressed to Yongxin Feng; fengyongxin@263.net

Received 22 May 2013; Accepted 6 August 2013

Academic Editor: Baochang Zhang

Copyright © 2013 Ye Tian et al. This is an open access article distributed under the Creative Commons Attribution License, which permits unrestricted use, distribution, and reproduction in any medium, provided the original work is properly cited.

A virtual channels scheduling algorithm with broad applicability based on movable boundary is proposed. According to the types of data sources, transmission time slots are divided into synchronous ones and asynchronous ones with a movable boundary between them. During the synchronous time slots, the virtual channels are scheduled with a polling algorithm; during the asynchronous time slots, the virtual channels are scheduled with an algorithm based on virtual channel urgency and frame urgency. If there are no valid frames in the corresponding VC at a certain synchronous time slot, a frame of the other synchronous VCs or asynchronous VCs will be transmitted through the physical channel. Only when there are no valid frames in all VCs would an idle frame be generated and transmitted. Experiments show that the proposed algorithm yields much lower scheduling delay and higher channel utilization ratio than those based on unmovable boundary or virtual channel urgency in many kinds of sources. Therefore, broad applicability can be achieved by the proposed algorithm.

1. Introduction

To meet the requirements of new space systems and new space missions, Consultative Committee for Space Data Systems (CCSDS) expanded the contents of the conventional recommendations [1, 2] and put forward Advanced Orbiting Systems (AOS) recommendations [3, 4], which provide flexible and various data processing businesses. In AOS, a two-layer multiplexing mechanism, which includes packet multiplexing and virtual channel multiplexing mechanisms, is used to share one physical channel between multiusers. Packet channel multiplexing mechanism is a mechanism in which various data packets share one virtual channel (VC), and some achievements have been made in this respect [5–8]. Virtual channel multiplexing mechanism is a mechanism in which a number of virtual channels share one physical channel.

Virtual channels are a group of logic channels formed by dividing the physical channel into different time slots. Each VC transmits the user data with the same or similar properties. The specific algorithm used in this mechanism, namely, VC scheduling algorithm, decides the order of VCs

occupying the physical channel as well as the transmission efficiency of the physical channel. Therefore, the way to design the VC scheduling algorithm will be the focus of AOS systems.

Some research conclusions on virtual channel scheduling algorithms have been achieved [9–11], most of which are designed for a certain satellite data source, so their application scopes are limited. Even the dynamic scheduling algorithm (DSA) [11], which provides good performance for some types of data sources, could hardly meet the transmission requirements of all types of satellite data sources. In addition, it pays little attention to the difference between VC urgency and frame urgency, which will cause performance reduction.

To address the problems above, a virtual channels scheduling algorithm with broad applicability based on movable boundary is proposed, in which the transmission time slots are divided into synchronous ones and asynchronous ones; furthermore, the boundary between them is movable. During the synchronous time slots, the virtual channels are scheduled with a polling algorithm. If there are no valid frames in the corresponding synchronous VC at a certain synchronous time slot, a frame of the other synchronous VCs

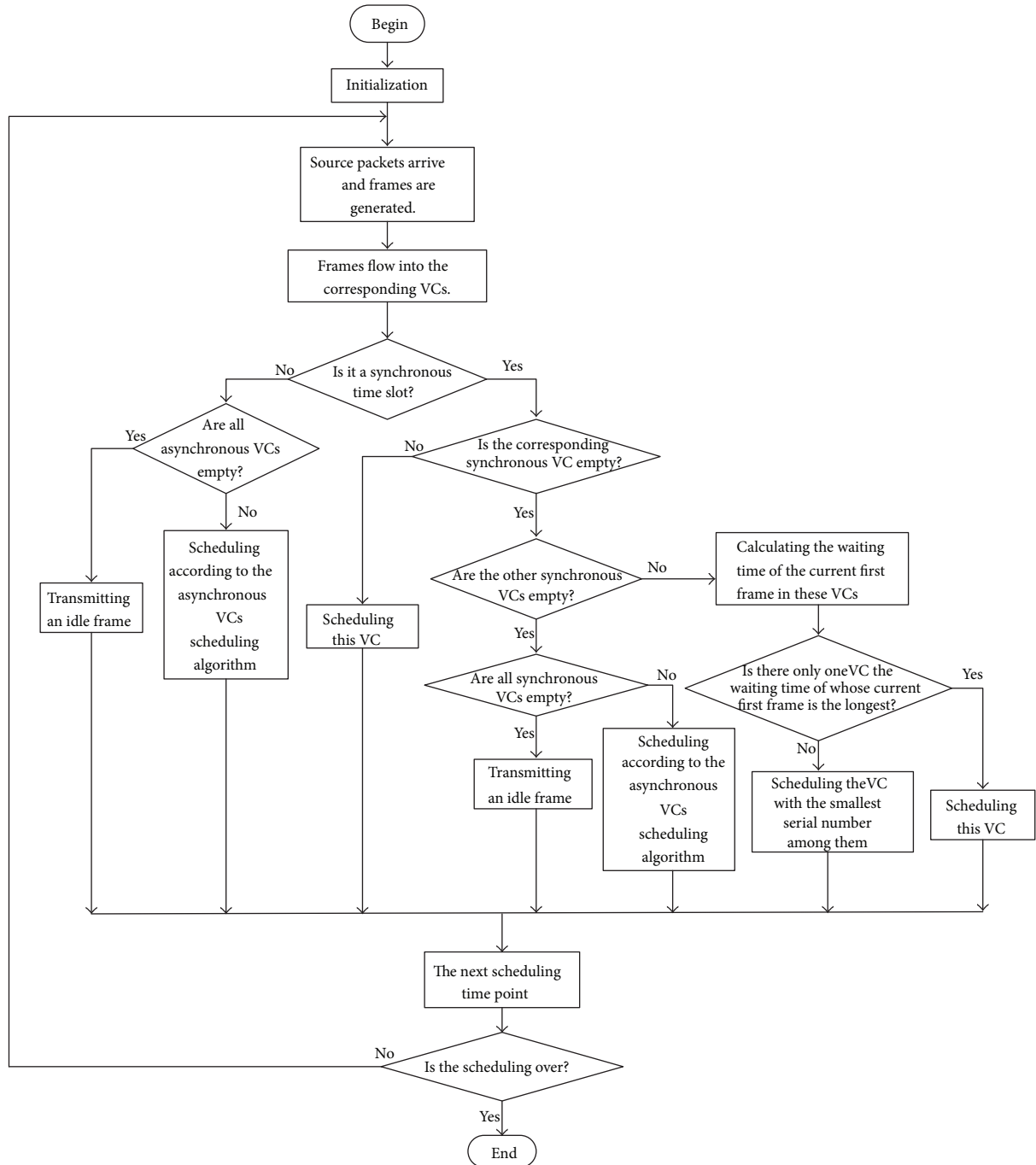


FIGURE 1: The proposed scheduling algorithm.

or asynchronous VCs will be selected to occupy this time slot according to the scheduling mechanism; if there are no valid frames in all VCs, an idle frame is generated and transmitted. During the asynchronous time slots, the virtual channels are scheduled with an algorithm based on VC urgency and frame urgency. Simulation results show that the proposed algorithm produces much less scheduling delay and higher channel utilization ratio than the DSA algorithm.

2. Scheduling Algorithm with Broad Applicability Based on Movable Boundary

There are three kinds of virtual channels multiplexing modes [12]: the full synchronous multiplexing mode, the full asynchronous multiplexing mode, and the synchronous/asynchronous multiplexing mode. For the full synchronous multiplexing mode, the order of virtual channels occupying

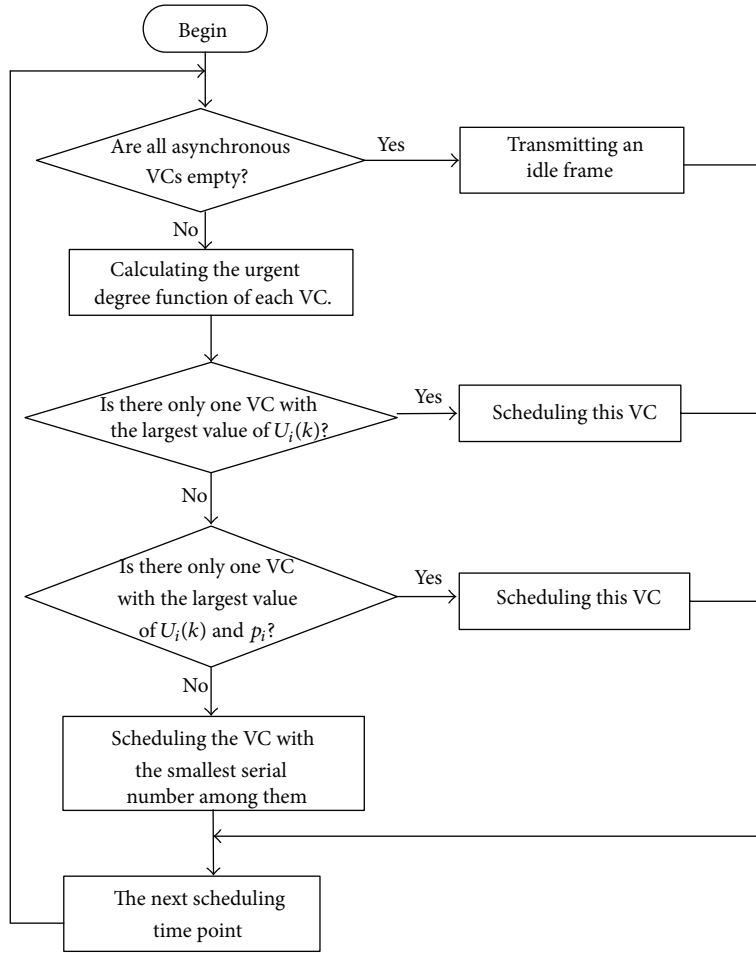


FIGURE 2: Asynchronous VCs scheduling algorithm.

a physical channel is fixed and repetitive, so it is suitable for the case in which most business data are synchronous and data rates of all the VCs are equivalent. However, it is not suitable for handling burst business and cannot achieve high channel utilization ratio. For the full asynchronous multiplexing mode, when two or more virtual channels are waiting to be scheduled, they are scheduled according to the priority assigned or calculated; therefore, this mode is suitable for burst business and low data rate information. However, this mode usually results in the delay wobbling of synchronous data [12]. For the synchronous/asynchronous multiplexing mode, the virtual channels are divided into synchronous and asynchronous ones. Synchronous virtual channels are scheduled with the full synchronous multiplexing mode, while asynchronous virtual channels are scheduled with the full asynchronous multiplexing mode. Although the system complexity is increased in this mode, the shortcomings of the first two modes mentioned above can be avoided.

In order to reduce the scheduling delay and improve the channel utilization ratio, a virtual channels scheduling algorithm based on movable boundary is proposed. In the proposed algorithm, the synchronous/asynchronous

multiplexing mode is adopted. Time slots are divided into synchronous and asynchronous ones, which are used to schedule synchronous and asynchronous virtual channels, respectively. The system distributes the number of synchronous and asynchronous time slots according to the VC data rates and the number of VCs [12]. In terms of the scheduling strategy, the polling scheduling strategy is used for synchronous virtual channels, while the virtual channel scheduling strategy based on VC urgency and frame urgency is used for asynchronous virtual channels. The flowchart of the proposed scheduling algorithm is shown in Figure 1.

2.1. Synchronous Virtual Channel Scheduling Algorithm. For synchronous virtual channels, the polling scheduling algorithm is used. The so-called polling scheduling algorithm is that each virtual channel occupies the physical channel exactly according to the order assigned before. If there are no valid frames in the corresponding VC at a certain synchronous time point, the frame with the longest waiting time from the other synchronous VCs will be transmitted; if two or more frames from the other synchronous VCs have

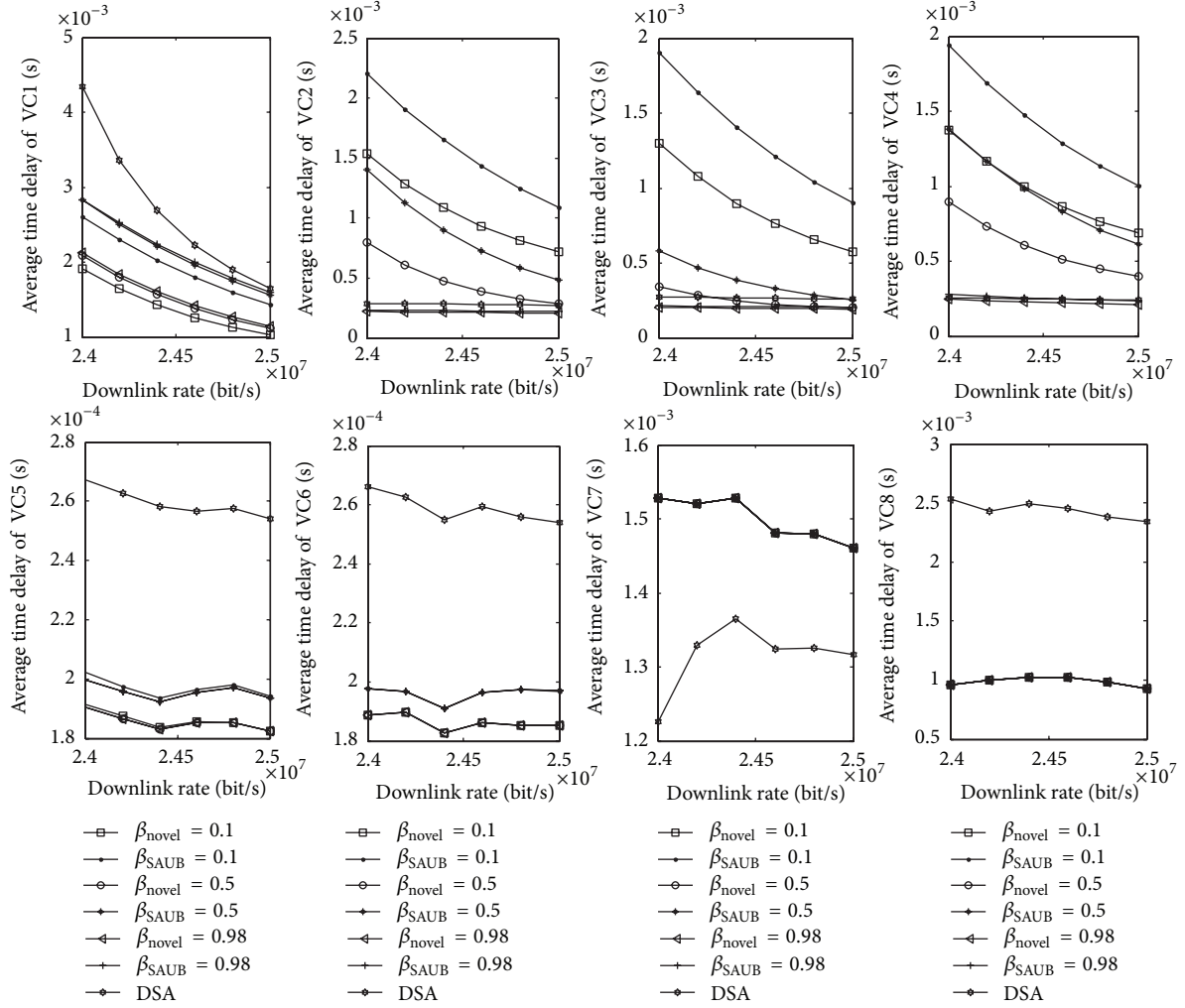


FIGURE 3: The average time delay of each VC of source model 1.

the longest waiting time, the first frame in the synchronous VC with the smallest VC serial number among them is transmitted; if there are no valid frames in all synchronous VCs, a valid asynchronous frame will be selected and transmitted according to the asynchronous scheduling mechanism. Otherwise, an idle frame will be generated and transmitted through the physical channel.

Define the waiting time of the current first frame in the i th VC (VC_i), T_{wi} , as:

$$T_{wi} = k\Delta t - T_{ia} \quad k = 1, 2, 3, \dots, \quad (1)$$

where $k\Delta t$ is the current scheduling time point, and T_{ia} is the arrival time of the current first frame in VC_i .

2.2. Asynchronous Virtual Channel Scheduling Algorithm. For asynchronous virtual channels, the scheduling algorithm based on VC urgency and frame urgency is exploited. First, the VC urgency and frame urgency are calculated, respectively, and then they are balanced with a weighting coefficient

β to form a new urgent degree function of VCs. VCs are scheduled according to the values of the function.

2.2.1. VC Urgency. Define the transmission urgency of VC_i , $U_{1i}(k)$, as

$$U_{1i}(k) = a_i(k) \cdot Q_i(k) \cdot p_i, \quad (2)$$

where $a_i(k)$ is the Boolean function, and it decides whether VC_i can participate in the competition of the physical channel. The values of $a_i(k)$ are shown as

$$a_i(k) = \begin{cases} 1, & \text{there are some valid frames in } VC_i \\ & \text{at the current scheduling time point} \\ 0, & \text{there are no valid frames in } VC_i \text{ at} \\ & \text{the current scheduling time point.} \end{cases} \quad (3)$$

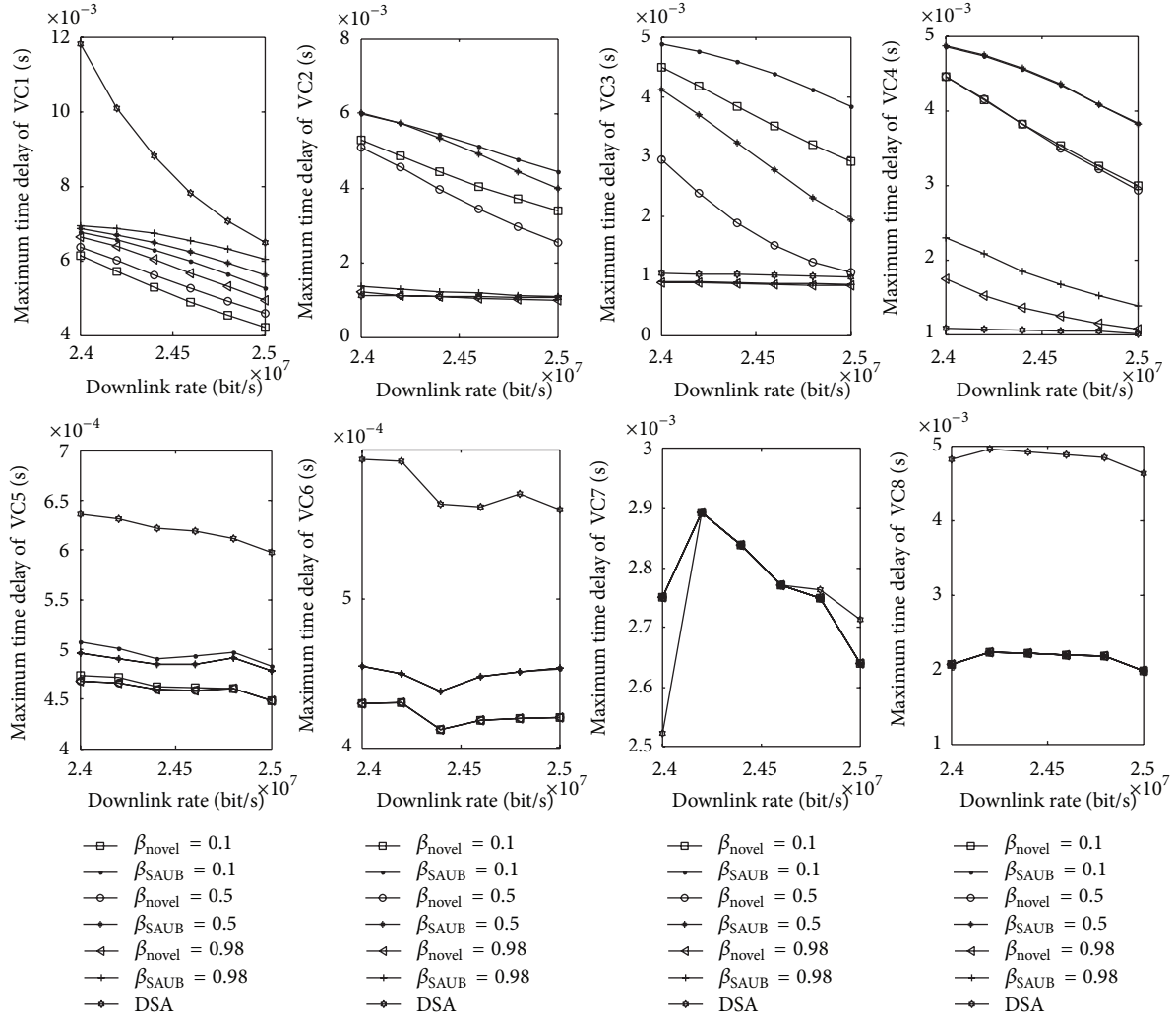


FIGURE 4: The maximum time delay of each VC of source model 1.

$Q_i(k)$ is the urgency base of VC_i , and it calculates the delay from the last time point when VC_i is scheduled to the current time point. The values of $Q_i(k)$ are shown as

$$Q_i(k) = \begin{cases} 0, & \text{there are some valid frames in } VC_i \\ & \text{and } VC_i \text{ is scheduled at the } k-1 \\ & \text{time point} \\ Q_i(k-1), & \text{there are some valid frames in } VC_i \\ & \text{and } VC_i \text{ is not scheduled at the } k-1 \\ & \text{time point} \\ Q_i(k-1)+1, & \text{there are no valid frames in } VC_i \\ & \text{at the } k-1 \text{ time point.} \end{cases} \quad (4)$$

p_i is the static priority of VC_i . If VC_i requests higher real-time performance, a larger value of p_i is assigned to it; otherwise, a smaller one is assigned.

2.2.2. Frame Urgency. Frame urgency can be calculated by the time that the current first frame has been waiting for. Define the frame urgency $U_{2i}(k)$ of VC_i as

$$U_{2i}(k) = a_i(k) \cdot \frac{(k\Delta t - T_{ia})}{\Delta t} \cdot p_i, \quad (5)$$

where T_{ia} is the arrival time of the current first frame in VC_i . Obviously, the smaller the value of T_{ia} is, the longer the waiting time of the current first frame is, which results in a larger value of $U_{2i}(k)$.

2.2.3. Urgent Degree Function of Virtual Channel. Define the urgent degree function of VC_i at the k th scheduling time point as

$$U_i(k) = \beta \cdot U_{1i}(k) + (1 - \beta) \cdot U_{2i}(k), \quad (6)$$

where β is the weighting coefficient, $0 < \beta < 1$.

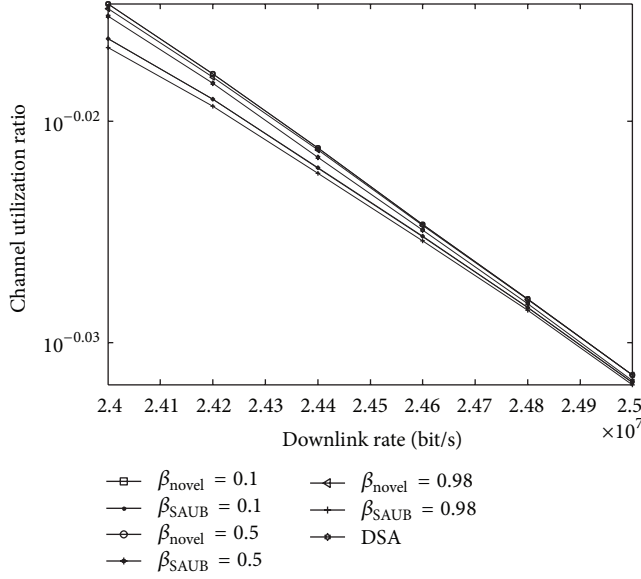


FIGURE 5: The channel utilization ratio of source model 1.

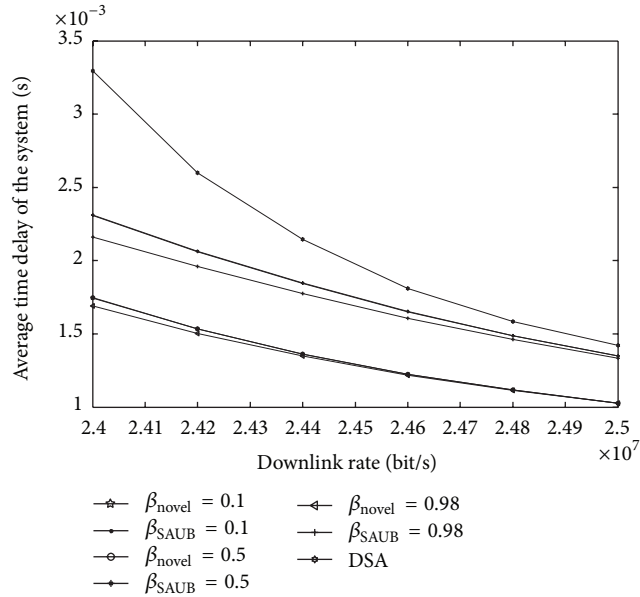


FIGURE 6: The average time delay of system of source model 1.

Substituting (5) into (6), we can get

$$U_i(k) = a_i(k) \cdot \left[\beta \cdot Q_i(k) + \frac{(1-\beta) \cdot (k\Delta t - T_{id})}{\Delta t} \right] \cdot p_i. \quad (7)$$

As is shown in (7), both the VC urgency and the frame urgency are estimated when calculating the urgent degree functions of VCs. On one hand, this will prevent the VC with large amount of data from monopolizing the physical channel; on the other hand, it overcomes the problem in the literature [11–14] that the waiting time of the other data

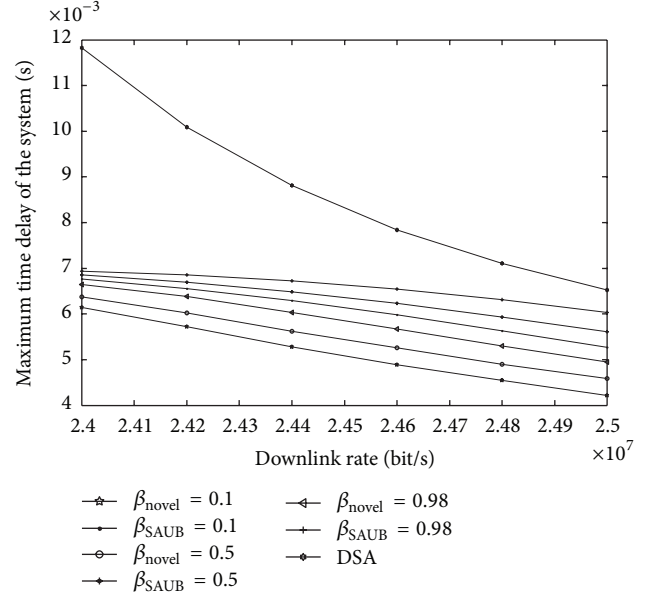


FIGURE 7: The maximum time delay of system of source model 1.

frames in a VC are reset when the first frame in this VC is transmitted, which will result in the decline of the VC urgency.

At any asynchronous scheduling time point, the VC with the largest value of $U_i(k)$ is scheduled; if there are two or more VCs with the largest value of $U_i(k)$, the VC with the largest values of $U_i(k)$ and p_i is scheduled; if there are two or more VCs with the largest values of $U_i(k)$ and p_i , the VC with the smallest VC serial number among them is scheduled. Otherwise, an idle frame is generated and transmitted through the physical channel. The flowchart of asynchronous VCs scheduling algorithm is shown in Figure 2.

2.2.4. Strategy of Selecting Weighting Coefficient. For different types of satellite data sources, we can select an appropriate β by computer simulation to get good urgent degree functions of VCs so as to achieve good scheduling performance. Therefore, the proposed algorithm can be applied to diverse satellite data sources.

Consider the following three kinds of satellite data sources.

- (a) Sources with large difference among VC loads. For this kind of sources, there is usually one or more VCs with large amount of data, whose number of data frames is much larger than the others. For VCs with large amount of data, the values of frame urgency are relatively large and the values of VC urgency are relatively small at most scheduling time points; for VCs with little amount of data, whose time of occupying physical channel is limited, the values of VC urgency are relatively large and the values of frame urgency are relatively small at most scheduling time points. In order to prevent VCs with large amount of

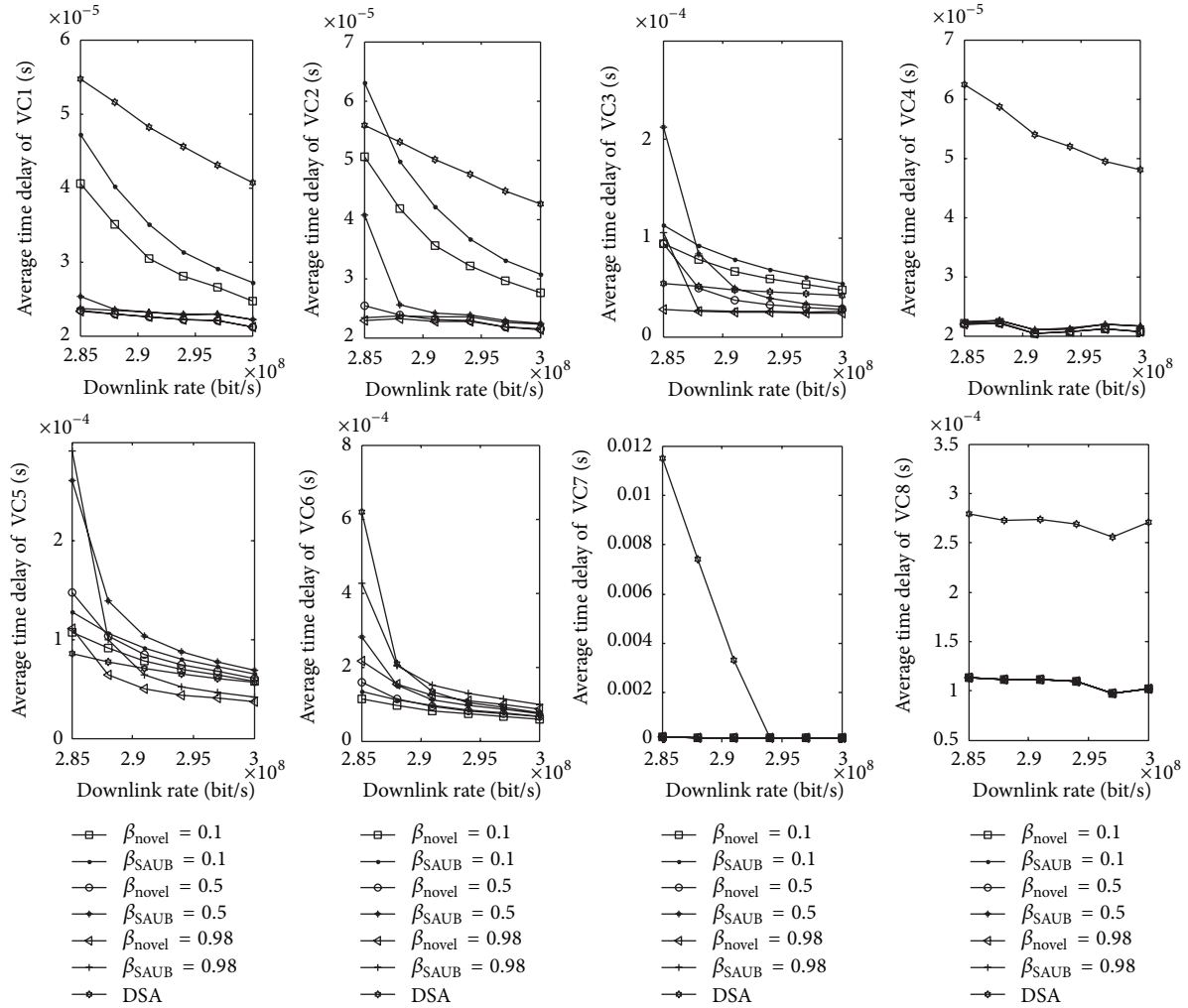


FIGURE 8: The average time delay of each VC of source model 2.

data from monopolizing the physical channel, we can select large values for β .

- (b) Sources with moderate difference among VC loads. For this kind of sources, there are no VCs with enough data to monopolize physical channel, so the value of β should be smaller than that of the first kind of sources. For the VCs with high data rates, the data frame urgency is dominant, so the smaller the value of β is, the better the delay performance is; for the VCs with low data rates, the VC urgency is dominant, so the larger the value of β is, the better the delay performance is. The right value of β can be determined by VC loads and real-time requirements.
- (c) Sources with little difference among VC loads. For this kind of sources, data rates of various VCs are relatively equivalent. Neither the VC urgency nor the frame urgency is dominant in the urgent degree function of VC, so the value of β has little effect on the performance of VCs scheduling delay, which makes it easy to be selected.

3. Simulation Results

Simulation is performed to compare the performance of the novel algorithm we proposed with those of the SAUB algorithm and the DSA algorithm. It is worth mentioning that the SAUB algorithm is the algorithm in which the same scheduling strategies as those used in the proposed algorithm are adopted, except that the boundary between the synchronous time slots and asynchronous ones is unmovable. Performance parameters include mainly the average scheduling delay of each VC, the maximum scheduling delay of each VC, the average scheduling delay of system, and the maximum scheduling delay of system and the channel utilization ratio.

3.1. Simulation on Sources with Large Difference among VC Loads. For this kind of sources, a source is selected whose VCs' division and parameter settings are shown in Table 1. VC1~VC6 are asynchronous VCs as that in the literature [15]. VC7 and VC8 are synchronous VCs. In addition, VC9 is used to generate and transmit idle frames. The highest data rate

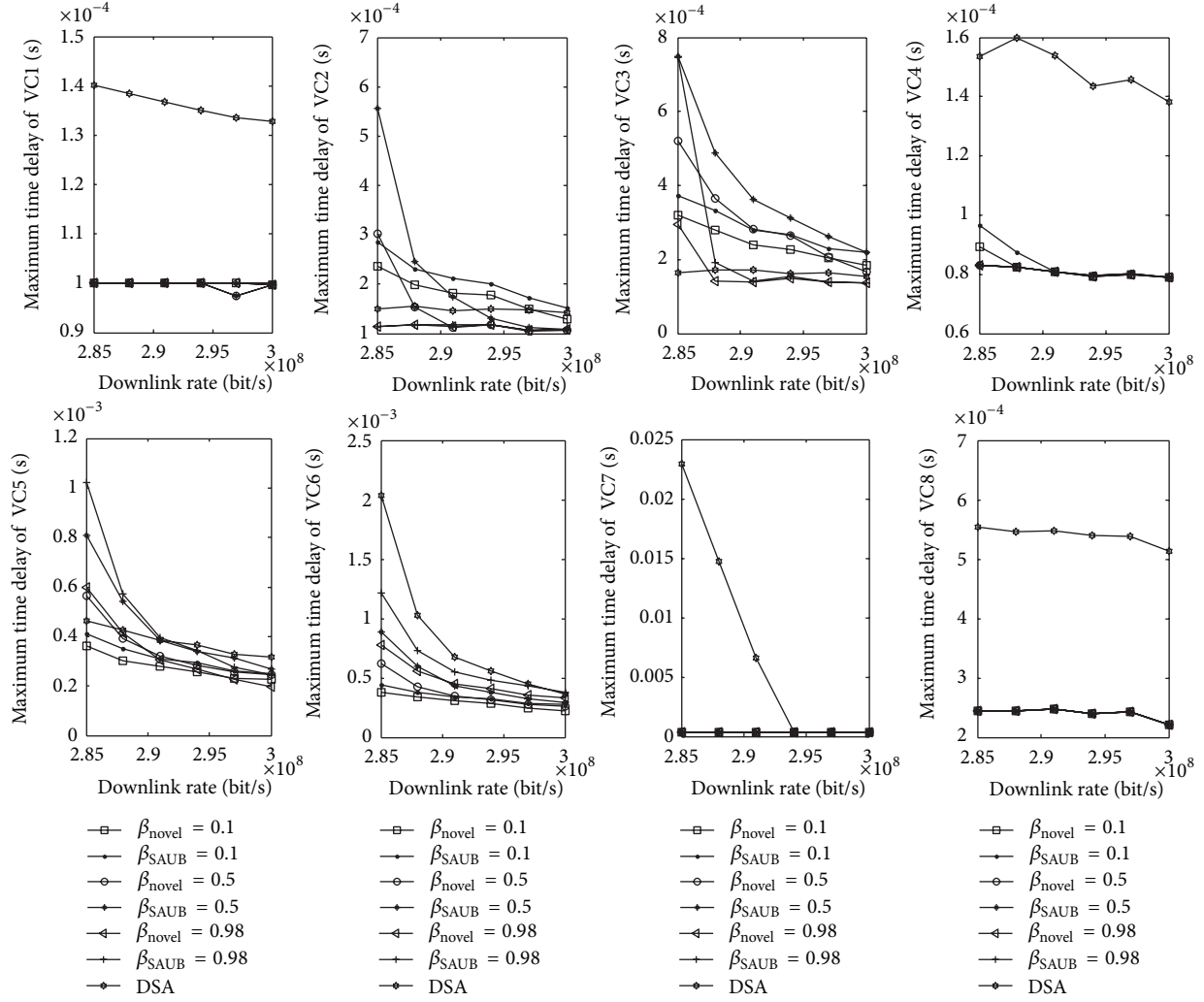


FIGURE 9: The maximum time delay of each VC of source model 2.

TABLE 1: Source with large difference among VC loads.

	VC1	VC2	VC3	VC4	VC5	VC6	VC7	VC8	VC9
Type of source	High data rate source	High data rate source	Middle data rate source	High data rate source	Middle-low data rate source	Low data rate source	High data rate source	High data rate source	Idle frame
Type of service	Path service	Path service	Path service	Path service	Path service	Multiplexing service	Path service	Path service	—
Data rate (Mbps)	15	1.3	0.1	1.5	0.06	0.05	3.3	1.1	—

(VC1) is 300 times as large as the lowest data rate (VC6). The other simulation parameters are set as follows: (1) the length of data frame is 6000 bits; (2) downlink rate ranges from 2.4×10^7 bps to 2.5×10^7 bps; (3) the static priority values of VCs are $p_1 = 1.1$, $p_2 = 1.2$, $p_3 = 1.3$, $p_4 = 1.4$, $p_5 = 1.5$, and $p_6 = 1.6$, respectively.

Simulation results are shown in Figures 3, 4, 5, 6, and 7.

It is shown from the previous figures that for all the VCs, performance of the scheduling delay and the channel

utilization ratio achieved by the proposed algorithm are better than those achieved by the SAUB algorithm, no matter what the value of β is. For example, when the downlink rate is 2.46 Mbps and β is 0.98, the average scheduling delay of VC3, the maximum scheduling delay of VC3, and the channel utilization ratio achieved by the SAUB algorithm are 2.093×10^{-4} s, 8.671×10^{-4} s, and 0.9432, respectively, while those achieved by the proposed algorithm are 1.983×10^{-4} s, 8.485×10^{-4} s, 0.9447, respectively. Therefore, the average scheduling

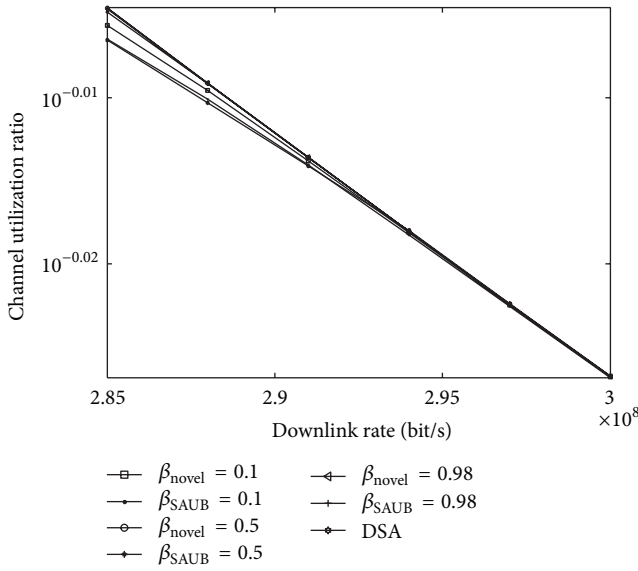


FIGURE 10: The channel utilization ratio of source model 2.

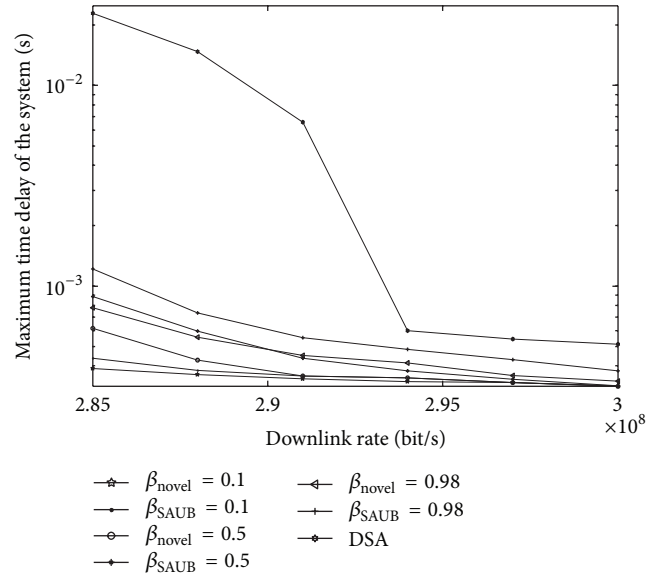


FIGURE 12: The maximum time delay of system of source model 2.

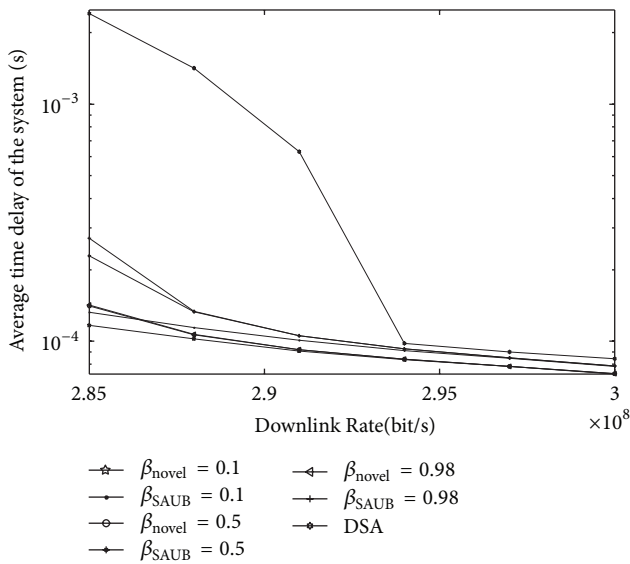


FIGURE 11: The average time delay of system of source model 2.

delay and the maximum scheduling delay of VC3 achieved by the proposed algorithm are 5.26% and 2.15% lower than those achieved by the SAUB algorithm, respectively, and the channel utilization ratio achieved by the proposed algorithm is 0.15% higher than that achieved by the SAUB algorithm. It is also shown that for most of the VCs, when the value of β is large, performance achieved by the proposed algorithm is better than that achieved by the DSA algorithm. For example, when the downlink rate is 2.46 Mbps and β is 0.98, the average scheduling delay of VC3, the maximum scheduling delay of VC3, and the channel utilization ratio achieved by the DSA algorithm are 2.664×10^{-4} s, 1.001×10^{-3} s, and 0.9442, respectively. Therefore, the average scheduling delay and the maximum scheduling delay of VC3 achieved by

the proposed algorithm are 25.56% and 15.25% lower than those achieved by the DSA algorithm, respectively, and the channel utilization ratio achieved by the proposed algorithm is 0.05% higher than that achieved by the DSA algorithm.

When the value of β is small, the performance of the proposed algorithm declines. This is consistent with our theoretical analysis. For all the VCs, scheduling delay varies with the change of β . In practice, we can select an appropriate value of β to meet the delay requirements of all VCs without increasing the downlink rate. Obviously, such an advantage cannot be achieved by the DSA algorithm.

3.2. Simulation on Sources with Moderate Difference among VC Loads. For this kind of sources, manned spacecraft source model [16] is used, whose VCs' division and parameter settings are shown in Table 2. VC1~VC6 are asynchronous VCs. VC7 and VC8 are synchronous VCs. In addition, VC9 is used to generate and transmit idle frames. The highest data rate (VC6) is 47.5 times as large as the lowest data rate (VC4). The other simulation parameters are set as follows: (1) the length of data frame is 8000 bits; (2) downlink rate ranges from 2.85×10^8 bps to 3.0×10^8 bps; (3) the static priority values of VCs are $p_1 = 1.6$, $p_2 = 1.5$, $p_3 = 1.4$, $p_4 = 1.3$, $p_5 = 1.2$, and $p_6 = 1.1$, respectively.

Simulation results are shown in Figures 8, 9, 10, 11, and 12.

Similar to model 1, for most of the VCs, the performance of the proposed algorithm is better than that of the SAUB algorithm and that of the DSA algorithm, no matter what the value of β is. For example, when the downlink rate is 2.91 Mbps and β is 0.5, the average scheduling delay of VC3, the maximum scheduling delay of VC3, and the channel utilization ratio achieved by the SAUB algorithm are 1.123×10^{-4} s, 4.358×10^{-4} s, and 0.9691, respectively, those achieved by the DSA algorithm are 1.339×10^{-4} s, 6.734×10^{-4} s, and 0.9680, respectively, and those achieved by the proposed

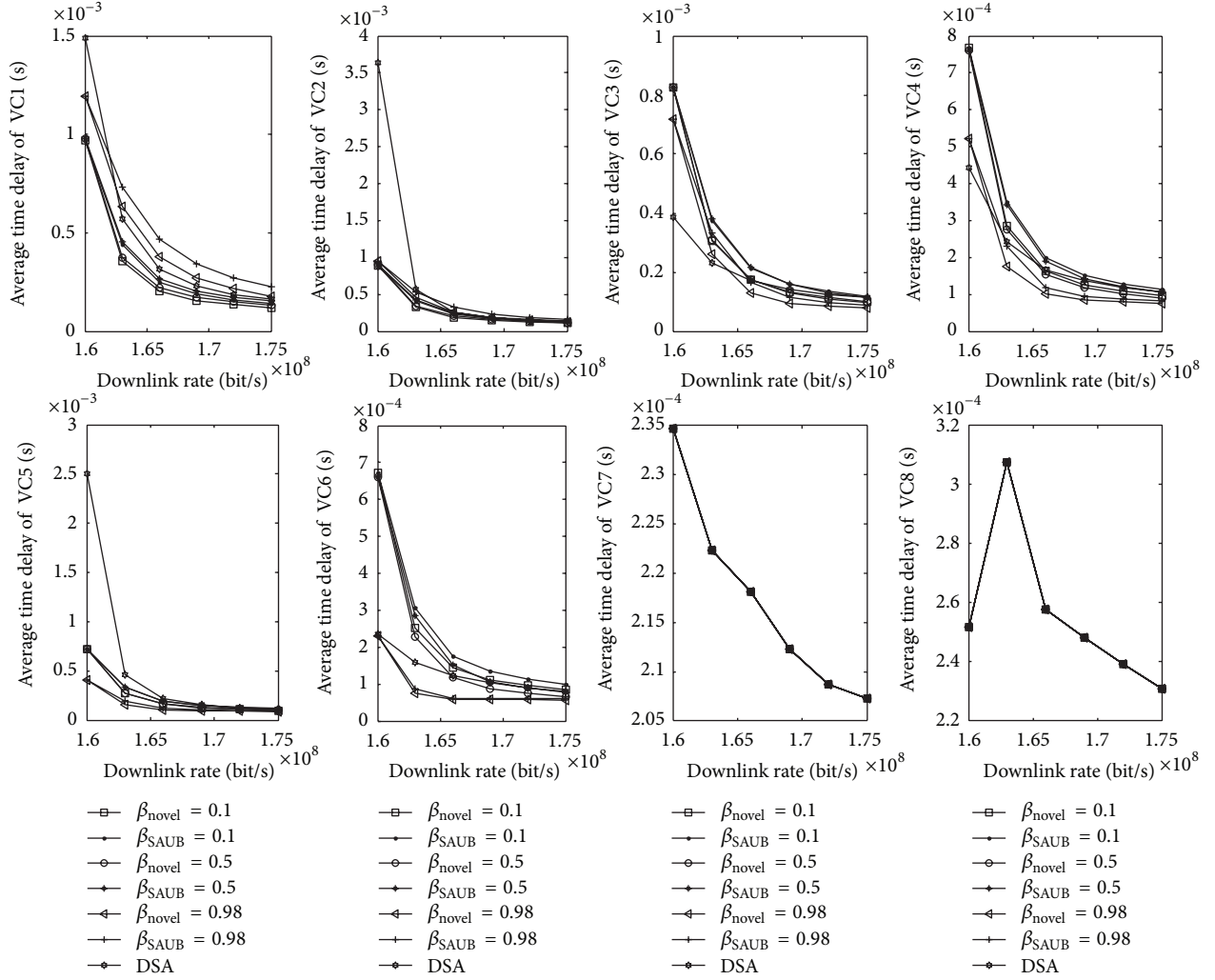


FIGURE 13: The average time delay of each VC of source model 3.

TABLE 2: Manned spacecraft source model.

	VC1	VC2	VC3	VC4	VC5	VC6	VC7	VC8	VC9
Type of source	Platform network data	Physiological telemetry data	Delayed telemetry data	Internet data	Test data	CCD image data	Video surveillance data	Video conference data	Idle frame
Type of service	Path service	Path service	Path service	Internet service	Path service	Bit-stream service	Bit-stream service	Bit-stream service	—
Data rate (Mbps)	10	10	35	2	75	95	44	11	—

algorithm are 9.287×10^{-5} s, 3.459×10^{-4} s, and 0.9692, respectively. Therefore, compared with those achieved by the SAUB algorithm, the average scheduling delay and the maximum scheduling delay of VC3 achieved by the proposed algorithm are 17.30% and 20.63% lower, respectively, and the channel utilization ratio achieved by the proposed algorithm

is 0.01% higher; compared with those achieved by the DSA algorithm, the average scheduling delay and the maximum scheduling delay of VC3 achieved by the proposed algorithm are 30.64% and 48.63% lower, respectively, and the channel utilization ratio achieved by the proposed algorithm is 0.12% higher.

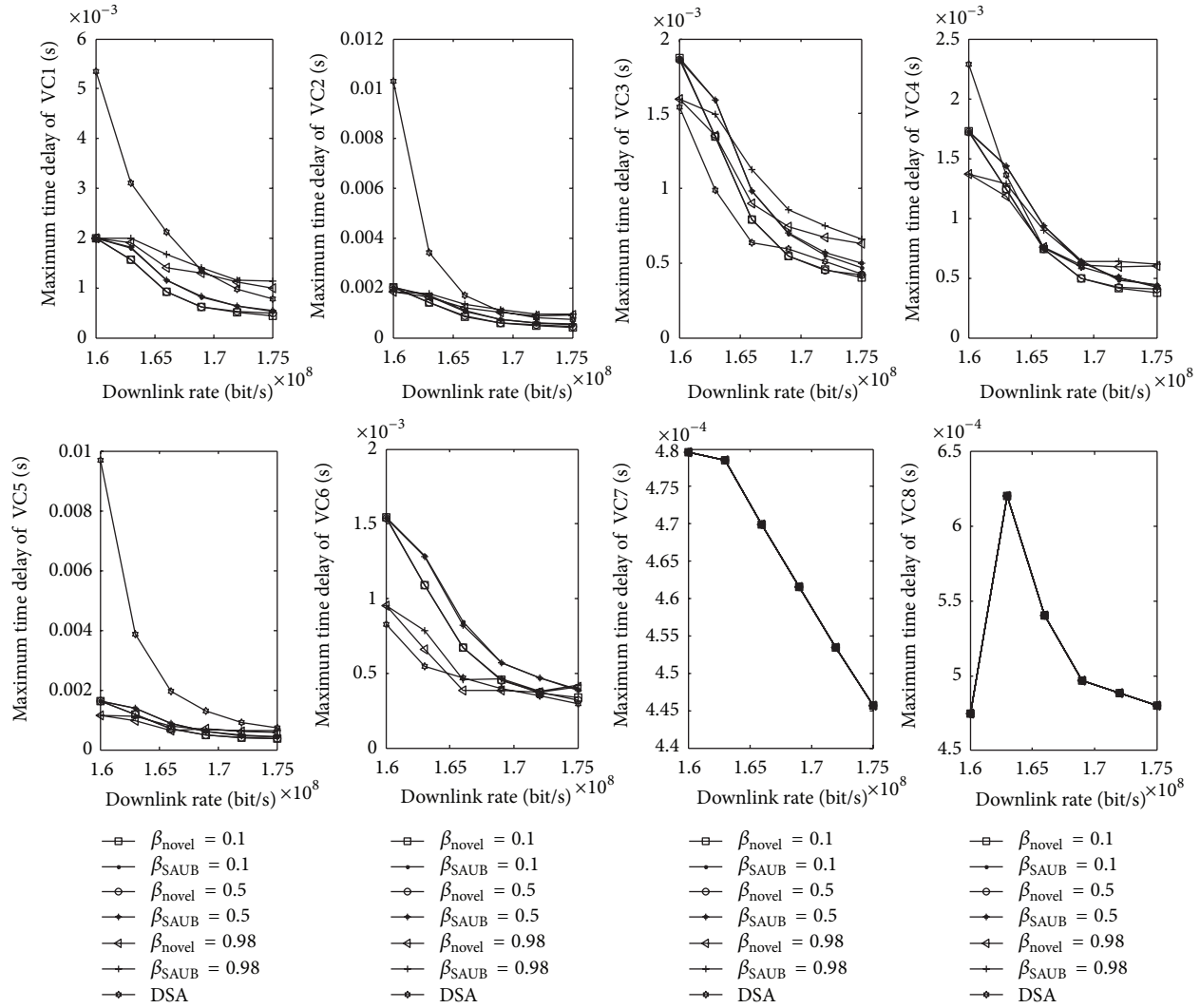


FIGURE 14: The maximum time delay of each VC of source model 3.

For the VCs with high data rates (e.g., VC6), the smaller the value of β is, the shorter the scheduling delay is; for the VCs with lower data rates (e.g., VC3), the larger the value of β is, the shorter the scheduling delay is, which is consistent with theoretical analysis.

3.3. Simulation on Sources with Little Difference among VC Loads. For this kind of sources, a source is selected whose VCs' division and parameter settings are shown in Table 3. VC1~VC6 are asynchronous VCs as shown in the literature [17]. VC7 and VC8 are synchronous VCs. In addition, VC9 is used to generate and transmit idle frames. In order to make the experimental results reflect balanced loads in general sense, the data rates of VC1~VC8 are set around 20 Mbps, but they are slightly different. The other simulation parameters are set as follows: (1) the data frame length is 6000 bits; (2) downlink rate ranges from 1.6×10^8 bps to 1.75×10^8 bps;

(3) the static priority values of VCs are $p_1 = 1.1$, $p_2 = 1.2$, $p_3 = 1.3$, $p_4 = 1.4$, $p_5 = 1.5$, and $p_6 = 1.6$, respectively.

Simulation results are shown in Figures 13, 14, 15, 16, and 17.

Similar to source model 1 and model 2, for most of the VCs, the performance of the proposed algorithm is better than that of the SAUB algorithm and the DSA algorithm, no matter what the value of β is. For example, when the downlink rate is 1.63 Mbps and β is 0.1, the average scheduling delay of VC3, the maximum scheduling delay of VC3, and the channel utilization ratio achieved by the SAUB algorithm are 4.882×10^{-4} s, 1.978×10^{-3} s, and 0.9833, respectively; those achieved by the DSA algorithm are 8.443×10^{-4} s, 5.943×10^{-3} s, and 0.9827, respectively, and those achieved by the proposed algorithm are 4.204×10^{-4} s, 1.889×10^{-3} s, and 0.9833, respectively. Therefore, compared with those achieved by the SAUB algorithm, the average scheduling delay and the maximum scheduling delay of VC3 achieved by the

TABLE 3: Source with little difference among VC loads.

	VC1	VC2	VC3	VC4	VC5	VC6	VC7	VC8	VC9
Type of source	High data rate source	High data rate source	High data rate source	High data rate source	High data rate source	High data rate source	High data rate source	High data rate source	Idle frame
Type of service	Path service	Path service	Path service	Path service	Path service	Path service	Path service	Path service	—
Data rate (Mbps)	20	21	19.5	19	22	18.5	19	21	—

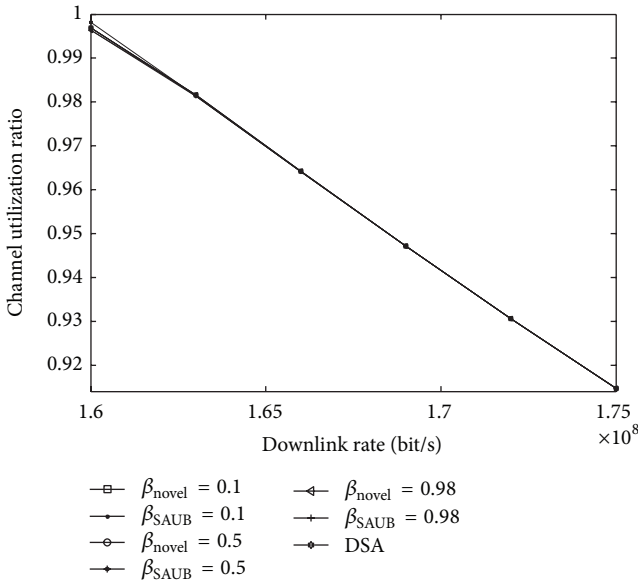


FIGURE 15: The channel utilization ratio of source model 3.

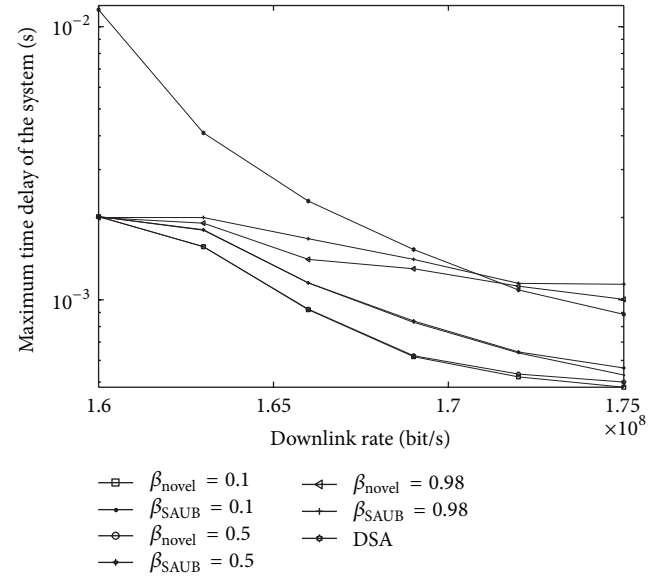


FIGURE 17: The maximum time delay of system of source model 3.

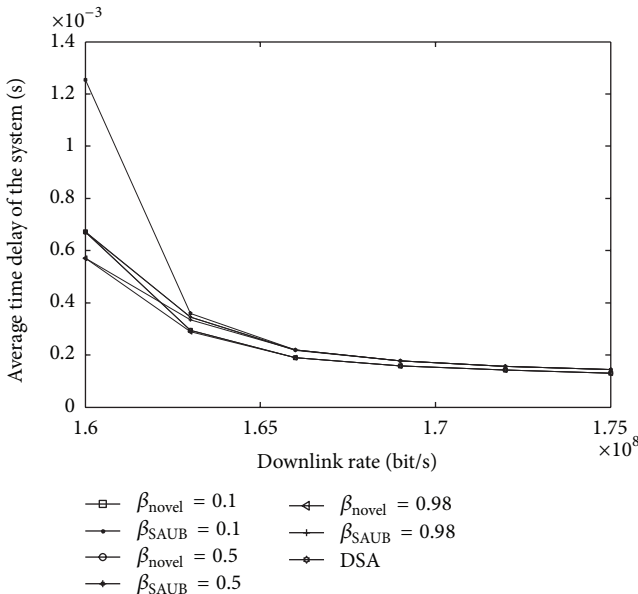


FIGURE 16: The average time delay of system of source model 3.

proposed algorithm are 13.89% and 4.50% lower, respectively; compared with those achieved by the DSA algorithm, the average scheduling delay and the maximum scheduling delay of VC3 achieved by the proposed algorithm are 50.21% and 68.21% lower, respectively, and the channel utilization ratio achieved by the proposed algorithm is 0.06% higher. Because data rates of all the VCs are equivalent, the value of β has relatively little effect on the performance of scheduling delay.

4. Conclusions

We proposed a novel algorithm for virtual channel scheduling based on movable boundary, in which time slots are divided into synchronous ones and asynchronous ones. During the synchronous time slots, the polling scheduling algorithm is used, while during the asynchronous ones, the VC scheduling algorithm based on VC urgency and frame urgency is used. When there are no valid synchronous data frames in the corresponding VC at a certain synchronous time slot, a frame of the other synchronous VC or asynchronous VCs will be transmitted. If there are no valid frames in all VCs, an idle frame will be generated and transmitted. Compared with

the SAUB algorithm, the proposed algorithm can reduce the scheduling delay and improve the channel utilization ratio, while compared with the DSA algorithm, the proposed algorithm is much better as far as the time delay and applicability scope are concerned. In addition, the proposed algorithm is suitable for the scheduling of diverse data sources.

Acknowledgments

This work was supported by the Natural Science Foundation of China (61101116), the Outstanding Young Scholar Plan of Liaoning Province (LJQ2012018), the Innovative Team Project of Liaoning (LT2011T005), and the Open Foundation of Key Laboratory of Shenyang Ligong University (4771004kfs06).

References

- [1] Space Packet Protocol, *Recommendation For Space Data System Standards, CCSDS 133.0-B-1*, Blue Book, Issue 1, CCSDS, Washington, DC, USA, 2003.
- [2] Overview of Space Link Protocols, *Consultative Committee For Space Data System. CCSDS 130. 0-G-1*, Draft Green Book, CCSDS, 2004.
- [3] AOS space data link protocol, *Recommendation For Space Data System Standards, CCSDS 732.0-B-1*, Blue Book, Issue 1, CCSDS, Washington, DC, USA, 2003.
- [4] AOS space data link protocol, *Recommendation For Space Data System Standards, CCSDS 732.0-B-2*, Blue Book, Issue 2, CCSDS, Washington, DC, USA, 2006.
- [5] Y. Tian, X. Na, Y. Xia, X.-L. Gao, and L.-S. Liu, "Research on the performance and application of adaptive frame generation algorithm in AOS protocol," *Journal of Astronautics*, vol. 33, no. 2, pp. 242–248, 2012.
- [6] Y. Tian, C.-S. Pan, Z.-J. Zhang, and Y.-Q. Zhang, "Research on adaptive frame generation algorithm in AOS protocol," *Journal of Astronautics*, vol. 32, no. 5, pp. 1171–1178, 2011.
- [7] Y. Tian, D. Zhang, Z. Tan, C. Pan, and X. Gao, "Research on the packet time delay of frame generation algorithms in advanced orbiting systems," *Chinese High Technology Letters*, vol. 21, no. 11, pp. 1121–1128, 2011.
- [8] Y.-T. Zhao, C.-S. Pan, Y. Tian, Z.-J. Zhang, and M.-X. Bi, "Research on multiplexing efficiency of MPDU based on CCSDS advanced orbiting systems," *Journal of Astronautics*, vol. 31, no. 4, pp. 1195–1199, 2010.
- [9] Y. Wen, *Study of Advanced Orbiting System Multiplexer*, Inner Mongolia University of Technology, Hohhot, China, 2007.
- [10] Y. Q. Gu and W. Z. Tan, "CCSDS downlink virtual channel schedule and performance analysis," *Chinese Space Science and Technology*, vol. 21, pp. 29–35, 2001.
- [11] A. P. Riha and C. Okino, "An advanced orbiting systems approach to quality of service in space-based intelligent communication networks," in *Proceedings of the 27th IEEE Aerospace Conference*, Big Sky, March 2006.
- [12] Y.-X. Bie, C.-S. Pan, and R.-Y. Cai, "Research and simulation on AOS virtual channel multiplexing technique," *Journal of Astronautics*, vol. 32, no. 1, pp. 193–198, 2011.
- [13] G. Z. Shao, Z. B. Hua, J. J. Sun et al., "Design and Implementation of On-board Packard Telemetry Equipment," *Journal of Telemetry, Tracking, and Command*, vol. 22, pp. 9–14, 2001.
- [14] Q. Liu, C. Pan, G. Wang, and W. Liu, "CCSDS advanced orbiting systems, data links protocol: Study on virtual channels scheduling algorithm," in *Proceedings of the 8th International Conference on Intelligent Systems Design and Applications (ISDA '08)*, pp. 351–355, November 2008.
- [15] Y. K. Ma, Z. Z. Zhang, and N. T. Zhang, "Simulation study on data processing system based on CCSDS AOS," *Journal of Telemetry, Tracking, and Command*, vol. 23, pp. 26–30, 2002.
- [16] Z. Tian and Q. J. Zhang, "Research on advanced orbiting systems virtual channels scheduling strategy of manned spacecraft," *Spacecraft Engineering*, vol. 15, pp. 20–26, 2006.
- [17] Y. Zhao, *High Data Rate Multi-Connect Encoder*, Xidian University, Xi'an, China, 2007.

Research Article

Comprehensive Models for Evaluating Rockmass Stability Based on Statistical Comparisons of Multiple Classifiers

Longjun Dong and Xibing Li

School of Resources and Safety Engineering, Central South University, Changsha 410083, China

Correspondence should be addressed to Longjun Dong; rydong001@csu.edu.cn

Received 14 July 2013; Accepted 7 August 2013

Academic Editor: Baochang Zhang

Copyright © 2013 L. Dong and X. Li. This is an open access article distributed under the Creative Commons Attribution License, which permits unrestricted use, distribution, and reproduction in any medium, provided the original work is properly cited.

The relationships between geological features and rockmass behaviors under complex geological environments were investigated based on multiple intelligence classifiers. Random forest, support vector machine, bayes' classifier, fisher's classifier, logistic regression, and neural networks were used to establish models for evaluating the rockmass stability of slope. Samples of both circular failure mechanism and wedge failure mechanism were considered to establish and calibrate the comprehensive models. The classification performances of different modeling approaches were analyzed and compared by receiver operating characteristic (ROC) curves systematically. Results show that the proposed random forest model has the highest accuracy for evaluating slope stability of circular failure mechanism, while the support vector Machine model has the highest accuracy for evaluating slope stability of wedge failure mechanism. It is demonstrated that the established random forest and the support vector machine models are effective and efficient approaches to evaluate the rockmass stability of slope.

1. Introduction

Since their introduction, researches into the areas of machine learning and their applications continue to captivate scientists and engineers from a variety of disciplines. This growing interest among researchers is stemming from the fact that these learning machines have an excellent performance in the issues of pattern recognition and the modeling of nonlinear relationships of multivariate dynamic systems [1]. The widely used and representative classification methods include random forest, support vector machine, bayes' classifier, fisher's classifier, logistic regression, and neural networks.

Comprehensive classification of slope rockmasses, an important activity during exploration, design, and construction for underground openings, is restrained by our limitations in defining the complex geological environments and modeling the relationships between geological features and rockmass behaviors [2, 3]. The published literatures reporting on learning machines provided effective and efficient approaches to establish the nonlinear relationships between geological features and rockmass behaviors [4, 5].

Some recent publications on various geotechnical engineering topics using different methods are given as follows:

remote sensing and GIS based landslide susceptibility assessment [6]; landslide susceptibility mapping [7–9]; early warning landslide susceptibility model using geographic information system (GIS) [10]; regional prediction of landslide hazard [11]; predicting of rockburst classification [12, 13]; predicting destructive effect of masonry structure under blasting vibration of open-pit mine [14]; prediction of seismic liquefaction of sand soil [15]; classification of rocks surrounding in tunnel [16, 17]; classification of top coal cavability of the steep seam [18]; comprehensive evaluation for seismic stability of slopes [19]; prediction rock mechanical behaviors [4]; predicting landslide deformation [20, 21]; predicting of P-wave velocity and anisotropic property of rock [22]; estimating rock properties using sound levels produced during drilling [23]; automated tunnel rock classification using rock engineering systems [24]; estimation of the rock mass deformation modulus using a rock classification system [25]; predicting blast disaster in open pit blasting operation [26, 27]; evaluation of penetration rate of tunnel boring machine in hard rock condition [28]; comparative study of cognitive systems for ground vibration measurements [29]; prediction of longitudinal wave velocity [30]; optimization of tunnel construction [31]; prediction of the rock mass diggability

index [32]; prediction of rock properties from sound levels produced during drilling [5]; modeling mine gas gushing forecasting on virtual environment [33]; rainfall reliability evaluation for stability of municipal solid waste landfills on slope [34]; determination of reservoir induced earthquake [35]; seismic event identification [36]; and prediction of elastic modulus of jointed rock mass [37].

However, researchers study the applications of support vector machine, bayes' classifier, fisher's classifier, logistic regression, and neural networks for evaluating rockmass stability, but few focus on applications of the advanced random forest method in the area, especially that few focus on the overall comparison of performances of different classifiers.

This paper investigated the validity of utilizing different learning machines in the physical problem of slope stability prediction. Random forest, support vector machine, bayes' classifier, fisher's classifier, logistic regression, and neural networks were used to establish comprehensive models for evaluating rockmass stability of slope, and the classification performances of different modeling approaches are analyzed and compared using ROC curves.

2. Data, Models, and Results

2.1. Data. The main scope of this work is to implement the random forest, support vector machine, bayes' classifier, fisher's classifier, logistic regression, and neural networks in the problem of slope stability estimation. In order to forecast the status of stability (S) in the case of rock or soil slopes, the factors that influence S have to be determined. The input layer data consist of six input parameters in the case of circular failure and eight input parameters in the case of wedge failure. The output layer is composed of a single output parameter, the status of stability (S). In this work, the status of stability is considered as a function approximation problem taking values in the range of $[0, 1]$, instead of the discrete values 0 and 1, with 1 indicating stable and 0 indicating failed.

The datasets used in this paper were collected from the publication by Sakellariou and Ferentinou [1]. The first dataset consists of 46 case studies of slopes analyzed for circular critical failure mechanism. Of them, 23 cases are dry (13 failed and 10 stable) and 23 cases are wet (16 failed and 7 stable). The second dataset consists of 22 case studies of rock slopes analyzed for wedge failure mechanism. All cases are dry (10 failed and 12 stable). The original data covering the 46 case studies are presented in Table 1, while the original data covering the 22 case studies are presented in Table 2. In the tables, F is the safety factor. The parameters that have been selected are related to the geotechnical properties and the geometry of each slope. More specifically, the parameters used for circular failure (Figure 1(a)) were unit weight (γ), cohesion (c), angle of internal friction (ϕ), slope angle (β), height (H), and pore water pressure (r_u). In the case of wedge failure (Figure 1(b)), the corresponding input parameters were unit weight (γ), cohesions (c_A) and (c_B), angles of internal friction (ϕ_A) and (ϕ_B), angle of the line of intersection of the two joint sets (ψ_p), slope angle (ψ_s), and height (H), where A and B refer to the two joint sets.

2.2. Random Forest Models. The random forest [38] is an ensemble approach that can also be thought of as a form of the nearest neighbor predictor. Random forests are an ensemble learning method for classification (and regression) that operates by constructing a multitude of decision trees at training time and outputting the class that is the model of the classes output by individual trees. The algorithm for inducing a random forest was developed by Breiman [38] and Adele Cutler, and "Random Forests" is their trademark.

The principle of random forests (RFs) is the aggregation of a large ensemble of decision trees [38]. During training, each individual tree in the ensemble is fitted by sampling the training data with replacement (bootstrap) and growing the tree to full depth on the training sample. The optimal data split at each tree node is determined by randomly choosing m of the available P input variables and selecting the one which splits the node best.

This implementation is based on the original Fortran code authored by Breiman, the inventor of RFs. We considered different parameter configurations for the values of $n_{\text{tree}} = 300, 500, \text{ and } 1000$ (number of trees to build) and $\text{nodesize} = 2$ (minimal size of the terminal nodes of the tree). The results for circular failure mechanism and wedge failure mechanism are listed in Tables 1 and 2.

2.3. Support Vector Machine Models. The extensive applications literature on text categorization, image recognition, rock mechanics and other fields shows the excellent empirical performance of support vector machine (SVM) in many more domains [4, 39]. The underlying idea of SVM classifiers is to calculate a maximal margin hyperplane separating two classes of the data.

To learn nonlinearly separable functions, the data are implicitly mapped to a higher-dimensional space by means of a kernel function, where a separating hyperplane is found. New samples are classified according to the side of the hyperplane they belong to [22]. Many extensions of the basic SVM algorithm can handle multiclass data. The "one-versus-rest" SVM works better for multiclass microarray data [1, 6], so this method was adopted for the analysis of multiclass datasets in the present study. In summary, this approach involves building a separate SVM model to classify each class against the rest and then predict the class of a new sample using the SVM model with the strongest vote.

We used SVM implementation in the DPS software with RBF kernel. The type of support vector machine is C-SVC, the kernel function is RBF, and C value is 1. The results for circular failure mechanism and wedge failure mechanism are listed in Tables 1 and 2, respectively.

2.4. Bayes' Classification Models. The aim of the naive bayesian classifier (NBC), as with other classifiers, is to assign an object I to one of discrete sets of categories C_1, C_2, \dots, C_m based on its observable attributes X_1, X_2, \dots, X_n . NBCs are used in a variety of applications, including document classification, medical diagnosis [40], systems performance management, probability classification of rockburst [41], and other fields. Domingos and Pazzani [42] proved optimality of

TABLE 1: Samples for circular failure mechanism and results.

Case no.	γ (KN/m ³)	C (kPa)	Φ (°)	β (°)	H (m)	r_u	S	F	Moisture	Bayes	Fisher	SVM	LR	BP	RF
1	18.68	26.34	15	35	8.23	0	Failed	1.11	Dry	0	0	0	0	0	0
2	21.4	10	30.34	30	20	0	Stable	1.7	Dry	1	1	1	1	1	1
3	23	0	20	20	100	0.3	Failed	1.2	Wet	0	0	0	0	0	0
4	16	70	20	40	115	0	Failed	1.11	Dry	0	0	0	0	0	0
5	18.84	14.36	25	20	30.5	0.45	Failed	1.11	Wet	0	1	0	0	0	0
6	20	0	36	45	50	0.5	Failed	0.67	Wet	0	0	0	0	0	0
7	18.5	12	0	30	6	0	Failed	0.78	Dry	0	0	0	0	0	0
8	22	20	36	45	50	0	Failed	1.02	Dry	0	0	0	0	0	0
9	12	0	30	35	4	0	Stable	1.46	Dry	0	0	1	0	1	1
10	21.43	0	20	20	61	0.5	Failed	1.03	Wet	0	0	0	0	0	0
11	22	0	40	33	8	0.35	Stable	1.45	Wet	1	1	1	1	1	1
12	20.6	16.28	26.5	30	40	0	Failed	1.25	Dry	1	1	0	1	0	0
13	18	5	30	20	8	0.3	Stable	2.05	Wet	1	1	1	1	1	1
14	23.47	0	32	37	214	0	Failed	1.08	Dry	0	0	0	0	0	0
15	20	20	36	45	50	0.5	Failed	0.83	Wet	0	0	0	0	0	0
16	20.41	24.9	13	22	10.67	0.35	Stable	1.4	Wet	0	0	1	0	0	1
17	18	24	30.15	45	20	0.12	Failed	1.12	Wet	0	0	0	0	0	0
18	28.44	39.23	38	35	100	0	Stable	1.99	Dry	1	1	1	1	1	1
19	21.51	6.94	30	31	76.81	0.38	Failed	1.01	Wet	0	0	0	0	0	0
20	22.4	10	35	45	10	0.4	Failed	0.9	Wet	0	0	0	0	0	0
21	14	11.97	26	30	88	0	Failed	1.02	Dry	0	0	0	0	0	0
22	22	0	36	45	50	0	Failed	0.89	Dry	0	0	0	0	0	0
23	20	0	24.5	20	8	0.35	Stable	1.37	Wet	1	1	1	1	1	1
24	28.44	29.42	35	35	100	0	Stable	1.78	Dry	1	1	1	0	1	1
25	25	120	45	53	120	0	Stable	1.3	Dry	1	1	1	1	1	1
26	19.63	11.97	20	22	12.19	0.405	Failed	1.35	Wet	0	0	0	0	0	0
27	20.41	33.52	11	16	45.72	0.2	Failed	1.28	Wet	0	0	0	0	0	0
28	22.4	100	45	45	15	0.25	Stable	1.8	Wet	1	1	1	1	1	1
29	18.84	14.36	25	20	30.5	0	Stable	1.875	Dry	1	1	1	1	1	1
30	12	0	30	45	8	0	Failed	0.86	Dry	0	0	0	0	0	0
31	18.84	15.32	30	25	10.67	0.38	Stable	1.63	Wet	1	1	0	1	1	0
32	21.82	8.62	32	28	12.8	0.49	Failed	1.03	Wet	1	1	0	1	1	0
33	16.5	11.49	0	30	3.66	0	Failed	1	Dry	0	0	0	0	0	0
34	9.06	11.71	28	35	21	0.11	Failed	1.09	Wet	0	0	0	0	0	0
35	12	0	30	45	8	0	Failed	0.8	Dry	0	0	0	0	0	0
36	18.5	25	0	30	6	0	Failed	1.09	Dry	0	0	0	0	0	0
37	20	20	36	45	50	0.25	Failed	0.96	Wet	0	0	0	0	0	0
38	18.84	57.46	20	20	30.5	0	Stable	2.045	Dry	1	1	0	1	0	0
39	24	0	40	33	8	0.3	Stable	1.58	Wet	1	1	0	1	1	1
40	26	150.05	45	50	200	0	Stable	1.2	Dry	1	1	1	0	0	1
41	14.8	0	17	20	50	0	Failed	1.13	Dry	0	0	0	0	0	0
42	12	0	30	35	4	0	Stable	1.44	Dry	0	0	0	0	1	1
43	22.4	10	35	30	10	0	Stable	2	Dry	1	1	1	1	1	1
44	18.84	0	20	20	7.62	0.45	Failed	1.05	Wet	0	0	0	0	0	0
45	20	0	36	45	50	0.25	Failed	0.79	Wet	0	0	0	0	0	0
46	14	11.97	26	30	88	0.45	Failed	0.625	Wet	0	0	0	0	0	0

TABLE 2: Samples for wedge failure mechanism and results.

No.	γ (KN/m ³)	c_A (KPa)	c_B (KPa)	ϕ_A (°)	ϕ_B (°)	Ψ_p (°)	Ψ_s (°)	H (m)	S	F	Moisture	Bayes	Fisher	LR	NN	RF	SVM
1	27	0	0	30	30	37.5	26	110	Stable	2.09	Dry	1	1	1	1	1	1
2	26	0	0	30.6	22.8	30.6	33	270	Stable	1.4	Dry	1	1	1	1	1	1
3	23.24	19.15	28.73	22.6	19.1	29	40	46	Failed	1	Dry	0	0	0	0	0	0
4	25.14	23.94	47.88	20	30	31.2	65	30.5	Stable	1.36	Dry	1	1	1	1	1	1
5	27	0	0	15	15	43	26	60	Failed	0.97	Dry	0	0	0	0	0	0
6	26	20	20	27	27	60	70	44	Stable	2.35	Dry	1	1	1	0	1	1
7	27	0	0	20	30	37.5	26	50	Stable	1.65	Dry	1	1	1	0	1	1
8	27	0	0	10	10	43	26	60	Failed	0.64	Dry	0	0	0	0	0	0
9	26.66	0	0	45	45	35	50	150	Stable	2.48	Dry	1	1	1	1	1	1
10	20	0	0	40	40	45	60	100	Failed	0.86	Dry	0	0	0	0	0	0
11	27	20	20	20	30	43	26	60	Stable	2.18	Dry	1	1	1	1	1	1
12	19.9	40	19	22	22	37	42	140	Failed	0.9	Dry	0	0	0	1	0	0
13	27	0	0	20	30	37.5	26	110	Stable	1.65	Dry	1	1	1	1	1	1
14	18.84	0	0	30	30	37.5	45	61	Failed	0.78	Dry	0	0	0	0	0	0
15	18.84	30.07	3.6	30	36.7	37.5	45	61	Failed	1.12	Dry	0	0	0	0	0	0
16	26.66	0	0	35	35	30	42	150	Stable	1.73	Dry	1	1	1	1	1	1
17	26	0	0	39	39	60	70	44	Failed	0.9	Dry	1	1	1	0	1	1
18	25	14.36	16.76	28	18	30	45	37	Failed	1	Dry	0	0	0	0	1	0
19	22.8	0	0	35	35	38	47	110	Failed	1.1	Dry	0	0	0	0	0	0
20	24	24.5	49	20	30	65	31	40	Stable	1.77	Dry	1	1	1	1	1	1
21	25	0	0	32.4	32.4	30	48	50	Stable	1.9	Dry	0	0	0	0	1	1
22	27	0	0	20	30	43	26	50	Stable	1.65	Dry	1	1	1	0	1	1

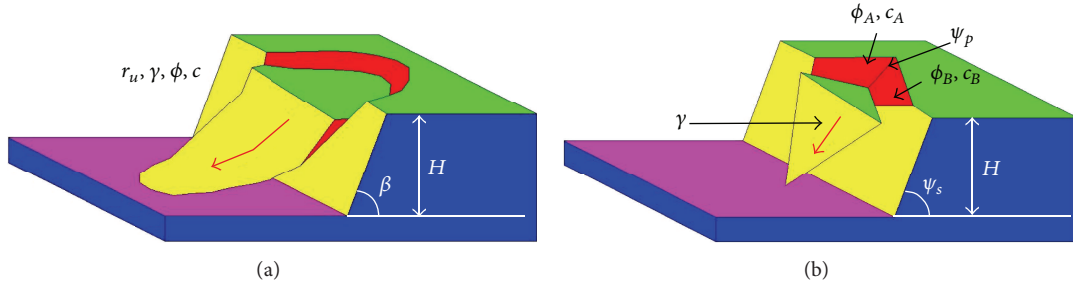


FIGURE 1: Failure models: (a) circular failure mechanism and (b) wedge failure mechanism.

the NBC under certain conditions even when the conditional independence assumption is violated.

This probability calculation is straightforward; conditioning on the observed attributes, we want to find the probability that I belongs to each category, that is, $P(I \in C_i | X_1, X_2, \dots, X_n)$.

Applying Bayes' Theorem [39], this is rewritten as

$$P(I \in C_i | X_1, X_2, \dots, X_n) = \frac{P(I \in C_i) P(X_1, X_2, \dots, X_n | I \in C_i)}{P(X_1, X_2, \dots, X_n)}. \quad (1)$$

Under the mutual conditional independence assumption [39], this reduces to

$$P(I \in C_i | X_1, X_2, \dots, X_n) = \frac{P(I \in C_i) \prod_{j=1}^n P(X_j | I \in C_i)}{P(X_1, X_2, \dots, X_n)} \quad (2)$$

for each category C_i . Since the denominator will be the same for all categories, we only need to calculate the numerator for each category i , choosing

$$i^* \in \arg \max P(I \in C_i) \prod_{j=1}^n P(X_j | I \in C_i) \quad (3)$$

and assigning I to category C_{i^*} . Then, the probability that an event I belongs to category C_i is computed by (2).

In the present study, unit weight (γ), cohesion (c), angle of internal friction (ϕ), slope angle (β), height (H), and pore water pressure (r_u) for circular failure mechanism were expressed as X_1, X_2, X_3, X_4, X_5 , and X_6 . The implementation was through the SPSS software with actual sizes of samples as a priori probabilities, and the discriminant function was given as follows:

$$Y_{\text{Failed}} = 1.6940X_1 - 0.0891X_2 - 0.3232X_3 + 0.6099X_4 - 0.0186X_5 + 8.1056X_6 - 22.9527,$$

$$Y_{\text{Stable}} = 1.9005X_1 - 0.0341X_2 + 0.0287X_3 + 0.2657X_4 - 0.0603X_5 - 1.1166X_6 - 24.3608. \quad (4)$$

For the case of wedge failure mechanism, unit weight (γ), cohesions (c_A) and (c_B), angles of internal friction (ϕ_A) and (ϕ_B), angle of the line of intersection of the two joint sets (ψ_p), slope angle (ψ_s), and height (H) are expressed as X_{w1} , X_{w2} , X_{w3} , X_{w4} , X_{w5} , X_{w6} , X_{w7} , and X_{w8} . Bayes' functions are given as follows:

$$Y_{\text{Failed}} = 15.14X_{w1} - 0.53X_{w2} - 0.82X_{w3} - 1.60X_{w4} + 4.57X_{w5} + 1.16X_{w6} + 0.31X_{w7} + 0.36X_{w8} - 253.77, \quad (5)$$

$$Y_{\text{Stable}} = 17.98X_{w1} - 0.42X_{w2} - 1.22X_{w3} - 2.28X_{w4} + 5.90X_{w5} + 1.45X_{w6} + 0.30X_{w7} + 0.47X_{w8} - 365.60.$$

According to the above established models, the results of circular failure mechanism and wedge failure mechanism cases were obtained and listed in Tables 1 and 2, respectively.

2.5. Fisher's Classification Models. Fisher's discriminant analysis is a classification method that projects high-dimensional data onto a line and performs classification in this one-dimensional space, which is widely used to determine which variable discriminates between two or more classes and to derive a classification model for predicting the group membership of new observations with high accuracy [14–16, 43, 44]. In the present work, the Fisher discriminant analysis was used to establish discriminator for discriminating between failed and stable statuses of slope.

Based on the Fisher discriminant theory, the score of Fisher discriminator can be calculated by

$$Y_{\text{Fisher}} = C_0 + \sum_{i=1}^n C_i X_i, \quad (6)$$

where C_i is the coefficient of the Fisher discriminator. And the Fisher scores of the center for failed and stable statuses can be calculated as \bar{Y}_f and \bar{Y}_s , respectively. Then, the threshold can be obtained by $0.5(\bar{Y}_f + \bar{Y}_s)$. Every case has a set of values of X_i , and corresponding to a Fisher score, if the Fisher score is greater than the threshold, the slope belongs to stable the slope, otherwise to the failed slope.

The indicators unit weight (γ), cohesion (c), angle of internal friction (ϕ), slope angle (β), height (H), and pore

water pressure (r_u) for circular failure mechanism are also expressed as X_1 , X_2 , X_3 , X_4 , X_5 , and X_6 . The calculation was executed through the SPSS software. The discriminant function is

$$Y_{\text{Fisher}} = -0.09X_1 - 0.02X_2 - 0.15X_3 + 0.14X_4 + 0.02X_5 + 3.87X_6 + 0.04. \quad (7)$$

The \bar{Y}_f and \bar{Y}_s are 0.874 and -1.509 , respectively.

For the case of wedge failure mechanism, as in Section 2.4, unit weight (γ), cohesions (c_A) and (c_B), angles of internal friction (ϕ_A) and (ϕ_B), angle of the line of intersection of the two joint sets (ψ_p), slope angle (ψ_s), and height (H) are also expressed as X_{w1} , X_{w2} , X_{w3} , X_{w4} , X_{w5} , X_{w6} , X_{w7} , and X_{w8} . The Fisher discriminant function is given as follows, and the \bar{Y}_f and \bar{Y}_s are -2.743 and 2.134 , respectively, as

$$Y_{\text{Fisher}} = 0.58X_{w1} - 0.02X_{w2} + 0.08X_{w3} - 0.14X_{w4} + 0.27X_{w5} + 0.06X_{w6} + 0.003X_{w7} + 0.02X_{w8} - 23.23. \quad (8)$$

According to the above established Fisher models, the results of circular failure mechanism and wedge failure mechanism cases were also obtained and listed in Tables 1 and 2, respectively.

2.6. Logistic Regression Models. Logistic regression (LR) is a statistical modeling technique in which the probability of a category is related to a set of explanatory variables. An explanation of logistic regression begins with an explanation of the logistic function, which always takes values between zero and one. The logistic model is defined by the following equations:

$$z = a_0 + \sum_{i=1}^n a_i x_i, \quad (9)$$

$$P(z) = \frac{e^z}{1 + e^z},$$

where z is a measure of the contribution of the explanatory variables x_i ($i = 1, \dots, n$), a_i are the regression coefficients which are obtained by maximum likelihood in conjunction with their standard errors Δa_i , and $P(z)$ is the categorical response of variables that represents the probability of a particular outcome. In this particular application, x_i are the slope rockmass parameters of interest, and $P(z)$ is the probability of having stable and failed statuses. The calculation of LR is finished through the SPSS software, and logistic functions for circular failure mechanism and wedge failure mechanism cases are given as follows:

$$P(z_c) = \frac{e^{0.459x_1 - 0.145x_2 + 0.515x_3 - 0.47x_4 - 0.147x_5 - 13.936x_6 - 4.262}}{1 + e^{0.459x_1 - 0.145x_2 + 0.515x_3 - 0.47x_4 - 0.147x_5 - 13.936x_6 - 4.262}}, \quad (10)$$

$$P(z_w) = \frac{e^{8.201x_{w1} + 0.567x_{w2} + 0.344x_{w3} - 1.264x_{w4} + 3.185x_{w5} + 0.558x_{w6} - 0.05x_{w7} + 0.225x_{w8} - 304.38}}{1 + e^{8.201x_{w1} + 0.567x_{w2} + 0.344x_{w3} - 1.264x_{w4} + 3.185x_{w5} + 0.558x_{w6} - 0.05x_{w7} + 0.225x_{w8} - 304.38}}.$$

The threshold of the above two logistic regression models is 0.5, and the results are listed in Tables 1 and 2.

2.7. Neural Networks Models. Neural networks (NNs) have long been used in problems such as this, with a lot of data, many variables, and the possibility of noise in the data.

Each input point is a high-dimensional vector. The neural network is organized in a series of layers, where the input vector enters at the left side of the network, which is then projected to a “hidden layer.” Each unit in the hidden layer is a weighed sum of the values in the first layer. This layer then projects to an output layer, which is where the desired answer appears.

In the present work, a multi-layer perceptron network model is used. Training took place for the specific range of values that cover the training dataset. Trying to achieve the best network’s performance, several networks with different architectures were developed using all of the possible variations of the backpropagation algorithms available in MATLAB 2010b. The final network architecture for the prediction of safety factor against circular failure it is (6-10-1), whereas in the case of wedge failure is (8-12-1). The learning rate was set to 0.01 and the error goal was set to 0.0001. The results for circular failure mechanism and wedge failure mechanism are listed in Tables 1 and 2, respectively.

3. Comparisons and Discussions

The ROC curve is used to evaluate and compare the established RF, SVM, Bayes, Fisher, LR, and NN classification models in slope stability evaluation. ROC is a graphical plot which illustrates the performance of a binary classifier system as its discrimination threshold is varied [45]. It is created by plotting the fraction of true positives out of the positives (TPR = true positive rate) versus the fraction of false positives out of the negatives (FPR = false positive rate), at various threshold settings.

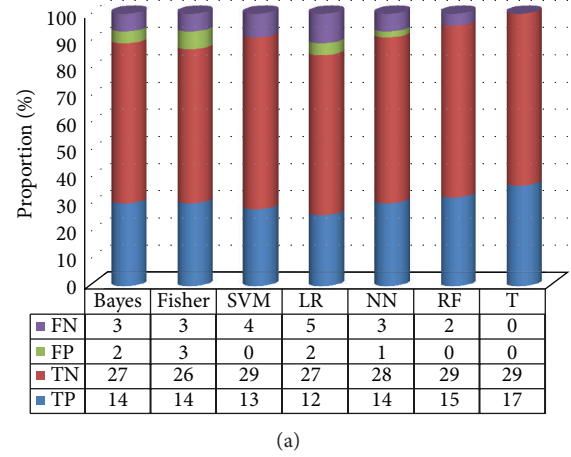
ROC analysis provides tools to select possibly optimal models and to discard suboptimal ones independently from (and prior to specifying) the cost context or the class distribution. ROC analysis is related in a direct and natural way to cost/benefit analysis of diagnostic decision making.

In the present study, the stable and failed statuses of slope were considered a two-class prediction problem (binary classification), in which the outcomes were labeled either as positive (p , stable) or negative (n , failed). There are four possible outcomes from a binary classifier. If the outcome from a prediction is p' and the actual value is also p , then it is called true positive (TP); however, if the actual value is n , then it is said to be false positive (FP). Conversely, a true negative (TN) value has occurred when both the prediction outcome and the actual value are n , and a false negative (FN) value is when the prediction outcome is n' while the actual value is p .

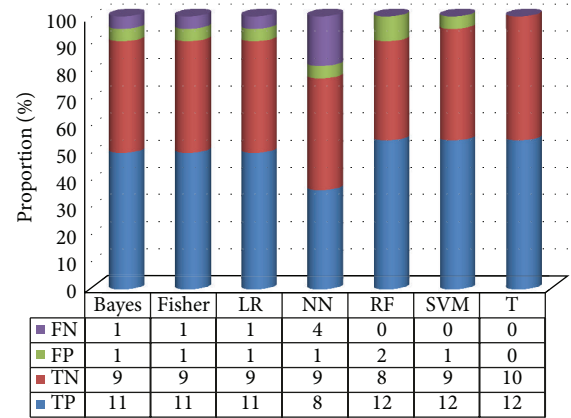
An experiment from p positive and n negative was defined for instances. The four outcomes can be formulated in a 2×2 contingency table or a confusion matrix, as follows in Table 3.

TABLE 3: Contingency matrix for the two-class prediction problem.

		Actual value		Total
		p	n	
Prediction outcome	p'	True positive (TP)	False positive (FP)	p
	n'	False negative (FN)	True negative (TN)	n
Total		p	n	



(a)



(b)

FIGURE 2: Proportions of TP, TN, FP, and FN for the RF, SVM, Bayes, Fisher, LR, and NN classification models: (a) circular failure mechanism and (b) wedge failure mechanism.

The specificity or the true negative rate (TNR) is defined as the percentage of slope which is correctly identified as being failed:

$$\text{Specificity} = \frac{\text{TN}}{\text{TN} + \text{FP}}. \quad (11)$$

The quantity $1 - \text{specificity}$ is the false positive rate and is the percentage of slopes that are incorrectly identified as being stable statuses. The sensitivity or the true positive rate (TPR) is defined as the percentage of slope which is correctly identified as being stable status:

$$\text{Sensitivity} = \frac{\text{TP}}{\text{TP} + \text{FN}}. \quad (12)$$

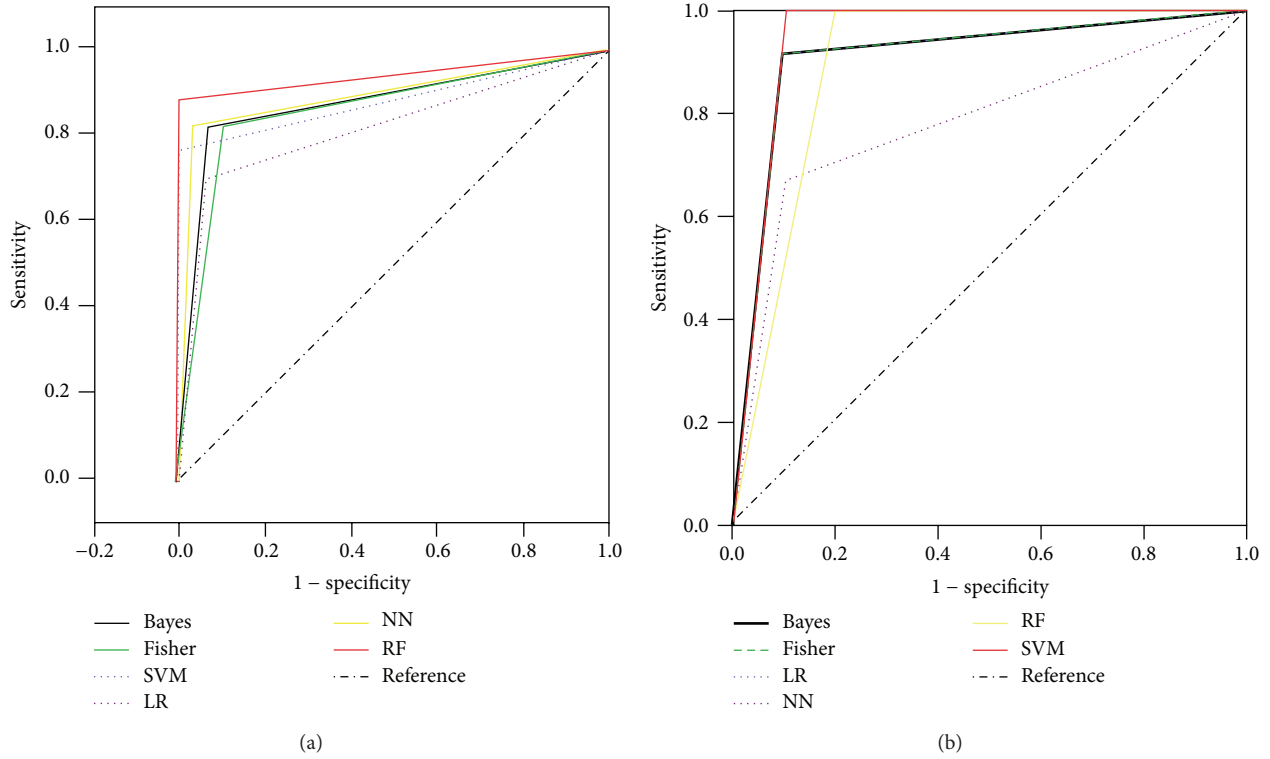


FIGURE 3: ROC curves for the RF, SVM, Bayes, Fisher, LR, and NN classification models: (a) circular failure mechanism and (b) wedge failure mechanism.

TABLE 4: Areas under ROC curves for cases of circular failure mechanism.

Methods	Areas	Standard error	P value	95% confidence interval	
				Upper	Lower
Bayes	0.877	0.061	0.0000	0.7573	0.9973
Fisher	0.860	0.064	0.0001	0.7355	0.9846
SVM	0.882	0.064	0.0000	0.7579	1.0000
LR	0.819	0.073	0.0004	0.6757	0.9612
BP	0.895	0.059	0.0000	0.7794	1.0000
RF	0.941	0.047	0.0000	0.8497	1.0000

For the cases of circular failure mechanism, the proportions of TP, TN, FP, and FN for the RF, SVM, Bayes, Fisher, LR, and NN classification models are shown in Figure 2(a). ROC curves are shown in Figure 3(a). And the areas under the ROC curves of RF, SVM, Bayes, Fisher, LR, and NN classification models are listed in Table 4. Figure 2(a) shows that the accuracy of RF model is the highest with the TP of 15 and TN of 29. Figure 3(a) and Table 4 show that RF has the biggest area (0.941), followed by NN (0.895), SVM (0.882), Bayes (0.877), Fisher (0.860), and LR (0.819). For the cases of wedge failure mechanism, the proportions of TP, TN, FP, and FN for RF, SVM, Bayes, Fisher, LR, and NN classifiers are shown in Figure 2(b). ROC curves are shown in Figure 3(b). And the areas under ROC curves of RF, SVM, Bayes, Fisher, LR, and NN classifiers are listed in Table 5. Figure 2(b) shows that the accuracy of SVM models is the highest with the TP of 12 and TN of 9. Figure 3(b) and Table 5 show that SVM has the

biggest area (0.95), and followed by Bayes' and Fisher models, and LR, which have the same area (0.908), and then followed by RF (0.9) and NN (0.783). Figures 2(a) and 2(b) clearly show that both the RF and SVM models have the highest TP and TN. It is suggested that the evaluated methods for different failure mechanism slopes are different, and RF and SVM models can be the preferred ones for circular failure and wedge failure landslides, respectively. It is noted that the trained and calibrated models are influenced by the size of training samples, and the reliability and applicability of the proposed models in this paper can be improved with increasing training samples.

4. Conclusions

This paper demonstrates the applicability and feasibility of the RF, SVM, Bayes (NBC), Fisher, LR, and NN classification

TABLE 5: Areas under ROC curves for cases of wedge failure mechanism.

Methods	Areas	Standard error	P value	95% confidence interval	
				Upper	Lower
Bayes	0.908	0.073	0.0010	0.7650	1.000
Fisher	0.908	0.073	0.0010	0.7650	1.000
LR	0.908	0.073	0.0010	0.7650	1.000
NN	0.783	0.102	0.0250	0.5830	0.984
RF	0.900	0.079	0.0020	0.7460	1.000
SVM	0.950	0.057	0.0000	0.8380	1.000

models to evaluate the rockmass stability of slopes. Samples of both circular failure mechanism and wedge failure mechanism were considered to establish and calibrate discriminant models. The classification performances of different modeling approaches are analyzed and compared by ROC curves. Results show that the established RF, SVM, Bayes, Fisher, LR, and NN classification models can evaluate the slope statuses with a high accuracy. RF models have the highest accuracy for slope cases for circular failure mechanism, while SVM models have the highest accuracy for slope cases for wedge failure mechanism. Both the RF and SVM models have the highest TP and TN. It is suggested that the established models for different failure mechanism slopes are different, and RF and SVM models can be the preferred ones for evaluating the stability of circular failure and wedge failure landslides, respectively.

Conflict of Interests

The authors declare that there is no conflict of interests regarding the publication of this paper.

Acknowledgments

The support of the National Natural Science Foundation of China (50934006), National Basic Research (973) Program of China (2010CB732004), China Scholarship Council, Doctoral Candidate Innovation Research Support Program by Science & Technology Review (kjdb201001-7), and Scholarship Award for Excellent Doctoral Student from Ministry of Education of China is gratefully acknowledged.

References

- [1] M. G. Sakellariou and M. D. Ferentinou, "A study of slope stability prediction using neural networks," *Geotechnical and Geological Engineering*, vol. 23, no. 4, pp. 419–445, 2005.
- [2] L.-J. Dong and X.-B. Li, "Interval non-probabilistic reliability method for surrounding jointed rock mass stability of underground caverns," *Chinese Journal of Geotechnical Engineering*, vol. 33, no. 7, pp. 1007–1013, 2011.
- [3] L.-J. Dong and X.-B. Li, "Interval parameters and credibility of representative values of tensile and compression strength tests on rock," *Chinese Journal of Geotechnical Engineering*, vol. 32, no. 12, pp. 1969–1974, 2010.
- [4] L. Dong, X. Li, and Z. Zhou, "Nonlinear model-based support vector machine for predicting rock mechanical behaviors," *Advanced Science Letters*, vol. 5, pp. 806–810, 2012.
- [5] B. Rajesh Kumar, H. Vardhan, M. Govindaraj, and G. Vijay, "Regression analysis and ANN models to predict rock properties from sound levels produced during drilling," *International Journal of Rock Mechanics and Mining Sciences*, vol. 58, pp. 61–72, 2013.
- [6] S. Kundu, A. Saha, D. Sharma, and C. Pant, "Remote sensing and GIS based landslide susceptibility assessment using binary logistic regression model: a case study in the Ganeshganga Watershed, Himalayas," *Journal of the Indian Society of Remote Sensing*, 2013.
- [7] H. R. Pourghasemi, A. G. Jirandeh, B. Pradhan, C. Xu, and C. Gokceoglu, "Landslide susceptibility mapping using support vector machine and GIS at the Golestan Province, Iran," *Journal of Earth System Science*, vol. 122, no. 2, pp. 349–369, 2013.
- [8] S. Pascale, S. Parisi, A. Mancini et al., "Landslide susceptibility mapping using artificial neural network in the urban area of Senise and San Costantino Albanese (Basilicata, Southern Italy)," in *Computational Science and Its Applications—ICCSA 2013*, pp. 473–488, Springer, 2013.
- [9] H. Wang, J. Li, B. Zhou, Z. Yuan, and Y. Chen, "Application of a hybrid model of neural networks and genetic algorithms to evaluate landslide susceptibility," *Natural Hazards and Earth System Sciences Discussions*, vol. 1, pp. 353–388, 2013.
- [10] M. Venkatesan, A. Thangavelu, and P. Prabhavathy, "An improved Bayesian classification data mining method for early warning landslide susceptibility model using GIS," in *Proceedings of the 7th International Conference on Bio-Inspired Computing: Theories and Applications (BIC-TA '12)*, pp. 277–288, 2013.
- [11] D. T. Bui, B. Pradhan, O. Lofman, I. Revhaug, and Ø. B. Dick, "Regional prediction of landslide hazard using probability analysis of intense rainfall in the Hoa Binh province, Vietnam," *Natural Hazards*, vol. 66, no. 2, pp. 707–730, 2013.
- [12] L. Dong, X. Li, and K. Peng, "Prediction of rockburst classification using Random Forest," *Transactions of Nonferrous Metals Society of China*, vol. 23, pp. 472–477, 2013.
- [13] A. C. Adoko, C. Gokceoglu, L. Wu, and Q. J. Zuo, "Knowledge-based and data-driven fuzzy modeling for rockburst prediction," *International Journal of Rock Mechanics and Mining Sciences*, vol. 61, pp. 86–95, 2013.
- [14] L. Dong, X. Li, G. Zhao, and F. Gong, "Fisher discriminant analysis model and its application to predicting destructive effect of masonry structure under blasting vibration of open-pit mine," *Chinese Journal of Rock Mechanics and Engineering*, vol. 28, no. 4, pp. 750–756, 2009.

- [15] L. J. Dong, F. Y. Wang, Y. F. Bai, and Y. F. Liu, "A Fisher discriminant analysis model for prediction of seismic liquefaction of sand soil," *Near-Surface Geophysics and Human Activity*, pp. 146–150, 2008.
- [16] L. J. Dong, Y. H. Fu, Y. F. Liu, and Y. F. Bai, "A Fisher discriminant analysis model for classification of rocks surrounding in tunnel," in *Proceedings of the Information Technology and Environmental System Sciences (Itess '08)*, vol. 2, pp. 632–636, 2008.
- [17] L. J. Dong, D. T. Hu, Y. F. Bai, and Y. F. Liu, "Unascertained average grade model for surrounding rock classification on hydraulic tunnels," *Progress in Safety Science and Technology*, vol. 7, pp. 2227–2231, 2008.
- [18] L.-J. Dong, X.-B. Li, and Y.-F. Bai, "A Fisher discriminant analysis model for classifying top coal cavability of the steep seam," *Journal of the China Coal Society*, vol. 34, no. 1, pp. 58–63, 2009.
- [19] L. Dong and F. Wang, "Comprehensive evaluation seismic stability of slopes based on unascertained measurement," *The Chinese Journal of Geological Hazard and Control*, vol. 18, pp. 74–78, 2007.
- [20] L. Dong and X. Li, "An application of grey-general regression neural network for predicting landslide deformation of Dahu Mine in China," *Advanced Science Letters*, vol. 6, pp. 577–581, 2012.
- [21] X. B. Li, L. J. Dong, G. Y. Zhao et al., "Stability analysis and comprehensive treatment methods of landslides under complex mining environment—A case study of Dahu landslide from Linbao Henan in China," *Safety Science*, vol. 50, no. 4, pp. 695–704, 2012.
- [22] T. N. Singh, R. Kanchan, K. Saigal, and A. K. Verma, "Prediction of p-wave velocity and anisotropic property of rock using artificial neural network technique," *Journal of Scientific and Industrial Research*, vol. 63, no. 1, pp. 32–38, 2004.
- [23] H. Vardhan, G. R. Adhikari, and M. Govinda Raj, "Estimating rock properties using sound levels produced during drilling," *International Journal of Rock Mechanics and Mining Sciences*, vol. 46, no. 3, pp. 604–612, 2009.
- [24] R. Huang, J. Huang, N. Ju, and Y. Li, "Automated tunnel rock classification using rock engineering systems," *Engineering Geology*, vol. 156, pp. 20–27, 2013.
- [25] A. Khabbazi, M. Ghafoori, G. Lashkaripour, and A. Cheshomi, "Estimation of the rock mass deformation modulus using a rock classification system," *Geomechanics and Geoengineering*, vol. 8, pp. 46–52, 2013.
- [26] K. Manoj and M. Monjezi, "Prediction of flyrock in open pit blasting operation using machine learning method," *International Journal of Mining Science and Technology*, vol. 23, no. 3, pp. 313–316, 2013.
- [27] L. Dong, X. Li, M. Xu, and Q. Li, "Comparisons of random forest and support vector machine for predicting blasting vibration characteristic parameters," in *Proceedings of the 1st International Symposium on Mine Safety Science and Engineering (ISMSSSE '11)*, vol. 26, pp. 1772–1781, October 2011.
- [28] A. Salimi and M. Esmaeili, "Utilising of linear and non-linear prediction tools for evaluation of penetration rate of tunnel boring machine in hard rock condition," *International Journal of Mining and Mineral Engineering*, vol. 4, pp. 249–264, 2013.
- [29] A. Verma and T. Singh, "Comparative study of cognitive systems for ground vibration measurements," *Neural Computing and Applications*, vol. 22, no. 1, supplement, pp. 341–350, 2013.
- [30] A. K. Verma and T. N. Singh, "A neuro-fuzzy approach for prediction of longitudinal wave velocity," *Neural Computing and Applications*, vol. 22, no. 7-8, pp. 1685–1693, 2013.
- [31] J. Xing, A. Jiang, Z. Wen, and J. Qin, "A nonlinear optimization technique of tunnel construction based on DE and LSSVM," *Mathematical Problems in Engineering*, vol. 2013, Article ID 980154, 11 pages, 2013.
- [32] O. Saeidi, S. R. Torabi, and M. Ataei, "Prediction of the rock mass diggability index by using fuzzy clustering-based, ANN and multiple regression methods," *Rock Mechanics and Rock Engineering*, 2013.
- [33] T. Wang, L. Cai, Y. Fu, and T. Zhu, "A wavelet-based robust relevance vector machine based on sensor data scheduling control for modeling mine gas gushing forecasting on virtual environment," *Mathematical Problems in Engineering*, vol. 2013, Article ID 579693, 4 pages, 2013.
- [34] Y. L. Tsai, "Rainfall reliability evaluation for stability of municipal solid waste landfills on slope," *Mathematical Problems in Engineering*, vol. 2013, Article ID 653282, 10 pages, 2013.
- [35] P. Samui and D. Kim, "Determination of reservoir induced earthquake using support vector machine and Gaussian process regression," *Applied Geophysics*, vol. 10, pp. 229–234, 2013.
- [36] L. Dong, X. Li, C. Ma, and W. Zhu, "Comparisons of logistic regression and Fisher discriminant classifier to seismic event identification," *Disaster Advances*, vol. 6, p. 8, 2013.
- [37] P. Samui, "Multivariate adaptive regression spline (Mars) for prediction of elastic modulus of jointed rock mass," *Geotechnical and Geological Engineering*, vol. 31, pp. 249–253, 2013.
- [38] L. Breiman, "Random forests," *Machine Learning*, vol. 45, no. 1, pp. 5–32, 2001.
- [39] F. Wang, L. Dong, and Z. Xu, "Phreatic line predicted method-based SVM for stability analysis of tailing dam," *Applied Mechanics and Materials*, vol. 44–47, pp. 3398–3402, 2011.
- [40] P. Berchiulla, F. Foltran, and D. Gregori, "Naïve Bayes classifiers with feature selection to predict hospitalization and complications due to objects swallowing and ingestion among European children," *Safety Science*, vol. 51, pp. 1–5, 2013.
- [41] Y.-H. Fu and L.-J. Dong, "Bayes discriminant analysis model and its application to the prediction and classification of rock-burst," *Journal of China University of Mining and Technology*, vol. 38, no. 4, pp. 528–533, 2009.
- [42] P. Domingos and M. Pazzani, "On the optimality of the simple Bayesian classifier under zero-one loss," *Machine Learning*, vol. 29, no. 2-3, pp. 103–130, 1997.
- [43] A. P. Worth and M. T. D. Cronin, "The use of discriminant analysis, logistic regression and classification tree analysis in the development of classification models for human health effects," *Journal of Molecular Structure: THEOCHEM*, vol. 622, no. 1-2, pp. 97–111, 2003.
- [44] Y. Bai, J. Deng, L. Dong, and X. Li, "Application of Fisher discriminant method in goaf collapse prediction," *Mining Research and Development*, vol. 28, no. 5, p. 5, 2008.
- [45] A. P. Bradley, "The use of the area under the ROC curve in the evaluation of machine learning algorithms," *Pattern Recognition*, vol. 30, no. 7, pp. 1145–1159, 1997.

Research Article

A Routing Algorithm for WiFi-Based Wireless Sensor Network and the Application in Automatic Meter Reading

Li Li,¹ Xiaoguang Hu,¹ and Baochang Zhang²

¹ School of Automation Science and Electrical Engineering, BeiHang University, Beijing 100191, China

² Science and Technology on Aircraft Control Laboratory, School of Automation Science and Electrical Engineering, BeiHang University, Beijing 100191, China

Correspondence should be addressed to Li Li; lilihe@buaa.edu.cn

Received 25 May 2013; Revised 20 July 2013; Accepted 27 July 2013

Academic Editor: Gelan Yang

Copyright © 2013 Li Li et al. This is an open access article distributed under the Creative Commons Attribution License, which permits unrestricted use, distribution, and reproduction in any medium, provided the original work is properly cited.

The Automatic Meter Reading (AMR) network for the next generation Smart Grid is required to possess many essential functions, such as data reading and writing, intelligent power transmission, and line damage detection. However, the traditional AMR network cannot meet the previous requirement. With the development of the WiFi sensor node in the low power cost, a new kind of wireless sensor network based on the WiFi technology can be used in application. In this paper, we have designed a new architecture of WiFi-based wireless sensor network, which is suitable for the next generation AMR system. We have also proposed a new routing algorithm called Energy Saving-Based Hybrid Wireless Mesh Protocol (E-HWMP) on the premise of current algorithm, which can improve the energy saving of the HWMP and be suitable for the WiFi-based wireless sensor network. The simulation results show that the life cycle of network is extended.

1. Introduction

Many countries have been carrying their own Smart Grid plan into reality [1, 2]. Although the focuses of their plans are different, the intellectualization of power utilization for terminal users is important work in most countries. As the footstone of the Smart Grid, the new generation of AMR system in Smart Grid not only can collect the data of power meters remotely, but also can have functions of power rationing, multirate billing, remote on-off control, power line loss test, antistealing, and the monitoring and management of power line and meters. Those functions should send data to terminal users, such as power meters, which is different from the old AMR systems. So a new generation of AMR architecture should be researched to meet the Smart Grid's new requirements [3].

There are many kinds of AMR communication technologies in the world now, such as Radio Frequency (RF) [4, 5], ZigBee-based wireless sensor network (WSN) [6–8], GPRS and 3G [9, 10], Power Line Carrier Communication (PLC) [11–13], and 485 bus. Among these technologies, WSN and

PLC are considered to be the key technologies to build a new generation of Smart Grid AMR systems in the future. In this paper, we mainly discuss the wireless sensor network for AMR and management of the terminal users.

The communication technologies of Wireless Sensor Networks used in short-range wireless are ZigBee, Ultrawide Band (UWB) WiFi (Wireless Fidelity), and so forth. With the development of SoC technology in recent years, the ultralow power WiFi System on SoC chip has emerged [14, 15]. As a result, WiFi-based wireless sensor networks come into use [16–22]. WiFi-based wireless sensor network has many special characteristics, such as high bandwidth, a large range covering, direct accessing to the WiFi hotspots at intelligent buildings, and smart home without additional equipment. The characteristics make it possible to decrease the costs, so WiFi-based wireless sensor network is more suitable for the AMR and management system in intelligent buildings and smart home.

Recently, many researchers and developers pay much attention to WiFi-based wireless sensor networks. GainSpan,

a company invested by Intel, developed the famous low-power WiFi sensor chips GS 1010 [14], and G2 Microsystems developed the G2C5x series chips [15]. It was reported that power consumption of GS 1010 sensor nodes is so low that a WiFi node can work five to ten years with an AA battery; of course, the working time also depends on the frequencies and time when the chip wakes up to work. Yu-Ping Chen compared GS 1010 with ZigBee sensors in standby and startup power consumption and got the conclusion that the average standby and startup power consumption of the WiFi sensor chip is less than the ZigBee sensor [23].

In China, some researchers have done much work in this area too. Shuang has developed a WiFi-based sensor node with GS 1010 chip and realized data transition and node positioning function [16]. Hongyi et al. have also realized remote environments monitoring system indoor and outdoor with GS 1010 chip [17]. Bin and Qiang have also done much application research work in these fields [18, 19]. Wu has designed and developed the hardware of a WiFi-based wireless sensor network node with ARM9-based S3C2440 processor [20]. There are more researchers who discussed and described the new applications with WiFi sensor network node [21, 22].

The aforementioned researchers mainly focus on hardware design and application of WiFi sensor node. However, the research work on routing protocols and security algorithm of WiFi-based wireless sensor network is much less. The current WiFi's AP is powered by a power line with unrestricted power and has higher calculation ability and large storage space. The routing protocols and security algorithms of the current WiFi technology are complex and nodes' energy saving has not been considered in the protocols. Nodes of wireless sensor networks are powered by batteries and are usually used in an unattended area. So the cost is higher when it is used in large-scale application. And the hardware's storage space and calculating ability of the WSN node are very limited. For the pervious reason, current WiFi technology cannot be directly applied to wireless sensor networks. We must upgrade the protocols and improve the security algorithms to meet the new requests.

On the basis of study work of original WiFi routing protocol HWMP, new method on improving the energy saving ability of HWMP to adapt the new features is described in this paper. Simulation work on the new routing protocol has been done with NS2, and the simulation results show that the life cycle of the network is extended to some degree.

2. The Architecture of Remote AMR Referring Wireless Mesh

In general, the network topologies of a large scale wireless sensor network are of a hierarchical network structure. The nodes of hierarchical wireless sensor network include several clusters and each of them consists of a cluster head and several cluster members. Cluster head is responsible for coordinating the work of nodes in the cluster and data integration and cluster members are common nodes. According to the difference between the cluster head and normal nodes,

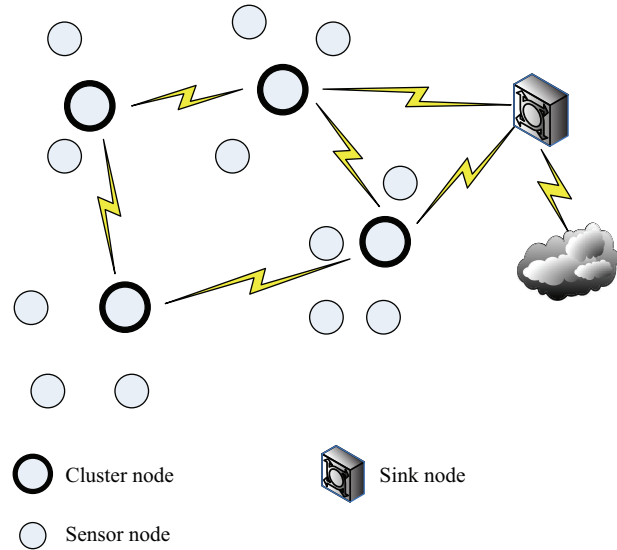


FIGURE 1: The topology of heterogeneous hierarchical network.

the hierarchical network structures are divided into two types, isomorphic hierarchical structure and heterogeneous hierarchical structure. In isomorphic hierarchical structure network, the cluster head nodes and the common members are the same, and the cluster head is selected from common cluster members using a specific clustering algorithm. In heterogeneous hierarchical structure network, the nodes' energy of the cluster head and the common members are different. And the cluster head is usually a special one with more powerful processing and communication capabilities, whose node energy is more powerful or unrestricted.

On the Internet of Things, natural gas meters, water meters, and power meters are nodes of the wireless sensor network. Because power meters can be powered by power line, its node energy can be unrestricted. But for water meters and natural gas meters, it is difficult to be powered by power line. They can be powered only by batteries and their node energy is restricted. For these reasons, the heterogeneous hierarchical structure is suitable for remote meter reading network. The power meter is the smart control center and the head of heterogeneous clusters. Besides reading and transmitting local data, power meter can be used to collect and transfer the data from water meters and natural gas meters in the wireless network. Further more, it is easy to act as control center of other kinds of nodes at home in the future. The heterogeneous hierarchical structure network is shown in Figure 1 [24].

There are three types of topologies in the WiFi network, point to point, point to multipoints in Star Network, and wireless mesh structure. The standards for WiFi are IEEE 802.11 series, in which IEEE 802.11s is specially made for wireless mesh structure. Wireless mesh structure is shown in Figure 2. In mesh network, routing protocols are used to build mesh paths between Mesh Points and Mesh Access Points and each Mesh Point works just like a route to provide relay services. Mesh Access Point (MAP) can be Mesh Point or

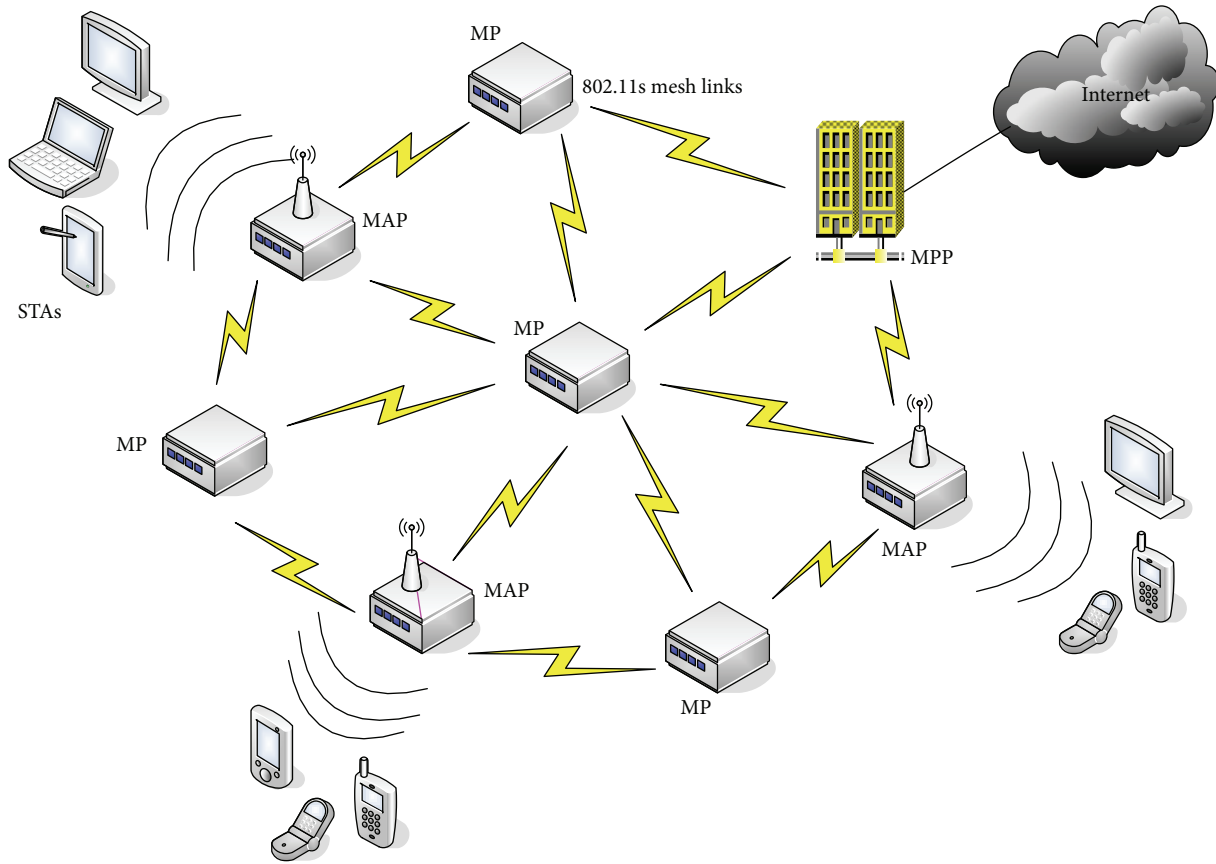


FIGURE 2: 802.11s structure of Wireless Mesh Network.

Access Point which can provide access services to the mobile client terminals in the mesh network [25].

If we compare the structure of Mesh Network on IEEE 802.11s with heterogeneous hierarchical wireless sensor network, we can find that they are very similar. Mesh Portal can work as a gateway and provide access to other networks, Mesh Portal is similar to the sink node of wireless sensor network, MAP is similar to the cluster head of heterogeneous hierarchical network, and mobile client terminals are similar to the common nodes in wireless sensor network. So, the protocol of WiFi Wireless Mesh Network can be used with the WiFi-based wireless sensor network after being optimized, such as routing protocol and security technology.

We have designed the architecture of WiFi-based new generation of remote Automatic Meter Reading Network which is shown in Figure 3 [3], which can be used in intelligent community buildings.

Comparing Figure 3 with Figure 2, we can find that they are very similar in the topology structure. The concentration server is similar to MPP, the concentrator of buildings is similar to MAP, and the meters are similar to mobile terminal. Because the energy of power meter is unrestricted, the power meters can be connected to build a tree, which is like the bone of network. And this character is very similar to HWMP's tree routing expanding. In addition, power meter is also

responsible for bidirectional data transmission between water meter and gas meter.

So we can refer to the structure of wireless mesh to realize remote AMR network. For example, we can design the network topology and route referring to the routing protocols of Mesh Network, and we can build security system of AMR network referring to the security protocols of Mesh Network. But we must note that most of the nodes of wireless sensor network are powered by batteries, so their node energy is restricted and the calculating capability and storage capacity are limited. So the network protocols of WiFi Wireless Mesh Network can only be used in the new generation of remote AMR network after being optimized. Since the default routing protocol of Wireless Mesh is HWMP, we should reduce the energy consumption of nodes running with HWMP.

3. Routing Protocol of HWMP

Hybrid Wireless Mesh Protocol (HWMP) is the default routing protocol of Wireless Mesh Standard IEEE 802.11s [26, 27], which is the hybrid of reactive routing protocol and tree topology-based proactive routing protocol. It is a routing protocol specifically for Wireless Mesh, in which the nodes of Mesh are relatively fixed and the nodes in trunk vary a little.

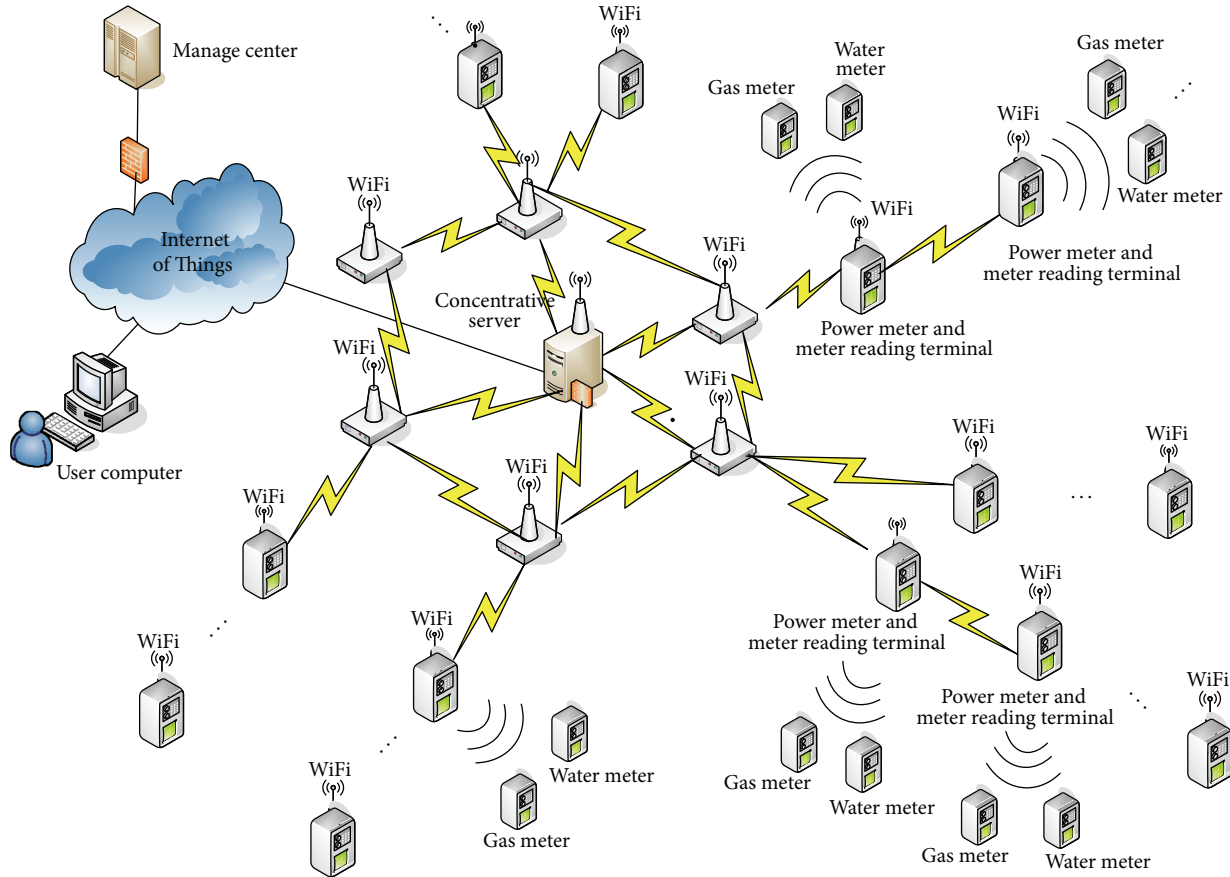


FIGURE 3: The structure of WiFi-based AMR network.

According to HWMP, Mesh nodes can be added or deleted easily.

Being a kind of hybrid routing protocol, HWMP includes reactive routing protocol and proactive routing protocol. The tree-based proactive routing protocol is adopted in backbone network, and the Radio-Metric AODV (RM-AODV) is adopted in variable network topology, which is evolved from AODV. AODV is an IP-based routing protocol and works in network layer, which uses the number of hops as metric. RM-AODV is MAC address-based routing protocol and works in physical layer, which uses Radio-Aware routing metric to choose path.

A Mesh Point acts as the MPP (Mesh Portal Point) and the root node of the tree routing network when a mesh network begins. Other MP Points proactively maintain the path to root node and the root node maintains the paths to each Mesh Point. In this way, a two-way proactive path tree of distance vector can be built. When there is data to be sent in an MP, it will send the data to the gateway node according to the path tree first. If the data should be sent to an external network, the MPP gateway will send the data packet to destination via external network link. Otherwise, if the data is sent to other MPs in the Mesh Network, the gateway will send it to the right Mesh Point. When the destination MP receives the data from the source node in inner network, it will send

back the corresponding routing request packet by starting the Radio-Metric Ad hoc On-Demand Distance Vector (RM-AODV). When the source node receives the packet, it will add the paths directly according to the received packet, through which the source node and the destination node are hop connected. If the transmission efficiency of a new path is higher, it will be used in the following transmission work. Since there is distance between gateway node and other Mesh Points in a Mesh Network, the hop transmission through nodes in inner network is more efficient and needs less network resources. The hybrid routing configuration process is shown in Figure 4.

HWMP uses the serial number of destination address to check the timeout and invalid routing information. If the newly received serial number of routing information is smaller than the known serial number of the Mesh Point, the routing information will be discarded for being timeout. In such way, the problems of routing loops and traditional distance vector protocol, such as counting infinitely, can be avoided. Every path in the routing table has a time limit. All invalid routing paths will be deleted automatically. Validity of every path will be reset when frames with data are sent or new routing information is generated.

A default Radio-Aware routing metric is defined for IEEE 802.11s devices according to the routing protocol HWMP

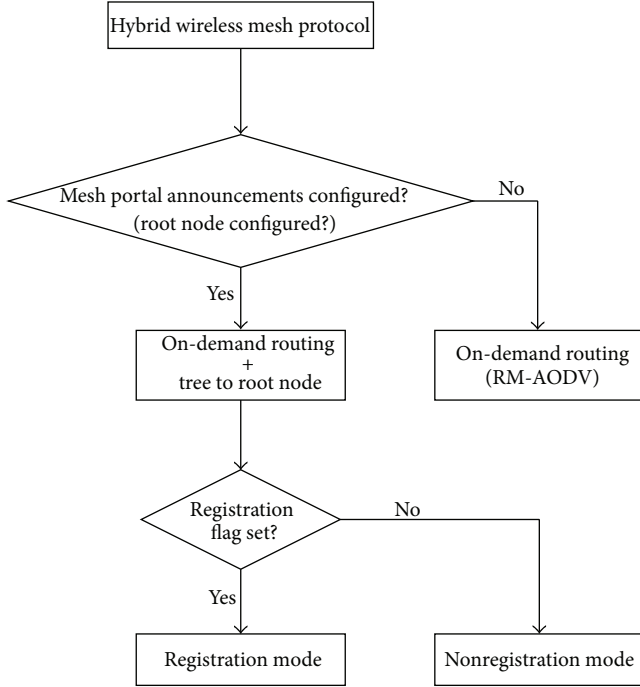


FIGURE 4: Configuration process of HWMP.

in the newly issued formal standard 802.11s [26]. Airtime link metric is a measure to calculate the channel resources consumed in the data frame sending via a specific wireless link. Formula (1) is used in calculating the consumption of spare time in every link. The path metric is the sum of all link metrics. Consider the following:

$$C_a = \left[O + \frac{B_t}{r} \right] \frac{1}{1 - e_{fr}}, \quad (1)$$

where O is channel Access Overhead; B_t is number of bits in test frame; and r is transmission bit rate; e_{fr} is error rate of every frame.

O is all the Channel Access Overheads, which include frame headers, training sequences, and access protocol frames. It varies depending on the technology of physical layer, such as IEEE 802.11b or 802.11g. B_t is the number of bits in test frame which is 8192 bits. The input parameters r and e_{fr} are the data rates in Mb/s and the frame error rate for the test frame size B_t , respectively. The rate r represents the data rate at which the mesh STA would transmit a frame of standard size B_t based on current conditions and its estimation is dependent on local implementation of rate adaptation. The frame error rate e_{fr} is the probability that when a frame of standard size B_t is transmitted at the current transmission bit rate r , the frame is corrupted due to transmission error.

4. Analysis and Improvement of HWMP Routing Protocol

4.1. HWMP Work Flow Analysis. After analyzing the simulation code of HWMP in NS-2.33 developed by Wireless Software Research and Development Group of Institute

of Information Transmission Problems under the Russian Academy of Sciences [28], we find that HWMP code is similar to AODV protocol code of NS2. They are all mainly composed of protocol body, routing table, broadcast timer, route cache timer, cache broadcast ID timer, and route cache queue.

When a packet is received, which means the function $\text{recv}(\text{Packet}^*, \text{Handler}^*)$ is called, different functions are called to deal with it according to the packet type.

(1) If it is a protocol packet, function $\text{recvHWMP}()$ will be called to deal with it. The TTL will be minus 1 before different functions are called according to different packet types.

(a) If it is a routing requested packet, the function $\text{recvPREQ}(\text{Packet}^*)$ will be called to deal with it. If the packet is generated by the node itself or has already been received, the node will discard it and the process will be ended. Otherwise, the node will deposit the serial number of the packet in cache, add the path sent by the packet to reverse route and forward the packet. After that, the node will call the corresponding function to deal with it according to the destination address. If the node is the destination node, the function sendPREP will be called. If the node is not the destination node and the route to destination node is known, the function sendPREP will insert the next hop node into the precursor list between source node and destination node. If the route to destination node is unknown, the number of hops will be plus 1 and the function forward will be called to broadcast the packet.

(b) If it is routing response packet, the function $\text{recvPREP}(\text{Packet}^*)$ will be called. The node should query the route to destination node. If there is no such route, a new route should be added. After the new route is added, the node should update the route information to the destination node and distribute the related packets. If the node is not the destination node but it knows the route to destination, the number of hops will be plus 1 and the function forward will be called to distribute the packet. Accordingly, the response precursor list will be updated. If the node is not the destination node and it does not know the route to destination, the packet will be discarded.

(2) If what the node received is an already sent data packet or TTL of the packet equals 0, the node will terminate the process. If the packet is generated by upper-layer protocol, the node will add data header to it. HWMP works according to the path selection protocol in the second layer and its addressing mode is MAC address, but in the source code the IP address is used instead for technical reasons. Finally the node handles it according to destination route.

The aforementioned is the routing process of HWMP protocol. In fact, there is a precompiling switch in the head file of hwmp.cc. The switch, “#define ROOT_INDEX(4)”, is used to start the tree proactive routing protocol and call a timer; thus, the route table can be updated every 10 seconds. If we disable the switch, the tree proactive routing protocol of HWMP will not start and there is no difference between HWMP and RM-AODV.

There should be a route error packet in the HWMP protocol, according to which the related node can take the right action when there is link error.

4.2. Improved Routing Protocol E-HWMP. By analyzing the work flow of HWMP protocol, it can be found that the node energy is not considered in routing selection. But, in fact, there are some nodes that are battery-powered in hybrid AMR network based on WiFi wireless sensor network, and their node energy is restricted. Nodes with adequate energy should be considered in priority when the next hop node should be selected. So it is necessary to adjust the original HWMP protocol to meet the requirements of the nodes with limited energy. The adjustment includes adding energy model to call the energy parameters of nodes, modifying the data packet header of protocol packet and original routing metric of HWMP in airtime. The adjusted protocol is called Energy saving-based Hybrid Wireless Mesh Protocol (E-HWMP) routing protocol.

4.2.1. The Improvement of Routing Metric in Airtime. The calculation method for routing airtime metric of HWMP is shown in formula (1). We know that it is irrelevant to node energy, so if we want the remaining energy of nodes to be considered in route selection according to HWMP, we can add parameter of node energy to it by multiplying original routing airtime metric E times. The method to get E is shown in formula (2):

$$E = \sum_{i=1}^{\text{Node}_{\text{cnt}}} \left(\frac{1}{\text{energy}_i} \right), \quad (2)$$

where Node_{cnt} is the collection of all nodes on the route and energy_i is current energy of node i .

The bigger the number of hops is, the bigger the value of E is in case that all the nodes in route have the same quantity of energy. If the number of hops is fixed, the more the rest energy in routing nodes is and the smaller the value of E is. By examining the remaining energy of nodes in route before the path is built, the case in which the nodes with high-energy consumption are selected can be avoided. In such way, the route loop problem can be effectively avoided.

The way to calculate the metric is shown in formula (3):

$$\text{Metric} = E * \sum C_a = \sum_{i=1}^{\text{Node}_{\text{cnt}}} \frac{1}{\text{energy}_i} * \sum_{j=1}^{\text{Link}_{\text{cnt}}} C_{aj}, \quad (3)$$

where C_{aj} is the airtime of the j th link and Link_{cnt} is the collection of all the links in the route.

4.2.2. Adding Node Energy Coefficient. As there is no node energy coefficient in the HWMP codes, the file that defines the node energy model, mobilenode.h, should be called. After that, the remaining energy in the current node can be read by a pointer. A pointer is defined in the previous codes to point to the current node and to get the remaining energy in the node. The pervious *index* means the ID of current node and energy_i is the energy value of current node.

4.2.3. Adjusting the Data Structure of the HWMP Packet Header. PREQ and PREP of RM-AODV are adopted to build the route tree and find on-demand routing in both proactive and reactive routing. There is no energy-related parameter in original path request packet (PREQ) and path response packet (PREP) of HWMP, so the packet headers of PREQ and PREP which use routing metric should be revised. A data variable named *energylost* should be used to record the sum of recipros the left energy value in current path, as is shown in formula (4):

$$\text{energylost+} = \frac{1}{\text{energy}_i}. \quad (4)$$

The revised packet header of path request (PREQ) is shown in Figure 5, and the revised packet header of path response (PREP) is shown in Figure 6. The energy parameter *energylost* is newly added to record the reciprocal sum of the left energy value in the current path automatically.

4.2.4. Analysis of Work Flow. By analyzing the codes of HWMP, we can learn that the PREQ request should be sent at first to build a path when an MP sends data to another MP or builds a path to root node. So, the routing metric should be revised in the function *recvPREQ* where the PREQ is received and processed. The value of the new routing metric equals the value of the original routing metric multiplied by the energy parameter, *energylost*.

There is a similar routing metric in function *recvPREP*. There might be a difference between the information in the PREP packet and the current network for the reason that the PREP packets might not be sent from the destination node and the PREP packets could also be sent from the nodes in the path to destination node. And the energy information is varying from time to time. So the path selection rules in function *recvPREP* do not need to be modified.

We name the improved protocol E-HWMP to distinguish it from the original protocol HWMP. We use a new routing metric related to node energy to get the network topology and route. In such way, we try to reduce the energy demand to the nodes, and the life cycle of network may be extended.

5. Simulation

In order to verify the effect of the improved E-HWMP protocol, we did simulation tests. In the tests, the energy model of NS2 is used. Energy model of NS2 can be started by TCL language in the energy simulation process and run according to the parameters set in TCL script. Surely the left energy information in the current node should be called

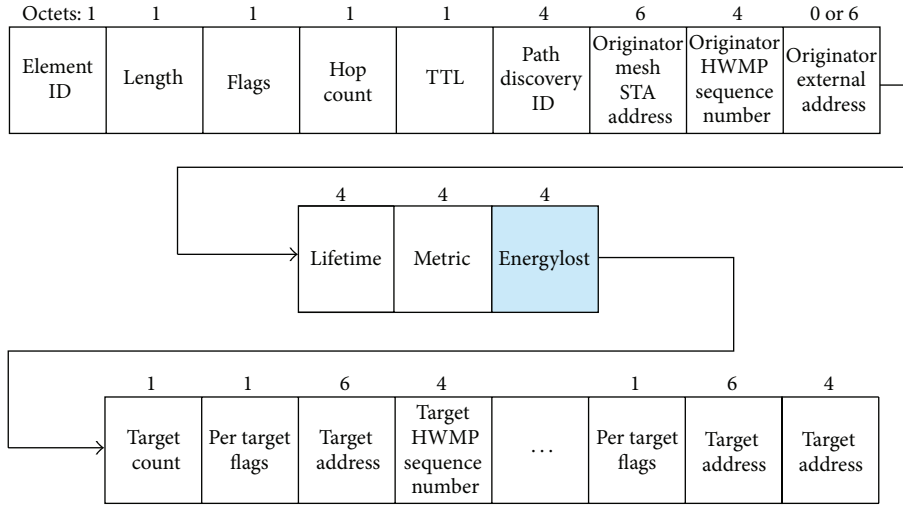


FIGURE 5: The modified packet header structure of PREQ.

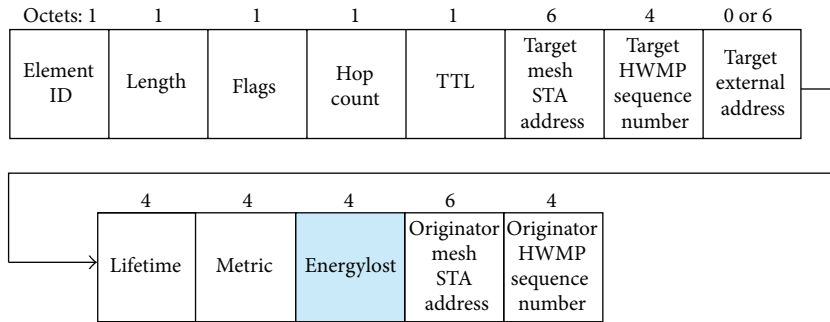


FIGURE 6: The modified packet header structure of PREP.

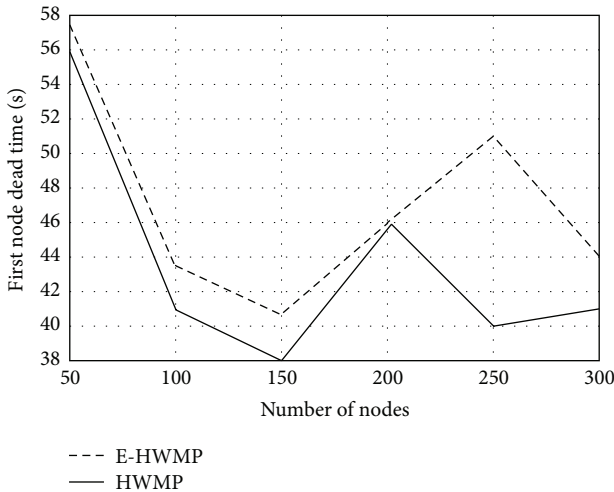


FIGURE 7: The time of first timeout node in different protocols.

in the codes if the energy information is considered in the routing protocol.

The simulation tests generate six different scenes which have 50, 100, 150, 200, 250, and 300 static nodes. The sensor

TABLE 1: Parameters of the passive routing test.

Simulation time	100 s
Transfer protocol	UDP
Packet types	CBR
Transmission rate	1 Mbps
Transmission distance	200 m
Mac layer	802.11 DCF
Antenna type	Omnidirectional antenna
Node moving speed	Fixed

nodes are random distributions in the scenes and each scene is 1000 m * 1000 m large. At the same time, when the number of nodes is 100, more tests were taken with three grades of initial energy, 5 J, 10 J, and 15 J. The details of the parameters are shown in Table 1.

The time of the first timeout node in the original HWMP and the improved E-HWMP is shown in Figure 7. The initial energy of all nodes is 15 J, the transmission power is 1 W, the receiving power is 1 W, and the waiting power is 0.05 W.

The figure shows that the life cycle of the first timeout node in the case of E-HWMP is obviously extended when the number of nodes is not 200, and there is little difference

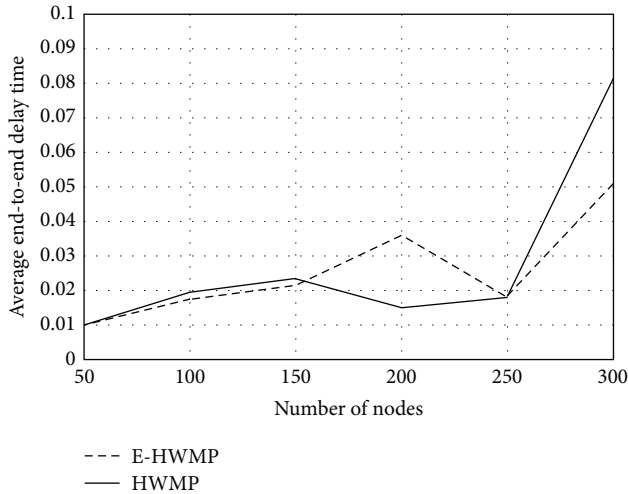


FIGURE 8: End-to-end time delay in the environment of different nodes.

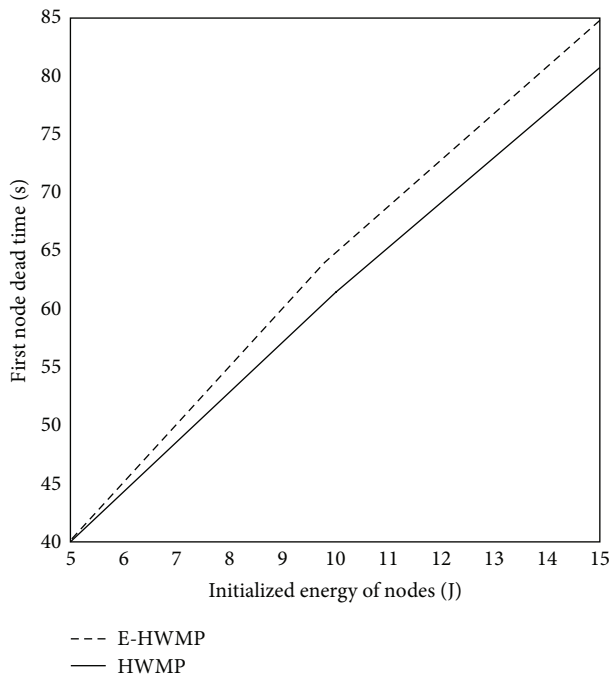


FIGURE 9: The simulation result of E-HWMP and HWMP with 100 nodes and different initial energies.

between the life cycles of two protocols in the scale of 200 nodes. It should be noted that there is a 10-second extension, improved by 25 percent, when the number of nodes is 250.

The average end-to-end delay time in different situations is shown in Figure 8.

The figure shows that there is little difference between the two protocols when the number of nodes is 250. There is a decrease in time delay in E-HWMP when the number of

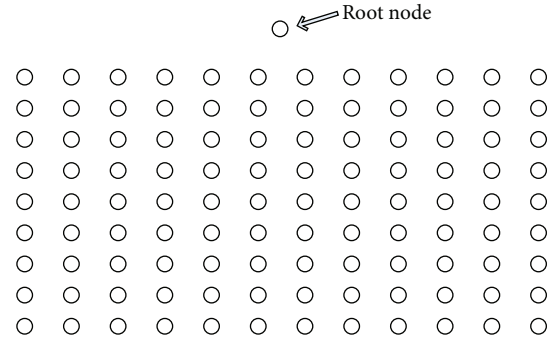


FIGURE 10: The topology of proactive routing for test.

nodes is 100, 150, or 300. But there is more time delay when the number of nodes is 200.

As is shown in Figure 9, the life cycle of the first timeout node in E-HWMP is extended to a certain degree when there are 100 nodes in the system and the initial energies are 5 J, 10 J, and 15 J, respectively.

Furthermore, in the proactive routing test an 8×12 point matrix is built, which can simulate the network topology of the building meter reading system. The distance between two adjacent nodes is 200 meters. The root node which simulates the concentrator of buildings is located on the top of the lattice, and it is connected with other nodes in the middle of lattice by one hop. The topology is shown in Figure 10.

The results of this simulation show that the time of the first timeout node of E-HWMP is 71.1927 s, while the time of the first timeout node of HWMP is 70.0268 s. There is more than a 1-second delay in the time of first timeout node in the E-HWMP protocol compared with HWMP protocol.

6. Conclusion

Compared with the original HWMP, the life cycle of the first timeout node in E-HWMP is extended to a certain degree and the existing period of the network is prolonged, at the same time, there is no large difference in the end-to-end time delay between E-HWMP and HWMP.

The result of the simulation of the AMR system under proactive routing model in the situation of apartment building shows that E-HMWP is more suitable than HWMP for the remote AMR network.

Acknowledgments

All authors do not have a direct financial relation with “Wireless Software Research and Development Group of Institute of Information Transmission Problems of the Russian Academy of Sciences (as in reference [28]),” which cannot lead to a conflict of interests for any of the authors. This work was supported in part by the Natural Science Foundation of China, under Contracts 61039003 and 61272052, and part by the Fundamental Research Funds for Central Universities.

References

- [1] Q. Song, J. Tang, and X. Feng, "Development and analysis of Smart Grid at home and abroad," *Electrotechnics Electric*, no. 3, pp. 1-4, 2010.
- [2] S. Fang, "Strategic plan for the Smart Grid in Europe and America," *Sino-Global Energy*, no. 6, p. 107, 2009.
- [3] L. Li, X. Hu, J. Huang, and K. He, "Design of new architecture of AMR system in Smart Grid," in *Proceedings of the 6th IEEE Conference on Industrial Electronics and Applications (ICIEA '11)*, pp. 2025-2029, June 2011.
- [4] A. Ali, N. A. Razali, N. H. Saad, and N. Vitee, "Implementation of Automatic Meter Reading (AMR) using radio frequency (RF) module," in *Proceedings of the IEEE International Conference on Power and Energy (PECon '12)*, pp. 876-879, December 2012.
- [5] C. Brasek, "Urban utilities warm up to the idea of wireless automatic meter reading," *IEE Computing and Control Engineering*, vol. 15, no. 6, pp. 10-14, 2004.
- [6] P. Corral, B. Coronado, A. C. de Castro Lima, and O. Ludwig, "Design of automatic meter reading based on Zigbee," *IEEE Latin America Transactions*, vol. 10, no. 1, pp. 1150-1155, 2012.
- [7] C. Prapasawad, K. Pornprasitpol, and W. Pora, "Development of an automatic meter reading system based on ZigBee PRO Smart Energy Profile IEEE 802. 15. 4 standard," in *Proceedings of the IEEE International Conference on Electron Devices and Solid State Circuit (EDSSC '12)*, pp. 1-3, December 2012..
- [8] N.-Q. Nhan, M.-T. Vo, T.-D. Nguyen, and H.-T. Huynh, "Improving the performance of mobile data collecting systems for electricity meter reading using Wireless Sensor Network," in *Proceedings of the International Conference on Advanced Technologies for Communications (ATC '12)*, pp. 241-246, October 2012.
- [9] T. Khalifa, K. Naik, and A. Nayak, "A survey of communication protocols for automatic meter reading applications," *IEEE Communications Surveys and Tutorials*, vol. 13, no. 2, pp. 168-182, 2011.
- [10] X. Chen, Y. Zhang, and L. Wang, "Hardware design of the wireless automatic meter reading system based on GPRS," in *Proceedings of the 10th World Congress on Intelligent Control and Automation (WCICA '12)*, pp. 4536-4540, July 2012.
- [11] B. Sivaneasan, P. L. So, and E. Gunawan, "A new routing protocol for PLC-based AMR systems," *IEEE Transactions on Power Delivery*, vol. 26, no. 4, pp. 2613-2620, 2011.
- [12] Q. Chen-Xi and H. Xiao-Guang, "The realization of broadband carrier communication in remote automatic meter reading system," in *Proceedings of the 10th IEEE International Conference on Industrial Informatics (INDIN '12)*, pp. 1073-1076, July 2012.
- [13] M. Popa, "Gateway design and implementation in an automatic meter reading system based on Power Line Communications," in *Proceedings of the 7th International Conference on Networked Computing and Advanced Information Management (NCM '11)*, pp. 295-298, June 2011.
- [14] D. M. Dobkin and B. Aboussouan, "Low power Wi-Fi (IEEE 802. 11) for IP smart objects," Gainspan Corporation White Paper, 2009.
- [15] G2 Microsystems, "Ultra Low-power Wi-Fi Datasheet V0. 95," 2006, <http://www.g2microsystems.com>.
- [16] H. Shuang, *Design and Application of a Wi-Fi Based Wireless Sensor Networks Node*, Beijing University of Posts and Telecommunications, 2010.
- [17] L. Hongyi, Z. Fang, L. Zhaohui et al., "Design and implementation of an indoor and outdoor environment remote monitoring system based on WiFi sensor network," *Journal of Computer Research and Development*, supplement, no. 47, pp. 361-365, 2010.
- [18] L. Bin, *The Design of Wireless Sensor Networks Detection System Based on Wi-Fi*, Southwest Jiaotong University, 2011.
- [19] Z. Qiang, *Design and Implementation of WIFI Wireless Sensor Networks*, North University of China, 2012.
- [20] C. Wu, Y. Zhen-Xing, H. Liang et al., "The design of Wireless Sensor Network node based on Wi-Fi," in *Proceedings of the 24th Chinese Control and Decision Conference*, August 2012.
- [21] L. Li, X. Hu, and H. Jian, "The applications of WiFi-based Wireless Sensor Network in Internet of Things and Smart Grid," in *Proceedings of the 6th IEEE Conference on Industrial Electronics and Applications (ICIEA '11)*, pp. 2025-2029, June 2011.
- [22] Z. Hongying, "The WiFi based on single chip microcomputer wireless sensor network products were reviewed," *Public Communication of Science and Technology*, no. 12, pp. 211-213, 2011.
- [23] Y.-P. Chen and Q. Wu, "Power consumption measurement and clock synchronization on low-power wireless sensor networks," in *Proceedings of the 14th International Conference on Advanced Communication Technology (ICACT '12)*, pp. 406-409, February 2012.
- [24] Z. Meng, S. Wang, and Q. Wang, "Research on the moving strategy for mobile sink in cluster wireless sensor networks," *Journal of Huazhong University of Science and Technology*, vol. 37, no. 6, pp. 67-70, 2009.
- [25] I. F. Akyildiz, X. Wang, and W. Wang, "Wireless mesh networks: a survey," *Computer Networks*, vol. 47, no. 4, pp. 445-487, 2005.
- [26] IEEE Computer Society, *IEEE Std 802. 11s-2011. 10*, 2011.
- [27] Y. Meng-Ke, Y. Yatao, and B. Zhongying, "Research on multi-portal routing protocol for wireless Mesh networks based on HWMP," *Microelectronics and Computer*, vol. 26, no. 12, pp. 4-8, 2009.
- [28] "HWMP for NS-2," Wireless Software Research and Development Group of Institute of Information Transmission Problems of the Russian Academy of Sciences (Wireless Software R&D Group of IITP RAS), <https://forge.iitp.ru/ns2/hwmp>.

Research Article

Accurate Counting Bloom Filters for Large-Scale Data Processing

Wei Li,¹ Kun Huang,² Dafang Zhang,¹ and Zheng Qin¹

¹ College of Information Science and Engineering, Hunan University, Changsha 410082, China

² Institute of Computing Technology, Chinese Academy of Sciences, Beijing 100190, China

Correspondence should be addressed to Dafang Zhang; dfzhang@hnu.edu.cn

Received 3 May 2013; Accepted 5 July 2013

Academic Editor: Gelan Yang

Copyright © 2013 Wei Li et al. This is an open access article distributed under the Creative Commons Attribution License, which permits unrestricted use, distribution, and reproduction in any medium, provided the original work is properly cited.

Bloom filters are space-efficient randomized data structures for fast membership queries, allowing false positives. Counting Bloom Filters (CBFs) perform the same operations on dynamic sets that can be updated via insertions and deletions. CBFs have been extensively used in MapReduce to accelerate large-scale data processing on large clusters by reducing the volume of datasets. The false positive probability of CBF should be made as low as possible for filtering out more redundant datasets. In this paper, we propose a multilevel optimization approach to building an Accurate Counting Bloom Filter (ACBF) for reducing the false positive probability. ACBF is constructed by partitioning the counter vector into multiple levels. We propose an optimized ACBF by maximizing the first level size, in order to minimize the false positive probability while maintaining the same functionality as CBF. Simulation results show that the optimized ACBF reduces the false positive probability by up to 98.4% at the same memory consumption compared to CBF. We also implement ACBFs in MapReduce to speed up the reduce-side join. Experiments on realistic datasets show that ACBF reduces the false positive probability by 72.3% as well as the map outputs by 33.9% and improves the join execution times by 20% compared to CBF.

1. Introduction

A Bloom filter [1] is a simple space-efficient randomized data structure for representing a set to support fast membership queries. A Bloom filter uses m bits to represent n elements by using k independent hash functions. Bloom filters allow false positives when querying an element, that is, returning true when the element is not in the set, but not false negatives, that is, returning false when the element is not in the set. Nevertheless, the space savings of Bloom filters often outweigh this drawback when the probability of false positives is made sufficiently low. Due to their simplicity and efficiency, Bloom filters have found widespread applications in databases, network applications [2], and distributed systems [3].

As standard Bloom filters do not support deleting elements, there has been a huge surge in the popularity of Bloom filters and variants. One well-known variant is the Counting Bloom Filter (CBF) [4] which allows the set to change dynamically via insertions and deletions of elements.

CBF extends Bloom filters by using a fixed-size counter instead of a single bit for each entry in the vector. When an element is inserted into CBF, the corresponding counters are incremented; deletions can now be safely done by decrementing the counters. To avoid counter overflow, we choose four bits per counter for most applications.

Large-scale data processing has been extensively used in the Cloud. MapReduce [5] is a popular program model for processing vast amounts of data on large clusters of commodity machines. The benefit of MapReduce is to provide *map* and *reduce* functions to users, hiding the details of parallelization, fault tolerance, and load balancing. Hadoop [6] is an open-source implementation of MapReduce. Hadoop is used on massive amounts of structured and unstructured datasets for data analytics applications. Due to its scalability and simplicity, Hadoop has recently been investigated and embraced by many big companies, such as Facebook, Yahoo!, IBM, JP Morgan Chase, New York Times, and China Mobile. So it is critical to study analytic techniques in the MapReduce framework.

However, large-scale data processing poses a significant challenge of performance to MapReduce. First, there are large amounts of data involved with data-intensive applications such as web search engines and log processing. For example, China Mobile has to process 5–8 TB of phone call records per day. Facebook gathers almost 6 TB new log data per day. For these applications, it is time consuming to distribute such data across hundreds or thousands of low-end machines for computations. Second, the join operation is very inefficient in the MapReduce framework. The join is one of fundamental query operations, which combines records from two different datasets based on a cross product. The main problem of the MapReduce join is that two entire datasets should be processed and distributed among a large amount of machines in the clusters. This causes high communication cost and even a performance bottleneck when a small fraction of data is relevant to the join operation. Third, there are not any auxiliary data structures such as indexes and filters in the MapReduce framework. This is due to the fact that MapReduce is initially designed to process only a single large dataset as its input. As all the records within a time period are analyzed together, dataset scans in the MapReduce framework therefore are preferable to index scans.

To address such challenge, CBFs have been widely used to accelerate large-scale data processing in MapReduce. In the reduce-side join [7, 8], CBF is used in the map phase to reduce dramatically the amount of redundant records shuffled across the network, improving the join performance. CBF is built on the smallest dataset in a distributed fashion and distributed via broadcast to all map tasks. To filter out more redundant traffic during the shuffle phase, the false positive probability of CBF should be made as low as possible to process ever-increasing datasets in the MapReduce join.

There are three performance metrics of CBF: processing overhead, memory consumption, and false positive probability. The processing overhead is the number of memory accesses for each primitive operation, which dominates the CBF throughput. The memory consumption is the counter vector size of CBF. Four bits per counter are typically used to support insertions and deletions. As the counters blow up the available memory space, several variants [9–13] have recently been proposed to minimize the memory consumption of CBF, fitting the whole filter in limited high-speed memory (i.e., SRAMs). The false positive probability is to claim an element to be a member in the set, though it is not. There is a tradeoff between the false positive probability and the memory consumption. Decreasing the false positive probability entails increasing the memory consumption. As datasets increasingly growing in size, it is vital to reduce the volume of datasets being processed and distributed across the network in MapReduce. Therefore, our goal is to minimize the false positive probability of CBF while maintaining its memory efficiency.

This paper presents a multilevel optimization approach to building an Accurate Counting Bloom Filter (ACBF). The goal of ACBF is to reduce the false positive probability. ACBF is constructed by partitioning the counter vector into multiple levels that are organized by offset indexing. In ACBF, the first level is used to perform set membership queries, while other

levels are used to calculate the counters on insertions and deletions. In order to minimize the false positive probability, we propose an optimized ACBF by maximizing the first level size while maintaining the same functionality as the standard CBF. Simulation results show that ACBF outperforms CBF in false positive probability at the same memory consumption. We also implement ACBFs in MapReduce to improve the reduce-side join performance by filtering out more redundant records shuffled. Experiments in Hadoop show that ACBF reduces the false positive probability by 72.3% as well as the map outputs by 33.9% and improves the total execution times by 20% compared to CBF.

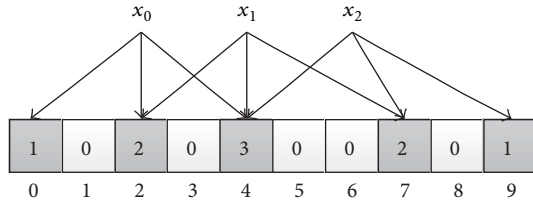
This paper makes the following main contributions.

- (1) We propose a novel multilevel optimization approach to building a variant of CBF called ACBF for reducing the false positive probability. ACBF is built by partitioning the counter vector into multiple levels. We propose an optimized ACBF by maximizing the first level size, in order to minimize the false positive probability.
- (2) We show that ACBF outperforms CBF in false positive probability at the same memory consumption. Simulation results show that the optimized ACBF reduces the false positive probability by up to 98.4% compared to CBF and performs the same functionality as CBF.
- (3) We implement ACBFs in MapReduce to improve the join performance. ACBF is constructed in a distributed fashion and distributed via broadcast to all map tasks for filtering out more redundant records transferred during the shuffle phase.
- (4) Experiments on realistic datasets show that ACBF reduces the false positive probability by 72.3% as well as the map outputs by 33.9% and improves the join execution times by 20% compared to CBF.

The rest of this paper is organized as follows. Section 2 introduces the background and related work on Bloom filters and CBFs. We describe the construction and optimization of ACBF and present simulation results in Section 3. Section 4 presents the ACBF implementation in MapReduce and presents experimental results on realistic datasets. Finally, we conclude this paper in Section 5.

2. Background and Related Work

2.1. Bloom Filters and CBFs. Bloom filters are space-efficient randomized data structures to perform approximate membership queries. A Bloom filter represents a set $S = \{x_1, x_2, \dots, x_n\}$ of n elements by using a bit vector of m bits, initially all set to 0. A Bloom filter uses k independent hash functions h_1, h_2, \dots, h_k with the range $[0, \dots, m - 1]$, each of which hashes an element to a random number uniform over the range. For an element x in S , the bits $h_i(x)$ are set to 1 for $1 \leq i \leq k$. To query whether an element y is in S , we check whether all bits $h_i(y)$ are set to 1. If not, then clearly y is not in S . If all bits $h_i(y)$ are set to 1, we assume that y is in S with a certain probability.

FIGURE 1: CBF with $m = 10$, $n = 5$, and $k = 3$.

A Bloom filter may yield false positives, but false negatives are not possible. The false positive probability is calculated as follows:

$$f = \left(1 - \left(1 - \frac{1}{m}\right)^{nk}\right)^k \approx \left(1 - e^{-kn/m}\right)^k, \quad (1)$$

where n is the number of elements in the set, m is the size of the bit vector, and k is the number of hash functions. Increasing the number k of hash functions can decrease the false positive probability f for a given ratio m/n . Thus, the false positive probability is minimized as $f \approx (1/2)^k$ when $k = (m/n) \ln 2$. For example, when $m/n = 10$ and $k = 7$, the false positive probability f is just over 0.008.

The standard Bloom filter allows insertion but not deletion. Deleting elements from the Bloom filter cannot be done simply by changing ones back to zeros. This is because a single bit in the vector may correspond to multiple elements inserted. The Counting Bloom Filter (CBF) [4] has been proposed to allow both insertions and deletions of elements. CBF extends the standard Bloom filter by using an array of m counters instead of bits. In CBF, counters are incremented on an insertion and decremented on a deletion. The counters are used to track the number of elements currently hashed to the same entries in the vector. The standard CBF can be derived from CBF by setting all nonzero counters to 1. To avoid counter overflow, four bits per counter have been shown to suffice for most applications. However, due to using counters of four bits, CBF blows up the memory space by a factor of four over the standard Bloom filter, even though most counters are zero.

2.2. Related Work on CBFs. CBFs have been widely used in a variety of applications such as networking [2] and distributed systems [3]. This is due to the fact that CBF is simple and efficient for performing fast membership queries and updates. In order to accommodate different applications, several variants [9–12] have been proposed to improve the performance of CBFs.

CBFs have one of key disadvantages of wasteful fourfold memory space. Several improvements on CBF have recently been proposed to minimize the memory consumption. The d -left CBF (d LCBF) [9, 10] is a simple hash-based alternative based on d -left hashing and fingerprints. d LCBF offers the same functionality as CBF but requires much less memory by a factor of above two at the same false positive probability. The Rank-indexed CBF (RCBF) [11] is a compact alternative based on rank-index hashing. RCBF uses a hierarchical structure

for chaining-based fingerprints at each entry, avoiding the costly storage overhead of pointers. RCBF outperforms CBF in memory space by a factor of above three for a false positive probability of 1% and also outperforms d LCBF in memory space by 27% at the same false positive probability. The Multilayer Compressed CBF (ML-CCBF) [12] is also another compact alternative using the idea of a hierarchical structure as well as the Huffman code. ML-CCBF reduces memory space by up to 50% as well as the lookup time compared to CBF. Unlike previous work on the memory consumption, this paper targets the false positive probability. Our goal is to design an accurate variant of CBF, which dramatically reduces the false positive probability while maintaining the same functionality and the memory consumption as CBF.

Moreover, other variants of Bloom filters have recently been proposed to improve the false positive probability. The power of two choices [14] is introduced to reduce the false positive probability by using more hashing. The main idea of this variant is to use two groups of hash functions for inserting elements into the filter and for checking membership queries. An improved variant using partitioned hashing [15] is proposed to improve the false positive probability while avoiding more hashing. This variant works well by partitioning elements into multiple groups and choosing proper combination of hash functions for each group. To reduce hash computations, only two hash functions can be used to derive other hash functions by using a linear combination of the two hash functions [16]. In addition, one memory access Bloom filter [17] is proposed to improve the processing overhead. However, this variant has a larger false positive probability than the standard Bloom filter. Although these previous variants can be generalized to CBF, they suffer from a higher processing overhead due to more hash computations and a larger false positive probability due to wasteful CBF counters. In this paper, ACBF is designed to improve the false positive probability by using multilevel optimization, avoiding these previous limitations.

3. Accurate Counting Bloom Filters

In this section, we describe a multilevel optimization approach to building an Accurate Counting Bloom Filter called ACBF. We first present the construction of ACBF and then describe the query and insertion/deletion algorithms. Next, we describe optimized ACBFs and then analyze the false positive probability. Finally, we show simulation results to compare optimized ACBFs with the standard CBF.

3.1. ACBF Construction. The basic idea of ACBF is to use a multilevel approach to partitioning the counter vector into multiple levels for higher accuracy. Using this approach, we separate the query operation and the insertion/deletion operations of ACBF. This separation is used to achieve a lower false positive probability while attaining updates on dynamic sets. This is done due to the observation of CBF. We observe that the counter vector of CBF is suitable to support quick updates by incrementing or decrementing the counters at the cost of the false positive probability. Figure 1 shows a simple

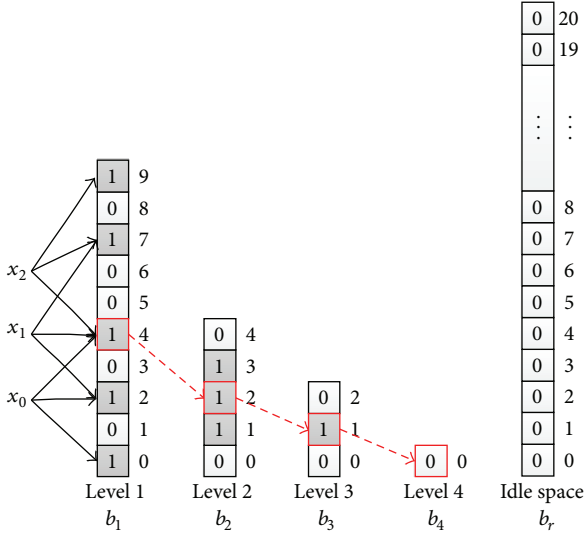


FIGURE 2: ACBF with four levels and an idle space.

example of CBF with $m = 10$, $n = 5$, and $k = 3$, where m is the number of counters, n is the maximal number of elements, and k is the number of hash functions.

We see that there are only three elements inserted into the filter, and the false positive probability is dominated by the number m of counters for given parameters n and k .

ACBF has a hierarchical structure which is composed of d levels b_1, b_2, \dots, b_d and an idle space b_r . In this hierarchy, b_1 is used to check the membership for each query, b_2, \dots, b_d is used to calculate the counters hashed by each element inserted, and b_r is used to remain for elements to be inserted. Figure 2 shows an example of ACBF with four levels b_1, b_2, b_3 , and b_4 and an idle space b_r . We see that b_1 has the same size of 9 bits as the counter vector of CBF, and there remain total 21 bits in b_r used for the idle space. Like the standard CBF, ACBF uses k hash functions h_1, h_2, \dots, h_k to hash an element x into k bits in the first level b_1 instead of the counter vector of CBF. Therefore, we only need to check k bits in b_1 on a membership query. Algorithm 1 shows the query operation in ACBF, where l_1 is the bit size of b_1 . If all bits $h_i(x)$ are set to 1, the algorithm claims that element x is in ACBF; otherwise, x is not in ACBF by returning false. Thus, ACBF has the same query complexity $O(k)$ as the standard CBF, denoting average k memory accesses per query.

ACBF is organized by using offset indexing for spanning the counters over different levels. We assume that each level b_i has a size of $l_i = |b_i|$ bits, where i is in the range $[1, \dots, d]$ and b_r has $l_r = |b_r|$ bits for the idle space. To span a counter, we recursively calculate an offset index in b_i by using a function $popcount(b_i, j)$ which computes the number of ones before position j in b_i . The offset value returned by $popcount(b_i, j)$ is used as an index to the bit in the next level b_{i+1} contained by the spanned counter. Therefore, we traverse this hierarchy to calculate a counter value by adding up the bits indexed by offset values that the counter responds to. For example, as shown in Figure 2, position 4 in b_1 is hashed by three elements x_0, x_1 , and x_3 inserted into ACBF, and its counter

spans over four levels b_1, b_2, b_3 , and b_4 . We traverse these levels to calculate the counter value at position 4. First, as bit 4 in b_1 is set to 1, we call $popcount(b_1, 4)$ that returns 2 as an offset index in b_2 . Second, we check to see that bit 2 in b_2 is set to 1 and then call $popcount(b_2, 2)$ that returns 1 as an offset index in b_3 . Third, we continue to call $popcount(b_3, 1)$ that returns 0 as an offset index in b_4 . Finally, we check to see that bit 0 in b_4 is set to 0 and then terminate the traversal, producing as output the counter value $1 + 1 + 1 + 0 = 3$ at position 4.

In order to insert or delete an element from ACBF, we must increment or decrement the counters hashed by the element. This is done by expanding or shrinking relative levels of the hierarchy. Algorithm 2 shows the insertion operation in ACBF. When an element is inserted into ACBF, we need to perform k lookups by traversing a series of levels b_1, \dots, b_j for each counter hashed by the element (see Lines from 3 to 9 in Algorithm 2). For incrementing a counter value, we expand the next level b_{j+1} by adding a one bit in b_j and shifting upward all bits of b_{j+1} by one position (see Lines from 11 to 16 in Algorithm 2). Like insertion, deletion also requires a lookup and a shift for each of k hashed counters. Algorithm 3 shows the deletion operation in ACBF. When an element is deleted from ACBF, we perform the same lookups by traversing a series of levels b_1, \dots, b_j for each counter hashed by the element (see Lines from 3 to 10 in Algorithm 3) and then shrink the last level b_j by shifting backward all the bits of b_j , at the same time of removing a one bit from b_{j-1} (see Lines from 12 to 14 in Algorithm 3). For example, we assume that element x_3 is deleted from ACBF as shown in Figure 2. As position 4 in b_1 is hashed by x_3 , we traverse level b_1 to level b_4 for its counter value. In order to decrement the counter value, we shrink b_4 by removing a zero bit at position 0 and shrink b_3 by removing a one bit at position 1.

From Algorithms 2 and 3, we see that both insertion and deletion have almost the same time complexity. Let φ be a counter value and λ be a popcount cost. Thus, the insertion/deletion complexity of ACBF is calculated as follows:

$$O(k \times [E(\varphi) \times (E(\lambda) + 1) + 1 + 1]), \quad (2)$$

where $E(\varphi)$ is the average counter value and $E(\lambda)$ is the average $popcount$ cost. $E(\lambda) + 1$ denotes a $popcount$ function and a read operation, and $1 + 1$ denotes a write operation and a shift for updating each counter. Equation (2) shows that ACBF has more complexity for the insertion/deletion than CBF with $O(k)$. A recent study [12] has shown a tight approximation $E(\varphi) \approx \ln 2$ when the false positive probability is minimized in ACBF. Thus, the insertion/deletion complexity depends on the average $popcount$ cost. Fortunately, the $popcount$ function is becoming increasingly common and very fast (e.g., one CPU cycle on a word) for most modern processors. Hence, $E(\lambda)$ is dominated by the word lengths of different levels in the ACBF hierarchy.

3.2. ACBF Optimization. To attain a lower false positive probability, we propose two optimization methods to improve the ACBF construction by increasing the first level size. We assume that ACBF consists of d levels b_1, b_2, \dots, b_d and an idle

```

(1) Query (Element  $x$ )
# ACBF is composed of  $d$  levels  $b_1, \dots, b_d$  and an idle space  $b_r$ 
# Each bitmap  $b_j$  has the size of  $l_j$ 
(2) for ( $i = 1; i \leq k; i++$ ) do
(3)    $\text{index} = h_i(x) \bmod l_1;$ 
(4)   if ( $b_1[\text{index}] == 0$ ) then
(5)     return false;
(6)   end if
(7) end for
(8) return true;

```

ALGORITHM 1: Query operation in ACBF.

```

(1) Insert (Element  $x$ )
(2) for ( $i = 1; i \leq k; i++$ ) do
# Traverse  $d$  bitmaps  $b_1, \dots, b_d$ 
(3)   for ( $j = 1; j \leq d; j++$ ) do
(4)     if ( $j == 1$ ) then
(5)        $\text{index} = h_i(x) \bmod l_1;$ 
(6)     end if
(7)     if ( $b_j[\text{index}] == 1$ ) then
(8)        $\text{offset} = \text{popcount}(b_j, \text{index});$ 
(9)        $\text{index} = \text{offset};$ 
# Expand bitmap  $b_{j+1}$  by one position
(10)    else
(11)       $b_j[\text{index}] = 1;$ 
(12)       $\text{offset} = \text{popcount}(b_j, \text{index});$ 
(13)       $\text{expand\_bitmap}(b_{j+1}, \text{offset});$ 
(14)       $\text{Index} = \text{offset};$ 
(15)       $b_{j+1}[\text{index}] = 0;$ 
(16)       $\text{exit}();$ 
(17)    end if
(18)  end for
(19) end for

```

ALGORITHM 2: Insertion operation in ACBF.

space b_r , each with a bit size $l_i = |b_i|$ for $1 \leq i \leq d$ or $i = r$. Thus, the false positive probability f is calculated as follows:

$$f = \left(1 - \left(1 - \frac{1}{l_1}\right)^{nk}\right)^k \approx \left(1 - e^{-kn/l_1}\right)^k, \quad (3)$$

where n is the maximal number of elements, l_1 is the bit size of the first level, and k is the number of hash functions. Equation (3) shows that the false positive probability f is dominated by the first level size l_1 for given parameters n and k .

The basic idea of the first optimization method is to simply increase the first level size by a multiplicative factor. Let c be an integer value, and let m be the number of CBF counters. Using this method, we set the first level size as $l_1 = cm$ for $1 \leq c \leq 4$ and improve the false positive probability f_c as follows:

$$f_c = \left(1 - \left(1 - \frac{1}{cm}\right)^{nk}\right)^k \approx \left(1 - e^{-kn/cm}\right)^k. \quad (4)$$

If $l_1 = m$, ACBF has the same false positive probability f_1 as CBF. If $l_1 = 4m$, ACBF has the lowest false positive probability f_4 but cannot allow deletions of elements. Hence, the key of optimizing ACBF is to set the optimal size of the first level for minimizing the false positive probability while maintaining the same functionality of insertions and deletions as CBF.

To achieve this goal, we propose the second optimization method for improving the ACBF construction. This method is designed based on the following observation: if up to n elements are inserted in ACBF, we need to have at least kn bits available for $j \geq 2$ levels in the hierarchy:

$$l_2 + \dots + l_d = kn. \quad (5)$$

The bit size l_1 of the first level b_1 is maximized as follows:

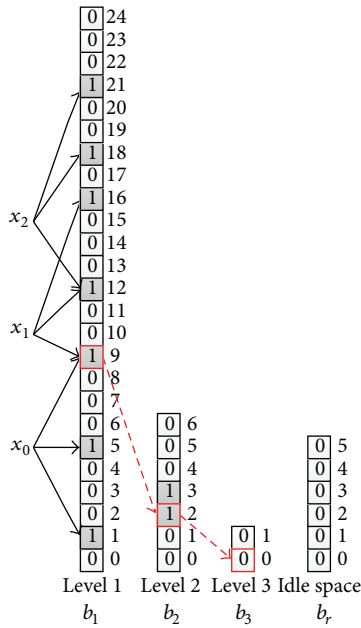
$$l_1 = 4m - (l_2 + \dots + l_d) = 4m - kn. \quad (6)$$

```

(1) Delete (Element  $x$ )
(2) for ( $i = 1; i \leq k; i++$ ) do
# Traverse  $d$  bitmaps  $b_1, \dots, b_d$ 
(3)   for ( $j = 1; j \leq d; j++$ ) do
(4)     if ( $j == 1$ ) then
(5)        $\text{index} = h_i(x) \bmod l_1$ ;
(6)     end if
(7)     if ( $b_j[\text{index}] == 1$ ) then
(8)        $\text{offset} = \text{popcount}(b_j, \text{index})$ ;
(9)        $\text{pre} = \text{index}$ ;
(10)       $\text{index} = \text{offset}$ ;
(11)    else
# Shrink bitmap  $b_j$  by one position
(12)       $\text{shrink\_bitmap}(b_j, \text{offset})$ ;
(13)       $b_{j-1}[\text{pre}] = 0$ ;
(14)       $\text{exit}()$ ;
(15)    end if
(16)  end for
(17) end for

```

ALGORITHM 3: Deletion Operation in ACBF.

FIGURE 3: Optimized ACBF with $m = 10$, $n = 5$, and $k = 3$.

Thus, the optimal false positive probability f_o is calculated as follows:

$$f_o = \left(1 - \left(1 - \frac{1}{4m - kn} \right)^{nk} \right)^k \approx \left(1 - e^{-kn/(4m - kn)} \right)^k. \quad (7)$$

When $k = (m/n) \ln 2 < m/n$, the upper and lower bounds of the first level size l_1 are derived as follows:

$$3m < l_1 = 4m - kn < 4m. \quad (8)$$

Hence, we can derive the upper and lower bounds of the optimal false positive probability f_o as

$$f_4 < f_o < f_3. \quad (9)$$

Equation (9) shows that the second method has a lower false positive probability than the first method with $l_1 = 3m$. Using the second method, ACBF remains kn bits for performing the same functionality of insertions and deletions as the standard CBF, avoiding space overflow.

Figure 3 shows an example of an optimized ACBF with $m = 10$, $n = 5$, and $k = 3$, where m is the number of 4-bit counters. There are only three elements x_0 , x_1 , and x_2 inserted in the filter. Using (5), we need at most $kn = 15$ bits for $j \geq 2$ levels of the hierarchy. Thus, we set the optimal bit size $l_1 = 4m - kn = 25$ of the first level b_1 and remain the idle space b_r of 6 bits for allowing other two elements inserted in the filter. We also see that the bit size l_2 of the second level b_2 is set to the number of ones in the first level b_1 , and the bit size l_3 of the third level b_3 is set to the number of ones in the second level b_2 . For example, we assume that position 9 in b_1 is hashed by two elements x_0 and x_1 (see Figure 3). We span the counter value at position 9 over b_1 and b_2 by using offset indexing described in Section 3.1.

Next, we compare the theoretical false positive probability of ACBFs with CBF in two cases of $k = 3$ and $k = \text{optimal}$ as shown in Figure 4. Note that $k = \text{optimal}$ means the optimal number of hash functions $k = (m/n) \ln 2$ for minimizing the false positive probability. Figure 4 shows that ACBF_o with the optimal first level size $l_1 = \text{optimal}$ outperforms both CBF and ACBF_i with $l_1 = im$ for $1 \leq i \leq 3$ by using the first optimization method. For instance, Figure 4(a) shows that ACBF_o reduces the false positive probability by up to 97.6%, up to 83.7%, and up to 48.1% in case of $k = 3$ compared to CBF/ACBF₁, ACBF₂, and ACBF₃, respectively. We note that ACBF₁ has the same false positive probability as CBF due to

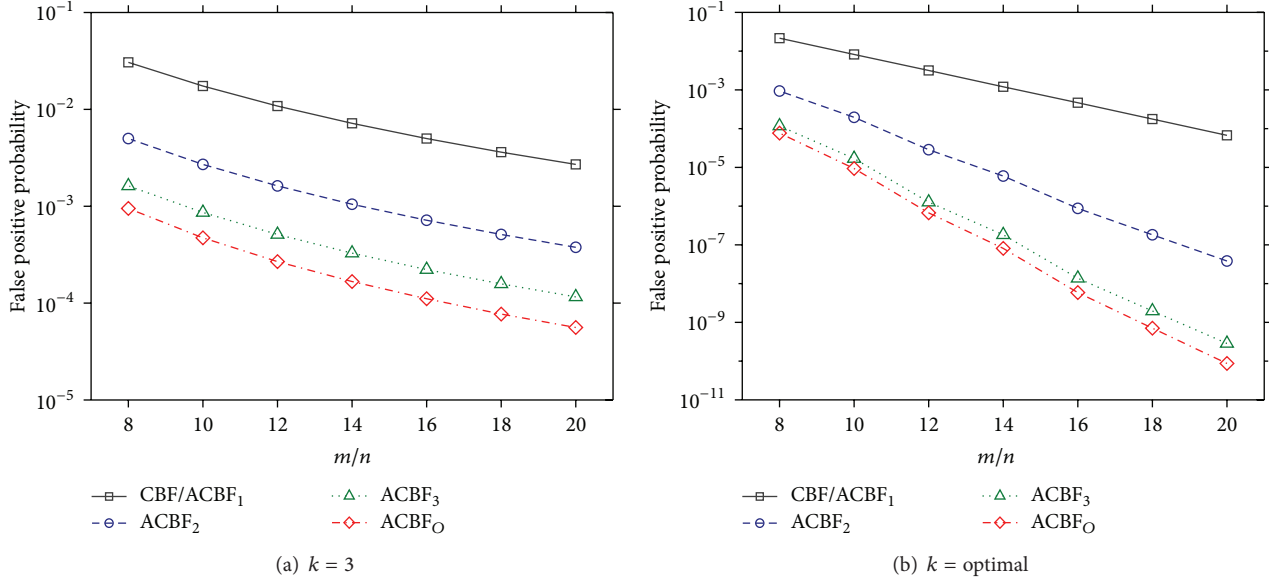


FIGURE 4: Theoretical false positive probability of CBF and ACBFs.

$l_1 = m$. Figure 4(b) also shows that in case of $k = \text{optimal}$, ACBF_O reduces the false positive probability by up to five orders of magnitude compared to CBF/ACBF₁ as well as the false positive probability by up to 99.8% and up to 69.6% compared to ACBF₂ and ACBF₃.

3.3. Simulation Results. We conduct simulation experiments to test the performance of ACBFs on synthetic datasets. As a standard CBF has the same memory consumption as its previous variants, we mainly compare ACBFs with the standard in the experiments. We compare ACBF_O with CBF, ACBF₁, ACBF₂, and ACBF₃ in terms of the false positive probability, the query overhead, and the update overhead, at the same memory consumption. In the experiments, both CBF and ACBFs have the same parameters such as m , n , and k , where m/n varies from 8 to 20 and k is set to 3 or the optimal integer value $\lceil (m/n) \ln 2 \rceil$.

For each synthetic experiment, we synthesize a data set and a query set. The data set contains 100 K unique strings that we represent with CBF and ACBFs, while the query set contains 1000 K strings that are tested through the filters. During an update period, 20 K elements are deleted from the filters, and another 20 K elements are inserted into the filters, maintaining constant 100 K elements in the filters. We do ten experimental trials and average the results.

Figure 5 depicts the false positive probability of CBF, ACBF₁, ACBF₂, ACBF₃, and ACBF_O. From the figure, we demonstrate that ACBF_O achieves significant reductions in the false positive probability compared to CBF, ACBF₁, ACBF₂, and ACBF₃. As shown in Figure 5(a), ACBF_O with $k = 3$ reduces the false positive probability by up to 96.0%, up to 76.6%, and up to 35.5%, compared to CBF/ACBF₁, ACBF₂, and ACBF₃, respectively. Figure 5(b) shows that compared to CBF/ACBF₁, ACBF_O with $k = \text{optimal}$ reduces the false positive probability by up to 98.4%. We also see that when

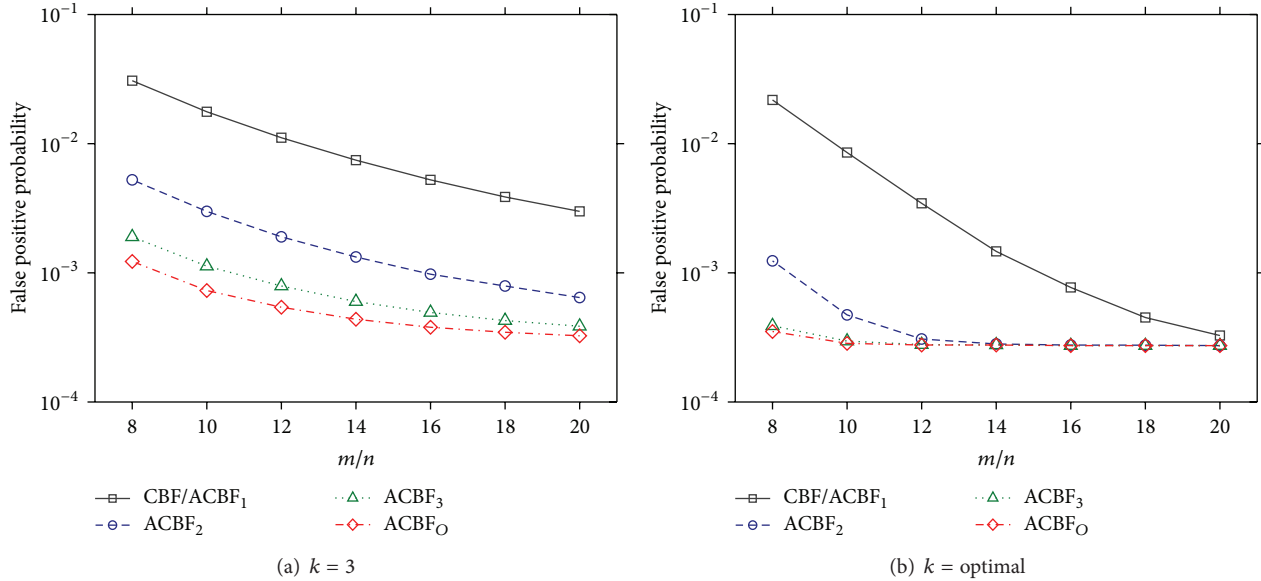
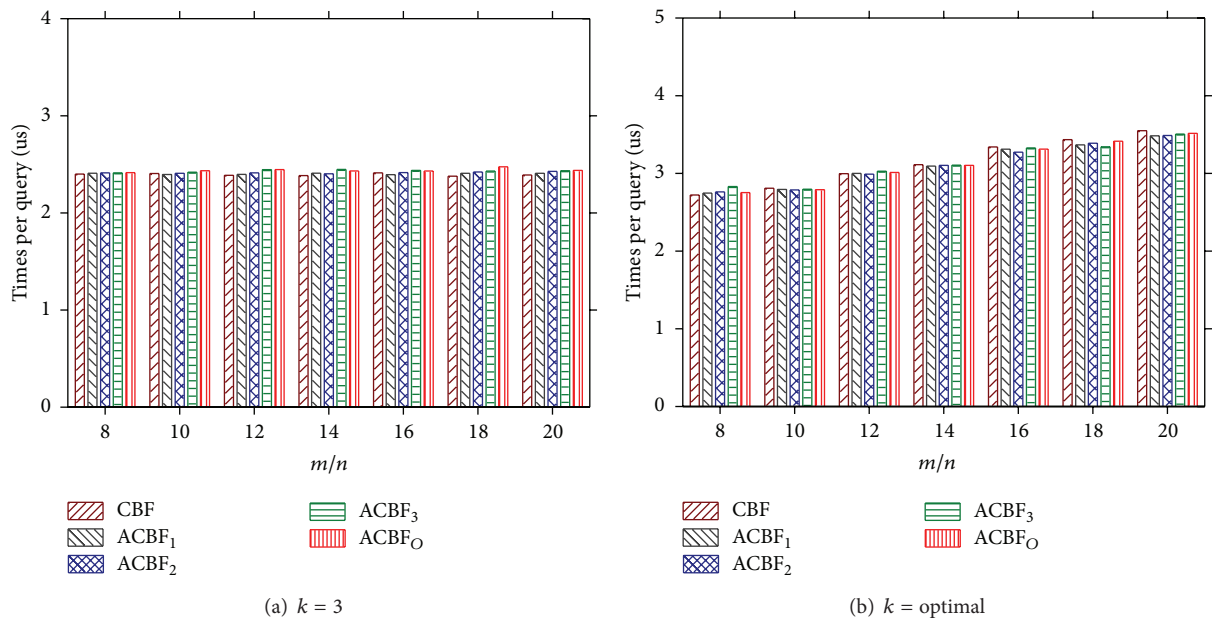
m/n is from 16 to 20 in case of $k = \text{optimal}$, ACBF₃ has the same false positive probability as ACBF_O. This is because the first level size l_1 of ACBF_O is very close to $3m$.

Figure 6 depicts the query overhead of CBF, ACBF₁, ACBF₂, ACBF₃, and ACBF_O in two cases of $k = 3$ and $k = \text{optimal}$. We see that ACBF_O has almost the same query times as CBF, ACBF₁, ACBF₂, and ACBF₃. This reason is that all the filters have the same number k of hash functions. We do examine the query overhead of CBF and ACBFs on a server with 2.4 GHz Intel Core Duo CPU P8600 and 3 GB main memory. Figure 6 shows that the query overhead of CBF and ACBFs is dominated by the number of hash functions. For instance, all the filters have about 2.4 us per query in case of $k = 3$ (see Figure 6(a)), while they require 2.7–3.6 us per query in case of $k = \text{optimal}$ (see Figure 6(b)).

Figure 7 depicts the update overhead of CBF, ACBF₁, ACBF₂, ACBF₃, and ACBF_O in two cases of $k = 3$ and $k = \text{optimal}$. We see that ACBFs require more update overhead than CBF. This is because ACBFs use the hierarchical structure to span the counters, which incurs more computations and I/O overhead. Figure 7 shows that ACBFs have more three orders of magnitude update times compared to CBF. For instance, CBF with $k = 3$ in Figure 7(a) requires 2.6–3.2 us per update, while ACBFs requires 1.4–4.2 ms per update. From the figure, we demonstrate that ACBFs dramatically reduce the false positive probability at the cost of the update overhead as analyzed in (2) of Section 3.1.

4. Implementation in MapReduce

In this section, we implement ACBFs in MapReduce to accelerate reduce-side joins for large-scale data processing. We first present the MapReduce overview and then describe the optimized reduce-side join with ACBF in MapReduce. Finally, we report experimental results on realistic datasets.

FIGURE 5: False positive probability of CBF, ACBF₁, ACBF₂, ACBF₃, and ACBF₀.FIGURE 6: Query overhead of CBF, ACBF₁, ACBF₂, ACBF₃, and ACBF₀.

4.1. MapReduce Overview. MapReduce [5] is a programming model for large-scale data processing on large clusters of commodity machines. The MapReduce model offers automatic parallel execution to allow users to only focus on their data processing strategies, hiding the details of parallel and distributed executions.

A MapReduce program provides *map* and *reduce* functions to users. The *map* function takes a set of key-value pairs (K, V) from input files as the input and produces intermediate key-value pairs (K', V') as the output. The *reduce* function takes pairs $(K', LIST(V'))$ as the input, where $LIST(V')$ is a list of all values V' that are grouped on a given key K' by

sorting and merging. Yet, the *reduce* function produces the final output key-value pairs. Typically, both the input and the output of a MapReduce job are files in a distributed file system (DFS), that is, Google File System (GFS). DFS is a block-based file system that supports fault tolerance by data partitioning and replication.

When a MapReduce job is launched, a job tracker creates a total of m map tasks and r reduce tasks. Each map task works on a nonoverlapping data block called a split of the input file. Each map task Map_i ($i = 1, \dots, m$) reads the file split, converts the records into a sequence of key-value pairs, and then executes the user-defined *map* function with each

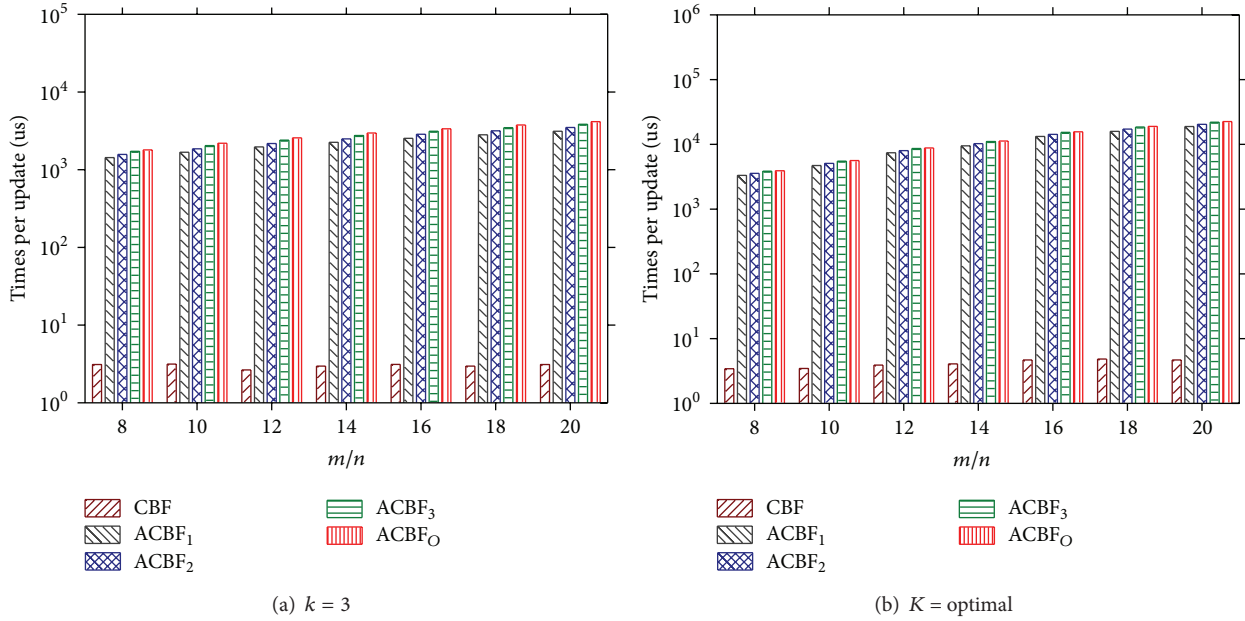


FIGURE 7: Update overhead of CBF, ACBF₁, ACBF₂, ACBF₃, and ACBF₀.

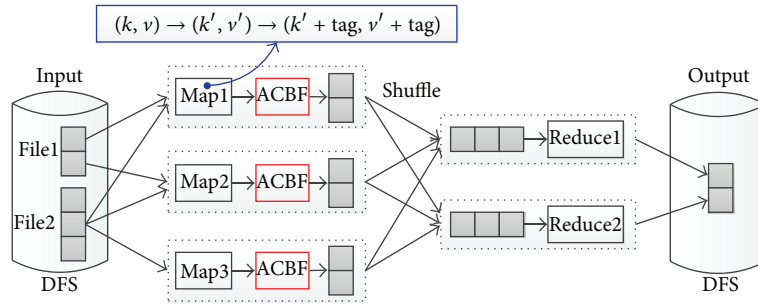


FIGURE 8: Reduce-side join with ACBF in MapReduce.

pair (K, V) . The output pairs (K', V') are partitioned into r chunks, one for each reduce task. This partitioning is basically done by a hash function to guarantee that pairs with the same key are allocated to the same chunk. The pairs in each chunk are sorted by K' and written to local storage. Each reduce task $Reduce_j$ ($j = 1, \dots, r$) fetches the j th chunk outputted by each map task remotely. This is referred to the shuffle phase in MapReduce, where each chunk is assigned to only a single reduce task by one-to-one shuffling strategy. $Reduce_j$ merges these chunks, produces the intermediate pairs $(K', LIST(V'))$ sorted by K' , and then invokes the user-defined *reduce* function for each pair $(K', LIST(V'))$. The final output is stored and tripled in DFS before the MapReduce job terminates.

4.2. Reduce-Side Join with ACBF. The join operation is one of fundamental query operations. It combines records from two different datasets based on a cross product [18]. We consider a join between two datasets R and S on attribute A of R and attribute B of S . The join result contains the pairs of records from R and S when $R \cdot A = S \cdot B$.

There are two main join implementations in MapReduce: the map-side join and the reduce-side join. As their own names imply, the map-side join implements the join during the map phase, while the reduce-side join implements the join during the reduce phase [19]. The map-side join is more efficient than the reduce-side join because it produces the final results of the join in the map phase. However, the map-side join is used only in particular circumstances, lacking the generality of the reduce-side join. This is because its efficiency requires the two input datasets to be partitioned and sorted on the join keys in advance.

The reduce-side join is the most general join approach implemented in MapReduce. The basic idea behind the reduce-side join is that a map task tags each key-value pair with its source and uses the join keys as the map output keys, so that the pairs with the same key are grouped for a reduce task. Figure 8 shows the tagging in the map phase. The map task reads a key-value pair (K, V) and produces a tagged pair $(K' + tag, V' + tag)$ as the output. Next, the map outputs $(K' + tag, V' + tag)$ with the same K' are sent to the same reduce task. The pairs $(K' + tag, V' + tag)$ are sorted primarily

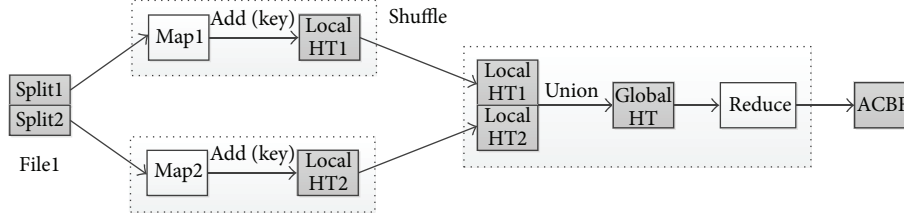


FIGURE 9: ACBF construction in MapReduce.

TABLE 1: Reduce-side join performance comparisons in Hadoop.

Filter parameters $m/n = 10, k = 3$	False positive probability	Map inputs (MB)	Map outputs (MB)	Filter construction times (s)	Total execution times (s)
Join + CBF	0.01772	252.5	45.1	62	115
Join + ACBF _O	0.00491	252.5	29.8	68	92

on K' and secondarily on tag and grouped only on K' . Finally, the *reduce* function separates a list of all values V' associated with the same join key K' into two sets according to tag and performs a cross product between values in the two sets as the final output.

To mitigate I/O cost of the reduce-side join, CBF is widely used in the map phase to filter the map outputs shuffled across the network. We use ACBF to replace CBF in the reduce-side join for minimizing the amount of traffic during the shuffle phase. ACBF has so lower false positive probability that more redundant map outputs can be reduced. Figure 8 shows an example of the reduce-side join with ACBF in MapReduce. The smallest input file, that is, $File_1$, is often used to construct an ACBF in a distributed way. The job tracker then broadcasts the ACBF to all the map tasks, that is, Map_1 , Map_2 , and Map_3 , by an efficient facility called *DistributedCache* which is provided by the MapReduce framework to cache data needed by the applications. Each map task uses the ACBF to filter out the redundant records. After that all the reduce tasks, that is, $Reduce_1$ and $Reduce_2$, perform the joins and produces the final results.

Figure 9 shows the ACBF construction in MapReduce. First, a job tracker splits the input file, that is, $File_1$, and then each map task (i.e., Map_1 or Map_2) reads an input split, that is, $Split_1$ or $Split_2$. A local hash table is created in each map task by adding the unique keys of each file split. Note that each map task consists of the *map* function only, without additional I/O cost. Each local filter (i.e., HT_1 or HT_2) is a chained hash table which has the same number of buckets and uses the same hash function called *MurmurHash* implemented in MapReduce. When each map task is completed, all local hash tables are assigned to one reduce task (i.e., $Reduce_1$), which creates a global hash table. All the local hash tables are merged by a union function that eliminates duplicated keys. Next, the reduce task creates an ACBF by adding the keys of the global hash table in the filter. Finally, the ACBF is written to local storage in DFS and submitted via broadcast to all other map tasks for performing the reduce-side join (see Figure 8).

4.3. Experimental Results. To evaluate the optimized reduce-side join, we implement ACBFs in Hadoop that is an open-source Java implementation of MapReduce. We obtain the NBER US patent citations data files [20] for evaluation. We use the patent citations file named *cite75_99.txt* of 16,522,438 records as the input dataset. We extract 65,771 records from the patent data file named *pat63_99.txt* as the join keys. Our Hadoop prototype runs on three servers each with 2.8 GHz Intel Core 2 Duo CPU and 4 GB main memory. We run Hadoop version 0.20.203 on Red Hat Enterprise Linux 6, perform ten experimental trials, and average the results.

Table 1 shows reduce-side join performance comparisons in Hadoop. We compare the join with CBF to that with the optimized ACBF named ACBF_O. From the table, we see that ACBF_O dramatically reduces the false positive probability by 72.3% as well as the map outputs by 33.9% compared to CBF. We also see that the reduce-side join with ACBF_O requires less 20% total execution times than that with CBF. This is because ACBF_O filters out more redundant records in the map phase. In addition, ACBF_O requires only more 9.7% construction times than CBF. This is due to the hierarchical structure of ACBF_O.

5. Conclusions

We propose a multilevel optimization approach to building an accurate CBF called ACBF for reducing the false positive probability. ACBF is constructed by partitioning the counter vector into multiple levels. We propose an optimized ACBF named ACBF_O which maximize the first level size as $4m-kn$, minimizing the false positive probability while maintaining the same functionality as CBF, where m is the number of counters, n is the number of elements, and k is the number of hash functions. Simulation results show that ACBF_O reduces the false positive probability by up to 96.0% in case of $k = 3$ and by up to 98.4% in case of $k = optimal$ compared to CBF.

We implement ACBFs in MapReduce to improve the reduce-side join performance. ACBF is used in the map phase to filter out redundant records shuffled. ACBF is constructed in a distributed way by merging local hash tables of all map

tasks. Experiments on realistic patent citations data files show that $ACBF_{\mathcal{O}}$ reduces the false positive probability by 72.3% as well as the map outputs by 33.9% and improves the join execution times by 20% compared to CBF. We show that ACBF is an accurate data structure suitable for large-scale data processing.

Acknowledgments

This work was supported in part by the National Basic Research Program (973 Program) of China under Grant no. 2012CB315805, the National Natural Science Foundation of China under Grant no. 61173167, no. 61100171, and no. 61272546, and the Scientific and Technological Project of Hunan Province, China, under Grant no. 2013SK3149.

References

- [1] B. B. Bloom, "Space/time tradeoffs in hash coding with allowable errors," *Communications of the ACM*, vol. 13, no. 7, pp. 422–426, 1970.
- [2] A. Broder and M. Mitzenmacher, "Network applications of Bloom filters: a survey," *Internet Mathematics*, vol. 1, no. 4, pp. 485–509, 2004.
- [3] S. Tarkoma, C. E. Rothenberg, and E. Lagerspetz, "Theory and practice of bloom filters for distributed systems," *IEEE Communications Surveys and Tutorials*, vol. 14, no. 1, pp. 131–155, 2012.
- [4] L. Fan, P. Cao, J. Almeida, and A. Z. Broder, "Summary cache: a scalable wide-area Web cache sharing protocol," *IEEE/ACM Transactions on Networking*, vol. 8, no. 3, pp. 281–293, 2000.
- [5] J. Dean and S. Ghemawat, "MapReduce: simplified data processing on large clusters," in *Proceedings of the 6th Symposium on Operating System Design and Implementation (OSDI '04)*, pp. 137–149, San Francisco, Calif, USA, 2004.
- [6] Hadoop [EB/OL], 2012, <http://hadoop.apache.org>.
- [7] C. Lam, *Hadoop in Action*, Manning Publications Press, Shelter Island, NY, USA, 2010.
- [8] T. Lee, K. Kim, and H. Kim, "Join processing using Bloom filter in MapReduce," in *Proceedings of the 2012 ACM Research in Applied Computation Symposium*, pp. 100–105, San Antonio, Tex, USA, 2012.
- [9] F. Bonomi, M. Mitzenmacher, R. Panigrahy, S. Singh, and G. Varghese, "Beyond Bloom filters: from approximate membership checks to approximate state machines," in *Proceedings of the ACM Conference on Applications, Technologies, Architectures, and Protocols for Computer Communications (SIGCOMM '06)*, pp. 315–326, Pisa, Italy, October 2006.
- [10] F. Bonomi, M. Mitzenmacher, R. Panigrahy, S. Singh, and G. Varghese, "An improved construction for counting Bloom filters," in *Proceedings of the 14th Annual European Symposium on Algorithms (ESA '06)*, pp. 684–695, Zurich, Switzerland, September 2006.
- [11] N. Hua, H. Zhao, B. Lin, and J. Xu, "Rank-indexed hashing: a compact construction of bloom filters and variants," in *Proceedings of the 16th IEEE International Conference on Network Protocols (ICNP '08)*, pp. 73–82, Orlando, Fla, USA, October 2008.
- [12] D. Ficara, S. Giordano, G. Procissi, and F. Vitucci, "MultiLayer compressed counting bloom filters," in *Proceedings of the 27th IEEE Communications Society Conference on Computer Communications (INFOCOM '08)*, pp. 311–315, Phoenix, Ariz, USA, April 2008.
- [13] O. Rottenstreich, Y. Kanizo, and I. Keslassy, "The variable-increment counting Bloom filter," in *Proceedings of the 31th IEEE International Conference on Computer Communications (INFOCOM '12)*, pp. 1880–1888, Orlando, Fla, USA, 2012.
- [14] S. Lumetta and M. Mitzenmacher, "Using the power of two choices to improve Bloom filters," *Internet Mathematics*, vol. 4, no. 1, pp. 17–33, 2009.
- [15] F. Hao, M. Kodialm, and T. V. Lakshman, "Building high accuracy Bloom filters using partitioned hashing," in *Proceedings of the ACM International Conference on Measurement and Modeling of Computer Systems (SIGMETRICS '07)*, pp. 277–287, San Diego, Calif, USA, 2007.
- [16] A. Kirsch and M. Mitzenmacher, "Less hashing, same performance: building a better bloom filter," *Random Structures and Algorithms*, vol. 33, no. 2, pp. 187–218, 2008.
- [17] Y. Qiao, T. Li, and S. Chen, "One memory access bloom filters and their generalization," in *Proceedings of the 30th IEEE International Conference on Computer Communications (INFOCOM '11)*, pp. 1745–1753, Shanghai, China, April 2011.
- [18] F. N. Afrati and J. D. Ullman, "Optimizing multiway joins in a map-reduce environment," *IEEE Transactions on Knowledge and Data Engineering*, vol. 23, no. 9, pp. 1282–1298, 2011.
- [19] S. Blanas, J. M. Patel, V. Ercegovac, J. Rao, E. J. Shekita, and Y. Tian, "A comparison of join algorithms for log processing in MapReduce," in *Proceedings of the ACM International Conference on Management of Data (SIGMOD '10)*, pp. 975–986, Indianapolis, Ind, USA, June 2010.
- [20] NBER U.S. patent citation data file [EB/OL], 2012, <http://data.nber.org/patents>.

Research Article

Analysis and Denoising of Hyperspectral Remote Sensing Image in the Curvelet Domain

Dong Xu,¹ Lei Sun,¹ Jianshu Luo,¹ and Zhihui Liu²

¹ College of Science, National University of Defense Technology, Changsha, Hunan 410073, China

² Department of Radiation Oncology, The 89th Hospital of PLA, Weifang, Shandong 261045, China

Correspondence should be addressed to Dong Xu; xu_don@163.com

Received 7 May 2013; Accepted 1 July 2013

Academic Editor: Yue Wu

Copyright © 2013 Dong Xu et al. This is an open access article distributed under the Creative Commons Attribution License, which permits unrestricted use, distribution, and reproduction in any medium, provided the original work is properly cited.

A new denoising algorithm is proposed according to the characteristics of hyperspectral remote sensing image (HRSI) in the curvelet domain. Firstly, each band of HRSI is transformed into the curvelet domain, and the sets of subband images are obtained from different wavelength of HRSI. And then the detail subband images in the same scale and same direction from different wavelengths of HRSI are stacked to obtain new 3-D datacubes of the curvelet domain. Again, the characteristics analysis of these 3-D datacubes is performed. The analysis result shows that each new 3-D datacube has the strong spectral correlation. At last, due to the strong spectral correlation of new 3-D datacubes, the multiple linear regression is introduced to deal with these new 3-D datacubes in the curvelet domain. The simulated and the real data experiments are performed. The simulated data experimental results show that the proposed algorithm is superior to the compared algorithms in the references in terms of SNR. Furthermore, MSE and MSSIM in each band are utilized to show that the proposed algorithm is superior. The real data experimental results show that the proposed algorithm effectively removes the common spotty noise and the strip noise and simultaneously maintains more fine features during the denoising process.

1. Introduction

Hyperspectral remote sensing image (HRSI) can be viewed as three-dimensional data consisting of one-dimensional spectral information and two-dimensional spatial information. With the fast development of hyperspectral remote sensing technology, HRSI can describe the characteristics of Earth objects more comprehensively and explicitly therefore, it is widely applied in many fields including agriculture, forestry, geological surveys, environmental monitoring, and military recon. Although over the last decades the development of imaging spectrometers is rapid, HRSI is still affected by many complex factors during the processing of acquisition and transmission, which will produce a mass of noises. The data that are contaminated with noise can cause a failure to extract valuable information and hamper further interpretation. In presence of noise in the image, extraction of all the useful information becomes difficult and noise can lead to artefacts and loss of spatial resolution [1]. The noise also affects the target detection, classification, and segmentation, so it is necessary to study the characteristic of HRSI for denoising [2].

Though the spatial correlation of HRSI is weaker than the nature image, the two-dimensional spatial information of HRSI is similar to the nature image [3]. When some traditional linear denoising methods are used to denoise the HRSI, they cannot get the satisfactory results for application such as Wiener filter. Compared with the nature image, the one-dimensional spectral information of HRSI is its particular characteristic. Minimum noise fraction (MNF), Savitzky-Golay filter, and wavelet denoising are the most popular among the existing denoising methods of hyperspectral imagery [4–7]. These methods are able to smooth the spectral while they have a negative impact on the sharp signal features.

In recent years, many denoising methods for HRSIs are constantly introduced with the development of hyperspectral remote sensing technology. Most of denoising methods combine correlation of spatial and spectral domain. Currently, wavelet denoising methods are widely used. The seminal work on signal denoising via wavelet thresholding or shrinkage proposed by Donoho and Johnstone [6, 7] shows that various wavelet thresholding schemes for denoising have

near-optimal properties in the minimax sense. The observed noisy data in a local neighborhood is utilized to perform an approximate maximum a posteriori estimation of the variance for each coefficient [8]. Then, the predicted image coefficients are obtained by an approximate minimum mean squared error estimation procedure. Şendur and Selesnick developed a bivariate shrinkage function for image denoising [9, 10]. Their results show that the estimated wavelet coefficients depend on the parent coefficients. The smaller parent coefficients mean the greater shrinkage. In [11], Buades et al. proposed a new filter called the nonlocal means (NLM) filter, which takes account of the two most important attributes of a denoising algorithm: detail preservation and noise removal. Unfortunately, as most of filtering methods, NLM filter is also based on the additive Gaussian signal-independent (SI) noise assumption, so it cannot be directly applied for HRSI with signal-dependent (SD) noise [12]. In order to fully utilize the spatial information and the spectral information, Atkinson et al. proposed a denoising method that uses discrete Fourier transforms, 2-D discrete wavelet transforms, and soft thresholding of wavelet coefficients to denoise HRSI [13]. In [14], Othman and Qian developed a noise reduction algorithm—hybrid spatial-spectral noise-reduction algorithm (HSSNR) for hyperspectral datacube. The algorithm resorts to the spectral derivative domain, where the noise level is elevated, and benefits from the dissimilarity of the signal regularity in the spatial and spectral domains. Chen and Qian [15] combined wavelet denoising with dimensionality reduction for HRSI by using bivariate wavelet thresholding, wavelet packets, and principal component analysis (PCA). In [16], Chen and Qian developed a new denoising method using PCA and wavelet shrinkage to avoid removing the fine features of the datacubes during denoising process. PCA is used to decorrelate the fine features of the datacube from noise for detail preservation. In this paper the method in [16] is named as PCABS.

Since wavelet has good time-frequency-localization property and multiresolution analysis property, it is widely and successfully applied in several fields [17]. However, wavelet is not perfect. Wavelet is mainly applied to representation of isotropic singularity object, while for anisotropic singularity, such as boundary and linear features of an image, it is not a good representation tool. In other words wavelet is good representation for point singularity, but for the curves it is relatively weak [18–20]. The complex wavelet [18], curvelet transform [19], and contourlet transform [20] are proposed to overcome the drawbacks of the wavelet transform. This paper focuses on the curvelet transform applied for HRSI.

Compared with normal three-dimensional data cube of fixed variance of additive noise, the noise level of HRSI may vary dramatically from band to band. The noise standard deviation in each band of HRSI is not constant; in particular, there exist some bands at which the atmosphere absorbs so much light that the signal received from the surface is unreliable [21]. And SD noise may no longer be neglected with respect to the SI noise in the new-generation hyperspectral sensors [22, 23]. In this paper, the proposed denoising method is available for the both SD noise and SI noise. The representation of HRSI in another domain is proposed for detail preservation. By analyzing spectral correlation of HRSI

in the new representation domain, we know the fact that the spectral correlation of HRSI in the new representation domain is strong. So the multiple linear regression (MLR) method is proposed to predict the representation of pure signal in the curvelet domain, in order to remove the noise of HRSI.

In the rest of this paper, the mathematical tools curvelet transform and MLR model are introduced in Section 2. Section 3 gives the analysis of HRSI in the curvelet domain. In Section 4 the denoising process is proposed in the curvelet domain. The simulated data experiment and the real data experiment are performed, and the experimental results are presented in Section 5. Finally, Section 6 draws the conclusion.

2. Mathematical Tools

In the section, the mathematical tools curvelet transform and MLR model are introduced. The curvelet transform, pioneered by Candès and Donoho, is shown to be optimal in a certain sense for functions in the domain with curved singularities [19]. Due to the strong spectral correlation of HRSI, MLR model has been widely applied to the HRSI [24, 25].

2.1. The Curvelet Transform. The curvelet transform is a new multiresolution analysis framework and widely applied in various image processing problems. The curvelet decomposition can be equivalently stated in the following four steps: (1) subband decomposition, (2) smooth partitioning, (3) renormalization, and (4) ridgelet transform. In short, the curvelet obtained by bandpass filtering of multiscale ridgelets with passband is rigidly linked to the scale of spatial localization. The discrete curvelet transform [26] is given as follows.

The digital image is used as an example to introduce the discrete curvelet transform. I stands for the original image, whose size is $N \times N$. And then I is decomposed by binary wavelet transform with J scales, and we have

$$I = C_J + \sum_{j=1}^J D_j, \quad (1)$$

where C_J is low-frequency component in the coarsest scale J , while $\{D_j\}_{j=1,2,\dots,J}$ is high-frequency component in different scale. Here, $j = 1$ is the finest scale. We now employ a sketch of the discrete curvelet transform algorithm.

- (1) Perform the binary wavelet transform with J scales on the original image I , and obtain subband sequence C_J and $\{D_j\}_{j=1,2,\dots,J}$.
- (2) Let the size of initial block (the subband in the finest scale) be B_{\min} , and set $B_1 = B_{\min}$.
- (3) For $j = 1, 2, \dots, J$
 - (a) partition the subband D_j with a block size B_j ;
 - (b) apply the digital ridgelet transform to each block;
 - (c) If j module 2 = 1 $B_{j+1} = 2B_j$, and else $B_{j+1} = B_j$.

Since each step of the previous decomposition process is invertible, the inverse curvelet transform is an invertible process.

The curvelet transform overcomes the major drawback that wavelets cannot really represent two-dimensional objects with edges sparsely and captures more directional information besides the horizontal, vertical, and diagonal directions. The system approximately obeys the scale relationship $\text{width} \approx \text{length}^2$. Therefore, it is optimal in a certain sense for functions in the domain with curved singularities.

It is known that the curvelet transform competes surprisingly well with the ideal adaptive rate. The approximation error is obtained as

$$\|f - \tilde{f}_m^C\|_2^2 \leq C \cdot m^{-2}(\log m)^3, \quad m \rightarrow \infty, \quad (2)$$

where \tilde{f}_m^C is the m biggest terms in the curvelet frame expansion to approximate f .

Curvelet is optimal in the sense that no other representation can yield a smaller asymptotic error with the same number of terms. Because of its surprising properties for image processing, a fast and accurate discrete curvelet transform operating on digital data is necessary. Candès et al. [27, 28] presented two 2-D discrete curvelet transforms for the second generation curvelet, which is curvelet via transforms and curvelet via wrapping of specially selected Fourier samples. Compared with the first generation curvelet, they are conceptually simpler, faster, and far less redundant. The curvelet transform used in this work is based on unequally-spaced fast Fourier transform.

2.2. Multiple Linear Regression (MLR). Due to the strong spectral correlation of new 3-D datacubes in the curvelet domain, the MLR model is introduced to predict the representation of pure HRSI in the curvelet domain. It is assumed that the HRSI has B spectral bands and each band of HRSI has $M \times N$ pixels. Let X denote a $P \times B$ matrix of the B spectral observed vectors of size P ($P = M \times N$). The $P \times 1$ vector X_k ($k = 1, 2, \dots, B$) is the k th column vector of the matrix X , namely, lexicographically arranging k th band image into a column vector X_k . In this paper, \hat{X}_k is the vector predicted for the signal X_k of band k . The L adjacent bands (not including itself) are utilized to perform MLR, where L is even; that is,

$$\hat{X}_k = X_{\lambda k} \beta_k \quad (k = 1, 2, \dots, B), \quad (3)$$

where the $P \times L$ matrix $X_{\lambda k}$ consists of the adjacent column vectors of X_k (not including the k th column vector). $X_{\lambda k}$ has the form

$$X_{\lambda k} = \begin{cases} [X_1, \dots, X_{k-1}, X_{k+1}, \dots, X_L] & 1 \leq k \leq \frac{L}{2} \\ [X_{k-L/2}, \dots, X_{k-1}, X_{k+1}, \dots, X_{k+L/2}] & \frac{L}{2} < k < B - \frac{L}{2} \\ [X_{B-L+1}, \dots, X_{k-1}, X_{k+1}, \dots, X_B] & B - \frac{L}{2} \leq k \leq B. \end{cases} \quad (4)$$

β_k is the regression vector of size $L \times 1$. For $k = 1, 2, \dots, B$, the least squares estimator of the regression vector β_k is given by

$$\hat{\beta}_k = (X_{\lambda k}^T X_{\lambda k})^{-1} X_{\lambda k}^T X_k. \quad (5)$$

3. Analysis of HRSI in the Curvelet Domain

HRSI is a datacube, having two spatial dimensions and a third spectral dimension. Fixing the wavelength band yields a 2-D image of the scene at a particular wavelength. So it may also be visualized as a stack of 2-D band images, each corresponding to a certain wavelength [3]. Since the bands are so closely spaced in wavelength, images in adjacent bands are highly correlated. In the rest of the section, HRSI is transformed into the curvelet domain band by band and the spectral correlation of the HRSI in the curvelet domain will be mainly discussed to denoise by performing the MLR.

Let $C(\cdot)$ and $C^{-1}(\cdot)$ denote the 2-D curvelet transform and 2-D inverse curvelet transform. Let $\{X_i\}_{i=1}^B$ be HRSI, where X_i is the i th band image and B is the number of bands. $C_i = C(X_i)$ stands for the coefficients of band X_i in the curvelet domain. A J -level curvelet transform is performed on each X_i . Setting aside the coarsest coefficients C_i^L of C_i , the same scale and same directional coefficients from each high frequency coefficient C_i^H ($C_i^H = C_i/C_i^L$) are stacked as a new 3-D datacube. The previous process is shown in Figure 1. In this way, several new 3-D datacubes $\{F^t\}_{t=1}^S$ are obtained where S is the number of data. However, transforming $\{F^t\}_{t=1}^S$ into C_i ($i = 1, 2, \dots, B$) is an inverse transform of the previous process. The spatial size of each datacube F^t varies with the scale and the direction, but each datacube has the same B spectral bands. The new three-dimensional datacubes are new representation of HRSI in the curvelet domain. The spectral correlation of F^t will be discussed. In this paper, each band X_i is decomposed into 5 levels. The first scale is coarsest scale with only one direction. From the second scale to the fourth scale, there are eight directions. At the finest scale, one direction is obtained. Setting aside the first scale, the total number of the other directions from different scale is 25; that is, $S = 25$.

Let $F_i^t(m, n)$ denote the value of the position (m, n, l) of the datacube. Let H denote the set of spatial coordinates of F^t , and let $|H|$ denote the element number of set H .

The spectral correlation factor of F^t between band k and band l is defined as

$$\rho_t(k, l) = \frac{\sum_{(m,n) \in H} [F_k^t(m, n) - u_k] [F_l^t(m, n) - u_l]}{\sqrt{(\sum_{(m,n) \in H} [F_k^t(m, n) - u_k]^2) (\sum_{(m,n) \in H} [F_l^t(m, n) - u_l]^2)}}, \quad (6)$$

where $u_k = (1/|H|) \sum_{(m,n) \in H} F_k^t(m, n)$ and $u_l = (1/|H|) \sum_{(m,n) \in H} F_l^t(m, n)$. In this paper, let $k = l + 1$; thus $\rho_t(k, k + 1)$ stands for the correlation factor of neighboring bands for datacube F^t . In order to analyze the spectral correlation of HRSI in the curvelet domain, AVIRIS hyperspectral data

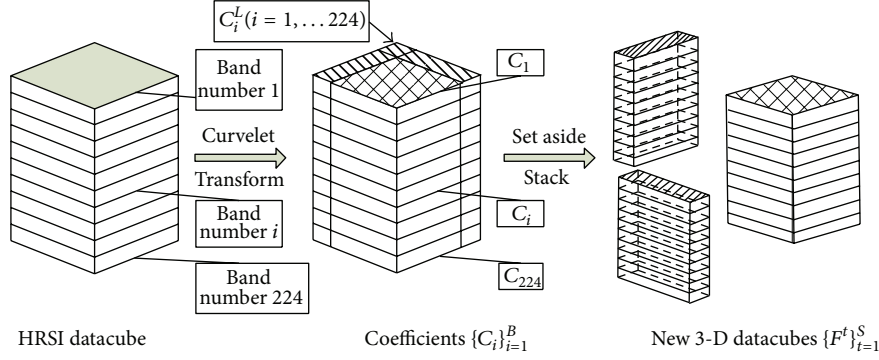


FIGURE 1: The process of obtaining new 3-D datacubes $\{F^t\}_{t=1}^S$.

Jasper Ridge whose size is $256 \times 256 \times 224$ (width \times height \times band) is used as an experimental example. Figure 2 shows the spectral correlation of each datacube F^t in the curvelet domain and the spectral correlation of the datacube Jasper Ridge.

From Figure 2, it is clear that the absolute value of linear correlation factor between neighboring bands is close to 1 from the second scale to the fourth scale except for the bands 1–5, 105–115, and 150–170, which is due to water absorption and low signal-to-noise ratio (SNR) for the HRSI. These bands are often viewed as junk band. From the second scale to the finest scale, the correlation factor of junk bands in the curvelet domain becomes much lower, but the other bands are still keeping close to 1. The result in the curvelet domain is consistent with the original HRSI. It also indicates that the curvelet coefficients of hyperspectral data between neighboring bands have significant linear correlation from the same scale and the same direction. The curvelet transform keeps the strong spectral correlation of HRSI, and specially at some directions from the second scale to the forth scale the spectral correlation in the curvelet domain becomes stronger. The reason for this phenomenon is the strong spectral correlation of HRSI, which means that the pixels in the same spatial location of each band image are similar. Images at different wavelengths capture the same scene, which has the same physical structure; thus the profiles of different wavelength images are similar [29]. After the curvelet transform, the coefficients of datacube F^t at close wavelengths maintain this similarity as well and have significant linear correlation. Since the most of subtle noise of HRSI is maintained in the finest scale, the correlation factor of the finest scale is lower than the other scales. But in the finest scale, the most of the correlation factors are still greater than 0.85. Due to the strong spectral correlation of HRSI in the curvelet domain, a new denoising algorithm based on MLR is proposed in the next section.

4. Proposed Denoising Algorithm

In this section, we summarize our denoising algorithm. According to the correlation factor of HRSI in the curvelet domain in Section 3, the MLR model is performed on the datacubes $\{F^t\}_{t=1}^S$ for denoising.

The denoising process is as follows (Figure 3).

- (1) Input the noisy datacube X .
- (2) A J -level curvelet transform (CT) is performed on X_i , and $C_i = C(X_i)$ ($i = 1, 2, \dots, B$) is obtained.
- (3) Set aside the coarsest scale coefficients C_i^L of C_i , and then the same scale and same directional coefficients from each high frequency coefficients C_i^H ($C_i^H = C_i/C_i^L$) are stacked as a 3-D datacube. The 3-D datacubes $\{F^t\}_{t=1}^S$ are obtained.
- (4) MLR is performed on F^t , $t = 1, 2, \dots, S$, and \hat{F}^t ($t = 1, 2, \dots, S$) is obtained.
- (5) For $i = 1, 2, \dots, B$, combine the new high frequency coefficients \hat{C}_i^H extracted from each \hat{F}_i^t ($t = 1, 2, \dots, S$) with the corresponding coarsest scale coefficients C_i^L to obtain the prediction coefficients \hat{C}_i of the C_i .
- (6) The inverse curvelet transform (ICT) is performed to obtain the denoised image \hat{X}_i ; that is, $\hat{X}_i = C^{-1}(\hat{C}_i)$.
- (7) Output the denoised datacube \hat{X} .

5. Experiment

Signal-to-noise ratio (SNR) is a key parameter on measuring the HRSI quality. So in this paper, we utilize SNR to evaluate the proposed algorithm. Here the SNR is defined as

$$\text{SNR} = \frac{P_X}{P_N}, \quad (7)$$

where P_X is the power of the pure signals $PX(i, j, k)$, and P_N is the noise power in the noisy signals $X(i, j, k)$, while (i, j, k) stands for the position of the pixel in the HRSI; that is,

$$\text{SNR} = \frac{\sum_{i=1, j=1, k=1}^{M, N, B} |PX(i, j, k)|^2}{\sum_{i=1, j=1, k=1}^{M, N, B} |PX(i, j, k) - X(i, j, k)|^2}. \quad (8)$$

5.1. Simulated Data Experiment. The simulated experiment of the noise reduction is carried out on AVIRIS images, Cuprite, Jasper Ridge, Low Altitude, Lunar Lake, and Moffett

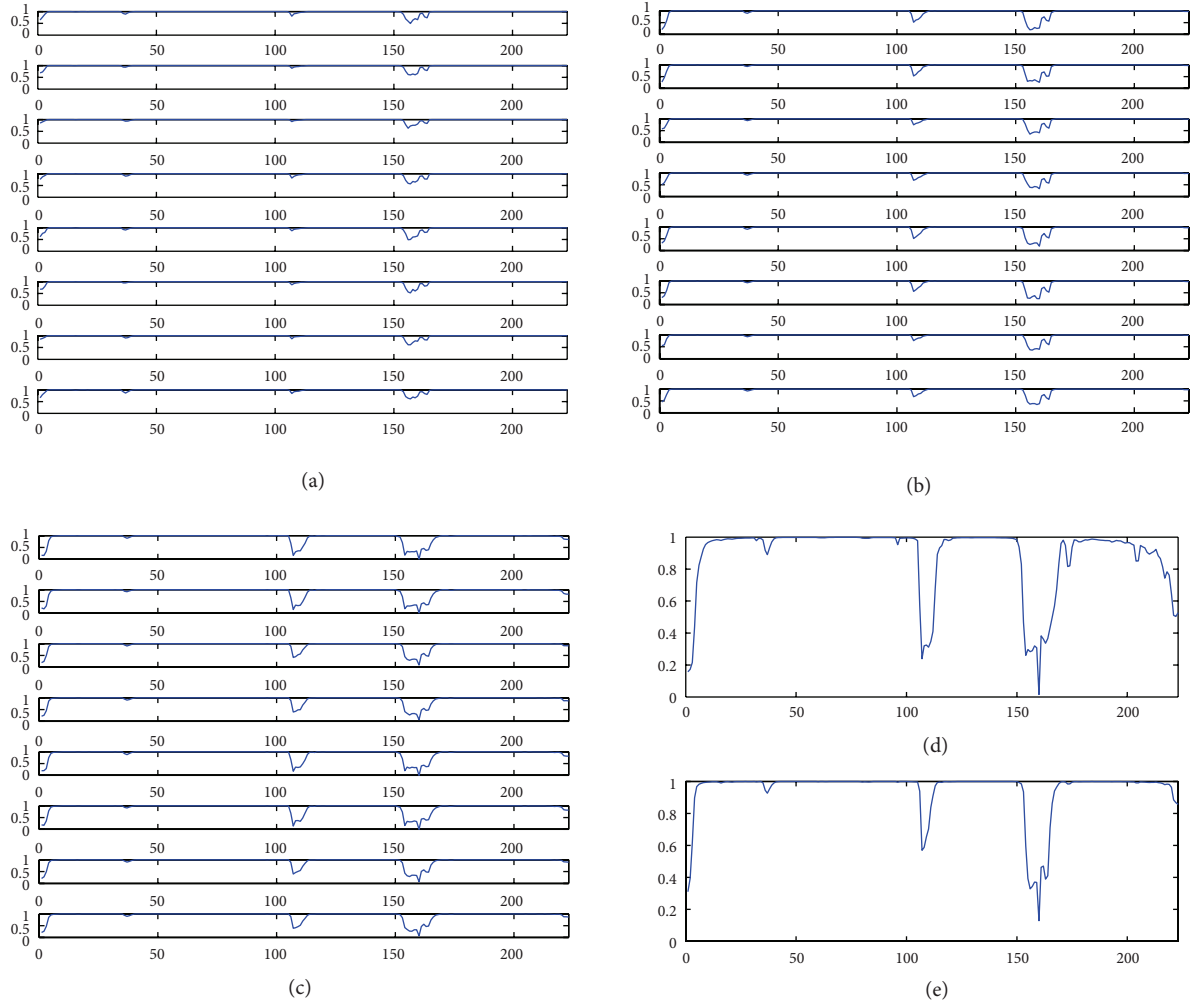


FIGURE 2: The spectral correlation factor of $\{F^t\}_{t=1}^S$ (a) eight directions of the second scale, (b) eight directions of the third scale, (c) eight directions of the fourth scale, (d) the finest scale, and (e) the spectral correlation factor of the Jasper Ridge.

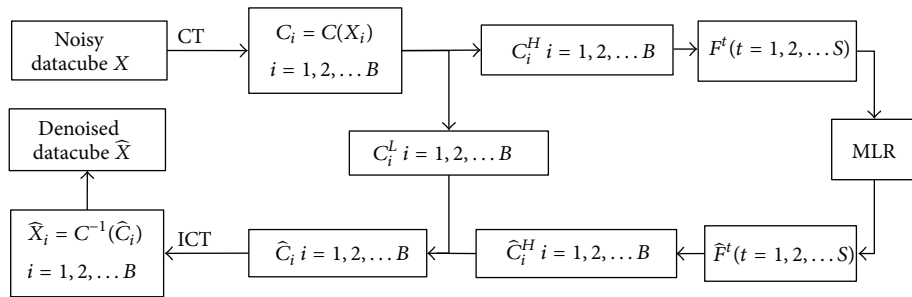


FIGURE 3: Block diagram of the proposed method in this paper.

Field provided by JPL, NASA. The size of datacube we extracted from the Cuprite, Jasper Ridge, Low Altitude, Lunar Lake, and Moffett Field for testing is $256 \times 256 \times 224$ (width \times height \times band). Figure 4 shows the band no.40 of these HRSIs. For the AVIRIS images a 28 m \times 28 m ground sample distance (GSD) datacube is derived by spatially averaging the 4 m \times 4 m GSD datacube elevating the nominal SNR to 7000:1. Having such high SNR, this datacube is viewed as a

pure datacube [14], which is used as a reference to measure the SNR before and after denoising. The image is corrupted by Gaussian white noise. It is different from the simple stationary additive noise model that is simulated by adding noise with a fixed standard deviation to the datacube; the noise variance is proportional to the average signal amplitude of each band, but the noise in each band is still additive noise. The SNR of the simulated noisy data is 600:1, which is chosen by

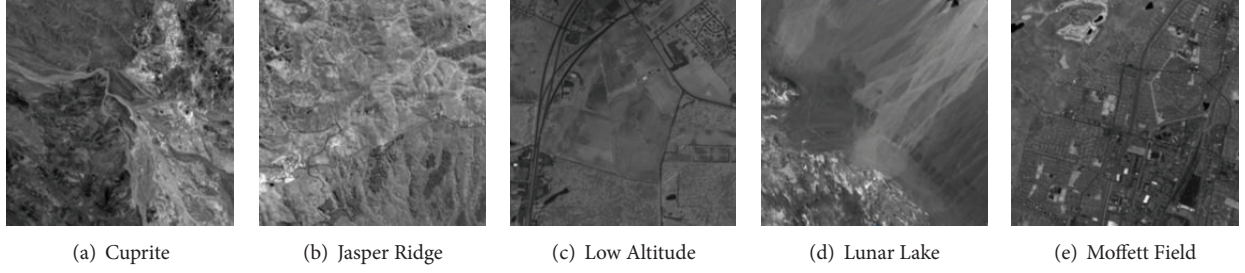


FIGURE 4: Band no.80 of AVIRIS images.

comprehensive requirement of the users and the machine design parameters.

In order to indicate that the nature image denoising methods cannot be immediately used for HRSI noise reduction, the 2-D complex wavelet with bivariate shrinkage (CWBS) [10] and the curvelet denoising (CD) [26] are used for comparison. From Table 1, it is shown that the denoised results in terms of SNR are obtained by the two nature image denoising methods; even the lower SNR is obtained. In order to illustrate the superiority of the proposed algorithm in our paper, the HSSNR [14] and the PCABS [16] are also performed to compare with the proposed method in this paper. The parameters chosen for the PCABS are consistent with [16]. In this paper, through utilizing $[0.2 \times B]$ bands to get the best result through the lots of simulated experiments, the proposed algorithm utilizes $[0.2 \times B]$ bands to perform the MLR, where $[x]$ means getting the nearest even integer of x . Table 1 shows the SNR of the hyperspectral datacubes Cuprite, Jasper Ridge, Low Altitude, Lunar Lake, and Moffett Field after denoising by the HSSNR, the PCABS, and the proposed algorithm. The results indicate that the proposed method is best method for denoising HRSI in terms of SNR.

In order to deeply analyze the proposed algorithm, the mean square of errors (MSE) in each band and the mean structural similarity (MSSIM) [30] between before and after denoising are utilized in each band. The lower MSE means that the denoised image is more similar to the original pure image, while MSSIM is close to 1 means that the denoised image is more similar to the original pure image. The MSE of band k denoised image is defined as

$$\text{MSE}_k = \frac{1}{MN} \sum_{i=1, j=1}^{M, N} |\widehat{X}_{i,j}^k - PX_{i,j}^k|^2, \quad (9)$$

and the MSSIM of band k denoised image is defined as

$$\text{MSSIM}_k(\widehat{X}^k, PX^k) = \frac{1}{Q} \sum_{q=1}^Q \text{SSIM}(\widehat{X}_q^k, PX_q^k), \quad (10)$$

where \widehat{X}_t^k and PX_t^k are the image contents at the q th local window, and Q is the number of local windows of the image. According to [30], the SSIM is defined as

$$\text{SSIM}(\mathbf{x}, \mathbf{y}) = \frac{(2\mu_x\mu_y + C_1)(2\sigma_{xy} + C_2)}{(\mu_x^2 + \mu_y^2 + C_1)(\sigma_x^2 + \sigma_y^2 + C_2)}, \quad (11)$$

TABLE 1: SNR of AVIRIS data Cuprite, Jasper Ridge, Low Altitude, Lunar Lake, and Moffett Field.

	SNR	CWBS	CD	HSSNR	PCABS	The proposed
Cuprite		1368.3	907.6	2712.6	8192.8	10952.0
Jasper Ridge		720.6	387.8	2365.9	6135.2	7503.0
Lunar Lake	600	2869.5	1844.2	2791.4	9787.5	12516.0
Low Altitude		530.7	220.8	2000.4	4351.5	5140.3
Moffett Field		530.1	253.7	2267.8	5757.7	6427.1

where $C_1 = (K_1V)^2$ and $C_2 = (K_2V)^2$ ($K_1 \ll 1$ and $K_2 \ll 1$ are two small constants, $K_1 = 0.01$ and $K_2 = 0.03$) and V is the dynamic range of the pixel values. In this paper, we use 11×11 circular-symmetric Gaussian weighting function $\mathbf{w} = \{w_i \mid i = 1, 2, \dots, N\}$, with standard deviation of 1.5 samples, normalized to unit sum ($\sum_{i=1}^N w_i = 1$). The estimates of local statistics μ_x , σ_x and σ_{xy} are then modified accordingly as

$$\mu_x = \sum_{i=1}^N w_i x_i, \quad (12)$$

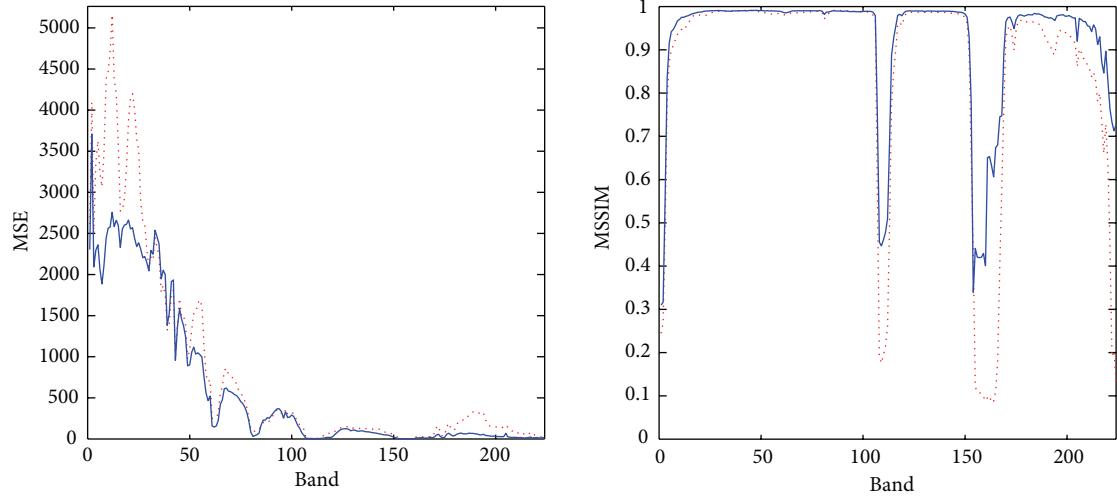
$$\sigma_x = \left(\sum_{i=1}^N w_i (x_i - \mu_x)^2 \right)^{1/2}, \quad (13)$$

$$\sigma_{xy} = \sum_{i=1}^N w_i (x_i - \mu_x)(y_i - \mu_y), \quad (14)$$

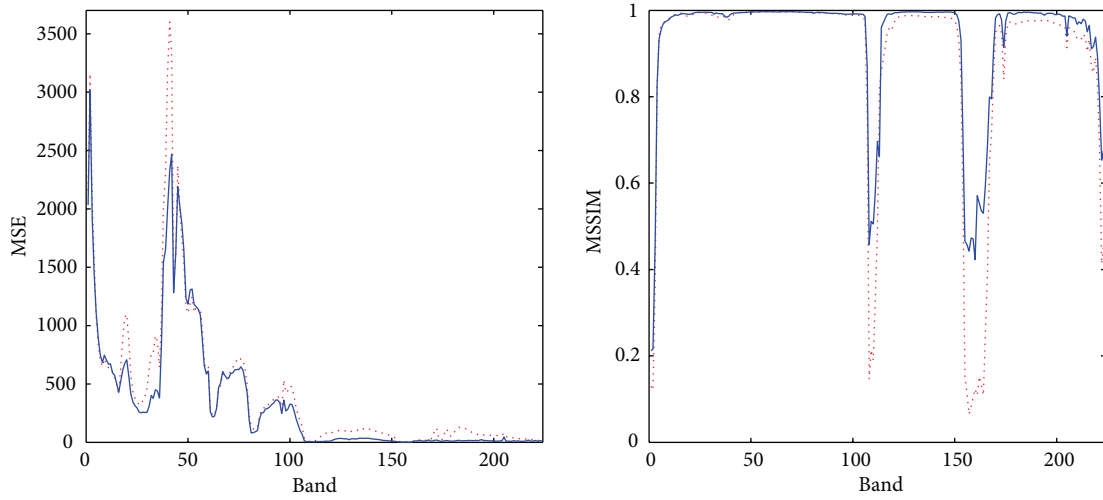
where μ_y and σ_y are consistent with the form μ_x and σ_x .

From Table 1, it is shown that the PCABS method and the proposed method obtain higher SNR. As a result, Figure 5 only shows MSE and MSSIM in each band of the AVIRIS datacubes denoised by the proposed algorithm and the PCABS. The MSE of each band obtained by the proposed algorithm is lower than the PCABS in nearly all bands, and the MSSIM of each band obtained by the proposed algorithm is closer to 1 than the PCABS, which indicates that the proposed algorithm is superior to PCABS.

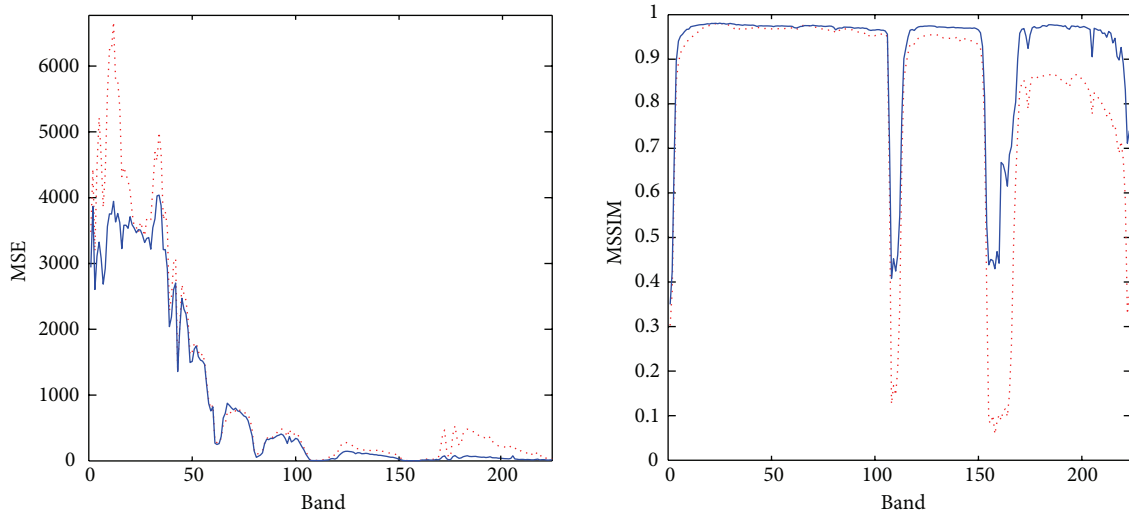
The computational complexity, that is, the number of floating-point operations (flops), of the proposed method can be analyzed as follows. The complexity of the curvelet transform is in order of $O(PB \cdot \log(\sqrt{P}))$ flops, where P is the number of pixels in the spatial domain and B is the number of bands. The complexity of the MLR is approximately the number of floating-point operations $4PLB + 2PL^2B + L^3B$ flops



(a) Cuprite



(b) Jasper Ridge



..... PCABS
— The proposed

..... PCABS
— The proposed

(c) Lunar Lake

FIGURE 5: Continued.

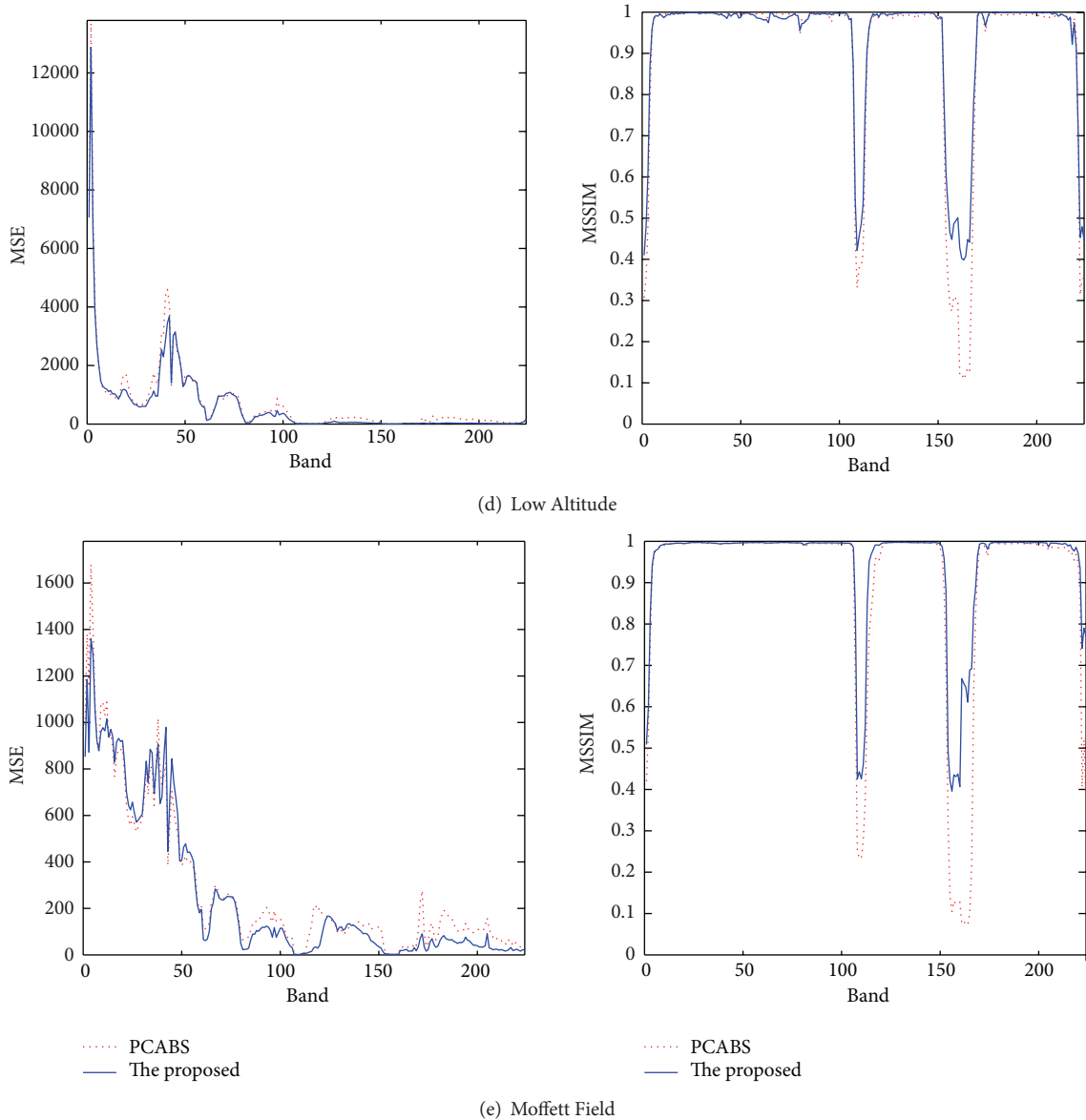


FIGURE 5: The MSE and the MSSIM in each band obtained by PCABS and the proposed method.

where P and B are defined as before and L is the number of bands used to perform MLR. Therefore, the computational complexity of the proposed method is mainly contributed by the MLR. The computational complexity of the proposed method is greater than that of the HSSNR and PCABS. The computational times of the HSSNR, the PCABS, and the proposed method are given in Table 2. The previous denoising approaches are implemented using the *Matlab* programming language and run on a PC with a Pentium 2.70 GHz Dual-Core CPU and a 1024 MB RAM.

5.2. Real Data Experiment. In this paper the OMIS (operational modular imaging spectrometer) data that is developed by the Shanghai Institute of Technical Physics of the Chinese Academy of Sciences is used for real data experiment to verify the correctness and performance of algorithm. It has

TABLE 2: The computational time of AVIRIS data Cuprite, Jasper Ridge, Low Altitude, Lunar Lake, and Moffett Field (units: s).

	HSSNR	PCABS	The proposed
Cuprite	145.12	185.25	810.09
Jasper Ridge	145.12	188.29	847.60
Lunar Lake	148.58	184.10	809.97
Low Altitude	146.98	201.05	860.91
Moffett Field	146.65	185.30	858.04

128 spectral bands ranging from visible to thermal infrared wavelength. The size of datacube we extracted from OMIS data for testing is $256 \times 256 \times 128$ (width \times height \times band). We perform denoising for the original OMIS data. Figure 6 shows band nos. 20, 40, 60, 80, and 100 of the original image

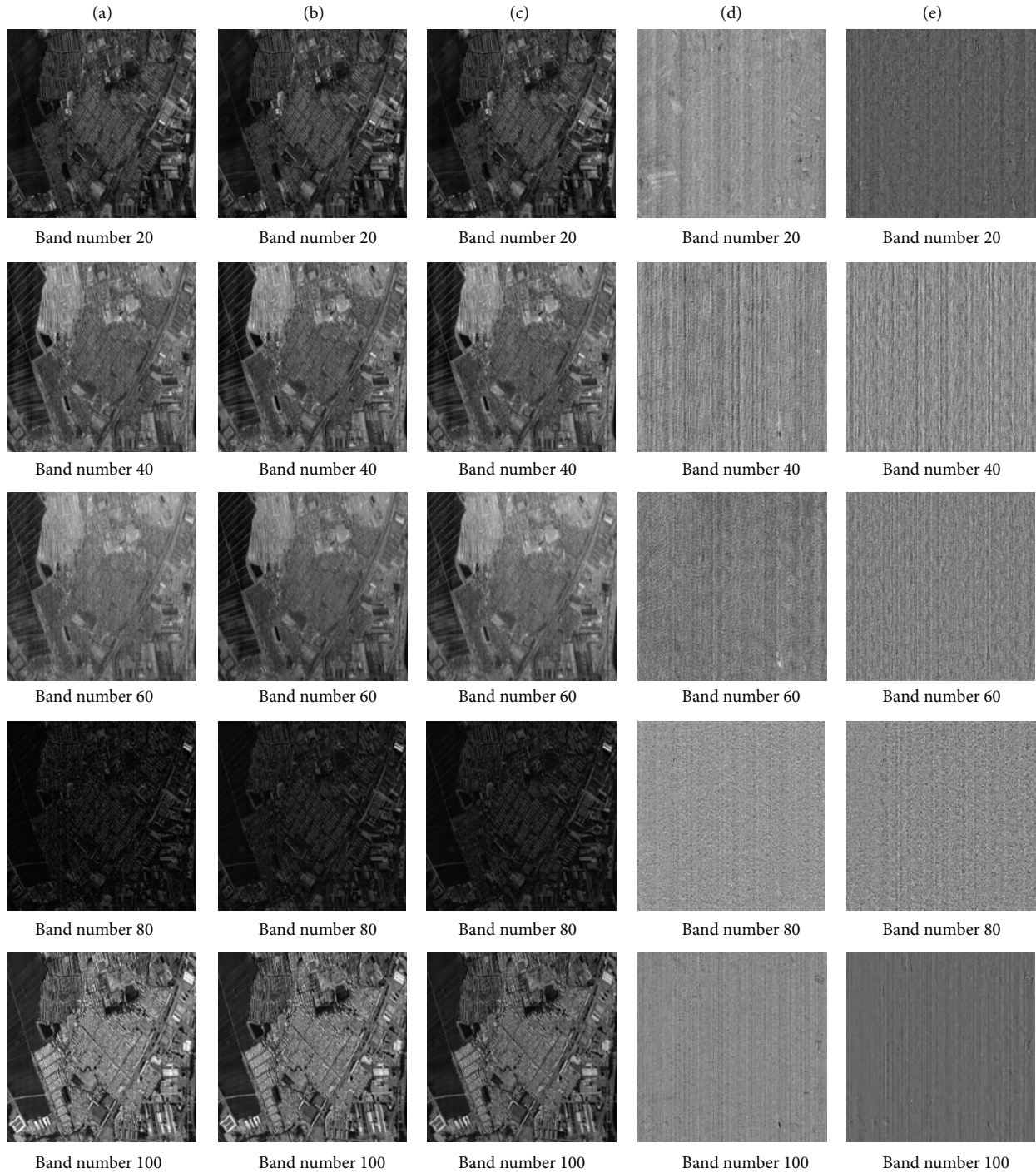


FIGURE 6: Band nos. 20, 40, 60, 80, and 100 of (a) the original image and (b) the denoised image obtained by the PCABS, (c) the proposed algorithm, and (d) the difference between the original image and the denoised image obtained by PCABS, as well as (e) the difference between the original image and the denoised image obtained by the proposed algorithm.

and the denoised image obtained by PCABS and the proposed method, as well as the difference between the original image and the denoised image obtained by PCABS and the proposed method. In Figure 6, the denoised images (b) and (c) show that the proposed method is feasible; especially the band no. 80 can be seen obviously. The image (d) is the difference between the original image and the denoised image obtained

by PCABS, and the image (e) is the difference between the original image and the denoised image obtained by the proposed algorithm. The difference shows that the two algorithms can effectively remove the common spotty noise and the strip noise from the noisy OMIS. But the features such as the edge of the image can be observed in the difference. The reason for this phenomenon is that the fine features

are removed as noise during the denoising process. So the less fine features in the difference mean the better denoised results. From Figures 6(d) and 6(e), the image (d) contains more fine features than the image (e), which is easy to distinguish by human eyes. The result shows that the PCABS method removes more fine features during the denoising process. Therefore the proposed algorithm is superior to the PCABS in terms of removing noise and simultaneously maintaining fine features during the denoising process.

6. Conclusions

In this paper, the spectral correlation of HRSI in the curvelet domain is discussed. By the analysis, in the curvelet domain, the strong spectral correlation of the hyperspectral remote sensing image is kept; even in some directions and scales it becomes stronger. So a new denoising algorithm is proposed; the MLR is performed in the curvelet domain to denoise the HRSI.

Simulated experimental result shows that the proposed method improves the quality of HRSI significantly in terms of SNR, MSE of each band, and MSSIM of each band. It is also seen that the denoised results obtained by the two algorithms are not content in the bands 1–5. This is a problem that will be studied in the future. For the real OMIS data, the results show that the proposed method is valid. The proposed method obtains better results in terms of detail preservation and noise removal during the denoising process.

Acknowledgment

This work was supported by the National Natural Science Foundation of China under Project 61101183 and Project 41201363.

References

- [1] D. Letexier and S. Bourennane, "Noise removal from hyperspectral images by multidimensional filtering," *IEEE Transactions on Geoscience and Remote Sensing*, vol. 46, no. 7, pp. 2061–2069, 2008.
- [2] L. Ebadi, H. M. Shafri, S. Mansor, and R. Ashurov, "A review of applying second-generation wavelets for noise removal from remote sensing data," *Environmental Earth Sciences*, pp. 1–12, 2013.
- [3] A. C. Zelinski and V. K. Goyal, "Denoising hyperspectral imagery and recovering junk bands using wavelets and sparse approximation," in *Proceedings of IEEE International Geoscience and Remote Sensing Symposium (IGARSS 06)*, pp. 387–390, August 2006.
- [4] A. A. Green, M. Berman, P. Switzer, and M. D. Craig, "Transformation for ordering multispectral data in terms of image quality with implications for noise removal," *IEEE Transactions on Geoscience and Remote Sensing*, vol. 26, no. 1, pp. 65–74, 1988.
- [5] J. Chen, P. Jönsson, M. Tamura, Z. Gu, B. Matsushita, and L. Eklundh, "A simple method for reconstructing a high-quality NDVI time-series data set based on the Savitzky-Golay filter," *Remote Sensing of Environment*, vol. 91, no. 3–4, pp. 332–344, 2004.
- [6] D. L. Donoho and J. M. Johnstone, "Ideal spatial adaptation by wavelet shrinkage," *Biometrika*, vol. 81, no. 3, pp. 425–455, 1994.
- [7] D. L. Donoho, "De-noising by soft-thresholding," *IEEE Transactions on Information Theory*, vol. 41, no. 3, pp. 613–627, 1995.
- [8] M. K. Mihçak, I. Kozintsev, K. Ramchandran, and P. Moulin, "Low-complexity image denoising based on statistical modeling of wavelet coefficients," *IEEE Signal Processing Letters*, vol. 6, no. 12, pp. 300–303, 1999.
- [9] L. Şendur and I. W. Selesnick, "Bivariate shrinkage functions for wavelet-based denoising exploiting interscale dependency," *IEEE Transactions on Signal Processing*, vol. 50, no. 11, pp. 2744–2756, 2002.
- [10] L. Şendur and I. W. Selesnick, "Bivariate shrinkage with local variance estimation," *IEEE Signal Processing Letters*, vol. 9, no. 12, pp. 438–441, 2002.
- [11] A. Buades, B. Coll, and J. M. Morel, "A review of image denoising algorithms, with a new one," *Multiscale Modeling and Simulation*, vol. 4, no. 2, pp. 490–530, 2005.
- [12] A. Buades, B. Coll, and J.-M. Morel, "A non-local algorithm for image denoising," in *Proceedings of IEEE Computer Society Conference on Computer Vision and Pattern Recognition (CVPR '05)*, vol. 2, pp. 60–65, June 2005.
- [13] I. Atkinson, F. Kamalabadi, and D. L. Jones, "Wavelet-based hyperspectral image estimation," in *IEEE International Geoscience and Remote Sensing Symposium (IGARSS '03)*, pp. 743–745, July 2003.
- [14] H. Othman and S.-E. Qian, "Noise reduction of hyperspectral imagery using hybrid spatial-spectral derivative-domain wavelet shrinkage," *IEEE Transactions on Geoscience and Remote Sensing*, vol. 44, no. 2, pp. 397–408, 2006.
- [15] G. Chen and S.-E. Qian, "Denoising and dimensionality reduction of hyperspectral imagery using wavelet packets, neighbour shrinking and principal component analysis," *International Journal of Remote Sensing*, vol. 30, no. 18, pp. 4889–4895, 2009.
- [16] G. Chen and S.-E. Qian, "Denoising of hyperspectral imagery using principal component analysis and wavelet shrinkage," *IEEE Transactions on Geoscience and Remote Sensing*, vol. 49, no. 3, pp. 973–980, 2011.
- [17] T. H. Yi, H. N. Li, H. N. Li, and X. Y. Zhao, "Noise smoothing for structural vibration test signals using an improved wavelet thresholding technique," *Sensors*, vol. 12, pp. 11205–11220, 2012.
- [18] I. W. Selesnick, R. G. Baraniuk, and N. G. Kingsbury, "The dual-tree complex wavelet transform," *IEEE Signal Processing Magazine*, vol. 22, no. 6, pp. 123–151, 2005.
- [19] E. J. Candes and D. L. Donoho, "Curvelets—a surprisingly effective nonadaptive representation for objects with edges," in *Curve and Surface Fitting*, pp. 105–120, Saint-Malo, France, 2000.
- [20] M. N. Do and M. Vetterli, "The contourlet transform: an efficient directional multiresolution image representation," *IEEE Transactions on Image Processing*, vol. 14, no. 12, pp. 2091–2106, 2005.
- [21] J. A. Richards and X. Jia, *Remote Sensing Digital Image Analysis*, Springer, Berlin, Germany, 3rd edition, 1999.
- [22] M. L. Uss, B. Vozel, V. V. Lukin, and K. Chehdi, "Local signal-dependent noise variance estimation from hyperspectral textual images," *IEEE Journal on Selected Topics in Signal Processing*, vol. 5, no. 3, pp. 469–486, 2011.
- [23] N. Acito, M. Diani, and G. Corsini, "Signal-dependent noise modeling and model parameter estimation in hyperspectral images," *IEEE Transactions on Geoscience and Remote Sensing*, vol. 49, no. 8, pp. 2957–2971, 2011.

- [24] J. M. Bioucas-Dias and J. M. P. Nascimento, "Hyperspectral subspace identification," *IEEE Transactions on Geoscience and Remote Sensing*, vol. 46, no. 8, pp. 2435–2445, 2008.
- [25] N. Acito, M. Diani, and G. Corsini, "Residual striping reduction in hyperspectral images," in *Proceedings of the 17th International Conference on Digital Signal Processing (DSP '11)*, pp. 1–7, July 2011.
- [26] J.-L. Starck, E. J. Candès, and D. L. Donoho, "The curvelet transform for image denoising," *IEEE Transactions on Image Processing*, vol. 11, no. 6, pp. 670–684, 2002.
- [27] E. J. Candès and D. L. Donoho, "New tight frames of curvelets and optimal representations of objects with piecewise C^2 singularities," *Communications on Pure and Applied Mathematics*, vol. 57, no. 2, pp. 0219–0266, 2004.
- [28] E. Candès, L. Demanet, D. Donoho, and L. Ying, "Fast discrete curvelet transforms," *Multiscale Modeling and Simulation*, vol. 5, no. 3, pp. 861–899, 2006.
- [29] L. Sun and J.-S. Luo, "Junk band recovery for hyperspectral image based on curvelet transform," *Journal of Central South University of Technology*, vol. 18, no. 3, pp. 816–822, 2011.
- [30] Z. Wang, A. C. Bovik, H. R. Sheikh, and E. P. Simoncelli, "Image quality assessment: from error visibility to structural similarity," *IEEE Transactions on Image Processing*, vol. 13, no. 4, pp. 600–612, 2004.